INVESTIGATION OF VARIATONS IN PERFORMANCE PROPERTIES OF ASPHALT CONCRETE USING IMAGE-BASED FINITE ELEMENT MODEL

A THESIS SUBMITTED TO
THE GRADUATE SCHOOL OF NATURAL AND APPLIED SCIENCES
OF
MIDDLE EAST TECHNICAL UNIVERSITY

BY

YALÇIN KARAKAYA

IN PARTIAL FULFILLMENT OF THE REQUIREMENTS
FOR
THE DEGREE OF DOCTOR OF PHILOSOPHY
IN
CIVIL ENGINEERING

JULY 2022

Approval of the thesis:

INVESTIGATION OF VARIATONS IN PERFORMANCE PROPERTIES OF ASPHALT CONCRETE USING IMAGE-BASED FINITE ELEMENT MODEL

submitted by **YALÇIN KARAKAYA** in partial fulfillment of the requirements for the degree of **Doctor of Philosophy** i**n Civil Engineering, Middle East Technical University** by,

Prof. Dr. Halil Kalıpçılar
Dean, Graduate School of **Natural and Applied Sciences** _____

Prof. Dr. Erdem Canbay
Head of the Department, **Civil Engineering** _____

Prof. Dr. Murat Güler
Supervisor, **Civil Engineering, METU** _____

Examining Committee Members:

Prof. Dr. İsmail Özgür Yaman
Civil Engineering, METU _____

Prof. Dr. Murat Güler
Civil Engineering, METU _____

Prof. Dr. Mustafa Şahmaran
Civil Engineering, Hacettepe University _____

Prof. Dr. Osman Nuri Çelik
Civil Engineering, Konya Technical University _____

Assoc. Prof. Dr. Hande Işık Öztürk
Civil Engineering, METU _____

Date: 20.07.2022

I hereby declare that all information in this document has been obtained and presented in accordance with academic rules and ethical conduct. I also declare that, as required by these rules and conduct, I have fully cited and referenced all material and results that are not original to this work.

Name Last name: Yalçın Karakaya

Signature:

ABSTRACT

INVESTIGATION OF VARIATONS IN PERFORMANCE PROPERTIES OF ASPHALT CONCRETE USING IMAGE-BASED FINITE ELEMENT MODEL

Karakaya, Yalçın
Doctor of Philosophy, Civil Engineering
Supervisor: Prof. Dr. Murat Güler

July 2022, 361 pages

The objective of this study is to evaluate variations in performance properties of asphalt concrete using a two-dimensional image-based finite element model. Two different asphalt mixtures are used in both laboratory tests and in FEM analyses representing different conditions. A flatbed scanner is then used to capture cross-sectional images of the samples and various image processing techniques are applied to prepare the images for FEM. A unique image vectorization method has been developed to transform cross-sectional images into the finite element mesh to minimize computational time in FEM, where AC is modeled as a composite material consisting of individual components of aggregate and asphalt binder. In the experimental program, three different testing programs; resilient modulus, repeated creep and indirect tensile fatigue tests are conducted to obtain different performance indicators. The laboratory experiments are performed using ten replicates, to establish the variability in performance properties. Sample variability is also studied in the FEM for identical specimens by changing their microstructures using a previously developed redistribution algorithm. Finally, the performance indicators

obtained from the laboratory tests and the FEM analyses are compared to evaluate the variability in the performance tests.

Various results show that the two-dimensional finite element model created in this study works successfully for two completely different mix designs under different test conditions. Furthermore, with the particle redistribution method, the inherent variability of the asphalt concrete on the test results is identified and it was found to correspond to values as low as about one eighth.

Keywords: 2D Image-Based Finite Element Model, Image Vectorization, Resilient Modulus Test, Repeated Creep Test, Indirect Tensile Fatigue Test

ÖZ

ASFALT BETONUN PERFORMANS ÖZELLİKLERİNDEKİ DEĞİŞİMLERİN GÖRÜNTÜ TABANLI SONLU ELEMANLAR MODELİ KULLANILARAK İNCELENMESİ

Karakaya, Yalçın
Doktora, İnşaat Mühendisliği
Tez Yöneticisi: Prof. Dr. Murat Güler

Temmuz 2022, 361 sayfa

Bu çalışmanın amacı, iki boyutlu görüntü tabanlı bir sonlu elemanlar modeli kullanılarak asfalt betonun performans özelliklerindeki değişimlerin değerlendirilmesidir. Hem laboratuvar testlerinde hem de sonlu elemanlar yöntemi analizlerinde, farklı koşulların temsil eden iki farklı asfalt karışımı kullanılmıştır. Daha sonra numunelerin kesit görüntülerinin yakalanması için düz yataklı bir tarayıcı kullanılmış ve bu görüntüleri sonlu elemanlar modeline hazırlamak için çeşitli görüntü işleme teknikleri uygulanmıştır. Asfalt betonun agrega ve bitümlü bağlayıdan oluşan ayrı bileşenlerinin kompozit bir malzeme olarak modellendiği sonlu elemanlar modelinde hesaplama süresinin en aza indirilmesi için kesit görüntüleri sonlu elemanlar ağına dönüştürülürken eşsiz bir görüntü vektörleştirme yöntemi geliştirilmiştir. Denel programında farklı performans göstergelerinin elde edilebilmesi için üç farklı test programı uygulanmıştır; esneklik modülü, tekrarlı sünme ve dolaylı yorulma deneyleri. Laboratuvar deneyleri, performans özelliklerindeki değişkenliklerin tespit edilebilmesi için on tekrar kullanılarak gerçekleştirilmiştir. Numune değişkenliği, özdeş numuneler üzerinde mikroyapıları

değiştiren daha önce geliştirilmiş bir yeniden dağıtım algoritması kullanılarak sonlu elemenlar analizlerinde de incelenmiştir. Son olarak, laboratuvar testleri ve sonlu elemanlar yöntemi analizleri sonuçları karşılaştırılarak performans testlerindeki değişkenlikler değerlendirilmiştir.

Çeşitli sonuçlar, bu çalışmada oluşturulan iki boyutlu sonlu elemanlar modelinin, farklı test koşulları altında tamamen farklı iki karışım tasarımı için başarılı ile çalıştığını göstermiştir. Ayrıca, bu çalışmada önerilen parçacık yeniden dağıtma yöntemi ile, asfalt betonun test sonuları üzerindeki doğal değişkenliği belirlenmiş ve yaklaşık sekizde bir gibi değerlere kadar düştüğü tespit edilmiştir.

Anahtar Kelimeler: İki Boyutlu Görüntü Tabanlı Sonlu Elemanlar Modeli, Görüntü Vektörleştirme, Esneklik Modülü Deneyi, Tekrarlanan Sünme Deneyi, Dolaylı Yorulma Deneyi

This dissertation is dedicated to my wife Tuba and my lovely daughter Hayat, who have supported me sacrificially and unstintingly throughout the process.

ACKNOWLEDGMENTS

First and foremost, I would like to express my sincere gratitude to my supervisor Prof. Dr. Murat Güler for his invaluable guidance, continuous support, and endless patience throughout during my PhD study. His immense knowledge and plentiful experience have encouraged me in all the time of my academic research and daily life.

Besides my advisor, I would like to thank the rest of my thesis committee: Prof. Dr. İsmail Özgür Yaman, Prof. Dr. Mustafa Şahmaran, Prof. Dr. Osman Nuri Çelik and Assoc. Prof. Hande Işık Öztürk for their insightful comments and encouragements.

Finally, I would like to thank my dear friends Ayhan Öner Yücel, Meltem Tangüler and Sertaç Günay for their friendship and support.

TABLE OF CONTENTS

ABSTRACT v

ÖZ vii

ACKNOWLEDGMENTS x

TABLE OF CONTENTS xi

LIST OF TABLES xvi

LIST OF FIGURES xviii

LIST OF ABBREVIATIONS xxxii

CHAPTERS

1 INTRODUCTION 1

1.1 Background 1

1.2 Hypothesis 3

1.3 Research Objectives 4

1.4 Scope 5

1.5 Outline of Research 6

2 LITERATURE REVIEW 9

2.1 Introduction 9

2.2 Finite Element Analysis of Asphalt Mixtures 9

2.2.1 3D Finite Element Modeling 11

2.2.2 2D Finite Element Modeling 16

2.3 Image Based Finite Element Modeling of Asphalt Mixtures 19

2.4 Digital Image Processing 25
2.4.1 X-Ray Tomography 26
2.4.2 Cameras and Scanners 28
2.5 Material Modeling 30
2.5.1 Aggregate 31
2.5.2 Asphalt Binder 34
2.5.3 Air Voids 38
2.6 Mechanical Testing of Asphalt Mixtures 41
2.6.1 Resilient Modulus Test 42
2.6.2 Repeated Creep Test 44
2.6.3 Indirect Tensile Fatigue Test 47
3 LABORATORY TESTING OF ASPHALT MIXTURES 49
3.1 Introduction 49
3.2 Sample Preparation 49
3.2.1 Aggregate 50
3.2.2 Gradation 52
3.2.3 Asphalt Binder 56
3.2.4 Mixing and Compaction Temperatures 58
3.2.5 Superpave Mixture Design 63
3.2.6 Specimen Cutting 70
3.3 Resilient Modulus Test 75
3.3.1 Test Setup 75
3.3.2 Mounting the LVDTs 76
3.3.3 Testing Procedure 79

3.4 Repeated Creep Test 83
3.4.1 Test Setup 83
3.4.2 Mounting the LVDTs 85
3.4.3 Testing Procedure 87
3.4.4 Calculation of the Flow Number 89
3.5 Indirect Tensile Fatigue Test 93
3.5.1 Test Setup 94
3.5.2 Mounting the LVDTs 95
3.5.3 Testing Procedure 96
4 NUMERICAL MODELING OF ASPHALT MIXTURES 101
4.1 Introduction 101
4.2 Image Processing 101
4.2.1 Image Acquisition 102
4.2.2 Image Enhancement 104
4.3 Image Vectorization 113
4.3.1 Size Distribution Analysis of Aggregates 114
4.3.2 Edge Detection 118
4.3.3 Vectorization 120
4.3.4 Pixel Reduction 124
4.4 Particle Redistribution 126
4.5 From Digital Images to Finite Element Model 128
4.5.1 Geometric Model 129
4.5.2 Material Model 134
4.5.3 Meshing 147

4.6 Finite Element Modeling of Resilient Modulus Test 150
4.6.1 Materials 150
4.6.2 Steps 151
4.6.3 Boundary Conditions and Loading 153
4.6.4 Amplitude 154
4.6.5 Calculations 155
4.7 Finite Element Modeling of Repeated Creep Test 164
4.7.1 Materials 164
4.7.2 Steps 164
4.7.3 Boundary Conditions and Loading 166
4.7.4 Amplitude 167
4.7.5 Calculations 168
4.8 Finite Element Modeling of Indirect Tensile Fatigue Test 172
5 RESULTS AND DISCUSSION 173
5.1 Introduction 173
5.2 Specimen Coding 173
5.3 Experimental Test Results 174
5.3.1 Resilient Modulus Test Laboratory Results 174
5.3.2 Repeated Creep Test Laboratory Results 180
5.3.3 Indirect Tensile Fatigue Test Laboratory Results 187
5.4 Finite Element Model Results 193
5.4.1 Resilient Modulus FEM Results 193
5.4.2 Repeated Creep FEM Results 204
6 CONCLUSIONS 213

6.1 Conclusions 213
6.2 Future Recommendations 217
REFERENCES 219
APPENDICES
A. Superpave Mixture Design Results 233
B. Laboratory Test Setups 235
C. Experimental Results of Indirect Tensile Fatigue Tests 241
D. MATLAB Code for Finding the Edge Pixels 261
E. ANSYS Mechanical APDL Script for Creating the Geometric Models 263
F. Synthetic Images Created by Particle Redistribution Method 266
G. Finite Element Models of the Specimens 279
H. FE Results of the Resilient Modulus Tests 320
I. FE Results of the Repeated Creep Tests 340
CURRICULUM VITAE 360

LIST OF TABLES

TABLES

Table 3.1. Physical properties of coarse aggregate (larger than 4.75 mm) 51
Table 3.2. Physical properties of fine aggregate (finer than 4.75 mm) 51
Table 3.3. Bulk specific gravity calculation 52
Table 3.4. Aggregate gradation control points for TGDH binder course design 53
Table 3.5. Aggregate gradation control points for FAA binder course design 54
Table 3.6. Tolerance limits used in FAA binder course design 55
Table 3.7. Measured properties of unmodified asphalt binder 56
Table 3.8. Measured properties of modified asphalt binder 57
Table 3.9. Mixing and compaction temperatures 63
Table 3.10. Superpave mix design parameters 66
Table 3.11. Results with different bitumen contents of the TGDH design 68
Table 3.12. Test results and design requirements of the TGDH mix design..... 69
Table 3.13 Test results and design requirements of the FAA mix design..... 69
Table 3.14. Test results and requirements of the TGDH mix design 81
Table 3.15. Constant values for the RM test (ASTM D7369, 2020)..... 82
Table 3.16. Effective test temperatures for the FN tests 89
Table 4.1. Comparison of actual and calculated gradations of the TGDH design 116
Table 4.2. Comparison of actual and calculated gradations of the FAA design ... 117
Table 4.3. Comparison of linear elastic material properties used in the literature 134
Table 4.4. Selected linear elastic material properties used in the study 135
Table 4.5. Prony series parameters of neat binder at 25 °C 145
Table 4.6. Prony series parameters of modified binder at 25 °C..... 145
Table 4.7. Prony series parameters of neat binder at 36 °C 146
Table 4.8. Prony series parameters of modified binder at 44 °C..... 146
Table 4.9. Model results under various step sizes 152
Table 5.1. Resilient modulus test results of TGDH samples..... 175

Table 5.2. Resilient modulus test results of FAA samples 177
Table 5.3. Flow number and power model results of TGDH samples..... 183
Table 5.4. Flow number and power model results of FAA samples..... 184
Table 5.5. Permanent strain results of TGDH samples at different cycles 186
Table 5.6. Permanent strain results of FAA samples at different cycles 187
Table 5.7. Fitted power model parameters of TGDH samples 189
Table 5.8. Fitted power model parameters of FAA samples 190
Table 5.9. IDTF test results of TGDH samples 191
Table 5.10. IDTF test results of FAA samples 192
Table 5.11. Numerical and laboratory M_R results of TGDH samples 194
Table 5.12. Numerical and laboratory Poisson's ratio results of TGDH samples 196
Table 5.13. Resilient modulus analysis results of synthetic TGDH samples 198
Table 5.14. Numerical and laboratory M_R results of FAA samples 199
Table 5.15. Numerical and laboratory Poisson's ratio results of FAA samples ... 201
Table 5.16. Resilient modulus analyzes results of synthetic FAA samples..... 203
Table 5.17. Comparison of fitted power model parameters of TGDH samples ... 206
Table 5.18. Fitted power model results of synthetic TGDH samples 208
Table 5.19. Comparison of fitted power model parameters of FAA samples 209
Table 5.20. Fitted power model results of synthetic FAA samples 211
Table A.1. Design number of gyrations..... 233

LIST OF FIGURES

FIGURES

Figure 2.1. Comparison of 2D and 3D model responses (Hau, 2000) 12
Figure 2.2. Idealized microstructural model (Wu et al. 2011) 14
Figure 2.3. Measured and predicted longitudinal strains (Mulungye et al., 2006).. 18
Figure 2.4. Load versus displacement curve (Dai et al., 2005) 20
Figure 2.5. Dynamic modulus (E^*) predictions and laboratory measurements (Adhikari et al., 2008) 20
Figure 2.6. Steps to create 2D finite element microstructure (Rami et al., 2017) ... 23
Figure 2.7. Example of an image capture: a) Captured by a flatbed scanner, b) Resulting binary image 25
Figure 2.8. (a) Cross-sectional images produced from X-ray imaging, (b) Visualizing in 3D of an asphalt concrete specimen (Arshadi, 2015) 26
Figure 2.9. Illustration of rheological models 35
Figure 2.10. Rheological models with multiple Maxwell/Voigt units 36
Figure 2.11. Verification of the linear viscoelastic binder model; plane stress, $\Delta t = 1s$ (Papagiannakis et al., 2002) 37
Figure 2.12. Three-dimensional asphalt mixture model from X-ray CT images: (a) Image with all three domains, (b) Air void distribution with in the asphalt mixture (Coleri et al. 2012) 40
Figure 2.13. Distribution of air voids based on the “bathtub” shape (Arshadi, 2015) 41
Figure 2.14. Schematic representation of RM test setup 43
Figure 2.15. Typical creep deformation of asphalt mixtures 45
Figure 2.16. Schematic representation of repeated permanent deformation test (Witczak et al. 2002) 45
Figure 2.17. Indirect tensile fatigue test setup 48
Figure 2.18. Stress distribution in indirect tensile fatigue test 48

Figure 3.1. Gradation chart for TGDH binder course design 53
Figure 3.2. Gradation chart for FAA binder course design 55
Figure 3.3. Brookfield rotational viscometer 57
Figure 3.4. Viscosity measurements of neat and polymer modified asphalt binder 58
Figure 3.5. Determination of the mixing and compaction temperatures of the unmodified binder 59
Figure 3.6. Dynamic shear rheometer used in the laboratory 60
Figure 3.7. Frequency sweep test results of the modified binder at four temperatures 61
Figure 3.8. Modified binder master curve at 100 ºC 62
Figure 3.9. Gyratory compactor used in the laboratory 64
Figure 3.10. Compacted mix design samples 65
Figure 3.11. Compaction curve of the TGDH-1 design sample 66
Figure 3.12. Superpave volumetric test results of the TGDH design 68
Figure 3.13. Superpave volumetric test results of the FAA design 70
Figure 3.14. Cylindrical specimen section for the FN test 71
Figure 3.15. Core drilling procedure 71
Figure 3.16. Specimen after coring 72
Figure 3.17. End treatment of the cylindrical specimens 73
Figure 3.18. Cylindrical specimens after end treatment 73
Figure 3.19. Specimen section for the indirect loading 74
Figure 3.20. IDT test specimens after cutting 74
Figure 3.21. Dynamic testing system used in the study 76
Figure 3.22. Drawing of LVDTs mounted on specimen (ASTM D7369, 2002) 77
Figure 3.23. LVDT assembly of the RM test 78
Figure 3.24. Example specimen in the RM test: a) Placed between the loading strips, b) Mounted LVDTs on the surface 79
Figure 3.25. The IDT strength test results of the TGDH samples 80
Figure 3.26. The IDT strength test results for the FAA samples 81
Figure 3.27. An example of applied load versus deformation pulse in the RM test 83

Figure 3.28. The FN test setup 84
Figure 3.29. Mounting the metal fixtures 85
Figure 3.30. The steel components that are going to hold the LVDTs 86
Figure 3.31. The mounted specimen in the FN test setup 86
Figure 3.32. FN test result for the specimen ID LUCR03 90
Figure 3.33. Power model fit example (sample ID LUCR03) 91
Figure 3.34. Coefficient of determination as a function of number of least square fit operations (sample ID LUCR03) 91
Figure 3.35. Rate of strain versus number of cycles (sample ID LUCR03) 93
Figure 3.36. Indirect tensile fatigue test setup 94
Figure 3.37. LVDT mounting procedures of IDTF tests 95
Figure 3.38. Permanent deformation graph (sample ID BMIF03-2) 97
Figure 3.39. Stiffness modulus versus number of cycles (sample ID BMIF03-2) 98
Figure 3.40. Reduction in stiffness vs number of cycles (sample ID BMIF03-2) 99
Figure 4.1. Flowchart of the image processing steps 102
Figure 4.2. Flatbed scanner used to obtain cross sectional images 103
Figure 4.3. RGB image captured by the scanner 103
Figure 4.4. A digital image composed of pixels 105
Figure 4.5. Zoomed section of an example image: a) Original RGB image, b) Grayscale image 106
Figure 4.6. Smoothing by averaging filter, the center pixel value would be changed from “*e*” to “*E*” 106
Figure 4.7. a) Grayscale image before smoothing, b) After smoothing 107
Figure 4.8. Example histogram of an image: (a) Before contrast stretching, (b) After contrast stretching 108
Figure 4.9. a) Smoothened image, b) After contrast enhancement 109
Figure 4.10. a) At the end of the contrast enhancement, b) Binary form 110
Figure 4.11. a) Binary image, b) After filling holes 111
Figure 4.12. a) After filling holes, b) After particle separation 112
Figure 4.13. Image processing steps 112

Figure 4.14. Aggregate shape parameters 114
Figure 4.15. An example of the sample ID LURM01-1 in the Vision Assistant software 115
Figure 4.16. Graphical comparison of actual and estimated gradations of the TGDH design 117
Figure 4.17. Graphical comparison of actual and estimated gradations of the FAA design 118
Figure 4.18. Binary image: a) Before, c) After particle removal (ID LURM01-1) 119
Figure 4.19. Edge detection method in MATLAB 119
Figure 4.20. Image matrices in MATLAB: a) Total aggregates, b) The edge pixels 120
Figure 4.21. Example aggregate particle creation procedure in the ANSYS 122
Figure 4.22. Resultant aggregate particle in the ANSYS 122
Figure 4.23. a) Binary image at the end of image processing, b) Vector form of the image in ANSYS 123
Figure 4.24. a) Original image, b) Reduced image after skipping 2 pixels, c) Reduced image after skipping 4 pixels 125
Figure 4.25. Aggregate redistribution of the specimen ID LURM02-1: a) Original image, b) Redistributed synthetic image 127
Figure 4.26. Aggregate redistribution of the specimen ID LUCR06: a) Original image, b) Redistributed synthetic image 128
Figure 4.27. Imported IGES file as a sketch model: a) Circular specimen (ID LURM02-1), b) Rectangular specimen (ID LUCR09) 130
Figure 4.28. Created 2D aggregate parts: a) Circular specimen (ID LURM02-1), b) Rectangular specimen (ID LUCR09) 131
Figure 4.29. Created 2D binder parts by subtracting the aggregate parts: a) Circular specimen (ID LURM02-1), b) Rectangular specimen (ID LUCR09) 132
Figure 4.30. Completed geometric models: a) Circular specimen (ID LURM02-1), b) Rectangular specimen (ID LUCR09) 133

Figure 4.31. Frequency sweep test results of neat binder 139
Figure 4.32. Frequency sweep test results of modified binder 140
Figure 4.33. Master curves of modified and unmodified asphalt binder at 25 °C 143
Figure 4.34. Shift factors at 25 °C 143
Figure 4.35. Master curves of unmodified asphalt binder at 36 °C and modified binder at 44 °C 144
Figure 4.36. Shift factors of unmodified asphalt binder at 36 °C and modified binder at 44 °C 144
Figure 4.37. 2D FE mesh of the aggregate phase 147
Figure 4.38. 2D FE mesh of the binder phase 148
Figure 4.39. 2D FE mesh of the model 148
Figure 4.40. Completed 2D FE mesh: a) Circular model (ID LURM02-1), b) Rectangular model (ID LUCR09) 149
Figure 4.41. Maximum horizontal deformation results with different step sizes .. 153
Figure 4.42. Boundary conditions of the RM test (specimen ID LURM02-1) 154
Figure 4.43. Amplitude input of the RM simulations 155
Figure 4.44. Loading pattern of the RM analysis 155
Figure 4.45. Maximum horizontal stresses of the sample ID LURM02-1 156
Figure 4.46. Maximum vertical stresses of the sample ID LURM02-1 157
Figure 4.47. FE results of the sample ID LURM02-1: a) Maximum horizontal deformation, b) Permanent horizontal deformation at the end of the loading cycle 158
Figure 4.48. FE results of the sample ID LURM02-1: a) Maximum vertical deformation, b) Permanent vertical deformation at the end of the loading cycle . 159
Figure 4.49. Nodal displacement locations of the RM analyze 160
Figure 4.50. Comparison of laboratory and FEM results of a TGDH design sample: a) Horizontal deformations, b) Vertical deformations 162
Figure 4.51. Comparison of laboratory and FEM results of a FAA design sample: a) Horizontal deformations, b) Vertical deformations 163
Figure 4.52. Boundary conditions of the FN test (specimen ID LUCR09) 166

Figure 4.53. Amplitude input of the FN tests 167
Figure 4.54. Loading pattern of the FN tests 167
Figure 4.55. First 10 cycles of axial deformations..... 168
Figure 4.56. Axial deformation graphs: a) TGDH design sample ID LUCR09, b) FAA design sample ID BMCR01 169
Figure 4.57. Permanent strain versus number of cycles of the TGDH design sample ID LUCR09..... 170
Figure 4.58. Permanent strain versus number of cycles of the FAA design sample ID BMCR01..... 171
Figure 5.1. Resilient modulus test results of TGDH samples..... 176
Figure 5.2. Resilient modulus test results of FAA samples..... 177
Figure 5.3. Variations among four different readings of TGDH samples 178
Figure 5.4. Variations among four different readings of FAA samples 178
Figure 5.5. M_R comparison of experimental test results..... 179
Figure 5.6. Poisson's ratio comparison of experimental test results..... 180
Figure 5.7. FN test results of each 10 TGDH samples 181
Figure 5.8. FN test results of each 10 FAA samples 182
Figure 5.9. Flow number comparison of experimental test results..... 185
Figure 5.10. Fatigue life comparison of experimental test results..... 192
Figure 5.11. Comparison of numerical and laboratory M_R results of TGDH samples 195
Figure 5.12. Comparison of numerical and laboratory Poisson's ratio results of TGDH samples..... 196
Figure 5.13. Resilient modulus analysis results of synthetic TGDH samples..... 198
Figure 5.14. Comparison of numerical and laboratory M_R results of TGDH samples 200
Figure 5.15. Comparison of numerical and laboratory Poisson's ratio results of TGDH samples..... 202
Figure 5.16. Resilient modulus analysis results of synthetic FAA samples 203
Figure 5.17. Comparison of intercept point (a) results of TGDH samples..... 206

Figure 5.18. Comparison of slope (b) results of TGDH samples 207
Figure 5.19. Comparison of intercept point (a) results of FAA samples 209
Figure 5.20. Comparison of slope (b) results of FAA samples 210
Figure A.1. Compaction curves of TGDH samples 234
Figure A.2. Compaction curves of FAA samples 234
Figure B.1. Resilient modulus test setup 235
Figure B.2. Repeated creep test setup 237
Figure B.3. Indirect tensile fatigue test setup 239
Figure C.1. IDTF test results of sample ID LUIF02-2: a) Stiffness modulus, b) Reduction in stiffness 241
Figure C.2. IDTF test results of sample ID LUIF07-2: a) Stiffness modulus, b) Reduction in stiffness 242
Figure C.3. IDTF test results of sample ID LUIF08-2: a) Stiffness modulus, b) Reduction in stiffness 243
Figure C.4. IDTF test results of sample ID LUIF11-2: a) Stiffness modulus, b) Reduction in stiffness 244
Figure C.5. IDTF test results of sample ID LUIF13-1: a) Stiffness modulus, b) Reduction in stiffness 245
Figure C.6. IDTF test results of sample ID LUIF14-1: a) Stiffness modulus, b) Reduction in stiffness 246
Figure C.7. IDTF test results of sample ID LUIF14-2: a) Stiffness modulus, b) Reduction in stiffness 247
Figure C.8. IDTF test results of sample ID LUIF15-1: a) Stiffness modulus, b) Reduction in stiffness 248
Figure C.9. IDTF test results of sample ID LUIF15-2: a) Stiffness modulus, b) Reduction in stiffness 249
Figure C.10. IDTF test results of sample ID LUIF17-1: a) Stiffness modulus, b) Reduction in stiffness 250
Figure C.11. IDTF test results of sample ID BMIF02-2: a) Stiffness modulus, b) Reduction in stiffness 251

Figure C.12. IDTF test results of sample ID BMIF03-2: a) Stiffness modulus, b) Reduction in stiffness 252
Figure C.13. IDTF test results of sample ID BMIF05-2: a) Stiffness modulus, b) Reduction in stiffness 253
Figure C.14. IDTF test results of sample ID BMIF07-2: a) Stiffness modulus, b) Reduction in stiffness 254
Figure C.15. IDTF test results of sample ID BMIF09-2: a) Stiffness modulus, b) Reduction in stiffness 255
Figure C.16. IDTF test results of sample ID BMIF12-2: a) Stiffness modulus, b) Reduction in stiffness 256
Figure C.17. IDTF test results of sample ID BMIF15-1: a) Stiffness modulus, b) Reduction in stiffness 257
Figure C.18. IDTF test results of sample ID BMIF15-2: a) Stiffness modulus, b) Reduction in stiffness 258
Figure C.19. IDTF test results of sample ID BMIF16-2: a) Stiffness modulus, b) Reduction in stiffness 259
Figure C.20. IDTF test results of sample ID BMIF17-1: a) Stiffness modulus, b) Reduction in stiffness 260
Figure F.1. Genuine image of sample ID LURM02-1 266
Figure F.2. Synthetic images of sample ID LURM02-1 267
Figure F.3. Genuine image of the sample ID BMRM02-1 269
Figure F.4. Synthetic images of sample ID BMRM02-1 270
Figure F.5. Genuine image of sample ID LUCR06 272
Figure F.6. Synthetic images of sample ID LUCR06 273
Figure F.7. Genuine image of sample ID BMCR03 275
Figure F.8. Synthetic images of sample ID BMCR03 276
Figure G.1. Sample ID LURM01-1: a) Captured RGB image, b) Binary form, c) Processed image, d) 2D FE model in ABAQUS 280
Figure G.2. Sample ID LURM02-1: a) Captured RGB image, b) Binary form, c) Processed image, d) 2D FE model in ABAQUS 281

Figure G.3. Sample ID LURM03-1: a) Captured RGB image, b) Binary form, c) Processed image, d) 2D FE model in ABAQUS 282
Figure G.4. Sample ID LURM06-1: a) Captured RGB image, b) Binary form, c) Processed image, d) 2D FE model in ABAQUS 283
Figure G.5. Sample ID LURM07-1: a) Captured RGB image, b) Binary form, c) Processed image, d) 2D FE model in ABAQUS 284
Figure G.6. Sample ID LURM08-1: a) Captured RGB image, b) Binary form, c) Processed image, d) 2D FE model in ABAQUS 285
Figure G.7. Sample ID LURM09-1: a) Captured RGB image, b) Binary form, c) Processed image, d) 2D FE model in ABAQUS 286
Figure G.8. Sample ID LURM10-1: a) Captured RGB image, b) Binary form, c) Processed image, d) 2D FE model in ABAQUS 287
Figure G.9. Sample ID LURM11-1: a) Captured RGB image, b) Binary form, c) Processed image, d) 2D FE model in ABAQUS 288
Figure G.10. Sample ID LURM12-1: a) Captured RGB image, b) Binary form, c) Processed image, d) 2D FE model in ABAQUS 289
Figure G.11. Sample ID BMRM01-1: a) Captured RGB image, b) Binary form, c) Processed image, d) 2D FE model in ABAQUS 290
Figure G.12. Sample ID BMRM02-1: a) Captured RGB image, b) Binary form, c) Processed image, d) 2D FE model in ABAQUS 291
Figure G.13. Sample ID BMRM07-1: a) Captured RGB image, b) Binary form, c) Processed image, d) 2D FE model in ABAQUS 292
Figure G.14. Sample ID BMRM08-1: a) Captured RGB image, b) Binary form, c) Processed image, d) 2D FE model in ABAQUS 293
Figure G.15. Sample ID BMRM09-1: a) Captured RGB image, b) Binary form, c) Processed image, d) 2D FE model in ABAQUS 294
Figure G.16. Sample ID BMRM10-1: a) Captured RGB image, b) Binary form, c) Processed image, d) 2D FE model in ABAQUS 295
Figure G.17. Sample ID BMRM11-1: a) Captured RGB image, b) Binary form, c) Processed image, d) 2D FE model in ABAQUS 296

Figure G.18. Sample ID BMRM12-1: a) Captured RGB image, b) Binary form, c) Processed image, d) 2D FE model in ABAQUS 297
Figure G.19. Sample ID BMRM13-1: a) Captured RGB image, b) Binary form, c) Processed image, d) 2D FE model in ABAQUS 298
Figure G.20. Sample ID BMRM14-1: a) Captured RGB image, b) Binary form, c) Processed image, d) 2D FE model in ABAQUS 299
Figure G.21. Sample ID LUCR03: a) Captured RGB image, b) Binary form, c) Processed image, d) 2D FE model in ABAQUS 300
Figure G.22. Sample ID LUCR05: a) Captured RGB image, b) Binary form, c) Processed image, d) 2D FE model in ABAQUS 301
Figure G.23. Sample ID LUCR06: a) Captured RGB image, b) Binary form, c) Processed image, d) 2D FE model in ABAQUS 302
Figure G.24. Sample ID LUCR07: a) Captured RGB image, b) Binary form, c) Processed image, d) 2D FE model in ABAQUS 303
Figure G.25. Sample ID LUCR08: a) Captured RGB image, b) Binary form, c) Processed image, d) 2D FE model in ABAQUS 304
Figure G.26. Sample ID LUCR09: a) Captured RGB image, b) Binary form, c) Processed image, d) 2D FE model in ABAQUS 305
Figure G.27. Sample ID LUCR10: a) Captured RGB image, b) Binary form, c) Processed image, d) 2D FE model in ABAQUS 306
Figure G.28. Sample ID LUCR11: a) Captured RGB image, b) Binary form, c) Processed image, d) 2D FE model in ABAQUS 307
Figure G.29. Sample ID LUCR12: a) Captured RGB image, b) Binary form, c) Processed image, d) 2D FE model in ABAQUS 308
Figure G.30. Sample ID LUCR13: a) Captured RGB image, b) Binary form, c) Processed image, d) 2D FE model in ABAQUS 309
Figure G.31. Sample ID BMCR01: a) Captured RGB image, b) Binary form, c) Processed image, d) 2D FE model in ABAQUS 310
Figure G.32. Sample ID BMCR02: a) Captured RGB image, b) Binary form, c) Processed image, d) 2D FE model in ABAQUS 311

Figure G.33. Sample ID BMCR03: a) Captured RGB image, b) Binary form, c) Processed image, d) 2D FE model in ABAQUS 312
Figure G.34. Sample ID BMCR04: a) Captured RGB image, b) Binary form, c) Processed image, d) 2D FE model in ABAQUS 313
Figure G.35. Sample ID BMCR05: a) Captured RGB image, b) Binary form, c) Processed image, d) 2D FE model in ABAQUS 314
Figure G.36. Sample ID BMCR06: a) Captured RGB image, b) Binary form, c) Processed image, d) 2D FE model in ABAQUS 315
Figure G.37. Sample ID BMCR07: a) Captured RGB image, b) Binary form, c) Processed image, d) 2D FE model in ABAQUS 316
Figure G.38. Sample ID BMCR08: a) Captured RGB image, b) Binary form, c) Processed image, d) 2D FE model in ABAQUS 317
Figure G.39. Sample ID BMCR09: a) Captured RGB image, b) Binary form, c) Processed image, d) 2D FE model in ABAQUS 318
Figure G.40. Sample ID BMCR10: a) Captured RGB image, b) Binary form, c) Processed image, d) 2D FE model in ABAQUS 319
Figure H.1. Resilient modulus simulation results of the specimen ID LURM01-1: a) Maximum horizontal deformation, b) Maximum vertical deformation 320
Figure H.2. Resilient modulus simulation results of the specimen ID LURM02-1: a) Maximum horizontal deformation, b) Maximum vertical deformation 321
Figure H.3. Resilient modulus simulation results of the specimen ID LURM03-1: a) Maximum horizontal deformation, b) Maximum vertical deformation 322
Figure H.4. Resilient modulus simulation results of the specimen ID LURM06-1: a) Maximum horizontal deformation, b) Maximum vertical deformation 323
Figure H.5. Resilient modulus simulation results of the specimen ID LURM07-1: a) Maximum horizontal deformation, b) Maximum vertical deformation 324
Figure H.6. Resilient modulus simulation results of the specimen ID LURM08-1: a) Maximum horizontal deformation, b) Maximum vertical deformation 325
Figure H.7. Resilient modulus simulation results of the specimen ID LURM09-1: a) Maximum horizontal deformation, b) Maximum vertical deformation 326

Figure H.8. Resilient modulus simulation results of the specimen ID LURM10-1: a) Maximum horizontal deformation, b) Maximum vertical deformation..... 327
Figure H.9. Resilient modulus simulation results of the specimen ID LURM11-1: a) Maximum horizontal deformation, b) Maximum vertical deformation..... 328
Figure H.10. Resilient modulus simulation results of the specimen ID LURM12-1: a) Maximum horizontal deformation, b) Maximum vertical deformation..... 329
Figure H.11. Resilient modulus simulation results of the specimen ID BMRM01-1: a) Maximum horizontal deformation, b) Maximum vertical deformation..... 330
Figure H.12. Resilient modulus simulation results of the specimen ID BMRM02-1: a) Maximum horizontal deformation, b) Maximum vertical deformation..... 331
Figure H.13. Resilient modulus simulation results of the specimen ID BMRM07-1: a) Maximum horizontal deformation, b) Maximum vertical deformation..... 332
Figure H.14. Resilient modulus simulation results of the specimen ID BMRM08-1: a) Maximum horizontal deformation, b) Maximum vertical deformation..... 333
Figure H.15. Resilient modulus simulation results of the specimen ID BMRM09-1: a) Maximum horizontal deformation, b) Maximum vertical deformation..... 334
Figure H.16. Resilient modulus simulation results of the specimen ID BMRM10-1: a) Maximum horizontal deformation, b) Maximum vertical deformation..... 335
Figure H.17. Resilient modulus simulation results of the specimen ID BMRM11-1: a) Maximum horizontal deformation, b) Maximum vertical deformation..... 336
Figure H.18. Resilient modulus simulation results of the specimen ID BMRM12-1: a) Maximum horizontal deformation, b) Maximum vertical deformation..... 337
Figure H.19. Resilient modulus simulation results of the specimen ID BMRM13-1: a) Maximum horizontal deformation, b) Maximum vertical deformation..... 338
Figure H.20. Resilient modulus simulation results of the specimen ID BMRM14-1: a) Maximum horizontal deformation, b) Maximum vertical deformation..... 339
Figure I.1. Repeated creep simulation results of the specimen ID LUCR03: a) Vertical deformations at the end of the test, b) Resulting vertical deformation graph 340

Figure I.2. Repeated creep simulation results of the specimen ID LUCR05: a) Vertical deformations at the end of the test, b) Resulting vertical deformation graph 341
Figure I.3. Repeated creep simulation results of the specimen ID LUCR06: a) Vertical deformations at the end of the test, b) Resulting vertical deformation graph 342
Figure I.4. Repeated creep simulation results of the specimen ID LUCR07: a) Vertical deformations at the end of the test, b) Resulting vertical deformation graph 343
Figure I.5. Repeated creep simulation results of the specimen ID LUCR08: a) Vertical deformations at the end of the test, b) Resulting vertical deformation graph 344
Figure I.6. Repeated creep simulation results of the specimen ID LUCR09: a) Vertical deformations at the end of the test, b) Resulting vertical deformation graph 345
Figure I.7. Repeated creep simulation results of the specimen ID LUCR10: a) Vertical deformations at the end of the test, b) Resulting vertical deformation graph 346
Figure I.8. Repeated creep simulation results of the specimen ID LUCR11: a) Vertical deformations at the end of the test, b) Resulting vertical deformation graph 347
Figure I.9. Repeated creep simulation results of the specimen ID LUCR12: a) Vertical deformations at the end of the test, b) Resulting vertical deformation graph 348
Figure I.10. Repeated creep simulation results of the specimen ID LUCR13: a) Vertical deformations at the end of the test, b) Resulting vertical deformation graph 349
Figure I.11. Repeated creep simulation results of the specimen ID BMCR01: a) Vertical deformations at the end of the test, b) Resulting vertical deformation graph 350

Figure I.12. Repeated creep simulation results of the specimen ID BMCR02: a) Vertical deformations at the end of the test, b) Resulting vertical deformation graph 351
Figure I.13. Repeated creep simulation results of the specimen ID BMCR03: a) Vertical deformations at the end of the test, b) Resulting vertical deformation graph 352
Figure I.14. Repeated creep simulation results of the specimen ID BMCR04: a) Vertical deformations at the end of the test, b) Resulting vertical deformation graph 353
Figure I.15. Repeated creep simulation results of the specimen ID BMCR05: a) Vertical deformations at the end of the test, b) Resulting vertical deformation graph 354
Figure I.16. Repeated creep simulation results of the specimen ID BMCR06: a) Vertical deformations at the end of the test, b) Resulting vertical deformation graph 355
Figure I.17. Repeated creep simulation results of the specimen ID BMCR07: a) Vertical deformations at the end of the test, b) Resulting vertical deformation graph 356
Figure I.18. Repeated creep simulation results of the specimen ID BMCR08: a) Vertical deformations at the end of the test, b) Resulting vertical deformation graph 357
Figure I.19. Repeated creep simulation results of the specimen ID BMCR09: a) Vertical deformations at the end of the test, b) Resulting vertical deformation graph 358
Figure I.20. Repeated creep simulation results of the specimen ID BMCR10: a) Vertical deformations at the end of the test, b) Resulting vertical deformation graph 359

LIST OF ABBREVIATIONS

2D: Two-dimensional

3D: Three-dimensional

AASHTO: American Association of State Highway and Transportation Officials

AC: Asphalt Concrete

APDL: ANSYS Parametric Design Language

ASTM: American Society for Testing and Materials

CCD: Charged-Couple Device

CMA: Cold Mix Asphalt

CT: Computed Tomography

CZM: Cohesive Zone Modeling

DAS: Data Acquisition System

DEM: Discrete Element Method

DPI: Dot per Inch

DSR: Dynamic Shear Rheometer

DTS: Dynamic Testing System

EN: European Norm

ESAL: Equivalent Single Axle Load

FAA: Federal Aviation Administration

FE: Finite Element

FEM: Finite Element Model

FN: Flow Number

HMA: Hot Mix Asphalt

IDT: Indirect Tensile

IDTF: Indirect Tensile Fatigue

IGES: Initial Graphics Exchange Specification

LTTP: Long Term Pavement Performance

LVDT: Linear Variable Displacement Transducer

NCHRP: National Cooperative Highway Research Program

PG: Penetration Graded

PMB: Polymer Modified Bitumen

RAP: Reclaimed Asphalt Pavement

RGB: Red, Green, and Blue

RM: Resilient Modulus

RTD: Resistance Temperature Detector

SBS: Styrene Butadiene Styrene

SHRP: Strategic Highway Research Program

SUPERPAVE: Superior Performing Asphalt Pavements

TGDH: Turkish General Directorate of Highways

UMAT: User-defined Material

UTM: Universal Testing Machine

VFA: Voids Filled with Asphalt

VMA: Voids in Mineral Aggregate

CHAPTER 1

INTRODUCTION

1.1 Background

Asphalt concrete, also known as hot mix asphalt (HMA), is a composite material consisting of mineral aggregate, asphalt binder and air voids. It is possible to produce many different asphalt mixtures with different components, such as combinations of binder and aggregates, gradations of aggregates and techniques for modifying the asphalt binder. The mechanical properties of these mixtures vary widely and depend on the characteristics of their constituents, e.g., aggregate properties (particle size, shape, texture, modulus, etc.), binder properties (rheological properties, grade, etc.), proportions (mix design), size and distribution of aggregates. Furthermore, the air voids, although they cannot withstand the applied load, play an important role in the overall performance of asphalt mixtures through their distribution and content. In addition to its very complex microstructure, the macro behavior of asphalt concrete is even more complicated due to the rate-dependent material nature of the asphalt binder. Therefore, it is of great importance to understand the effects of asphalt mix constituents on its overall performance.

There are several empirical test methods for measuring and analyzing the response of HMA mixtures to loading and environmental conditions. However, in some cases, replicating laboratory tests can be quite difficult, costly and time-consuming. It is well known that empirical tests are not reliable when conditions differ from those for which the tests were developed (Roberts et al., 1996).

In addition, the availability of the equipment needed for technical characterization is not always possible. Therefore, there is a need virtually simulate asphalt mixtures and evaluate the mechanical behavior based on the properties of their constituents.

Numerical simulation techniques such as the finite element method (FEM) and the discrete element method (DEM) can be used to estimate the performance of materials under field conditions without having to measure them directly. Many researchers have developed numerical models to predict the response of asphalt concrete and avoid the expensive and time-consuming tests (Hashin, et al., 1963; Mori, et al., 1973; Uddin et al., 1995; Lu & Wright, 1998; Kose, 2002; Christensen, et al., 2003; Arshadi, 2015).

Early numerical methods for evaluating the performance of HMA used the continuum mechanics and the discrete particle mechanics approach. In the continuum mechanics approach, the properties of the composite material are considered as if they were a single-phase, homogeneous continuum unit. Since most of these models are based on the material properties characterized from the experimental test results where the samples were treated as homogeneous materials, they usually do not consider the effects of factors such as aggregate gradation, air void content or aggregate surface texture on the overall performance of the HMA. In the discrete particle mechanics approach, the aggregates are represented as discrete elastic particles whose properties are considered individually. The usual approach is to model the aggregates as given shapes such as discs, spheres, elliptical or polygonal elements. Apart from being able to handle complex and changing contact geometries and large displacements, DEM has limited success in modeling HMA. The problem with DEM simulations is that shear resistance is usually underestimated when simple discs or spheres are used (Jensen et al., 1999). Furthermore, it has been found in the literature that the sphere-based DEM yields lower strengths than the actual strengths of the soils (Ting & Rowell, 1995). In their study, Jensen et al. (1999) stated that better qualitative results could be obtained if more complex shapes such as arbitrary polygonal elements were used instead of circles and ellipses, but this would significantly increase the computational time.

Later finite element modeling studies employed imaging techniques to achieve a better geometric representation of aggregates in asphalt concrete specimens (AC). Advances in computer technology made it possible to produce both 2D and 3D microstructures of the real specimens. The digital representation of the real microstructure of the physical sample, also called the digital image, can then be transferred to FEM to perform computational simulations in which the response of the asphalt mixture is evaluated based on the real microstructure of the material. The experimental results can then be used to validate the numerical model through comparisons to understand the underlying mechanisms of deformation in HMA. These techniques have been used to accurately capture the actual microstructure of HMA (Kose et al., 2000; Masad & Somadevan, 2002; Abbas, 2004; Wang, 2007; Arshadi, 20015).

Given the challenges in applying empirical testing and identifying the underlying causes of asphalt concrete deterioration, there is a need to introduce and improve numerical methods for testing HMA mixes.

1.2 Hypothesis

Virtual testing of asphalt mixture samples can be an effective tool for evaluating their performance. It is expected that such a test method will reduce the number of combinations associated with actual physical testing and can be used as an effective alternative when laboratory testing is not available. The finite element method (FEM) can be an effective virtual test method in this context. One of the main difficulties for the success of FEM is that an accurate geometric model is required. To overcome this difficulty, image processing can be used at this point. With this approach, the HMA can be modeled as a composite material consisting of individual components, namely aggregate, binder and air voids. Using the actual microstructure of the samples to create the geometric model also helps to increase the accuracy of the model. Therefore, it is hypothesized in this topic that FEM together with the use of imaging can combine the advantages of continuum and discrete methods, as it is

able to characterize the discrete nature of HMA while treating the material as a continuum.

1.3 Research Objectives

The aim of this research is to develop a virtual model for HMA that will help reduce the amount of work required for actual physical testing of specimens. A two-dimensional finite element model based on digital imaging techniques is used to investigate the tensile variations within the HMA. The following objectives can be summarized in this context:

(1) Development of a suitable method for the acquisition of digital images of real asphalt samples and their conversion into a finite element model.

(2) Creation of a 2D micromechanical finite element model based on the digital images of the samples.

(3) Evaluation and validation of the FEM through experimental and numerical simulation techniques.

(4) Use of the virtual model by redistributing the aggregate particles to create different microstructures and determine variations in the tensile strength of the samples.

Asphalt concrete samples are prepared in the laboratory using two different mixture designs and laboratory tests are carried out. Two-dimensional images of the samples are captured using a flatbed scanner. Image processing techniques are then applied to transform the images into finite element geometry. Image based FEM is created and the same laboratory tests are simulated in the finite element environment. The finite element model is verified by comparing the experimental and numerical test results from resilient modulus test, repeated creep test and indirect tensile fatigue test. In addition, the effect of variations in the tensile strength of AC is evaluated by

creating different microstructures from the same cross-sectional images of asphalt concrete specimens using the particle redistribution method.

It is expected that the virtual model of this study will be used in future studies to evaluate the performance of AC specimens. The evaluation of asphalt concrete specimens under different conditions can be easily repeated using the virtual model created in this study. In this regard, the labor required for laboratory experiments can be reduced and great convenience is provided in the absence of test equipment.

1.4 Scope

This study was conducted in three main phases. The first phase includes laboratory study in which two mix designs with different asphalt binders, aggregates and pavement types were performed. Prior to the mix design, various tests were conducted on the materials, i.e., the aggregates and binders, to determine their properties. Then the Superpave mix design methods were carried out and a number of test specimens were prepared. To input the material model in FEM, frequency sweep tests on the asphalt binders were also carried out at this stage. After preparing the required number of specimens from the Superpave mix design method, a laboratory test program was carried out. Three main test methods were used in this program: Resilient modulus (RM) test, repeated creep, also known as flow number (FN) test, and indirect tensile fatigue (IDTF) test.

In the second phase, an image processing technique was developed to obtain high-resolution 2D cross-sectional images of real asphalt samples. To obtain clean images, the samples had to have a smooth surface. For this purpose, a diamond-tipped saw was available in the laboratory. A simple flatbed scanner was then used to capture images from the smooth surfaces of the samples. Before further analysis, the cross-sectional images were enhanced through a series of image processing methods. The processed and enhanced images were then converted into a finite element geometric model in ANSYS® software. The ANSYS® scripting language, also called

Mechanical APDL (Parametric Design Language), was used to convert binary images into their geometric model using a unique method called image vectorization. The geometric models were then transferred into ABAQUS® software and the finite element models were finalized by applying the other input parameters such as material models for aggregate and binder, boundary conditions, and loading. In order to validate the FEM, the same laboratory experiments were simulated in the finite element environment and the post-processing was carried out to obtain numerical test results. These test results were then compared with the laboratory test results to determine the accuracy of the virtual model.

Finally, the same cross-sectional images were used to redistribute the aggregate particles, resulting in a different microstructure. A MATLAB® algorithm was developed to detect and distribute all aggregate particles to random locations in the same cross-sectional area. Synthetic cross-sectional images were created using this method. By generating numerous artificial microstructures based on the real samples, sample repetition and the effects of homogeneity on the tensile strength of asphalt concrete could be studied.

1.5 Outline of Research

Chapter 1 sets out the background to the study, the research objectives, scope and outline of the research. A detailed literature review on numerical modeling of asphalt concrete is presented in Chapter 2. The literature review includes previous numerical modeling methods as well as their validation techniques. A large part of the literature review relates to two-dimensional image-based finite element modeling of asphalt concrete. This chapter also provides brief information on the performance and analysis of the laboratory test methods used in this study.

Chapter 3 is dedicated to the laboratory testing program of the study. In this chapter, basically all the laboratory work of this study is described in detail. First, the design and preparation of the asphalt concrete samples are presented. Selected test

parameters as well as detailed test procedures are also presented in this chapter. Finally, the analyzes of the test data to obtain the results are explained in detail. Chapter 4 presents in detail the numerical modeling of the asphalt samples compacted in the laboratory. The image processing techniques used to convert the cross-sectional images of the real samples into their FEM model are explained. The rest of the finite element modeling techniques are illustrated to show how the numerical calculations are performed. In addition, the aggregate redistribution method used to study the tensile variations is also explained in detail in this chapter.

All empirical and numerical test results are presented in Chapter 5. First, the results of the laboratory tests are presented and compared. Then the numerical results are presented and compared with the previous empirical test results to validate the FEM. Besides, the tensile variations of the asphalt concrete samples are investigated using the test results of the artificially constructed numerical models. Finally, Chapter 6 summarizes the conclusions of this study and provides recommendations for the future to improve the constructed model.

CHAPTER 2

LITERATURE REVIEW

2.1 Introduction

This chapter presents a comprehensive literature review on two-dimensional image-based microstructural characterization of asphalt concrete. Current numerical methods for characterizing asphalt mixtures are discussed in detail. Previously proposed methods for finite element modeling of asphalt specimens are compared. Finally, laboratory test methods for resilient modulus, repeated creep and indirect tensile fatigue tests are briefly described.

2.2 Finite Element Analysis of Asphalt Mixtures

Asphalt concrete has a very complicated heterogeneous nature, consisting mainly of three components: Aggregates, asphalt binders and air voids. The aggregates in pavements usually have an irregular shape, random orientation and vary in size from less than 1 μm to as much as 30 mm. The asphalt binder, on the other hand, has a very complex behavior under different loading and temperature conditions. While it behaves like a viscous liquid at mixing temperatures, it becomes a viscoelastic solid at service temperatures (Meegoda & Chang, 1994). Although air voids are not believed to have inherent strength, their profound effect on the overall strength of asphalt concrete is a known fact. This complex structure of asphalt concrete makes its nature very difficult to understand and evaluate. Finite element analysis is a qualified and efficient tool for predicting the behavior of such a material (Lakes, et al., 2002).

Apart from the fact that it was first introduced systematically in aerospace engineering by Turner et al. (1956), finite element analysis is based on the creation of a surrogate structure whose parts are separated from the problem domain by grid lines. Each of these parts is called an element and is connected to the neighboring elements at the nodes or vertices. This process is called discretization, and the collection of nodes and elements is called a mesh. Based on the nodal displacements of an element, the displacements, strains and stresses can be determined over the area or volume of that element. The relationship between the strain and the nodal displacement is shown as follows:

$$\{\varepsilon\} = [B]\{U\} \tag{2.1}$$

where ε is the strain vector; B is the matrix of linear operators (derivatives of shape functions); U is the nodal displacement vector.

The element stiffness matrices are than can be calculates as:

$$K^e = \int B^T D B \, dv \tag{2.2}$$

where D is the constitutive matrix. The element stiffness matrices should be combined to form an overall stiffness matrix, and the resulting system of equation Eq. (2.3) should be solved for unknown nodal displacements.

$$\{F\} = [K]\{U\} \tag{2.3}$$

where K is the overall stiffness matrix; U is the nodal displacement vector; F is the equivalent nodal force element. The stresses and strains can be then calculated from the nodal displacements (Arshadi, 2015).

2.2.1 3D Finite Element Modeling

Over the years, many researchers have attempted to simulate and study the microstructure of asphalt mixtures using FEM. Chen et al (1986) studied the effects of heavy axle loads on the performance of asphalt mixtures by using 3D FEM instead of an elastic layer model, which was commonly used for pavement design at that time. They showed that the asphalt layers exhibited greater tensile strains under uniform pressure than under non-uniform pressure (Chen, et al., 1986).

In a study by Zaghloul and White (1993), a three-dimensional finite element model was used to analyze flexible pavements subjected to dynamic loads at various rates. They used a series of material models to represent the actual material properties such as viscoelasticity and elastoplasticity. The study proved that FEM provides a reliable prediction of the actual pavement behavior under moving loads (Zaghloul & White, 1993).

Cho et al. (1996) investigated the applicability of three FEM methods (plane strain, axisymmetric, and three-dimensional) and their drawbacks to facilitate the selection of an appropriate model and element type for simulating the effects of live loads. It was found that the 3D simulation FEM provides a reasonable approximation if the boundary conditions and geometry are well controlled (Cho et al., 1996).

In another study, Helwany et al. (1998) used another 3D finite element analysis to illustrate the usefulness of the finite element method. A variety of material constitutive models, such as linear elastic, nonlinear elastic, and viscoelastic, were used, and it was concluded that the finite element method, if validated, is an extremely useful tool as it allows direct estimation of the primary response parameters without the need for costly field tests (Helwany et al., 1998).

After comparing the rutting results between 2D and 3D FE analyzes, Hua (2000) found that the maximum rut depth between the two methods was less than 2% (Figure 2.1), and therefore decided to use 2D analysis instead of 3D analysis. Considering the time and resources required to run the 3D FE model, 2D analysis is the more practical option in most cases (Hua et al., 2000).

Erkens et al. (2002) developed a finite element implementation of a three-dimensional, strain rate sensitive, temperature and load history dependent constitutive model. The simulations showed the influence of geometry and material properties on the development of damage. They concluded that accurate nonlinear material models would lead to a better understanding of pavement distress phenomena and the parameters that affect them (Erkens et al., 2002).

Another 3D implementation of a material model for the load- bearing behavior of asphalt pavements was carried out by Oeser & Möller (2004). The constitutive model was first described mathematically in differential form and one-dimensional configuration and extended to the general 3D stress-deformation state using an energy hypothesis (Oeser & Möller, 2004).

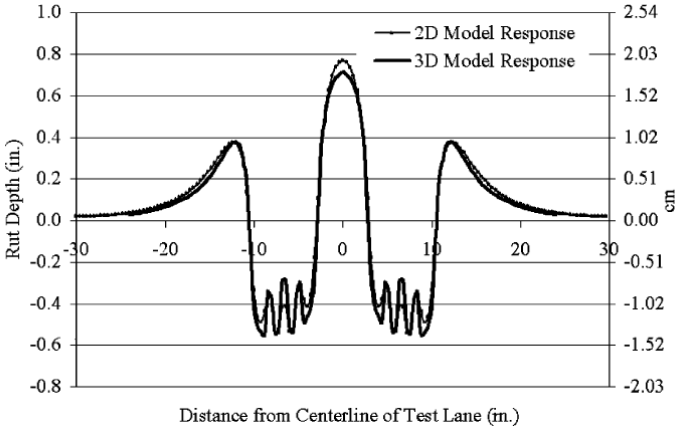

Figure 2.1. Comparison of 2D and 3D model responses (Hau, 2000)

Collop et al. (2006) investigated the viscoelastic behavior of asphalt mixtures using discrete element modeling. An idealized 3D mixture model was generated from spherical aggregate shapes to perform uniaxial and triaxial compression creep tests, and the numerical results were validated with experimental data (Collop et al., 2006).

Wang (2007) investigated a computational simulation method that incorporates the microstructure of AC with three-dimensional FEM. The rutting potential of asphalt mixtures was evaluated based on the actual microstructure reconstructed from X-ray tomography images. The results of the simulation tests showed good agreement with the experimental results (Wang, 2007).

Mo et al. (2008) presented 2D and 3D finite element models for the analysis of open-pore asphalt concrete rupture at the mesoscale. Different models were developed to gain insight into the effects of geometric aspects, including 2D representations of different particle packing and 3D representations of the highest particle packing. It was found that the 3D model tended to be more stressed compared to the equivalent 2D representation and the calculated stresses in the 3D model were 2.6 to 3.5 times greater than in the 2D model (Mo et al., 2008).

Kim et al. (2009) investigated nonlinear modeling of pavement foundations for three-dimensional finite element analysis. Nonlinear stress-dependent modular models were programmed in the User Material Subroutine (UMAT) of ABAQUS® to properly characterize the elastic behavior of pavement foundations. The predictive capability of the developed nonlinear model was validated by measuring and comparing the responses with those of field sections. The predicted pavement responses agreed well with the displacements and stresses measured in the field and the 3D FE analyzes (Kim et al., 2009).

Another discrete element and idealized 3D microstructure model (Figure 2.2) to simulate constant compression tests with different strain rates at different temperatures was carried out by Wu et al. (2011). Again, the model results were found to agree well with the experimental data (Wu et al., 2011). Ameri et al. (2011)

used 3D finite element analysis to investigate the top-to-bottom transverse cracking under traffic loading. They were able to successfully calculate the stress intensity factors by using a large number of 3D finite element models. Although it provides a more accurate simulation of actual conditions, a 3D finite element model requires more analytical effort and expertise than a 2D model due to its complex modeling (Ameri et al., 2011).

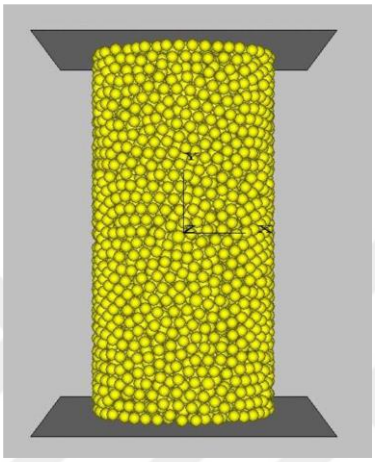

Figure 2.2. Idealized microstructural model (Wu et al. 2011)

Abu Al-Rub et al. (2012) conducted a comprehensive evaluation of the effects of different finite element modeling techniques and material constitutive models used to predict rutting in asphalt pavements under repeated loading conditions. 2D and 3D models were compared and it was found that two-dimensional models predict much larger permanent deformations than three-dimensional models, resulting in overestimation.

The influence of asphalt micromechanical surface morphology on rubber block friction was studied by Srirangam et al. (2017). The morphology of the asphalt surface of the mixes was recorded using the X-ray tomography method, from which the finite element micromechanical structure was developed. After validating the model, they suggested that it could be used to evaluate the performance of different mixtures against skidding without the need to build a test track (Srirangam et al., 2017). Liu et al. (2017) evaluated the effects of heavy traffic loads on asphalt

pavements using the SAFEM® program, which requires a three-dimensional FE program that requires only a two-dimensional mesh. Then the semi-analytical finite element method was applied using Fourier series in the third dimension. The experimental studies showed that the method is able to predict the mechanical responses of asphalt pavements (Liu et al., 2017).

Shanbara et al. (2018) described the development of a three-dimensional finite element model of flexible fiber-reinforced cold mix asphalt (CMA) pavements. A 3D finite element model was used to predict the viscoelastic response using Prony series parameter properties. The permanent deformation of flexible CMA pavements was validated by laboratory tests and numerical predictions. Good agreement was obtained between the predicted rutting and experimental results (Shanbara et al., 2018).

Klimczak & Cecot (2019) focused on efficient numerical modeling using the Burgers viscoelastic material model. A straightforward algorithm was presented for the generation of random AC structures in conjunction with the finite element meshes. It was based on the predefined shapes of inclusions and the relocation of nodes of the regular grid. This coarser FE mesh system saved a lot of computational time and resources. Despite its simplicity, this low-cost 3D representation of AC mesostructure and multiscale modeling was very useful (Klimczak & Cecot, 2019).

Taherkhani & Tajdini (2020) investigated the effects of crack type, position, length, tire pressure and axle load on the behavior of cracked asphalt pavements using the 3D finite element method in ABAQUS®. The results showed that the pavement responses increased more with increasing tire pressure and axle load for the cracked pavements. Cardenes et al. (2020) investigated sample size correction factors for indentations in asphalt bitumen using the finite element method. Although the correction factors for lateral dimensions obtained from the finite element method were higher than those obtained from the analytical results, the reason was explained by the neglected volumetric effects captured in the finite element analysis in the previous analytical approach (Cardenes et al., 2020). Furthermore, the results of the

asymmetric 2D model were compared with a 3D model with second-order hexahedral elements. The results showed no significant difference between the two models and the work continued with the 2D model only. Yang et al. (2020) introduced a recurrent neural network to investigate the fatigue damage model of asphalt binders. The proposed model was validated using the 3D finite element method with continuum, 20 nodes and 3D element type. In their study, it was proved that FEM effectively utilizes the computational advantages of vectorization, so that FEM has a high convergence rate (Yang et al., 2020). Wang et al. (2021a) used a three-dimensional discrete element method (3D DEM) to study the permanent deformation of asphalt mixtures. The results showed the success of the discrete element method in simulating rutting behavior (Wang et al., 2021a).

One of the most recent studies on 3D FE viscoelastic analysis of crack propagation from top to bottom in asphalt pavements was conducted by Alae et al. (2021). The viscoelastic fracture analyzes enabled the researchers to identify the critical point of TDG growth. Han et al. (2021a) presented a 3D finite element method based on random reconstruction of aggregate particles. Heat transfer models were then performed on the virtual samples to predict the thermal parameters of asphalt mixtures. The effects of the design parameters and material properties of each component on the thermal properties of asphalt mixtures were investigated. The results showed that FEM is a reliable method for predicting the thermal properties of asphalt mixtures (Han et al., 2021).

2.2.2 2D Finite Element Modeling

Myers et al. (2001) evaluated the discrepancies between two- and three-dimensional FE models and the suitability of a modified two-dimensional analysis to be used as a reasonable approximation of the three-dimensional behavior of asphalt pavements. Based on the comparisons, it was concluded that the modified two-dimensional analysis developed in the study can be used to provide a reasonable approximation to the 3D tensile stresses (Myers et al., 2001). It should be noted that such a study

was necessary due to the high cost of 3D FEM analysis, especially for predictions involving constantly changing structures and thousands of load applications of varying magnitude and position (Myers et al., 2001).

A lattice-based micromechanical approach was adopted by Guddati et al. (2002) to characterize the cracking behavior of asphalt concrete. To determine the effectiveness of lattice modeling of heterogeneous materials, a typical elastic structure with rigid inclusions was analyzed and the results compared with those obtained using a very fine finite element mesh. In general, the results agree well with the exact results for both displacements and reactions (Guddati et al., 2002).

In his dissertation, Abbas (2004) described a method for characterizing the micromechanical behavior of asphalt mastic and asphalt mixtures using the discrete element method. Asphalt mastic was represented by cylindrical 2D particles that were randomly generated. The 2D results from DEM compared well with experimental mastic data and were able to capture the high stiffening rate typically observed when testing asphalt mastic at relatively low volume concentrations (Abbas, 2004).

A 2D finite element analysis of the microstructure and macroscopic properties of HMA was carried out by Dessouky (2005) in a PhD thesis. Several FE analyzes were performed to simulate experimental measurements and they all agreed with the experimental data (Dessouky, 2005).

Mulungye et al. (2006) used the finite element method to investigate the effects of tire pressure, wheel configuration and axle load variations on the structural performance of a flexible pavement. The structure of the pavement was modeled in ANSYS® as a two-dimensional four-layer structure. Model comparisons with full-scale measured test data (Figure 2.3) showed good convergence, indicating that the finite element method is an efficient tool for estimating potential distresses (Mulungye et al., 2006).

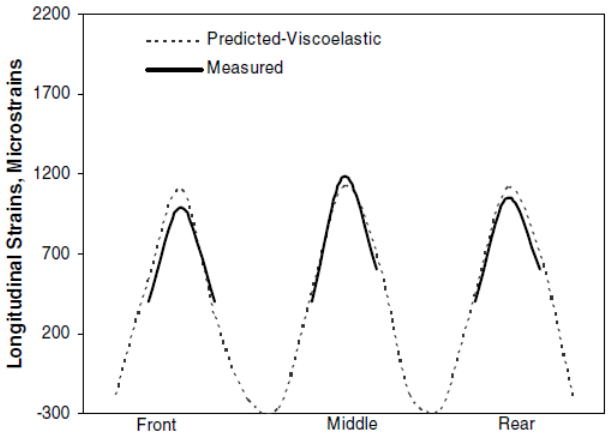

Figure 2.3. Measured and predicted longitudinal strains (Mulungye et al., 2006)

Gu et al. (2016) investigated the development of a finite element model to simulate a flexible roadway structure reinforced with geogrids. A user-defined material (UMAT) subroutine was programmed in to simulate the nonlinear cross-anisotropic behavior of unbound granular material reinforced with geogrids. The finite element models were then validated through a well-designed large-scale tank test program (Gu et al., 2016).

In his study, Bekele et al. (2021) modeled the development of low temperature micro-damage in asphalt concrete due to differential thermal contraction using a 2D finite element micromechanical model. The results of the micromechanical model agreed well with the experimental observations.

After reviewing the extensive studies in the literature, it was found that although the three-dimensional (3D) finite element model can solve all the problems solved by the two-dimensional (2D) finite element model, the use of the 3D finite element model is expensive in terms of computation time and data preparation. Since asphalt pavements have a large extension compared to the other dimensions, the 2D plane strain condition can be used instead of 3D modeling (Arshadi, 2015).

2.3 Image Based Finite Element Modeling of Asphalt Mixtures

In recent years, the application of the image-based finite element method in the study of the microstructure of asphalt mixtures has greatly increased. This method is a very important and effective tool for simulating the complex multiphase nature of asphalt concrete and its mechanical behavior. The visualization of asphalt concrete constituents has helped to create better and more effective finite element models that capture the internal structure of asphalt mixtures and the distribution of air voids.

In his dissertation, Kose (2002) developed a 2D image-based finite element model in ABAQUS® that helps reduce the number of combinations required for mixture development in actual physical tests. Although the virtual model was successfully created from cross-sectional images of asphalt concrete samples, the results underestimated the actual mix properties measured in the laboratory (Kose, 2002).

Dai et al (2005) used a micromechanical model to simulate the two-dimensional damage behavior of asphalt concrete. The aggregate-mastic microstructure was simulated using an equivalent finite element model generated numerically from photographic surface data of actual asphalt specimens. Comparisons of the overall load-deformation behavior and internal damage/failure responses between the test data and the simulation results were made and good agreement was found (Figure 2.4, Dai et al., 2005).

You & Dai (2007) investigated the dynamic complex modulus (E^*) of hot mix asphalt (HMA) using a micromechanical finite element model. The microstructure of the mixtures was obtained from two-dimensional scanned images of a sawed surface, and the study focused on modeling this structure at several preselected low and medium temperatures and at preselected loading frequencies. After comparison between the numerical simulation and laboratory measurements, the FE model provided satisfactory predictions for the moduli of the HMA at different loading frequencies and test temperatures (You & Dai, 2007).

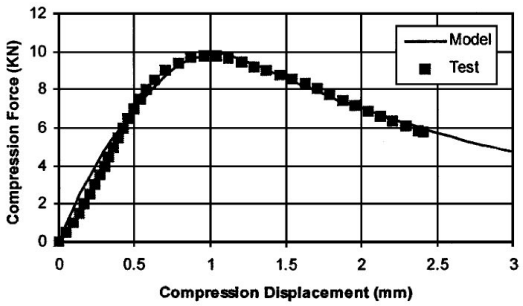

Figure 2.4. Load versus displacement curve (Dai et al., 2005)

One of the studies on 3D microstructure models for asphalt mixtures was conducted by Adhikari and You (2008). Images from X-ray CT were used for modeling using both two-dimensional and three-dimensional unique distinct element methods. Comparison of experimental measurements with 2D and 3D predictions showed that the 3D unique element models predicted the dynamic modulus of the asphalt mixture much better than the 2D models (Figure 2.5, Adhikari & You, 2008).

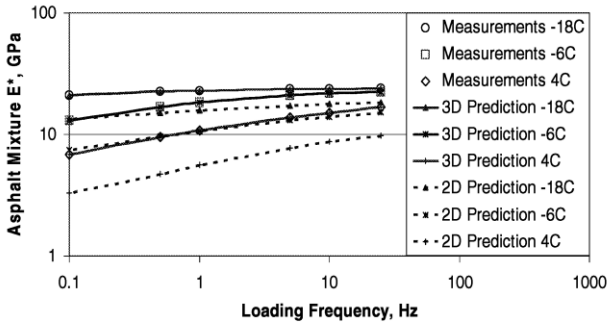

Figure 2.5. Dynamic modulus (E^*) predictions and laboratory measurements (Adhikari et al., 2008)

Aragao et al. (2011) used a finite element method to predict crack-induced fracture damage in asphalt pavements. The assessment of microstructural damage was based on a 2D finite element model that incorporated digital imaging techniques and was validated through laboratory testing. It was found that the successfully developed numerical model provided better and more accurate insights into the effects of mix constituents on overall mix performance, while minimizing modeling effort and achieving significant savings in testing costs and time (Aragao et al., 2011).

Coleri et al. (2012) developed 2D and 3D micromechanical finite element models to predict the shear modulus of asphalt mixtures whose internal microstructures were determined using X-ray computed tomography images. The X-ray images were then processed to create 2D and 3D mesh structures for asphalt mixtures FE in ABAQUS®. The aggregate and mastic subdomains were then modeled using elastic and viscoelastic assumptions, respectively. Shear modulus predictions for 2D and 3D models were compared with measured values to determine the effectiveness of each model type for simulating shear frequency sweep at constant height (FSCH). It was found that the 3D micromechanical FE model is able to predict such shear modulus at relatively high test temperatures with high accuracy over a range of loading frequencies (Coleri et al., 2012).

In his dissertation, You (2013) developed both two-dimensional (2D) and three-dimensional (3D) microstructural modeling of asphalt concrete. The 3D model was reconstructed from sections of 2D X-ray CT images consisting of matrix and aggregate phases. His model combines nonlinear constitutive models, finite element analyzes and the unique capabilities of X-ray CT in capturing material microstructure and provides the ability to link microstructural properties to macroscopic responses (You, 2013). Wang et al. (2013) investigated the crack propagation of rubber-modified asphalt mixtures using the extended finite element method. The internal microstructure of the mixtures was created using the X-ray CT imaging technique. After the semi-circular bending (SCB) tests, the model proved that it can provide a theoretical guide for predicting and controlling the fracture damage caused by crack growth, which is one of the most important distresses of rubber-modified asphalt pavements (Wang et a., 2013).

Recently, researchers have also looked at modeling the complex behavior of asphalt concrete using user-interface finite element software such as ABAQUS® and ANSYS®. In his dissertation, Arshadi (2015) investigated 2D multiscale finite element analysis to predict fatigue damage in asphalt mixtures. In addition to the four scales of asphalt binder, mastic, mortar and asphalt mix, the study included an

approach to consider particle contacts in each of the scales where mineral particles are present. The viscoelastic continuum damage model was implemented in ABAQUS® via UMAT to simulate the binder phase. Artificial 2D images of mastic and mortar scales were generated and used for the scales of mastic and mortar. Finally, scanned 2D images of asphalt mixtures were used for the scale of the asphalt mixture. After comparing experimental and FE simulation results, it was found that the 2D model FE was able to predict the effects of asphalt binder properties and aggregate microstructure on the mechanical behavior of asphalt concrete (Arshadi, 2015).

In another dissertation, the 2D digital image processing technique was used to convert images into finite element models using ABAQUS® and MATLAB® (Ling, 2016). The image-based model was successful in predicting the rutting behavior of asphalt mixtures. Huang et al. (2016) presented an image-based 3D micromechanical modeling approach for predicting the viscoelastic behavior of asphalt mixtures. An improved image analysis technique on X-ray CT images was used to develop a voxel-based 3D digital reconstruction model of asphalt mixtures. After comparing the numerical predictions with the observed laboratory results of flexural bending tests, it was concluded that the presented image-based digital model could be suitable for predicting the mechanical behavior of asphalt mixtures if all the mechanical properties of the different phases are available (Huang et al., 2016).

Rami et al. (2017) presented a computational microstructure model using multiple two-dimensional finite element microstructures as an alternative and efficient approach to predict the actual 3D fracture behavior of asphalt mixtures. The 2D microstructures generated using image processing techniques (Figure 2.6) and the simulation results were able to capture the 3D viscoelastic fracture behavior. The study found that multiple 2D microstructures can adequately represent the complex viscoelastic fracture behavior of 3D mixtures, which significantly reduces the experimental and computational costs (Rami et al., 2017).

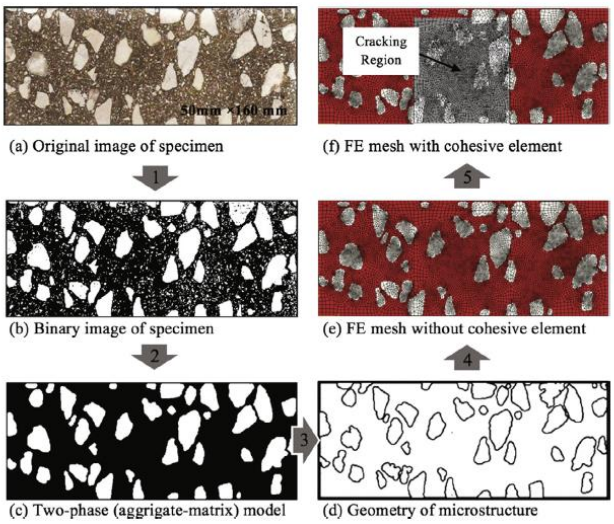

Figure 2.6. Steps to create 2D finite element microstructure (Rami et al., 2017)

Kollmann et al. (2019) applied two-dimensional cohesive zone modeling (CZM) techniques to simulate the microscale crack initiation and propagation in asphalt mixtures. X-ray computed tomography (X-ray CT) and digital image processing (DIP) were used to reproduce the microstructure of asphalt samples in finite element simulations. To validate the FE model, the maximum reaction forces of eleven samples were evaluated in the simulated IDT test and compared with the experimental results. The results showed very good agreement when comparing the simulation results and the experimental results (Kollmann et al., 2019). Zhang et al. (2019) used digital images of two-dimensional sections of the laboratory samples to construct the ideal binary mixed RAP mixtures. Finite element analyzes were performed to determine the modulus values of the digital RAP mixtures.

Zhao et al (2020) used X-ray CT scanning technology to obtain a large number of internal mesostructured images of asphalt mixtures and image-based finite element modeling to construct 2D FE models to simulate beam bending tests. The model was verified by comparing the simulation and laboratory test results and it was found that the 2D FE models were able to reduce the number of tests and improve the computational efficiency while ensuring the accuracy of the BBT simulations (Zhao et al., 2020). Another microstructure-based multiscale finite element method was

investigated by Sun et al. (2020). An image-based 2D finite element model was used to investigate the effects of temperature fields on damage development in asphalt pavements under traffic loading. The results showed that the developed multi-scale FE model, provides insight into the damage behavior of asphalt pavements under temperature exposure (Sun et al., 2020). Du et al. (2020) presented the study on the development of a multiscale finite element model to quantitatively investigate the distributions of cohesive and adhesive damage and their effects on the overall damage behavior of asphalt pavements. The microstructure of the asphalt mixture and the macrostructure of the asphalt pavement were simultaneously included in a single 2D finite element model. The results showed the effects of heterogeneity on stress concentrations, which could be the main factors for pavement cracking (Du et al., 2020).

Wang et al. (2021b) investigated the effect of ultraviolet ageing on cracking at the interface of an asphalt mortar modified with warm crumb rubber. Digital image correlation technique and finite element method were combined to determine the factors affecting the crack propagation path at the interface. The model created with ABAQUS® showed good agreement with the test results (Wang et al., 2021b).

Many other researchers have applied image analysis and micromechanical FE methods to investigate the effects of microstructure of AC on its complex behavior (Kose et al. 2000; Sadd et al. 2003; Al-Rub et al. 2011; Dai et al. 2006; Sefidmazgi et al. 2012). Based on the literature review on finite element analysis of asphalt mixtures, image-based 2D plane strain FE modeling is adopted in this study. Laboratory compacted and cut specimens are used to generate 2D images of the specimens using a flatbed scanner. The phases of the aggregate and binder are determined from the processed images and the model is created from the two-phase microstructure of the asphalt mixture samples.

2.4 Digital Image Processing

The use of image analysis techniques to study the microstructure of asphalt mixtures has increased dramatically in recent years. The first step in digital image processing is the acquisition of images in the computer environment by an image acquisition method. The images, acquired by either destructive or non-destructive methods, provide a good estimate of the geometric structure of asphalt pavements in the finite element models. In the destructive method, the samples have to be cut into slices to obtain a smooth surface from which images can later be taken with flatbed scanners or digital cameras (Figure 2.7). X-ray computed tomography, on the other hand, is a non-destructive imaging method widely used to obtain 2D and 3D images of the internal structure of asphalt mixtures (Figure 2.8). After acquisition, image enhancement techniques such as smoothing, contrast stretching, etc. are applied to the raw images.

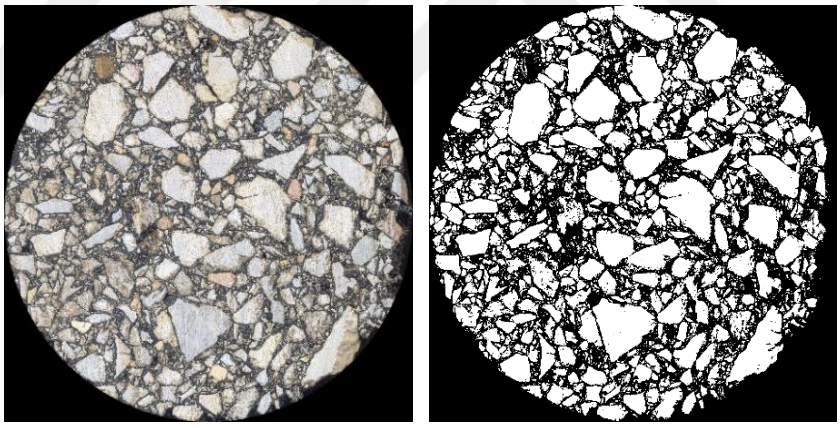

(a) (b)

Figure 2.7. Example of an image capture: a) Captured by a flatbed scanner, b) Resulting binary image

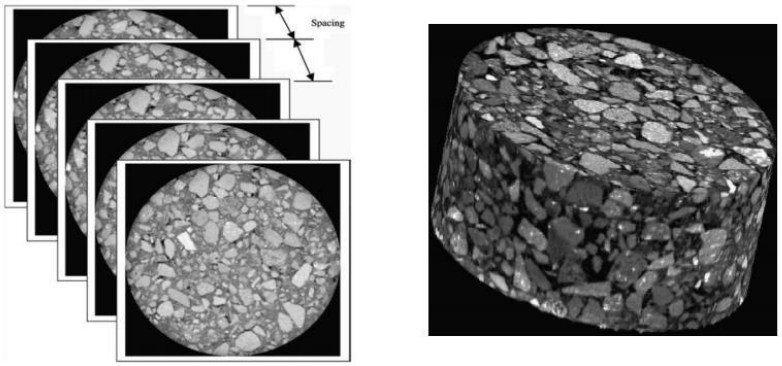

(a) (b)

Figure 2.8. (a) Cross-sectional images produced from X-ray imaging, (b) Visualizing in 3D of an asphalt concrete specimen (Arshadi, 2015)

2.4.1 X-Ray Tomography

In this non-destructive method, the X-rays penetrate the scanned material and are partially absorbed depending on the composition and density. The remaining X-ray intensity (number of photons per second) is then measured by detectors to produce an intensity profile called an image. Several studies have shown the potential application of X-ray CT technology to characterize various properties or to quantify the air void distribution of AC mixtures.

Masad et al. (1999) proposed several parameters to measure aggregate orientation, gradation and air void distribution in asphalt mixtures. In their study, X-ray tomography-based image analysis techniques were used to characterize the internal structure of asphalt concrete mixtures. The percentage air voids measured from X-ray tomography images agreed well with the air voids measured in the laboratory (Masad et al., 1999).

Mased et al. (2002) investigated the air void distribution in asphalt mixtures using the X-ray CT system together with image analysis techniques, and the air void distribution in Superpave gyratory compacted specimens exhibited a bathtub shape. Tashman et al. (2002) investigated the air void distribution in circular compacted

specimens using image analysis techniques and X-rays CT. The method for non-destructive characterization of air void distribution showed that the air voids were more concentrated in the upper and lower areas in contact with the bottom plates and in the outer areas in contact with the mold (Tashman et al., 2002).

In another study, image analysis techniques were used by Al-Rousan et al. (2007) to quantify the shape characteristics of aggregates. It was found that image techniques have been shown to be able to objectively quantify the shape features of aggregate particles (Al-Rousan et a., 2007).

Zelelew et al (2008) presented an automated digital image processing algorithm called Volumetrics-based Global Minima (VGM) thresholding algorithm, for processing asphalt concrete X-ray computed tomography images. The proposed VGM method significantly improved the X-ray CT images significantly (Zelelew et al., 2008).

Hu et al. (2015) investigated the effects of the internal structure of asphalt mixtures on deformation at high temperatures. The internal microstructures of the samples were determined using X-ray CT data, and three-dimensional models were processed using digital image processing technology. After finding that the results of the improved image segmentation algorithm could effectively separate the target and background, they concluded that the method developed in their study is an effective tool for investigating high-temperature failure mechanisms of asphalt mixtures (Hu et al., 2015).

Han et al. (2021b) investigated the influence of aggregate morphology on the dynamic modulus of asphalt mixtures. A two-dimensional digital image processing method was used to obtain statistical laws of fractal dimension and aspect ratio of aggregate profiles. The results showed the significant influence of aggregate morphology on the dynamic modulus of asphalt mixtures (Han et al., 2021b).

2.4.2 Cameras and Scanners

Over the years, X-ray tomography has gained acceptance in the field of imaging asphalt mixtures, but the high cost of the procedure remains a problem. Therefore, researchers have been trying to find a way to improve the accuracy of images when imaging HMA components and make visualization a more effective tool. 2D scanning is an important alternative in this context. Charged-couple device (CCD) is a special type of image capture device that detects light intensity and is considered the backbone of image capture in both scanners and cameras.

One of the first studies on 2D microstructure characterization of asphalt mixtures was conducted by Yue et al. (1995). A flatbed scanner was used to convert images into digital files that could be processed by computer. The resolution of the scanner was set to the highest practical value to increase the accuracy of the measurements. The digital image processing method, which seemed to be a major revolution at the time, was successfully used to quantify the distribution, orientation and shape of coarse aggregates in AC mixtures (Yue et al., 1995).

Hunter et al. (2004) investigated the structure of the internal aggregate-bitumen matrix of laboratory-produced specimens using different compaction methods and compared it with mechanical performance. Three compaction methods were used: Gyroscopic, vibratory and slab compaction, and 2D images taken with a digital camera were analyzed using image analysis techniques. Overall, the quantitative information provided by the image analysis techniques on the asphalt mixture samples showed that the aggregates are circumferentially aligned in gyratory and vibratory compaction (Hunter et al., 2004).

Coenen et al. (2012) used two-dimensional image analysis to characterize aggregate structure. The orientation of the aggregate in the image, the spatial distribution and the contact zones were analyzed as crucial features to describe the aggregate structure. Laboratory compacted asphalt concrete samples were used to capture the 2D images directly with a flatbed scanner. The images were then processed and

analyzed. In addition to improving the image philter method by matching it to the actual measured volumes, their work also proved that it can be used to quantify gradation (Coenen et al., 2012). Bruno et al. (2012) used an image analysis method to automatically detect aggregates in asphalt mixtures from planar images without having to separate bitumen and aggregates. The study was based on 2D digital images taken with a digital camera from different slices of asphalt mixture cores. The proposed method allowed estimation of aggregate gradation without time-consuming tests that not only require specialized laboratory equipment but also pose a health risk to users due to the use of solvents and other hazardous substances (Bruno et al., 2012).

Ozen & Guler (2014) proposed a method for determining the particle size distribution of aggregates from 2D cross-sectional images of concrete samples. The images were obtained using a flatbed scanner and an algorithm was introduced to determine the optimal threshold for image analysis of the cross-sections. The result of the study proved to be of practical value for the evaluation of concrete in terms of the degree of segregation (Ozen & Guler, 2014).

Another study on the particle size distribution of asphalt mixtures was conducted by Moon et al. (2015). A simple two-dimensional digital image processing technique was applied to obtain aggregate gradation curves. A flatbed scanner was capable of generating the required RGB images. Following the procedure, the diameters of the aggregates in the binary image were determined and used to generate aggregate size distribution curves, which were then graphically and statistically compared to the original mixture gradations. While predictions were good for particle sizes of 4.75 mm or more, poor gradations were determined for particle sizes of 2.38 mm or less (Moon et al. 2015).

Shi et al. (2020) investigated in-depth analyzes of the mechanisms involved in coarse aggregate movement and rutting under stress. A digital image processing technique was employed and a digital camera was used to obtain cross-sectional images of asphalt mixtures. Finally, a mesostructural model of coarse aggregate movement was proposed (Shi et al., 2020).

Many other studies, whether using a digital camera or a flatbed scanner, have been conducted to model the microstructure of asphalt mixtures using 2D digital imaging techniques and have demonstrated their effectiveness and accuracy (Tashman et al., 2011; Bessa et al., 2012; Vadood et al., 2013; Obaidat et al., 2017).

In this study, a flatbed scanner is used to capture 2D color images of laboratory compacted samples from their sawn surfaces. A series of image processing techniques are then applied to create the microstructure of the asphalt samples in the finite element model. The details are described in the following sections. It is concluded that 2D digital image processing is a very effective, time-saving and accurate method to work with.

2.5 Material Modeling

As mentioned earlier, asphalt mix is a multiphase material containing aggregates, binders and air voids. The bearing capacity of the asphalt mix, either through the stiffness of the mastic or through the contact between the aggregates, depends largely on these components. In other words, the performance of the HMA is determined by the mix properties resulting from the properties of each component (Kose, 2002). Each of these components is modeled differently in the finite element method.

2.5.1 Aggregate

Some researchers have looked for ways to reduce the computational costs and resources caused by high element numbers in the finite element method. Modeling aggregates as rigid bodies was one of these methods. This was useful because aggregates are assumed to be rigid compared to the binder under the loads that a pavement is subjected to during its lifetime. The rigid bodies in a finite element model are represented by a single reference node and move through space without changing their shape. The advantage of such elements over deformable elements is that a rigid body has many fewer degrees of freedom at a reference node, whereas deformable elements have many degrees of freedom and require expensive element calculations to determine the deformations. By neglecting such deformations, modeling a component as a rigid body leads to significant savings in calculations without affecting the overall results.

Kose (2002) used rigid elements to model aggregate particles in his dissertation. Since about 80% of the total mix consists of aggregates, a considerable reduction in computational effort was expected. After comparing the results with those of conventional models, it was found that the results were almost identical (up to the sixth significant digit) (Kose, 2002).

The dissertation by Abbas (2004) dealt with the simulation of the micromechanical behavior of asphalt mixtures using DEM. It was assumed that the aggregates are rigid. This was justified by the significant difference in stiffness between aggregate and mastic, which leads to high deformation within the mastic compared to that of the aggregate (Abbas, 2004). Dai et al. (2006) investigated the behavior of asphalt mixtures with the finite element method, using a combination of rigid and continuum elements for aggregate and asphalt mastic respectively.

Dai & You (2007) also used rigid-body elements to model the aggregate particles in their 2D finite element model. The reason for this was the much stiffer nature of the aggregate compared to the mastic. However, the results showed that the creep stiffness of the mixture was over-predicted at the beginning of the loading period, which was due to the rigid aggregates with infinite stiffness (Dai & You, 2007). In another study, Wang (2007) digitally simulated the asphalt mixtures using a finite element model. To identify and compare the 3D aggregate particles before and after testing, a pattern recognition algorithm was introduced based on the morphological characteristics of the particles. Once the particles were tracked, the movements of the particles, such as rotation and translation, were quantified. In addition, the particles were assumed to be rigid bodies and their deformation under wheel load was neglected, so that the permanent deformation of the asphalt concrete was mainly due to the rotation and translation of the particles (Wang, 2007).

Alternatively, a more common assumption, the linear elastic material law, has been used in the literature to simulate the aggregate particles in finite element models or discrete element analyzes. Papagiannakis et al. (2002) analyzed the microstructure of asphalt concrete using the finite element method based on X-ray images. The two phases of the microstructure, aggregate and binder, were modeled as linear elastic and viscoelastic, respectively. In another study, You & Dai (2007) used the elastic modulus of the aggregate and the viscoelastic properties of the mastic to predict the dynamic complex modulus of HMA in a micromechanical finite element model. They also investigated the sensitivity of the aggregate modulus and found that a very high aggregate modulus does not significantly affect the prediction of the E^* of HMA, as the curve becomes flatter when the aggregate modulus is above the value of 50 GPa (You & Dai, 2007).

Adhikari & You (2008) also used the elastic modulus of aggregate and dynamic modulus of sand mastic in microstructure-based models with different elements to predict the complex mixing moduli. Graham (2009) used an isotropic linear elastic material model with elastic modulus and Poisson's ratio to simulate aggregates in his

dissertation. You (2013) also investigated two- and three-dimensional microstructural modeling of asphalt composites, considering aggregates as a linear-isotropic elastic material.

Another linear elastic property (Young's modulus and Poisson's ratio) for aggregates was used by Aragao et al. (2011) in their study. They measured the elastic modulus of coarse aggregates using the nanoindentation technique. After comparing the results of the model with the experimental results, good agreement was found (Aragao et al., 2011).

Furthermore, the method of estimating the aggregate modulus instead of direct measurement is a fairly common approach. Coleri et al. (2012) estimated the aggregate modulus to be 55 GPa instead of performing tests, justifying this with the small influence of aggregate stiffness on shear deformation at high temperatures. However, it should be noted that the modulus of the aggregate has a significant influence on the modulus of the asphalt mixture at low temperatures (You et al., 2008).

Huang et al. (2016) proposed an image-based finite element approach to predict the viscoelastic behavior of asphalt mixtures. In the 3D model, the aggregates and air voids were assumed to be linearly elastic materials, while the asphalt mastic phase was considered to be linearly viscoelastic. The linear elastic properties of the aggregate, the modulus of elasticity and Poisson's ratio, were estimated.

Another assumption of linear elastic properties of aggregates in a finite element model was made by Kollman et al. (2019). They chose an elastic modulus of 55 GPa and a Poisson's ratio of 0.2 to define the material properties in the 2D finite element model. Other studies used the linear elastic material model for the aggregate particles within their microstructure-based finite element models (Sun et al. 2020; Zhao et al. 2021; Wang et al. 2021a).

It should be noted that Luo & Lytoon (2011) investigated inverse and forward micromechanical modeling of asphalt mixtures and based on their work, valid results were found for frequency dependence of aggregate moduli and unexpected stiffening of aggregates with increasing age of mixtures, suggesting that a viscoelastic law may be more appropriate for aggregates. It was noted that this result could be due to the binder absorption of the aggregates (Luo & Lytoon, 2011). No further studies on this topic were found.

After a thorough review of the existing literature, this study also uses the linear elastic material model to characterize the aggregates in the finite element model. It has been shown that this approach is much more widely used than the others and can simulate the behavior of aggregates in practice much better.

2.5.2 Asphalt Binder

Asphalt binder is a viscoelastic material, which means that its behavior depends on the rate (or time) of loading and temperature. Therefore, it should be modeled to determine its stress-strain relationship and predict the mechanical response under a given loading condition. The relationship between the nature and propagation of stresses in asphalt mixtures and the time-dependent (i.e., viscoelastic) properties of the asphalt binder has been demonstrated in studies, so that it became almost impossible to characterize asphalt concrete without the viscoelastic properties of the asphalt binder. Linear viscoelasticity theory has been widely used by researchers because of its simplicity. In this method, combinations of springs and dashpots represent the elastic and viscous components of viscoelastic behavior, respectively. This results in various viscoelastic models such as the Maxwell model, the Voigt model and the Burger model. The Maxwell model is a combination of spring and dashpot in series; the Voigt model is a combination of both in parallel. Burger's model is a combination of these two entities in series (Figure 2.9).

Many researchers have used these models since the early 1940s to describe the rheological behavior of asphalt binders (Lethersich, 1942; Saal & Labout, 1958; Meegoda & Chang, 1994). Although Burger's model is better suited to simulate the behavior of asphalt binders compared to Kelvin's and Maxwell's models, it has been quite difficult to do so. Kose (2002) attempted to integrate Burger's model into ABAQUS® in his dissertation, but due to the obstacles involved, the formulation of viscoelasticity in the frequency domain was eventually adapted. In their study, Grabowski et al. (2002) found that while the models of Maxwell, Voigt and Burger were suitable for characterizing viscoelastic behavior, Burger's model had significant limitations as the curves were not fully compatible with laboratory results. They indicated that the generalized Maxwell model was the most appropriate (Grabowski et al., 2002). Finally, more complex models were developed, such as the generalized Maxwell model, which consists of N Maxwell units connected in parallel, and the generalized Voigt model, which consists of N Voigt units in series (Figure 2.10).



(a) Maxwell Model

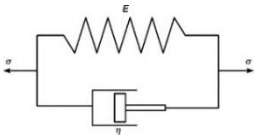

(b) Voight Model

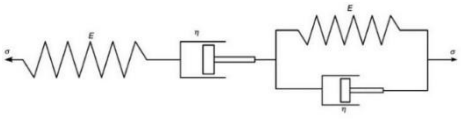

(c) Burger’s Model

Figure 2.9. Illustration of rheological models

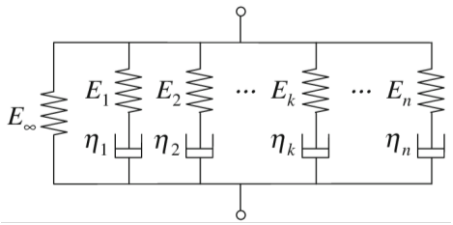

(a) Generalized Maxwell Model

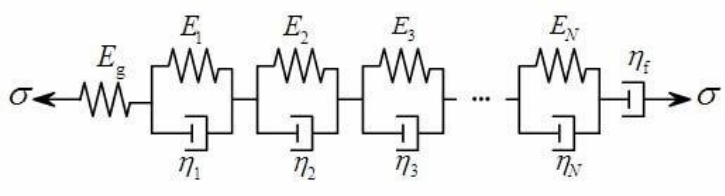

(b) Generalized Voigt Model

Figure 2.10. Rheological models with multiple Maxwell/Voigt units

The generalized Maxwell model, also known as the Wiechert model, is the most general form of linear viscoelasticity. It takes into account the fact that relaxation occurs in a time distribution rather than at a single point in time, and that within the model the same strain is distributed to all elements. An additional isolated spring (E_∞) is added to represent arrheodictic behavior (i.e., materials that do not exhibit steady-state flow behavior). Within the model, each Maxwell element is expressed:

$$\dot{\varepsilon}_k = \frac{\dot{\sigma}_k}{E_k} + \frac{\sigma_k}{\eta_k}, \quad k = 1,2, \ldots, n \tag{2.4}$$

where E_k is the elastic modulus of the spring; η_k is the viscosity of the dashpot. If a constant strain ε_0 is imposed at $t = 0$, the solution of Eq. 2.4 is obtained as:

$$\sigma_k(t) = \sigma_{k,0}\, exp\left(-\frac{t}{\tau_k}\right) \tag{2.5}$$

$$\tau_k = \frac{\eta_k}{E_k}, \quad \sigma_{k,0} = E_k \varepsilon_0 \tag{2.6}$$

where $\sigma_{k,0}$ is the initial stress at $t = 0$; τ_k is therelaxation time of the kth element. Then the total stress $\sigma(t)$ and the relaxation modulus $E(t)$ can be calculated as:

$$\sigma(t) = E_\infty \varepsilon_0 + \sum_{k=1}^{n} \sigma_{k,0} \tag{2.7}$$

$$E(t) = \frac{\sigma(t)}{\varepsilon_0} = E_\infty + \sum_{k=1}^{n} E_k \exp\left(-\frac{t}{\tau_k}\right) \tag{2.8}$$

where E_∞ is the long-term modulus once the material is totally relaxed. By relating the modulus of elasticity to the long-term modulus:

$$E_0 = E_\infty + \sum_{k=1}^{n} E_k \tag{2.9}$$

where E_0 is the instantaneous modulus. Therefore, an alternative can be derived as:

$$E(t) = E_0 - \sum_{k=1}^{n} E_k \left[1 - \exp\left(-\frac{t}{\tau_k}\right)\right] \tag{2.10}$$

A pair of E_k and τ_k is called as a Prony pair.

The Prony series form, which follows the generalized Maxwell model, has been preferred by many researchers in fitting asphalt rheological test data because of its precise fit and efficiency. Papagiannakis et al (2002) used a generalized Maxwell model in the form of a Prony series to describe the viscoelastic behavior of asphalt binders and implemented it in finite element analysis software. Figure 2.11 shows the effectiveness of the model (Papagiannakis et al., 2002).

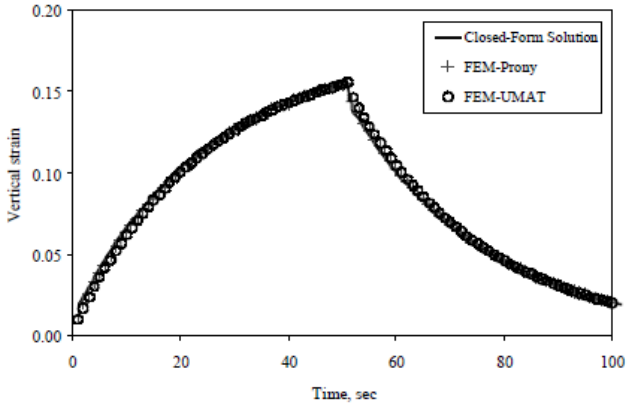

Figure 2.11. Verification of the linear viscoelastic binder model; plane stress, $\Delta t = 1s$ (Papagiannakis et al., 2002)

Dai & You (2008) applied a regression fitting method to the creep compliance test data using a generalized Maxwell model. The model included one spring and four Maxwell elements in parallel and successfully predicted the complex modulus of asphalt mixtures. Arshadi (2015) also used the same model with one spring and four Maxwell units in his dissertation. The model was validated through a series of laboratory experiments. There are several other studies in the literature that use the Prony series model to predict the viscoelastic behavior of asphalt binders (Mulungye et al. 2007; Aragao et al. 2011; Al-Rub et al. 2012; Coleri et al. 2012; Wang et al. 2013; Gu et al. 2016; Arshadi & Bahia 2015; Huang et al. 2016; Ling 2016; Shanbara et al. 2018; Kollmann et al 2019; Cardenas et al. 2021; Bekele et al. 2021; Alae et al. 2021).

In this study, the linear viscoelastic material model of asphalt binder is represented by a Prony series method based on the generalized Maxwell model. In order to determine the master curve of the complex shear moduli, frequency sweep tests are performed on the binder. Then, the Prony series parameters are determined by regression analysis. Finally, the Prony series are used as input parameters for the viscoelastic behavior of the asphalt binder in the FEM software ABAQUS®.

2.5.3 Air Voids

Although X-ray CT imaging can identify air voids in asphalt concrete to some extent based on density differences between different phases, air voids cannot be reliably detected with current 2D imaging techniques because there is no color contrast between air voids and background asphalt. In addition, most air voids are inevitably filled during the cutting process due to the smearing of the binder. Therefore, the inclusion of air voids in finite element modeling of asphalt concrete has always been a challenge for researchers.

Sepehr et al. (1994) used small stiffness values for some elements in their finite element model. It was a very rough estimate, but the analysis showed the significant effect of air voids on the deflection of the pavement (Sepehr et al., 1994).

One way to capture air voids is to fill them with a substance that is a different color than the binder and aggregate, so that they can be easily seen in the image. In his image-based finite element model, due to the importance of air voids, Kose (2002) made considerable efforts to capture the air void content and distribution using a special impregnation method. He tried to use a fluorescent dye together with epoxy resin to impregnate the air voids in the samples. With this mixture of resin and dye, the air voids were successfully detected when using scanners (Kose 2002).

Yongping (2007) determined the three-phase microstructure of AC using X-ray tomography images. Based on the density differences of the three phases (i.e., mastic, aggregate and voids), the brightness of each component differed from each other. After separating the three groups of elements, the air voids were removed during the loading steps in the simulations (Yongping, 2007).

Coleri et al. (2012) developed a micromechanical finite element model from X-ray CT images. Based on the intensity differences between aggregates, air voids and mastic, they successfully distinguished these three different structures using X-ray images (Figure 2.12). Subsequently, the region of air voids was excluded from the material structure and left as empty, as it does not exhibit stiffness (Coleri et al. 2012).

In another microstructural modeling of asphalt concrete, You (2013) did not consider the effect of air voids due to the high computational cost. Discrete 3D element models were created from 2D X-ray CT images and although the distribution of air voids could be captured, the air voids and the mastic were considered as one phase, the matrix (You, 2013).

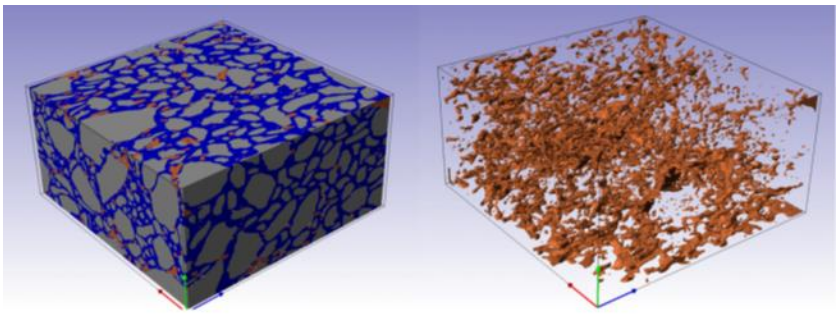

(a) (b)

Figure 2.12. Three-dimensional asphalt mixture model from X-ray CT images: (a) Image with all three domains, (b) Air void distribution with in the asphalt mixture (Coleri et al. 2012)

Huang et al. (2016) created an image-based three-dimensional FE model containing aggregates, asphalt mastic, and air voids. X-ray technique was used to detect the internal microstructure of asphalt mixtures. After successful localization, the air void phase was considered as an elastic material with a Young's modulus of 0.5 MPa and a Poisson's ratio of 0.3.

Another study, based on 2D finite element microstructural analysis, assumes two primary phases: Aggregates and a binding matrix phase containing asphalt binders, fine aggregates and entrapped air voids (Rami et al. 2017).

Kollmann et al. (2019) investigated the microstructural fracture behavior of asphalt mixtures using the finite element method. To build the model in ABAQUS®, the X-ray CT method was used, which contains only aggregates and air voids. The regions corresponding to the air voids were then cut out of the model (Kollmann et al., 2019).

Arshadi (2015) attempted to use an artificially created circular geometry in the macroscale images to represent air voids based on the bathtub shape distribution found by (Masad et al., 2002). Subsequently, the air voids were represented by empty spaces in ABAQUS® without assigning any material properties to them (Figure 2.13). Ling (2016) later used the same method.

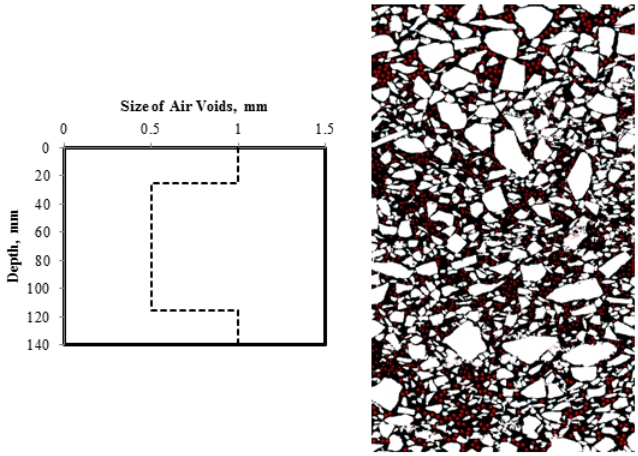

Figure 2.13. Distribution of air voids based on the "bathtub" shape (Arshadi, 2015)

Due to the difficulties in identifying air voids in 2D image processing techniques and the fact that this study is concerned with other aspects of image-based finite element modeling, air voids are not evaluated in this study. However, air voids have a major impact on the overall strength of asphalt concrete and it is of great importance that these air voids are accurately and effectively considered and integrated into the finite element method in future studies.

2.6 Mechanical Testing of Asphalt Mixtures

The traditional method for modeling and validating the microstructure of asphalt concrete in a finite element model is to compare the model results with the results of empirical testing methods, as many researchers have done. However, the type of mechanical testing chosen is very important to be able to observe the influence of the micromechanical properties on the macromechanical performance of the asphalt mixture. In addition, a numerical model may give good results under a certain test condition, but may not be as accurate under completely different conditions, e.g., due to the methods used, the handling, the assumptions made or the level of precision chosen. To ensure that the numerical model in this study is accurate under different conditions, three different test methods were chosen: Resilient modulus (RM) test, repeated creep (FN) test and indirect tensile fatigue (IDTF) test.

2.6.1 Resilient Modulus Test

Although asphalt concrete exhibits viscoelastic behavior (time and temperature dependent response to applied load), its behavior under repeated loading can be considered elastic if sufficient time is allowed for strain recovery between load repetitions. Several parameters are used to determine the moduli of asphalt concrete, including the elastic modulus or resilient modulus, the complex modulus and the dynamic modulus. The resilient modulus (M_R), the ratio between the applied stress and the recoverable strain, is used to describe material behavior, evaluate material quality, and predict pavement performance in many pavement design procedures. The modulus of elasticity is determined from a repeated load. The peak stress and recoverable (elastic) deformation values are used to calculate an M_R value. The size and loading frequency of the test are designed to simulate the dynamic loads applied to the pavement structure by the traffic.

Measuring the elastic modulus of pavements is a complex and difficult procedure because it is a non-linear, stress-dependent measurement. Nevertheless, the determination of the modulus of elasticity is critical to any mechanistic-based pavement design or analysis procedure.

There are several methods for determining the resilient modulus. Measurement by the indirect tension method (ASTM D 7369, 2020) is the most common form of stress-strain measurement used to characterize the elastic properties of asphalt concrete. The tests are usually performed on cylindrical specimens subjected to compressive loading on two opposite sides, resulting in a relatively uniform tensile stress acting perpendicular to and along the diameter plane of the applied load (Figure 2.14). First, the Poisson's ratio is calculated from either the instantaneous or the total vertical and horizontal deformation values. The Poisson's ratio is independent of the specimen diameter if the ratio between the width of the stress strip and the specimen diameter is 1/8 (Zhang et al., 1997). The resilient modulus

can then be calculated from the Poisson's ratio and the recoverable horizontal deformations (Zhang et al., 1997).

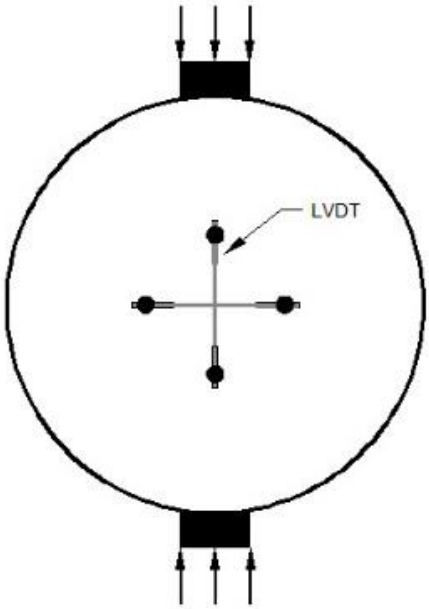

Figure 2.14. Schematic representation of RM test setup

The 1986 AASHTO Pavement Design Guide recommendation to use of M_R to characterize pavements has led to a rapid increase in the use of this type of testing. Various test protocols and methods have been developed to determine the indirect resilient modulus of asphalt concrete (ASTM D 7369, 2020; Barksdale et al. 1997; AASHTO TP -31, (1996); Roque & Buttlar 1992; Buttlar & Rogue 1994; Roque et al. 1998; SHRP-LTTP P07 2001; Witczak 2002).

Boudreau et al. (1992) studied the M_R of laboratory compacted asphalt concrete specimens and found that the values of M_R depended on many factors, such as the system used, the test equipment, the compaction method, the temperature, the frequency of loading, the duration of loading and the degree of diametrical strain caused by the loading. It has also been noted that M_R can be measured as total or instantaneous, which differs in the interpretation of recoverable strain at unloading (Boudrequ et al. 1992). Shalaby et al. (2004) found that the values of resilient modulus vary greatly depending on the mix design and testing method. McCann &

Sebaaly (2003) concluded that the modulus of elasticity is the best method for evaluating the moisture sensitivity of mixtures when the difference in strength between the unconditional and conditional samples is small.

In this study, the resilient modulus of specimens compacted in the laboratory is determined using the indirect tensile test method. The indirect tensile test uses aspects of the ASTM D7369 (2020) test standard. Details can be found in the following sections.

2.6.2 Repeated Creep Test

Creep in asphalt pavements is the continuous time-dependent deformation under constant or repeated loading. A typical creep curve under repeated loading develops in three stages (Figure 2.15). Under an initial load, the material behaves elastically and sudden deformation occurs as soon as the initial load is applied. The strains at this stage are still fully recoverable. In the primary zone, the pavement continues to deform under continuous load application, but at a decreasing rate, i.e., the permanent strain rate slows down over time. The hardening effect results from compaction and the reduction of air voids. In the second phase, steady-state creep occurs and microcracks develop. The rate of permanent deformation becomes almost constant and the slope of deformation is almost linear in this zone. In the final zone, the rate of permanent deformation increases with further loading cycles and plastic flow of the material occurs. The flow number is referred to as the cycle number at which the tertiary zone begins.

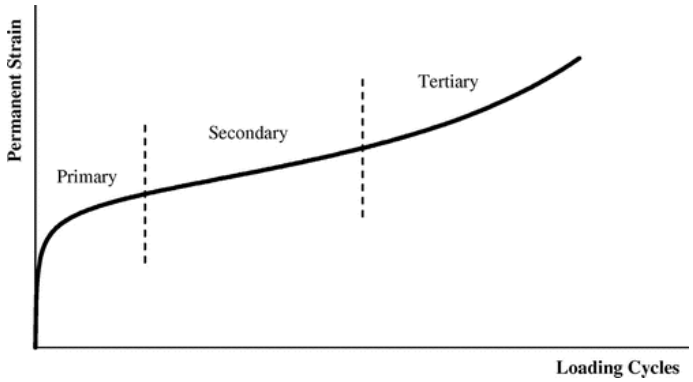

Figure 2.15. Typical creep deformation of asphalt mixtures

The repeated creep test, also known as the flow number test (FN), is described in NCHRP Report 465 (Witczak et al., 2002) as applying a loading cycle of 1 Hz compressive loading with 0.1 s loading and 0.9 s rest. The test procedure is performed at a single effective test temperature with a design stress level and both constrained and unconstrained applications are possible. The test temperature is selected taking into account the service conditions of the asphalt concrete. Once the test conditions are selected and applied, the specimen is tested until it reaches 10,000 cycles or 5% cumulative permanent strain, whichever comes first.

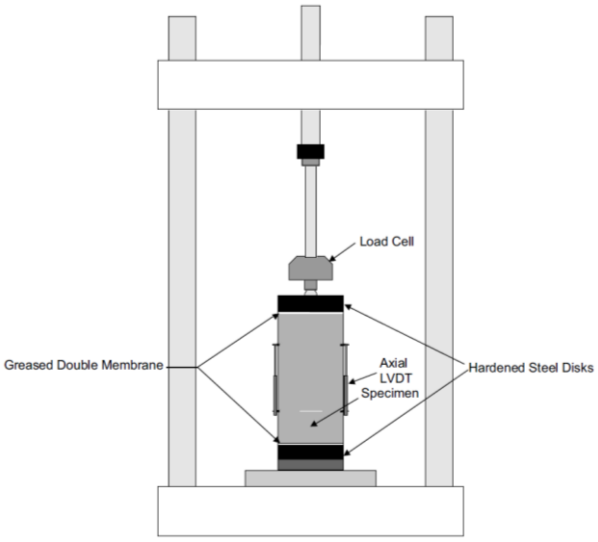

Figure 2.16. Schematic representation of repeated permanent deformation test (Witczak et al. 2002)

A schematic representation of the repeated creep test can be found in Figure 2.16. To ensure that the test response reflects the basic engineering properties, a minimum height to diameter ratio of 1.5 was required (Witczak et al., 2002). The number of cycles versus cumulative permanent axial strain is plotted on a logarithmic scale and the flow number values are determined based on the plastic deformation measurements.

There are several methods for calculating flow numbers, none of which is generally accepted by researchers. Witczak et al. (2002) proposed a polynomial curve fit through five points, and FN was equal to the cycle number where the rate of change of strain is zero. Bonaquist et al. (2003) calculated and smoothed the strain rates for all loading cycles using the moving average method through five points. The flow number is considered to be the cycle number at which the minimum strain rate is reached (Bonaquist et al., 2003). Zhou (2004) used the "three-stage model" to determine the flow numbers from the maximum number of cycles in the second stage. Francken (1977) presented his model for calculating flow numbers from regression constants as follows:

$$\varepsilon_P(N) = AN^B + C(e^{DN} - 1) \tag{2.11}$$

where ε_P is the permanent deformation or permanent strain; N is the number of loading cycles; $A, B, C,$ and D are the regression constants.

The model was developed based on triaxial repeated load tests at different temperatures and stress levels. The regression constant *C* indicates whether plastic failure would occur or not. Since the model is composed of a power and an exponential component, a very good representation of all three stages of permanent deformation test data is possible, including the tertiary stage. Several studies have adopted this model. Ameri et al. (2014) evaluated and compared different methods for calculating the flow number. The results showed that the Francken model had the least variability and therefore this model was recommended. Other studies also confirmed the effectiveness and accuracy of the model (Dongre et al. 2009; Biligiri

et al., 2007). However, in this study, the power model was used to calculate the flow numbers, the details of which are explained in the following sections.

2.6.3 Indirect Tensile Fatigue Test

Fatigue cracking, one of the most important deteriorations of asphalt pavements, is a load-induced deterioration caused by a weakened base course or subgrade, inadequate pavement thickness, excessive repetitive loading, or a combination of these factors. The classic form of fatigue cracking usually starts at the bottom of the HMA, where the tensile stress is highest, and then propagates to the surface. This type of failure, called bottom-up cracking, usually occurs in thin pavements. The other type of top-down cracking, on the other hand, usually starts at the surface of thick pavements where the local stress is high due to the interaction between the tire and the pavement.

There are two main approaches to fatigue crack assessment; stress-controlled and strain-controlled testing. In stress-controlled testing, the cyclic loading of the stress amplitude is kept constant during the test, while the tensile strains increase due to the decrease in material stiffness. In strain-controlled fatigue testing, on the other hand, loads are applied to produce a specific strain amplitude. As the test progresses, these required loads decrease to maintain the strain amplitude.

The indirect tensile fatigue test (IDTF) is one of the most commonly used test methods for measuring the fatigue behavior of asphalt mixtures. This test method also follows a similar design procedure to the resilient test method (Figure 2.17). The prepared samples are placed in a temperature-controlled cabinet and brought to the specified test temperature. The load is applied by means of loading strips arranged parallel to and centered on the vertical diametral plane. Then the haversine load is applied repeatedly with 0.1 s loading time and 0.4 s rest time. The resulting stresses in the sample are shown in Figure 2.18.

The IDT test has many advantages over other tests, such as simple and easy sample preparation, available equipment, and the fact that the stress state at the center is similar to that at the bottom of the asphalt layer. Mehta et al (2005) reported that the IDT test can be used to characterize pavement structures of resilient modulus, indirect tensile strength and failure strain. In this study, indirect tensile fatigue (IDTF) tests are performed according to the test standard EN 12697-24 (2018) to measure the fatigue life of specimens compacted in the laboratory.



Figure 2.17. Indirect tensile fatigue test setup

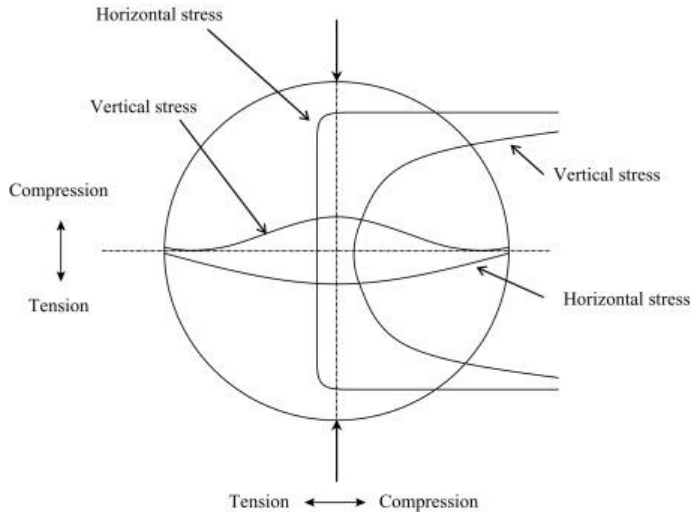

Figure 2.18. Stress distribution in indirect tensile fatigue test

CHAPTER 3

LABORATORY TESTING OF ASPHALT MIXTURES

3.1 Introduction

This chapter describes the methodology for mechanical testing of asphalt specimens. First, the design and preparation of asphalt mixture specimens are explained in detail. The materials and methods used in the development of AC samples are described, including the detailed procedure for developing the Superpave mix designs. The laboratory compacted specimens are produced using two different mix design types and then tested in the laboratory. The experimental program for the performance measurements includes resilient modulus test, repeated creep test and indirect tensile fatigue test. The detailed methodology for conducting these tests has been explained thoroughly. It is worth noting that the results of the laboratory experiments are not given in this chapter. Instead, they are presented in detail in Chapter 5.

3.2 Sample Preparation

One of the main objectives of this study is to ensure that the numerical model works under different conditions. After a thorough review of the literature, as presented in the previous chapter, it was found that numerical modeling of asphalt concrete is a very complex method involving many different variables. Although it works correctly in many cases, it was found that numerical results can vary under different conditions. To ensure the accuracy of the model, two very different mix designs were used in this study.

The first design was based on the traditional asphalt pavement of highways. TGDH (Turkish General Directorate of Highways) specifications for binder course were followed to prepare the specimens to meet AASHTO Superpave volumetric design standards (AASHTO M 323, AASHTO R 35). For the second design, the FAA (Federal Aviation Administration) design criteria for airport runways were adopted using the FAA manual (AC 150/5370-10H). In the FAA design, the specifications were much more stringent and the resulting samples were of relatively higher quality than those of the regular pavement design. The two designs were based not only on different mix specifications, but also on different aggregates, binders and aggregate gradations. The aim was to prove that the numerical model would work under two completely different conditions.

3.2.1 Aggregate

Two different aggregates, limestone and basalt, were used in this study. The limestone aggregate was supplied from Ankara, Yapracık region, and has a relatively light color. The basalt aggregate, which came from Istanbul, Ağaçlı, had a darker color. Basalt was used for the FAA design, while limestone was used for the TGDH design. The measured physical properties of the two aggregates are shown in Tables 3.1 and 3.2. The coarse, fine and filler contents of the aggregates were tested separately and the specific gravities were calculated separately for each group. The overall properties of these two aggregates are very different. The basalt aggregates have relatively lower abrasion values and are of a relatively firmer nature than the limestone aggregates. This was also observed when processing these aggregates in the laboratory environment. For example, during the sawing operations explained in the following chapters, it was observed that the samples with basalt aggregate were more difficult to cut and more stable.

Table 3.1. Physical properties of coarse aggregate (larger than 4.75 mm)

Properties	**Aggregate Type**		**Specification**
	Limestone	**Basalt**	
Bulk Specific Gravity	2.695	2.706	ASTM C127 (2015)
Absorption (%)	0.454	0.679	ASTM C127 (2015)
Apparent Specific Gravity	2.711	2.733	ASTM C127 (2015)
Los Angeles Abrasion (%)	30	14	ASTM C131 (2020)

Table 3.2. Physical properties of fine aggregate (finer than 4.75 mm)

Properties	**Aggregate Type**		**Specification**
	Limestone	**Basalt**	
Bulk Specific Gravity	2.684	2.697	ASTM C128 (2015)
Absorption (%)	0.421	0.780	ASTM C128 (2015)
Apparent Specific Gravity*	2.704	2.756	ASTM D854 (2014)

* (Finer than 0.075 mm)

After calculating the specific gravities of the coarse aggregate, the fine aggregate and the filler separately, the bulk specific gravity of the combined aggregate (G_{sb}) is calculated for each type of aggregate using Equation 3.1.

$$G_{sb} = \frac{P_1+P_2+P_3}{\frac{P_1}{G_1}+\frac{P_2}{G_2}+\frac{P_3}{G_3}} \tag{3.1}$$

where G_{sb} is the bulk specific gravity of the combined aggregate; P is the percentage; and G is the bulk specific gravity of different portions. The percentages of coarse, fine and filler aggregates in the two different blend are given in Table 3.3 together with the calculated specific bulk densities.

Table 3.3. Bulk specific gravity calculation

	Limestone	**Basalt**
Coarse Aggregate (%)	65	62
Fine Aggregate (%)	32	35
Filler (%)	4	3
Calculated G_{sb}	2.692	2.703

3.2.2 Gradation

The specifications (Karayolları Teknik Şartnamesi, 2013) of the Turkish General Directory of Highways (TGDH) were used for the first mix type. The gradation limits for the binder course were determined using TGDH control points. The upper and lower limits of gradation are shown in Table 3.4. Figure 3.1 shows the selected aggregate gradations according to the design limits in an aggregate gradation diagram with scaled to power 0.45. When selecting the aggregate gradation, the maximum density line of 0.45 provides a good indication of the link between the origin and the maximum aggregate size. The design curve in Figure 3.1 was determined through several tries to meet the design specifications.

For the FAA runway design, basalt aggregates were used. The aggregate gradation for the mix design was determined according to the FAA limits (Table 3.5) for the binder course (AC 150/5370-10H). In addition, Table 3.6 shows the limits set by the FAA for aggregate gradation, bitumen content and VMA tolerance. Finally, Figure 3.2 shows the mix gradation and tolerance limits of the FAA design criteria on the 0.45 curve scale.

In both gradations, the binder course design was adopted. The reason for this is that the binder layer contains a larger nominal maximum aggregate size than the wearing course and that a larger proportion of aggregate helps to reduce the amount of work required for image analysis and finite element modeling.

Table 3.4. Aggregate gradation control points for TGDH binder course design

Sieve Size (mm)	Percent Passing		
	Min.	Max.	Design
25	100	100	100
19	80	100	95
12.5	58	80	80
9.5	48	70	68
4.75	30	52	35
2.00	20	40	21.5
0.425	8	22	10
0.180	5	14	6.5
0.075	2	7	4

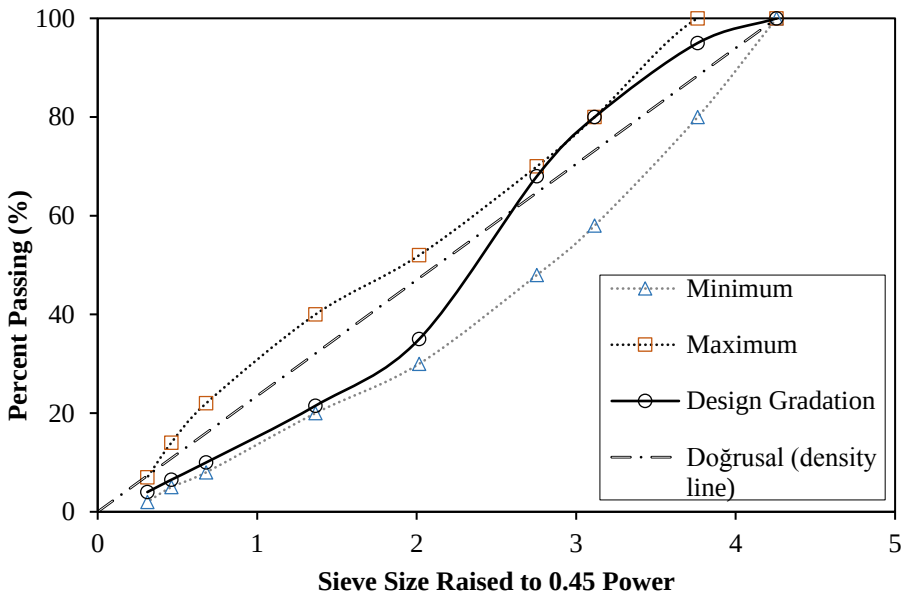

Figure 3.1. Gradation chart for TGDH binder course design

Table 3.5. Aggregate gradation control points for FAA binder course design

Sieve Size	**Percent Passing**		
(mm)	**Min**	**Max**	**Design**
25	100	100	100.0
19	92	100	98.0
12.5	85.3	97.3	91.2
9.5	77.7	89.7	83.7
4.75	42	54	47.7
2.36	26.5	37.1	31.5
1.18	18.6	28.6	23.1
0.6	12.7	20.1	15.7
0.3	8.9	14.9	10.9
0.15	5.5	10.1	6.4
0.075	2.9	6.9	3.0

Table 3.6. Tolerance limits used in FAA binder course design

Sieve No	Sieve Size (mm)	Tolerance Values
1″	25	±6%
3/4″	19	±6%
1/2″	12.5	±6%
3/8″	9.5	±6%
No. 4	4.75	±6%
No. 8	2.36	±5,3%
No. 16	1.18	±5%
No. 30	0.6	±3.7%
No. 50	0.3	±3%
No. 100	0.15	±2,3%
No. 200	0.075	±2%
AC (%)		±0.45%
VMA (%)		-0.5

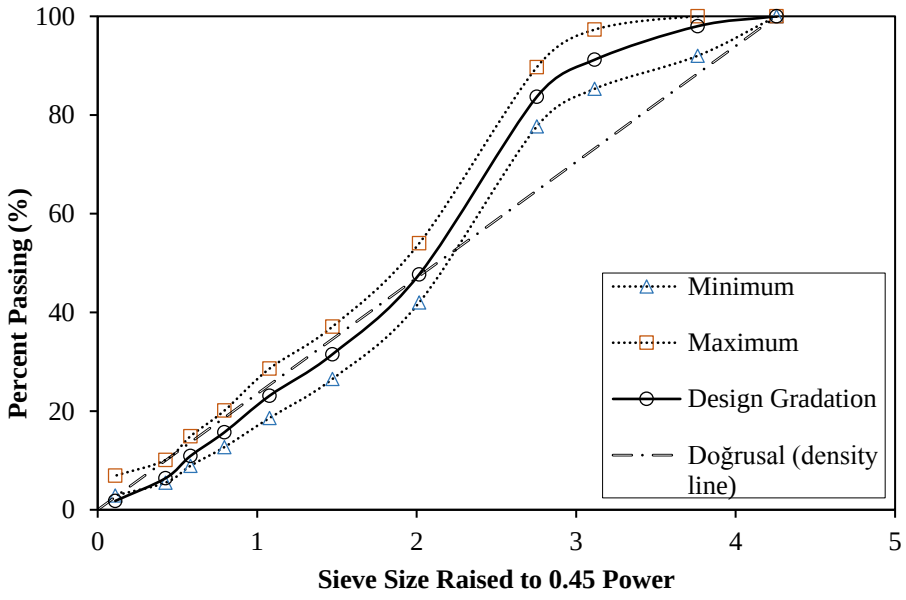

Figure 3.2. Gradation chart for FAA binder course design

3.2.3 Asphalt Binder

Two different asphalt binder types were used in this study. For the TGDH design, a typical 50/70 penetration grade binder was used without any modification. For the FAA design, a polymer modified bitumen (PMB) modified with SBS PG 76-16 was used. The measured properties of the asphalt binders can be found in Table 3.7 and 3.8. In order to determine the rheological behavior of the two asphalt binders, the viscosity tests were performed using the Brookfield rotational viscometer (Figure 3.3). According to ASTM D2493 (2016), the rotational viscosity values were determined at a constant speed of 20 rpm. Starting at 120 °C, viscosity values were measured at 10 °C intervals until the final temperature of 180 °C. The temperature-controlled software was able to reach the target temperatures within 30 minutes, and after a 15-minute equilibrium period, the viscosity values were read at each step. At each temperature, six data points were measured at 30-second intervals and finally the viscosities were calculated from the average values of the data points. The results are shown in Figure 3.4.

Table 3.7. Measured properties of unmodified asphalt binder

Properties	**Measured Value**	**Specification**
Penetration	54	ASTM D5 (2020)
Specific gravity (kg/m^3)	1.036	ASTM D36 (2020)
Softening point	47.5	ASTM D70 (2021)
Flash point (ºC)	+300	ASTM D92 (2018)
Ductility (5 cm/min, 25 ºC)	+100	ASTM D113 (2017)
Kinematic viscosity @135 ºC (cP)	372	ASTM D445 (2021)

Table 3.8. Measured properties of modified asphalt binder

Properties	**Measured Value**	**Specification**
Type and % of modifier	SBS, 4%	-
Penetration	39	ASTM D5 (2020)
Specific gravity (kg/m^3)	1.029	ASTM D36 (2020)
Softening point	74	ASTM D70 (2021)
Flash point (ºC)	+300	ASTM D92 (2018)
Ductility (5 cm/min, 25 ºC)	+100	ASTM D113 (2017)
Kinematic viscosity @135 ºC (cP)	3445	ASTM D445 (2021)



Figure 3.3. Brookfield rotational viscometer

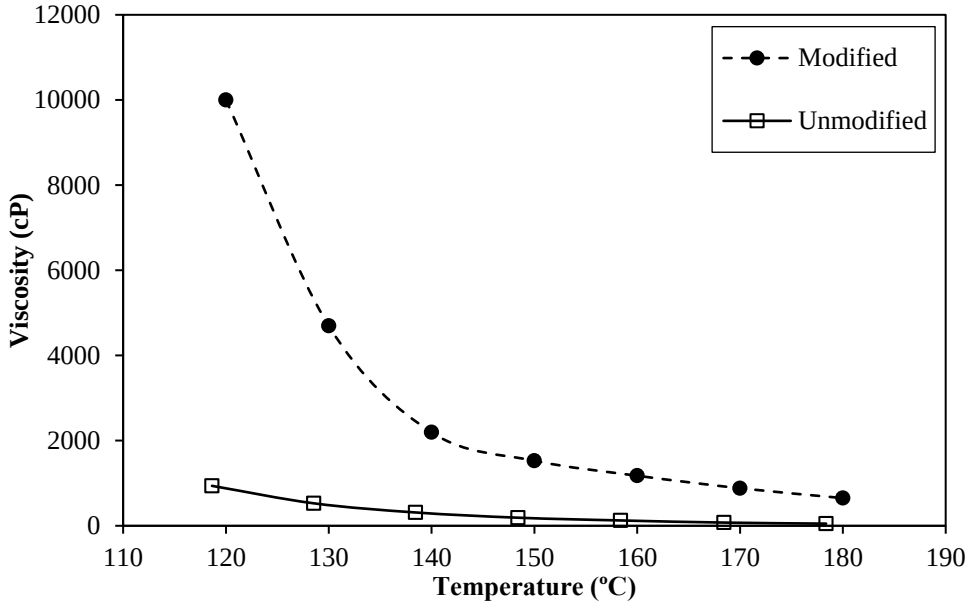

Figure 3.4. Viscosity measurements of neat and polymer modified asphalt binder

3.2.4 Mixing and Compaction Temperatures

After the material characterization of the aggregate and the asphalt binder, it was necessary to determine the mixing and compaction temperatures of the two different types of bitumen to be used in the design. The mixing and compaction temperatures of the asphalt binder are one of the most important factors in the production and laying of hot mix asphalt (HMA) and must be determined with great care. These temperatures play an important role in improving the aggregate coating and maintaining an appropriate density. While optimum temperatures regulate aggregate dryness, workability and compaction, excessively high mixing and compaction temperatures can lead to construction problems, higher emissions, degradation of binders, etc.

3.2.4.1 Unmodified Asphalt Binder

PG 50/70 bitumen with a penetration value of 54 was used for the tests. To determine the mixing and compaction temperatures of the neat binder, the viscosity results were plotted against temperature on a logarithmic scale (see Figure 3.4). The target viscosities for the mixing and compaction temperatures were set at 170 cP and 280 cP respectively. It should be noted that these target viscosity values were selected from the recommended ranges (0.17 Pa.s ± 0.02 and 0.28 Pa.s ± 0.03) of AASHTO T316 (2019). Using Figure 3.5, the mixing and compaction temperatures were determined from the target viscosities.

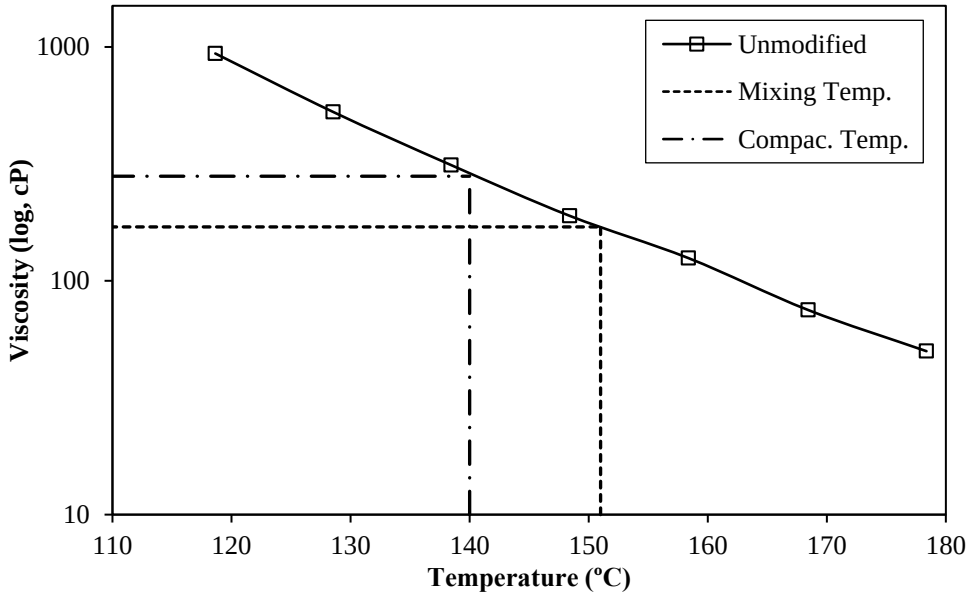

Figure 3.5. Determination of the mixing and compaction temperatures of the unmodified binder

3.2.4.2 Modified Asphalt Binder

In contrast, determining the mixing and compaction temperatures of the modified asphalt binder was a more complicated procedure. It is well known that most mixes prepared by modification should be mixed and compacted at relatively higher temperatures, both in the laboratory and in the field, to achieve the same degree of workability. However, most authorities rely on the asphalt binder manufacturer's instructions to determine mixing and compaction temperatures as there is no specific procedure to follow. Since the application of the Brookfield rotational viscometer method to modified binders would result in dramatic changes in the rheological properties of the binder at excessively high temperatures, a dynamic shear rheometer (DSR) was used to determine the mixing and compaction temperatures of modified asphalt binder (Figure 3.6).



Figure 3.6. Dynamic shear rheometer used in the laboratory

NCHRP Report 648 (West et al., 2010) presented a method (Casola method) for determining the transition point of the binder from viscous to viscoelastic behavior. The frequency corresponding to this transition point has been related to the temperatures at which asphalt binders provide good aggregate coating during mixing and good lubrication during compaction. Therefore, calculating the mixing and compaction temperatures of the modified binder using this point is considered a valid method. The method, also known as the phase angle method, used a DSR with 25 mm parallel plate geometry with a 1 mm gap in oscillating shear mode. The angular frequencies varied from 0.1 to 10 Hz (0.6283 to 62.83 rad/s) with a decade of 10 points, and a shear strain rate of 12% was applied to ensure that the binder behaved in the linear range. The phase angle (δ) and complex shear modulus (G*) were calculated at four different temperatures: 90 ºC, 100 ºC, 110 ºC, 120 ºC (Figure 3.7).

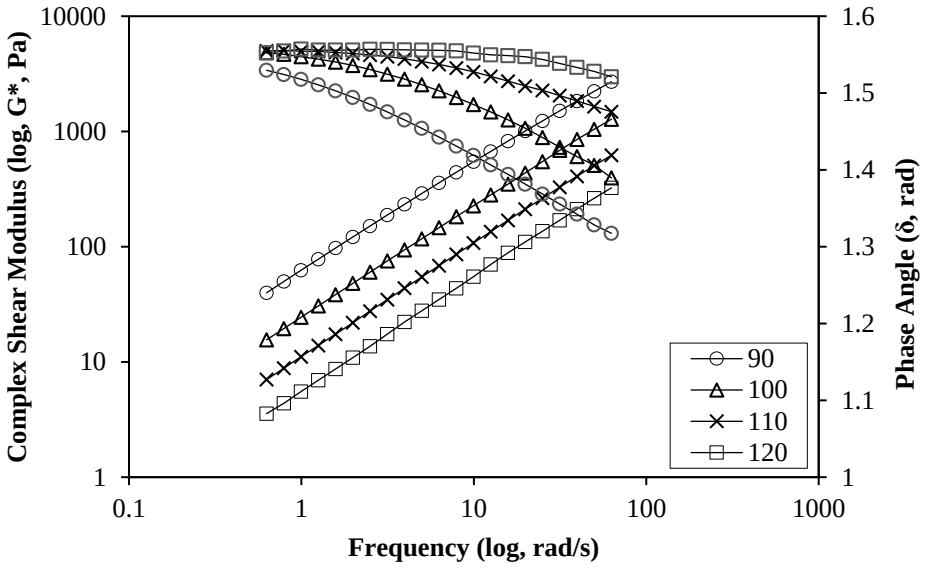

Figure 3.7. Frequency sweep test results of the modified binder at four temperatures

To see the transition from elastic to viscous behavior, the reference temperature was set at 100 ºC. Then the master curve of the modified binder was created with reduced frequencies at the reference temperature (Figure 3.8). The phase angle method states that the transition from viscoelastic to absolute viscous behavior occurs in the region

between the 85º and 90º phase angles of the master curve. Therefore, the frequency corresponding to δ = 88º was chosen as the reference point for the temperature calculations. Finally, the mixing and compaction temperatures of the modified binder were calculated from the test results using the following equations (West et al., 2010):

$$Mixing\ Temperature\ (°F) = 325\omega^{-0.0135} \quad (3.2)$$

$$Compaction\ Temperature\ (°F) = 300\omega^{-0.012} \quad (3.3)$$

where ω is the frequency in rad/s for the phase angle of 88° as taken from the master curve at the reference temperature.

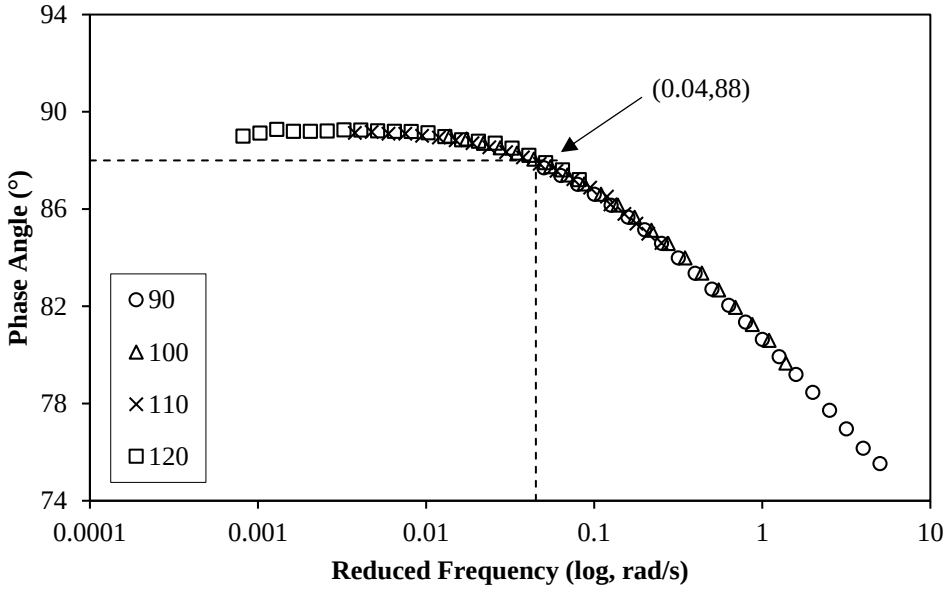

Figure 3.8. Modified binder master curve at 100 ºC

Using the Equations 3.2 and 3.3, 170 ºC was calculated as the mixing temperature and 155 ºC as the compaction temperature. After determining the respective mixing and compaction temperatures for both types of binders, the results are shown in Table 3.9.

Table 3.9. Mixing and compaction temperatures

Binder Type	Mixing Temperature (ºC)	Compaction Temperature (ºC)
Unmodified	151	140
SBS modified	172	156

3.2.5 Superpave Mixture Design

The Superpave mixture design method was one of the key outputs of the Strategic Highway Research Program (SHRP) and was developed to replace older methods such as Marshall and Hveem. This method is much more innovative than the older ones and has a thorough approach that takes into account the climatic conditions, traffic volume and structural cross-section for a given pavement. The old compaction equipment of the Hveem and Marshall methods have been replaced by a modern gyratory compactor, and the compaction effort in the mix design is selected based on the expected traffic volume. The main objective of the Superpave method is to produce a mixture of asphalt binder and aggregate that has sufficient void and asphalt binder content so that the performance expectations of the pavement are met during its service life.

After determining the mixing and compaction temperatures, gradation and physical properties of the aggregates, the Superpave mix design method could be carried out in accordance with the AASHTO T312 (2019) standard. First, the aggregates and asphalt binder were stored in ovens for 2 hours at the mixing temperatures to establish thermal equilibrium. Then batches weighing about 4,900 grams are prepared at the mixing temperature using a laboratory mixer. The batches are then stored in the oven for 2 hours ± 5 minutes at the compaction temperature to simulate short-term ageing (AASHTO R30, 2002). Short-term ageing occurs during the production of asphalt concrete in the mixing plant and then continues during storage and transport.

The batches were filled into molds that have 300 mm height and 150 mm diameter after being conditioned in ovens for 2 hours. The molds were then compacted using the ICT 250 gyratory compactor (Figure 3.9). The kneading action resulting from the rotating shear movements of the machine brings the particles closer together and results in a more densely packed aggregate structure. In addition, the rotational compaction of the samples matches the real compaction of the asphalt concrete in the field resulting from the movement of the tires and is therefore better than the traditional Marshall compaction hammer.



Figure 3.9. Gyratory compactor used in the laboratory



Figure 3.10. Compacted mix design samples

The specimens were compacted under a pressure of 600 kPa with an internal gyroscopic angle of 1.16º at 30 rpm (AASHTO T312, 2016). A special device was used to remove the compacted specimens from the molds while they were still hot, and then the specimens were cooled. At this stage, 30 specimens were produced for each mixture design, for a total of 60 specimens (Figure 3.10). In the final step, volumetric measurements were taken on the samples that had cooled sufficiently to room temperature to determine the mixture designs.

Table 3.10 shows the parameters of the Superpave mixture design procedures. The example compaction curve for sample TGDH-1 is shown in Figure 3.11. During the designs, the density of the samples was evaluated using the compaction curve. The aggregate and asphalt binder were selected so that the compaction curve was 96% of the theoretical maximum specific gravity at the design number of gyrations (N_{design}). In other words, the mix must be compacted to have 4% air voids at the design number of gyrations in the TGDH design. The design number of gyrations were selected based on the estimated traffic volume on site. See Appendix A for more details. For the FAA design, the number of gyrations was set at 75, with a target air void ratio of at least 3.5% (AC 150/5370-10H).

Table 3.10. Superpave mix design parameters

Design Parameter	Selected/Calculated Values	
	TGDH Design	FAA Design
Number of gyrations (N_{des})	100	75
Cumulative traffic assumed	3 to 10 Million	0.3 to 3 Million
Mixing temperature	151 °C	172 °C
Compaction temperature	140 °C	156 °C
Air void content for the design	4%	3.5%

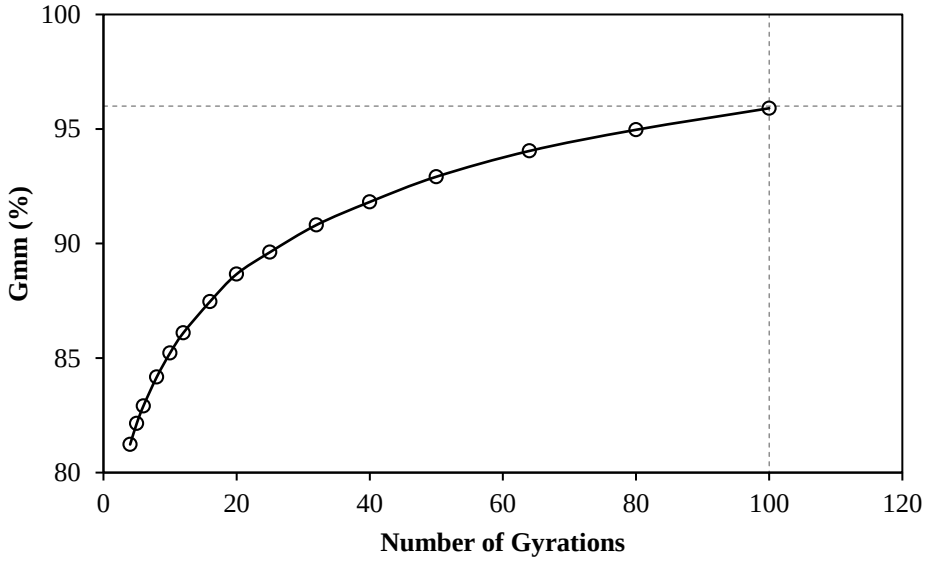

Figure 3.11. Compaction curve of the TGDH-1 design sample

The first 36 specimens were made with 4,900 grams of aggregate and the resulting specimens were about 121 mm high. However, repeated creep tests require specimens with a height of 150 mm and a diameter of 100 mm. Therefore, specimens having heights of more than 150 mm had to be produced. In addition, a certain amount of material has to be cut off at both ends of the test specimens. To achieve such heights, 7,000 grams of aggregate weights were determined after several trials to ensure a minimum height of 150 mm. As can be seen in Figure 3.10, 12 test specimens were produced in this way for each mix design, giving a total of 24 test specimens. However, when compacting larger quantities of test specimens than the

initial design, the required compaction effort should be higher, so that the same physical structure can be achieved. To ensure this, the calculated bulk densities of the designs were used. The target density to achieve 4% air voids was entered into the software. The software then immediately measures the sample heights and calculates the instantaneous density at each cycle based on the measured sample height, the entered sample weight and the mold diameter, which is 150 mm. Compaction continues until the target density value is reached.

3.2.5.1 Optimum Asphalt Content for the TGDH Design

In order to determine the optimum asphalt content, a sample gradation and an estimated asphalt content were selected. A series of specimens were prepared with four different asphalt contents, i.e., estimated asphalt content, estimated ±0.5%, estimated +1%, and three replicates. The volume calculations of these twelve samples were then performed and checked whether they met the design specifications or not. If not, the sample gradation was changed. This process was repeated until all required design parameters were met, i.e., air void content, voids in mineral aggregate (VMA), voids filled with asphalt (VFA), maximum density and dust to binder ratio. The AASHTO R35 (2017) standard was considered in the volumetric calculations. The results of these calculations are shown in Figure 3.12 and Table 3.11. AASHTO T166 (2016) and AASHTO T209 (2020) were used to determine the bulk specific gravity and theoretical maximum density, respectively. The optimum asphalt content was selected as the final content that yields 4 per cent of air voids.

For the TGDH mix design that has limestone aggregate and unmodified asphalt binder, 3.8 percent of the optimum asphalt content was determined at 4 percent air void content. Other design parameters corresponding to the optimum asphalt content were also checked for compliance with the standard and are shown in Table 3.12.

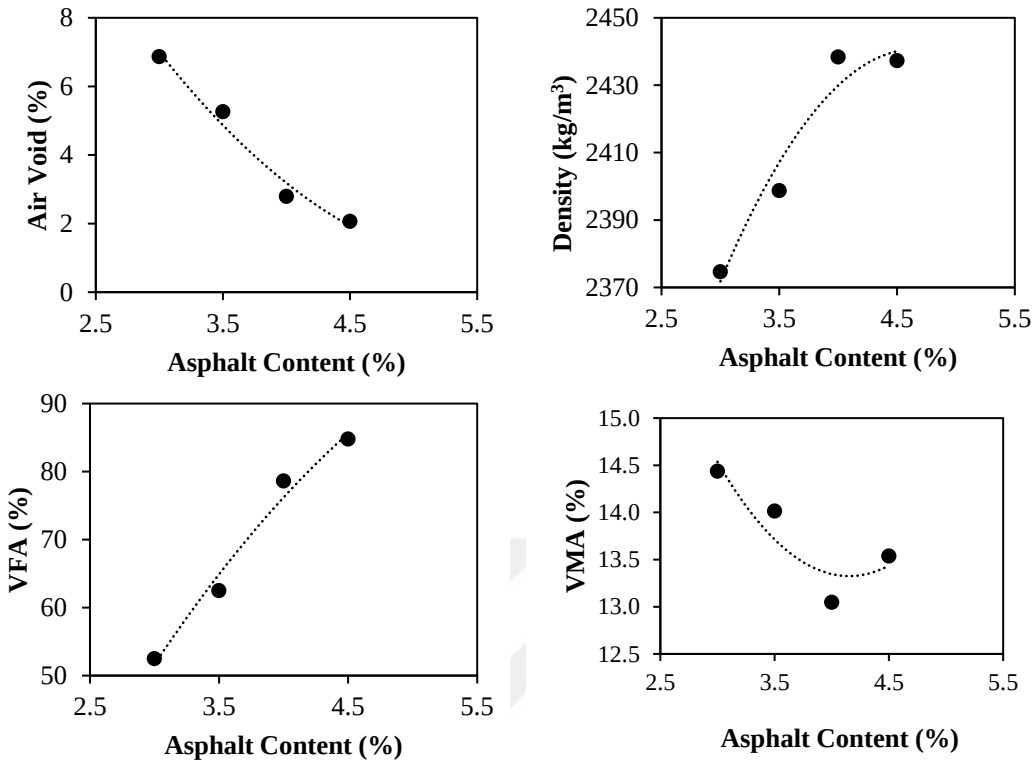

Figure 3.12. Superpave volumetric test results of the TGDH design

Table 3.11. Results with different bitumen contents of the TGDH design

Parameter	**Bitumen Content (%)**			
	3.0	**3.5**	**4.0**	**4.5**
Air Void (V_a), %	6.862	5.258	2.791	2.062
VMA, %	14.437	14.014	13.046	13.537
VFA, %	52.469	62.479	78.608	84.772
Density, kg/m^3	2374.6	2398.7	2438.3	2437.3

Table 3.12. Test results and design requirements of the TGDH mix design

Parameter	Test Results	Design Requirements
Opt. Asphalt Content, %	3.8	3.5 - 6.5
Air Void (V_a), %	4	-
VMA, %	13.5	13 - 15
VFA, %	71	60 - 75
Dust-to-Binder Ratio	0.752	< 1.4

3.2.5.2 Optimum Asphalt Content for the FAA Design

Finding the optimum asphalt content for the FAA design was more challenging due to the stringent design requirements. Similar procedures were repeated for the FAA design samples. After a series of trial and error, an optimum asphalt content of 4.7% by the weight of mix was determined for the FAA mix with basalt aggregate and SBS polymer modified SBS binder. The results of the FAA design are shown in Figure 3.13. As mentioned earlier, the binder mix design was prepared according to the 75 design gyrations. The minimum air void ratio of 3.5% was chosen to determine the optimum asphalt content. Other design requirements corresponding to the optimum asphalt content were compared to the design requirements and are shown in Table 3.13.

Table 3.13 Test results and design requirements of the FAA mix design

Parameter	Test Results	Design Requirements
Opt. Asphalt Content, %	4.7	> 4.5
Air Void (V_a), %	3.5	-
VMA, %	14.1	> 14
VFA, %	74.34	-
Tensile Strength Ratio, %	86.4	> 85
Asphalt Pavement Analyzer, mm	1.6	< 10

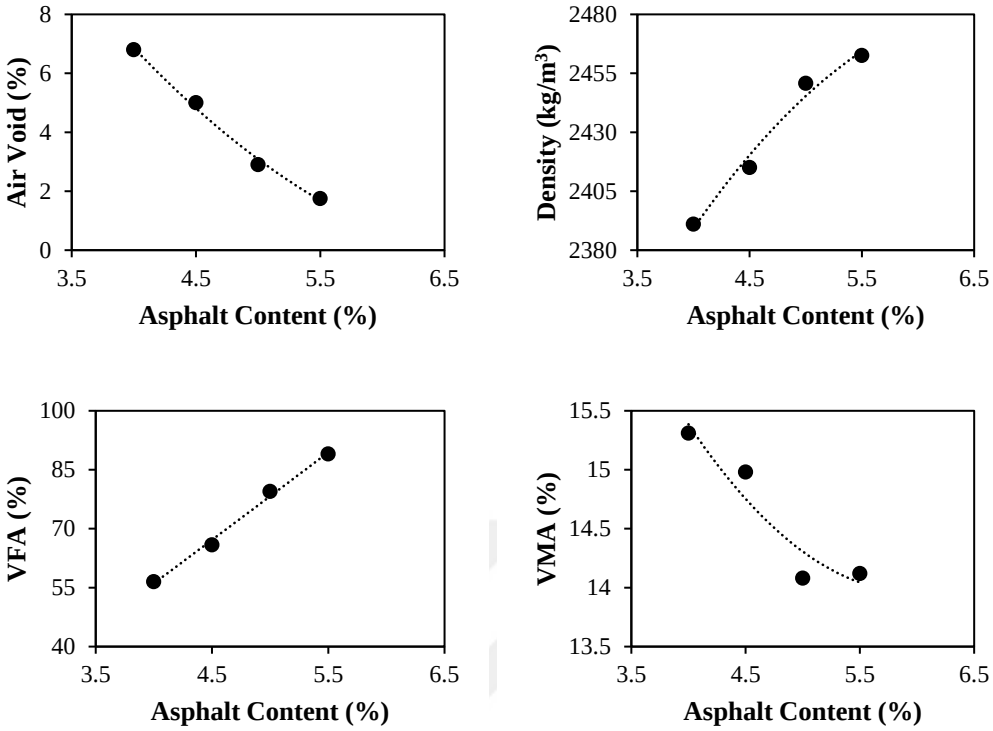

Figure 3.13. Superpave volumetric test results of the FAA design

3.2.6 Specimen Cutting

After fabricating the design samples, the next step was cutting. Two different types of specimens were mainly used in this study. In the first group, cylindrically shaped specimens were used. Cored specimens with a diameter of 100 mm and a height of 150 mm were needed for the repeated creep (FN) tests. As described in the previous sections, 24 specimens with a height of more than 150 mm were already prepared for this test method. Cylindrical samples were then taken from the compacted samples with a diameter of 150 mm using a core drill (Figure 3.14 and 3.15). A core bit with a 100 mm drill head was used and a wet cutting procedure was carried out to minimize disturbance to the samples and avoid overheating. The samples were placed on a thin rubber plate in the machine to prevent their rotation during the cutting process and to avoid damaging the base plate, and then the drill head and the samples were centered. Once the sample was fixed between two rounded steel

columns, the drilling method was applied manually. An example of a drilled sample can be found in Figure 3.16. It should be noted that the samples were placed in a freezer for 3 hours before drilling to avoid structural damage to the samples from friction and vibration. To avoid interruptions, the cutting process was carried out slowly.

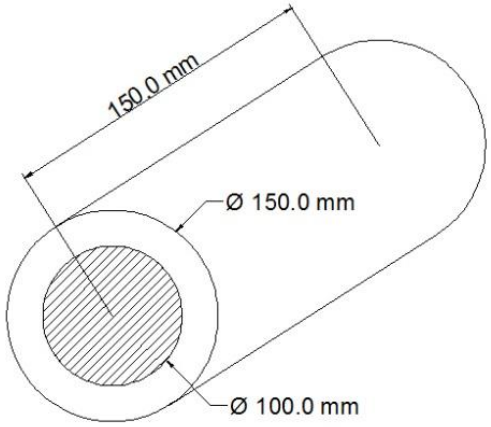

Figure 3.14. Cylindrical specimen section for the FN test



Figure 3.15. Core drilling procedure



Figure 3.16. Specimen after coring

After the side faces of the specimens, the next step was to prepare the upper and lower ends. To reduce friction between the specimens and the loading plates, end treatments were required for the repeated creep test. This is because without a smooth surface, frictional forces arise between the specimen and the loading plate and thus lead to unrealistic test results. The test specimens were made at this stage with a height of about 170 mm so that a thin layer could be cut from both ends with a diamond saw. The procedure is shown in Figure 3.17. Similar to drilling, the cut was made with water to avoid excessive heating of the system and damage to the sample. Equal sized sections were cut out at both ends to achieve an even distribution of air voids within the samples. The resulting samples after the final treatment are shown in Figure 3.18.

Great care was taken with the specimens during the final treatment. One of the greatest difficulties was that the surfaces not only had to be smooth, but also perpendicular to the axis of the specimen. If this could not be achieved, the eccentricity of the load would lead to a buckling effect, misleading deformations and even slippage of the specimen through the loading plates. Therefore, great efforts were made to ensure perpendicularity between the specimens and the saw axis. The necessary checks were made by taking measurements at at least three different points with a caliper gauge. If the ends were not parallel, the samples were recut if they still had sufficient height, otherwise they were not used for the experiments. It should not go unmentioned that a piece of rubber was placed between the sample surface and the clamping device to prevent damage and displacement of the sample. In the second group, circular, disc-shaped samples without coring were used.



Figure 3.17. End treatment of the cylindrical specimens



Figure 3.18. Cylindrical specimens after end treatment

The RM test can be performed on cored or laboratory-molded specimens with a diameter of 101.6 ± 3.8 mm (4 in.) or on non-cored specimens with a diameter of 152.4 ± 9 mm (6 in.) and a thickness of 38.1 mm (1.5 in.) to 63.5 mm (2.5 in.) (ASTM D7369, 2020). Similarly, the IDTF tests require a minimum thickness of 40 mm with a maximum aggregate size of 25 mm (EN 12697-24, 2018). Therefore, a thickness of 50 ± 1.0 mm and a diameter of 150 mm were specified for the second group of specimens (Figure 3.19). Since the Superpave mold had a diameter of 150 mm, coring was not required for this group of specimens. However, the specimens were

trimmed at both ends to bring them to the required thickness of 50 ± 1.0 mm and to obtain a suitable surface for further imaging procedures. Since the difference between the specimen thicknesses affects the test results, a tolerance margin of plus/minus 1.0 millimeter was chosen and applied during cutting.

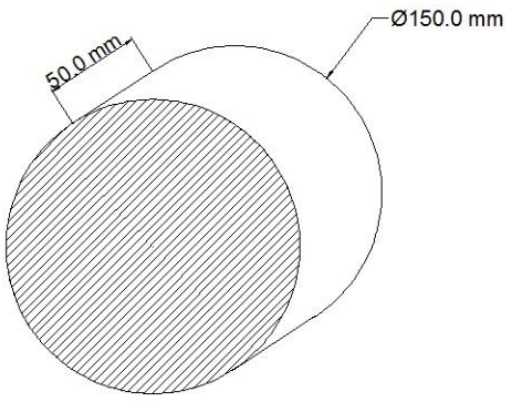

Figure 3.19. Specimen section for the indirect loading

The main reason for the equal thicknesses is that both the resilient modulus and the horizontal tensile stress of the specimen change inversely to its thickness under indirect loading. Using the same diamond-tipped saw, the specimens were cut to 50 ± 1.0 mm thickness and the necessary measurements were taken to ensure that the specimens were within the tolerance limits. The perpendicularity was also adjusted at this stage so that the thickness of the specimens was 50 mm uniformly around the entire circumference. All the samples after cutting are shown in Figure 3.20.



Figure 3.20. IDT test specimens after cutting

3.3 Resilient Modulus Test

The ASTM D7369 (2020) test standard was used to measure the resilient modulus of laboratory prepared asphalt specimens using a repeated load indirect tensile test. The tests were performed by repeatedly applying compressive loads in a haversine waveform. The compressive load was applied along the vertical diametral plane of the circular specimens. The resulting horizontal and vertical deformations were measured using LVDTs. Poisson's ratio values were calculated using the recoverable vertical and horizontal deformations. Finally, the values of the total elastic modules were calculated from the total recoverable deformations, which included both the instantaneous recoverable and the time-dependent sustained recoverable deformations during the recovery phase of the cycle.

3.3.1 Test Setup

All performance tests in this study were conducted using a dynamic testing system (DTS) with a capacity of 16 kN, as shown in Figure 3.21. The equipment (Universal Testing Machine - PAVETEST 2014) included a computer whose user interface software controlled the entire system, a data acquisition system (DAS) from which all measurements were recorded, and a pneumatic pressure system capable of generating a maximum static load of 20 kN and a dynamic load of 16 kN. The actuator applied pneumatic loads to the specimen via a loading frame. The cooled LMS environmental chamber could maintain an operating temperature range of -10 ºC to +60 ºC and had internal dimensions of 550 x 700 x 1170 mm. The data acquisition system (DAS) collected signals from various transducers with up to 16 channels and a sampling rate of 200,000 (200 kHz) per second. Finally, the standard material testing software Testlab® from Pavetest Ltd. was used to control all systems and apply the test procedures.

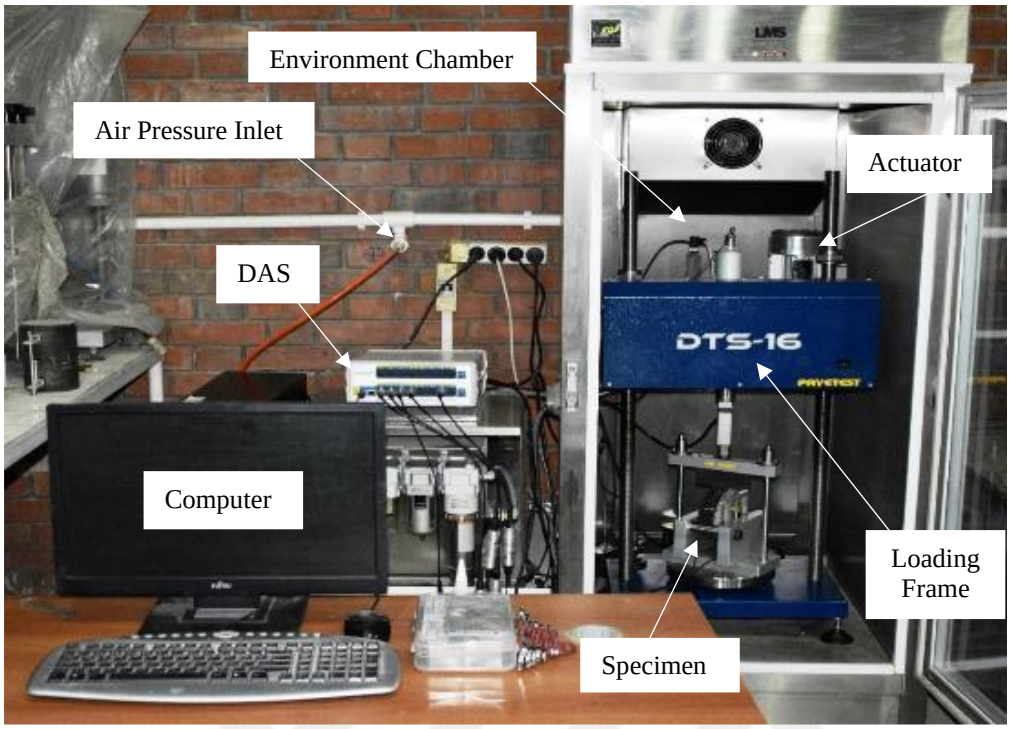

Figure 3.21. Dynamic testing system used in the study

3.3.2 Mounting the LVDTs

The linear variable differential transformer (LVDT) is a type of electrical transformer used to measure displacement. In the RM tests, both horizontal and vertical deformations had to be measured. Therefore, two LVDTs were needed on each side of the sample, one for horizontal and one for vertical measurements, so that a total of four LVDTs were needed for the deformation measurements (Figure 3.22).

Complete procedure of mounting the LVDTs is illustrated in Figure 3.23. First, round metal jigs were screwed into the template plate. As it can be seen in Figure 3.23b, there are two different sets of screws on the template plate. These are for two different gauge lengths in relation to the sample diameter: ¼ of the diameter (38.1 mm for a 152.4 mm diameter sample) or ½ of the diameter (76.2 mm for a 152.4 mm diameter sample). According to ASTM D7369 (2020), any of these gauge lengths

can be used and the smaller sets were chosen in the experiments. A sufficient amount of epoxy resin was applied to each fixture (Figure 3.23c). The template plate was then placed on the sample (Figure 3.23d) and at least one hour was waited for the epoxy to dry. It was very important that the template plate was placed exactly in the center of the sample and that the axes of the LVDTs were aligned so that accurate displacement measurements could be made. Any deviation or misalignment would affect the accurate detection of the deformations occurring in the center of the sample. The template plate was very helpful in this regard.

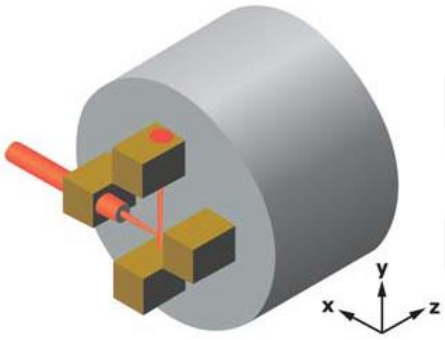

Figure 3.22. Drawing of LVDTs mounted on specimen (ASTM D7369, 2002)

After waiting for the epoxy to cure, the template plate was disassembled and brass mounts (two for each LVDT, for a total of four on each side) were screwed to the round metal mounts (Figure 3.23f). Two LVDTs were used for each of the elastic modulus measurements and the two brass holders were used to hold each piece of the LVDT. The same procedure was repeated for the other surface of the sample and the assembly of the eight brass holders was completed. Finally, the sample was placed in the machine between the steel loading bars and the connections of a total of four LVDTs, two on each side, were completed. It is worth noting that the loading rods had a concave contact surface tailored to the radius of curvature of the 150 mm diameter specimen. This allowed the load to be applied over the entire contact area rather than just a narrow area at the contact point of the sample. Another important aspect of the installation was the alignment of the load to the center of the specimen. An example of a specimen mounted in the testing machine is shown in Figure 3.24.

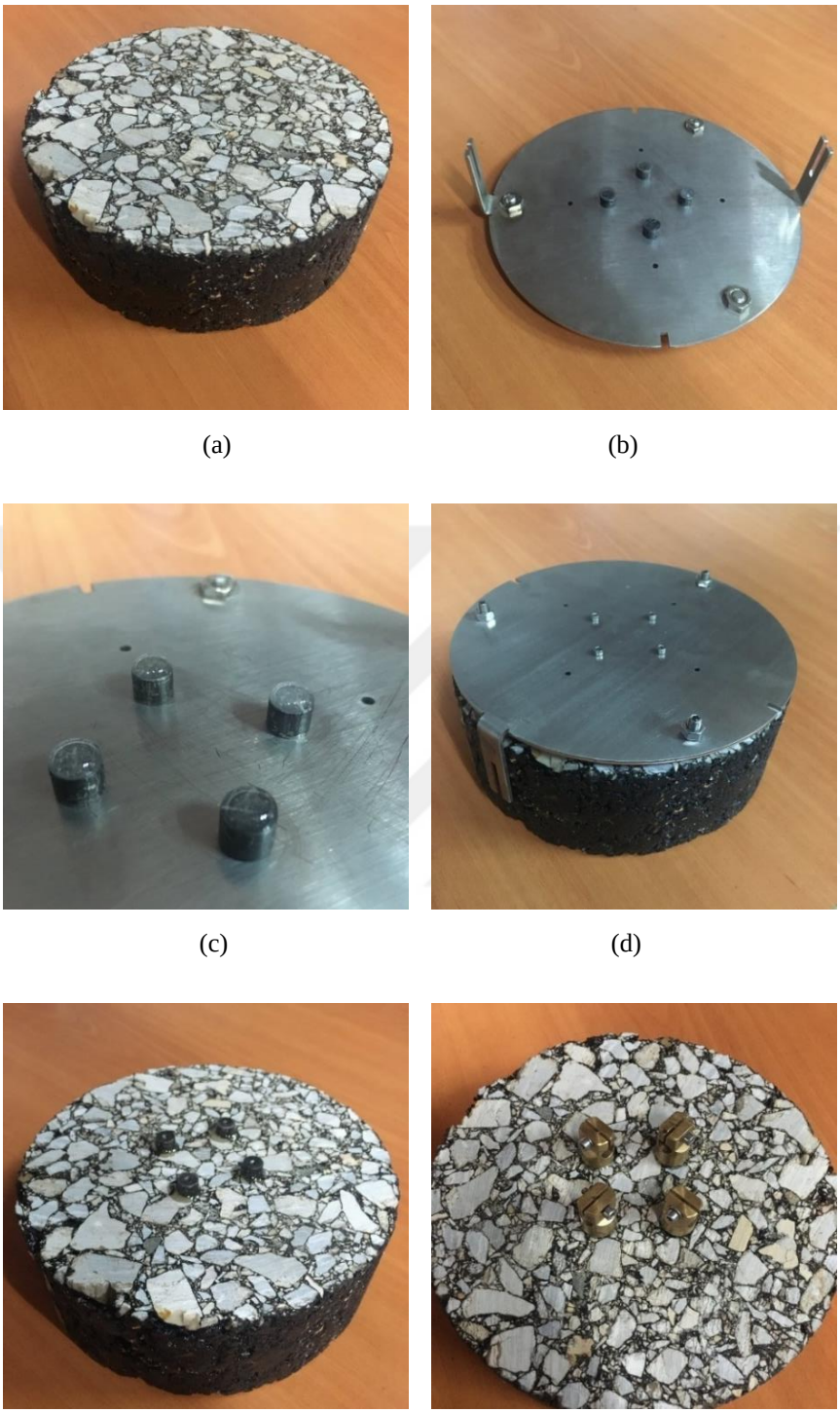

(a) (b)

(c) (d)

(e) (f)

Figure 3.23. LVDT assembly of the RM test



(a) (b)

Figure 3.24. Example specimen in the RM test: a) Placed between the loading strips, b) Mounted LVDTs on the surface

3.3.3 Testing Procedure

The procedure involved testing the resilient modulus at constant temperature, defined load and loading frequency. In accordance with ASTM D7369 (2020), the tests were conducted at a constant temperature of 25 ºC, which was kept constant by the temperature-controlled cabinet. This temperature was chosen because it is recognized as the average temperature value to which asphalt concrete is exposed in practice. The specimens were installed in the cabinet at least four hours prior to testing to ensure that thermal equilibrium existed both inside and outside the specimen. A resistance temperature detector (RTD) was attached to a dummy to check the temperature in situ.

The decision on the amount of applied cyclic load was a separate case. Prior to conducting the RM test, the indirect tensile strengths of the specimens were determined using (ASTM D6931, 2017). The same setup was used for the indirect tensile (IDT) tests on the same prepared specimens. Meaning, three specimens for each mix design type, 6 specimens in total, with a thickness of 50 mm and a diameter of 150 mm were tested at a constant temperature of 25 ºC. However, instead of cyclic

loading, the specimens were loaded with a vertical pressure ramp until the maximum load was reached. The target deformation rate was 50 mm/min. The loading and deformation results, including TGDH and FAA design, are presented in Figures 3.25 and 3.26. The IDT strength values were calculated as follows:

$$S_t = \frac{2000 \times P}{\pi \times t \times D} \tag{3.4}$$

where S_t is the IDT strength, kPa; P is the maximum load, N; t is the specimen height, mm; and D is the specimen diameter, mm. The mean of 3 results for each type of mixture was calculated as the average value of indirect tensile strength. The results are shown in Table 3.14. The IDT strength tests were carried out as a basis for selecting the load levels for the resilient modulus test. According to the test standard (ASTM D7369, 2020), the RM tests are performed with load values between 10 and 20% of the measured tensile strength values. Therefore, the cyclic load values used in the tests were chosen within this range to ensure the assumed linear behavior of the material in the RM tests. After some testing, it was concluded that the repeated loads of 1100 and 1550 N covered the required stress range.

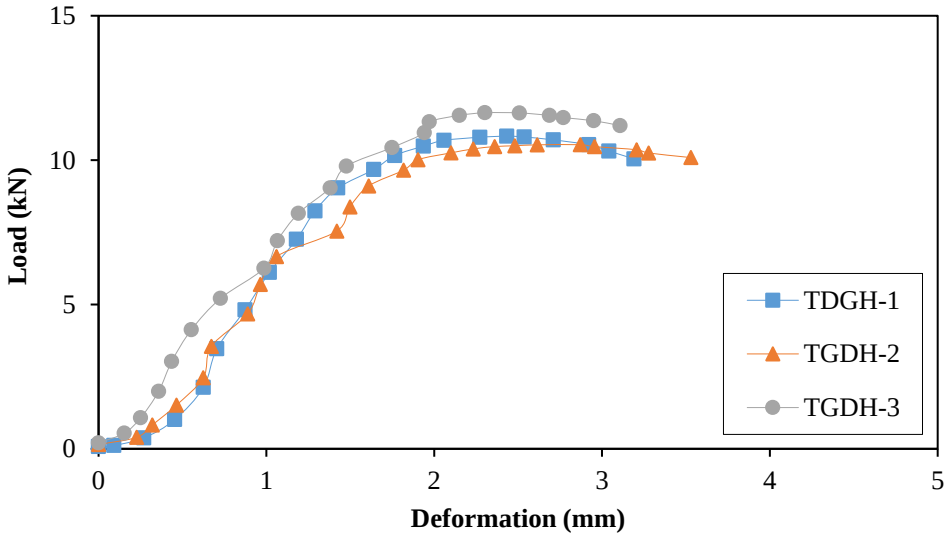

Figure 3.25. The IDT strength test results of the TGDH samples

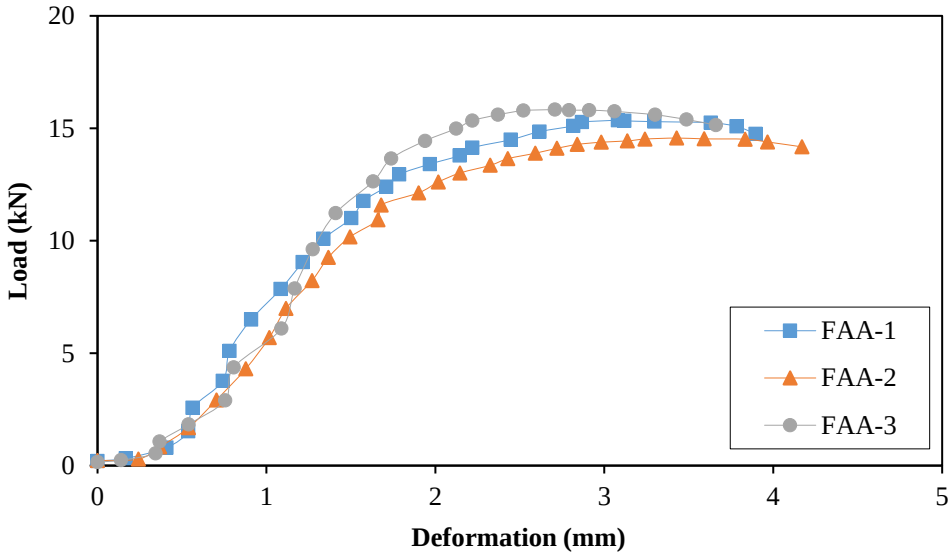

Figure 3.26. The IDT strength test results for the FAA samples

Table 3.14. Test results and requirements of the TGDH mix design

Parameter	**TGDH**	**FAA**
Max. Load, N	11000.7	15249.7
IDT strength, kPa	941.7	1296.7
St. dev. of IDT strength, kPa	32.2	24.9
%10 of max. load, N	1100.1	1525.0
%20 of max load, N	2200.2	3050.0
Selected load, N	1100	1550

The resilient modulus was first tested along the first diametrical axis and then by rotating the specimen 90º. At this point the LVDTs were also changed. The aim was to measure the same axis with the same LVDT. After waiting a few minutes, the same procedure was applied to the other axis of the specimen. The M_R and the Poisson's ratio values were calculated from the average of the eight different values for each axis, two directions and two sides. The computer generated haversine waveform was applied to each diametrical axis of the sample. Loading was applied for 0.1 seconds, followed by a rest period of 0.9 seconds, so that one loading cycle

lasted 1 second (1 Hz). In order for the deformations of the elastic modulus to reach stable values, 100 cycles were performed first. Stable means that the change in the elastic modulus is less than 1%. Using the average values of the last five cycles, the Poisson's ratio and the resilient modulus values were calculated as follows:

$$\mu = \frac{l4 - l1\frac{\delta_v}{\delta_h}}{l3 - l2\frac{\delta_v}{\delta_h}} \tag{3.5}$$

where μ is the Poisson's ratio; δ_v is the recoverable (instantaneous or total) vertical deformation; δ_h is the recoverable (instantaneous or total) horizontal deformation; l_i is the constants calculated by using gauge length and diameter of the specimen.

$$M_R = \frac{P}{\delta_h t}(l_1 - l_2\mu) \tag{3.6}$$

where M_R is the instantaneous or total resilient modulus; t is the thickness of the specimen; P is the applied load to specimen. The ratio of gauge length to sample diameter was 0.25, as explained in the previous section when assembling the LVDTs, and the constant values in the Equations 3.5 and 3.6 are given in Table 3.15. The details of the test setup used in the Testlab® software user interface and other test methods can be found in Appendix B.

Table 3.15. Constant values for the RM test (ASTM D7369, 2020)

Gauge length to dia.	$l1$	$l2$	$l3$	$l4$
0.25	0.144357	–0.450802	0.155789	–0.488592
0.50	0.233936	–0.780056	0.307445	–1.069463
0.75	0.265925	–0.952670	0.430875	–1.934486
1.00	0.269895	–1.000000	–0.062745	–3.587913

Figure 3.27 shows an example of the diagram of load and deformation impulse determined by the software. The figure shows a cycle time, i.e., 0.1 seconds of load and 0.9 seconds of rest. When the sample is loaded, the deformations also start to build up, but with a small delay. This delay is due to the viscoelastic behavior of the

asphalt concrete. The same delay is also observed when the load is removed and during the rest period. As can be seen from the figure, the typical viscoelastic behavior consists of the instantaneous deformation under the load, the recoverable (elastic) deformations and the non-recoverable (plastic) deformations after the load is removed. The results of the RM tests are described in Chapter 5.

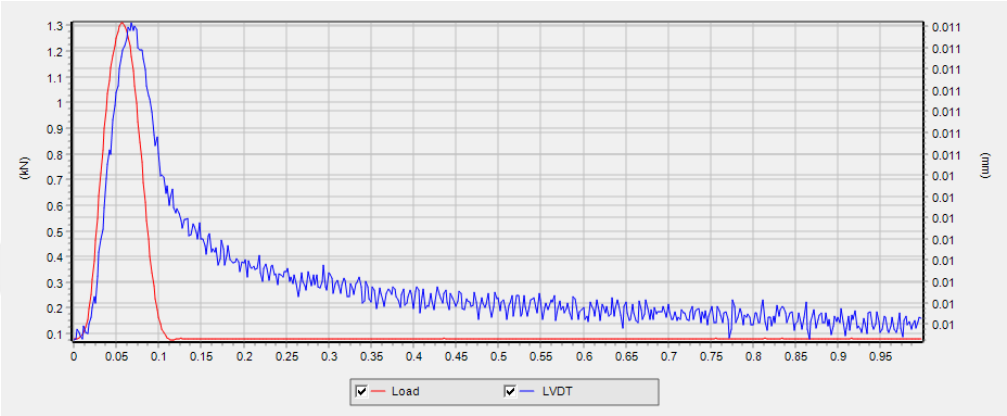

Figure 3.27. An example of applied load versus deformation pulse in the RM test

3.4 Repeated Creep Test

NCHRP Report 465 (2002) is a summary report by the Transportation Research Board on the design of asphalt mixtures to resist rutting. The report explains the detailed test procedure of the repetitive creep test, also called the dynamic creep test. Direct repetitive compressive loads were applied in 1 Hz at constant temperature. Vertical deformations were recorded along the length of the specimen. The flow numbers were calculated from the permanent strain values.

3.4.1 Test Setup

The same dynamic test system UTM - PAVETEST was used to carry out the repeated creep tests. The same climatic chamber, capable of maintaining the target temperature of the test with an accuracy of ± 0.5 ºC, was used with a pneumatic loading mechanism with a capacity of 16 kN. The machine was capable of generating

a cyclic load of up to 30 Hz. However, the test protocol and the LVDT equipment used differed from the resilient modulus test (Figure 3.28). First, the loading plates were changed to prepare the machine for direct loading. Two loading plates were used, one above and one below the specimen. The sample was first placed on the lower plate. The upper plate was then placed on top of the specimen to distribute the load evenly across the axis of the specimen. Testlab® software was used to make the necessary test settings such as load, measurements and calculations. Since the load and deformations are different from those of the resilient modulus tests, the LVDTs were replaced with less sensitive but more powerful ones. A detailed representation of the software layout for performing the repeated creep tests can be found in Appendix B.



Figure 3.28. The FN test setup

3.4.2 Mounting the LVDTs

The cylindrical test specimens with a diameter of 100 mm and a height of 150 mm were prepared as described in the previous sections. During the measurements, two identical LVDTs were used to measure the deformations along the specimen at a radial distance of 180º. To attach the LVDTs on the specimen surface, two sets of circular metal templates were glued to each side of the specimen using a reference steel template (Figure 3.29). The gage length of the plate was 100 mm. This distance was used to calculate the relative strains.



Figure 3.29. Mounting the metal fixtures

Once the epoxy had cured, the LVDT brackets were screwed onto the mounts as shown in Figure 3.30. The mount consisted of four parts for each side of the specimen. First, the lower and upper parts were screwed to the brackets. Then the shorter metal rod was screwed to the lower part. The LVDT was inserted into the opening between the upper and lower parts, with its tip touching the shorter metal rod. Since the LVDTs could not reach 100 mm of the opening, the shorter metal rod was used to shorten the distance. Finally, the longer metal rod was used to align the whole system and prevent it from rotating. While the longer metal rod was fixed at one end, the other end was released to allow the specimen to deform freely under the applied load. An example of the mounted sample in the environmental chamber is shown in Figure 3.31.



Figure 3.30. The steel components that are going to hold the LVDTs



Figure 3.31. The mounted specimen in the FN test setup

3.4.3 Testing Procedure

The guidelines of NCHRP Report 465 were used to establish the test parameters, i.e., the deviatoric stress, test temperature and loading frequency. First of all, the repeated creep tests could be performed both with and without confinement, and the protocol for the repeated tests without confinement was adopted in this study. According to the report, a stress level between 69 and 207 kPa was suggested for the tests without confinement. However, the maximum stress level recommended in the NCHRP report was not sufficient to produce adequate deformations (to be able to reach the 3rd stage) for the FAA design. Therefore, higher deviatoric stress levels were needed for the FAA design. For this type of design, a stress level of 690 kPa (0.69 N/mm^2) was chosen. For the TGDH design with limestone aggregate and unmodified binder, the same stress level of 690 kPa was considered appropriate, in order to compare the two design under similar conditions. When selecting the stress values, one of the considerations was to avoid excessive damage to the specimens so that they could later be used for imaging procedures. Therefore, the highest possible stress values were chosen that would cause the necessary deformations while not damaging the samples too much.

In addition, a contact pressure of about 5% of the cyclic load, i.e., 34.5 kPa, was applied to the specimens to ensure positive contact between the loading plates and the specimen. Then the cyclic load was applied at the test temperature with a frequency of 1 Hz, of which 0.1s was for loading and the rest for rest. The final criterion of the experiment was that either 10,000 cycles or 3 per cent of the cumulative permanent strain was achieved. NCHRP Report 465 recommends 5 per cent of total axial strain as the final criterion, but 3 per cent was chosen as the minimum. The reason for this is that the specimens were needed later in the image processing method. If the specimens were too damaged, the image acquisition could not be done properly. It was found that 3% of the axial strain did not affect the structure of the sample too much.

The effective test temperature (T_{eff}) is a selected single test temperature at which the elastic modulus tests are performed and should be calculated using average annual temperature values (Witczak et al., 2002). There are several methods for determining the effective test temperature for FN tests. The method proposed in the SHRP A-407 (Cominsky et al., 1994) report was adopted in this study. According to Cominsky et al. (1994), the effective temperature for ruts at a depth of 25 mm below the surface course of the pavement can be calculated based on the mean annual air temperatures as follows:

$$T_{eff} = 30.8 - 0.12Z_{cr} + 0.92MAAT_{design} \quad (3.7)$$

$$MAAT_{design} = MAAT_{average} + K_{\alpha}\sigma_{MAAT} \quad (3.8)$$

where T_{eff} is the effective rutting temperature, ºC; Z_{cr} is the critical depth from the pavement surface, mm; $MAAT$ is the mean annual air temperature from historical data, ºC; K_{α} is the normal probability value at an appropriate reliability level; σ_{MAAT} is the standard deviation of the distribution of mean annual air temperature.

The geographical locations were needed to determine and calculate the effective test temperature. Since the FAA test was conducted for airport runways, the location of Turkey's largest airport, Istanbul Airport, was selected. For the TGDH design, Ankara in Turkey was selected as the geographical location. Then, weather data for the two locations was collected from the Turkish State Meteorological Service. From 2019 (the last available year), the monthly annual averages for the last 20 years for Ankara and Istanbul were used to calculate the effective test temperatures (Table 3.16).

The average annual air temperatures for the last 20 years were calculated to be 13.2 and 15.8 ºC for Ankara and Istanbul, respectively. A confidence interval of 95 per cent was chosen. Then, the effective rut depth of the binder course of 62.5 mm was obtained from SHRP A-407 (1994) report. Finally, the effective test temperatures were calculated to be 36 and 44 ºC.

One of the most important aspects of the test was the avoidance of friction between the load plates and the test specimen. The first step in this regard was to precisely cut the surfaces of the specimens. Silicone grease oil with a viscosity of 12,500 cSt was also applied to two pieces of rubber membranes at room temperature. These membranes were then placed between the sample and the loading plates at both ends. The combination of the two provided a frictionless surface and prevented the build-up of stresses that could lead to premature cracking or false readings.

Table 3.16. Effective test temperatures for the FN tests

Parameter	**TGDH**	**FAA**
$MAAT_{average}$, ºC	13.2	15.8
σ_{MAAT}, ºC	0.665	0.721
K_{α}, (95 % reliability)	1.645	1.645
Z_{cr}, mm	62.5	62.5
T_{eff}, ºC	36	44

3.4.4 Calculation of the Flow Number

An example of a test result for the sample ID LUCR03 is shown in Figure 3.32. Deviatoric stresses were applied to the sample and the resulting permanent strains were recorded at the end of each cycle. As it can be seen from the figure, the permanent strains have not yet reached the tertiary zone in most cases. This is because, as explained earlier, lower loading stresses or lower target values for the permanent strains were chosen so that the specimens would not deform too much. However, this situation made the calculation of the flow numbers more difficult. As mentioned in the first sections, there are several methods to calculate the flow numbers, but in this study the power model was used. The reason for this is that the model ignores the tertiary zone and only considers the second zone of plastic deformations to calculate the flow numbers.

Initially, permanent strain as a function of the number of cycles was plotted on a logarithmic scale, as shown in Figure 3.33. MATLAB® was used to search for the linear part of the permanent strain data and the power model was fitted to this range using the non-linear regression method to obtain the highest R^2 value (Figure 3.34). The algorithm searched for the best fit line for the linear range based on the calculation of the R^2 values. The constants of the power model, i.e., the slope of the fitted model (b) and the intercept at the permanent strain value (a), were calculated using the MATLAB® algorithm. The mathematical representation of the power model is:

$$\varepsilon = aN^b \tag{3.9}$$

where ε is the permanent strain at N cycle; a is the intercept point that offset permanent strain at cycle N=1; b is the slope of the fitted model.

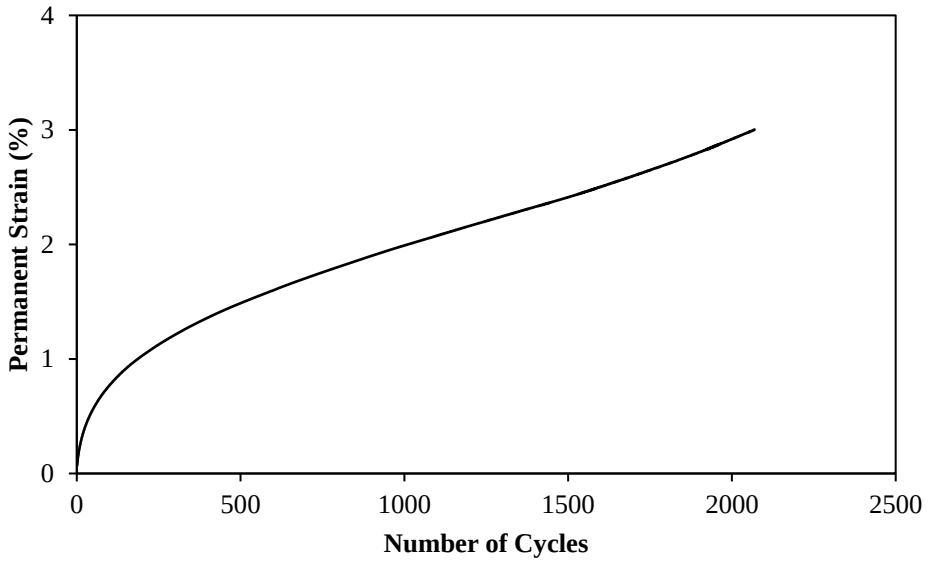

Figure 3.32. FN test result for the specimen ID LUCR03

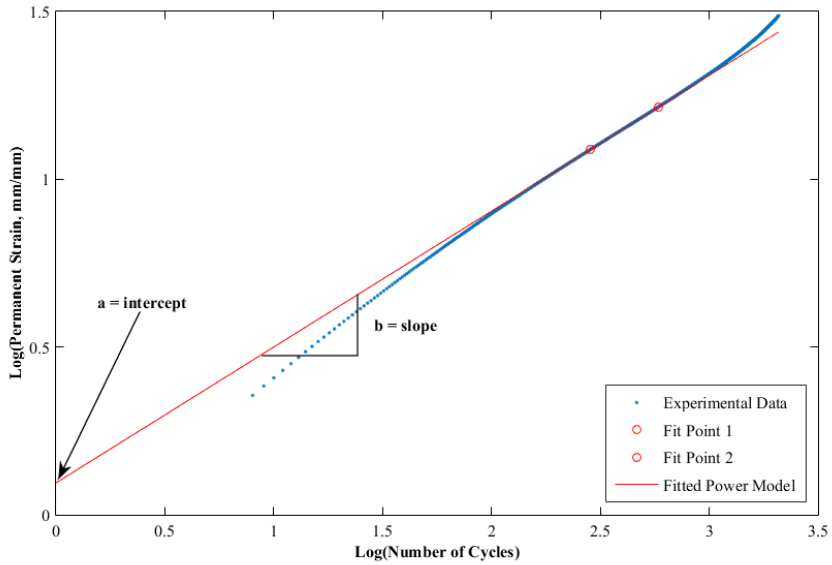

Figure 3.33. Power model fit example (sample ID LUCR03)

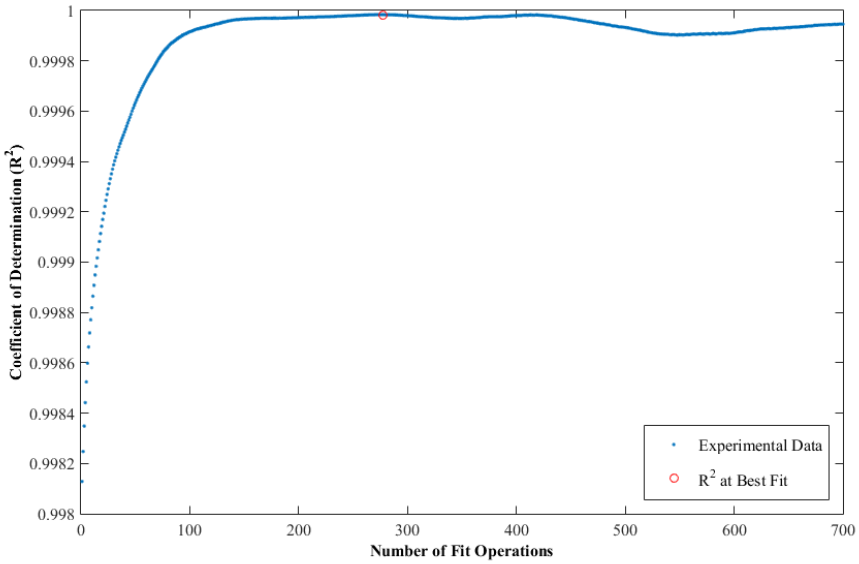

Figure 3.34. Coefficient of determination as a function of number of least square fit operations (sample ID LUCR03)

The flow number is calculated as the minimum point of the strain rate vs number of cycle plot (Figure 3.35). The power model can only be fitted to permanent strain if the permanent strain rate curve has a minimum. Whether there is a minimum or not can also be seen from the logarithmic scale by noting that the permanent strain rate curve bends upwards immediately after the linear part. To confirm the presence of such points in the experimental data, the strain rate of each loading cycle was first calculated as the difference between the adjacent cycles and then divided by twice the cycle interval:

$$\frac{\delta(\varepsilon_p)_i}{\delta N} = \frac{(\varepsilon_{pN_{i+1}} - \varepsilon_{pN_{i-1}})}{2\Delta N} \tag{3.10}$$

where $\delta(\varepsilon_p)_i/\delta N$ is the rate of change in permanent axial strain at cycle *i*; $\varepsilon_{pN_{i+1}}$, $\varepsilon_{pN_{i-1}}$ is the permanent axial strain of neighbouring cycles; ΔN is the cycle interval.

The calculated strain rate data was then smoothed to reduce the fluctuations. This was done using a moving average method that differentiates over an interval of 20 cycles. Without this method, the flow number calculations were misleading, as either the low accuracy of the measurements or the resulting electronic readings of the devices caused significant noise. The calculated flow numbers and their power model constants are presented in detail in Chapter 5.

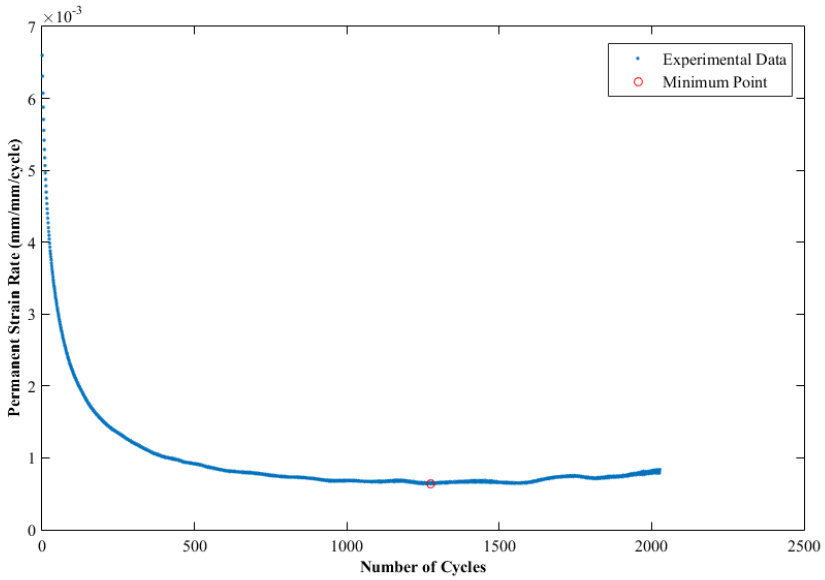

Figure 3.35. Rate of strain versus number of cycles (sample ID LUCR03)

3.5 Indirect Tensile Fatigue Test

The test standard EN 12697-24 (2012) was used to determine the fatigue behavior of asphalt mixtures under repeated indirect loading. The constant load mode was applied using the indirect tensile test (IDT). Laboratory-made cylindrical specimens were used under repeated compression and haversine load signals through the vertical diametral plane. Along the center, the horizontal deformations of the specimen were recorded, resulting from the tensile stress pulses perpendicular to the direction of the applied load. The stiffness values were calculated from the resilient deformations and Poisson's ratios. The Poisson's ratio values were already calculated in the resilient modulus test phase. Fatigue life was determined according to traditional fatigue criteria, i.e., the total number of load cycles corresponding to a 50% reduction in stiffness.

3.5.1 Test Setup

The same dynamic test system from UTM - PAVETEST was again used for the experiments. Another set of LVDTs was mounted on the machine. These longer LVDTs were able to measure over 3.75 mm with an accuracy of 0.1%. The required static test temperature was provided by the thermostatic chamber. The loading frame consisted of two loading bars. First, the sample was placed on the lower bar. Then the upper bar, which was attached to a beam, was placed on top of the specimen. A hemispherical piece of metal was placed between the upper loading bar and the loading arm of the machine. The upper beam was free to move in the loading direction. The loading beams had concave surfaces and rounded edges with a radius of curvature of 75 mm and a width of 19.1 mm to have equal loading surfaces along the loading beams for a nominal diameter of the specimen of 150 mm. Figure 3.36 shows an example of a specimen in the experimental setup. A detailed representation of the software layout for performing the indirect tensile fatigue tests can also be found in Appendix B.

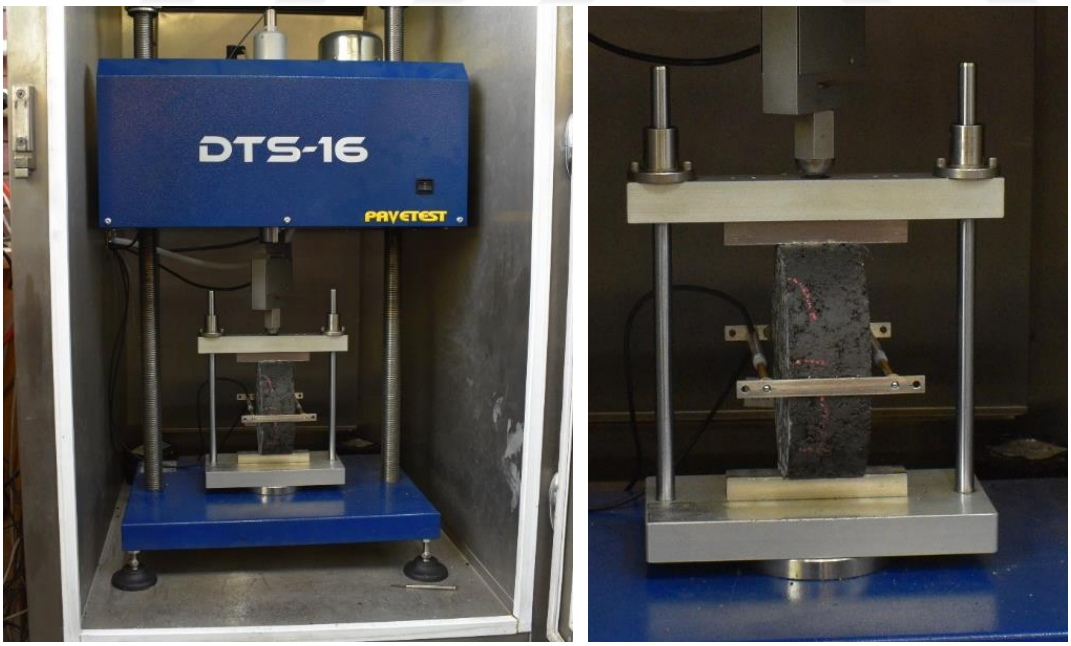

Figure 3.36. Indirect tensile fatigue test setup

3.5.2 Mounting the LVDTs

The dimensions of the samples were fixed at a minimum thickness of 40 mm and a diameter of 100 mm with a maximum grain size of 25 mm (this was the maximum grain size of the samples). Therefore, as explained earlier, the samples compacted in the laboratory were cut into 50 mm thick slices and used for the experiments. The deformation measurement system consisted of two deformation transducers and two metal strips (Figure 3.37). The strips were glued on opposite sides of the horizontal diametrical plane. A positioning device helped to position and glue the deformation strips and to assign the position of the load strips. After waiting for the epoxy to cure, the specimen was removed from the fixture and placed in the climate chamber. Finally, the installation of two LVDTs, one for each side of the specimen, was completed.

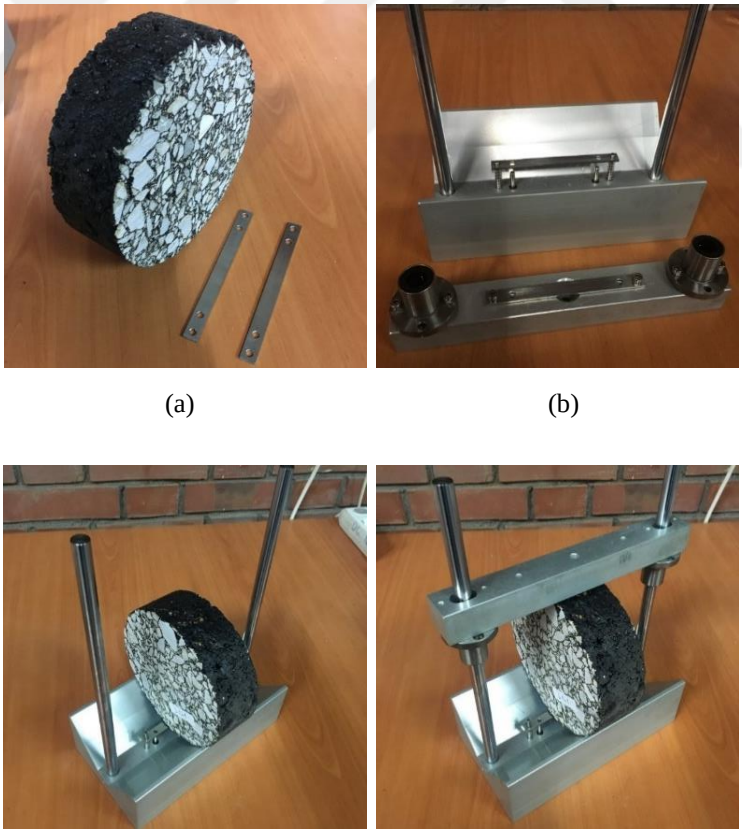

(a) (b)

(c) (d)

Figure 3.37. LVDT mounting procedures of IDTF tests

3.5.3 Testing Procedure

The tests were carried out at 25 ºC, which corresponds to the usual processing temperature of asphalt mixtures in practice. The test specimens were placed in the thermostatic chamber and exposed to the specified test temperature for at least four hours prior to testing to achieve thermal equilibrium. A haversine load was repeatedly applied with 0.1 s loading time and 0.4 s rest time.

The initial deformations were recorded during the first 100 cycles to calculate the initial strain amplitude. According to the test standard EN 12607-24 (2012), the initial strain amplitude should be between 50 μm/m and 200 μm/m. The loading stress is then adjusted and the load is applied again for 100 cycles until the target initial strain amplitude is reached. It was found that loading stresses of 1800 and 900 kPa could achieve the desired strain amplitudes for the FAA and TGDH designs respectively. Testing continued until either 1,000,000 cycles were reached, 2.5 times the initial strain value occurred, or the specimen fractured. Fatigue life was estimated using the conventional failure criterion $N_{f/50}$, i.e., the number of cycles at which a 50% decrease in stiffness modulus occurred. An example diagram of the permanent horizontal deformation of specimen ID BMIF03-2 as a function of the number of cycles is shown in Figure 3.38.

When a constant stress is applied to the specimen, permanent horizontal deformations begin to develop within the specimen. Although the initial deformations were relatively small at first, they increased exponentially as the load progressed, eventually leading to cracking. The horizontal tensile stress and strain at the center of the specimen were calculated as follows:

$$\sigma = \left(\frac{2F}{\pi \times t \times D}\right) \tag{3.11}$$

$$\varepsilon = \left(\frac{2\Delta H}{D}\right)\left(\frac{1 + 3\nu}{4 + \pi\nu - \pi}\right) \tag{3.12}$$

where σ is the horizontal tensile stress at the specimen center; F is the measured force; t is the specimen thickness; D is the specimen diameter; ε is the horizontal strain; ΔH is the horizontal deformation; and ν is the Poisson's ratio. Then the stiffness modulus of the specimen was calculated as:

$$S_{mix} = \frac{\sigma}{\varepsilon}(1 + 3\nu) \tag{3.13}$$

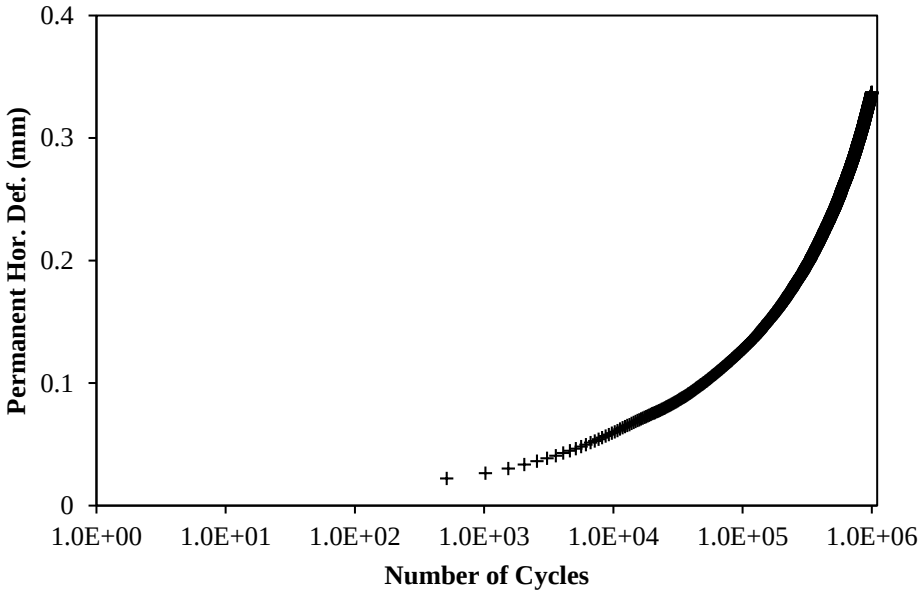

Figure 3.38. Permanent deformation graph (sample ID BMIF03-2)

The calculated stiffness modulus of sample BMIF03-2 was plotted on a logarithmic scale in Figure 3.39. Then, the decrease in stiffness modulus between two consecutive cycles was calculated and plotted in Figure 3.40. As can be seen from the figures, the calculated stiffness reductions could not reach the targeted 50%. A regression analysis was then performed to fit a power model to the reduction in stiffness values. It is known that the power model is the best method to represent fatigue data.

In fatigue experiments, the first phase of the test data is characterized by a rapid decrease in stiffness due to repeated loading of the specimen. The exact explanation for this decrease is not clear, but it has become common practice to remove this first

region in the fatigue tests. Thus, specification of the initial stiffness value is very hard work to determine. Although the fatigue experiments of asphalt mixtures have been used for nearly 40 years in the pavement industry, there is no exact validation nor verification of the initial stiffness. When examining the test data, a relatively rapid decrease in the stiffness modulus was observed during the first 2,500 - 3,000 cycles. These sudden decreases reduce significantly after about 2,500 cycles and the test data reaches the general trend of the graph. When this first range, which corresponds to about 0.25 to 1 percent of the total test data, is removed, the fitting success of the power model increases enormously. Therefore, when fitting the power model to the fatigue test results, the first 2,500 cycles were removed from the test data. Finally, the fatigue life of the specimens was determined as the number of cycles corresponding to a 50 per cent decrease in stiffness modulus. The detailed results are presented in Chapter 5. Additionally, all the laboratory experiment results for the total 20 tested specimens, together with the fitted power models are presented Appendix C.

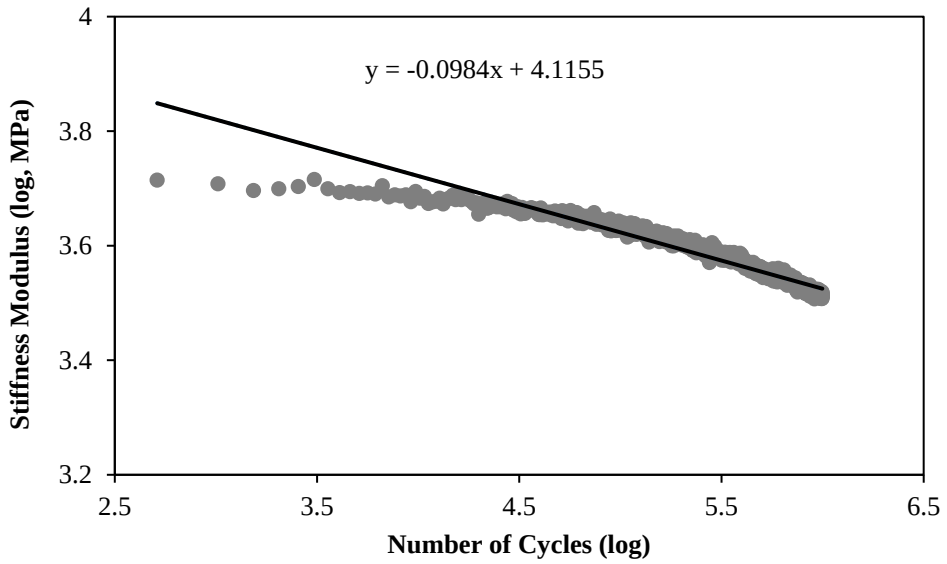

Figure 3.39. Stiffness modulus versus number of cycles (sample ID BMIF03-2)

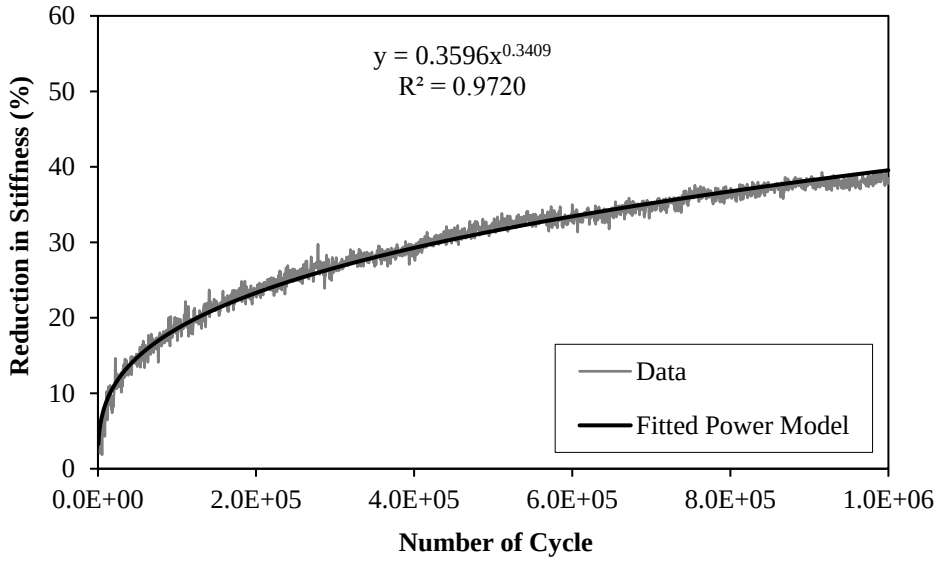

Figure 3.40. Reduction in stiffness vs number of cycles (sample ID BMIF03-2)

CHAPTER 4

NUMERICAL MODELING OF ASPHALT MIXTURES

4.1 Introduction

In this chapter, the finite element modeling of the asphalt mixture is explained. First, images of the samples prepared in the laboratory are acquired using image acquisition techniques. Then image processing methods are applied to the samples to prepare them for finite element modeling. A unique image vectorization method is developed to convert the processed images of the asphalt samples into two-dimensional finite element geometry. Then, the material modeling of the finite element model is explained in detail. After applying material models, boundary conditions and the other required operations, the numerical modeling of the asphalt mixtures is completed. All the procedures are explained in detail. The results of the numerical experiments are presented in Chapter 5.

4.2 Image Processing

Asphalt concrete specimens were prepared in the laboratory, cored and sliced as previously described. The finite element model created in this study was based on 2D images of these specimens. In order to create the numerical model, cross-sectional images of the specimens had to be acquired first. With the exception of the drilled specimens to be used for the repeated creep tests, all other specimens were suitable for image processing as they already had smooth surfaces after cutting. Therefore, images were taken of all these samples except the samples for the creep tests before the performance tests and the application of image processing methods was carried out. The samples for the creep tests, on the other hand, were cut in half

after the repeated creep tests and then subjected to the image processing methods. As mentioned earlier, image processing is the method used to prepare the specimens for finite element modeling, and it was mainly applied in three parts in this study: Image acquisition, image enhancement and vectorization of the images. The flowchart of the image processing steps is shown in Figure 4.1.

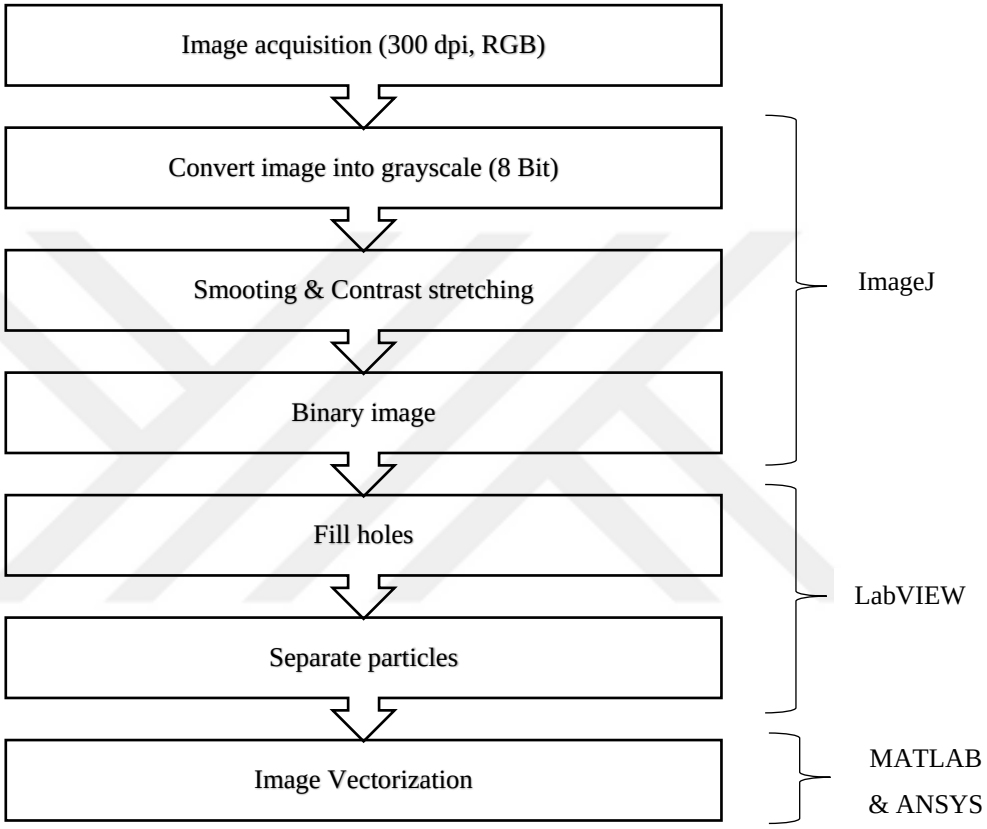

Figure 4.1. Flowchart of the image processing steps

4.2.1 Image Acquisition

The image acquisition technique, which is the first step of image processing, is the method of transferring the cross-sectional images of the asphalt concrete samples into the computer environment. There are various methods and devices for this procedure. In this study, a 2D flatbed scanner was used to capture cross-sectional images of the samples (Figure 4.2) because of its practicality and cheapness. All prepared or tested samples were scanned from each surface in the scanner in turn.



Figure 4.2. Flatbed scanner used to obtain cross sectional images

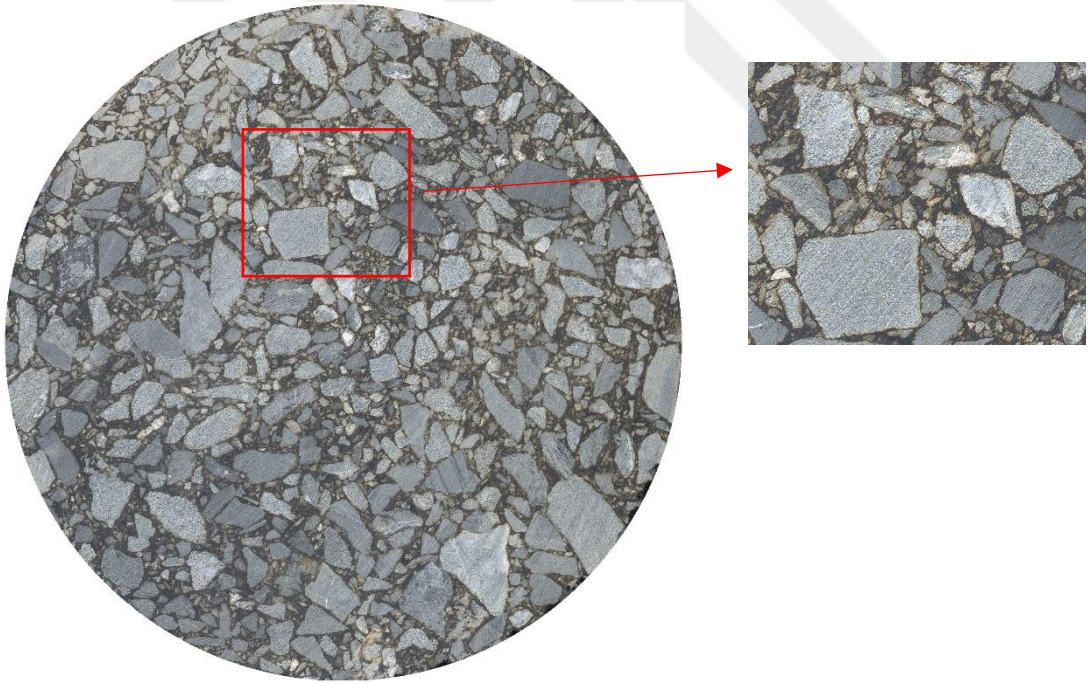

Figure 4.3. RGB image captured by the scanner

The images were taken in RGB format and with a resolution of 300 dpi. An example of an RGB image immediately after capturing with the flatbed scanner is shown in Figure 4.3. A high resolution was chosen so that all aggregate particles can be captured, even the smaller ones, in the structure. It has been shown that with this resolution, particles larger than 0.425 mm could be able to captured successfully.

4.2.2 Image Enhancement

In order to create a finite element model based on 2D images, the generated images first had to be improved. Random noise, color differences between individual aggregate particles or a single odd particle surface can cause distortions in the image and need to be corrected. At this stage, many methods were used to enhance the raw images and these processes were carried out using ImageJ software. ImageJ is a Java-based image processing software developed at the National Institutes of Health and the Laboratory for Optical and Computational Instrumentation (LOCI) at the University of Wisconsin (Schneider et al., 2012).

4.2.2.1 Smoothing

Digital images are represented as an array of discrete picture elements (pixels) in two dimensions (Figure 4.4). These arrays are represented by a matrix in computer memory with the origin point (0, 0) in the upper left corner of the image, unlike the traditional coordinate system:

$$f(x,y) = \begin{pmatrix} f(0,0) & \cdots & f(0,N-1) \\ \vdots & \ddots & \vdots \\ f(M-1,0) & \cdots & f(M-1,N-1) \end{pmatrix} \tag{4.1}$$

where $f(x,y)$ is represents the digital image; M, N are the resolution of the image (number of pixels in each direction).

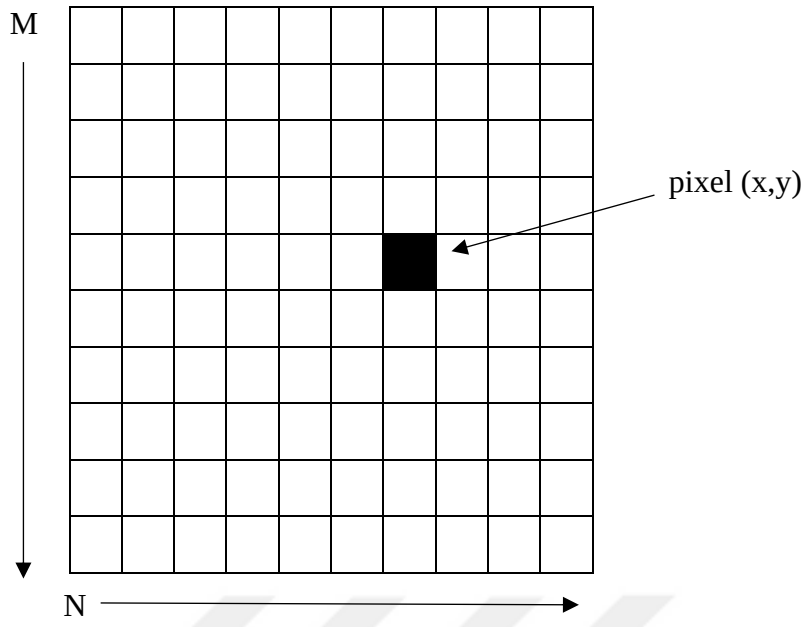

Figure 4.4. A digital image composed of pixels

Each element of the matrix indicates the intensity value of a pixel. In an RGB image, there are three different matrices for each pixel, representing different color spectra: Red, green and blue. The combination of the three matrices gives the color image. Therefore, at this stage, the captured RGB images need to be converted into a grayscale format. In a grayscale image, the intensity of each pixel is represented by a single matrix, on the basis of which image processing can be carried out. A grayscale image, also called an 8-bit image, consists of 256 intensity levels (28 = 256). This means that in the matrix each intensity value varies between 0 and 255, where 0 is black and 255 is white. The total number of elements in the matrix is called the resolution, and resolution is measured in dots per inch (dpi). Higher resolutions contain a greater number of pixels and therefore show more detail. To capture the entire structure, the images were scanned at a resolution of 300 dpi. At this stage, the images of the asphalt concrete samples were scanned, transferred to the computer in RGB format and then converted to grayscale (Figure 4.5).



(a) (b)

Figure 4.5. Zoomed section of an example image: a) Original RGB image, b) Grayscale image

The grayscale images contained unwanted noise resulted from the scanning procedure. Smoothing is one of the most commonly used and effective methods to remove random noise in images. In this method, all pixel values are simply replaced by the average of the intensity values in a given neighborhood. So, each pixel value was individually replaced by an average intensity value of its 3x3 neighborhoods. The method is shown in Figure 4.6. The average value became the new intensity value of the corresponding pixel. Figure 4.7 shows the zoomed image section before and after smoothing. Although this method makes the image appear blurred, this does not matter because of the binarization method in the following steps.

a	b	c
d	e	f
g	h	i

$$\Longrightarrow \quad E = \frac{1}{9}(a + b + c + d + e + f + g + h + i)$$

Figure 4.6. Smoothing by averaging filter, the center pixel value would be changed from "*e*" to "*E*"

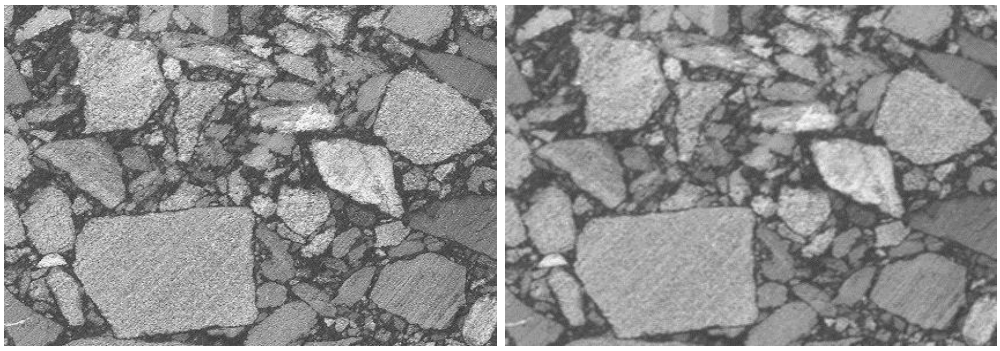

(a) (b)

Figure 4.7. a) Grayscale image before smoothing, b) After smoothing

4.2.2.2 Contrast Enhancement

The number of pixels in the image in relation to their intensity values is recorded at the end of the smoothing process and then plotted on a graph (see Figure 4.8a). Looking at this graph, called a histogram, it is clear that the range is relatively narrow. By stretching the contrast, also called normalization, the histogram was widened to cover the entire spectrum. This procedure was carried out in MATLAB®. An example histogram of an image before and after the normalization method can be found in Figure 4.8. This method not only improved the overall quality of the image and facilitated the detection of aggregate particles, but also made a positive contribution to the future binarization method. The improvement in overall image quality is shown in Figure 4.9.

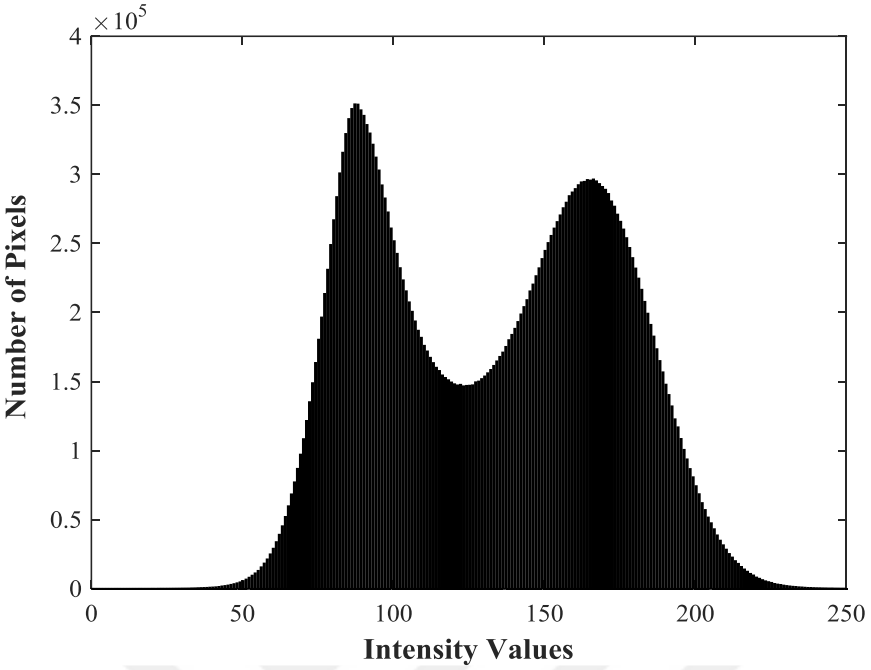

(a)

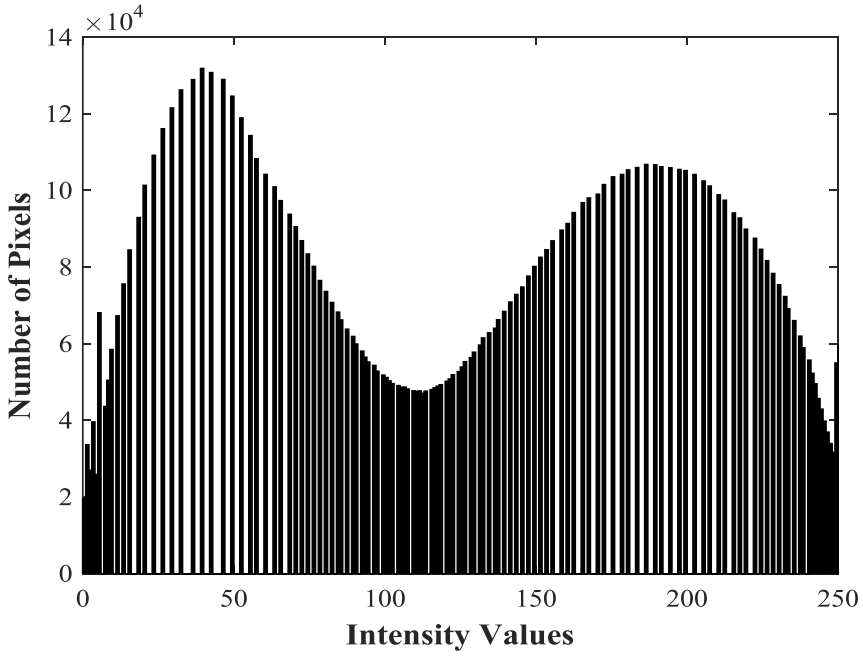

(b)

Figure 4.8. Example histogram of an image: (a) Before contrast stretching, (b) After contrast stretching

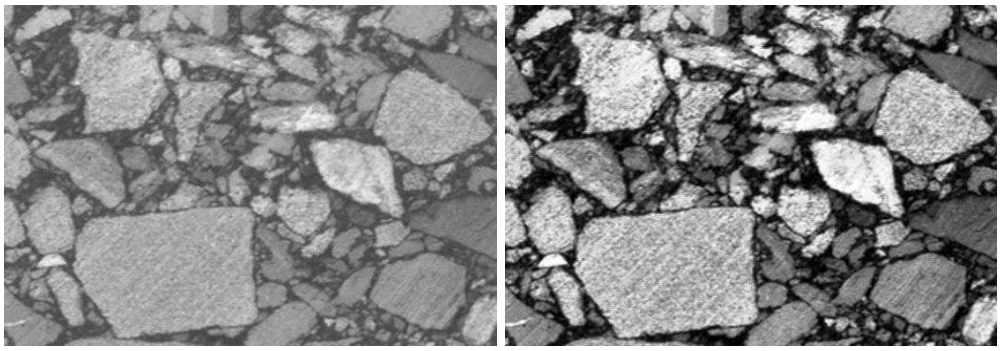

(a) (b)

Figure 4.9. a) Smoothened image, b) After contrast enhancement

4.2.2.3 Image Binarization

A binary image consists of pixels that can have two colors, black and white. This means that each pixel is stored as a single bit, i.e., 0 or 1. In this study, the binary images represent the aggregate particles as 0 and the binder as 1. Since these values were determined for each pixel, a reference intensity value first had to be selected as a threshold. Once this threshold was selected, the upper and lower intensity values could be assigned to the corresponding black or white phases. There are several methods in the literature to determine the threshold value manually or automatically. However, recently developed automated methods have been found to be very effective in avoiding human error. Therefore, an automated threshold method was also used in this study.

ImageJ software was used to convert the images to binary format. ImageJ's standard method, the "IsoData" algorithm, was used. This algorithm uses an iterative selection method to split the image into object and background by setting an initial threshold value (Ridler & Calvard, 1978). Then the mean values of the pixels at or below this threshold and the pixels above it are calculated. The means of the two are compared to the composite mean and a check is made to see if the mean is greater than the composite mean. If not, the process is repeated until it is greater. Once the threshold

value is determined, the image is converted to its binary form. The zoomed cross-sectional image before and after the binary condition is shown in Figure 4.10.

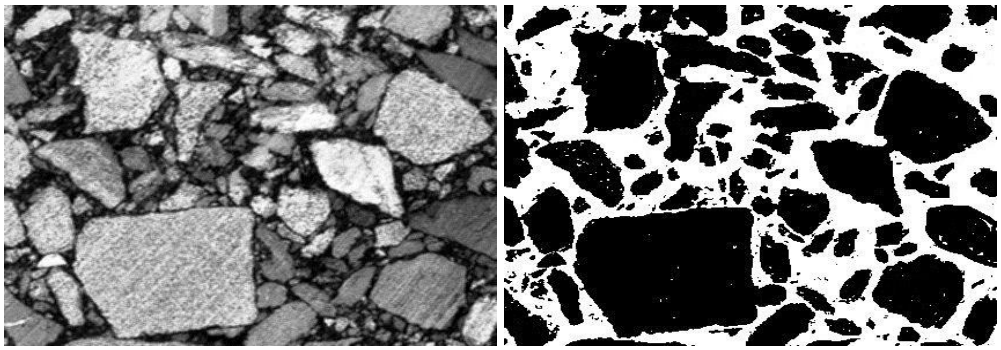

(a) (b)

Figure 4.10. a) At the end of the contrast enhancement, b) Binary form

4.2.2.4 Filling Holes

As it can be seen from Figure 4.10b, there are some inverse pixels in their relative zones. These inversions occur when the pixels are outside the desirable brightness range due to color deviations, noise, or holes in the aggregate or binder phase. During binarization, these pixels are inverted because they have an intensity value above or below the phase to which they belong, becoming so-called holes. To prepare the image for the two-dimensional geometric finite element model, these holes had to be eliminated according to the region in which they were located. A LabVIEW® algorithm was used to fill these holes using the four-connectivity element method. It should also be noted that at this stage and in the particle separation stage, which will be mentioned in the following section, some of the tasks that the algorithm could not detect were also performed manually using basic imaging software. The image after this procedure is shown in Figure 4.11.

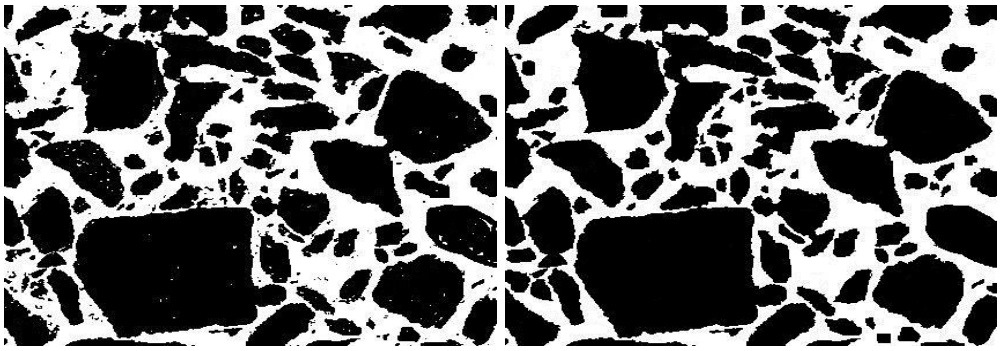

(a) (b)

Figure 4.11. a) Binary image, b) After filling holes

4.2.2.5 Particle Separation

At this stage, image enhancement was still incomplete. Eventually, the touching aggregate particles had to be separated, and this process was one of the most important steps in image processing. When two aggregate particles were very close to each other, the intensity gradients in the area between them became similar. After the image was converted to its binary form, these areas were difficult to distinguish, so the particles were perceived as touching each other. If left untreated, these anomalies would lead to an incorrect estimation of the aggregate structure and thus erroneous results. To separate these particles, the same LabVIEW® algorithm was used along with manual hand work. The final shape of the image at the end of the image enhancement process is shown in Figure 4.12.

So far, a small zoomed section of an image has been used to be able to see the details better. Figure 4.13 shows the transition of an actual image systematically through the stages of image enhancement. In summary, the 2D digital cross-sectional images of the asphalt samples were first captured using a flatbed scanner. The captured RGB image was then converted to its grayscale (8-bit) form. Smoothing and contrast enhancement methods were applied to improve the image quality. Binarization was then performed to identify the aggregate and binder states. After binarization, it was found that the image still contained many distortions, so the gap filling method was

applied. Finally, the touching aggregate particles were separated in the particle separation phase and image processing was completed.

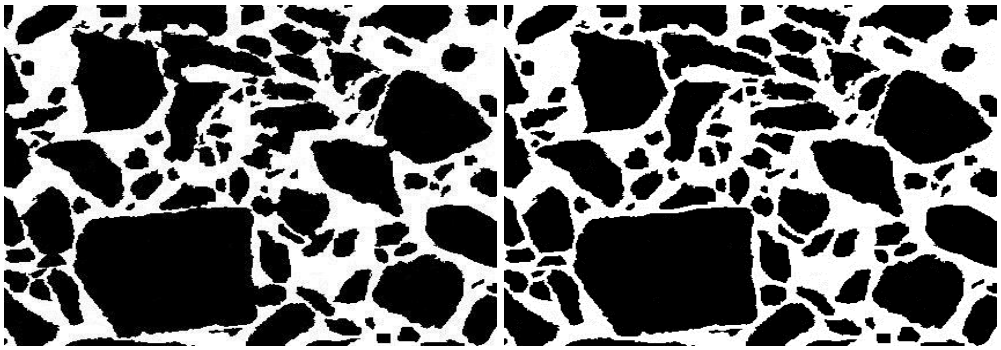

(a) (b)

Figure 4.12. a) After filling holes, b) After particle separation

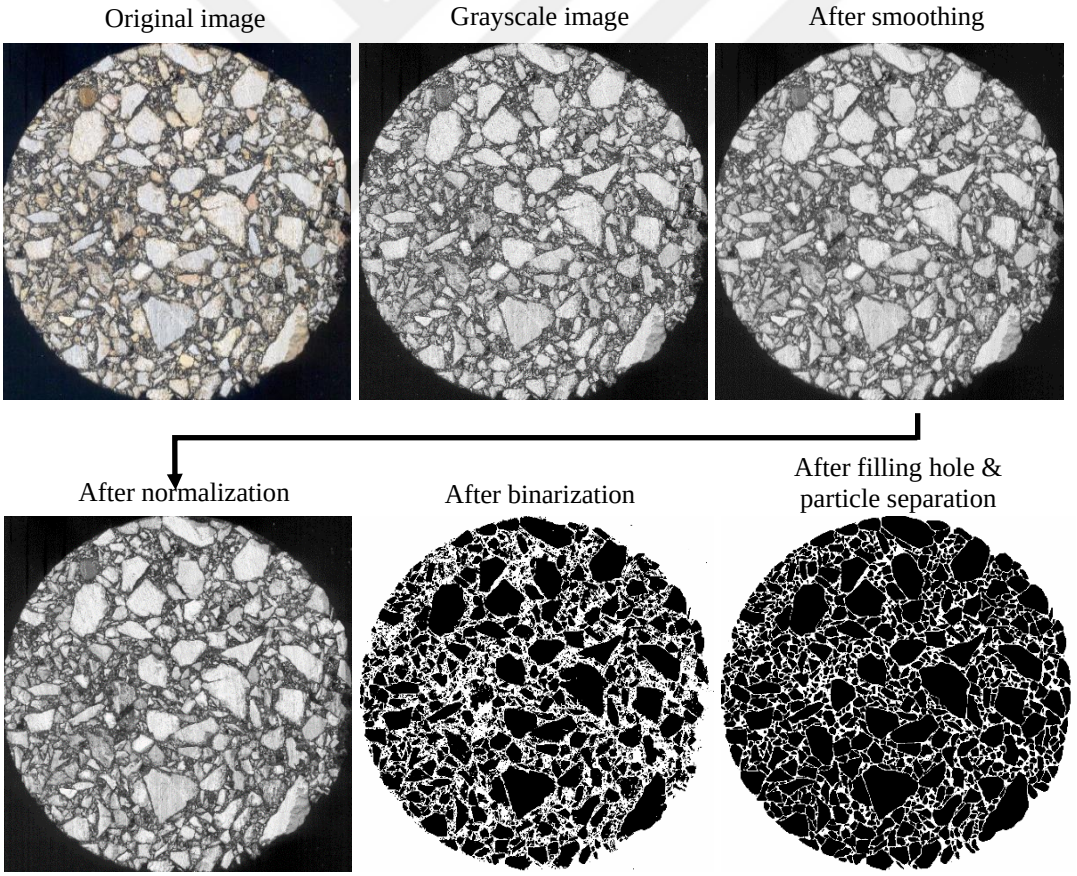

Figure 4.13. Image processing steps

4.3 Image Vectorization

One of the many advantages of finite element modeling (FEM) is its ability to handle complicated geometries (and boundaries) with relative ease. However, it is also very difficult to simulate these complex geometries, which are also found in the structure of asphalt concrete, in the finite element environment. In the early studies, artificial circular or irregular shaped elements were used to create the geometric model in FEM, which was quite far from the actual structure of the aggregates. With the development of the image processing method, it became possible to simulate the actual structure of the aggregate.

Initially, the complex structure of the AC, which consists of aggregate and binder, was evaluated in a pixel-based model, and all pixels corresponding to these sections were transferred as a whole to the finite element environment. This method usually required a large number of elements and very high computational costs, and thus the practicality of the finite element method could not be fully facilitated. This is because the pixel-based models must work with all pixels of the image, and increasing the resolution to capture smaller aggregate particles would result in a large number of pixels. Thus, some sacrifices have to be made between resolution and model accuracy. To overcome these problems while realistically simulating the aggregate structure in the finite element environment, a completely new image vectorization method was developed in this study. With this proposed method, specimen surfaces can be scanned at an arbitrarily high resolution without increasing the element sizes too much. A detailed explanation of this method can be found in the following sections.

4.3.1 Size Distribution Analysis of Aggregates

At the end of the image processing process, the images were scanned, enhanced, and converted to a binary state. Despite the processing, there were still many small clusters or individual pixels in the image. These clusters were due to intensity differences during scanning and were too small to actually represent aggregated particles and therefore had to be removed. At this stage, some parameters had to be defined to further process the aggregate particles in the images.

There are several methods and parameters in the literature that have been used to study the shape analysis of cross-sectional images of asphalt concrete. Ozen and Guler (2014) found that the optimal shape parameter to predict the actual aggregate size distribution was the use of the maximum Feret diameter. The binary images were analyzed using the shape parameters: Maximum Feret diameter and area. The area of an aggregate particle is the sum of all pixels contained in its cross-section. The maximum Feret diameter, on the other hand, is the length of the largest line segment that can be inserted into an aggregate particle (Figure 4.14).

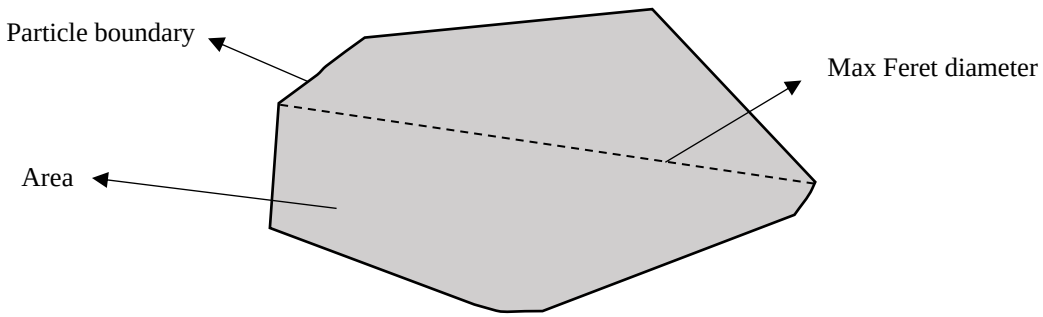

Figure 4.14. Aggregate shape parameters

The area and maximum Feret diameter of each aggregate particle were determined. To determine the percentage passing through a sieve size, the maximum Feret diameter was compared to the standard diagonal sieve size. The reason for this is that an elongated particle larger than the standard sieve size (square) can still pass through this sieve opening. Therefore, to determine the percentage of particles of each size that passed, the maximum Feret diameters were compared to the diagonal

opening of each sieve size. The particles whose maximum Feret diameter is equal to or smaller than the diagonal sieve size are considered to pass through that sieve.

Images were analyzed in LabVIEW®- Vision Assistant software to determine the size distribution of the cross-sectional images. To ensure that the captured image of the sample represents the actual gradation used in the mix design, the size distributions of the two were compared. To illustrate the particle size analysis, Figure 4.15 shows an example image of the specimen ID "LURM01-1" in the LabVIEW®- Vision Assistant software. The software was able to detect any closed form of aggregate shapes and calculate their areas and maximum Feret diameters. The sample contained 4115 particles, some of which were impractical, as mentioned earlier. After several trials and errors, it was concluded that the detection of particles smaller than 0.425 mm was impractical for size distribution analysis. The same method was also used by Yucel (2019) in his dissertation. In this example, 1536 small particles with a maximum ferret diameter of less than 0.425 mm were detected and these aggregates were removed from the image, resulting in a total of 2579 aggregate particles.

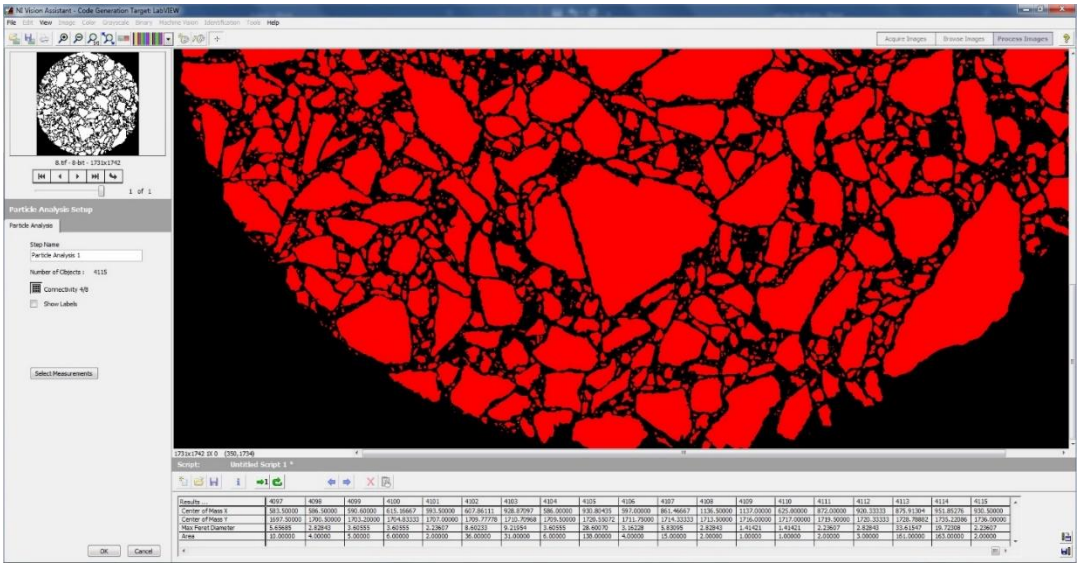

Figure 4.15. An example of the sample ID LURM01-1 in the Vision Assistant software

Later, the excluded particles were used to normalize the percentages to eliminate their influence on the results:

$$P_p = \frac{(100-P_e)}{100} P_i \quad (4.2)$$

where P_p is the normalized percent passing; P_e is the actual percentage area of excluded particles; P_i is the percentage passing calculated from the software.

The actual gradations used in the mix design and the estimated gradations from the size distribution analyzes are shown in Table 4.1 and 4.2. Three cross-sectional images were compared for each design type. The results show that the gradations of the captured 2D cross-sectional images of the samples are quite close to the original gradations used in the mix design. It was concluded that the images are capable of representing the actual aggregate gradation in the finite element environment.

The graphical comparisons of the results are shown in Figure 4.16 and 4.17. While the largest deviation for the TGDH design samples was 16.4% at sieve No. 4 (4.75 mm), for the FAA design it was 16.9% at the sieve No. 16 (1.18 mm). In general, the overall deviations for the other size fractions are negligible ($R^2 > 0.994$).

Table 4.1. Comparison of actual and calculated gradations of the TGDH design

Sieve size (mm)	**Percent Passing (%)**			
	Design Gradation	**Image-1**	**Image-2**	**Image -2**
25	100	100	100	100
19	95	90.8	91.4	97.2
12.5	80	78.5	77.2	85.3
9.5	68	66.9	64.2	70.7
4.75	35	39.9	38.5	32.2
2	21.5	18.2	19.8	22.5
0.425	10	10.2	9.8	9.9
R^2		0.994	0.996	0.996

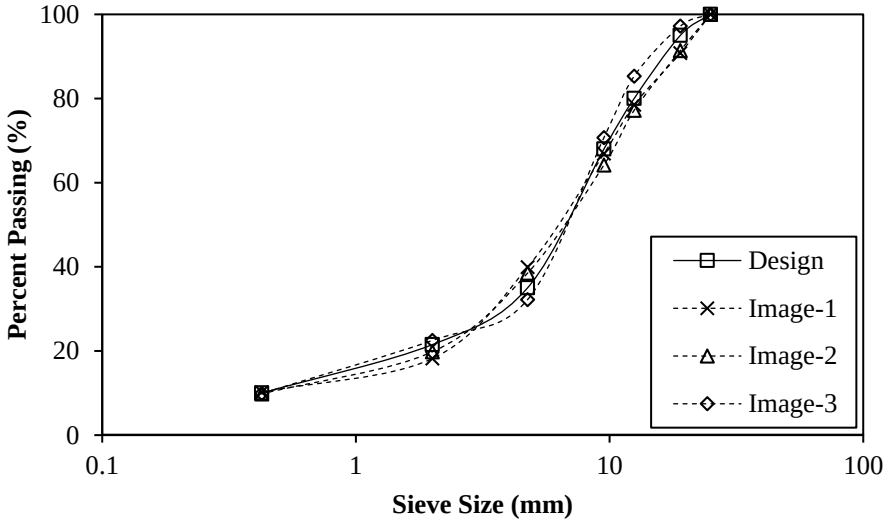

Figure 4.16. Graphical comparison of actual and estimated gradations of the TGDH design

Table 4.2. Comparison of actual and calculated gradations of the FAA design

Sieve size (mm)	**Percent Passing (%)**			
	Design Gradation	**Image-1**	**Image-2**	**Image -2**
25	100	100	100	100
19	98	98.1	98.7	97.2
12.5	91.2	89.2	88.9	89.5
9.5	83.7	85.5	80.5	79.2
4.75	47.7	43.1	43.5	50.8
2.36	31.5	32.3	33.1	30.6
1.18	23.1	25.5	25.1	27.0
0.6	15.7	15.8	15.8	15.7
R^2		0.996	0.996	0.995

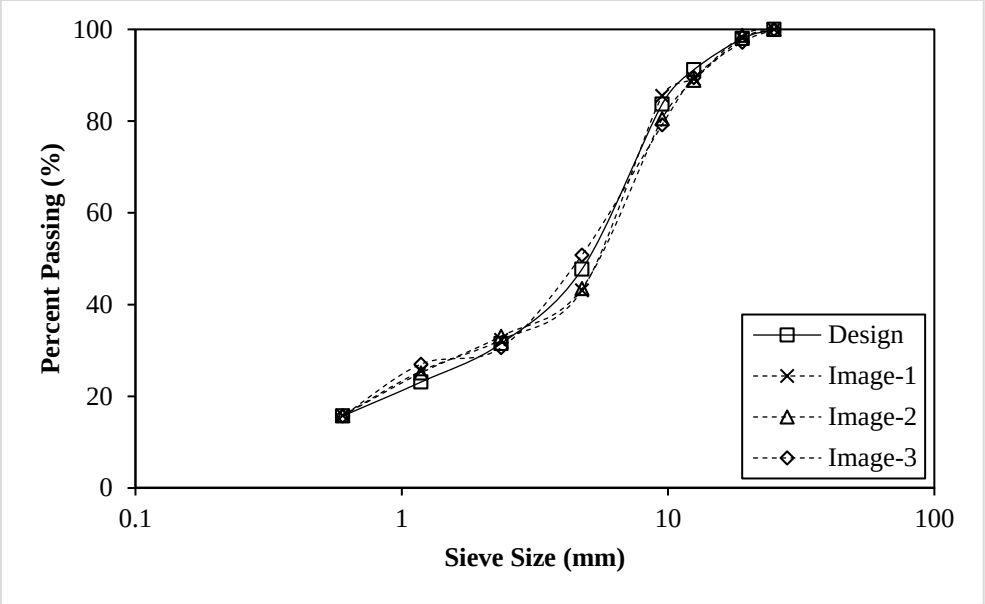

Figure 4.17. Graphical comparison of actual and estimated gradations of the FAA design

4.3.2 Edge Detection

In an asphalt mixture, while the mastic phase contains fillers ranging in size from 1 μm to 75 μm, the mortar phase contains fine aggregates smaller than 2.36 mm. Therefore, the scale of the asphalt mixture in this study was modeled with aggregates whose maximum Feret diameter is 2.36 mm and above. The particles below this value were removed from the images and these areas were evaluated in the binder phase. In addition, the flatbed scanning method is not able to filter out such smaller particles from the noise, and relatively higher thresholds for aggregates were required. An example image (ID LURM01-1) before and after particle removal for the finite element modeling is shown in Figure 4.18. The image had 4115 particles before this procedure, while a total of 1126 aggregate particles remained after particle removal. This procedure was very important for the success of the finite element modeling. This is because removing superfluous particles significantly reduced the number of elements in the finite element model and thus the required computing power.

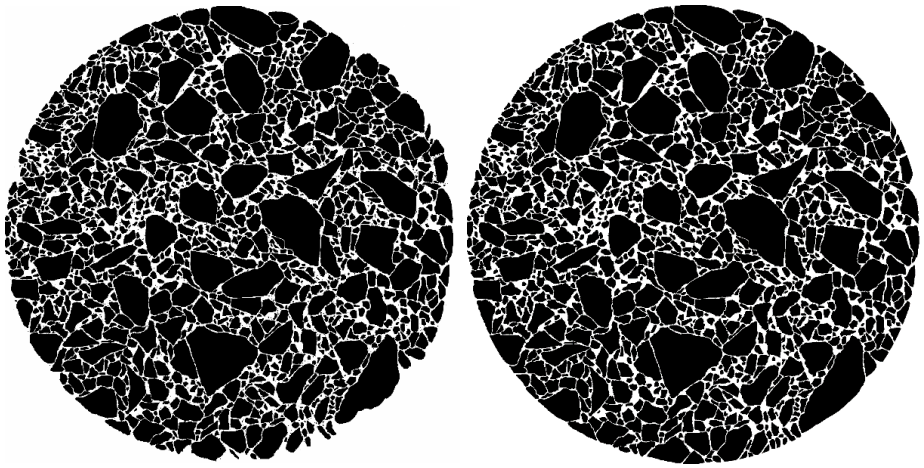

(a) (b)

Figure 4.18. Binary image: a) Before, c) After particle removal (ID LURM01-1)

The images were then transferred into MATLAB®. To create the vector format of the image, an algorithm was written to locate the edge pixels in the outermost periphery of each aggregate with a thickness of one pixel. The binary image was then converted back into its new form. This time, the edge pixels at the periphery of the aggregates took the place of their faces (Figure 4.19). The MATLAB® code for such an algorithm can be found in Appendix D.

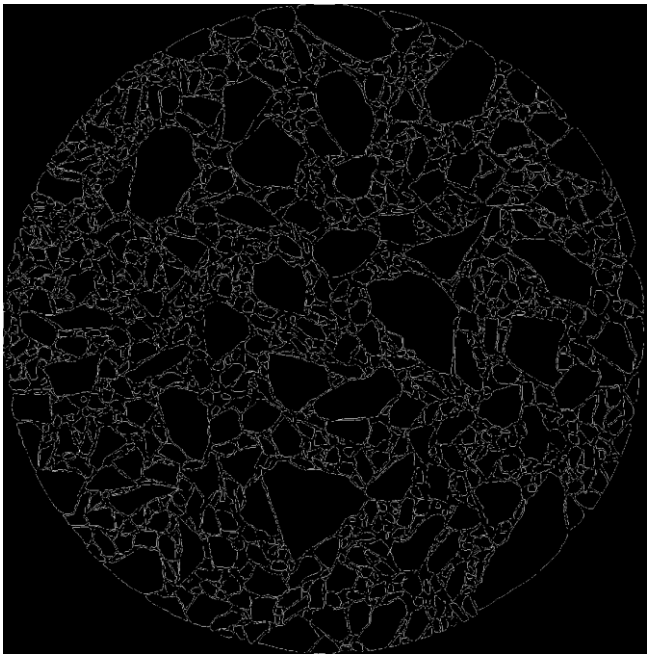

Figure 4.19. Edge detection method in MATLAB

4.3.3 Vectorization

The image whose edge pixels were located was ready in MATLAB® at this point. The coordinates of each edge pixel were then transferred to a file, with respect to their x and y axes within the image. It should be noted that the origin point of an image in MATLAB® is at the upper left corner. Each aggregate particle in the image was surrounded by several pixels, and the coordinates of these pixels were written to a file in relation to their positions in the image. Figure 4.20 shows an example image (ID LURM01-1) with 1126 aggregate particles. These particles with their edge pixels clusters are in an array of cells, where each cell represents an aggregate particle (Figure 4.20a). In Figure 4.20b, the vertical coordinates of the pixels are in the first column, while the horizontal coordinates are in the second column, and the combination of one row corresponds to one pixel. In the example, the coordinates of the 30 edge pixels of an aggregate particle can be seen, which form the aggregate in the 9th cell.

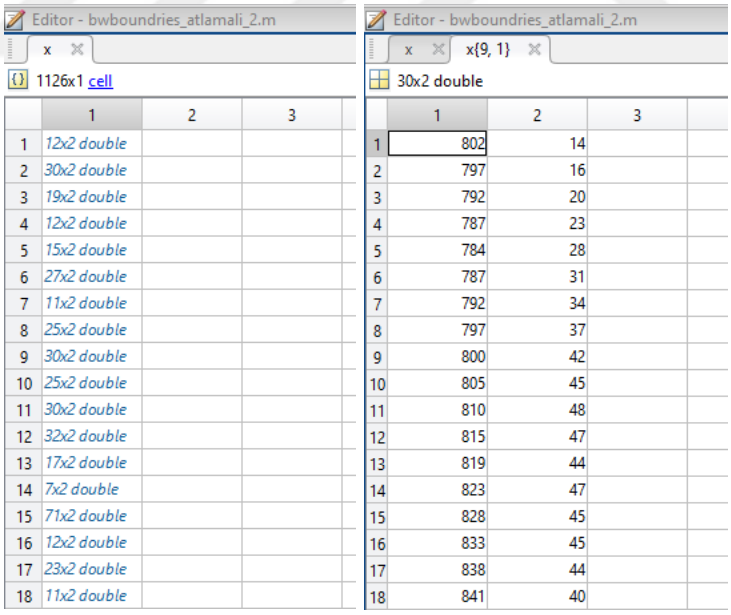

(a) (b)

Figure 4.20. Image matrices in MATLAB: a) Total aggregates, b) The edge pixels

Then, the obtained files, containing the total number of pixels and their coordinates, are imported into ANSYS®. ANSYS® is a mechanical finite element analysis software for simulating computer models of structures, electronic or machine components and can analyze strength, toughness, elasticity, temperature distribution, electromagnetism, fluid flow and other properties. However, the main reason for using ANSYS® at this stage was its efficiency, simplicity and the necessary capability of the APDL function to create the geometric model. ANSYS® Parametric Design Language (APDL) provides parameterization, macros, branches and loops, and also complex mathematical operations. All of these features were exactly what was needed at this stage. An algorithm was written in ANSYS® Mechanical APDL to convert the coordinate files into their geometric shapes in the finite element environment. The algorithm is given in Appendix E.

The basic operating principle of the algorithm was as follows: First, a single aggregate particle was treated at a time, and a keypoint was assigned to each pixel coordinate around that aggregate in turn. Then these keypoints were connected by lines and this process was continued clockwise until all surrounding pixels of an aggregate particle were completed (Figure 4.21). Finally, the closed aggregate geometry obtained was converted to an area using the area command (Figure 4.22). This process was continued until all the aggregate particles in the image were formed in sequence. The resulting geometric model with its original binary image is shown in Figure 4.23. In this model, the image was converted to its vector format, with polygon aggregate shapes formed from keypoints connected by lines.

A vector image has the unique advantage over the original raster image in that the points and lines can be scaled to any resolution without aliasing. In addition, the quality of the model was now independent of its resolution and could be meshed as desired in a finite element environment. Another advantage of the vector image was that the number of elements within the finite element was greatly reduced because pixels were completely eliminated. In this example, the image had 1740 pixels in each direction as it was scanned at a resolution of 300 dpi. The total number of pixels

within the binary image was over 3 million. In contrast, the vector format of the example image (ID LURM01-1) in ANSYS® consisted of a total of about 100,000 pixels, i.e., 100,000 keypoints and the same number of connecting lines. As it will be explained in the following chapters, the number of elements can be reduced even further.

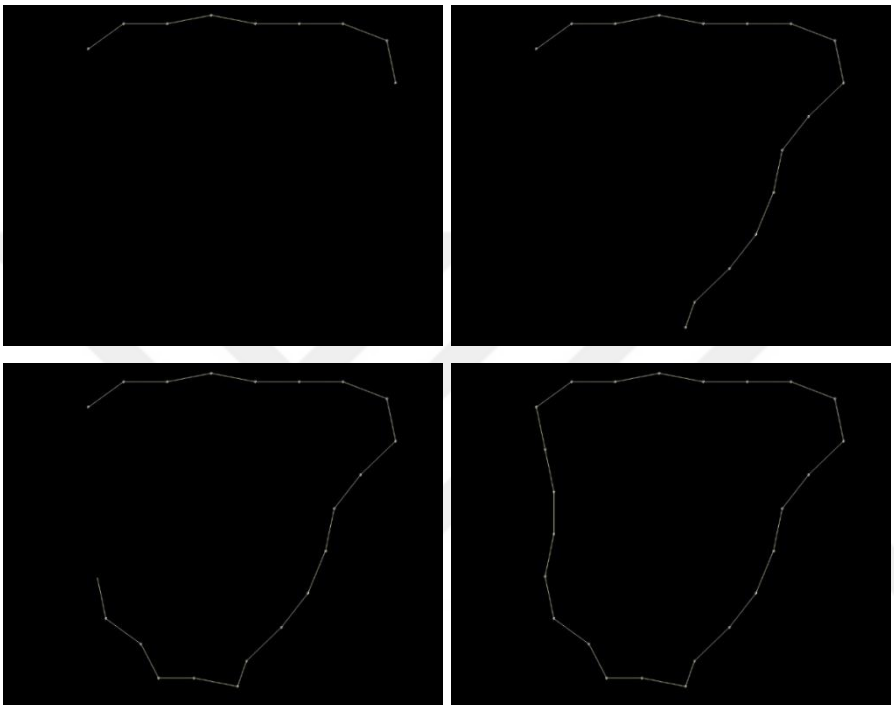

Figure 4.21. Example aggregate particle creation procedure in the ANSYS

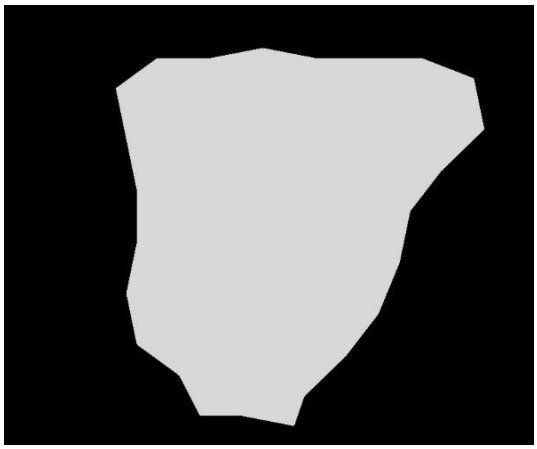

Figure 4.22. Resultant aggregate particle in the ANSYS

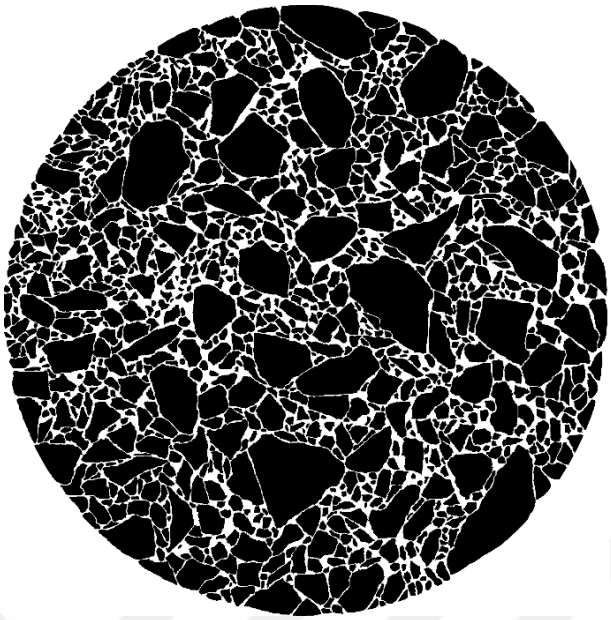

(a)

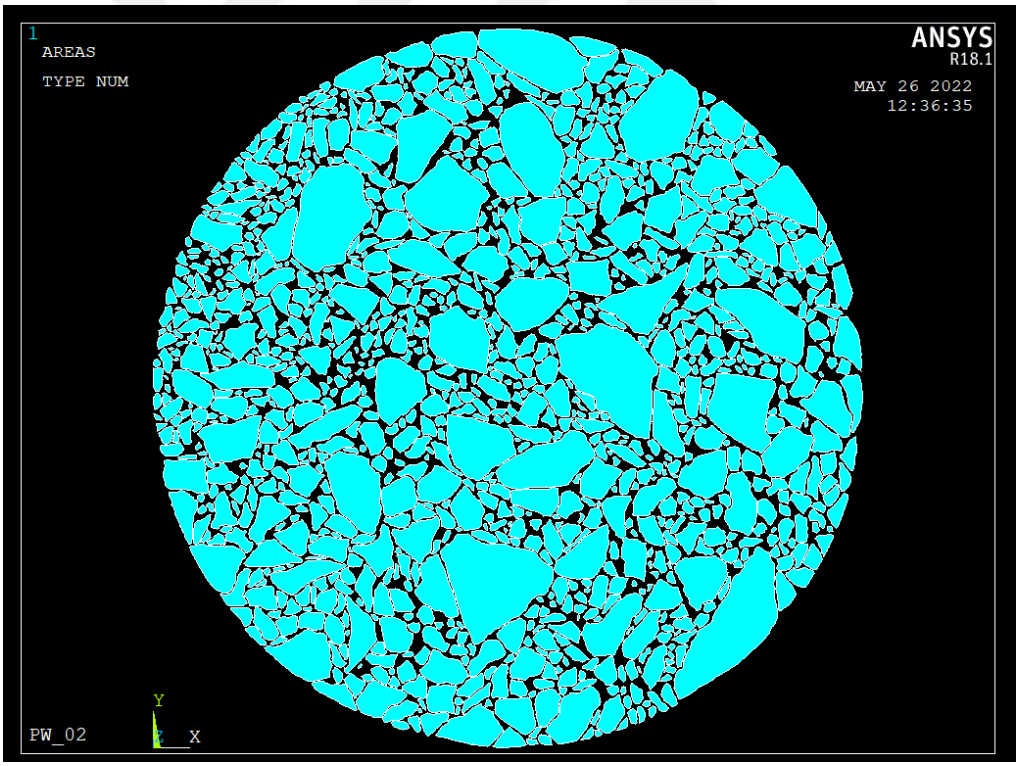

(b)

Figure 4.23. a) Binary image at the end of image processing, b) Vector form of the image in ANSYS

4.3.4 Pixel Reduction

Another problem associated with pixel-based models is the external shape of the aggregate particles used in the image-based geometric model. For images scanned at low resolution, the outer edges of the aggregate particles are rough due to the square shape of the pixels. The actual shape of the aggregate particles is much smoother than shown in the images. Although scanning at higher resolutions reduces this phenomenon, it cannot be completely eliminated. Furthermore, since higher resolutions would increase the number of pixels, leading to a significant increase in the processing and computational complexity of the model, and preventing efficient analysis.

In order to accurately model the actual shapes of the aggregates, pixel reduction was performed at this point. This involved skipping some of the pixel coordinates around the aggregate particles in a clockwise direction. First, a single pixel jump was performed and the result was compared to the previous model. The number of pixel jumps was increased until the desired smoothing was achieved. Finally, it was found that taking pixels in five intervals gave the best results (Figure 4.24). However, skipping more than seven pixels sometimes caused the loop to fail, because the number of pixels for some aggregate particles was insufficient to create a closed area. Eventually, the pixels were reduced to 1 in 5 and the model was rebuilt. The total number of keypoints in the final model was 28,834, and the same number of lines was used to create areas.

Vectorization of images brought several advantages. First, high-resolution images could be used to capture even the smallest aggregate particles. After the vectorization process, the number of elements used to create the high-resolution image was significantly reduced, which allowed both a high-quality geometric representation of the images and the use of relatively small element sizes. In addition, the particle shapes were more accurate compared to previous methods.

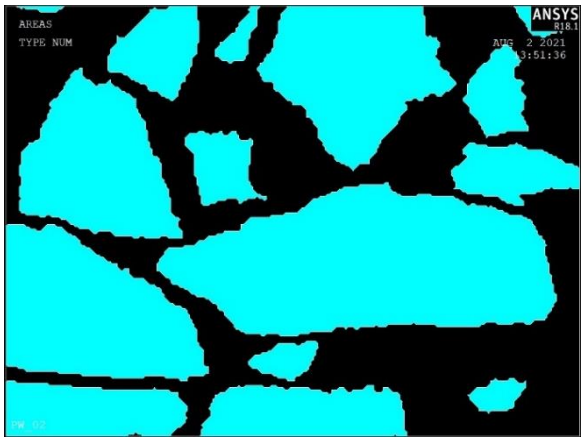

(a)

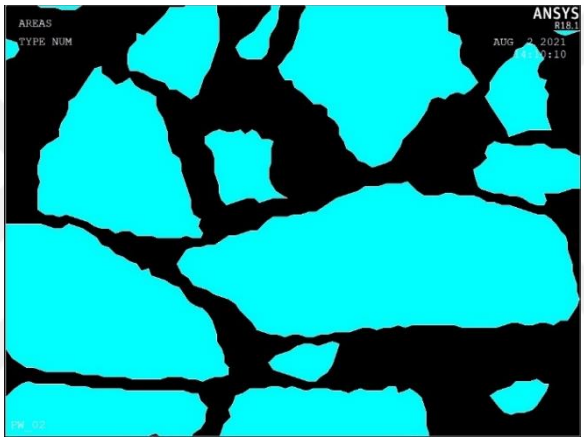

(b)

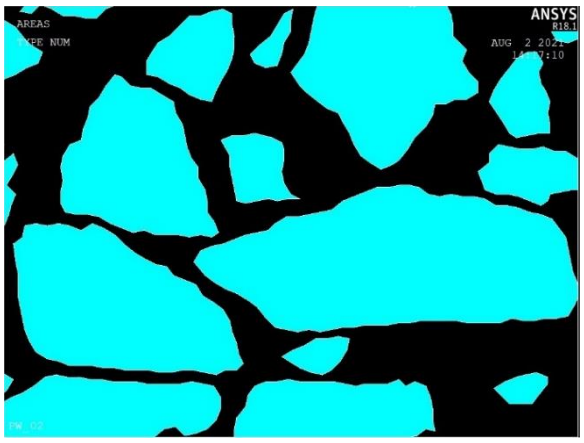

(c)

Figure 4.24. a) Original image, b) Reduced image after skipping 2 pixels, c) Reduced image after skipping 4 pixels

4.4 Particle Redistribution

One of the main objectives of this study is to facilitate replication of samples, which is difficult in laboratory studies, by taking advantage of the numerical method of analysis. Replicating the experiment allows researchers to estimate the variability of the results, identify patterns and trends, eliminates erroneous results and increases the precision of the estimate. Not to mention that testing a large number of samples, even preparing single asphalt sample for testing in the laboratory, requires quite a bit of work. However, with the numerical analysis method, it is easier to repeatedly apply a similar analysis once it has been prepared. For this reason, the goal is to create new artificial images based on the obtained images by changing only the positions and orientations of the aggregate particles in the image without changing the number or orientation of the original aggregate particles.

In his thesis work, A MATLAB® algorithm was developed and used by Yucel (2019), that can generate new artificial images based on existing processed images. A similar method was also used in this study. In these new images, the aggregate particles are the same in terms of their number and external shape, only their positions and directions within the image have been changed.

The algorithm first detects all aggregate particles individually and sorts them from large to small according to their maximum Feret diameter. It then spatially redistributes these aggregates at random locations. If any overlap is detected, the redistribution step is repeated until there is no more overlap. Although the resulting image is the same in terms of the total number of the pixels and pixels corresponding to each phase of the asphalt mixture, i.e., asphalt binder and aggregate, a completely new aggregate structure is created. Furthermore, this method can be used an unlimited number of times to perform as many sample replicates as desired. Thus, many sample repetitions can be applied in the finite element method while maintaining the original gradations of the samples prepared in the laboratory.

An example of such aggregate redistribution using the images of the samples ID LURM02-1 and ID LUCR06, can be found in Figures 4.25 and 4.26. The resulting binary output images are the same with the input images in terms of image size, number of aggregates, and shape of these aggregates. However, the positions of these aggregate particles and their directions are completely different from those of the original images. In these artificially generated synthetic images, a completely different aggregate structure is created with the help of the initial gradation. The remaining images resulting from the redistribution are listed in Appendix F.

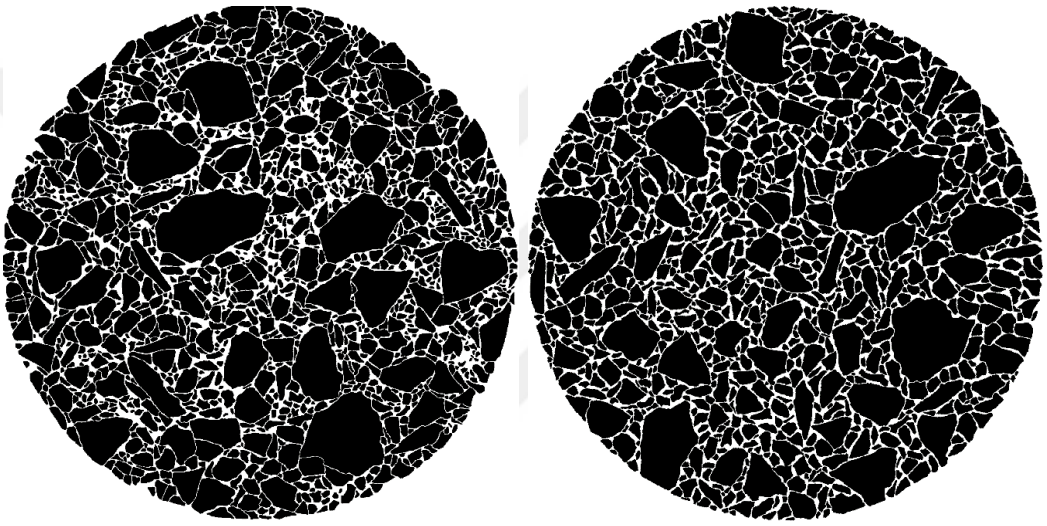

(a) (b)

Figure 4.25. Aggregate redistribution of the specimen ID LURM02-1: a) Original image, b) Redistributed synthetic image

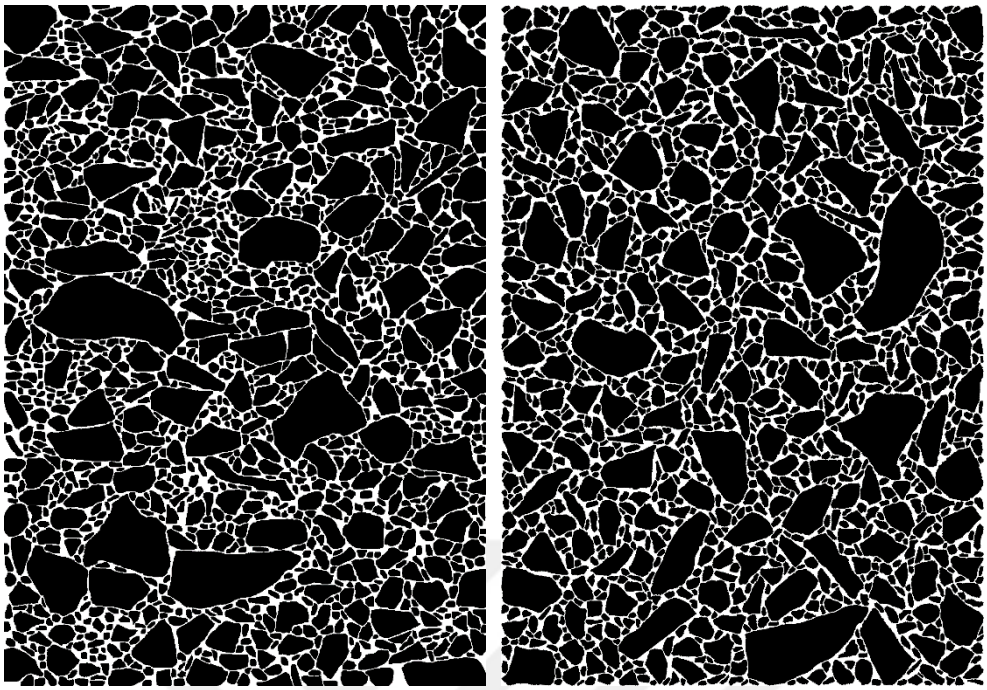

(a) (b)

Figure 4.26. Aggregate redistribution of the specimen ID LUCR06: a) Original image, b) Redistributed synthetic image

4.5 From Digital Images to Finite Element Model

Once the geometric model is completed in ANSYS® Mechanical APDL software, it can be exported to a single file in IGES format. This file contains the entire geometric model in the form of keypoints and lines created based on the edge pixels. At this point, all the necessary geometric elements required to create the finite element model are formed. The rest of the analysis is performed using ABAQUS® software. ABAQUS/CAE (computer-aided environment) is a software package for finite element analysis. It can solve all types of linear and nonlinear problems as well as contact problems.

4.5.1 Geometric Model

The IGES file, in which separate keypoints, lines, and surfaces were formed for each aggregate particle, was exported from ANSYS® and then imported into ABAQUS® as a sketch model. One such example is shown in Figure 4.27. The numerical model of this study consisted of two phases: The aggregate phase and the asphalt binder phase. First, the aggregate phase was created with a 2D planar part based on the sketch model (Figure 4.28). The corresponding parts were created in ABAQUS® using "2D Planar" modeling space because of the fact that the FE model in this study is a 2D model. At this stage, deformable parts with the "shell" base feature are used.

The binder phase was then created by subtracting the existing aggregate phase from the background portion, which had the dimensions of the original sample (Figure 4.29). By joining these two parts created in ABAQUS®, the geometric model was completed (Figure 4.30). A linear 2D element type with plane strain was used to represent the two parts. Two main types of specimens were used in this study: Circular specimens with a diameter of 150 mm for resilient modulus and indirect tensile fatigue tests, and cylindrical core specimens with a diameter of 100 mm and a height of 150 mm for repeated creep tests. Images of the smooth surfaces of the round specimens were taken before resilient modulus and indirect tensile fatigue tests. Only the specimens for the FN tests were cut and scanned after the tests in which they exhibited some degree of deformation. All binary images used in this study after image processing and their finite element models in ABAQUS® are listed in Appendix G.

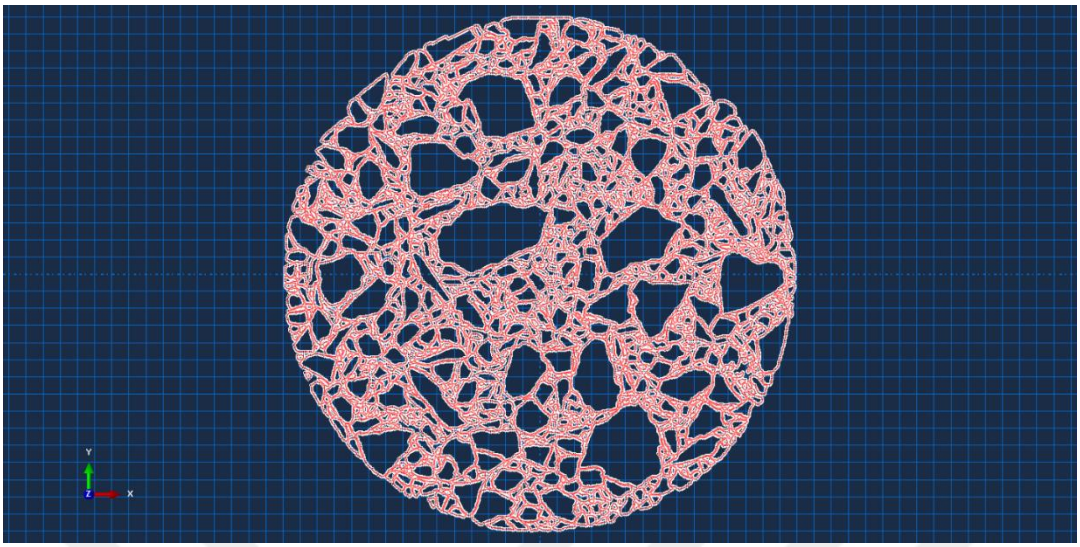

(a)

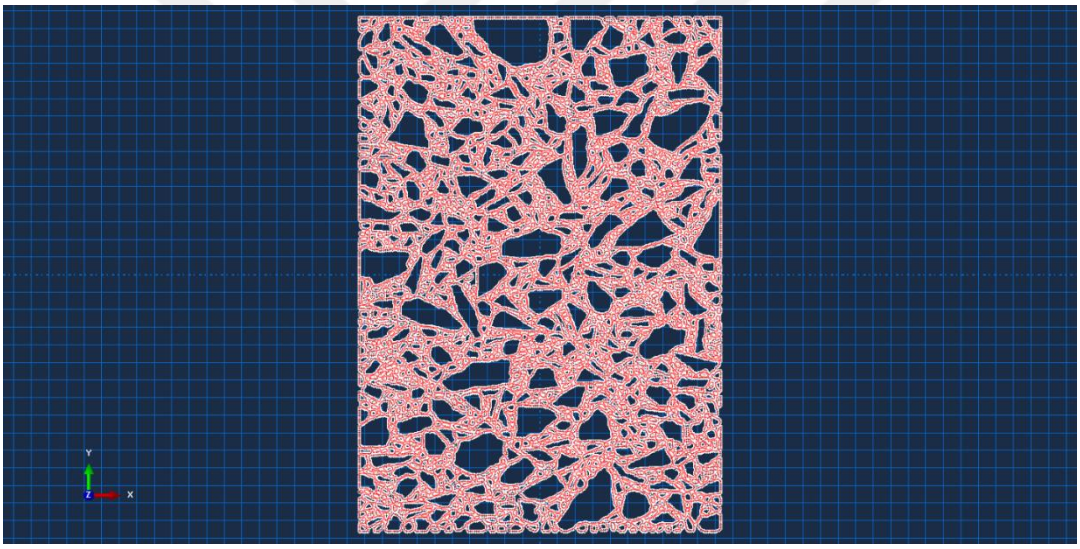

(b)

Figure 4.27. Imported IGES file as a sketch model: a) Circular specimen (ID LURM02-1), b) Rectangular specimen (ID LUCR09)

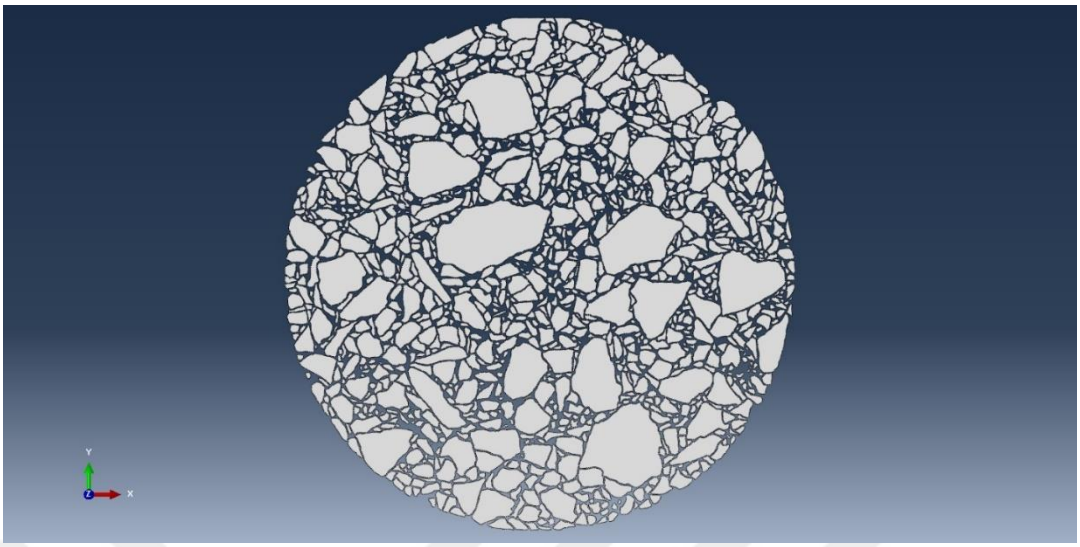

(a)

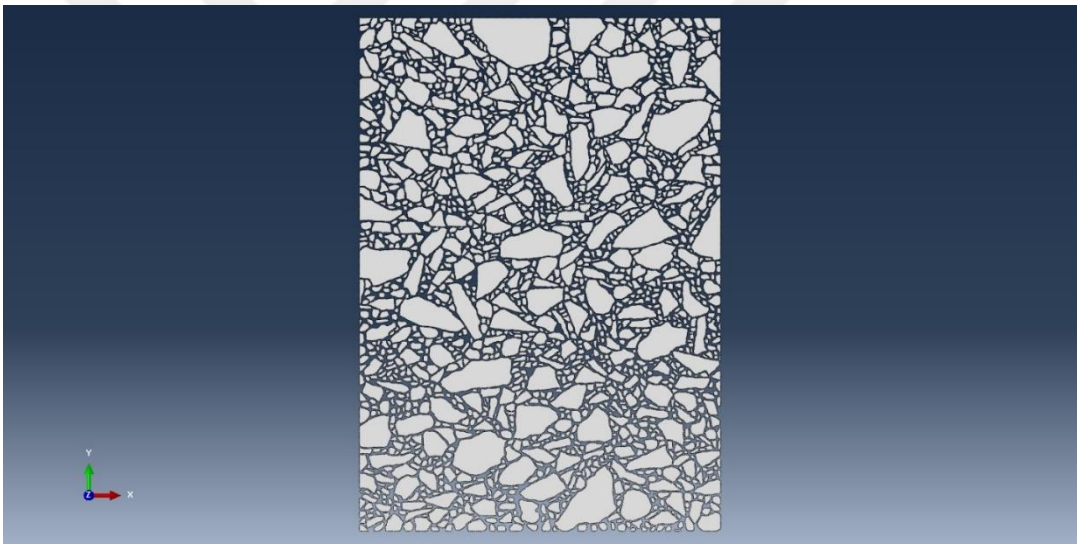

(b)

Figure 4.28. Created 2D aggregate parts: a) Circular specimen (ID LURM02-1), b) Rectangular specimen (ID LUCR09)

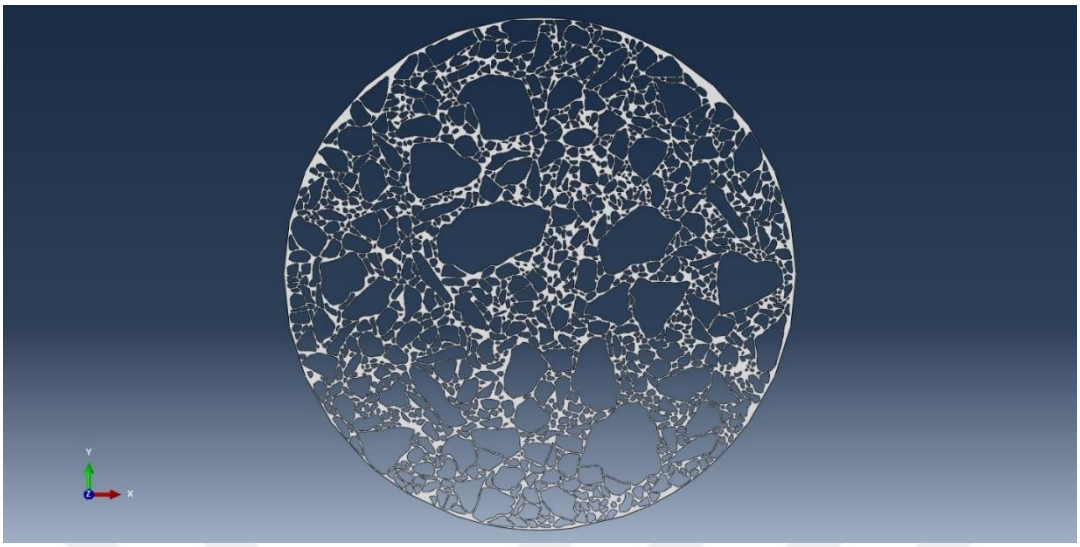

(a)

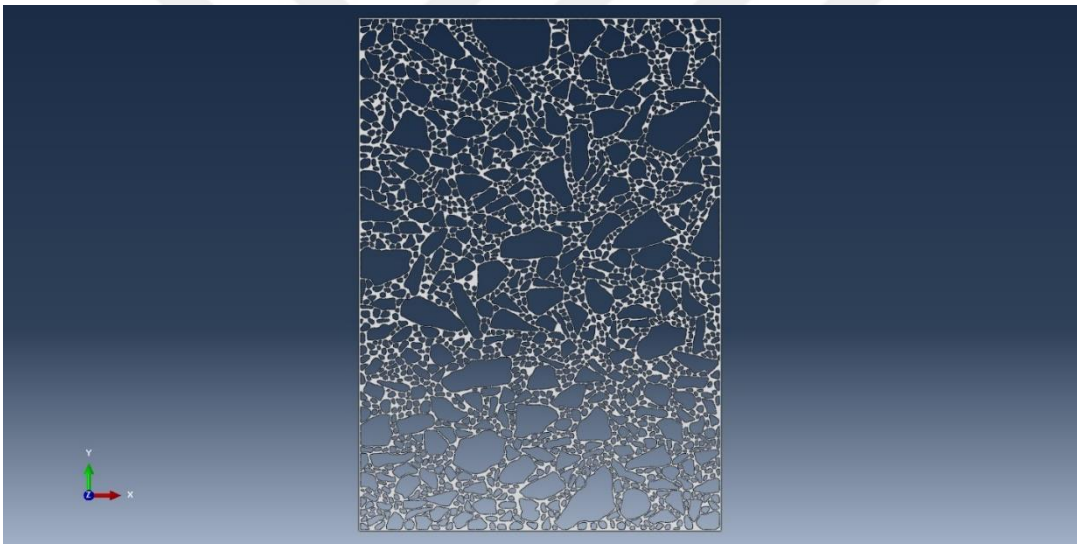

(b)

Figure 4.29. Created 2D binder parts by subtracting the aggregate parts: a) Circular specimen (ID LURM02-1), b) Rectangular specimen (ID LUCR09)

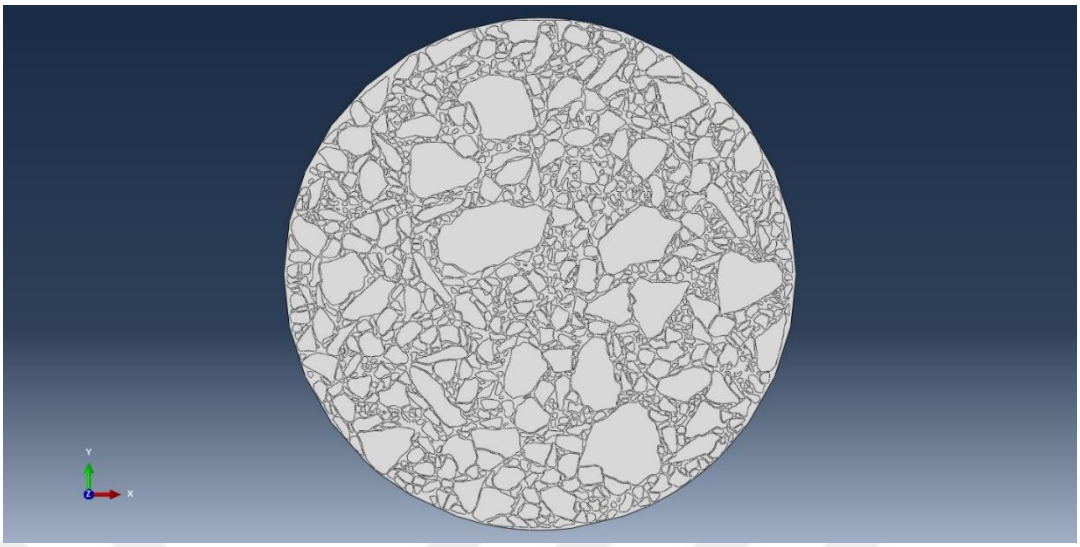

(a)

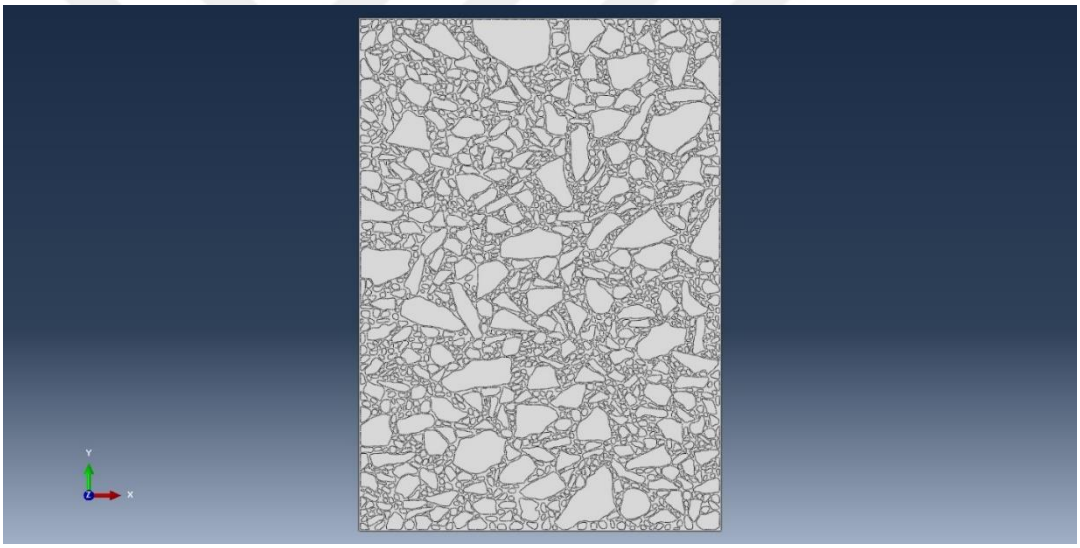

(b)

Figure 4.30. Completed geometric models: a) Circular specimen (ID LURM02-1), b) Rectangular specimen (ID LUCR09)

4.5.2 Material Model

4.5.2.1 Aggregate

The two-dimensional finite element model in this study consisted of two phases: Aggregate phase and binder phase. Linear elastic properties were used to model the aggregate phase. After a thorough review of the literature, it was found that this traditional method was also used in many studies. The elastic modulus and Poisson's ratio were frequently predicted by researchers. The linear elastic material properties used in these studies are summarized in Table 4.3.

Table 4.3. Comparison of linear elastic material properties used in the literature

Study	***E* (GPa)**	***ν***
Kose (2002)	25	0.25
Abbas (2004)	25	0.25
You et al. (2008)	55	0.20
Graham (2009)	1	0.16
Aragao et al. (2011)	60.9	0.35
Wang et al. (2013)	73.26	0.26
Arshadi & Bahia (2015)	25	0.25
Huang et al. (2016)	25	0.25
Rami et al. (2017)	63.5	0.15
Kollman et al. (2019)	55	0.2
Du et al. (2020)	80	0.2
Zhao et al. (2020)	63.5	0.15
Wang et al. (2021a)	60	0.25

Two types of aggregates were used in this study: Limestone in the TGDH samples and basalt in the FAA samples. The two aggregates differed significantly in quality. Los Angeles abrasion tests were conducted on the aggregates and the results were 30

and 14 percent for the limestone and basalt aggregates, respectively. Therefore, the elastic modulus of the basalt aggregate is believed to be much greater than that of the limestone. The properties of the linear elastic aggregates were determined as follows:

Table 4.4. Selected linear elastic material properties used in the study

Aggregate	***E* (GPa)**	***ν***
Limestone	55	0.25
Basalt	70	0.25

4.5.2.2 Asphalt Binder

Material modeling for the asphalt binder, on the other hand, was quite complicated due to its viscoelastic nature. In this study, the main principles of linear viscoelasticity were used to describe the asphalt binder phase. The basic uniaxial isothermal stress-strain equation for a linear viscoelastic material can be expressed by the Boltzmann superposition integral:

$$\sigma_{(t)} = \int_0^t E(t-\tau)\frac{d\varepsilon(\tau)}{d\tau}d\tau \tag{4.4}$$

where $E(t-\tau)$ is the relaxation modulus characterising the response of the material. The time-dependent character of this modulus can be represented by arbitrary rheological models consisting of various combinations of elastic (spring) and viscous (dashpot) elements, such as the generalized Maxwell model. As explained in the second chapter, the generalized Maxwell model is composed of a spring and several Maxwell units. A Maxwell unit is the simplest mechanical model that represents the linear viscoelastic behavior through a spring in series with a dashpot. The behavior of such an element can be represented as follows:

$$\varepsilon(t) = \frac{\sigma(t)}{E} + \frac{\sigma(t)}{\eta} \tag{4.5}$$

where E is the elastic modulus of the spring; η is the viscosity of the dashpot. If a constant strain (ε_0) is applied at $t = 0$ and held for a time, the above equation becomes:

$$\sigma(t) = E\varepsilon_0 e^{\left(\frac{-t}{\tau_M}\right)} \tag{4.6}$$

and

$$\tau_M = \frac{\eta}{E} \tag{4.7}$$

where, τ_M is the relaxation time. The above equation implies that the stress builds up with delay at the beginning and relaxes exponentially from its equilibrium value at the beginning. However, the Maxwell model is too simplified to describe real linear viscoelastic behavior, such as creep. Moreover, in reality, a viscoelastic material does not have a single relaxation time. Therefore, the generalized Maxwell model has been used by researchers to overcome these problems. The total stress of the generalized Maxwell model can be written as follows:

$$\sigma(t) = E_\infty\varepsilon_0 + \sum_{i=1}^{n} E_i\varepsilon_0 e^{\left(\frac{-t}{\tau_i}\right)} = \varepsilon_0\left[E_\infty + \sum_{i=1}^{n} E_i e^{\left(\frac{-t}{\tau_i}\right)}\right] \tag{4.8}$$

The relaxation modulus $E(t)$ then can be expressed by:

$$E(t) = \frac{\sigma(t)}{\varepsilon_0} = E_\infty + \sum_{i=1}^{n} E_i e^{\left(\frac{-t}{\tau_i}\right)} \tag{4.9}$$

where, E_∞ is the final or (equilibrium) modulus. This equation is also called the Prony series representation. The instantaneous modulus E_0 is:

$$E_0 = E_\infty + \sum_{i=1}^{n} E_i \tag{4.10}$$

So, the Eq. 4.9 then can be written as:

$$E(t) = E_0 - \sum_{i=1}^{n} E_i\left(1 - e^{\left(\frac{-t}{\tau_i}\right)}\right) \tag{4.11}$$

where, the pair of E_i and τ_i is referred to as a Prony pair.

In ABAQUS®, the rate-dependent viscoelastic behavior is described by a viscoelastic material model in the time domain and implemented by using Prony series. However, the shear and bulk responses are separated and represented by a Prony series expansion of the dimensionless relaxation modulus. Dividing then both sides of the relaxation modulus equation by the instantaneous modulus G_0 the shear modulus (G) and bulk modulus (K) can be written as follows:

$$G_R(t) = G_0\left[1 - \sum_{i=1}^{n} g_k\left(1 - e^{\left(\frac{-t}{\tau_i}\right)}\right)\right] \tag{4.12}$$

and

$$K_R(t) = K_0\left[1 - \sum_{i=1}^{n} k_k\left(1 - e^{\left(\frac{-t}{\tau_i}\right)}\right)\right] \tag{4.13}$$

where G_0 and K_0 are the instantaneous shear and bulk modulus determined by the ABAQUS® from the user-defined instantaneous elastic modulus E_0 and Poisson's ratio ν:

$$G_0 = \frac{E_0}{2(1+\nu)} \tag{4.14}$$

and

$$K_0 = \frac{E_0}{3(1-2\nu)} \tag{4.15}$$

or they can also be determined from the long-term elastic modulus, if so defined. In ABAQUS®, the necessary parameters of time-dependent volume and shear behavior can be defined in four ways: by directly specifying the parameters of the Prony series, from creep test data, from relaxation test data, or from frequency-dependent test data. In this study, the complex shear modulus master curve of the asphalt binder was determined using frequency sweep tests. A nonlinear curve fitting was then applied to the master curve to determine Prony pairs. The Prony pairs were then used in the ABAQUS® material model to simulate the viscoelastic behavior of the asphalt binder.

The Prony series terms can be calibrated with frequency-dependent test data. In this case ABAQUS® uses analytical expressions relating the relaxation functions of the Prony series to the storage and loss moduli. Then the Fourier transforms are used in a nonlinear least square fit to determine the storage and loss moduli:

$$G_s(\omega) = G_0[1 - \sum_{i=1}^{n} g_i] + G_0 \sum_{i=1}^{n} \frac{g_i \tau_i^2 \omega^2}{1+\tau_i^2 \omega^2} \tag{4.16}$$

and

$$G_l(\omega) = G_0 \sum_{i=1}^{n} \frac{g_i \tau_i \omega}{1+\tau_i^2 \omega^2} \tag{4.17}$$

where G_s is the storage modulus; G_l is the loss modulus; ω is the angular frequency; n is the number of terms in the Prony series. In the nonlinear least-square fit, the Prony series parameters are determined from the storage and loss moduli test data by minimizing the error function x^2:

$$x^2 = \sum_{i=1}^{m} \frac{1}{G_\infty^2} [(G_s - \bar{G}_s)_i^2 + (G_l - \bar{G}_l)_i^2] \tag{4.18}$$

where $\bar{G}_s, \bar{G}_l$ are the test data. For simplicity, only the shear modulus will be considered and isothermal compressibility is neglected. The nondimensional shear relaxation function in its Fourier transformation $g^*(\omega)$:

$$g(t) = \frac{G(t)}{G_\infty} - 1 \tag{4.19}$$

and the real and imaginary part of the function $\omega g^*(\omega)$ are:

$$\omega \Re(g^*) = \frac{G_l}{G_\infty} \tag{4.20}$$

and

$$\omega \Im(g^*) = 1 - \frac{G_s}{G_\infty} \tag{4.21}$$

First, frequency sweep tests were performed on the two types of asphalt binders using a dynamic shear rheometer testing machine (DSR) in accordance with the AASHTO T315 (2020) testing standard. The shear strain amplitudes were applied oscillatory

to the two types of binders. The study included two types of asphalt binders. The applied DSR strain values had to be lower than the maximum strain that can be used in the linear range. Therefore, strain sweep tests were first performed with both asphalt binders to determine the linear range. After the strain sweep tests, strain values of 1% for the unmodified binder and 0.1% for the SBS-modified binder were determined to be used for the frequency sweep tests.

The frequencies of the oscillating load ranged from 0.1 to 30 rad/s with 25 steps. To determine the master curve of the asphalt binders, the tests were conducted at different temperatures: 10 °C, 22 °C, 25 °C, 34 °C, 46 °C, 58 °C, and 70 °C. Two different stainless steel test plates were used for the tests. For tests up to 34 °C the plate with a diameter of 8 mm was used and from 34 °C the one with a diameter of 25 mm. The complex shear moduli G^* and phase angles δ were measured. The test results are shown in Figures 4.31 and 4.32 for the unmodified and modified binders, respectively.

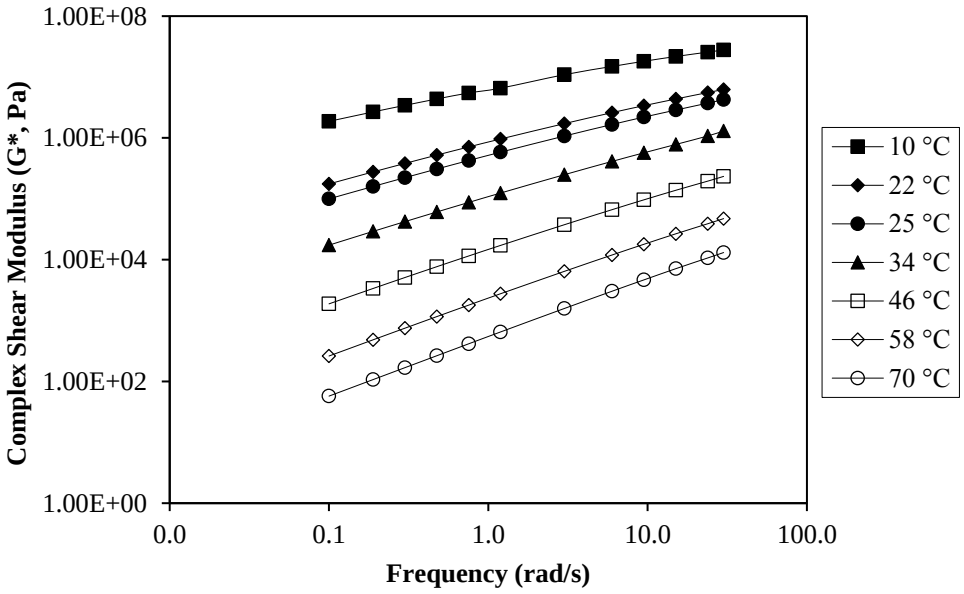

Figure 4.31. Frequency sweep test results of neat binder

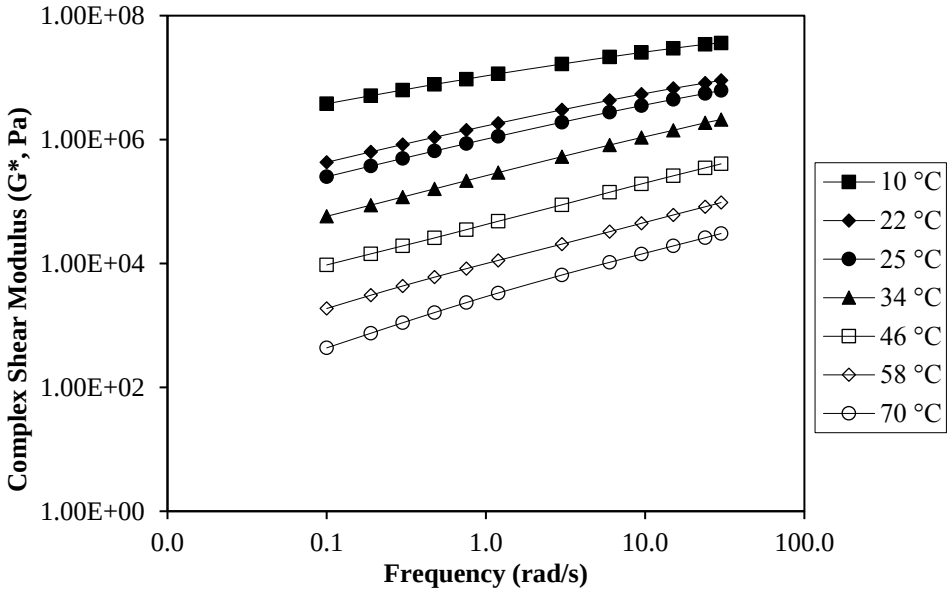

Figure 4.32. Frequency sweep test results of modified binder

Once the data for the frequency tests were obtained, master curves for asphalt binders were developed. Researchers have studied the concept of master curves for asphalt binders to fully characterize their flow properties (Anderson et al., 1991; Christensen and Anderson, 1992). The master curve characterizes the stiffness of asphalt binders under a variety of loading times and temperatures. The resulting master curve and associated temperature shift factors provide a complete characterization of the stiffness-temperature behavior of asphalt binders (Booshehrian et al., 2013). At this point, Christensen and Anderson's method was used to develop master curves for asphalt binders. The mathematical model that can fully characterize the viscoelastic properties of asphalt binders:

$$G^*(\omega) = G_g \left[1 + \left(\frac{\omega_c}{\omega_r}\right)^{\frac{log2}{R}}\right]^{\frac{-R}{log2}} \quad (4.22)$$

where $G^*(\omega)$ is the complex shear modulus; G_g is the glass modulus assumed equal to 1 GPa; ω_c is the cross over frequency at the defining temperature, rad/s; ω_r is the reduced frequency at the defining temperature, rad/s; ω is the frequency, rad/s; R is the rheological index.

In the Christensen-Anderson model, the main curve parameters are ω_c, R, and T_d. The hardness of the binder decreases with increasing crossover frequency. The rheological index, R, describes the rheological type. As the rheological index increases, the master curve becomes flatter, i.e., the behavior of the asphalt binder at intermediate loading times and temperatures becomes more rubbery and less brittle. The defining temperature, T_d, is an indicator of the temperature dependence of the material, which increases with increasing T_d (Anderson et al., 1991).

The reduced frequencies were calculated using Eq. 4.23. The shift factors indicate how much shift is required at each temperature to the defining temperature (T_d). The defining temperature was set to 10 °C.

$$\omega_r = \omega \times 10^{\log a(T)} \tag{4.23}$$

where $log\ a(T)$ is the shift factor; T is the temperature, °K. For temperatures above T_d, the shift factors are calculated using Williams-Landel-Ferry (WFL) equation:

$$\log a(T) = \frac{-19(T-T_d)}{92+T-T_d} \tag{4.24}$$

For the temperatures below the shift factors can be calculated using Arrhenius function (Anderson et al. 1991):

$$\log a(T) = 13016.07\left(\frac{1}{T} - \frac{1}{T_d}\right) \tag{4.25}$$

The shift factors were calculated using the above equations and then substituted into Eq. 4.23 to calculate the reduced frequencies (ω_r). The reduced frequencies were then inserted into the Christensen-Anderson model, Eq. 4.22, to create the first master curve at the defining temperature (T_d). To create the master curve, the three unknown parameters of the Christensen-Anderson model, ω_r, R, and T_d, were initially assigned assumed values. The initial values were calculated using the assumed parameters. Then, the Microsoft® Excel Solver Tool was used to minimize the sum of squared errors (SSE) of the logarithm of calculated and measured G^* by changing the three initial assumed parameters. With the SSE minimized, the three

parameters in Eq. 4.22 were used to construct the master curve. Finally, the G^* values at the determining temperature were shifted to the reference temperature (T_r).

Two types of asphalt binders and three different reference temperatures were used in this study. Laboratory experiments of resilient modulus and indirect tensile fatigue tests were conducted at 25 °C, while FN tests were conducted at 36 °C and 44 °C. At these temperatures, the above procedures were used to generate master curves and then the Prony pairs were calculated from the master curves.

The master curve of the unmodified and modified binders at 25 °C and their shift factors are shown in Figures 4.33, 4.34, 4.35, and 4.36. It can be seen that the polymer modification increases the viscosity and complex modulus. At the lower frequencies, the modified binder has higher moduli than the unmodified binder, and the difference decreases with increasing frequency. In general, the polymer modification of the asphalt binder improved the rheological properties of the asphalt binder. After the master curves were determined, the Prony pairs were calculated using the curve fitting method. The calculated Prony series parameters of the results are shown in Tables 4.5, 4.6, 4.7, and 4.8.

In addition to the Prony series parameters, Poisson's ratio values were needed to build the time domain viscoelastic material model in ABAQUS®. A review of the literature shows that the estimation of Poisson's ratio of asphalt binders has been considered in many studies and has proven to be successful. Therefore, in this study, the Poisson's ratio values for the unmodified and modified asphalt binder were estimated to be 0.42 and 0.32, respectively.

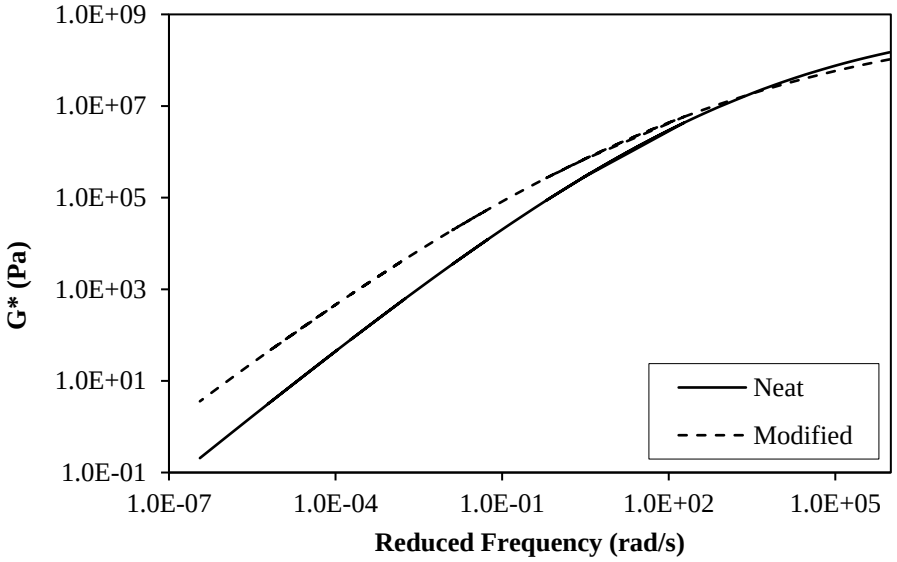

Figure 4.33. Master curves of modified and unmodified asphalt binder at 25 °C

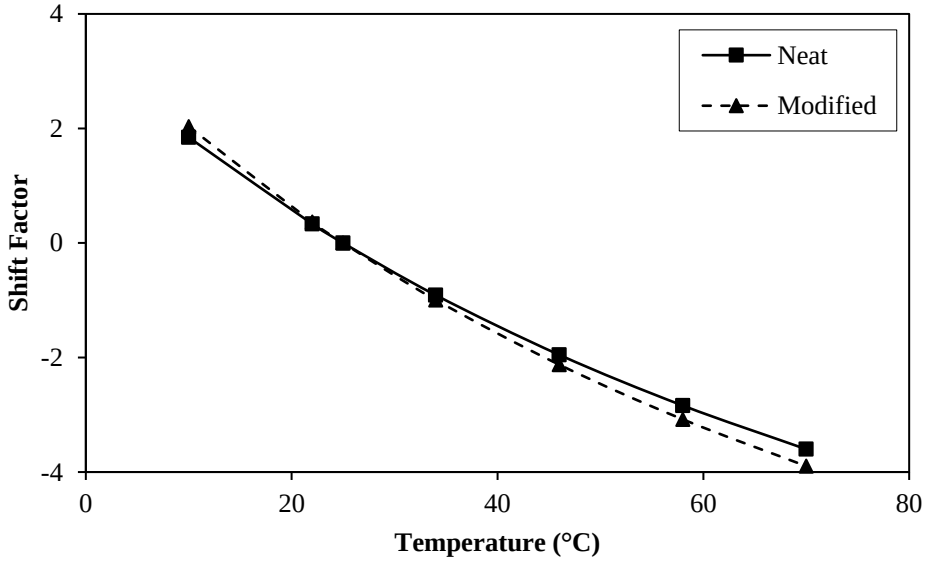

Figure 4.34. Shift factors at 25 °C

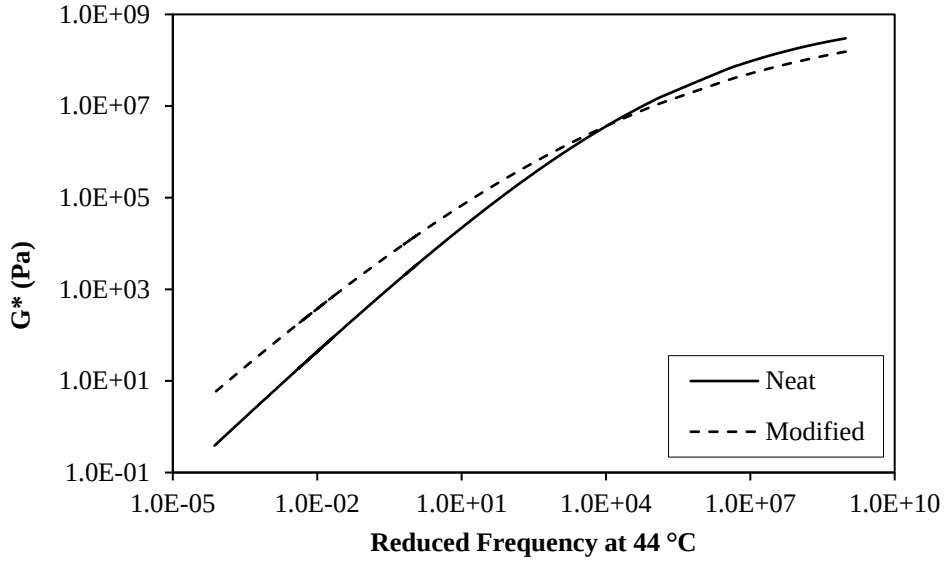

Figure 4.35. Master curves of unmodified asphalt binder at 36 °C and modified binder at 44 °C

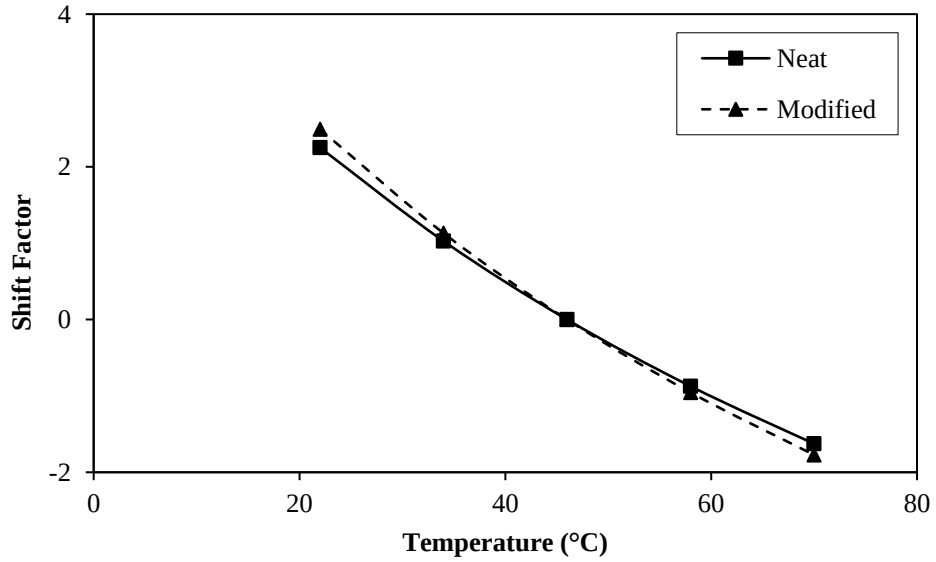

Figure 4.36. Shift factors of unmodified asphalt binder at 36 °C and modified binder at 44 °C

Table 4.5. Prony series parameters of neat binder at 25 °C

Prony Series Parameters	
G_0 (Pa) = 17.43E+06	
g_1 = 5.75E-01	τ_1 = 1.00E-03
g_2 = 2.50E-01	τ_2 = 1.00E-03
g_3 = 9.82E-02	τ_3 = 1.00E-01
g_4 = 2.69E-02	τ_4 = 1.00E+00
g_5 = 4.69E-03	τ_5 = 1.00E+01
g_6 = 1.16E-03	τ_6 = 1.00E+02
g_7 = 2.42E-04	τ_7 = 1.00E+03
g_8 = 1.80E-05	τ_8 = 1.00E+04

Table 4.6. Prony series parameters of modified binder at 25 °C

Prony Series Parameters	
G_0 (Pa) = 21.85E+06	
g_1 = 6.04E-01	τ_1 = 1.00E-03
g_2 = 2.16E-01	τ_2 = 1.00E-02
g_3 = 8.35E-02	τ_3 = 1.00E-01
g_4 = 3.87E-02	τ_4 = 1.00E+00
g_5 = 6.98E-03	τ_5 = 1.00E+01
g_6 = 7.85E-03	τ_6 = 1.00E+02
g_7 = 2.54E-04	τ_7 = 1.00E+03
g_8 = 2.10E-05	τ_8 = 1.00E+04

Table 4.7. Prony series parameters of neat binder at 36 °C

Prony Series Parameters	
G_0 (Pa) = 13.38E+06	
g_1 = 6.66E-01	τ_1 = 1.00E-03
g_2 = 2.26E-01	τ_2 = 1.00E-02
g_3 = 8.06E-02	τ_3 = 1.00E-01
g_4 = 2.02E-02	τ_4 = 1.00E+00
g_5 = 4.71E-03	τ_5 = 1.00E+01
g_6 = 1.21E-03	τ_6 = 1.00E+02
g_7 = 3.30E-04	τ_7 = 1.00E+03
g_8 = 2.20E-05	τ_8 = 1.00E+04

Table 4.8. Prony series parameters of modified binder at 44 °C

Prony Series Parameters	
G_0 = 15.22E+08	
g_1 = 6.83E-01	τ_1 = 1.00E-03
g_2 = 2.07E-01	τ_2 = 1.00E-02
g_3 = 6.47E-02	τ_3 = 1.00E-01
g_4 = 3.73E-02	τ_4 = 1.00E+00
g_5 = 4.47E-03	τ_5 = 1.00E+01
g_6 = 1.39E-03	τ_6 = 1.00E+02
g_7 = 3.97E-04	τ_7 = 1.00E+03
g_8 = 2.50E-05	τ_8 = 1.00E+04

4.5.3 Meshing

Once the geometric and material models were completed, meshing was performed. Another advantage of the model created in this study was that meshing could be performed freely. Since the model became independent of pixels through the process of image vectorization, node placement and thus mesh frequency and element sizes could be adjusted using global seed control. The created geometric model was meshed using the free triangle meshing method. The heteromorphic aggregate surfaces made it impossible to apply a quadruple element shape. It was determined that the triangular free element structure was the best method for meshing in ABAQUS®. An example model after meshing is shown in Figures 4.37 through 4.39. The approximate global size in this example was set to five, and the total element size was 79,457. Element sizes throughout the analysis ranged from 60,000 to 90,000, depending on the model type and the number of total aggregate particles that could be captured in the model. Compared to the initial pixel counts of more than 2 million, the element size in our model was significantly reduced. The complete meshed models of the two types of samples are shown in Figure 4.40.

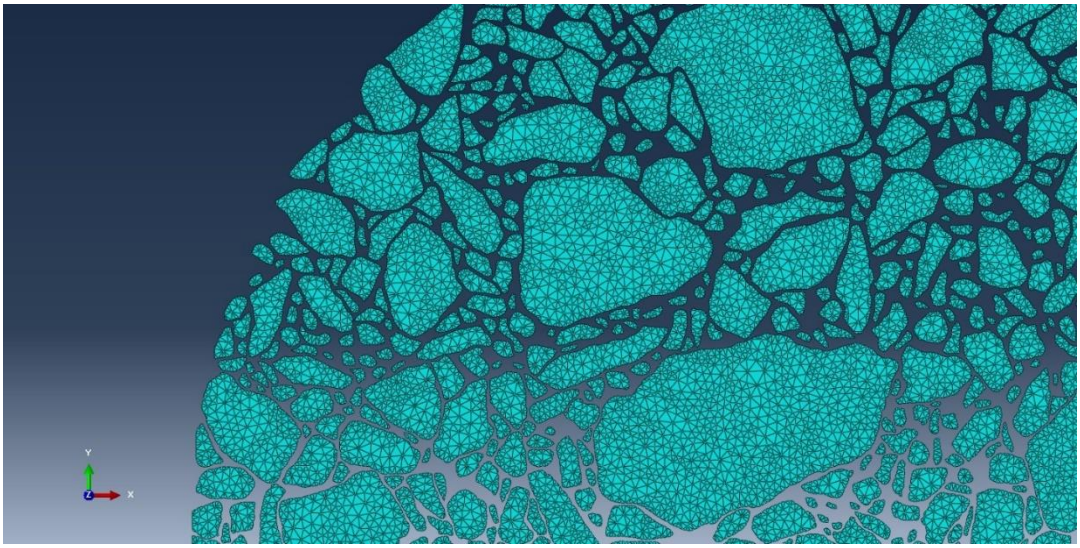

Figure 4.37. 2D FE mesh of the aggregate phase

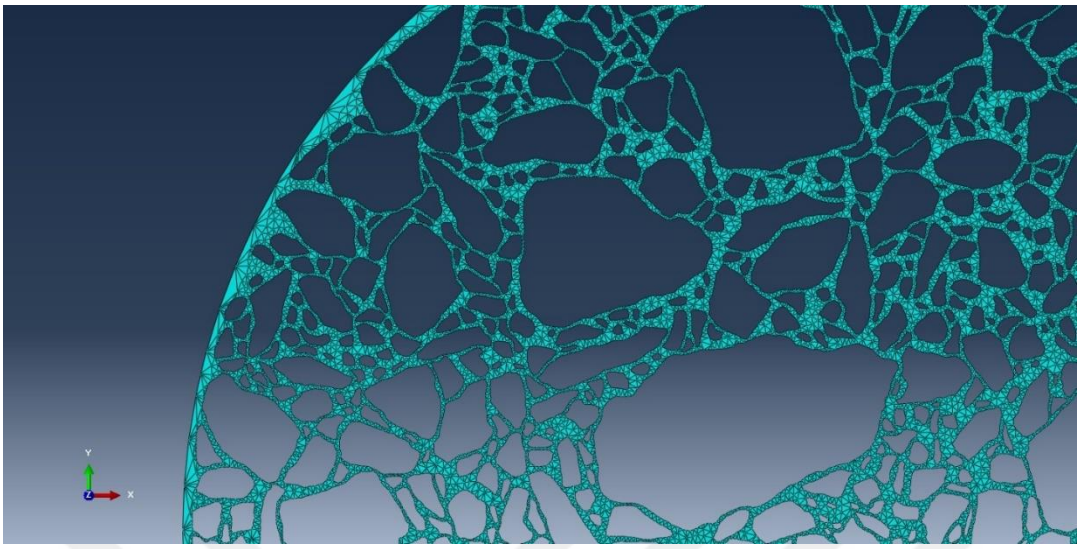

Figure 4.38. 2D FE mesh of the binder phase

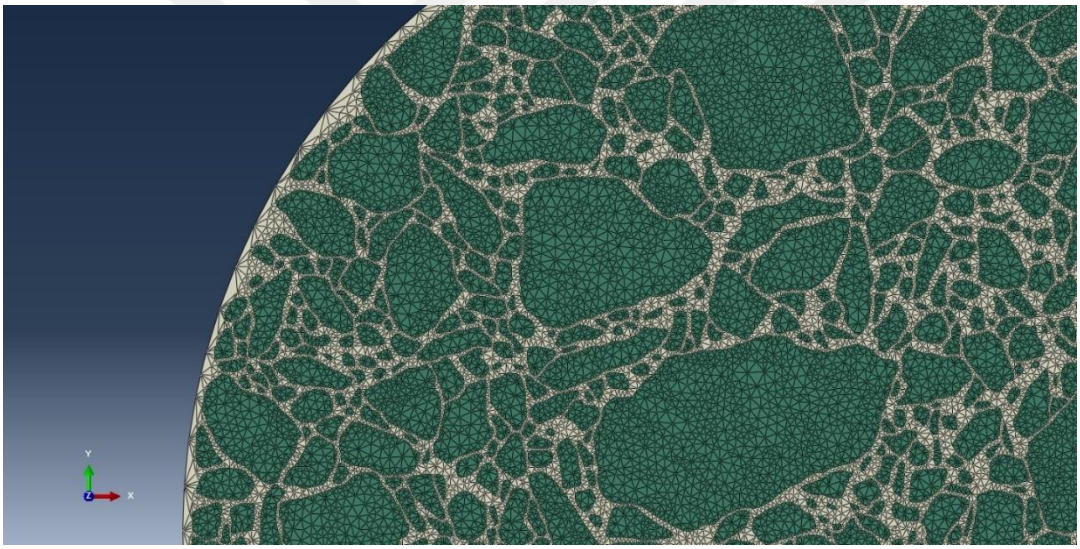

Figure 4.39. 2D FE mesh of the model

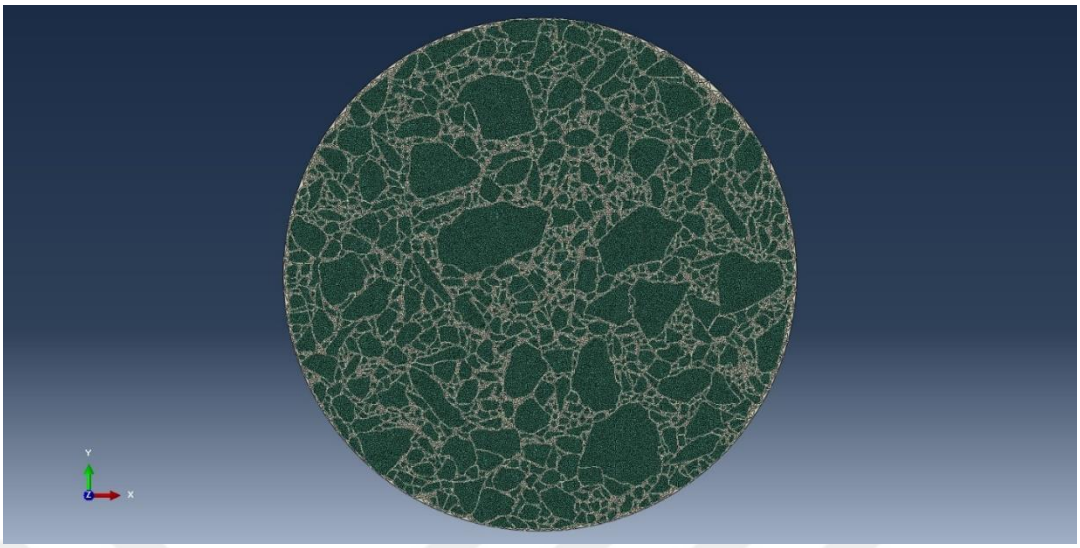

(a)

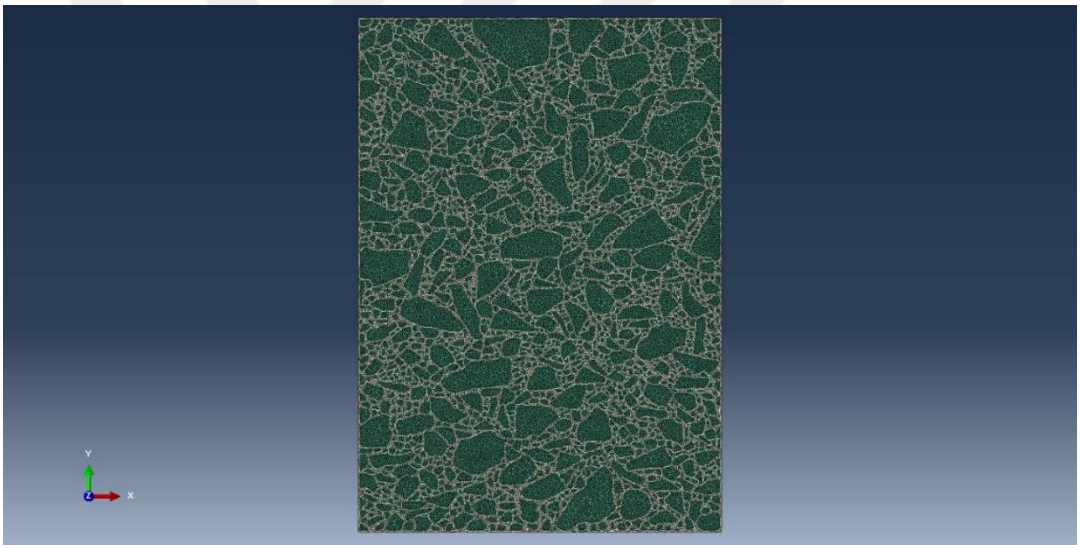

(b)

Figure 4.40. Completed 2D FE mesh: a) Circular model (ID LURM02-1), b) Rectangular model (ID LUCR09)

4.6 Finite Element Modeling of Resilient Modulus Test

To validate the numerical model created in this study, the same laboratory experiments were simulated this time in the finite element environment and the results were compared. These simulations are based on the parameters in the corresponding test standards. The created circular geometric models were used to simulate the resilient modulus tests. Similar to the laboratory experiments, the ASTM D7369 (2020) test standard was used for the finite element analysis.

4.6.1 Materials

The 2D geometry model of the circular specimens with a diameter of 150 mm was created and the meshing procedure was applied as described in the previous chapter. Then, material models were created for the two phases of the model, i.e., the aggregate phase and the binder phase. Linear elastic and viscoelastic material models were created using the previously mentioned model parameters. Isotropic elastic material behavior was chosen to define Young's Modulus and Poisson's ratio for both material types. However, for the linear elastic material model, the time scale of the long-time modulus was chosen, while the instantaneous modulus was used to represent the G_0 parameter of the viscoelastic material model. In addition to the elastic material behavior, the viscoelastic behavior under the elasticity part was used to generate the viscoelasticity in the time domain. Finally, 8 of the Prony pairs were inserted into this viscoelastic part to complete the viscoelastic material model representing the binder phase.

4.6.2 Steps

In ABAQUS®, the problem progression is divided into steps. The RM tests consisted of a single type of dynamic loading, namely indirect loading. Therefore, only one step was created to apply the dynamic indirect tensile loading. The loading process was performed in the visco-step form. The visco-step type is used in ABAQUS® to obtain a transient static response in an analysis with time-dependent material behavior, from which our viscoelastic material model was created. The time span of a cycle is one second and the increment size was set to 0.0025. An increment in ABAQUS® is part of a step. In nonlinear analyzes, the total load applied in a step is divided into smaller increments so that the nonlinear solution path can be determined. Determining the step size is one of the most important aspects for the success of finite element analysis. The step size can contribute to the truncation error and the condition error in the FEM. The truncation error is the difference between the exact value and the calculated value and increases with large step sizes, while the condition error is caused by the loss of numerical precision and generally increases with decreasing step size in finite element analyzes (Haftka, 1985).

To see the effect of step size on the RM simulation results, several different tests were performed under different step sizes. The values for maximum and permanent deformation (at the end of the loading cycle) were obtained from the model in both axes by starting with the highest value and then selecting an increasingly smaller step size range. The results are shown in Table 4.9. Examination of the results shows that the maximum deformation values are more affected by the changes in step size compared to the permanent deformation values. Moreover, similar trends were observed in the vertical and horizontal maximum deformation values and only the horizontal values are shown in Figure 4.41.

It was observed that the permanent deformations obtained at the end of the loading step remained at approximately the same throughout the change in step size. However, the maximum deformation values, which generally correspond to a point slightly anterior to the highest point of loading, gave much smaller values at

relatively large step size intervals than at much smaller step sizes. The maximum horizontal deformations also showed a flattening trend when the step size values were reduced (Figure 4.41). This is because the deformations obtained by the haversine waveform start at zero and gradually increase in the loading phase and gradually decrease in the rest phase. Therefore, the peak value of the deformation shifts when the step size is increased. After a few test runs, it was found that a step size of 0.0025 seconds was sufficient. With this selected value, 1 second of loading and unloading phase of the resilient modulus test could be calculated in 400 steps.

Table 4.9. Model results under various step sizes

		Horizontal		**Vertical**	
Step Size	**Increment**	**Maximum Def. (µm)**	**Permanent Def. (µm)**	**Maximum Def. (µm)**	**Permanent Def. (µm)**
0.00100	1000	2.590	9.37E-02	14.892	0.533
0.00125	800	2.589	9.37E-02	14.891	0.533
0.0025	400	2.586	9.37E-02	14.882	0.533
0.005	200	2.581	9.37E-02	14.785	0.534
0.01	100	2.565	9.37E-02	14.677	0.534
0.02	50	2.526	9.45E-02	14.543	0.538
0.03	34	2.471	9.46E-02	14.112	0.539
0.04	25	2.107	9.47E-02	12.162	0.539

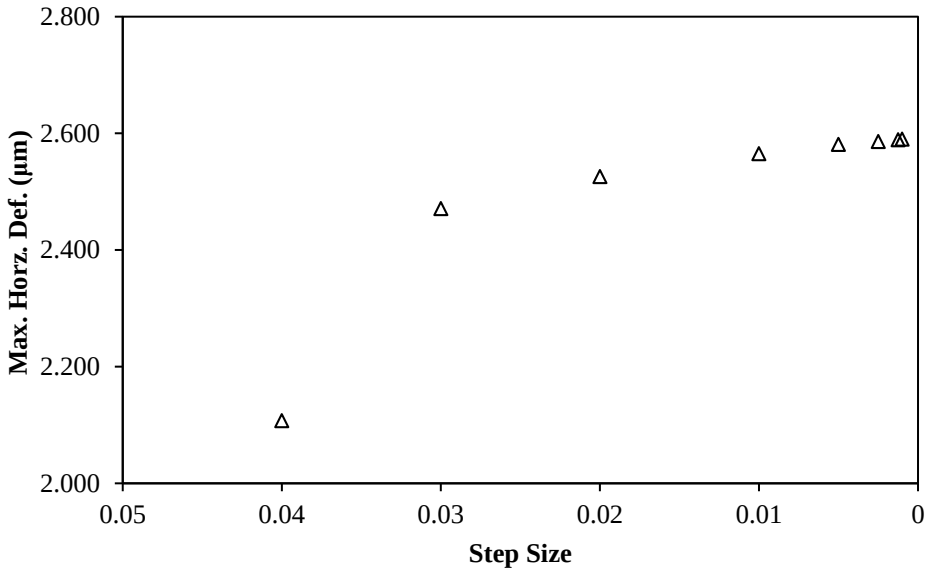

Figure 4.41. Maximum horizontal deformation results with different step sizes

4.6.3 Boundary Conditions and Loading

As shown in Figure 3.24a, specimens in the laboratory test were placed between two steel loading bars, one at the top and one at the bottom. Indirect haversine loading was then applied over the top rod. The surfaces of these bars that contacted the specimen were concave in shape and had a horizontal width of 19 mm. During the resilient modulus tests, these bars could only move in the vertical direction and were confined in the other 2 dimensions.

To apply the same laboratory test conditions in the 2D finite element analyzes, the same loading values were applied to a 19 mm wide surface in the upper part of the geometric model. In addition, the horizontal (in the X-axis) deformation of this upper 19 mm wide surface was set to 0 (U1 = 0). The lower part with the same width is encastered in all directions (U1 = U2 = U3 = 0). The final shape of the model after applying the loading and boundary conditions is shown in Figure 4.42.

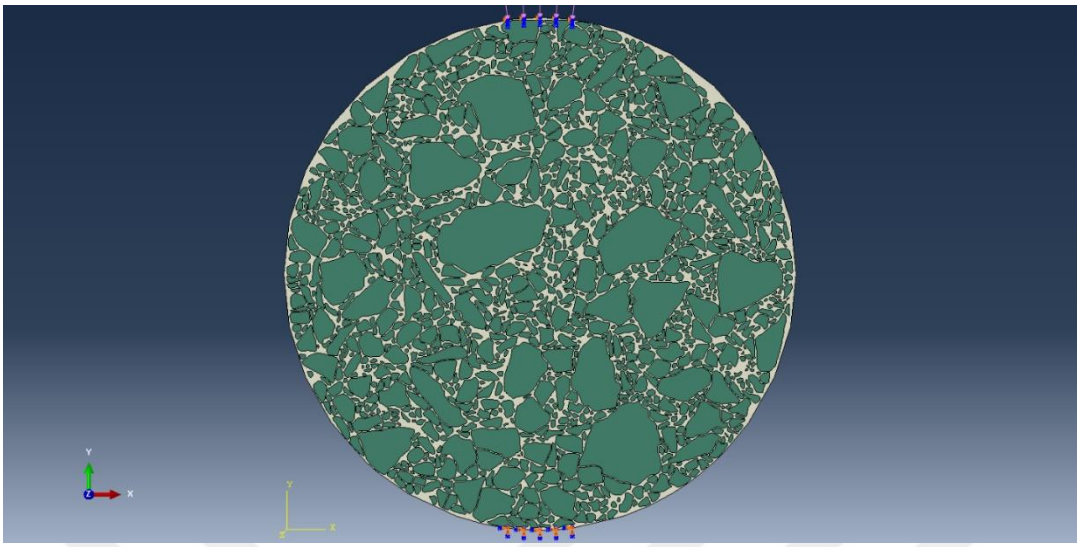

Figure 4.42. Boundary conditions of the RM test (specimen ID LURM02-1)

4.6.4 Amplitude

The loading pattern of the resilient modulus test method was explained in detail in Chapter 3. According to the ASTM D7369 (2020) test standard, the indirect load in the form of haversine should be applied to the specimen within 0.1 seconds and then allowed to rest for 0.9 seconds. This loading pattern was simulated in ABAQUS® using the "Smooth Step" amplitude type (Figure 4.43). Since the load is applied within 0.1 seconds, it is ensured that it reaches its highest value in half of this period by increasing and decreases to 0 in the other half by decreasing, so that the entire load is applied within the time interval of 0.1 seconds and the remaining 0.9 seconds are reserved as rest period. Completed 1-second loading cycle of the resilient modulus simulations in ABAQUS® is given in Figure 4.44.

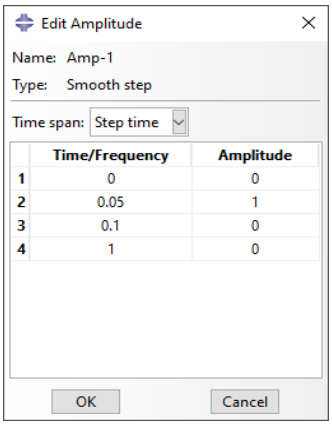

Figure 4.43. Amplitude input of the RM simulations

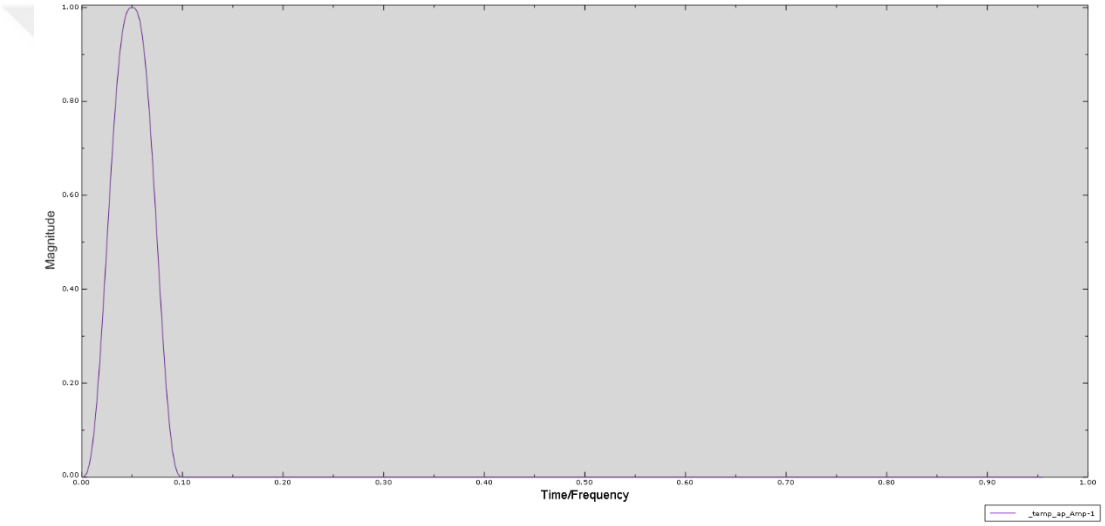

Figure 4.44. Loading pattern of the RM analysis

4.6.5 Calculations

The laboratory test procedure for the resilient modulus was simulated using finite element analysis. An indirect tensile load in the form of a haversine waveform was applied for 0.1 second of loading and the remaining 0.9 seconds of rest, giving a total of 1 cycle of 1 second. The numerical test results of the stress values for the specimen ID LURM02-1 are shown in Figures 4.45 and 4.46.

The maximum values of the vertical and horizontal stresses were determined and plotted. As explained earlier, the load on the specimen reached its highest value at 0.05 seconds, so the stresses formed in the specimen reached the highest value at this point. Moreover, these horizontal and vertical stresses are similar to the trends that occur due to the nature of the indirect tensile (IDT) test on asphalt mixture specimens as reported in the literature. In Figure 4.45, it can be seen that the horizontal stresses formed along the vertical axis tend to be constant and have lower stress values inside the specimen, while they increase sharply at the loading and support points and become compressive stresses. The vertical stresses are fully compressed and also increase at the loading and support points (Figure 4.46).

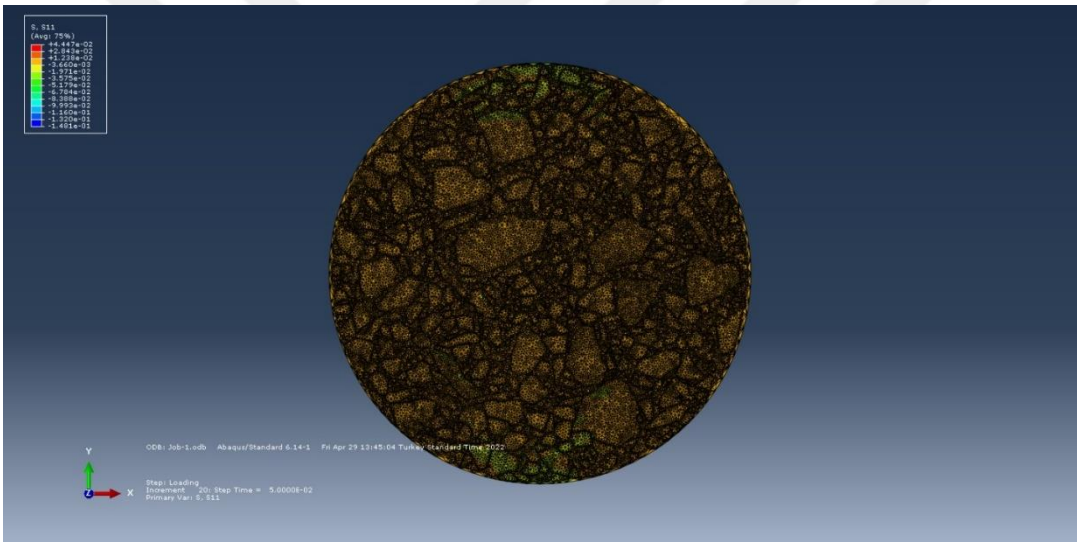

Figure 4.45. Maximum horizontal stresses of the sample ID LURM02-1

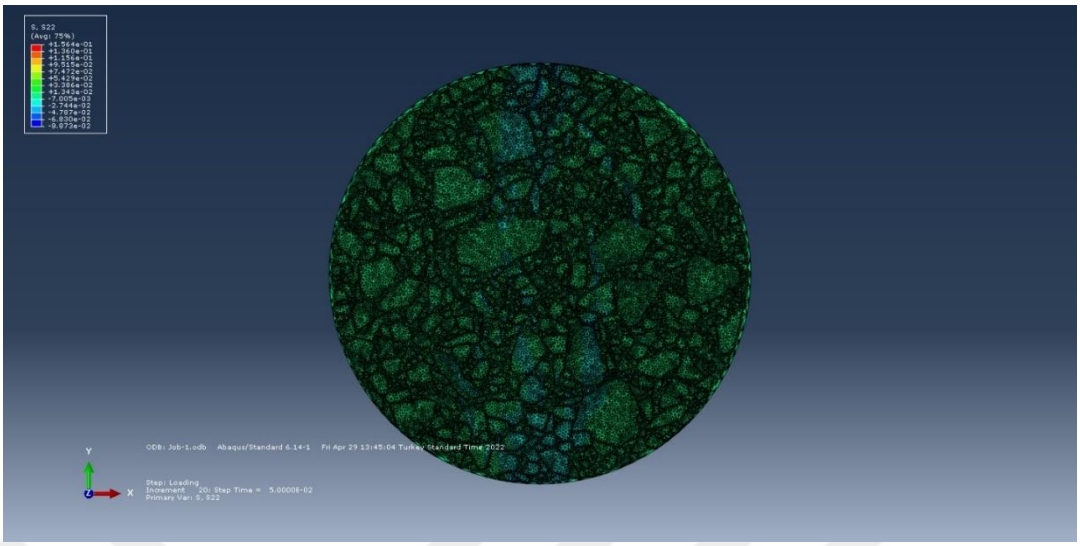

Figure 4.46. Maximum vertical stresses of the sample ID LURM02-1

The maximum deformations of the sample did not occur at 0.05 seconds, the peak of the stresses and also of the load, but at another point. It is clear that this situation is due to the viscoelastic behavior (phase lag) of the asphalt. Figures 4.47 and 4.48 show the deformation results of the same sample whose stress values are given above. The maximum deformation values were calculated as the maximum deformation of the sample during the entire loading cycle, while the permanent deformation values were calculated as the remaining deformation values of the sample at the end of the loading cycle.

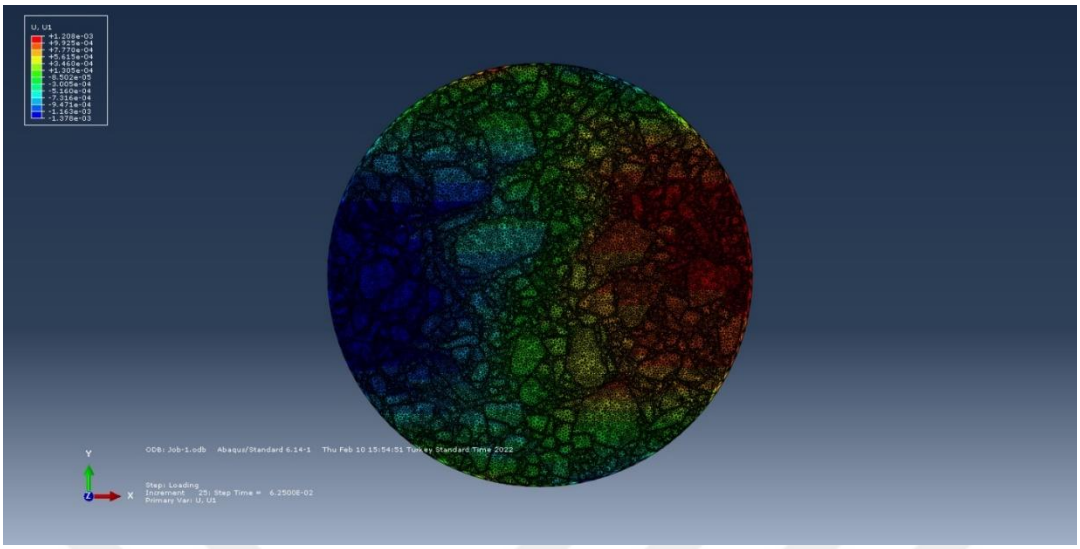

(a)

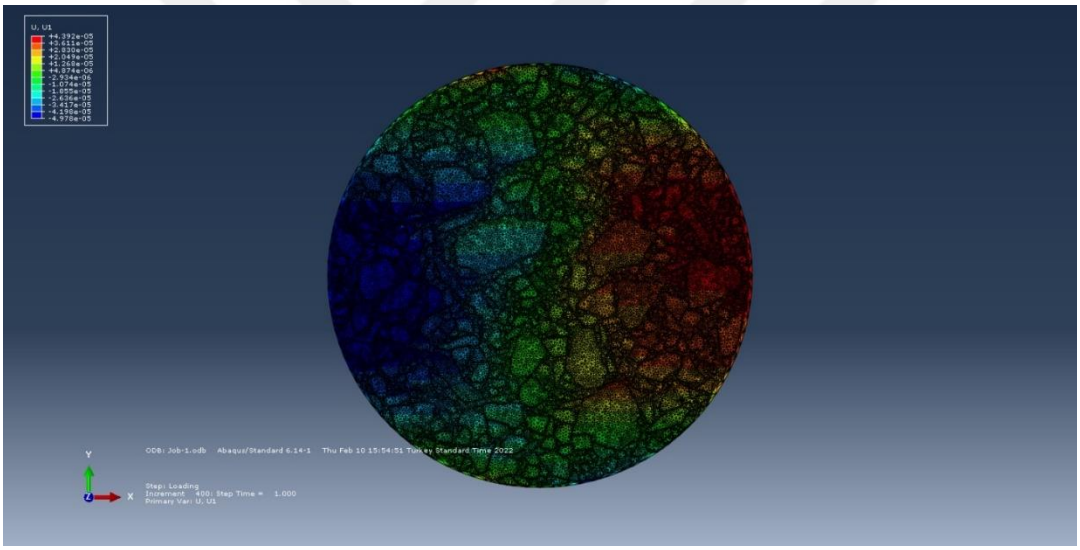

(b)

Figure 4.47. FE results of the sample ID LURM02-1: a) Maximum horizontal deformation, b) Permanent horizontal deformation at the end of the loading cycle

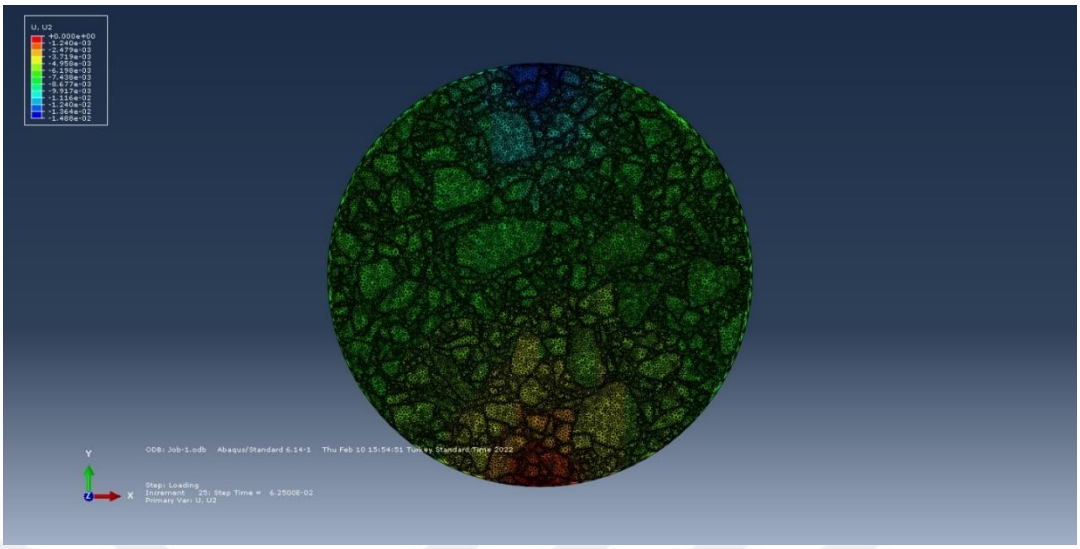

(a)

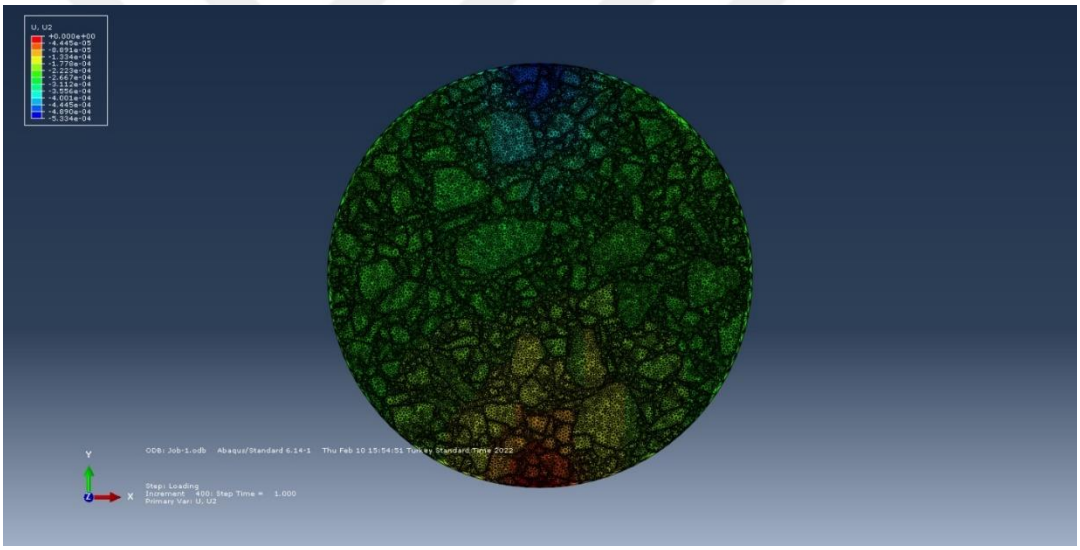

(b)

Figure 4.48. FE results of the sample ID LURM02-1: a) Maximum vertical deformation, b) Permanent vertical deformation at the end of the loading cycle

As it can be seen from the figures above, some of these deformations have similar characteristics. As expected, the horizontal deformations are quite small in the center of the sample and increase along the horizontal axis towards the outer edges in positive and negative directions. The vertical deformations are a complete contraction, they are small in the center of the sample and increase at near the loading and support points.

Finally, in order to compare the finite element results with the experimental results, the resilient modulus and Poisson's ratio were calculated using the total recoverable vertical and horizontal deformations. At this stage, equations 3.5 and 3.6, previously given in Chapter 3, are used to calculate the Poisson's ratio and M_R values, respectively.

The total recoverable horizontal and vertical deformations used in these equations were calculated at the same points in the numerical model that were measured in the laboratory tests. As can be seen in Figure 4.49, points A and B are located at a distance of 37.5 mm from each other (the same distance that corresponds to the gauge length of the laboratory tests) and represent the contact points of the LVDT that measures the vertical deformations of the sample. Points C and D are also at the same distance and correspond to the points where the LVDT, which measured the horizontal deformations, contacts the surface of the sample.

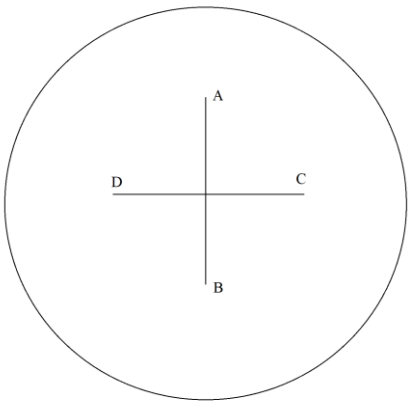

Figure 4.49. Nodal displacement locations of the RM analyze

In these calculations, the total vertical deformations were first calculated as the difference of the absolute values at A and B (Uv = A - B) and the total horizontal deformations were calculated as the sum of the absolute values at C and D (Uh = D + C). The same steps were performed at the point of maximum deformation and at the end of the loading cycle. The resilient modulus and Poisson's ratio were then calculated using the total recoverable deformations, i.e., the difference between the maximum deformation amount and the deformation at the end of the loading cycle.

The horizontal and vertical deformations occurring on the specimen due to the indirect loading are compared in Figures 4.50 and 4.51. From the figures, it can be seen that both types of finite element modeling (the TGDH model and the FAA model) successfully simulate the laboratory behavior of the specimens in the finite element environment. For both models, the horizontal and vertical deformations of the numerical models are quite close to the results obtained in the laboratory environment, which proves that the finite element model works successfully in terms of the resilient modulus analyzes. The detailed results of the numerical model are presented in Chapter 5. Additionally, in order to see the model results of the 20 genuine specimens tested in the RM simulations, the horizontal and vertical deformations at the maximum points are presented in Appendix H. It should be noted that the permanent deformations of these simulations at the end of the loading cycles along with the tested 20 other synthetic specimens (generated by particle redistribution method) cannot be included in Appendix H because it would be too long.

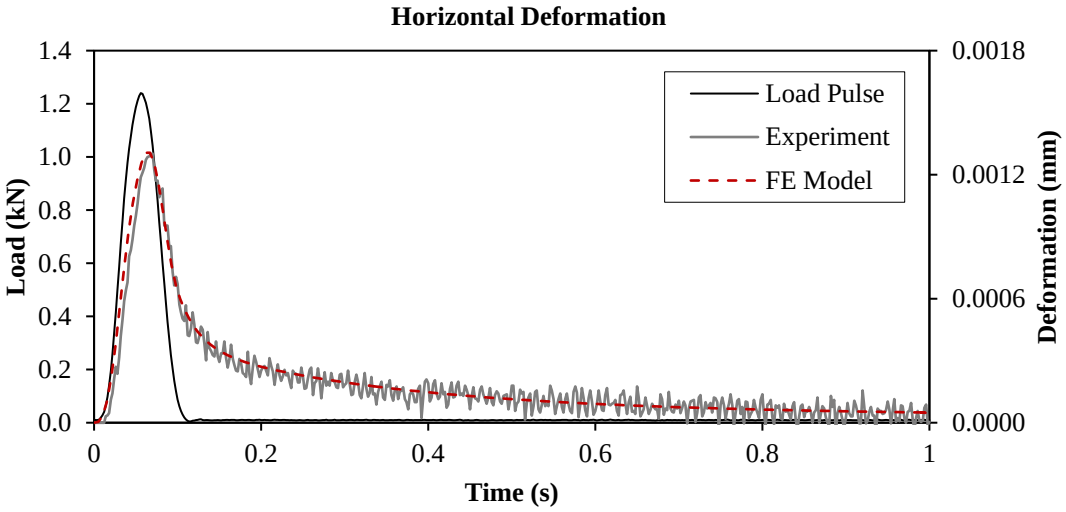

(a)

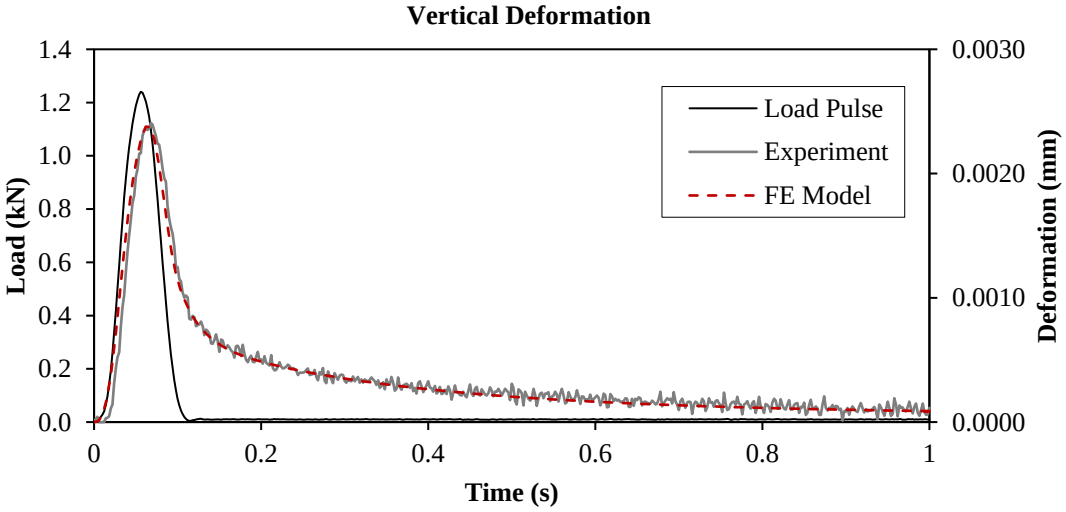

(b)

Figure 4.50. Comparison of laboratory and FEM results of a TGDH design sample: a) Horizontal deformations, b) Vertical deformations

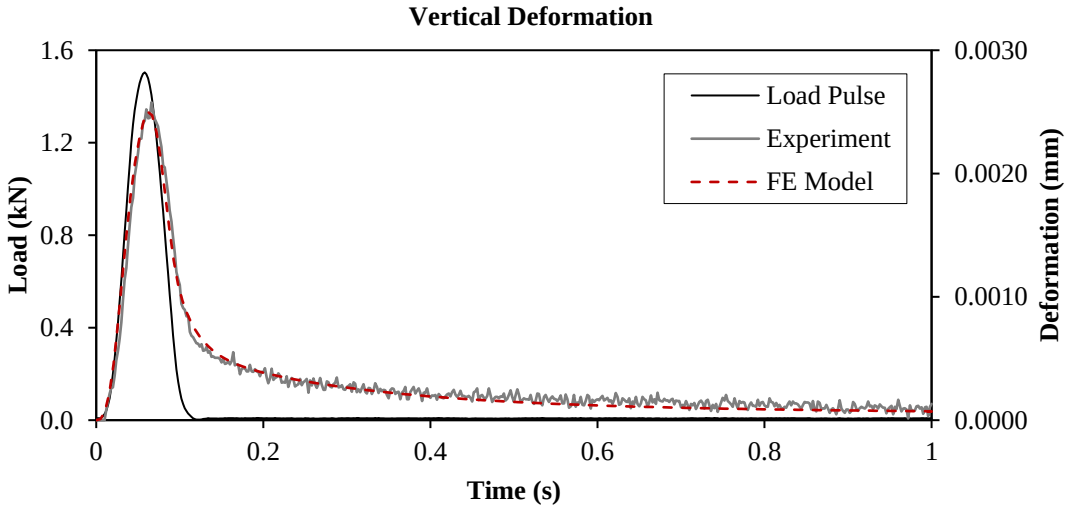

(a)

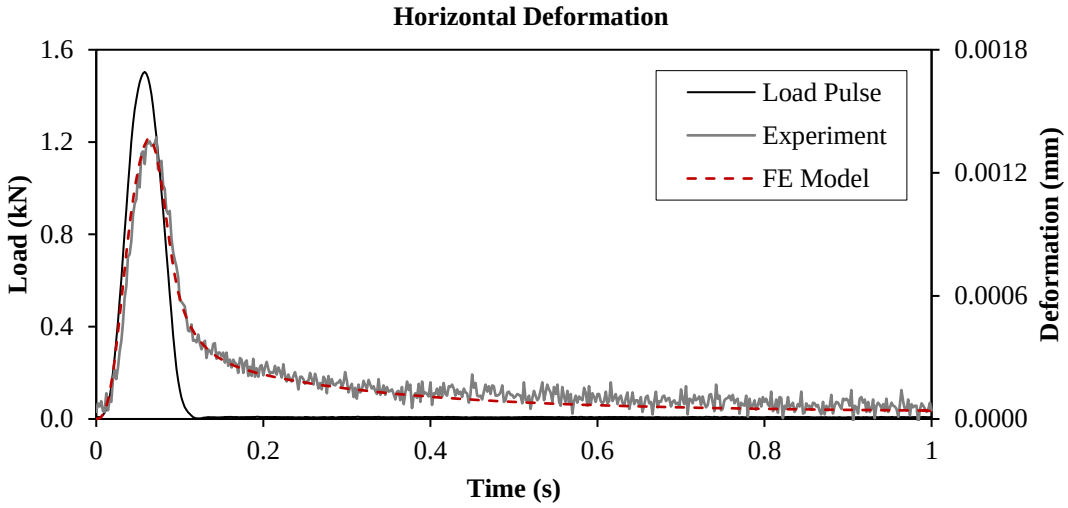

(b)

Figure 4.51. Comparison of laboratory and FEM results of a FAA design sample: a) Horizontal deformations, b) Vertical deformations

4.7 Finite Element Modeling of Repeated Creep Test

After the resilient modulus test, the repeated creep (FN) tests, carried out in the laboratory, were simulated in the 2D finite element model. Similarly, the test parameters selected based on NCHRP Report 465 (2002) were also applied in the simulations. The details are as follows:

4.7.1 Materials

The 2D geometric model of the repeated creep tests is based on a rectangular shape approximately 150 mm high and 100 mm wide. As explained in the previous chapters, the cylindrical specimens were cut along their vertical axis to capture the internal structure in the image processing analyzes. The cutting procedures were applied after testing the samples in the laboratory, therefore the final dimensions of the samples varied. An appropriate 2D geometric model was created for each sample, meshed, and the remaining model parameters were applied. A similar material model to that used in the simulations of the RM tests was also applied to the FN analyzes. However, since the effective test temperatures determined and applied in the laboratory tests for the repeated creep tests differed from those of the RM tests, the corresponding parameters were used for the material model of the asphalt binders. Apart from the 8 Prony pairs and the instantaneous moduli (G_0) of the asphalt binder, all other parameters of the material model were the same as those used in the resilient modulus simulations.

4.7.2 Steps

The "visco" step type is also used in ABAQUS® to perform the repeated creep simulations. However, the tests of RM consisted of 1-second loading, while the FN tests consisted of much longer dynamic loading cycles. As explained in Chapter 3.4, the repeated creep tests were performed in the laboratory according to the

specification of 10,000 cycles or 3% permanent axial strain. However, while the maximum number of cycles could be performed on the basalt samples before the target of 3% axial strain was reached, approximately 2,000 cycles could be performed on the limestone specimens. Therefore, an appropriate number of cycles had to be selected for the dynamic loading in our finite element model.

As will be explained in the following sections, the obtained values of permanent deformation in the first two regions of the creep behavior can be represented when a high number of cycles is applied in repeated creep simulations, and these values never go beyond the 2nd region. It was observed that beyond a certain point, the choice of a higher number of loading cycles did not affect the obtained test parameters, i.e., the slope of the fitted model and the intercept. The reason for this situation is the following: Since there is no damage model defined in the viscoelastic material model, there is no damage in the finite element environment and therefore the resulting permanent deformations are represented only in the first two regions of the creep behavior. It should be noted that the damage model in the finite element environment is a completely separate issue and is not addressed in this study. Since it was found that choosing very high cycles both increased analysis times and had no effect on test results, a value of 2,000 load cycles was used for the repeated creep simulations.

For the repeated creep simulations, the permanent deformations were needed, i.e., the final deformation values at the end of a load cycle. As seen in the previous sensitivity analysis, the deformations occurring on the specimen are much less affected by the change in step size at the end of the loading cycle than the maximum values. As can be seen in Table 4.9, the permanent deformations remained close for all values of step size compared to the maximum deformation values. Considering the high number of load cycles applied, a step size of 0.05 was considered appropriate and applied to avoid increasing the analysis times too much. With this step size, a repeated creep analysis of 2,000 cycles can be completed in 40,000 steps and in about 20 hours.

4.7.3 Boundary Conditions and Loading

As already shown in Figure 3.25, in the FN tests, the sample was placed between two loading plates, between which there were rubber membranes oiled with silicone grease. This allowed the samples to move freely in the entire X and Z planes. However, in finite element analysis, the specification of certain boundary conditions has a direct influence on the accuracy of the analysis results. By its very nature, it is not possible to complete the finite element analysis without specifying certain boundary conditions. For this purpose, the rectangular geometric model is encastered from bottom (U1 = U2 = U3 = 0). Then the deformation along the X-axis is prevented at the top (U1 = 0). It should be noted that in reality the top loading plate distributes the stresses uniformly and symmetry constraints should be provided on the X-axis of the specimen from its center. However, since the geometric model is not symmetrical along the X-axis, the symmetry constraints could not be applied and only the horizontal deformation of the upper part could be prevented. The load was also applied to the same upper part of the model. The final shape of the model after applying the load and constraints is shown in Figure 4.52.

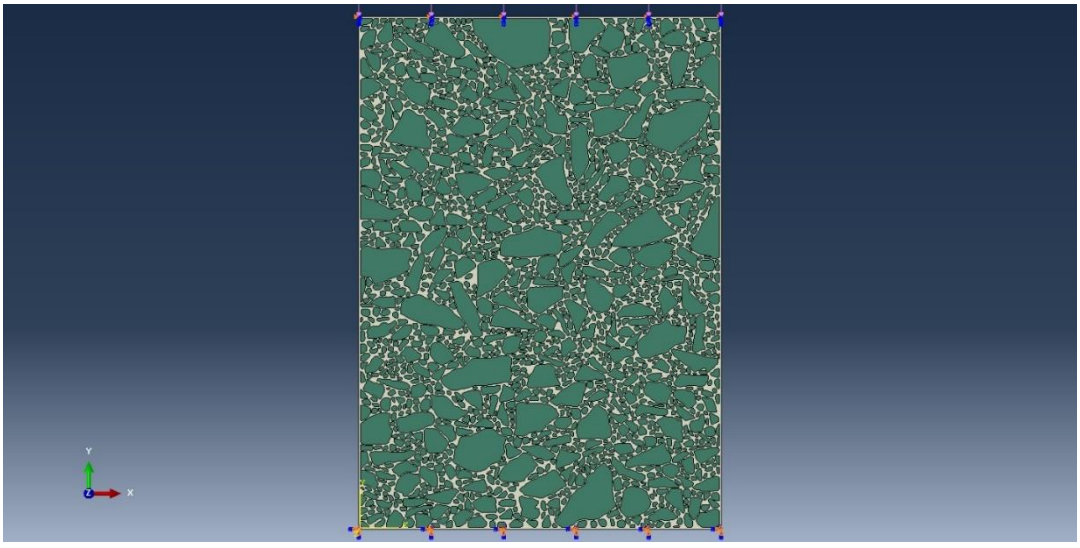

Figure 4.52. Boundary conditions of the FN test (specimen ID LUCR09)

4.7.4 Amplitude

The specified number of 2,000 cycles is defined at this stage as dynamic loading at a frequency of 1 Hz. The first 10 cycles of the entered amplitude values are shown as examples in Figures 4.53 and 4.54. It should be noted that, as described in NCHRP Report 465 (2002), the first 0.1 seconds of the 1 Hz loading is reserved for the application of the load and the remaining 0.9 seconds for the rest of the sample. In a similar application in the resilient modulus analyzes, the "smooth step" amplitude type was defined such that the load reached its maximum value in half of this 0.1-second loading and dropped back to zero in the other half. This amplitude pattern was continued until the maximum number of cycles of 2,000 was reached.

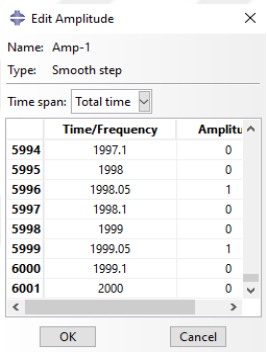

Figure 4.53. Amplitude input of the FN tests

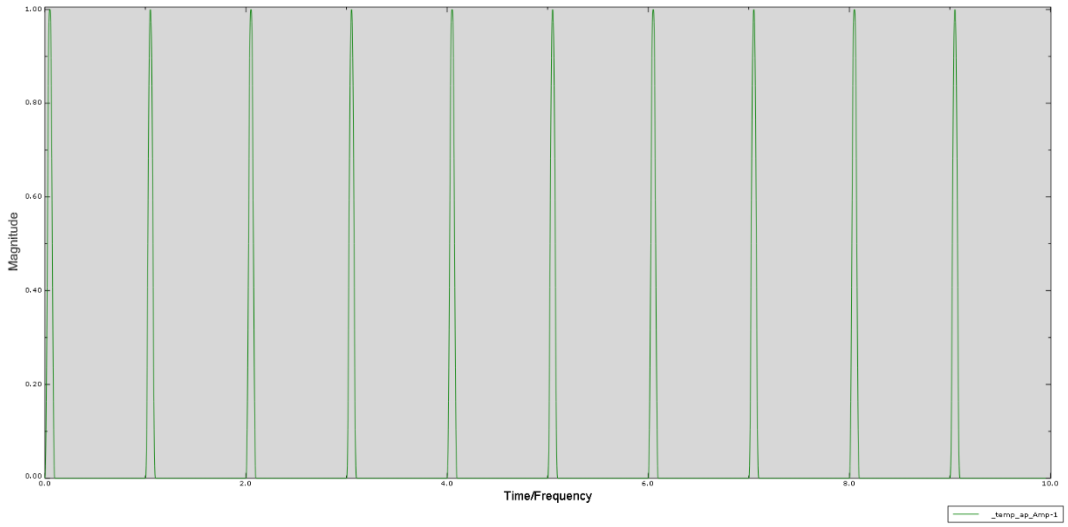

Figure 4.54. Loading pattern of the FN tests

4.7.5 Calculations

The axial deformation values that occur as a result of the repeated creep simulation on the example specimen ID LUCR09 are shown in Figure 4.55. To make the diagram clearer, the first 10 cycles are shown enlarged. As it can be seen from the diagram, the deformations of the specimen increase with the load for each 1 second cycle, and some of these deformations (recoverable or elastic deformations) are dispersed in the rest phase. At the end of each loading cycle, some of these deformations (permanent or plastic deformations) remain on the sample. Furthermore, these plastic deformations increase with each cycle and it is shown that the creep behavior of the specimen can be successfully simulated.

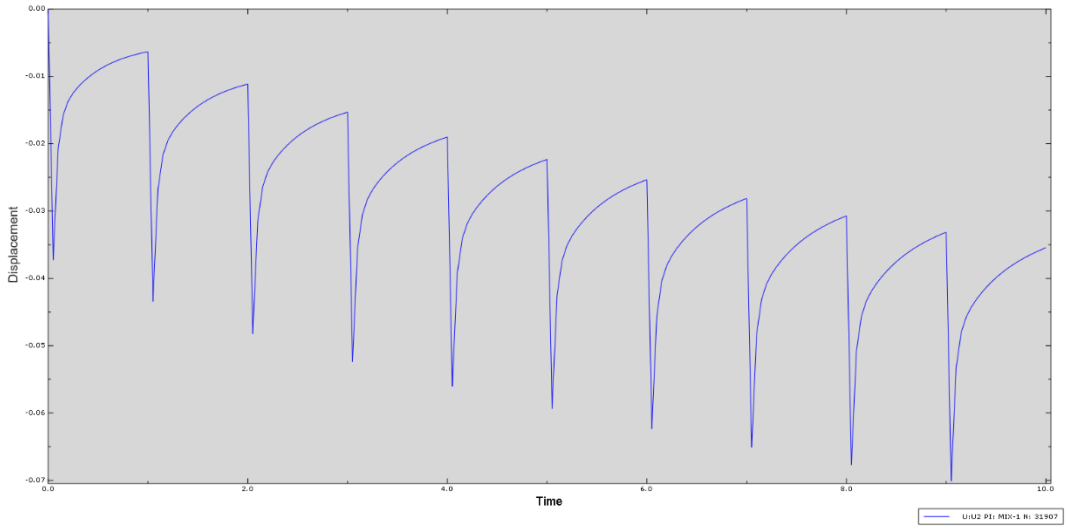

Figure 4.55. First 10 cycles of axial deformations

The axial deformation curves of the individual FAA and TGDH design examples formed at the end of 2,000 cycles are shown in Figure 4.56. From the graphs, it can be seen that both the total deformation and the permanent axial deformation increase with increasing number of cycles for both specimens. Similar to the laboratory experiments, the values of total deformation are much lower for the TGDH specimen than for the FAA specimen. It can also be seen that the recoverable deformations are higher for the basalt sample than for limestone, which again is consistent with the

results of the laboratory experiments. It can be concluded that the FAA specimens exhibit more elastic behavior than the TGDH specimens, allowing them to withstand higher dynamic loading cycles before creep failure occurs.

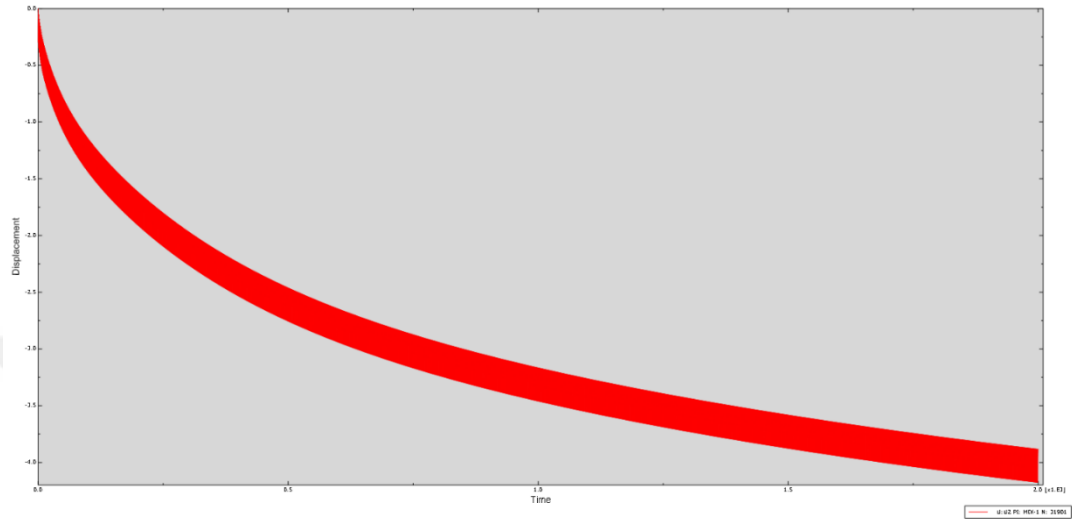

(a)

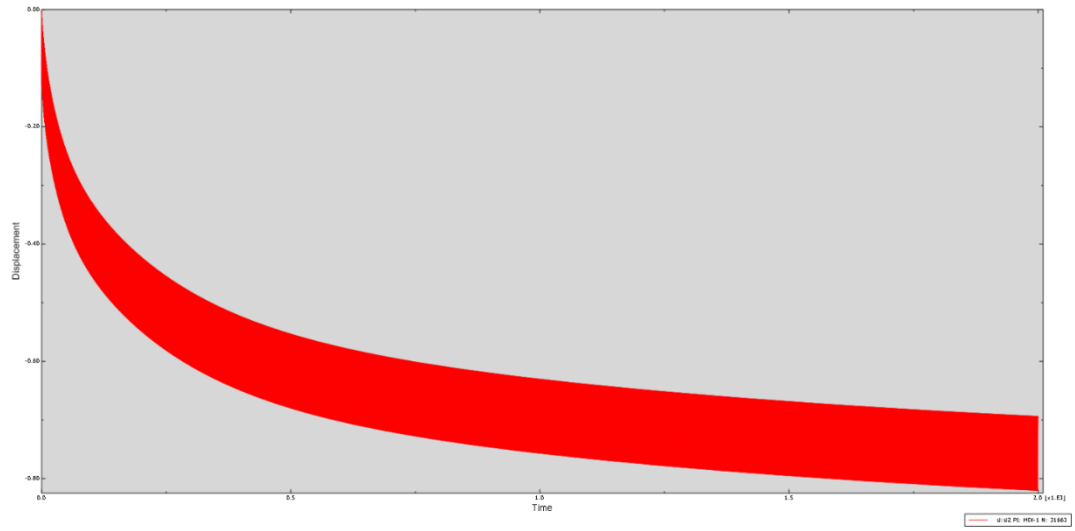

(b)

Figure 4.56. Axial deformation graphs: a) TGDH design sample ID LUCR09, b) FAA design sample ID BMCR01

To validate the numerical analyzes, the laboratory results had to be compared with the finite element results. For this purpose, the values of permanent axial deformation of the specimen at the end of each cycle were calculated. These deformation values were then used to calculate the resulting permanent strain values at the top of the specimen based on its overall length. The resulting permanent strain values are shown in Figures 4.57 and 4.58. In these figures, the values of the permanent strains at the end of each loading cycle in the finite element analysis of the specimens are given together with the results of the laboratory tests on the same specimens.

As it can be seen from the figures, the results of the finite element analysis and the laboratory results of the repeated creep tests are very close. Even at this initial stage, the numerical model appears to successfully model the laboratory results. In addition, it is clear that the finite element analysis results, unlike the laboratory results, reflect the creep behavior of the specimen only in the first two regions, which is due to the lack of a damage model, as explained earlier.

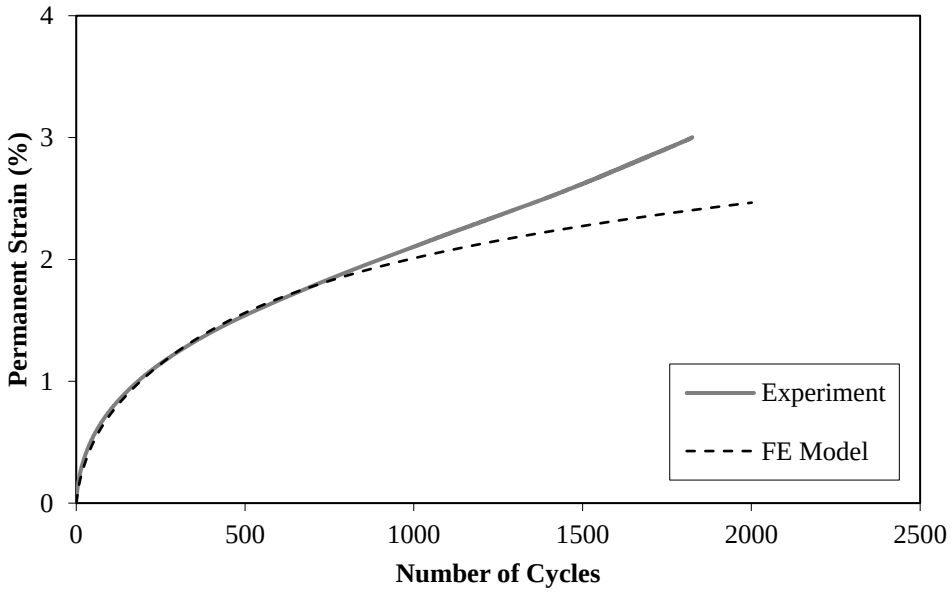

Figure 4.57. Permanent strain versus number of cycles of the TGDH design sample ID LUCR09

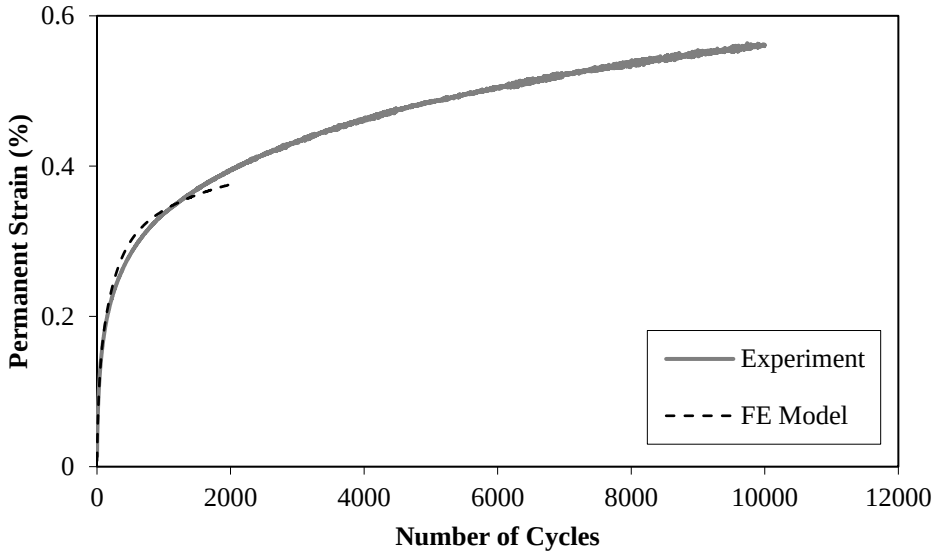

Figure 4.58. Permanent strain versus number of cycles of the FAA design sample ID BMCR01

Finally, the power model described in Chapter 3.4 is applied to the finite element results. The results are described in detail in the next chapter. Moreover, the validation of the FE model by comparing the numerical results with the experimental results is explained in the following chapter.

The final form of the 20 real specimens at the end of the repeated creep simulations is given in Appendix I. In these figures, the resulting vertical deformation curves are also given as a result of 2,000 loading cycles. However, the remaining results for the 20 synthetic specimens tested (generated using the particle redistribution method) are not included in Appendix I to avoid becoming too long.

4.8 Finite Element Modeling of Indirect Tensile Fatigue Test

At the beginning of this thesis work, one of the main objectives was to use 3 of the basic behaviors of asphalt concrete to validate the 2D finite element model. For this purpose, the resilient modulus test, the repeated creep test and the indirect tensile fatigue test were selected to determine the elastic, creep and fatigue properties of asphalt concrete. The resilient modulus and repeated creep tests were successfully performed using the finite element method, as explained above. However, the IDTF tests could not be successfully simulated in this study.

The main reason why the fatigue tests were not successful is the very high number of load cycles used in these experiments. The tests from RM did not last longer than 105 seconds in total and the simulation time in ABAQUS® was about 15 minutes, even with the very small step size values chosen. The repeated creep analyzes took about 20 hours to complete the selected 2,000 load cycles and the results file was about 250 GB in size. The fatigue experiments, on the other hand, required hundreds of thousands of load cycles in the laboratory, even in the worst case, hundreds of thousands of cycles were required for a successful finite element analysis. While it takes about 1 day to implement even 2,000 cycles in the repeated creep simulations, it was not possible to implement the IDTF tests in ABAQUS® at these cycle values. At least this was not possible with the method or equipment available in this study, and this situation was not foreseeable at the beginning of the study. Although these high cycle numbers may or may not be accomplished with supercomputers, it was not possible to simulate the indirect tensile fatigue tests in the finite element environment because no such capability currently exists.

CHAPTER 5

RESULTS AND DISCUSSION

5.1 Introduction

In this chapter, the results of the laboratory testing program are presented in detail. Resilient modulus, repeated creep, and indirect tensile fatigue tests were performed on the specimens compacted in the laboratory. Two different mixes were used to produce the specimens: TGDH mix with limestone and unmodified asphalt binder and FAA mix with basalt aggregate and polymer modified asphalt binder. A total of 60 specimens were tested in the laboratory environment, 10 for each test method and design type. The specimens were then modeled using the finite element method. A two-dimensional image-based finite element model was created from the cross-sectional images of the asphalt specimens compacted in the laboratory. The same test procedures were simulated in the numerical model to obtain results. The numerical results were compared with the empirical results to validate the 2D image-based FEM.

5.2 Specimen Coding

In this study, two different mix designs were used along with two different aggregate types and two different asphalt binders. In addition, three different tests were conducted to measure performance in both the laboratory and finite element model. For each test, up to 18 cylindrical Superpave gyratory compacted specimens were produced, and after cutting, up to two different specimens were produced from one cylindrical specimen. A coding system was developed to identify the samples: Aggregate type: L for limestone, B for basalt; Binder type: M for bitumen modified

with SBS polymers and U for unmodified bitumen; Test type: RM for resilient modulus test, CR for repeated creep test, and IF for indirect tensile fatigue test; Specimen number: 1 to 18 for each group of gyratory compacted cylindrical specimens; position within specimen: 1 for bottom of cylindrical specimen and 2 for top of cylindrical specimen. For example, code BMRM10-1 corresponds to the specimen with basalt aggregate and modified bitumen. The specimen was tested in the resilient modulus test and comes from the bottom part of the Superpave gyratory compacted specimen No. 10. It is worth noting that each of the cylindrical specimens used for the repeated creep tests comes from a single gyratory compacted specimen and therefore does not bear the last digit of the specimen code.

5.3 Experimental Test Results

In order to investigate the tensile variations of asphalt concrete and additionally to verify the numerical model, three different tests were performed: Resilient modulus (RM) test, repeated creep (FN) test, and indirect tensile fatigue (IDTF) test. The detailed test procedures were explained in the previous chapters. The results of these tests performed in the laboratory are presented in the following sections.

5.3.1 Resilient Modulus Test Laboratory Results

Resilient modulus (RM) tests were performed in accordance with ASTM D7369 (2020) test standard. The TGDH and FAA specimens were subjected to repeated loads of 1100 and 1550 N, respectively. The load was applied using a haversine waveform for 0.1 seconds, followed by a 0.9 second rest period at 25 °C. 100 cycles were performed until the resilient modulus deformations were stable. Using the average value of the last five cycles, the resilient modulus (M_R) and Poisson's ratio were calculated from the total vertical and horizontal deformations. A total of 20 specimens were tested, 10 for each design.

The results of resilient modulus and Poisson's ratio results for the specimens with limestone aggregate and unmodified binder are shown in Table 5.1, and it can be seen that they are quite consistent. The same results can also be seen in Figure 5.1. The TGDH specimens have an average resilient modulus of 5450.87 MPa and a Poisson's ratio of 0.341. The standard deviation of the M_R results is relatively small (179.13 MPa). Moreover, this deviation from the mean is quite small, only 3.3%. Similarly, the results of the Poisson's ratio of the TGDH samples are fairly consistent. The coefficient of variation is 4.9%, which indicates a good coherence between the test results.

Table 5.1. Resilient modulus test results of TGDH samples

Specimen	**Resilient Modulus (MPa)**	**Poisson's Ratio**
LURM01-1	5277.69	0.335
LURM02-1	5472.30	0.356
LURM03-1	5645.01	0.334
LURM06-1	5622.79	0.358
LURM07-1	5335.90	0.336
LURM08-1	5434.92	0.342
LURM09-1	5210.17	0.320
LURM10-1	5242.42	0.315
LURM11-1	5702.08	0.368
LURM12-1	5565.40	0.350
Avg.	5450.87	0.341
St. Dev.	179.13	0.017
CV, %	3.3	4.9

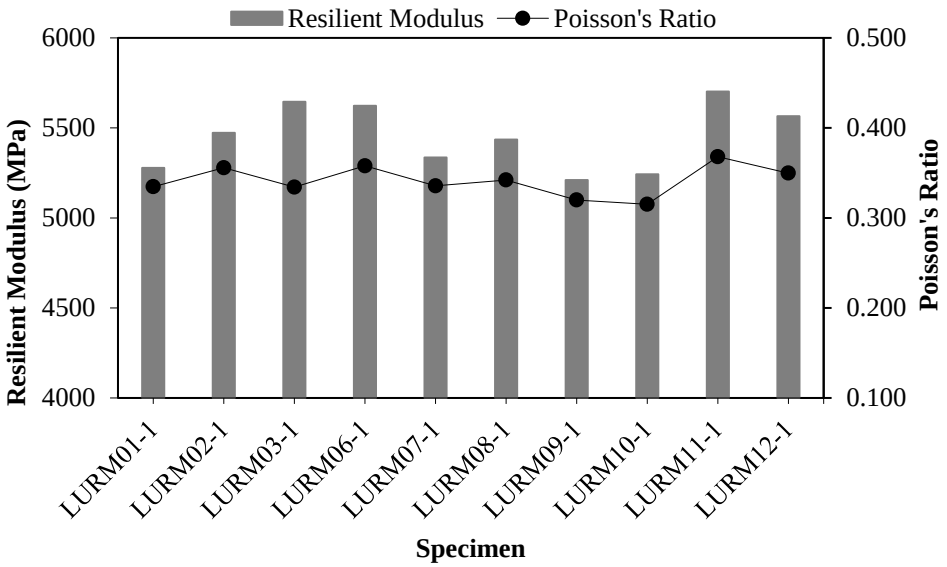

Figure 5.1. Resilient modulus test results of TGDH samples

The results of the RM tests on the FAA mix specimens are shown in Table 5.2 and Figure 5.2. The average resilient modulus and Poisson's ratio of these specimens with basalt aggregate and modified binder were 6793.25 MPa and 0.294, respectively. Similar to the TGDH specimens, the standard deviations (159.03 MPa and 0.012) and coefficient of variations (2.3% and 4.1%) between the FAA design specimens are also relatively low, indicating good agreement between the test results.

The values were calculated for each sample from the average of four different readings taken during the experiment: Two different readings from each side of the sample and two different axes by rotating the first axis 90° after the experiment and running the experiment again. The differences between these four different readings are shown in Figures 5.3 and 5.4. As it can be seen from the figures that the differences between the LVDT measurements and thus the M_R results between these readings are quite small. This indicates that the homogeneity of the specimens was quite consistent. Great care was taken in the preparation and compaction of the specimens. The mounting of the specimens in the test chamber and the placement of the LVDT devices were also critical in obtaining uniform readings.

Table 5.2. Resilient modulus test results of FAA samples

Specimen	Resilient Modulus (MPa)	Poisson's Ratio
BMRM01-1	6702.44	0.279
BMRM02-1	7043.61	0.310
BMRM07-1	6755.87	0.304
BMRM08-1	6833.34	0.294
BMRM09-1	6974.03	0.285
BMRM10-1	6614.56	0.284
BMRM11-1	6685.91	0.282
BMRM12-1	6927.18	0.311
BMRM13-1	6841.58	0.301
BMRM14-1	6553.94	0.288
Avg.	6793.25	0.294
St. Dev.	159.03	0.012
CV, %	2.3	4.1

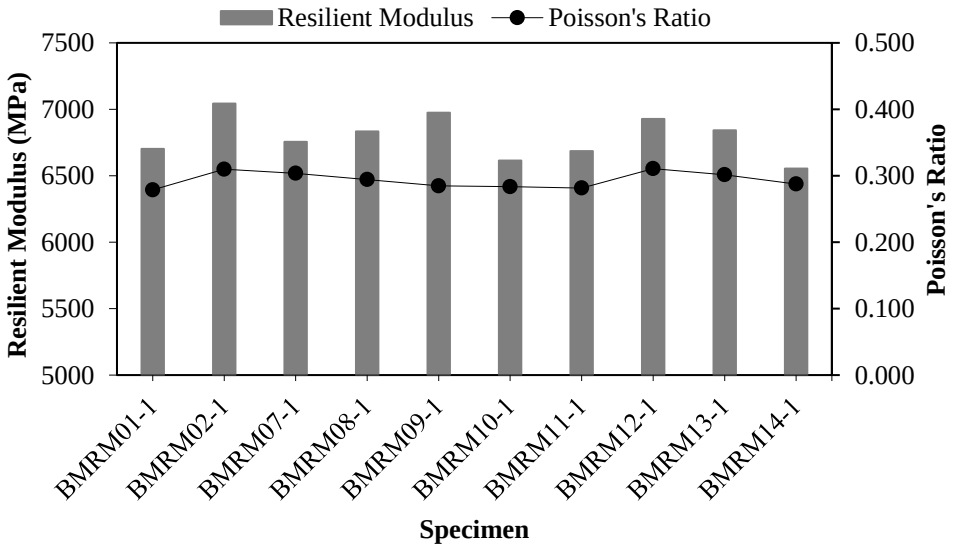

Figure 5.2. Resilient modulus test results of FAA samples

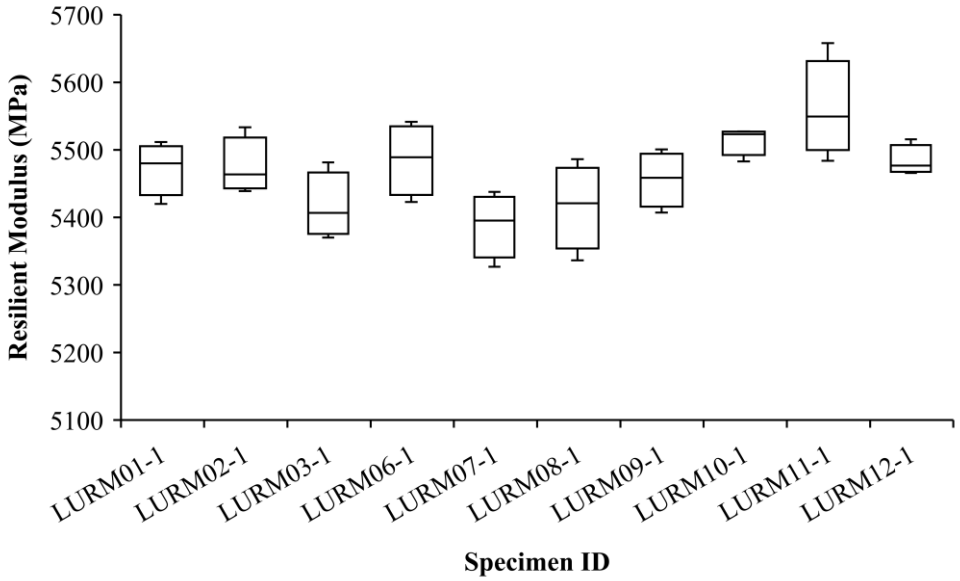

Figure 5.3. Variations among four different readings of TGDH samples

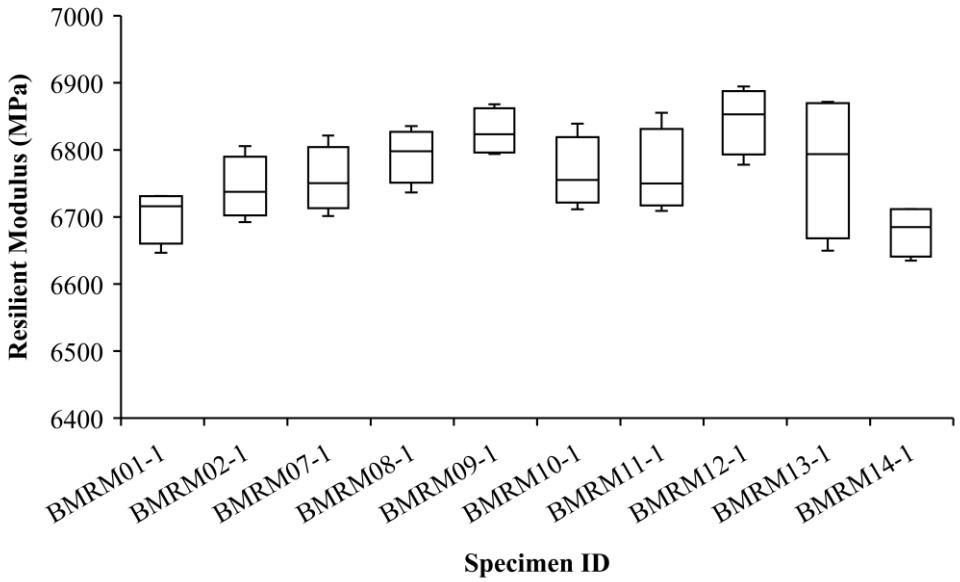

Figure 5.4. Variations among four different readings of FAA samples

The comparison between the two groups of test samples is shown in Figures 5.5 and 5.6. The MR results of the FAA specimens are generally 25% higher than those of the TGDH specimens. The main difference between the qualities and properties of basalt and limestone aggregates resulted in higher strength of the samples with basalt

aggregate. In addition, the modified asphalt binder improved the resilient modulus of the asphalt mixtures compared to the neat binder. Thus, the modification of the asphalt binder led to an improvement in the elastic properties of asphalt mixtures. This is due to the higher viscosity of the modified binder, which leads to better elastic properties. The results show that the use of basalt aggregate and modified asphalt binder leads to asphalt concrete with higher elastic properties and thus higher bearing capacity.

Poisson's ratios are relatively smaller for FAA specimens than for TGDH specimens. Since smaller Poisson's ratios are expected for stiffer materials than for relatively soft materials, these results are compatible. The combination of basalt aggregate and SBS polymer modification resulted in lower PR values and thus lower deformations in the transverse and longitudinal directions. Again, the main physical properties of the basalt aggregate and the viscosity increase of the polymer modified binder are believed to be the main reasons for this phenomenon.

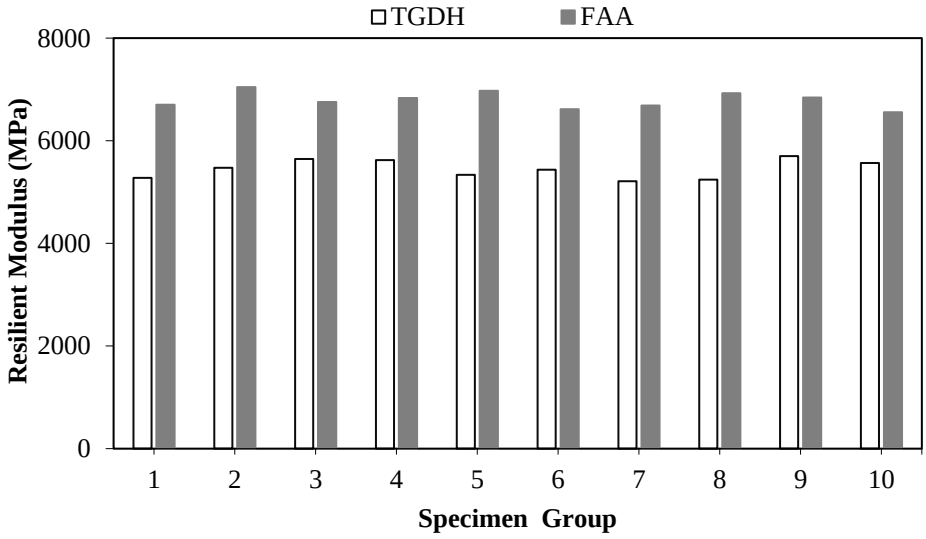

Figure 5.5. M_R comparison of experimental test results

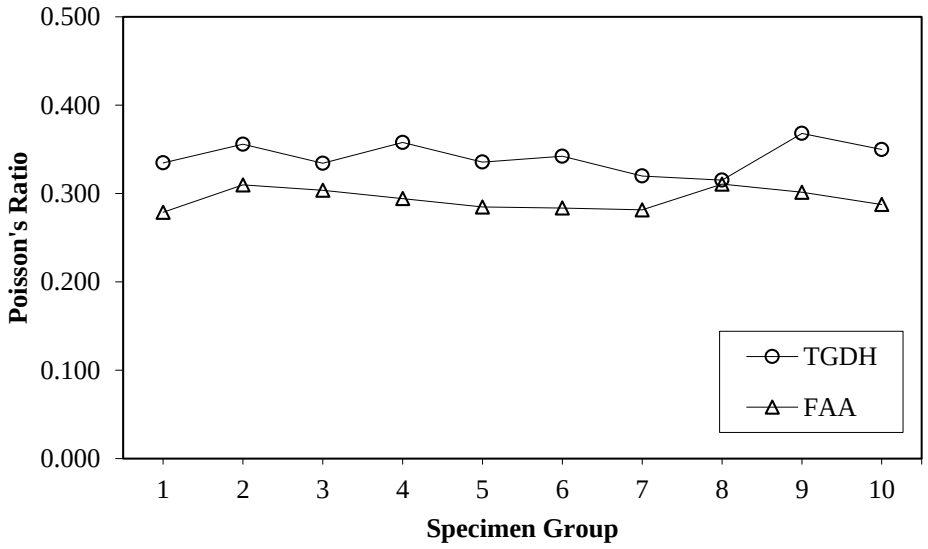

Figure 5.6. Poisson's ratio comparison of experimental test results

5.3.2 Repeated Creep Test Laboratory Results

Repeated creep tests, also known as flow number tests (FN), were performed in accordance with NCHRP Report 465 (2002). Direct repetitive compressive loads were applied at 1 Hz (0.1 second load followed by 0.9 second rest). The same stress value of 690 kPa was applied to the FAA and TGDH specimens. Effective test temperatures were calculated as 36 °C for the TGDH specimens and 44 °C for the FAA specimens. Testing continued until 10,000 cycles or 3% of the cumulative permanent strain was reached. For each type of design, 10 specimens were tested. The induced permanent strains at the end of each cycle were recorded. Finally, the flow numbers of the specimens were calculated using the power model.

Figures 5.7 and 5.8 show the permanent strains as a function of the number of cycles. As can be seen from the figures, the specimens with limestone aggregate and unmodified asphalt binder have relatively lower creep strength than the specimens with basalt aggregate and modified binder. The TGDH specimens generally reached the maximum strain value of 3% at about 1900 cycles. In contrast, all FAA

specimens were able to reached much lower permanent strain values of about 0.5% even after 10,000 cycles of loading. One possible reason for this is the higher physical properties of the basalt aggregates compared to those of the limestone aggregates. The higher toughness of the basalt aggregate results in a higher resistance to permanent deformation. At the end of the test, the permanent deformations of the basalt aggregates are about six times lower than those of the limestone aggregates. Looking at the curves in the graphs, it can be seen that the creep behavior of the TGDH specimens easily reaches the first and second regions, while for some samples it also reaches to the third region. However, for the FAA specimens, only the first two regions are seen even though they were loaded with five times more load cycles. As can be seen from Figures 5.7 and 5.8, the FAA specimens showed much higher resistance to repeated creep loading than the TGDH specimens.

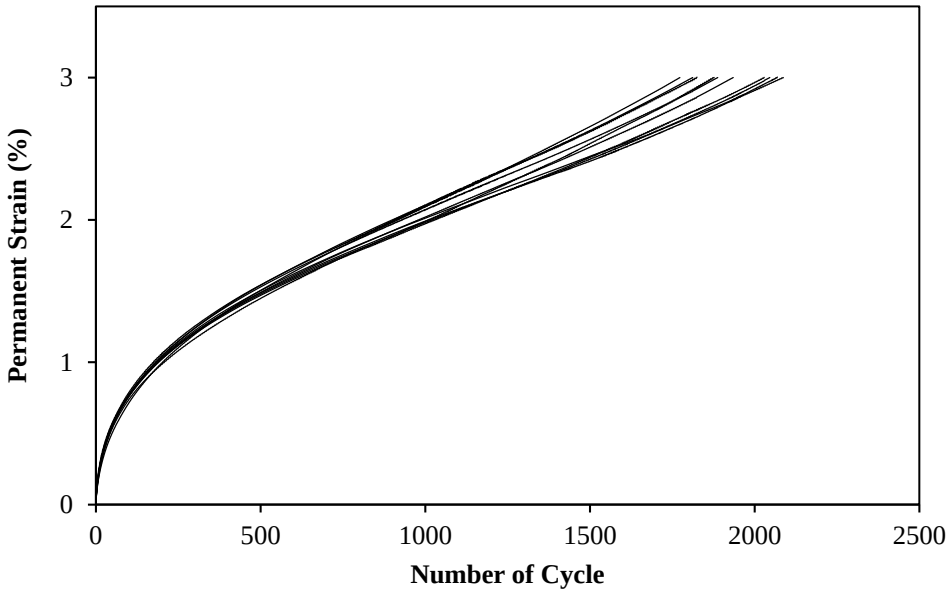

Figure 5.7. FN test results of each 10 TGDH samples

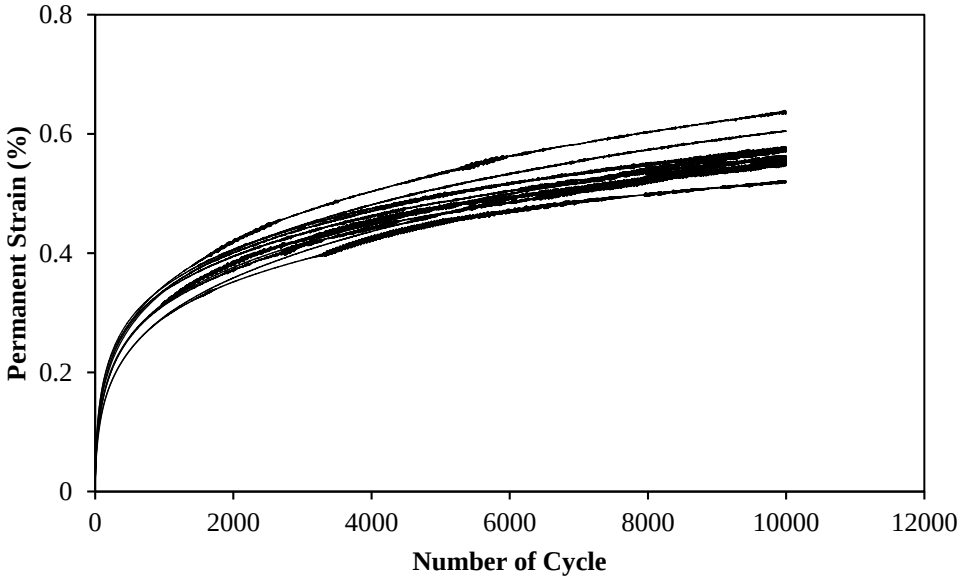

Figure 5.8. FN test results of each 10 FAA samples

Another reason for the lower permanent deformations could be the difference between the bitumen types. The SBS polymer modification of the asphalt binder increases the overall viscosity, elastic behavior, and complex modulus. Therefore, the polymer modification of the asphalt binder directly affects the permanent deformations that occur at relatively high loads. The FAA design procedure, combined with the basalt aggregate and modified bitumen, resulted in a much higher creep resistance of HMA than the TGDH design samples, which consisted of limestone aggregate and unmodified bitumen.

The results of the flow numbers calculated using the fitted power model are shown in Tables 5.3 and 5.4. The parameters of the power model, the intercept (a) and the slope of the fit (b) are also shown in the figures. A total of 10 specimens were tested for each of the design types. The TGDH specimens have an average flow number of approximately 1323 load cycles and an intercept at 0.090 on the logarithmic scale of the permanent strain axis. The slope constant averages 0.456. For the FAA specimens, an average flow number of 9033 was calculated, while the average intercept of the specimens is 0.050, with an average slope of 0.296.

Table 5.3. Flow number and power model results of TGDH samples

Specimen	Flow Number	Intercept (a)	Slope (b)	R^2
LUCR03	1278	0.095127	0.445027	0.9967
LUCR05	1340	0.086523	0.460160	0.9952
LUCR06	1443	0.081448	0.467673	0.9942
LUCR07	1212	0.079428	0.476811	0.9977
LUCR08	1107	0.087168	0.464116	0.9976
LUCR09	1182	0.091281	0.449617	0.9938
LUCR10	1381	0.094384	0.452536	0.9962
LUCR11	1376	0.095710	0.442765	0.9958
LUCR12	1427	0.093522	0.446101	0.9950
LUCR13	1488	0.090596	0.456501	0.9966
Avg.	1323.4	0.089519	0.456131	
St. Dev.	124.6	0.005727	0.011050	
CV, %	9.4	6.4	2.4	

The variations between the test results are also shown in the figures and tend to have relatively low values. The average flow numbers of the total 20 specimens tested are about 125 (9.4%) for the TGDH design and 545 (6%) for the FAA design. In addition, the slopes of the fitted power model show a deviation of 2.4% and 3.8% from the mean. Again, a good correlation can be seen between the test results in terms of their variability.

Figure 5.9 shows a comparison of the flow number test results between the two mixture designs. Looking at the results of the FN tests, it can be seen that the FAA specimens have almost seven times higher rutting resistance than the TGDH specimens. In addition, the power model constant, slope (b), is also an indicator of the asphalt concrete's resistance to permanent deformation (rutting). The combination of basalt aggregate and modified binder exhibits a lower slope constant

(b), indicating a higher resistance to rutting. These results are consistent with the literature, as the traditional treatment against permanent deformation in practice is to use polymer modified asphalt binder and/or aggregate with higher stiffness. In the literature, there is no clear relationship between the intersection (a) and rutting behavior. However, it is generally assumed that the higher the value of the intersection (a), the greater the rutting, and vice versa.

Table 5.4. Flow number and power model results of FAA samples

Specimen	**Flow Number**	**Intercept (a)**	**Slope (b)**	**R^2**
BMCR01	8721	0.049300	0.308924	0.9855
BMCR02	9175	0.047835	0.297688	0.9815
BMCR03	8509	0.050653	0.299417	0.9850
BMCR04	9779	0.054280	0.288041	0.9766
BMCR05	8847	0.049428	0.294722	0.9825
BMCR06	8471	0.042721	0.304189	0.9895
BMCR07	9595	0.058886	0.274608	0.9637
BMCR08	8995	0.042275	0.308871	0.9929
BMCR09	9841	0.057287	0.282302	0.9601
BMCR10	8401	0.046421	0.300376	0.9710
Avg.	9033.4	0.049909	0.295914	
St. Dev.	544.5	0.005595	0.011272	
CV, %	6.0	11.2	3.8	

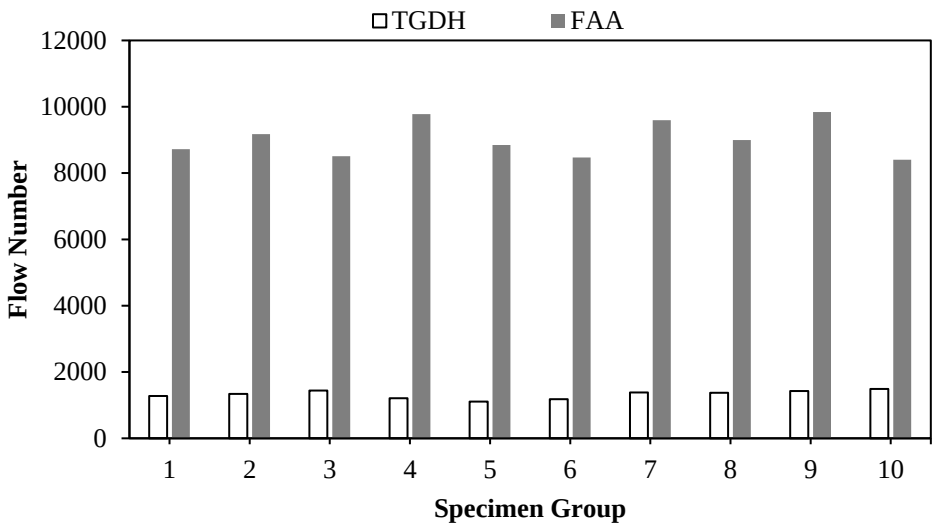

Figure 5.9. Flow number comparison of experimental test results

In addition, the permanent strains in the FN tests at different cycle numbers are given below (Tables 5.5 and 5.6). These cycle numbers were selected according to the two different designs, taking into account the total number of cycles applied. To compare the test results, the values of total permanent strain at the 1750th loading cycle were compared. It can be seen that the average permanent strain values at the 1750th cycle are much lower for the FAA specimens than for the TGDH specimens. Almost six times more permanent strain occurred in the TGDH specimens than in the FAA specimens. It can be seen from the figures that the airport runway mix design with basalt aggregate and polymer modified asphalt binder is about six times more resistant to rutting than the conventional roadway mix design with limestone aggregate and unmodified asphalt binder under the same cyclic loading.

Table 5.5. Permanent strain results of TGDH samples at different cycles

Specimen	**Permanent Strain (%)**		
	@500 Cycle	@1000 Cycle	@1750 Cycle
LUCR03	1.503	2.012	2.668
LUCR05	1.491	2.020	2.775
LUCR06	1.448	1.990	2.829
LUCR07	1.505	2.092	2.969
LUCR08	1.541	2.103	2.907
LUCR09	1.470	1.974	2.694
LUCR10	1.543	2.094	2.922
LUCR11	1.486	1.991	2.647
LUCR12	1.478	1.982	2.670
LUCR13	1.529	2.070	2.833
Avg.	1.499	2.033	2.791
St. Dev.	0.031	0.051	0.118
CV, %	2.1	2.5	4.2

Table 5.6. Permanent strain results of FAA samples at different cycles

Specimen	Permanent Strain (%)		
	@1000 Cycle	@1750 Cycle	@5000 Cycle
BMCR01	0.346	0.401	0.534
BMCR02	0.314	0.364	0.477
BMCR03	0.336	0.391	0.508
BMCR04	0.338	0.389	0.495
BMCR05	0.315	0.373	0.480
BMCR06	0.292	0.340	0.453
BMCR07	0.337	0.383	0.486
BMCR08	0.293	0.345	0.464
BMCR09	0.344	0.394	0.498
BMCR10	0.312	0.359	0.466
Avg.	0.323	0.374	0.486
St. Dev.	0.020	0.021	0.024
CV, %	6.3	5.7	4.9

5.3.3 Indirect Tensile Fatigue Test Laboratory Results

The test standard EN 12697-24 (2012) was used for the IDTF tests. The tests were conducted at 25 ºC, which is considered to be the usual working temperature of asphalt concrete in practice. Haversine loading was applied for 0.1 seconds, followed by a rest period of 0.4 seconds (2 Hz). Recurrent loads of 1800 kPa and 900 kPa were applied to the FAA and TGDH specimens, respectively, for 1,000,000 cycles. However, it took approximately 6 days to complete 1 million cycles. This high number of cycles could not be achieved for every specimen due to random problems with the laboratory conditions, random errors in the test setup, or premature cracking of the specimen.

A total of twenty specimens, ten for each design type, were tested. The resulting indirect tensile stresses and permanent horizontal deformations were recorded. The stiffness modulus values at the end of each loading cycle were calculated using the tensile stress and total cyclic horizontal strain at the center of the specimen. The stiffness values were then plotted as a function of the number of cycles on a log-log scale, and a nonlinear regression analysis was applied to estimate the fatigue life of the specimens, as explained in Chapter 3.5. It is known that the power model fit is the best numerical representation of the fatigue data. Therefore, the fatigue life values were estimated using the fitted power model as the required number of cycles corresponds to a 50% reduction in stiffness modulus.

The fitting parameters applied to the test results are shown in Tables 5.7 and 5.8. Looking at the results, one first notices that the applied fits are quite successful in terms of their relatively high R2 values. Almost all the coefficient of determination (R^2) values are above 95% for both sample groups and thus the regression analyzes agree very well with the actual data. It can also be seen that the results of the TGDH and FAA designs are consistent with each other. For the TGDH samples, the slopes of the fitted power model have a deviation of only 1.6% and the axis intercepts have a deviation of 8.2%. For the FAA design samples, the deviations between the values for the slope (1.9%) and the axis intercepts (8.5%) are also relatively small. A good correlation between the test results shows that the variability between the tested samples is relatively low and the results have a high credibility.

The slope of the power model averages 0.332 for the FAA samples, which is generally lower than for the TGDH samples (0.3691). This indicates that the FAA specimens experience less reduction in stiffness under fatigue loading and therefore have higher strength against fatigue failure. This can be better seen in the fatigue life calculations that follow.

Table 5.7. Fitted power model parameters of TGDH samples

Specimen	Intercept (a)	Slope (b)	R^2
LUIF02-2	0.3636	0.3683	0.9813
LUIF07-2	0.3976	0.3624	0.9890
LUIF08-2	0.3384	0.3765	0.9769
LUIF11-2	0.3206	0.3783	0.9775
LUIF13-1	0.3709	0.3654	0.9859
LUIF14-1	0.3735	0.3701	0.9419
LUIF14-2	0.3637	0.3714	0.9721
LUIF15-1	0.3377	0.3736	0.9860
LUIF15-2	0.4196	0.3615	0.9414
LUIF17-1	0.3888	0.3634	0.9525
Avg.	0.3674	0.3691	
St. Dev.	0.0300	0.0059	
CV, %	8.2	1.6	

The IDTF test results of the TGDH and FAA samples are shown in Table 5.9 and 5.10, respectively. The limestone specimens with unmodified asphalt binder have an average initial stiffness of 4225.65 MPa and a fatigue life of 610,479 cycles. In contrast, the basalt specimens with modified asphalt binder have an average initial stiffness of 5052.69 MPa and a fatigue life of 2,059,089 cycles. The standard deviation and coefficient of variation between the test results are very low, indicating good agreement. With a coefficient of variation of about 3%, the initial stiffness values are very close within each group. The variations between the fatigue lives of the TGDH and FAA specimens are also very consistent at about 7%.

Table 5.8. Fitted power model parameters of FAA samples

Specimen	Intercept (a)	Slope (b)	R^2
BMIF02-2	0.3739	0.3378	0.9730
BMIF03-2	0.4216	0.3287	0.9720
BMIF05-2	0.4224	0.3283	0.9850
BMIF07-2	0.3797	0.3335	0.9790
BMIF09-2	0.4337	0.3250	0.9589
BMIF12-2	0.3852	0.3370	0.9730
BMIF15-1	0.3608	0.3380	0.9802
BMIF15-2	0.4354	0.3272	0.9754
BMIF16-2	0.4613	0.3207	0.9839
BMIF17-1	0.3697	0.3392	0.9695
Avg.	0.4044	0.3315	
St. Dev.	0.0345	0.0064	
CV, %	8.5	1.9	

Although the average initial stiffness values of airport runway design samples were only about 20% higher than those of traditional highway design samples, their average indirect fatigue life was more than three times higher. This once again demonstrates the undeniable superiority of FAA design samples. The use of modified asphalt binder and stronger aggregates combined with the FAA design specifications that has much higher standards, made it possible to produce specimens having much higher resistance against fatigue deterioration.

Table 5.9. IDTF test results of TGDH samples

Specimen	Initial Stiffness (MPa)	Fatigue Life (N_f)
LUIF02-2	4203.13	639720
LUIF07-2	4121.42	621423
LUIF08-2	4244.34	578614
LUIF11-2	4168.54	626619
LUIF13-1	4276.04	673664
LUIF14-1	4389.54	557480
LUIF14-2	4087.91	571751
LUIF15-1	4109.94	644950
LUIF15-2	4308.70	553491
LUIF17-1	4346.97	637079
Avg.	4225.65	610479
St. Dev.	104.54	41760
CV, %	2.5	6.8

Table 5.10. IDTF test results of FAA samples

Specimen	Initial Stiffness (MPa)	Fatigue Life (N_f)
BMIF02-2	5125.34	1969246
BMIF03-2	5182.66	1935272
BMIF05-2	4913.98	2065837
BMIF07-2	5139.97	2266786
BMIF09-2	4959.47	2207701
BMIF12-2	5020.31	1865828
BMIF15-1	4924.27	2169706
BMIF15-2	5178.86	1977392
BMIF16-2	4819.44	2215401
BMIF17-1	5262.58	1917718
Avg.	5052.69	2059089
St. Dev.	145.16	145048
CV, %	2.9	7.1

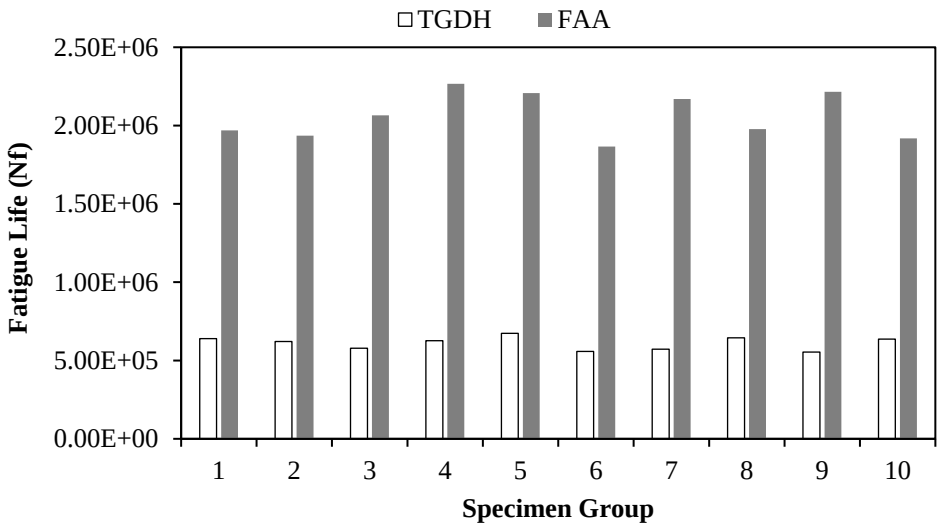

Figure 5.10. Fatigue life comparison of experimental test results

5.4 Finite Element Model Results

After the laboratory tests, the 2D finite element models were created using the images of the samples compacted in the laboratory. To validate the FEM, the same laboratory experiments, i.e., resilient modulus tests, repeated creep tests, and indirect tensile fatigue tests, were attempted to be repeated in the numerical environment. The details of the numerical model were explained in Chapter 4. The results of the numerical simulations and their comparison with the experimental tests are presented in the following sections.

5.4.1 Resilient Modulus FEM Results

For the analysis of the resilient modulus, conditions similar to those in the laboratory experiments were created in the finite element environment, as explained in Chapter 4, and the MR and Poisson's ratio were calculated using the total recoverable deformation values. The mechanical and numerical results of the resilient modulus of the TGDH specimens are presented in Table 5.11 and Figure 5.11.

It can be seen that the resilient modulus values of the TGDH design samples consisting of limestone aggregate and unmodified bitumen are quite close. As a result of the analyzes of ten different specimens, the average of the finite element values M_R is about 5.5 GPa, and this value is very close to the 5450.9 MPa of the experimental results. Although there are differences between the individual FE results and the laboratory results, the average M_R values after simulating the ten different models are very close to the laboratory results. These discrepancies are due to the sensitivity of the M_R values. Since very small changes in the total recoverable deformation values result in larger changes in the MR values, it can be seen that these inter-sample deviations disappear and approach the average value as the number of simulations increases.

In addition, lower deviations were observed in the finite element model with respect to the overall standard deviations of these 10 different simulations. The standard deviation decreased from 3.3 to 2.4% in the FE model. This indicates that the numerical simulations were more consistent than the laboratory tests. As a result, more consistent results in terms of elastic modulus analysis can be obtained with the image-based 2D finite element model presented in this study.

Table 5.11. Numerical and laboratory M_R results of TGDH samples

	Resilient Modulus (M_R)	
Specimen	**Experiment (MPa)**	**Finite Element (MPa)**
LURM01-1	5277.69	5366.69
LURM02-1	5472.30	5468.30
LURM03-1	5645.01	5654.37
LURM06-1	5622.79	5561.78
LURM07-1	5335.90	5256.81
LURM08-1	5434.92	5375.97
LURM09-1	5210.17	5397.67
LURM10-1	5242.42	5533.36
LURM11-1	5702.08	5605.67
LURM12-1	5565.40	5319.83
Avg.	5450.9	5454.0
St. Dev.	179.1	131.2
CV, %	3.3	2.4

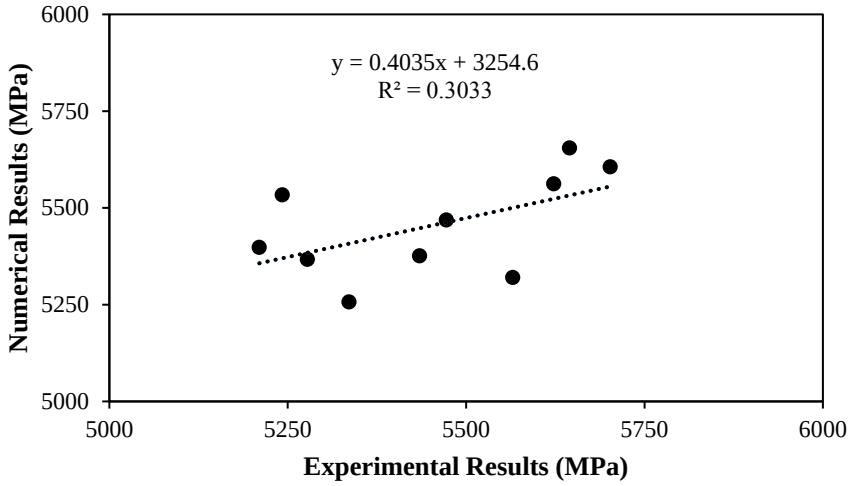

Figure 5.11. Comparison of numerical and laboratory M_R results of TGDH samples

The Poisson's ratio values calculated from the finite element results and the corresponding laboratory values for each specimen are given in Table 5.12 and Figure 5.12. From these results, it can be seen that the finite element and laboratory results are very close, similar to the resilient modulus results. The mean Poisson's ratio of the TGDH specimens was about 0.34 for both types of analysis, and the variations between these results were very small, amounting to 4.9%. From the results of M_R and the Poisson's ratio, it can be concluded that the finite element model based on 2D images successfully simulated the laboratory results for the TGDH specimens.

Synthetic models, created using the aggregate particle redistribution method, were then analyzed. One of the TGDH samples (ID: LURM02-1) was selected and the redistribution method described in Chapter 4 was applied to create a total of 10 different synthetic FE models based on the original structure. Resilient modulus simulations were then performed for these 10 models. The results are shown in Table 5.13 and Figure 5.13.

Table 5.12. Numerical and laboratory Poisson's ratio results of TGDH samples

		Poisson's Ratio
Specimen	**Experiment**	**Finite Element**
LURM01-1	0.335	0.331
LURM02-1	0.356	0.350
LURM03-1	0.334	0.368
LURM06-1	0.358	0.339
LURM07-1	0.336	0.348
LURM08-1	0.342	0.344
LURM09-1	0.320	0.317
LURM10-1	0.315	0.332
LURM11-1	0.368	0.318
LURM12-1	0.350	0.320
Avg.	0.341	0.336
St. Dev.	0.017	0.016
CV, %	4.9	4.9

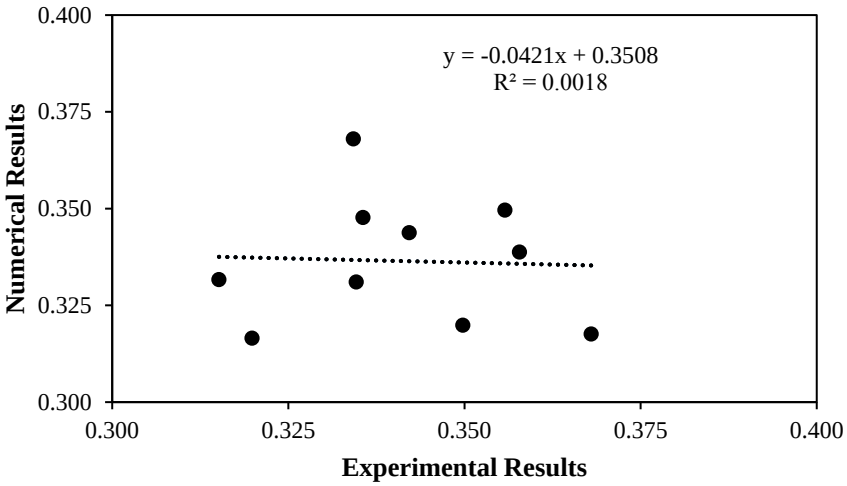

Figure 5.12. Comparison of numerical and laboratory Poisson's ratio results of TGDH samples

In the finite element analysis of the original sample, ID LURM02-1, M_R was calculated to be 5468.30 MPa and Poisson's ratio 0.350. It can be seen that the average values of the test results after ten repetitions, 5455.92 MPa and 0.334, are quite close to the initial values of the sample. Furthermore, the variation of the resilient modulus results within the synthetic samples 2.6%. It can be seen that this variation value is lower than the variation between the empirical results of the same number of TGDH samples, which was 3.3%. In the finite environment, it was found that only 2.6% variations within the test results are caused from specimen microstructure and macro behavior. The effect of testing equipment, laboratory conditions and human factor increases these variations about 25%.

For Poisson's ratio values, the coefficient of variation is 4.9% for the laboratory results and 5.2% for the redistribution results, which are very close. A look at the results shows that the aggregate particle redistribution method can successfully simulate the replication of TGDH samples from the laboratory environment. It is believed that the redistribution method in this study reduces the variability between test results, thus not only facilitating sample replication but also providing more consistent results.

Table 5.13. Resilient modulus analysis results of synthetic TGDH samples

Replicate No.	M_R (MPa)	Poisson's Ratio
	5468.30	**0.350**
1	5542.77	0.339
2	5251.41	0.322
3	5679.96	0.356
4	5548.08	0.324
5	5577.82	0.307
6	5368.48	0.349
7	5387.51	0.359
8	5539.28	0.331
9	5306.33	0.315
10	5357.52	0.337
Avg.	5455.92	0.334
St. Dev.	139.14	0.017
CV, %	2.6	5.2

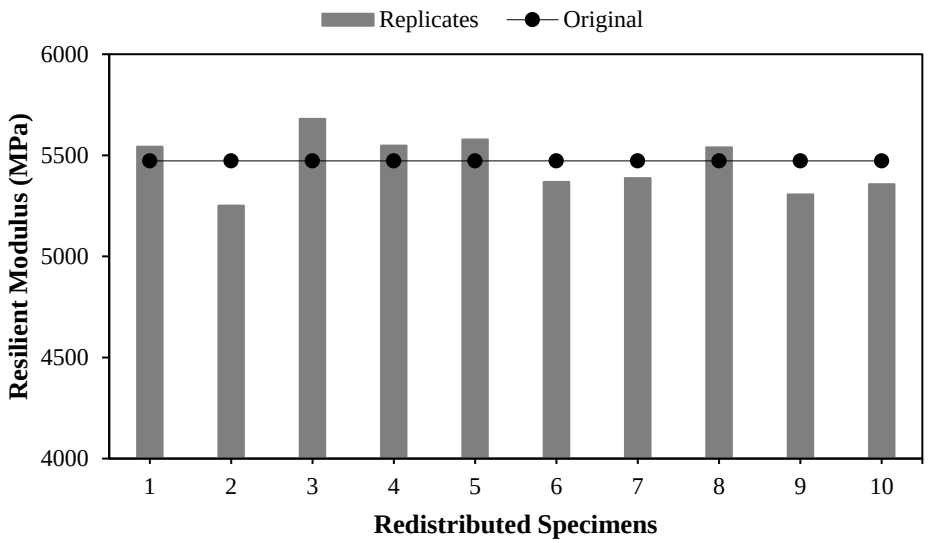

Figure 5.13. Resilient modulus analysis results of synthetic TGDH samples

The M_R results of the FAA design specimens can be found in Table 5.14 and Figure 5.14. The results of 10 different FAA specimens after laboratory tests and finite element analyzes are quite close. While the average resilient modulus in the laboratory experiments was 6793.25 MPa, it was increased to 6837.24 MPa by the FEM. Similar to the TGDH specimens, the standard deviations and thus the deviations between the finite element results for the FAA specimens also appear to be smaller than the laboratory results for these specimens. When the FAA samples were tested in the laboratory, the deviation between the results was 2.3%, but decreased to 1.7% when the FE models were applied. Thus, it can be assumed that not only the FE method can successfully simulate the laboratory experiments of the FAA design samples, but also provides more consistent results compared to the laboratory tests.

Table 5.14. Numerical and laboratory M_R results of FAA samples

	Resilient Modulus (M_R)	
Specimen	**Experiment (MPa)**	**Finite Element (MPa)**
BMRM01-1	6702.44	6865.53
BMRM02-1	7043.61	6615.39
BMRM07-1	6755.87	6756.73
BMRM08-1	6833.34	6900.80
BMRM09-1	6974.03	6844.49
BMRM10-1	6614.56	6689.10
BMRM11-1	6685.91	6927.07
BMRM12-1	6927.18	6896.34
BMRM13-1	6841.58	7018.63
BMRM14-1	6553.94	6858.33
Avg.	6793.25	6837.24
St. Dev.	159.03	119.00
CV, %	2.3	1.7

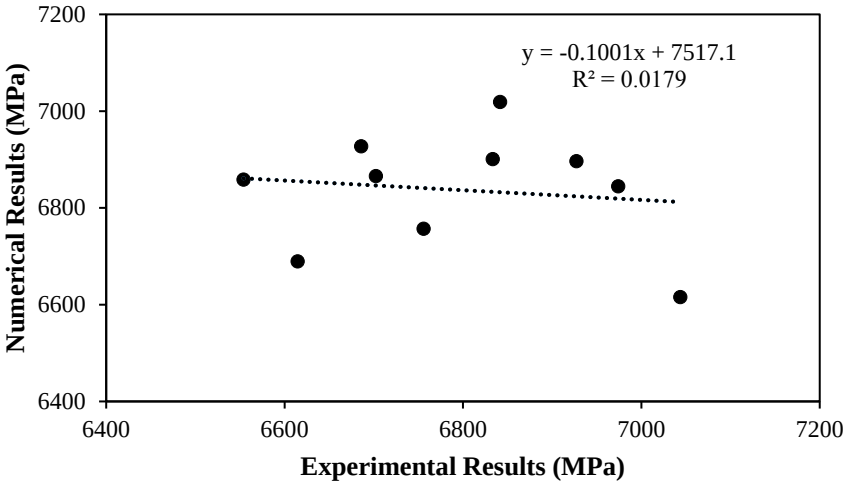

Figure 5.14. Comparison of numerical and laboratory M_R results of TGDH samples

Poisson's ratio results can be found in Table 5.15 and Figure 5.15. Similar to the MR results, the Poisson's ratio values of the FAA samples generated from the FE model are also quite close to the laboratory test values. The two analyzes have shown that the average Poisson's ratio values after testing ten different samples for each design type are 0.294 and 0.298. It is also noted that the variation between the data is smaller and the results of the finite element analyzes are more consistent. Therefore, it can be concluded that the finite element model based on 2D cross-sectional images of the specimens compacted in the laboratory successfully simulates the experimental results of the FAA design in terms of Poisson's ratio. The resilient modulus simulations of the two different models showed that the FE model works very well under two completely different mixture designs in this study.

The sample ID BMRM09-1 was then selected for the particle redistribution procedure. Ten different FE models were analyzed based on the synthetic images of the sample and the results are shown below. Table 5.16 and Figure 5.16 show the resilient modulus and Poisson's ratio results of these synthetic models along with their initial FE results. The original sample (ID BMRM09-1) had 6844.49 MPa of M_R, while the average of the ten synthetic models is 6837.81 MPa. With a standard deviation of 125.74 MPa, the particle redistribution method is successful in

simulating the replicate of the original sample. Additionally, the Poisson's ratio values of the ten synthetic specimens average at 0.292, which is very close to the average PR value of the ten initial laboratory results (0.294).

Table 5.15. Numerical and laboratory Poisson’s ratio results of FAA samples

		Poisson’s Ratio
Specimen	**Experiment**	**Finite Element**
BMRM01-1	0.279	0.308
BMRM02-1	0.310	0.296
BMRM07-1	0.304	0.298
BMRM08-1	0.294	0.285
BMRM09-1	0.285	0.297
BMRM10-1	0.284	0.287
BMRM11-1	0.282	0.307
BMRM12-1	0.311	0.302
BMRM13-1	0.301	0.305
BMRM14-1	0.288	0.294
Avg.	0.294	0.298
St. Dev.	0.012	0.008
CV, %	4.1	2.6

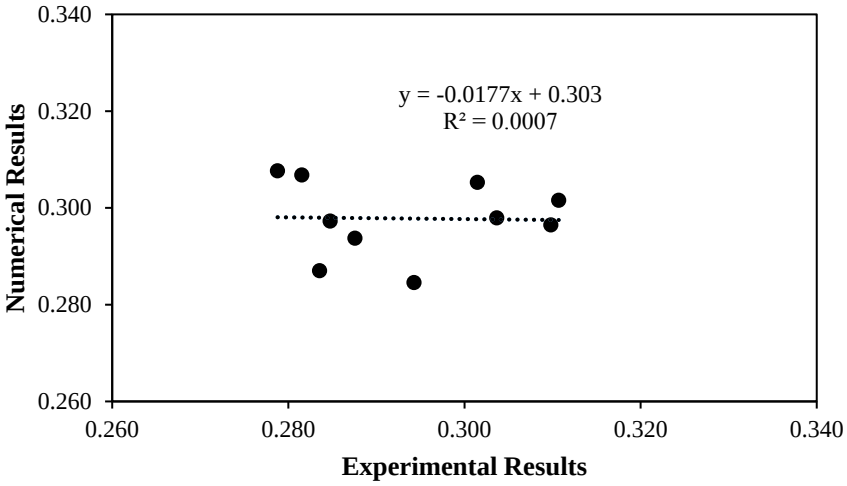

Figure 5.15. Comparison of numerical and laboratory Poisson's ratio results of TGDH samples

The standard deviation of the M_R values after the laboratory experiments was 159.03 MPa (2.3%). Replicates of these 10 specimens using the particle redistribution method yielded a smaller deviation of 125.74 MPa (1.8%), indicating the higher consistency of the image particle redistribution method. The average Poisson's ratio values remained almost the same between the original FE analyzes (0.294) and the redistributed analyzes (0.292). The standard deviations of the PR results between the redistributed samples are lower (2.6%) than those of the laboratory results (4.1%). Consequently, the particle redistribution method not only facilitated replication of samples in the vicinity of FE, which is difficult to do in the laboratory, but also was successful for developing more consistent results.

Based on the resilient modulus analyzes, the image-based 2D FE model created in this study was able to successfully simulate the laboratory tests of the two different asphalt mixtures in the finite element environment. A total of 20 simulations were compared with the same number of laboratory experiments and the numerical model was validated in terms of resilient modulus and Poisson's ratio results. In addition, the method for redistributing the aggregate particles in the FE environment was able to successfully simulate the sample replications performed in the laboratory.

Table 5.16. Resilient modulus analyzes results of synthetic FAA samples

Replicate No.	M_R (MPa)	Poisson's Ratio
	6844.49	**0.297**
1	6881.09	0.284
2	6962.96	0.288
3	6829.46	0.305
4	6614.97	0.300
5	6783.29	0.289
6	6962.13	0.297
7	6763.73	0.282
8	6692.80	0.286
9	7005.48	0.299
10	6882.20	0.295
Avg.	6837.81	0.292
St. Dev.	125.74	0.008
CV, %	1.8	2.6

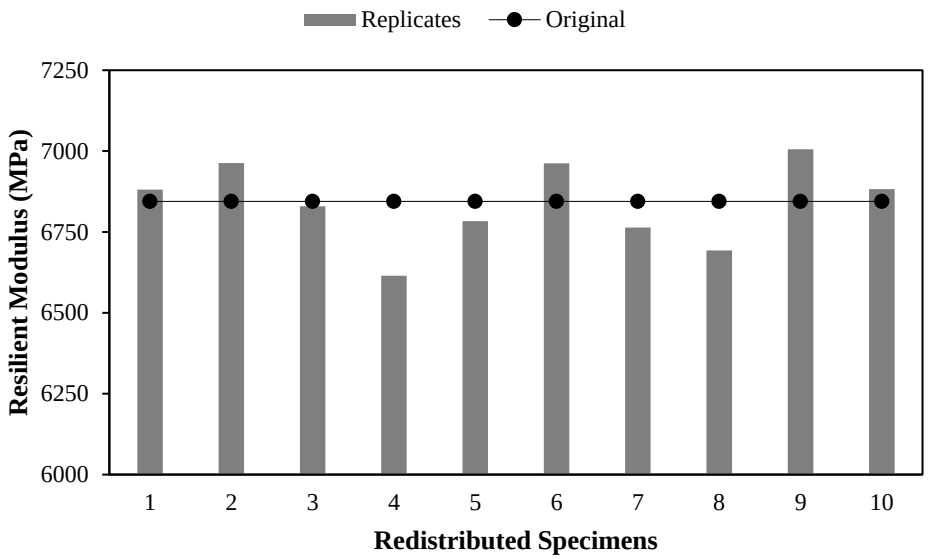

Figure 5.16. Resilient modulus analysis results of synthetic FAA samples

5.4.2 Repeated Creep FEM Results

Repeated creep tests were simulated in the finite element model created from the images of the specimens compacted in the laboratory. The necessary steps have already been described in Chapter 4. 2,000 cycles of repeated loading were applied to the FE model, and the total permanent strains at the end of each cycle were calculated. These permanent strains at the end of each loading cycle were then recorded and a power model was fitted to the numerical results, as in the analyzes of the laboratory results. Since, as mentioned before, no damage model is defined in the FEM, the creep behavior of the specimens was preserved only in the first two regions and could not pass to the tertiary zone where the rapid and unstable shear failures occur. Therefore, the flow numbers (FN) were not calculated from the model results, but only the parameters of the power model, i.e., the intercept (a) and the slope of the fitted model (b), were compared to validate the numerical model.

The fitted model parameters of the TGDH test samples that have the combination of limestone aggregate and unmodified binder are shown in Table 5.17. In this table, the model parameters of each specimen are listed together in relation to their laboratory and numerical test results. The comparisons of the power model parameters of the laboratory tests and the FE simulations are shown in Figures 5.17 and 5.18.

First of all, in the finite element results, it can be seen that the coefficients a and b of the power model are in better agreement with each other compared to the laboratory results. The standard deviations of the two coefficient values are much smaller for the numerical results than for the mechanical test results. In particular, the slopes of the fitted performance models have about 8 times lower coefficient of variation (0.3%) in the finite element simulations than the laboratory results (2.4%).

The same situation can be observed with the intercepts. While they have a variance of 6.4% in the laboratory results, this value was reduced to 1.9% by the finite element analyzes. It is therefore clear that the finite element method provides more consistent

results than the laboratory tests when fitting the power model. Although the coefficients of determination for the regression analyzes are lower than the laboratory results, the fitted models are considered successful for the FE results due to their high R-squared values (> 97%).

A look at Table 5.17 also shows that the applied parameters of the power model are very close in both types of analyzes. After 10 different applied analyzes, the mean value of the slopes (b) of the fitted power models in the laboratory experiments was 0.456131, while the same value in the finite element simulations was 0.453754. Similarly, the mean value of the intersection points (a) in the laboratory experiments was 0.089519, while the finite element result was 0.090149. Thus, considering the TGDH mix design, the 2D image-based finite element model in this study was able to successfully simulate the repeated creep tests in the finite element environment.

Table 5.17. Comparison of fitted power model parameters of TGDH samples

	Experiment			Finite Element		
Specimen	**Inter. (a)**	**Slope (b)**	**R^2**	**Inter. (a)**	**Slope (b)**	**R^2**
LUCR03	0.095127	0.445027	0.9967	0.091674	0.452193	0.9766
LUCR05	0.086523	0.460160	0.9952	0.090291	0.454069	0.9770
LUCR06	0.081448	0.467673	0.9942	0.089376	0.454520	0.9794
LUCR07	0.079428	0.476811	0.9977	0.091377	0.452082	0.9784
LUCR08	0.087168	0.464116	0.9976	0.091052	0.453620	0.9769
LUCR09	0.091281	0.449617	0.9938	0.087467	0.454792	0.9772
LUCR10	0.094384	0.452536	0.9962	0.091175	0.452371	0.9766
LUCR11	0.095710	0.442765	0.9958	0.086994	0.457261	0.9778
LUCR12	0.093522	0.446101	0.9950	0.091098	0.452815	0.9767
LUCR13	0.090596	0.456501	0.9966	0.090983	0.453820	0.9771
Avg.	0.089519	0.456131		0.090149	0.453754	
St. Dev.	0.005727	0.011050		0.001669	0.001567	
CV, %	6.4	2.4		1.9	0.3	

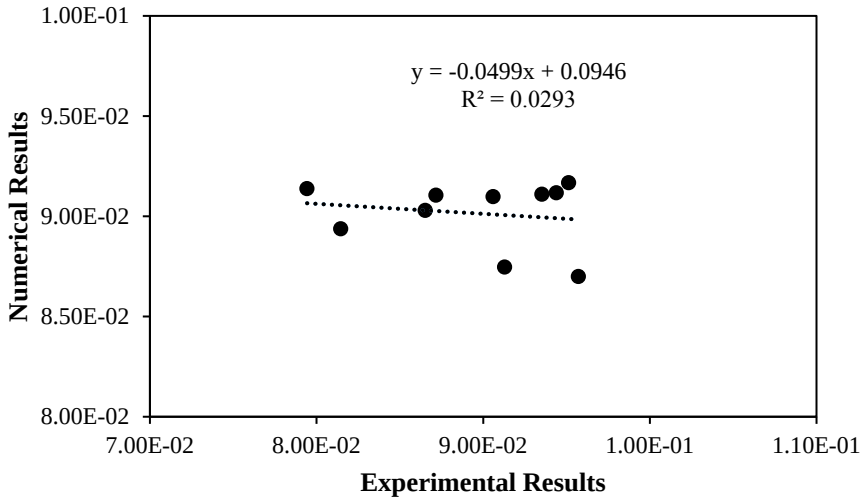

Figure 5.17. Comparison of intercept point (a) results of TGDH samples

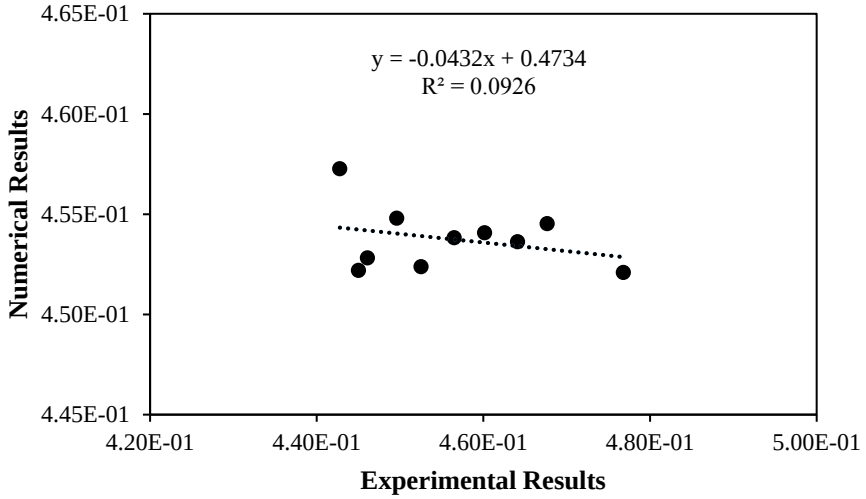

Figure 5.18. Comparison of slope (b) results of TGDH samples

To investigate the variations of the repeated creep experiments conducted in the laboratory, the sample ID LUCR06 was selected and the particle redistribution method was applied. Finite element models were then created and run on 10 different synthetic images. Similarly, power models were fitted to the FE results of the repeated creep simulations. The power model parameters, i.e., the intercept (a) and slope (b) of the fit, based on these 10 different synthetic model results are shown in Table 5.18 below. This table also includes the finite element results of the original model of the sample ID LUCR06. A look at the results in the table shows that the results of the created synthetic samples are quite close to the original finite element results. The standard deviations correspond to almost the same percentages as in the finite element analyzes of the real samples. Both the 10 real TGDH models and the 10 synthetic redistributions of the sample ID LUCR06 have a deviation of 1.9% at the intercept (a) and 0.3% at the slope (b). Therefore, the specimen replication performed in the laboratory environment, can be successfully simulated in the FEM using the image particle redistribution method presented in this study.

Table 5.18. Fitted power model results of synthetic TGDH samples

Replicate No	**Intercept (a)**	**Slope (b)**	**R^2**
	0.089376	**0.454520**	**0.9794**
1	0.090127	0.454287	0.9777
2	0.091065	0.452856	0.9786
3	0.090875	0.453889	0.9763
4	0.091013	0.452132	0.9793
5	0.088511	0.456098	0.9793
6	0.089220	0.454565	0.9783
7	0.090945	0.453696	0.9762
8	0.086123	0.454966	0.9799
9	0.089542	0.455563	0.9773
10	0.092296	0.453745	0.9782
Avg.	0.089972	0.454180	
St. Dev.	0.001737	0.001194	
CV, %	1.9	0.3	

The repeated creep simulation results of the FAA samples are shown in Table 5.19. The comparison of the power model parameters between the finite element analysis and the laboratory experiments is shown in Figures 5.19 and 5.20. Similar to the TGDH specimens, the parameters of the fitted power model applied to the finite element results of the FAA specimens are more consistent than the laboratory results. The intercept (a) of the power model has a variation of 11.2% in the experimental results, while the coefficient of variation is reduced to 2.9% after finite element modeling of the same specimens. Moreover, the coefficient of variation of the slope values (b) in the FEM has decreased more than five times and is 0.7%. Once again, the numerical model presented in this study can not only successfully simulate the repeated creep tests, but also reduce the variation between the test results.

Table 5.19. Comparison of fitted power model parameters of FAA samples

	Experiment			Finite Element		
Specimen	**Inter. (a)**	**Slope (b)**	**R^2**	**Inter. (a)**	**Slope (b)**	**R^2**
BMCR01	0.049300	0.308924	0.9855	0.050180	0.300469	0.9008
BMCR02	0.047835	0.297688	0.9815	0.050802	0.299609	0.9003
BMCR03	0.050653	0.299417	0.9850	0.051218	0.298558	0.8997
BMCR04	0.054280	0.288041	0.9766	0.052874	0.297668	0.8992
BMCR05	0.049428	0.294722	0.9825	0.051955	0.298459	0.8997
BMCR06	0.042721	0.304189	0.9895	0.052207	0.297914	0.8993
BMCR07	0.058886	0.274608	0.9637	0.049964	0.301405	0.9016
BMCR08	0.042275	0.308871	0.9929	0.049056	0.303340	0.9018
BMCR09	0.057287	0.282302	0.9601	0.053702	0.295520	0.8999
BMCR10	0.046421	0.300376	0.9710	0.053056	0.297720	0.8985
Avg.	0.049909	0.295914		0.051501	0.299066	
St. Dev.	0.005595	0.011272		0.001509	0.002218	
CV, %	11.2	3.8		2.9	0.7	

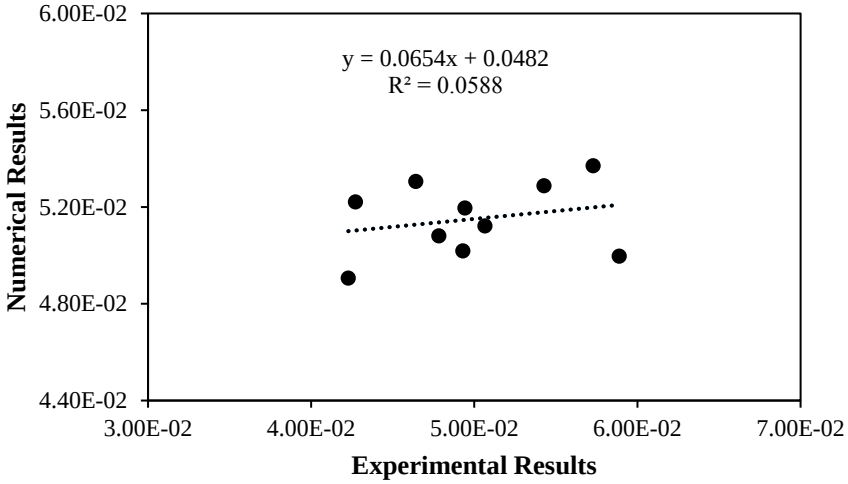

Figure 5.19. Comparison of intercept point (a) results of FAA samples

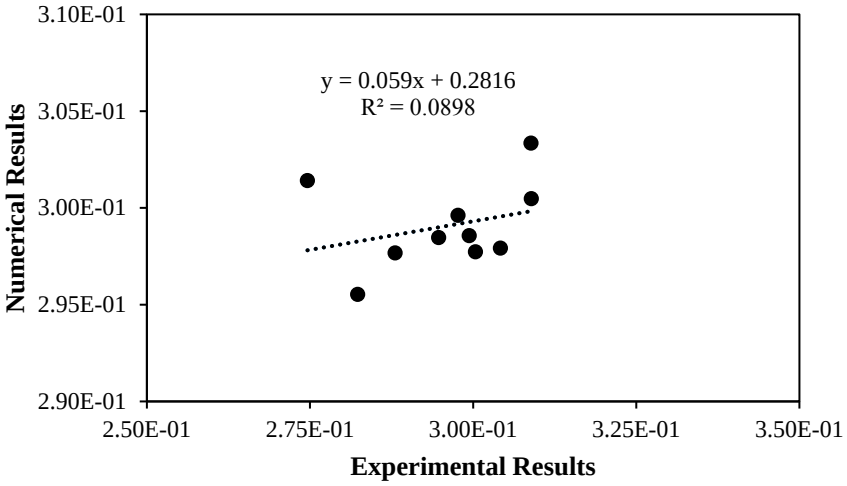

Figure 5.20. Comparison of slope (b) results of FAA samples

The results of the 10 synthetic samples (based on the sample ID BMCR03) prepared by applying the particle redistribution method are shown in Table 5.20. Again, the variations between these synthetic FE models are very close to the real FE models, proving that the aggregate redistribution method works as intended. The average slope (b) and average intercept (a) of the 10 synthetic samples are almost identical to the real original sample ID BMCR03. Therefore, the particle redistribution method for the FAA design samples in the finite element environment was able to successfully apply the specimen replicates performed in the laboratory.

The image-based 2D finite element model created in this study was validated by several repeated creep analyzes. By comparing 10 different specimens of two different designs, the numerical model was validated. Moreover, it was proved that the application of specimen repetition in the laboratory environment can be successfully simulated by the particle redistribution method presented in this study.

Table 5.20. Fitted power model results of synthetic FAA samples

Replicate No	**Intercept (a)**	**Slope (b)**	**R^2**
	0.051218	**0.298558**	**0.8997**
1	0.053247	0.295418	0.9046
2	0.052342	0.298243	0.8992
3	0.051347	0.297287	0.8923
4	0.050242	0.301123	0.8912
5	0.053123	0.294235	0.9012
6	0.052099	0.296234	0.9023
7	0.049234	0.300213	0.8989
8	0.049123	0.300023	0.9035
9	0.052347	0.297345	0.9012
10	0.050234	0.299123	0.8912
Avg.	0.051334	0.297925	
St. Dev.	0.001534	0.002234	
CV, %	3.0	0.7	

CHAPTER 6

CONCLUSIONS

6.1 Conclusions

In this study, a finite element method based on 2D images was developed to investigate the tensile variations of asphalt concrete. To prove that the FE model works under different conditions, two completely different asphalt mix designs were carried out. One of the designs contained a combination of limestone aggregate and unmodified binder and was based on a traditional binder course specification from the Turkish General Directorate of Highways (TGDH). The other design was based on Federal Aviation Administration (FAA) design criteria for a binder course for airport runways and included a combination of basalt aggregate and SBS polymer-modified asphalt binder (PMB). The required number of samples for each design combination was prepared in the laboratory using a Superpave gyratory compactor.

Three different test programs were conducted for empirical observation, namely the resilient modulus test (RM), the repeated creep test, also known as the flow number test (FN), and the indirect tensile fatigue test (IDTF). Each design type was tested with 10 different replicates under the three different test methods. The images of the laboratory compacted specimens were then scanned using a flatbed scanner and various image processing techniques were applied to prepare the images for the FEM. A unique image vectorization method was developed to transform the images of the asphalt samples into the finite element geometry model in ANSYS®. Finally, the image-based 2D finite element model was created in ABAQUS® and an attempt was made to replicate the originally selected three different test programs in the finite element environment. The aggregate particle redistribution method was used to

investigate the tensile variations of asphalt concrete. By comparing the numerical analyzes with the experimental results, an attempt was made to prove the accuracy of the finite element method. The following findings can be summarized from this study:

1- The size distribution analysis showed that the actual gradations of the asphalt concrete specimens can be successfully represented in the 2D cross-sectional images obtained with a flatbed scanner. The maximum ferret diameter and area of each aggregate particle were used on the scanned images to calculate the percent retention on each sieve size. Comparison of the calculated curves with the curves of the initial gradations showed that the scanned images successfully represented the initial gradations of the samples used in sample preparation.

2- By using image vectorization and pixel reduction methods, the external shapes of aggregate particles are successfully transferred to the finite element environment using the ANSYS® Mechanical APDL user interface. In addition, the image vectorization method reduces the required number of pixels to be used in a pixel-based geometric model by about 30 times, allowing more realistic outer shapes of aggregate particles to be modeled more rapidly.

3- The specimens with limestone aggregate and unmodified binder generally have lower elastic behavior than the specimens with basalt aggregate and polymer-modified binder. The FAA airport runway specimens have an average resilient modulus (M_R) that is about 25% higher than that of the TGDH specimens with a conventional pavement with a wearing course structure.

4- The average Poisson's ratio values are generally higher for the TGDH samples than for the FAA samples. A higher Poisson's ratio denotes that the material has larger elastic deformations and is softer. Consistent with the M_R results, the combination of basalt aggregate and SBS polymer-modified binder resulted in higher strength of the FAA runway specimens.

5- In the repeated creep experiments, the airport runway samples were able to withstand much longer load repetitions with much less permanent deformation compared to the conventional pavement samples. While the TGDH specimens reached an average maximum strain value of 3% at the end of about 1,900 repeated load cycles, the average maximum strain values for the FAA specimens remained at about 0.5%, even though the number of load repetitions was five times higher. The combination of basalt aggregate and PMB bitumen was found to make a significant contribution to the repeated creep strength of asphalt concrete compared to limestone aggregate and unmodified bitumen.

6- The comparisons of the flow numbers (FN) of the laboratory experiments showed that the rutting resistances of the FAA runway samples are about 5 times higher than those of the TGDH pavement samples. The axis intercept parameter (a) of the fitted power model in the repeated creep tests, which represents the permanent strain at the initial cycle, is generally lower for the FAA specimens, indicating lower rutting deformations. Accordingly, the slopes (b) of the fitted power models are generally lower for the FAA specimens than for the TGDH specimens, resulting in higher rutting resistance. A comparison of the FN test results at the 1750th loading cycle shows that the combination of basalt aggregate and polymer modified bitumen (PMB) exhibits more than 7 times higher resistance to permanent deformation than the neat bitumen and limestone aggregate at the same number of loadings.

7- Comparison of the indirect tensile fatigue test results shows that the FAA runway specimens performed better than the TGDH pavement specimens. While the average initial stiffness value of the FAA specimens is only about 20% higher than that of the TGDH specimens, their fatigue life (N_f) at the end of the indirect tensile fatigue tests is more than three times higher.

8- The slopes (b) of the fitted power model for the IDTF test results are generally lower for the FAA samples than for the TGDH samples. Consequently, the combination of basalt aggregate and modified binder in the airport runway design has better damping capabilities under indirect tensile loading, resulting in better

fatigue performance. The intercepts (a) of the power models are generally higher for the FAA specimens, indicating a higher fatigue life.

9- Comparing the resilient modulus of the TGDH and FAA samples, it can be seen that the values of MR, obtained from the FE models, are quite close to the values obtained from the laboratory experiments. Moreover, the Poisson's ratio results calculated at the end of the resilient modulus analyzes are almost identical for the specimens of both design types. Thus, the finite element model based on 2D images was validated with respect to the results of the resilient modulus tests for both the conventional highway and airport runway design samples.

10- The coefficients of variation (CV) of the resilient modulus analyzes are lower in the results of FE than in the laboratory experiments, except for the Poisson's ratios of the TGDH samples. Thus, as a result of each 10 different analyzes with two different design types, it was proved that the finite element model gives more consistent and less varying results than the results obtained in the laboratory.

11- Particle redistribution methods were applied to a sample of each mixture design and 10 different synthetic images were produced. Comparison of the resilient modulus simulation results for these 20 synthetic models showed that the sample replication performed in the laboratory can be successfully simulated in a FE environment using the particle redistribution method.

12- The validation of the 2D image-based finite element model created in this study is further supported by the repeated creep analyzes. The coefficients of the fitted power model, i.e., the intercept (a) and slope (b) of the fit, are compared for both the TGDH and FAA design results, and the FE results are very close to the results of the laboratory experiments. As with the resilient modulus experiments, the repeated creep analyzes confirmed that the FE analyzes give more consistent results than the laboratory tests due to their lower coefficient of variation.

13- The image particle redistribution method is also validated by the repeated creep tests. Based on the results of 10 different synthetic samples for both TGDH and FAA design samples, it is clear that the particle redistribution method successfully simulates the replication of laboratory samples in a FE environment.

14- Indirect tensile fatigue experiments, however, could not be simulated in the finite element environment. With the computer hardware available in hand, high loading numbers of the IDTF tests could not be made possible in the FE analyzes created in this study.

6.2 Future Recommendations

In light of the findings of this study, the following recommendations can be made for future studies:

- In this study, damage models were not defined in the creation of the image-based 2D finite element model. Simulated repeated creep tests characterized the material response within the first two regions. A damage model could be developed to give full credit to the simulated repeated creep tests or other similar test methods.

- IDTF tests could not be simulated due to the high number of loading cycles. Advanced computer hardware is needed to determine whether or not the FE model will perform at higher load repetitions.

- The two-phase FE model in this study does not consider air voids, which are known to have a major influence on the material response of asphalt concrete. These air voids, which can be identified by various methods such as dye, can be defined as a third phase in the finite element model and their effect can be investigated in future studies.

- During the preparation phase of the material model, an advanced viscoelastic material model, Burger's model, was to be implemented but could not be completed

due to time constraints and the focus of the study. Instead, the simpler and effective Prony series method was used. By using the material subroutine (UMAT) of ABAQUS®, more advanced material models such as Burger's model can be implemented together with the image vectorization method used in this study to further investigate the material behavior of asphalt concrete.

REFERENCES

Abbas, A. R. (2004). *Simulation of the micromechanical behavior of asphalt* mixtures *using the discrete element method*. (Doctoral dissertation, Washington State University). ProQuest Dissertations & Theses Global database. (UMI No. 3160461).

Abu Al-Rub, R. K., Darabi, M. K., Huang, C. W., Masad, E. A., & Little, D. N. (2012). Comparing finite element and constitutive modelling techniques for predicting rutting of asphalt pavements. *International Journal of Pavement Engineering*, *13*(4), 322-338.

Adhikari, S., & You, Z. (2008). 3D microstructural models for asphalt mixtures using X-ray computed tomography images. *International Journal of Pavement Research and Technology*, *1*(3), 94.

Alae, M., Ling, M., Haghshenas, H. F., & Zhao, Y. (2021). Three-dimensional finite element analysis of top-down crack propagation in asphalt pavements. *Engineering Fracture Mechanics*, *248*, 107736.

Al-Rousan, T., Masad, E., Tutumluer, E., & Pan, T. (2007). Evaluation of image analysis techniques for quantifying aggregate shape characteristics. *Construction and Building Materials*, *21*(5), 978-990.

Ameri, M., Mansourian, A., Khavas, M. H., Aliha, M., & Ayatollahi, M. R. (2011). Cracked asphalt pavement under traffic loading–A 3D finite element analysis. *Engineering Fracture Mechanics*, *78*(8), 1817-1826.

Ameri, M., Sheikhmotevali, A. H., & Fasihpour, A. (2014). Evaluation and comparison of flow number calculation methods. *Road materials and pavement design*, *15*(1), 182-206.

Aragão, F. T. S., Kim, Y. R., Lee, J., & Allen, D. H. (2011). Micromechanical model for heterogeneous asphalt concrete mixtures subjected to fracture failure. *Journal of Materials in Civil Engineering*, *23*(1), 30-38.

Arshadi, A. (2015). *Development of an image-based multi-scale finite element approach to predict fatigue damage in asphalt mixtures*. (Doctoral dissertation, The University of Wisconsin-Madison). ProQuest Dissertations & Theses Global database. (UMI No. 3704452).

Arshadi, A., & Bahia, H. (2015). Development of an image-based multi-scale finite-element approach to predict mechanical response of asphalt mixtures. *Road Materials and Pavement Design*, *16*(sup2), 214-229.

Barksdale, R. D., Lago Alba, J. A., Khosla, N. P., Kim, R., Lambe, P. C., & Rahman, M. S. (1997). Laboratory determination of resilient modulus for flexible pavement design. *No. NCHRP Project 1-28*.

Bekele, A., Balieu, R., Jelagin, D., Ryden, N., & Gudmarsson, A. (2021). Micro-mechanical modelling of low temperature-induced micro-damage initiation in asphalt concrete based on cohesive zone model. *Construction and Building Materials*, *286*, 122971.

Bessa, I. S., Branco, V. T. C., & Soares, J. B. (2012). Evaluation of different digital image processing software for aggregates and hot mix asphalt characterizations. *Construction and Building Materials*, *37*, 370-378.

Biligiri, K. P., Kaloush, K. E., Mamlouk, M. S., & Witczak, M. W. (2007). Rational modeling of tertiary flow for asphalt mixtures. *Transportation Research Record*, *2001*(1), 63-72.

Bonaquist, R. F., Christensen, D. W., & Stump, W. (2003). Simple performance tester for Superpave mix design: First-article development and evaluation (Vol. 513). *Transportation Research Board*.

Boudreau, R. L., Hicks, R. G., & Furber, A. M. (1992). Effects of test parameters on resilient modulus of laboratory-compacted asphalt concrete specimens. *Transportation Research Record*, (1353).

Bruno, L., Parla, G., & Celauro, C. (2012). Image analysis for detecting aggregate gradation in asphalt mixture from planar images. *Construction and Building Materials*, *28*(1), 21-30.

Buttlar, W. G., & Roque, R. (1994). Development and evaluation of the strategic highway research program measurement and analysis system for indirect tensile testing at low temperatures. *Transportation Research Record*, (1454).

Cárdenas, M., Filonzi, A., & Delgadillo, R. (2021). Finite element and experimental validation of sample size correction factors for indentation on asphalt bitumens with cylindrical geometry. *Construction and Building Materials*, *274*, 122055.

Chen, H. H., Marshek, K. M., & Saraf, C. L. (1986). Effects of truck tire contact pressure distribution on the design of flexible pavements: a three-dimensional finite element approach. *Transportation Research Record*, (1095).

Cho, Y. H., McCullough, B. F., & Weissmann, J. (1996). Considerations on finite-element method application in pavement structural analysis. *Transportation Research Record*, *1539*(1), 96-101.

Christensen Jr, D. W., Pellinen, T., & Bonaquist, R. F. (2003). Hirsch model for estimating the modulus of asphalt concrete. *Journal of the Association of Asphalt Paving Technologists*, *72*.

Coenen, A. R., Kutay, M. E., Sefidmazgi, N. R., & Bahia, H. U. (2012). Aggregate structure characterisation of asphalt mixtures using two-dimensional image analysis. *Road Materials and Pavement Design*, *13*(3), 433-454.

Coleri, E., Harvey, J. T., Yang, K., & Boone, J. M. (2012). Development of a micromechanical finite element model from computed tomography images for shear modulus simulation of asphalt mixtures. *Construction and Building Materials*, *30*, 783-793.

Collop, A. C., McDowell, G. R., & Lee, Y. W. (2006). Modelling dilation in an idealised asphalt mixture using discrete element modelling. *Granular Matter*, *8*(3), 175-184.

Dai, Q., Sadd, M. H., Parameswaran, V., & Shukla, A. (2005). Prediction of damage behaviors in asphalt materials using a micromechanical finite-element model and image analysis. *Journal of Engineering Mechanics*, *131*(7), 668-677.

Dai, Q., Sadd, M. H., & You, Z. (2006). A micromechanical finite element model for linear and damage-coupled viscoelastic behaviour of asphalt mixture. *International Journal for Numerical and Analytical Methods in Geomechanics*, *30*(11), 1135-1158.

Dai, Q., & You, Z. (2008). Micromechanical finite element framework for predicting viscoelastic properties of asphalt mixtures. *Materials and Structures*, *41*(6), 1025-1037.

Dessouky, S. H. (2005). *Multiscale approach for modeling hot mix asphalt*. (Doctoral dissertation, Texas A&M University). ProQuest Dissertations & Theses Global database. (UMI No. 3172018).

Dongré, R., D'Angelo, J., & Copeland, A. (2009). Refinement of flow number as determined by asphalt mixture performance tester: Use in routine quality control–quality assurance practice. *Transportation Research Record*, *2127*(1), 127-136.

Du, C., Sun, Y., Chen, J., Gong, H., Wei, X., & Zhang, Z. (2020). Analysis of cohesive and adhesive damage initiations of asphalt pavement using a microstructure-based finite element model. *Construction and Building Materials*, *261*, 119973.

Erkens, S. M. J. G., Liu, X., & Scarpas, A. (2002). 3D finite element model for asphalt concrete response simulation. *The International Journal Geomechanics*, *2*(3), 305-330.

Francken, L. (1977, January). Permanent deformation law of bituminous road mixes in repeated triaxial compression. In *Volume I of proceedings of 4th International Conference on Structural Design of Asphalt Pavements, Ann Arbor, Michigan, August 22-26, 1977.* (No. Proceeding).

Grabowski, W., Kuczma, M. S., & SŁOWIK, M. (2002). Mathematical modelling of rheological properties of polymer modified bitumens. *Foundations of Civil and Environmental Engineering*, *2*, 27-42.

Gu, F., Luo, X., Luo, R., Lytton, R. L., Hajj, E. Y., & Siddharthan, R. V. (2016). Numerical modeling of geogrid-reinforced flexible pavement and corresponding validation using large-scale tank test. *Construction and Building Materials*, *122*, 214-230.

Guddati, M. N., Feng, Z., & Kim, Y. (2002). Toward a micromechanics-based procedure to characterize fatigue performance of asphalt concrete. *Transportation Research Record*, *1789*(1), 121-128.

Iott, J., Haftka, R.T., Adelman, H.M. (1985). Selecting Step Sizes in Sensitivity Analysis by Finite Differences; *NASA Technical Memorandum:Greenbelt*, MD, USA, 1985; Volume 86382.

Han, D., Liu, G., Zhao, Y., Pan, Y., & Yang, T. (2021a). Research on thermal properties and heat transfer of asphalt mixture based on 3D random reconstruction technique. *Construction and Building Materials*, *270*, 121393.

Han, D., Yuan, M., & Hu, H. (2021b). Establishing prediction master curve of dynamic modulus of asphalt mixture considering randomness of aggregate morphology. *Construction and Building Materials*, *294*, 123575.

Hashin, Z., & Shtrikman, S. (1963). A variational approach to the theory of the elastic behaviour of multiphase materials. *Journal of the Mechanics and Physics of Solids*, *11*(2), 127-140.

Helwany, S., Dyer, J., & Leidy, J. (1998). Finite-element analyzes of flexible pavements. *Journal of Transportation Engineering*, *124*(5), 491-499.

Hu, J., Qian, Z., Liu, Y., & Zhang, M. (2015). High-temperature failure in asphalt mixtures using micro-structural investigation and image analysis. *Construction and Building Materials*, *84*, 136-145.

Hua, J. (2000). *Finite element modeling and analysis of accelerated pavement testing devices and rutting phenomenon* (Doctoral dissertation, Purdue University). ProQuest Dissertations & Theses Global database. (UMI No. 3020244).

Huang, W., Zhang, X., & Yin, Y. (2016). An image-based finite element approach for simulating viscoelastic response of asphalt mixture. *Advances in Materials Science and Engineering*, *2016*.

Hunter, A. E., Airey, G. D., & Collop, A. C. (2004). Aggregate orientation and segregation in laboratory-compacted asphalt samples. *Transportation Research Record*, *1891*(1), 8-15.

Jensen, R. P., Bosscher, P. J., Plesha, M. E., & Edil, T. B. (1999). DEM simulation of granular media-structure interface: effects of surface roughness and particle shape. *International Journal for Numerical and Analytical Methods in Geomechanics*, *23*(6), 531-547.

Kim, M., Tutumluer, E., & Kwon, J. (2009). Nonlinear pavement foundation modeling for three-dimensional finite-element analysis of flexible pavements. *International Journal of Geomechanics*, *9*(5), 195-208.

Klimczak, M., & Cecot, W. (2020). Towards asphalt concrete modeling by the multiscale finite element method. *Finite Elements in Analysis and Design*, *171*, 103367.

Kollmann, J., Liu, P., Lu, G., Wang, D., Oeser, M., & Leischner, S. (2019). Investigation of the microstructural fracture behaviour of asphalt mixtures using the finite element method. *Construction and Building Materials*, *227*, 117078.

Kose, S. (2002). *Development of a virtual test procedure for asphalt concrete*. (Doctoral dissertation, University of Wisconsin-Madison). ProQuest Dissertations & Theses Global database. (UMI No. 3089655)

Lakes, R. S., Kose, S., & Bahia, H. (2002). Analysis of high volume fraction irregular particulate damping composites. *Journal of Engineering Materials and Technology, 124*(2), 174-178.

Lethersich, W. (1942). The Mechanical behavior of bitumen. *Journal of the Society of Chemical Industry, 61(7),* 101-108, 1942.

Ling, C. (2016). *Using Image-based Multi-scale Finite Element Model to Predict Rutting Behavior of Asphalt Mixtures* (Doctoral dissertation, University of Wisconsin-Madison). ProQuest Dissertations & Theses Global database. (UMI No. 10251184).

Liu, P., Wang, D., & Oeser, M. (2017). Application of semi-analytical finite element method to analyze asphalt pavement response under heavy traffic loads. *Journal of Traffic and Transportation Engineering (English Edition)*, *4*(2), 206-214.

Lu, Y., & Wright, P. J. (1998). Numerical approach of visco-elastoplastic analysis for asphalt mixtures. *Computers & Structures*, *69*(2), 139-147.

Luo, R., & Lytton, R. L. (2011). Self-consistent micromechanics models of an asphalt mixture. *Journal of Materials in Civil Engineering*, *23*(1), 49-55.

Masad, E., Muhunthan, B., Shashidhar, N., & Harman, T. (1999). Internal structure characterization of asphalt concrete using image analysis. *Journal of Computing in Civil Engineering*, *13*(2), 88-95.

Masad, E., Jandhyala, V. K., Dasgupta, N., Somadevan, N., & Shashidhar, N. (2002). Characterization of air void distribution in asphalt mixes using X-ray computed tomography. *Journal of Materials in Civil Engineering*, *14*(2), 122-129.

Masad, E., & Somadevan, N. (2002). Microstructural finite-element analysis of influence of localized strain distribution on asphalt mix properties. *Journal of Engineering Mechanics*, *128*(10), 1105-1114.

McCann, M., & Sebaaly, P. E. (2003). Evaluation of moisture sensitivity and performance of lime in hot-mix asphalt: Resilient modulus, tensile strength, and simple shear tests. *Transportation Research Record*, *1832*(1), 9-16.

Mehta, Y. A., Sukumaran, B., Liddle, J., & Stevenson, J. (2005). Investigation of new devices for use in determining mechanistic properties and performance. No. WHRP 06-10. 2005.

Meegoda, J. N., & Chang, K. G. (1994). Modeling viscoelastic behavior of Hot Mix Asphalt (HMA) using discrete element methods. In *Proceedings of the third Materials Engineering Conference*, 804-811.

Mo, L. T., Huurman, M., Wu, S. P., & Molenaar, A. A. A. (2008). 2D and 3D meso-scale finite element models for ravelling analysis of porous asphalt concrete. *Finite Elements in Analysis and Design*, *44*(4), 186-196.

Moon, K. H., Falchetto, A. C., Wistuba, M. P., & Jeong, J. H. (2015). Analyzing aggregate size distribution of asphalt mixtures using simple 2D digital image processing techniques. *Arabian Journal for Science and Engineering*, *40*(5), 1309-1326.

Mori, T., & Tanaka, K. (1973). Average stress in matrix and average elastic energy of materials with misfitting inclusions. *Acta Metallurgica*, *21*(5), 571-574.

Mulungye, R. M., Owende, P. M. O., & Mellon, K. (2007). Finite element modelling of flexible pavements on soft soil subgrades. *Materials & Design*, *28*(3), 739-756.

Myers, L. A., Roque∗, R., & Birgisson, B. (2001). Use of two-dimensional finite element analysis to represent bending response of asphalt pavement structures. *International Journal of Pavement Engineering*, *2*(3), 201-214.

Obaidat, M. T., Ghuzlan, K. A., & Alawneh, M. M. (2017). Analysis of volumetric properties of bituminous mixtures using cellular phones and image processing techniques. *Canadian Journal of Civil Engineering*, *44*(9), 715-726.

Oeser, M., & Möller, B. (2004). 3D constitutive model for asphalt pavements. *International Journal of Pavement Engineering*, *5*(3), 153-161.

Ozen, M., & Guler, M. (2014). Assessment of optimum threshold and particle shape parameter for the image analysis of aggregate size distribution of concrete sections. *Optics and Lasers in Engineering*, *53*, 122-132.

Papagiannakis, A. T., Abbas, A., & Masad, E. (2002). Micromechanical analysis of viscoelastic properties of asphalt concretes. *Transportation Research Record*, *1789*(1), 113-120.

Rami, K. Z., Amelian, S., Kim, Y. R., You, T., & Little, D. N. (2017). Modeling the 3D fracture-associated behavior of viscoelastic asphalt mixtures using 2D microstructures. *Engineering Fracture Mechanics*, *182*, 86-99.

Roberts, F. L., Kandhal, P. S., Brown, E. R., Lee, D. Y., & Kennedy, T. W. (1991). Hot mix asphalt materials, mixture design and construction. *National Center for Asphalt Technologies (NCAT)*, NAPA Research and Education Foundation, Maryland.

Roque, R., Buttlar, W. G., Ruth, B. E., & Dickison, S. W. (1998). Short-loading-time stiffness from creep, resilient modulus, and strength tests using superpave indirect tension test. *Transportation Research Record*, *1630*(1), 10-20.

Ridler, T. W., & Calvard, S. (1978). Picture thresholding using an iterative selection method. *IEEE Transactions on Systems, Man and Cybernetics*, *8*(8), 630-632.

Saal, R. & Labout, J. (1958). Rheological properties of asphalts. *Rheology: Theory and Applications, (2),* 363-400.

Sadd, M. H., Dai, Q., Parameswaran, V., & Shukla, A. (2003). Simulation of asphalt materials using finite element micromechanical model with damage mechanics. *Transportation Research Record*, *1832*(1), 86-95.

Schneider, C. A., Rasband, W. S., & Eliceiri, K. W. (2012). NIH Image to ImageJ: 25 years of image analysis. Nature methods, 9(7), 671-675.

Sefidmazgi, N. R., Tashman, L., & Bahia, H. (2012). Internal structure characterization of asphalt mixtures for rutting performance using imaging analysis. *Road Materials and Pavement Design*, *13*(sup1), 21-37.

Sepehr, K., Svec, O. J., Yue, Z. Q., & El Hussein, H. M. (1994). Finite element modelling of asphalt concrete microstructure. *Computer Aided Assessment and Control of Localized Damage*, p225.

Shalaby, A., Liske, T., & Kavussi, A. (2004). Comparing back-calculated and laboratory resilient moduli of bituminous paving mixtures. *Canadian Journal of Civil Engineering*, *31*(6), 988-996.

Shanbara, H. K., Ruddock, F., & Atherton, W. (2018). Predicting the rutting behaviour of natural fibre-reinforced cold mix asphalt using the finite element method. *Construction and Building Materials*, *167*, 907-917.

Shi, L., Wang, D., Jin, C., Li, B., & Liang, H. (2020). Measurement of coarse aggregates movement characteristics within asphalt mixture using digital image processing methods. *Measurement*, *163*, 107948.

SHRP-A-407, (1994). The Superpave mix design manual for new construction and overlays. *National Research Council*, Washington, D.C.

SHRP-LTPP Protocol P07, (2001). Test method for determining the creep compliance, resilient modulus, and strength of asphalt materials using the indirect tensile test device. *TRB, National Research Council*, Washington, D.C.

Srirangam, S. K., Anupam, K., Kasbergen, C., & Scarpas, A. T. (2017). Analysis of asphalt mix surface-tread rubber interaction by using finite element method. *Journal of Traffic and Transportation Engineering (English Edition)*, *4*(4), 395-402.

Sun, Y., Du, C., Gong, H., Li, Y., & Chen, J. (2020). Effect of temperature field on damage initiation in asphalt pavement: A microstructure-based multiscale finite element method. *Mechanics of Materials*, *144*, 103367.

Tajdini, M., & Taherkhani, A. (2020). Investigating the Performance of Cracked Asphalt Pavement Using Finite Elements Analysis. Civil Engineering Infrastructures Journal, 53(1), 33-51.

Tashman, L., Masad, E., D'Angelo, J., Bukowski, J., & Harman, T. (2002). X-ray tomography to characterize air void distribution in superpave gyratory compacted specimens. International Journal of Pavement Engineering, 3(1), 19-28.

Tashman, L., Wang, L., and Thyagarajan, S. (2011). Microstructure characterization for modeling HMA behavior using imaging technology. Road Materials and Pavement Design, 8(2), 207–238.

Ting, J. M., Meachum, L., & Rowell, J. D. (1995). Effect of particle shape on the strength and deformation mechanisms of ellipse-shaped granular assemblages. *Engineering Computations*.

Turner, M. J., Clough, R. W., Martin, H. C., & Topp, L. J. (1956). Stiffness and deflection analysis of complex structures. *Journal of the Aeronautical Sciences*, *23*(9), 805-823.

Uddin, W., Hackett, R. M., Joseph, A., Pan, Z., & Crawley, A. B. (1995). Three-dimensional finite-element analysis of jointed concrete pavement with discontinuities. *Transportation Research Record, 1482*, 26-32.

Vadood, M., Johari, M. S., & Rahaei, A. R. (2014). Introducing a simple method to determine aggregate gradation of hot mix asphalt using image processing. *International Journal of Pavement Engineering*, *15*(2), 142-150.

Wang, H., Zhang, C., Yang, L., & You, Z. (2013). Study on the rubber-modified asphalt mixtures' cracking propagation using the extended finite element method. *Construction and Building Materials*, *47*, 223-230.

Wang, H., Zhou, Z., Huang, W., & Dong, X. (2021a). Investigation of asphalt mixture permanent deformation based on three-dimensional discrete element method. *Construction and Building Materials, 272,* 121808.

Wang, L., Cui, S., & Feng, L. (2021b). Research on the influence of ultraviolet aging on the interfacial cracking characteristics of warm mix crumb rubber modified asphalt mortar. *Construction and Building Materials, 281*, 122556.

West, R. C., Watson, D. E. & Turner, P. A. (2010). Mixing and compaction temperatures of asphalt binders in hot-mix asphalt (NCHRP Report 648). Transportation Research Board.

Witczak, M. W., Kaloush, K., Pellinen, T., El-Basyouny, M., & Von Quintus, H. (2002). NCHRP Report 465 simple performance test for Superpave mix design. *National cooperative highway research program report*, National Research Council, Washington, D.C.

Wu, J., Collop, A. C., & McDowell, G. R. (2011). Discrete element modeling of constant strain rate compression tests on idealized asphalt mixture. *Journal of Materials in Civil Engineering*, *23*(1), 2-11.

Yang, E., Tang, Y., Li, L., Yan, W., Huang, B., & Qiu, Y. (2021). Research on the recurrent neural network-based fatigue damage model of asphalt binder and the finite element analysis development. *Construction and Building Materials*, *267*, 121761.

Yongping, W. (2007). *Digital simulative test of asphalt mixtures using finite element method and X-ray tomography images* (Doctoral dissertation, Virginia Tech). ProQuest Dissertations & Theses Global database. (UMI No. DP19532).

You, Z., Adhikari, S., & Dai, Q. (2008). Three-dimensional discrete element models for asphalt mixtures. *Journal of Engineering Mechanics*, *134*(12), 1053-1063.

You, Z., & Dai, Q. (2007). Dynamic complex modulus predictions of hot-mix asphalt using a micromechanical-based finite element model. *Canadian Journal of Civil Engineering*, *34*(12), 1519-1528.

You, T. (2013). *Two-and three-dimensional microstructural modeling of asphalt particulate composite materials using a unified viscoelastic-viscoplastic-viscodamage constitutive model* (Doctoral dissertation, Texas A&M University). ProQuest Dissertations & Theses Global database. (UMI No. 3608036).

Yucel, A. Ö. (2019). Investigation of the impact of aggregate segregation on rutting resistance of asphalt concrete. (Doctoral dissertation, Middle East Technical University, Ankara).

Yue, Z. Q., Bekking, W., & Morin, I. (1995). Application of digital image processing to quantitative study of asphalt concrete microstructure. *Transportation Research Record*, *1492*, 53-60.

Zaghloul, S. M., & White, T. (1993). Use of a three-dimensional, dynamic finite element program for analysis of flexible pavement. *Transportation Research Record*, (1388).

Zelelew, H. M., Papagiannakis, A. T., & Masad, E. (2008, October). Application of digital image processing techniques for asphalt concrete mixture images. In *The 12th International Conference of International Association for Computer Methods and Advances in Geomechanics (IACMAG)* (pp. 119-124).

Zhang, W., Drescher, A., & Newcomb, D. E. (1997). Viscoelastic analysis of diametral compression of asphalt concrete. *Journal of Engineering Mechanics*, *123*(6), 596-603.

Zhang, K., Shen, S., Lim, J., & Muhunthan, B. (2019). Development of Dynamic Modulus–Based Mixture Blending Chart for Asphalt Mixtures with Reclaimed Asphalt Pavement. *Journal of Materials in Civil Engineering*, *31*(2), 04018382.

Zhao, Y., Jiang, J., Zhou, L., Dai, Y., & Ni, F. (2021). Meso-structure image pre-selection method for two-dimensional finite element modeling in beam bending simulation of asphalt mixture. *Construction and Building Materials*, *268*, 121129.

Zhou, F., Scullion, T., & Sun, L. (2004). Verification and modeling of three-stage permanent deformation behavior of asphalt mixes. *Journal of Transportation Engineering*, *130*(4), 486-494.

APPENDICES

A. Superpave Mixture Design Results

The gyratory compaction curves for each design are given below (Figure A.1 and A.2). The TGDH design contains limestone aggregate and unmodified binder, while the FAA design contains basalt aggregate and SBS polymer modified binder. The number of gyrations was selected based on the traffic volume according to the Superpave method (Table A.1).

Table A.1. Design number of gyrations

Number of Gyrations	**TGDH (3 - 10 million ESALs)**	**FAA (0.3 – 3 million ESALs)**
N_{init}	8	7
N_{design}	100	75
N_{max}	160	115

N_{max} and N_{init} can be selected from the Superpave diagrams based on the expected design traffic volume in ESAL (Equivalent Single Axle Loads) over a 20-year lifetime or calculated using the following equations:

$$\log N_{max} = 1.1 \log N_{design}$$

$$\log N_{init} = 0.45 \log N_{design}$$

The specific gravity of the mixture should not exceed 98 per cent and 89 per cent of the theoretical maximum specific gravity at the number of gyrations N_{max} and N_{init}, respectively. A total of 60 samples were prepared, 30 for each of the mixture design types (Figure 3.10). The calculated and corrected G_{mm} values from the measured bulk specific gravity (G_{mb}), the measured maximum theoretical specific gravity of a

loose sample (G_{mm}) and the sample heights instantaneously measured by the software were presented for each sample in Figures A.1 and A.2.

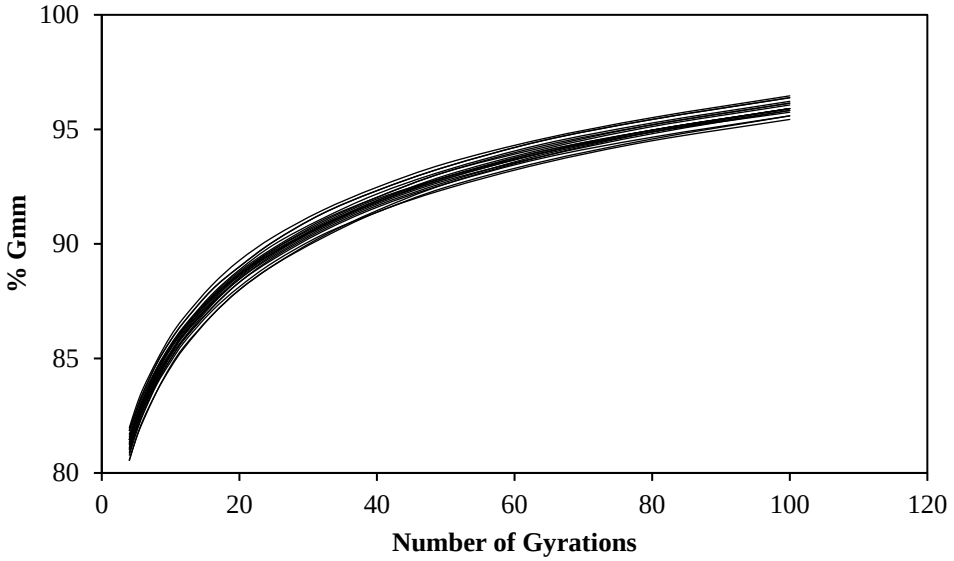

Figure A.1. Compaction curves of TGDH samples

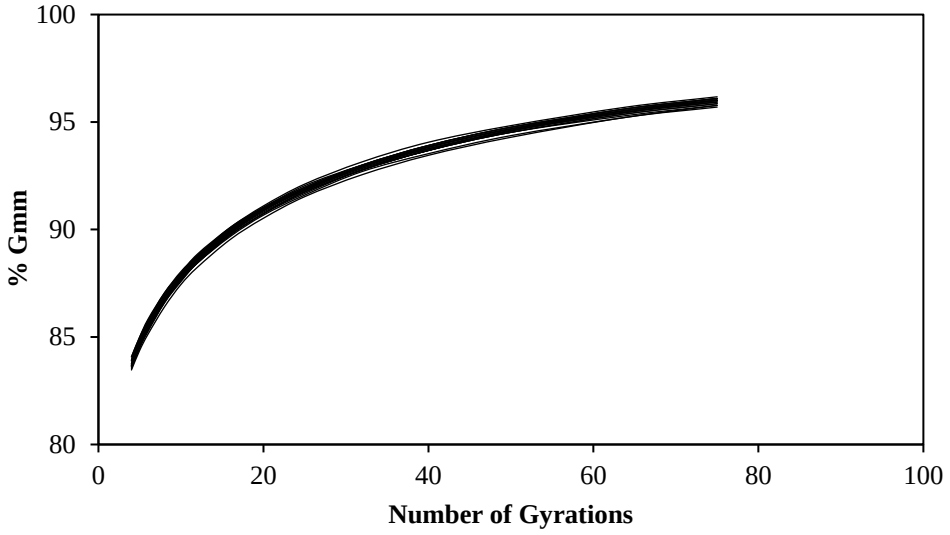

Figure A.2. Compaction curves of FAA samples

B. Laboratory Test Setups

In this study, all three mechanical test methods, i.e., the modulus test, the repeated creep test and the indirect tensile fatigue test were conducted using a dynamic testing system (DTS) in the laboratory environment. The test setup, the Universal Testing Machine (UTM), was controlled using the Testlab® user interface software from Pavetest Ltd. The various settings of this software used to perform these experiments are shown in Figures B.1 to B.3.

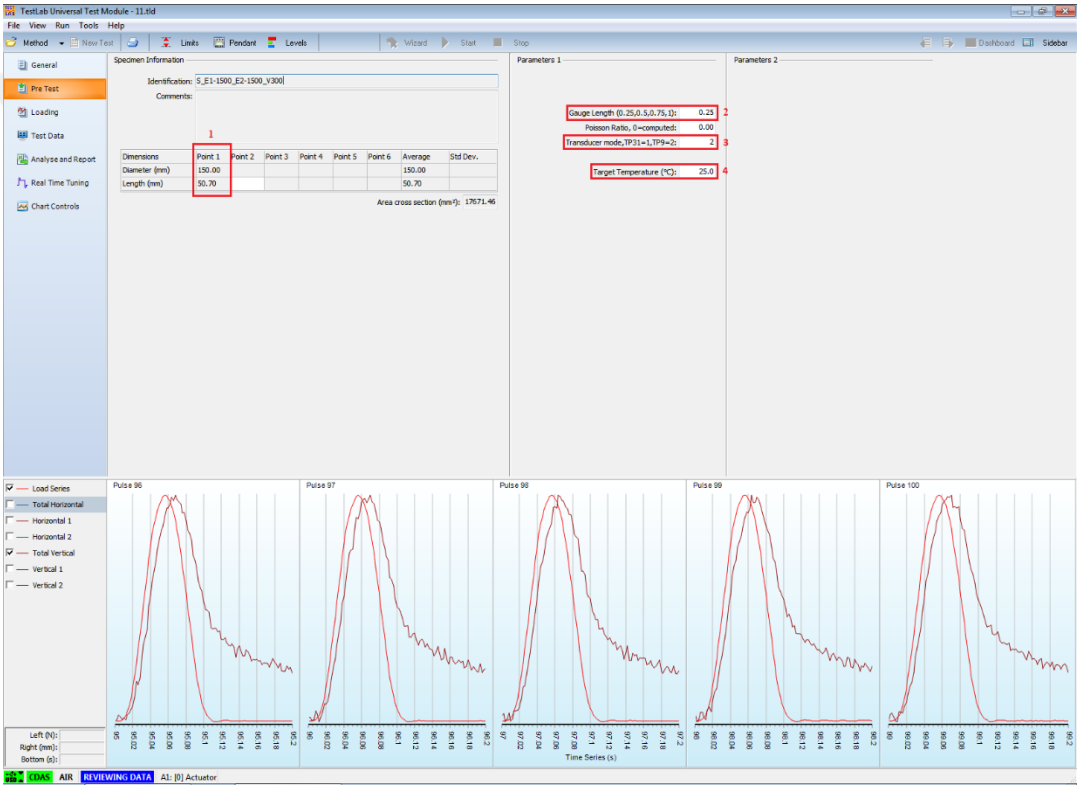

Figure B.1. Resilient modulus test setup

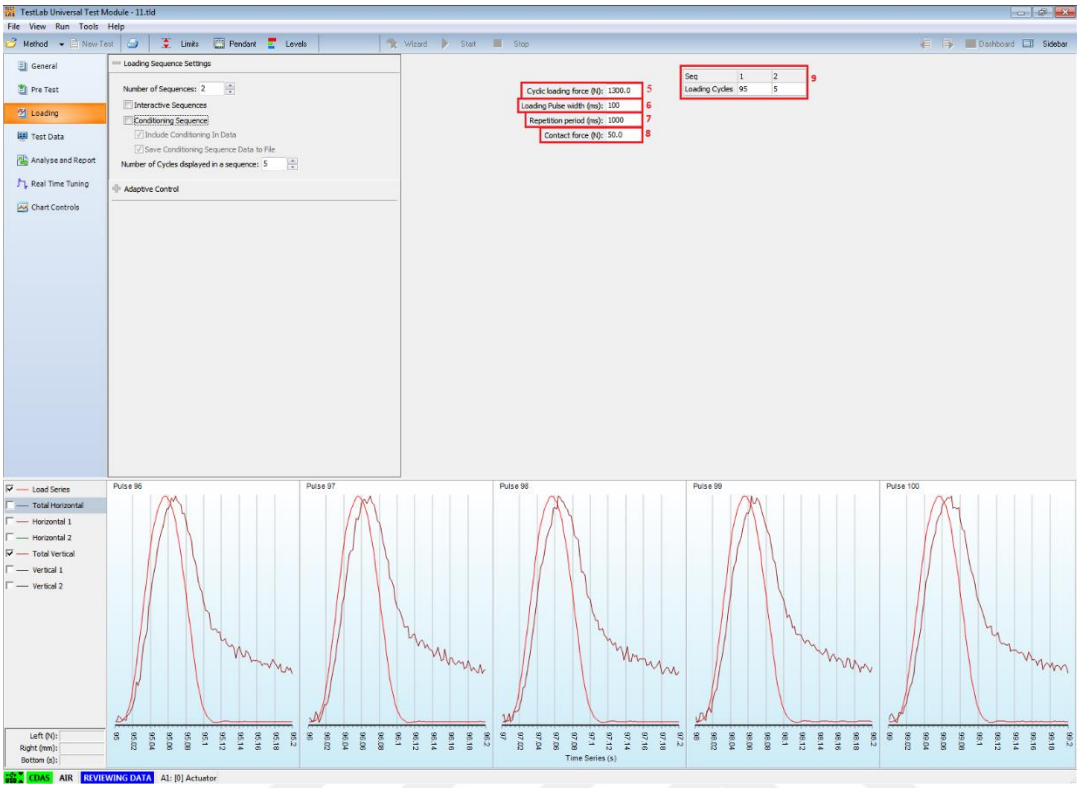

Figure B.1. (Continued)

where

1: Diameter and thickness of the sample (calculated by the average),

2: Ratio of gauge length to diameter (selected as ¼),

3: Transducer mode (selected as 2 because four LVDTs are used),

4: Test temperature,

5: Applied cyclic load (selected between 10 and 20 % of IDT strength),

6: Load portion of the cycle (0.1 s load),

7: Total duration for one cycle (0.1 load and 0.9 s rest combined),

8: Contact force applied to the sample during unloading to establish positive contact,

9: Number of preconditioning and test cycles (M_R values are calculated in the steady stage).

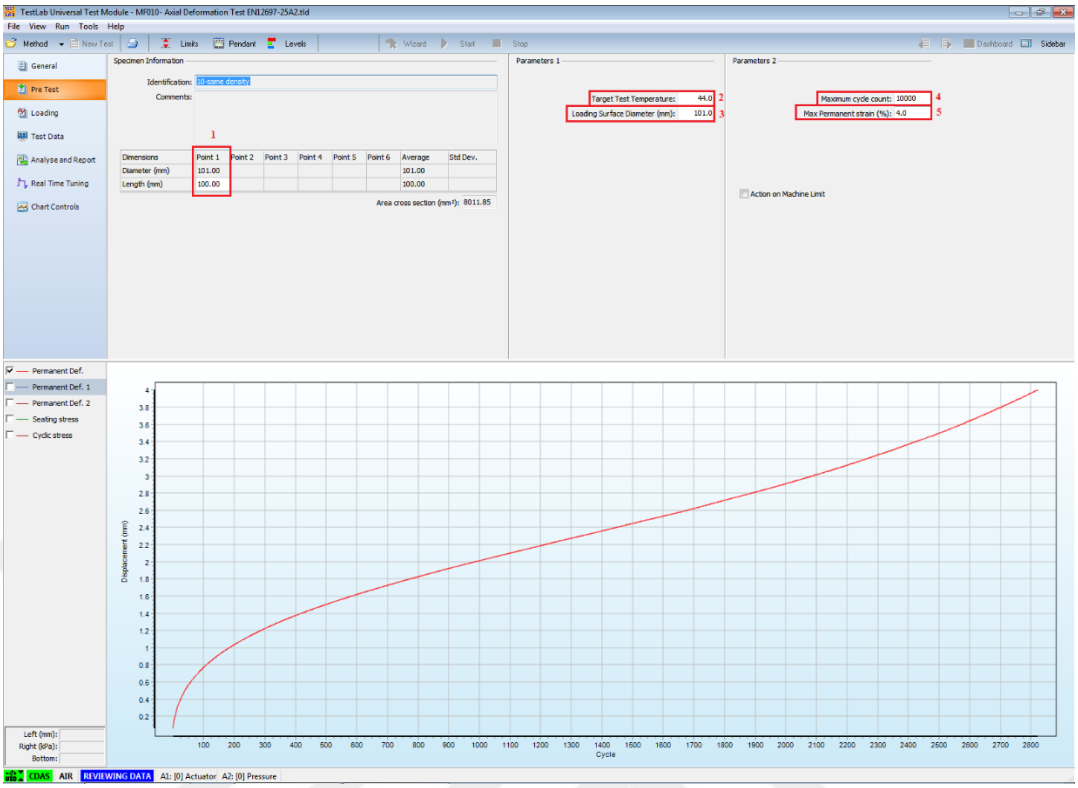

Figure B.2. Repeated creep test setup

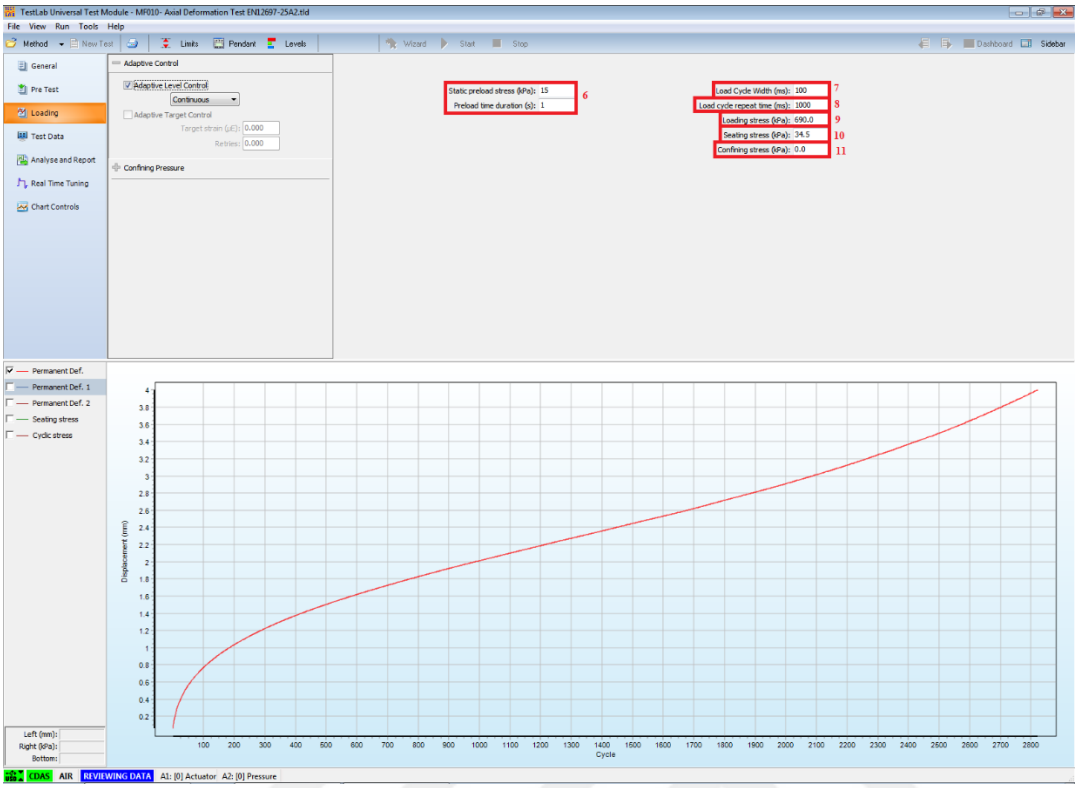

Figure B.2. (Continued)

where

1: Sample diameter and gauge length (the distance between the ends of the LVDTs),

2: Calculated effective test temperature (36.5 ºC for TGDH and 44 ºC for FAA),

3: The specimen diameter resulting from coring,

4: Termination criteria of 10,000 cycles or,

5: Termination criteria of 4 per cent cumulative permanent strain,

6: Static creep test portion of the software,

7: Loading portion of the cycle (0.1 s loading),

8: Total duration for one cycle (combined 0.1 s load and 0.9 s rest),

9: Applied deviatoric stress (300 kPa for the TGDH and 690 kPa for the FAA),

10: Contact force applied to the sample during unloading to provide positive contact,

11: Confined stress (0 for the unconfined condition).

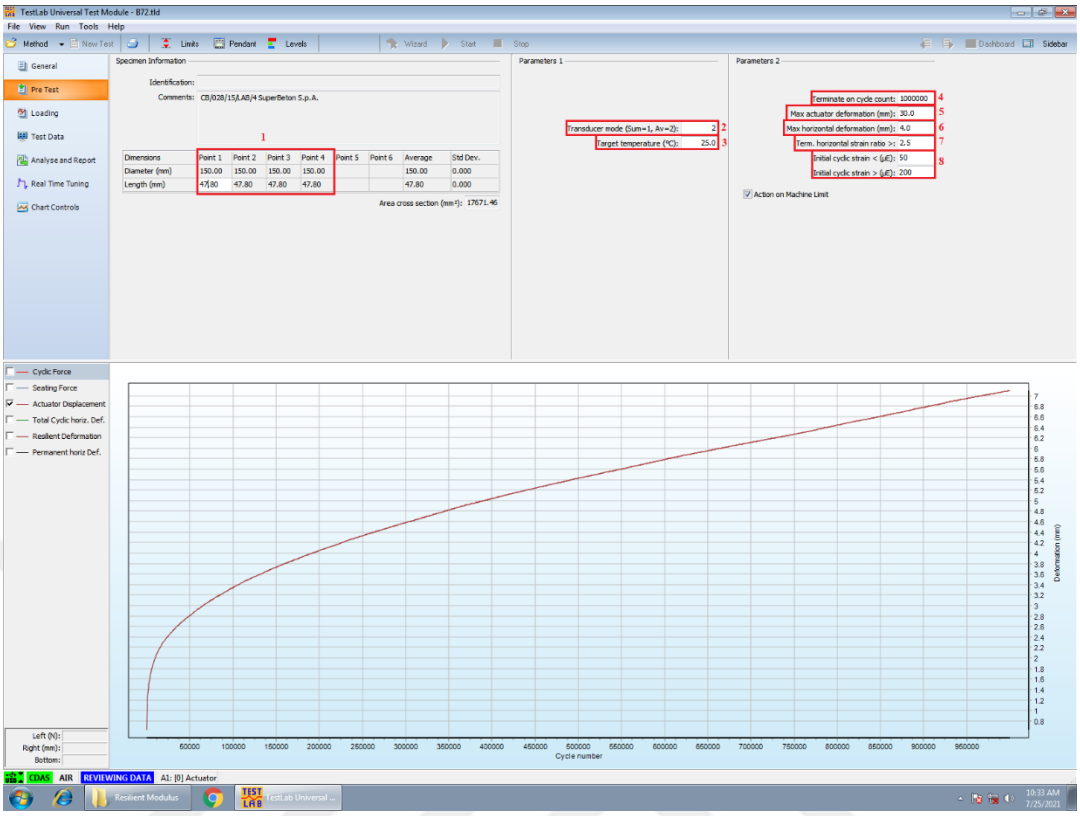

Figure B.3. Indirect tensile fatigue test setup

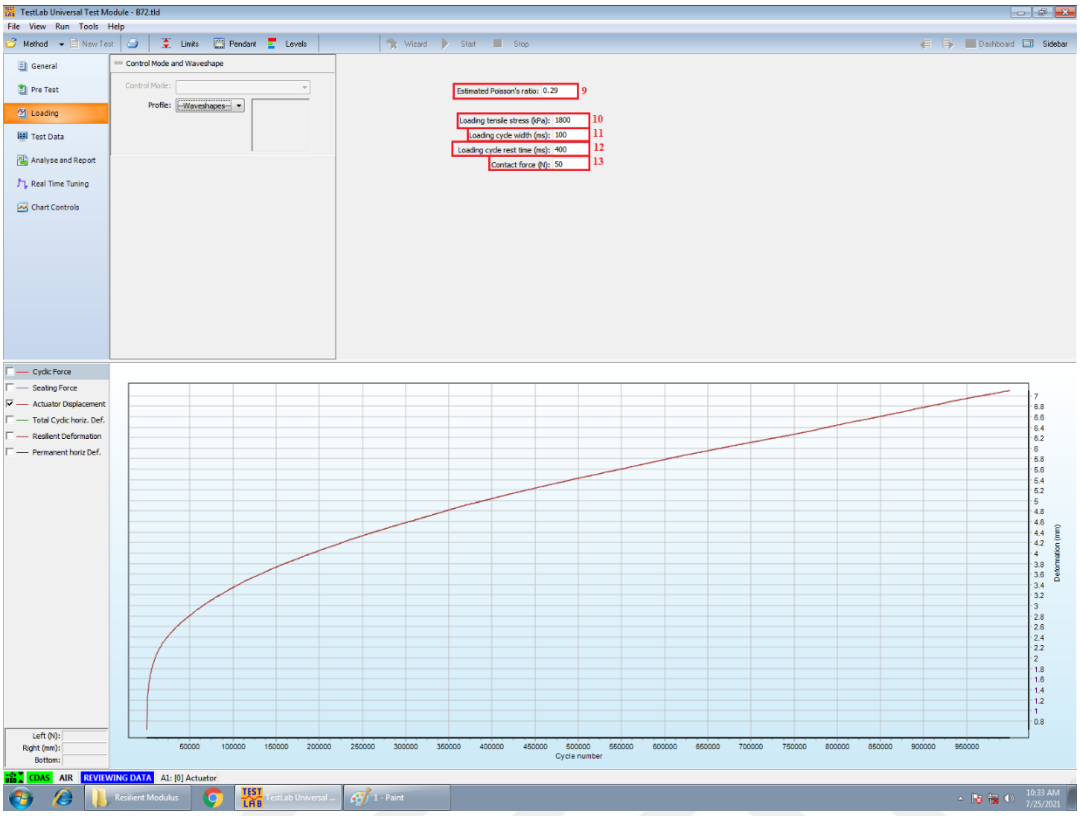

Figure B.3. (Continued)

where

1: Specimen dimensions measured at four different locations,

2: The LVDT setup,

3: Target test temperature,

4: One of the termination criteria, 10,000 cycles,

5: Maximum allowable vertical deformation of the load arm for safety,

6: Maximum allowable LVDT range,

7: Another termination criterion as 2.5 times the initial strain,

8: Minimum and maximum required value of initial strain,

9: Poisson's ratio from the resilient modulus tests,

10: Applied loading stress required for the initial strain rage,

11: Loading section of the cycle which was 0.1 s,

12: Resting section of the cycle which was 0.4 s,

13: Contact pressure to ensure that the specimen is stable.

C. Experimental Results of Indirect Tensile Fatigue Tests

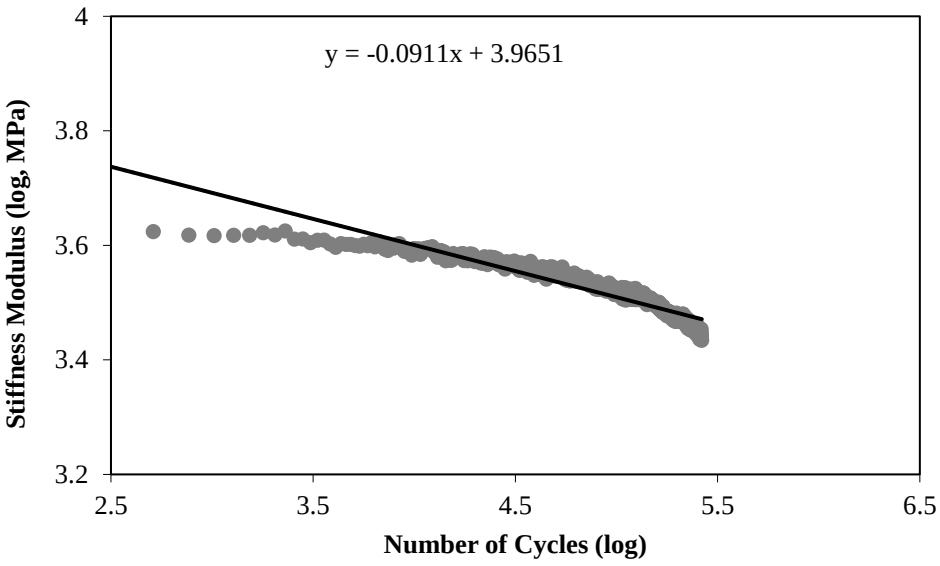

(a)

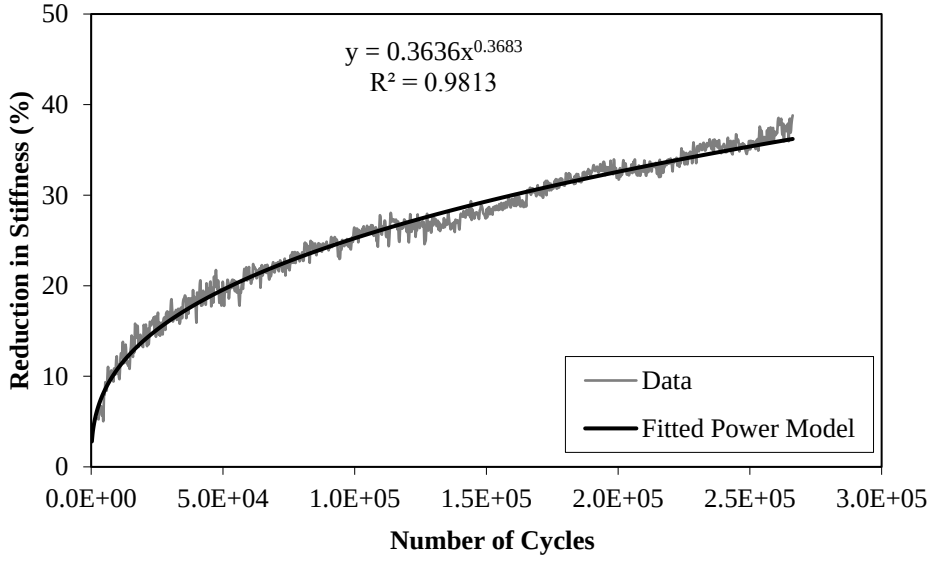

(b)

Figure C.1. IDTF test results of sample ID LUIF02-2: a) Stiffness modulus, b) Reduction in stiffness

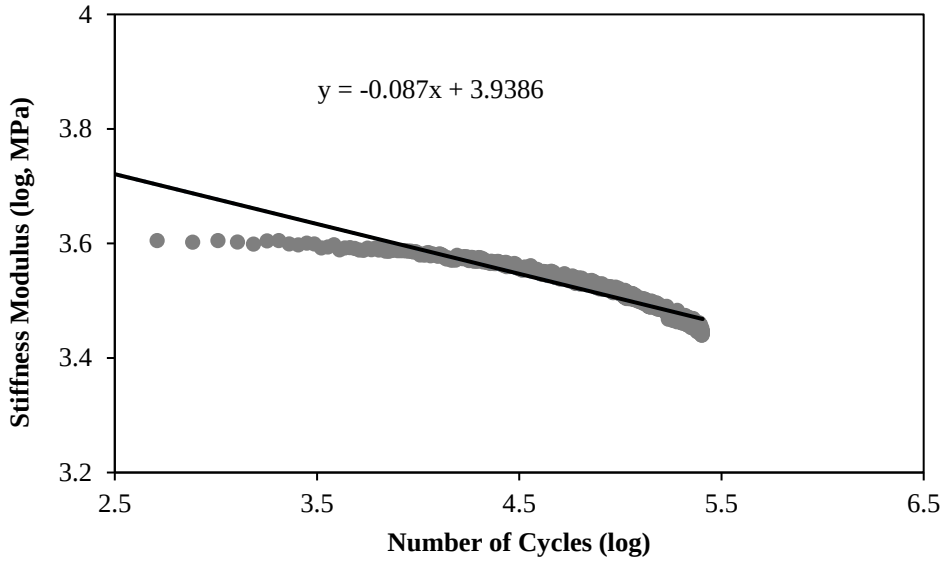

(a)

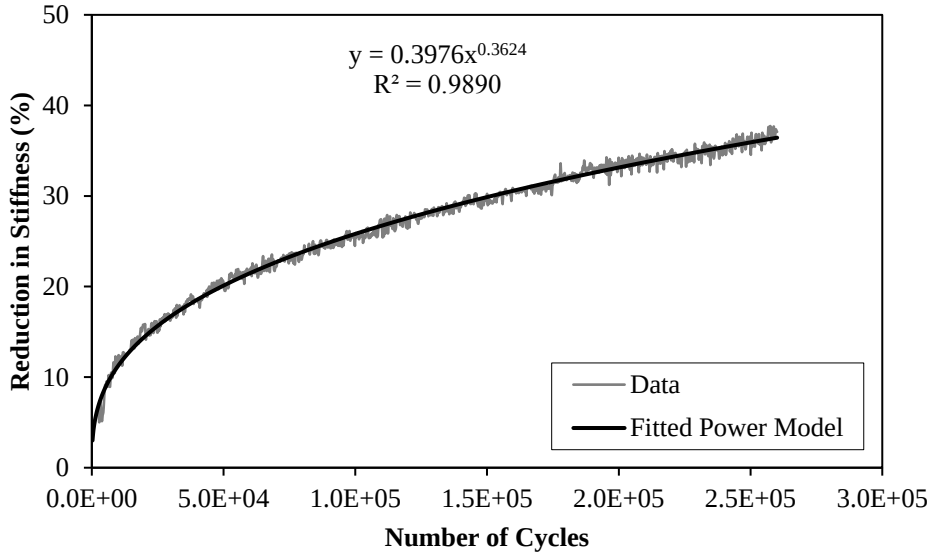

(b)

Figure C.2. IDTF test results of sample ID LUIF07-2: a) Stiffness modulus, b) Reduction in stiffness

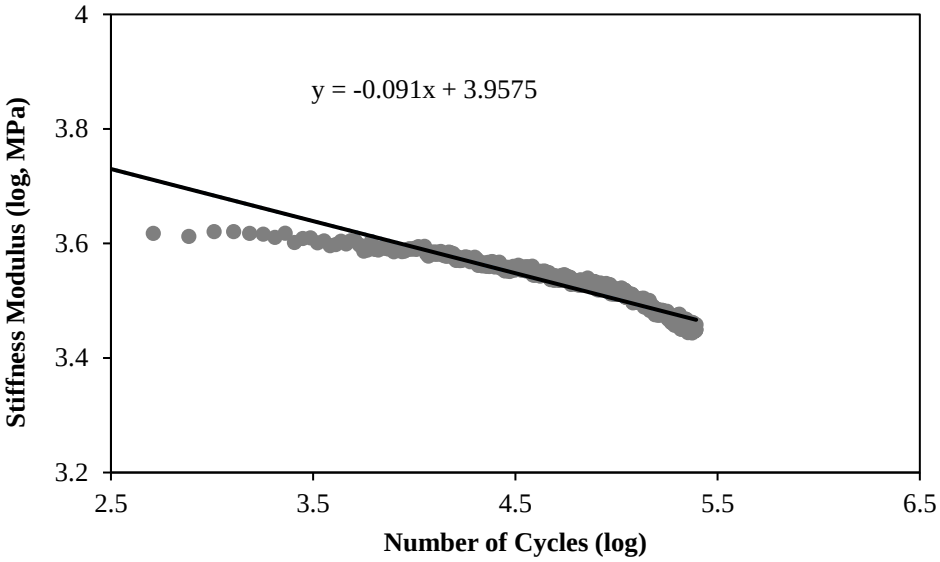

(a)

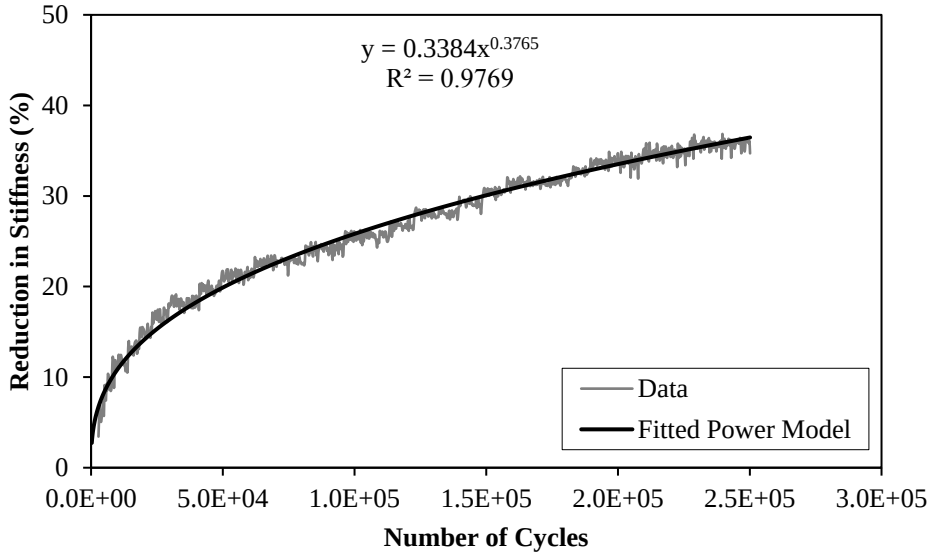

(b)

Figure C.3. IDTF test results of sample ID LUIF08-2: a) Stiffness modulus, b) Reduction in stiffness

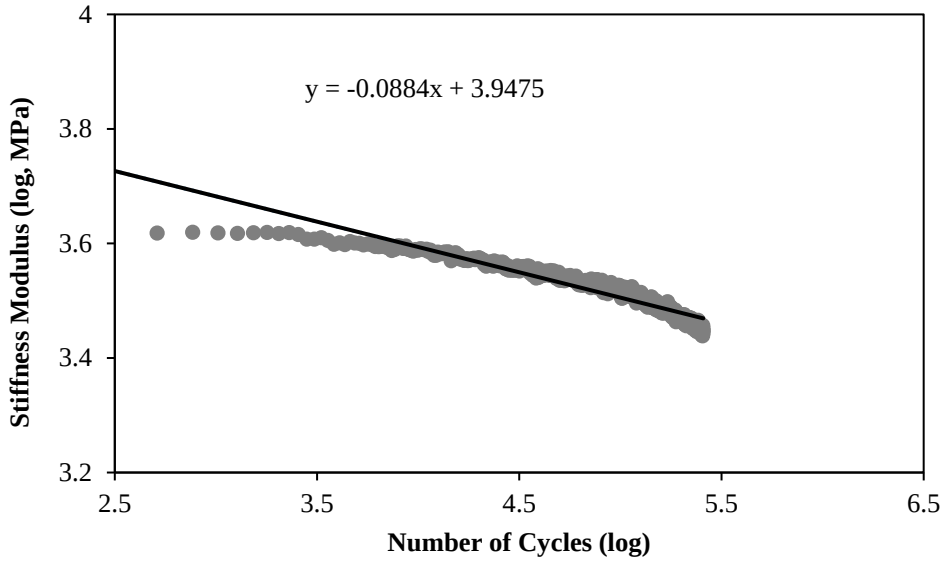

(a)

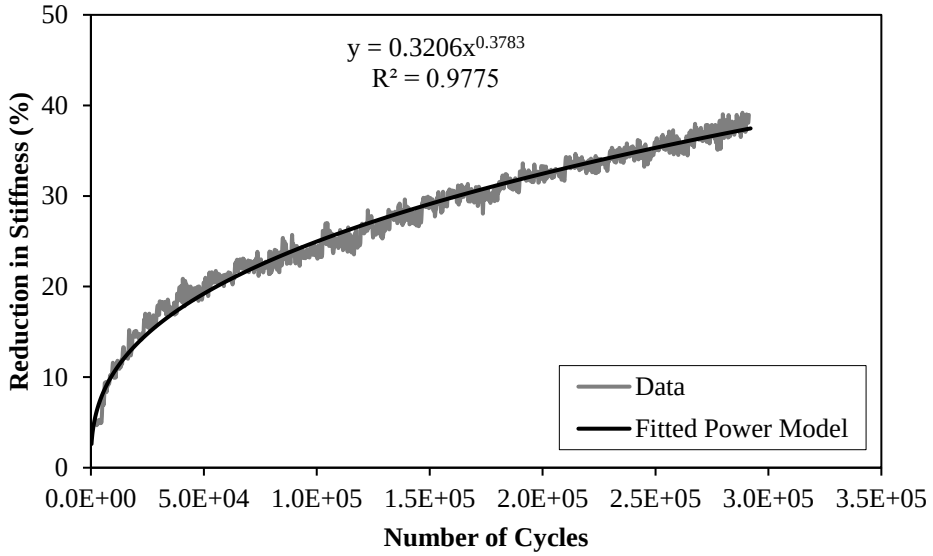

(b)

Figure C.4. IDTF test results of sample ID LUIF11-2: a) Stiffness modulus, b) Reduction in stiffness

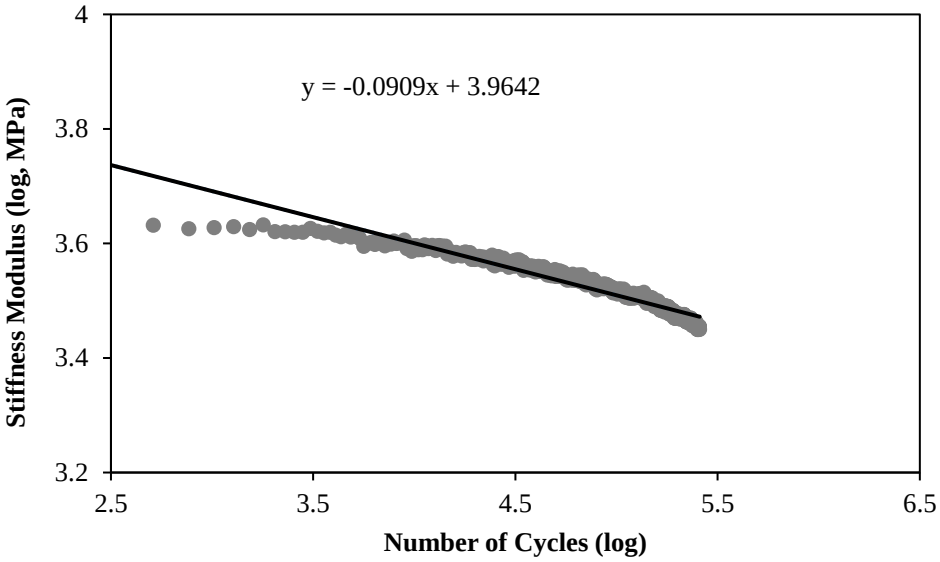

(a)

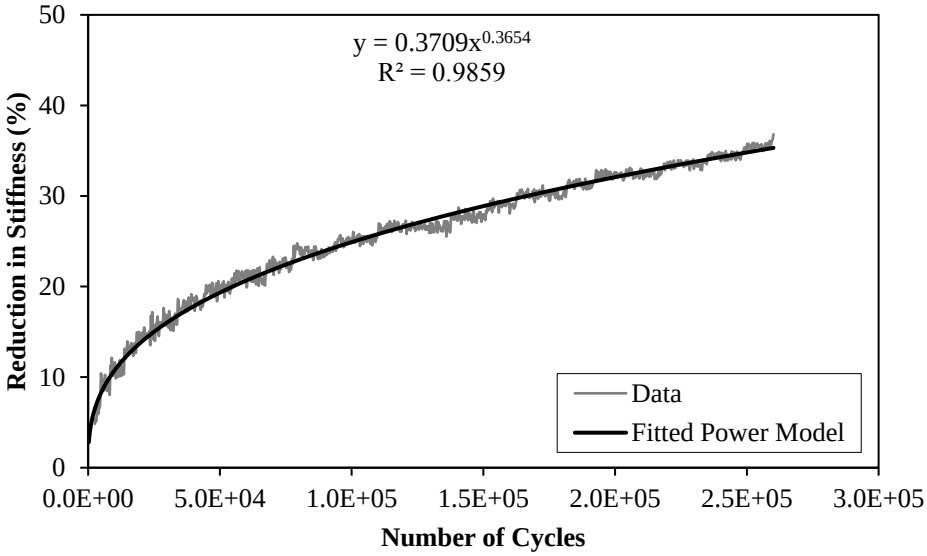

(b)

Figure C.5. IDTF test results of sample ID LUIF13-1: a) Stiffness modulus, b) Reduction in stiffness

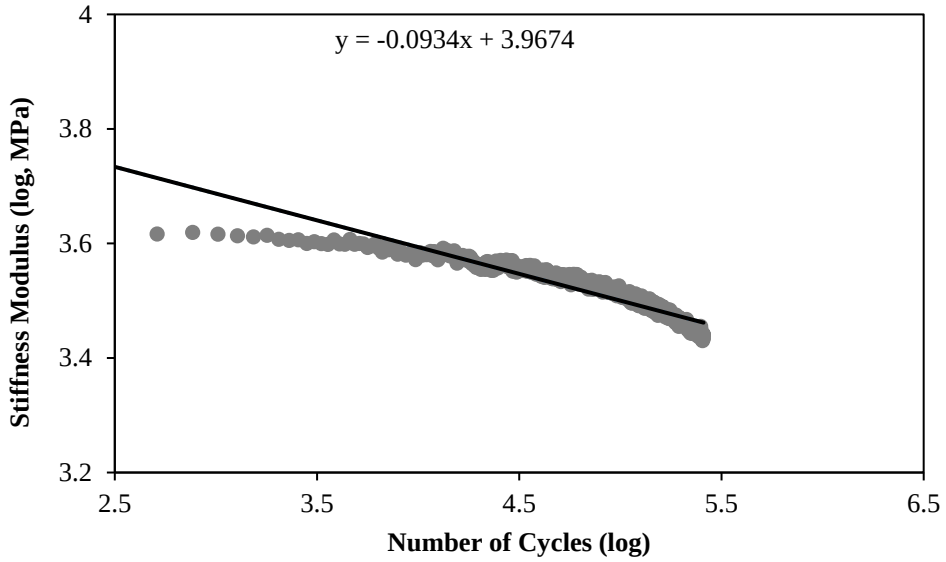

(a)

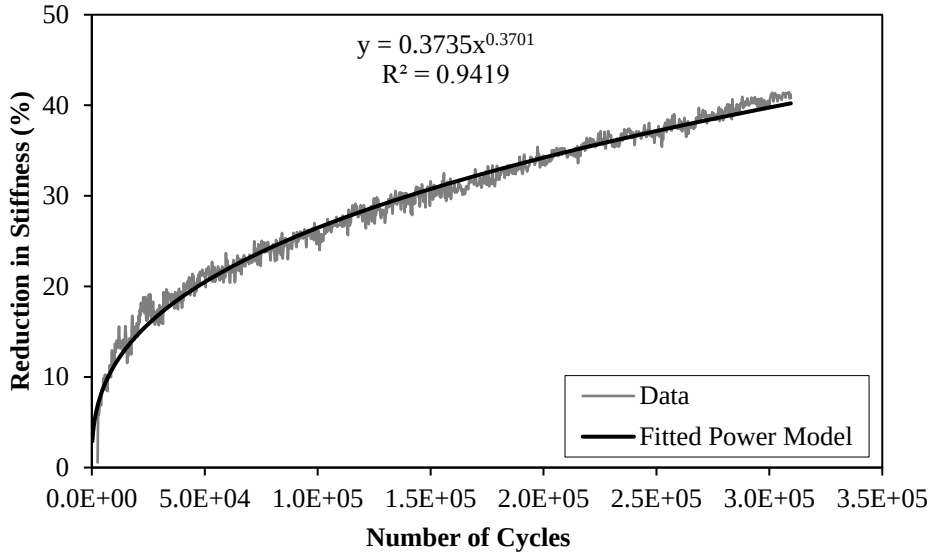

(b)

Figure C.6. IDTF test results of sample ID LUIF14-1: a) Stiffness modulus, b) Reduction in stiffness

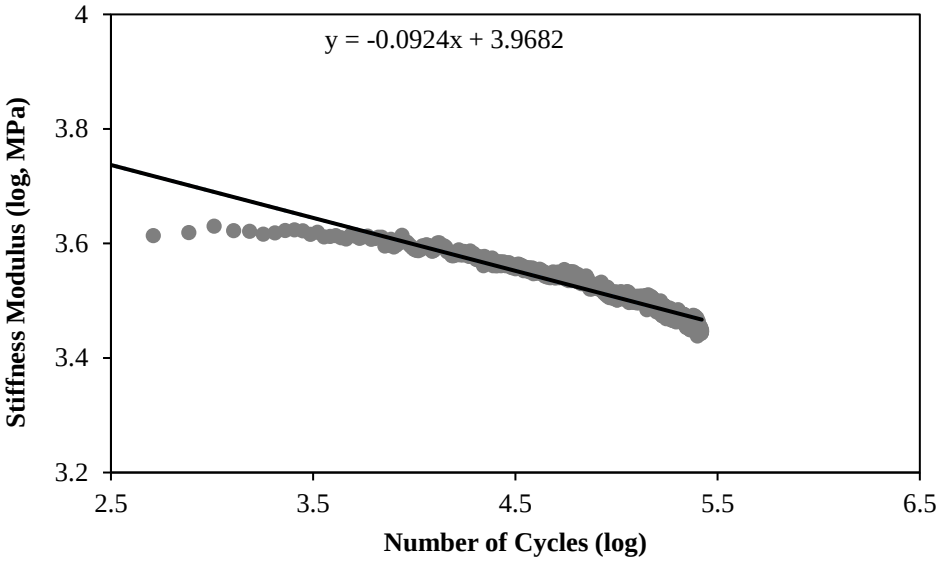

(a)

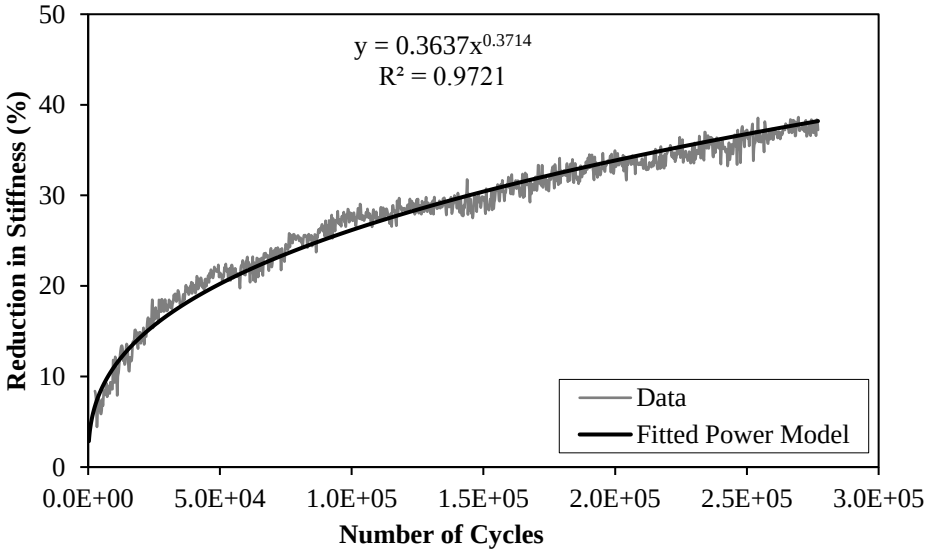

(b)

Figure C.7. IDTF test results of sample ID LUIF14-2: a) Stiffness modulus, b) Reduction in stiffness

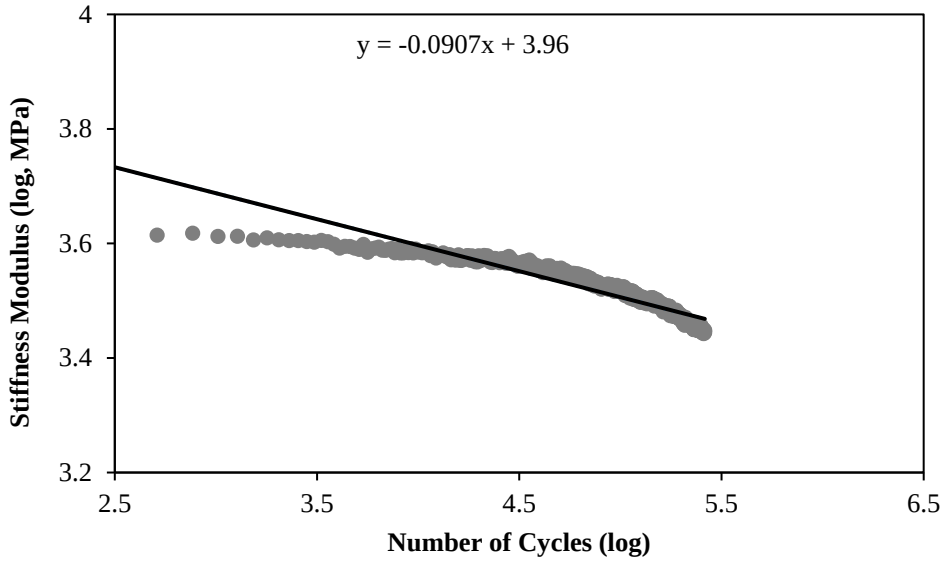

(a)

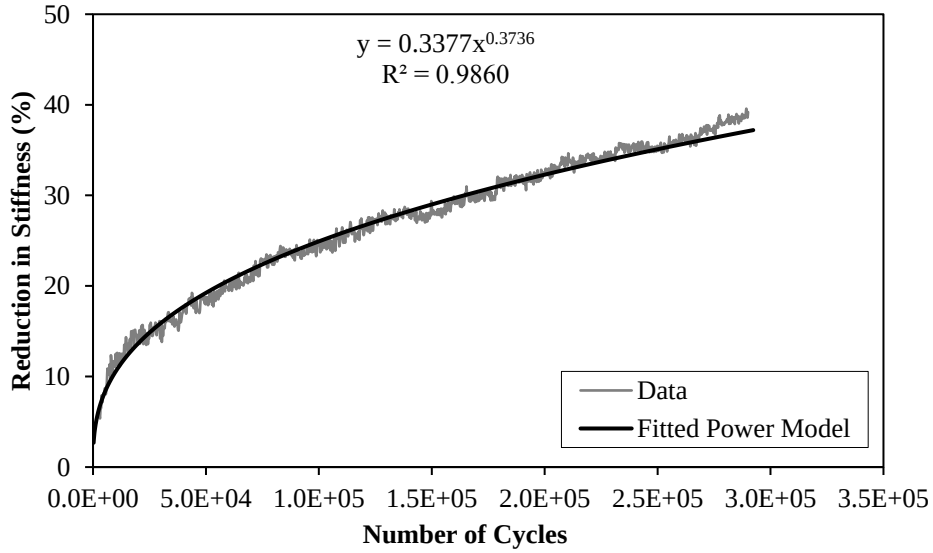

(b)

Figure C.8. IDTF test results of sample ID LUIF15-1: a) Stiffness modulus, b) Reduction in stiffness

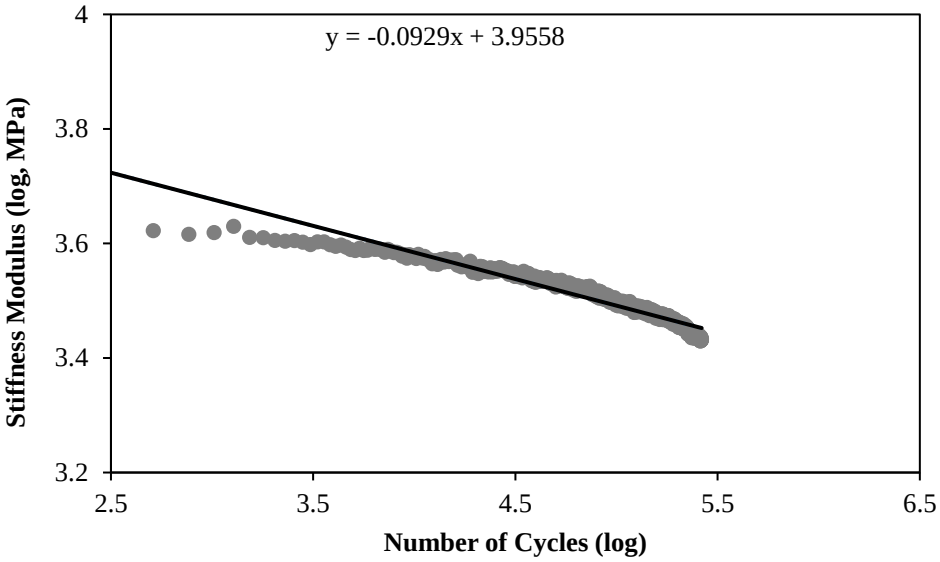

(a)

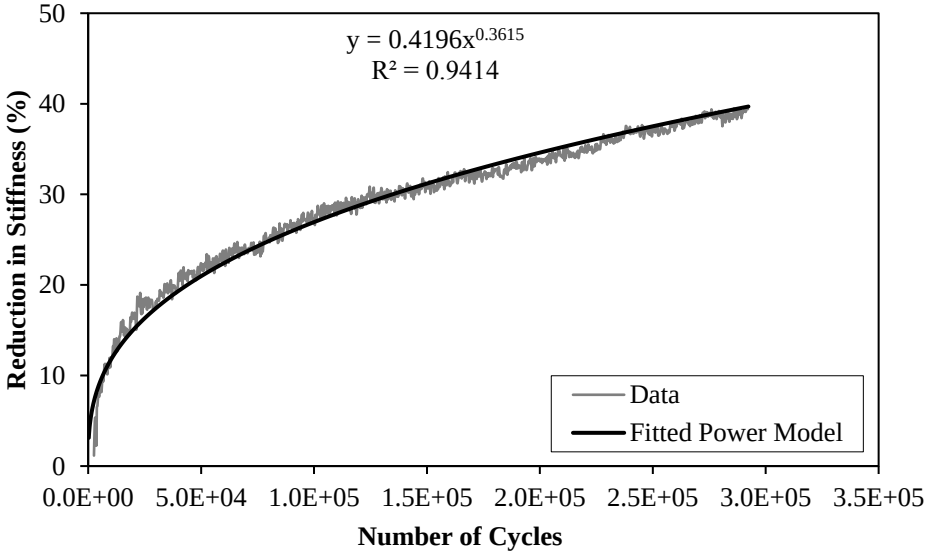

(b)

Figure C.9. IDTF test results of sample ID LUIF15-2: a) Stiffness modulus, b) Reduction in stiffness

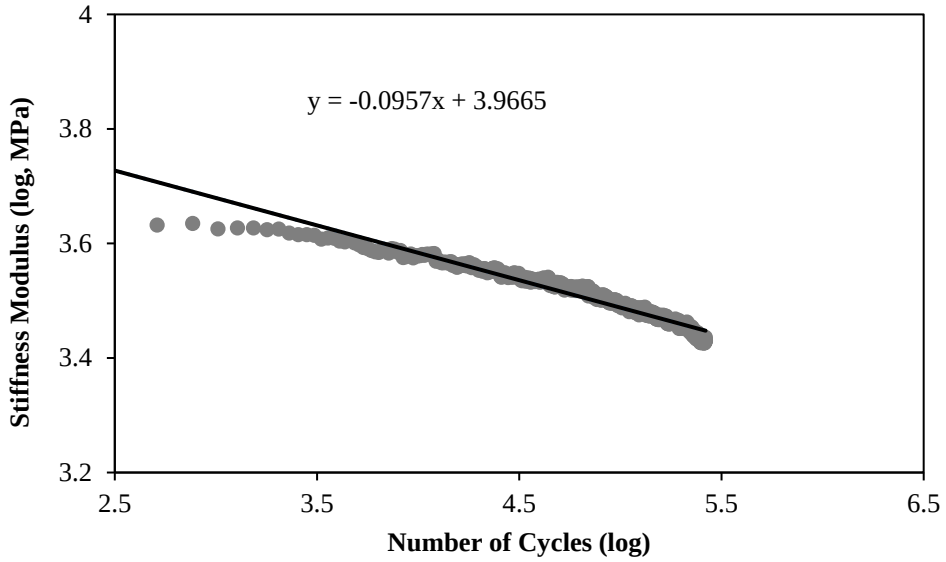

(a)

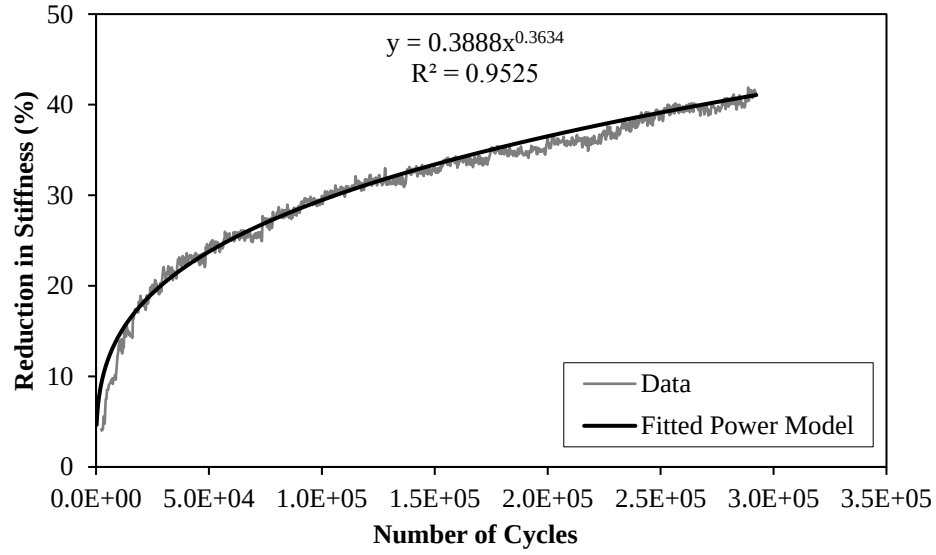

(b)

Figure C.10. IDTF test results of sample ID LUIF17-1: a) Stiffness modulus, b) Reduction in stiffness

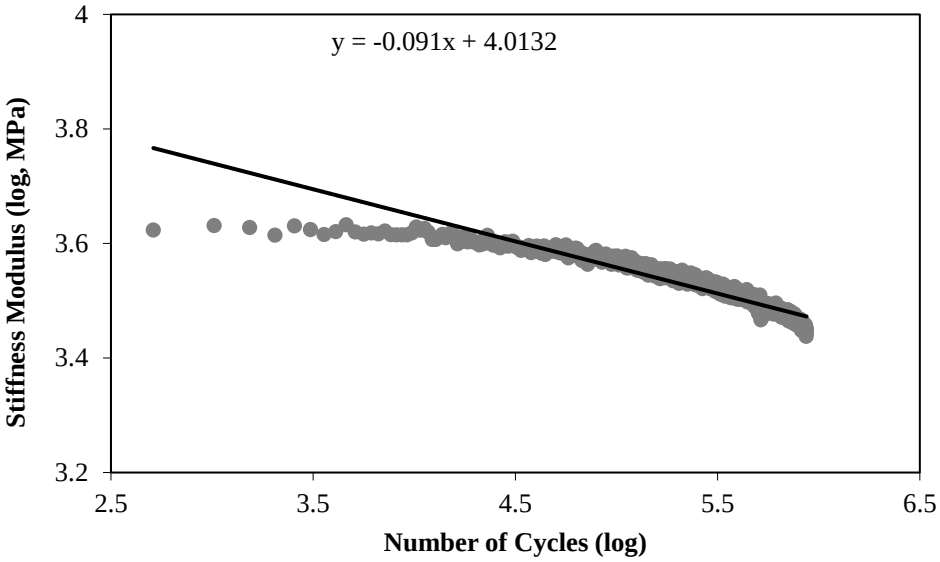

(a)

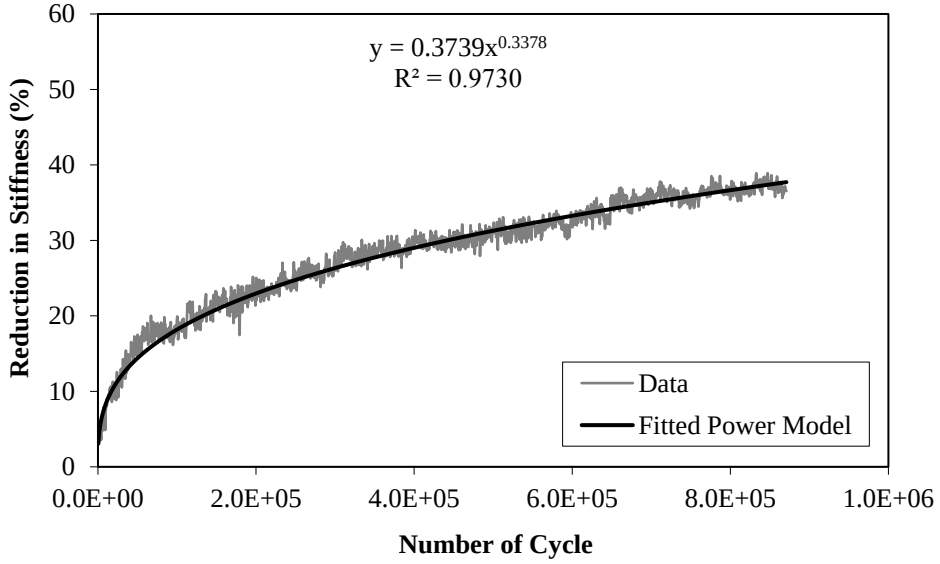

(b)

Figure C.11. IDTF test results of sample ID BMIF02-2: a) Stiffness modulus, b) Reduction in stiffness

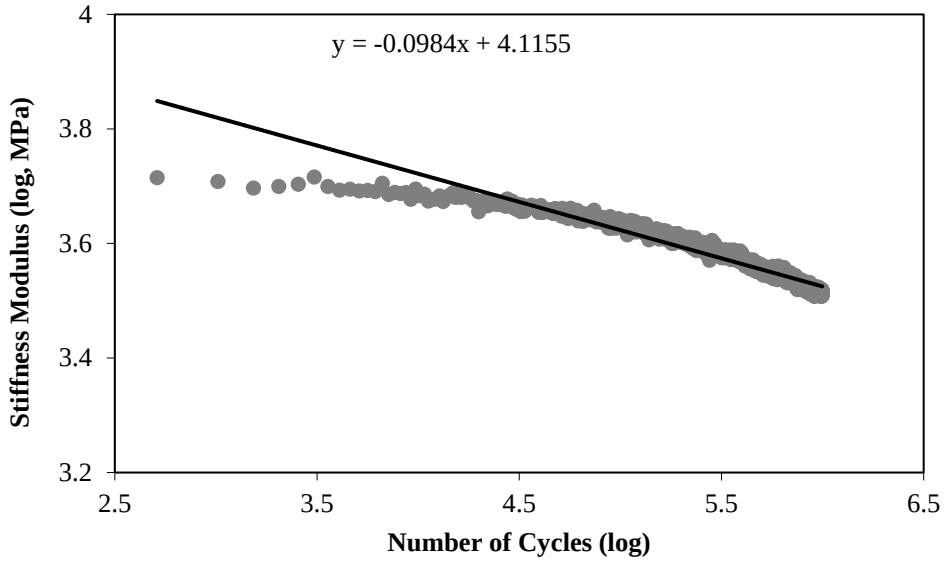

(a)

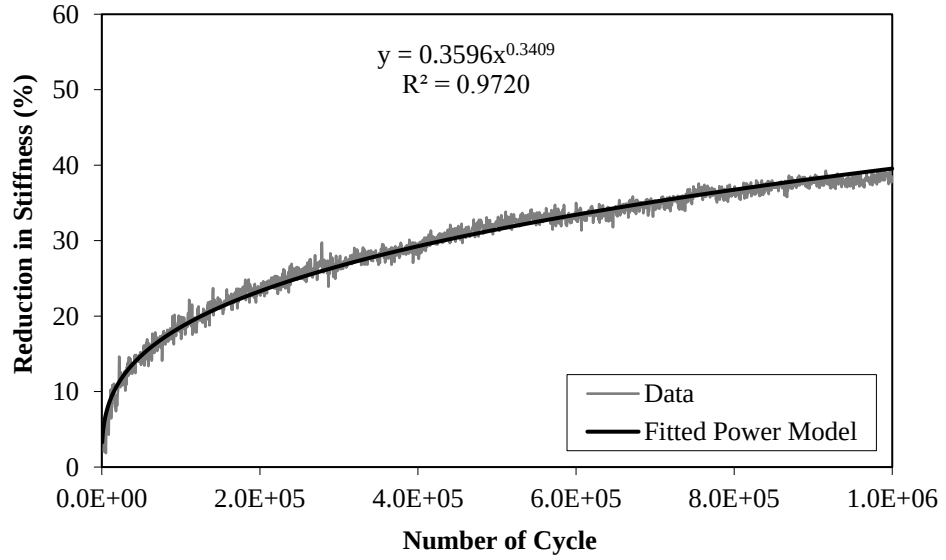

(b)

Figure C.12. IDTF test results of sample ID BMIF03-2: a) Stiffness modulus, b) Reduction in stiffness

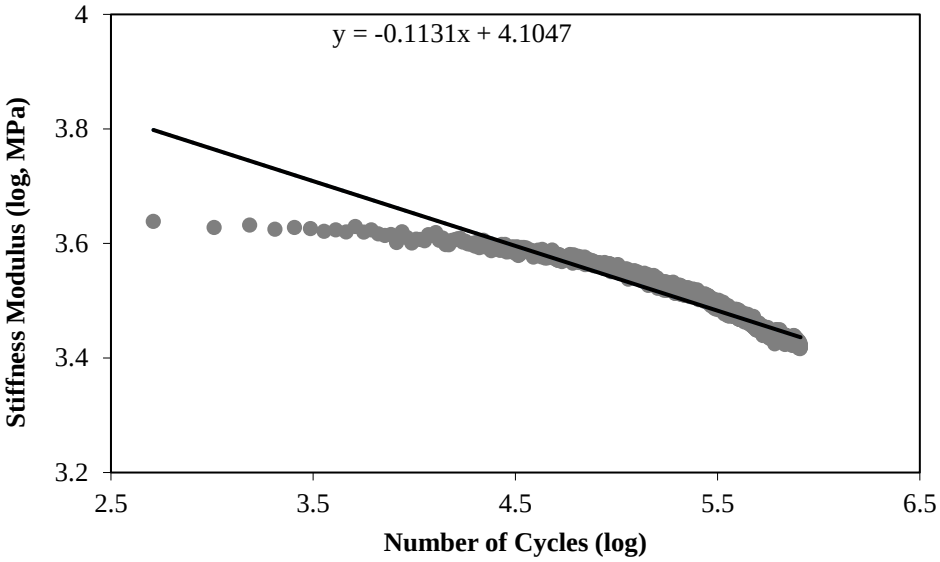

(a)

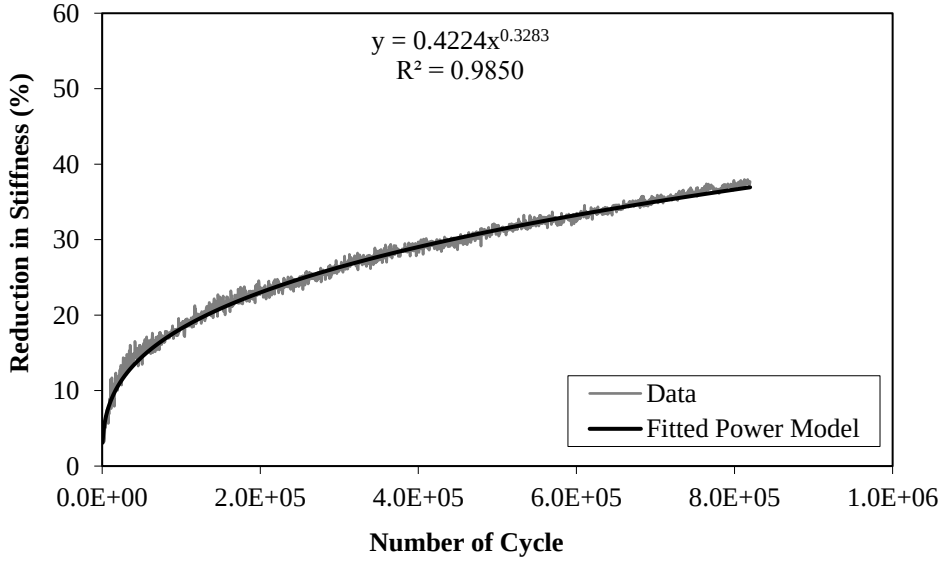

(b)

Figure C.13. IDTF test results of sample ID BMIF05-2: a) Stiffness modulus, b) Reduction in stiffness

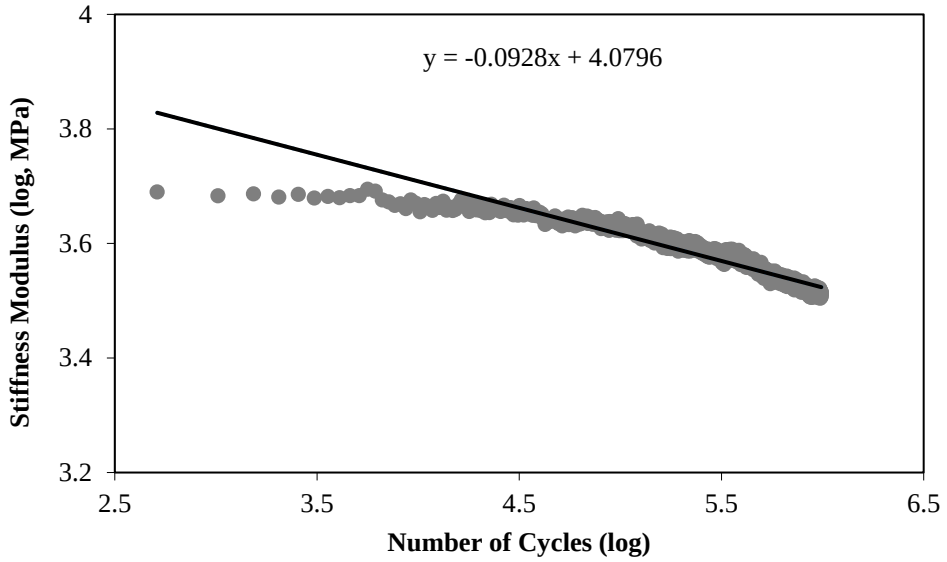

(a)

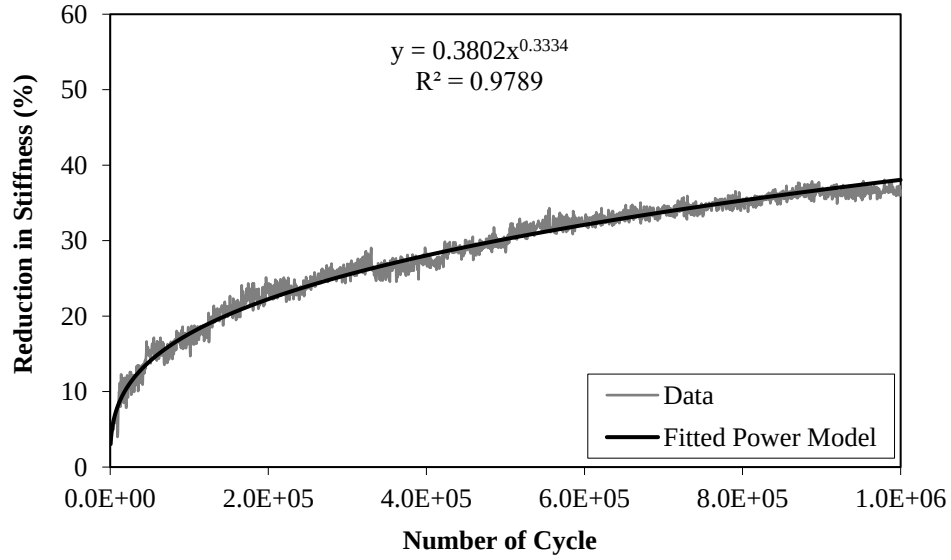

(b)

Figure C.14. IDTF test results of sample ID BMIF07-2: a) Stiffness modulus, b) Reduction in stiffness

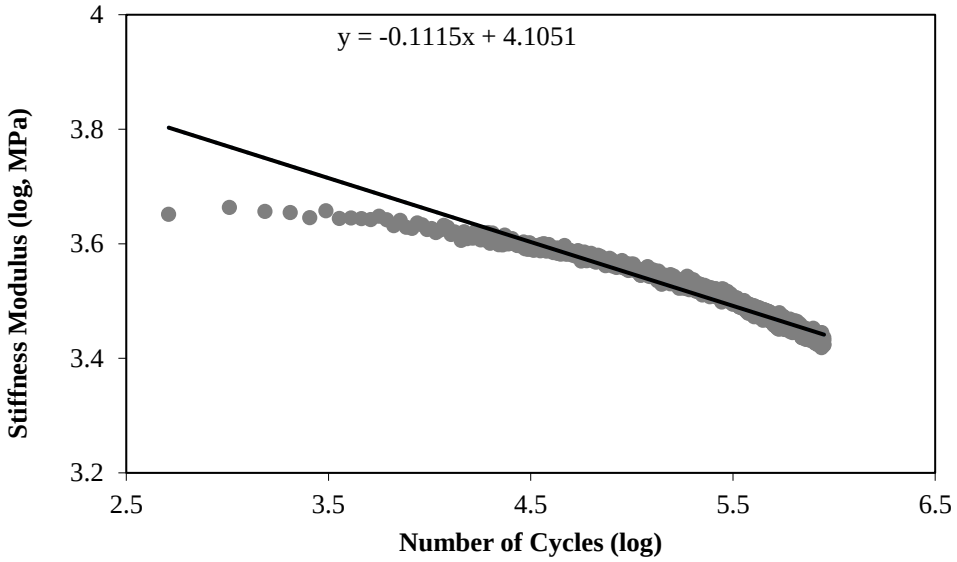

(a)

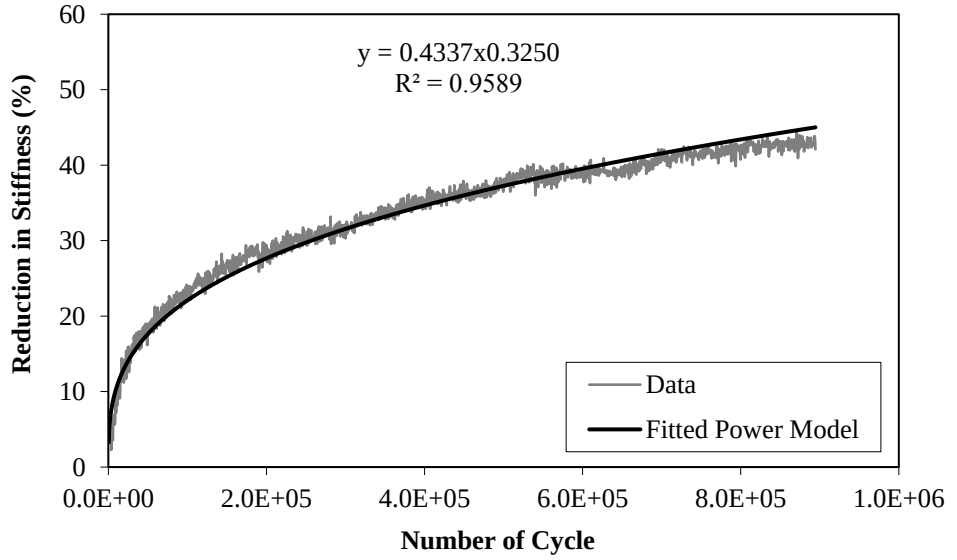

(b)

Figure C.15. IDTF test results of sample ID BMIF09-2: a) Stiffness modulus, b) Reduction in stiffness

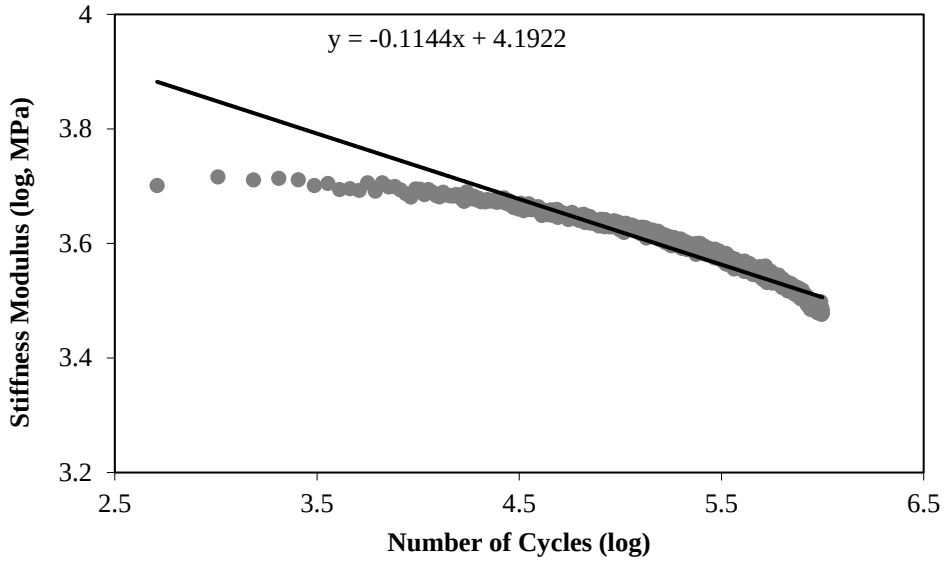

(a)

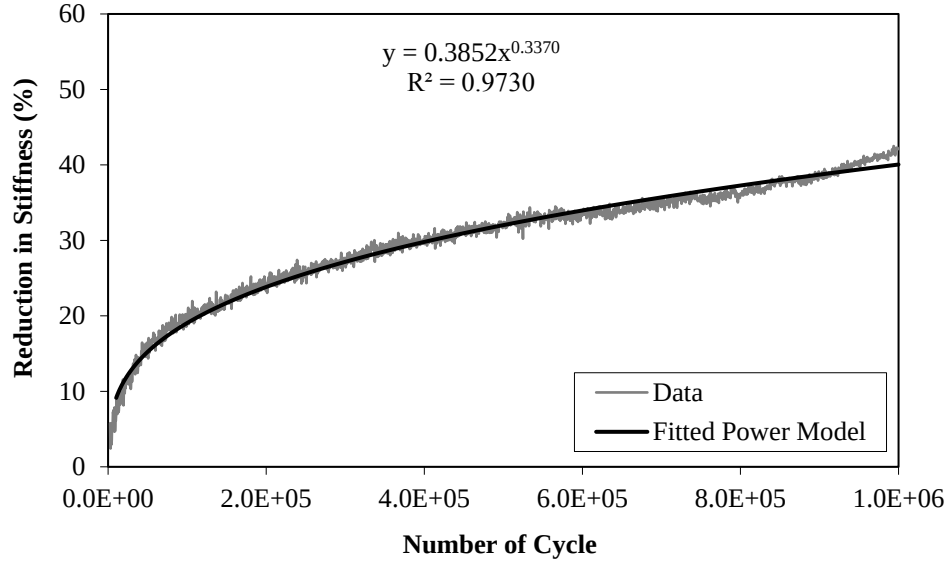

(b)

Figure C.16. IDTF test results of sample ID BMIF12-2: a) Stiffness modulus, b) Reduction in stiffness

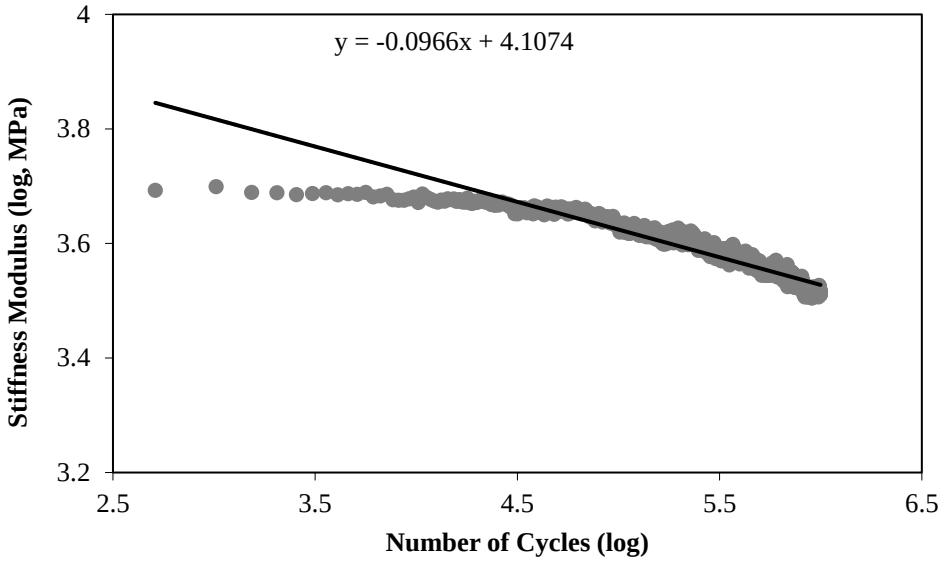

(a)

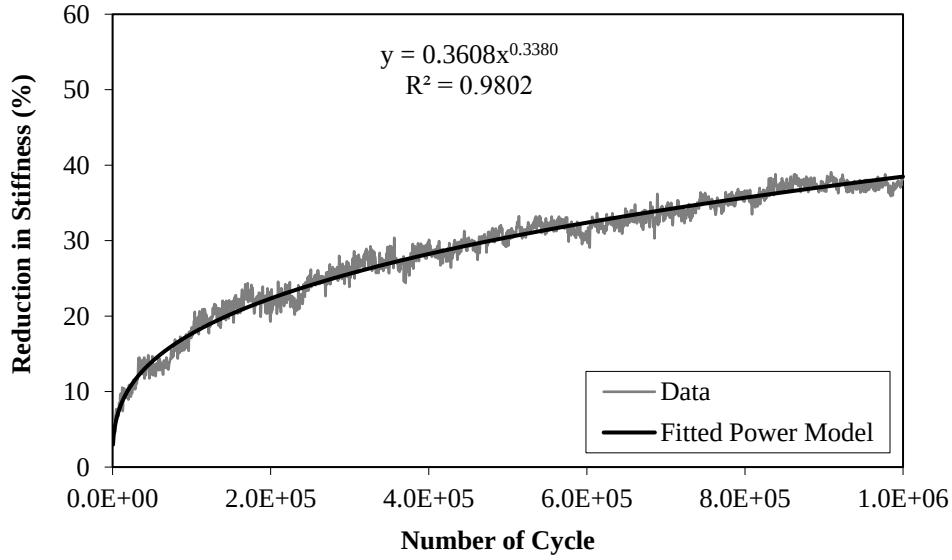

(b)

Figure C.17. IDTF test results of sample ID BMIF15-1: a) Stiffness modulus, b) Reduction in stiffness

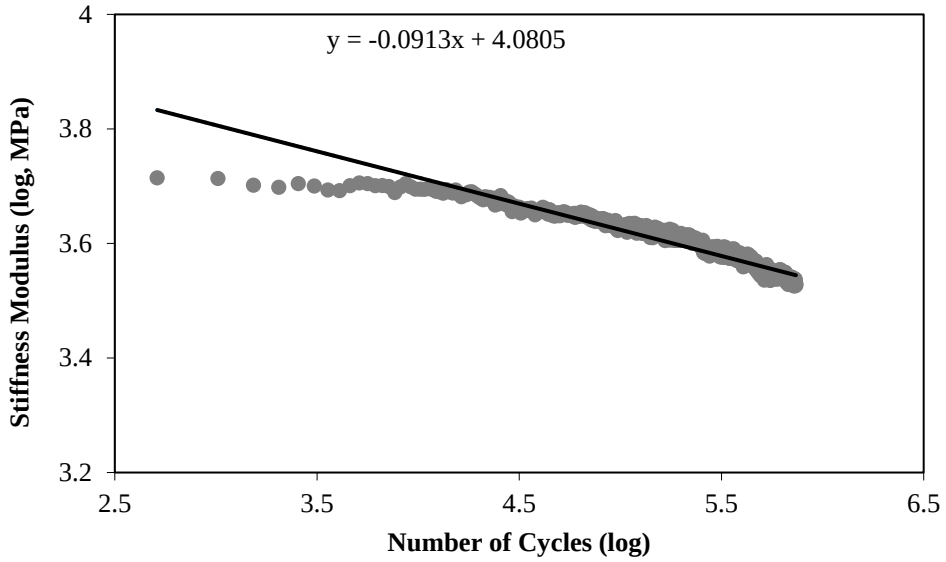

(a)

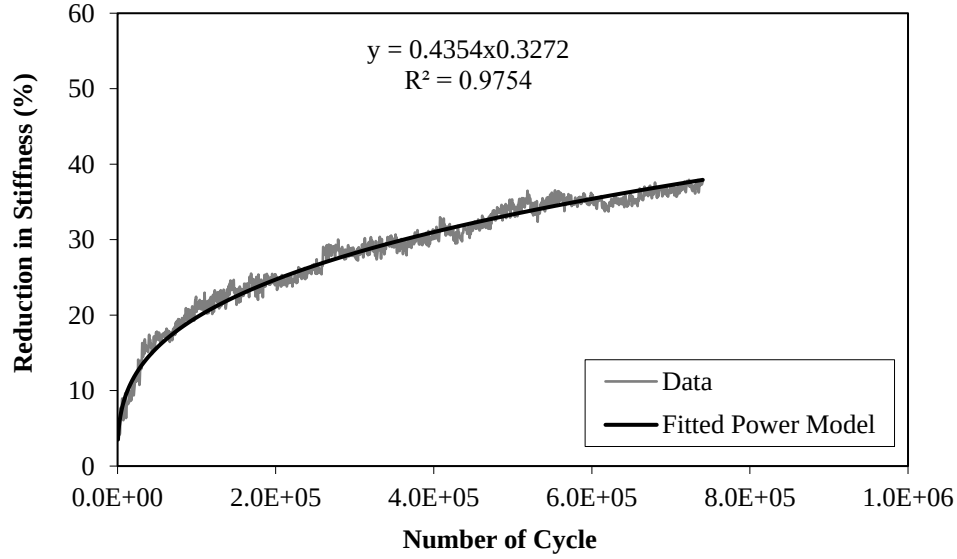

(b)

Figure C.18. IDTF test results of sample ID BMIF15-2: a) Stiffness modulus, b) Reduction in stiffness

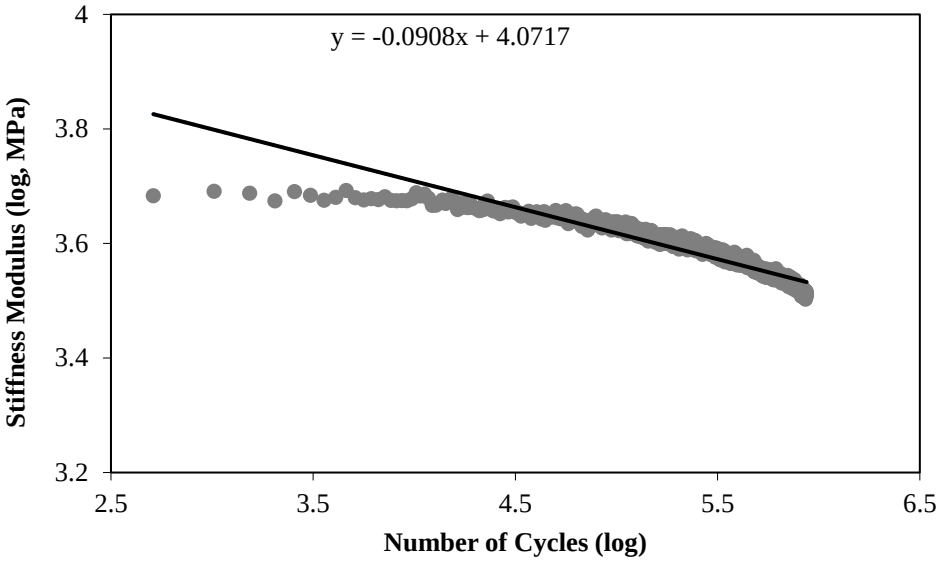

(a)

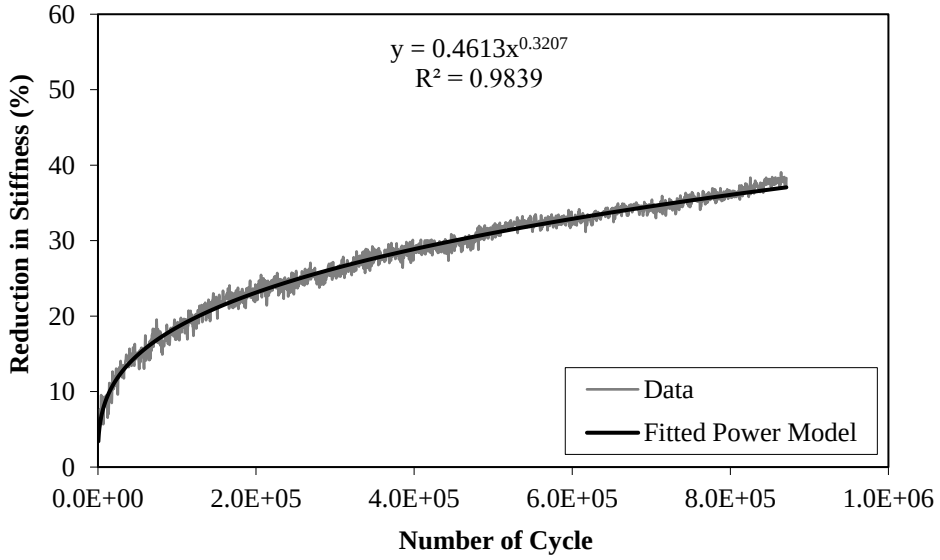

(b)

Figure C.19. IDTF test results of sample ID BMIF16-2: a) Stiffness modulus, b) Reduction in stiffness

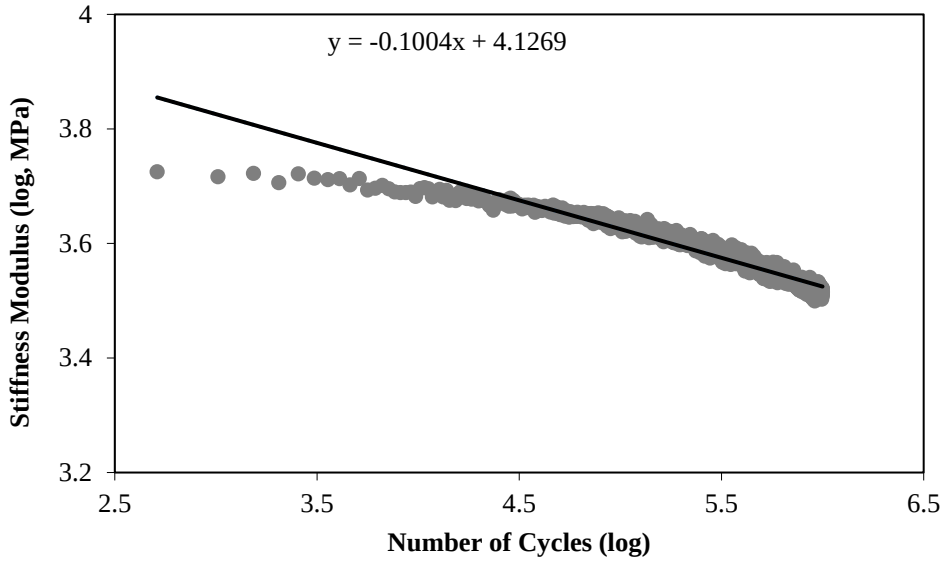

(a)

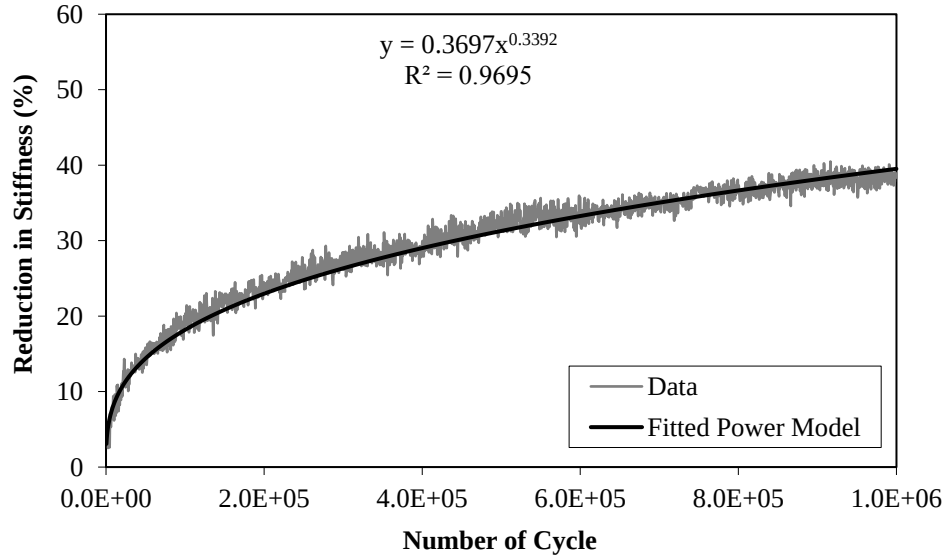

(b)

Figure C.20. IDTF test results of sample ID BMIF17-1: a) Stiffness modulus, b) Reduction in stiffness

D. MATLAB Code for Finding the Edge Pixels

```
clear all
clc

OrImage=imread('C:\Users\yalcin\Desktop\image\LURM12_1.tif');
%enhanced, final image read


BW=bwperim(OrImage);                                %image conversation
to binnary


imshow(BW);

[x,y]=bwboundaries(BW,'noholes');                   %find boundaries of
the binnary image x cell, y image


NumberofAggregates=numel(x);                        %total aggregate
number



for i=1:NumberofAggregates;
    Vector1=x{i};
    Size_of_Agg=size(Vector1,1);                    %Select first
vector
    Row_delete=1:Size_of_Agg;                       %Create the full
row to be deleted
    Row_keep=[1:5:Size_of_Agg];                     %Rows will be kept
    Row_delete(Row_keep)=[];                        %final rows will be
deleted

    Vector1(Row_delete, :)=[];                      %Final vector
    x{i}=Vector1;
end



[m,n]=size(OrImage);
NoP_Results=zeros(size(x));
for i=1:NumberofAggregates;
    Aggregate=x{i};
    NumberofPixels=length(Aggregate);
    NoP_Results(i)=NumberofPixels;
end


CoP_Results=cell2mat(x);

YDimension=m;
```

```
NumberofPixels=length(CoP_Results);CoP_Results2=zeros(NumberofPixel
s,2);


for i=1:NumberofPixels
    ValueY1=CoP_Results(i,1);
    ValueY2=YDimension-ValueY1;
    ValueX=CoP_Results(i,2);
    CoP_Results2(i,:)=[ValueX ValueY2];
end



csvwrite('CoP_results.csv',CoP_Results2); %write down the
coordinates

csvwrite('NoP_Results.csv',NoP_Results);
```

E. ANSYS Mechanical APDL Script for Creating the Geometric Models

```
/CLEAR,nostart          !reset ANSYS database.
*DEL,ALL,_PRM           !delete all parameters
*AFUN,DEG
/DELETE,Output,txt      !delete output file
/OUTPUT,Output,txt      !write output into TXT file
/UNITS,SI               !Length [m],Mass [kg],Force [N],Pressure
[Pa], Time [s]
/TITLE,PW_02


!*****************************************************************
!            PARAMETER
!*****************************************************************


!*****************************************************************
!            PREPROCESSING
!*****************************************************************
/PREP7


!Creating aggregate numbers and pixel numbers
/INQUIRE,NumbOfAgg,LINES,NoP_Results2,csv
*DIM,NumbOfPix_Table,TABLE,NumbOfAgg
*TREAD,NumbOfPix_Table,NoP_Results2,csv
*DIM,NumbOfPix,ARRAY,NumbOfAgg,2
*VFUN,NumbOfPix(1,1),copy,NumbOfPix_Table(1,0)
*VFUN,NumbOfPix(1,2),copy,NumbOfPix_Table(1,1)
*DEL,NumbOfPix_Table


!Creating arrays for aggregates and pixels of each aggregates
/INQUIRE,Total_NumbOPix,LINES,CoP_results,csv
*DIM,arr_table,TABLE,Total_NumbOPix
*TREAD,arr_table,CoP_results,csv
*DIM,Pix_arr,ARRAY,Total_NumbOPix,2
*VFUN,Pix_arr(1,1),copy,arr_table(1,0)
*VFUN,Pix_arr(1,2),copy,arr_table(1,1)
*DEL,arr_table


*SET,Agg_NOP_Strt,NumbOfPix(1,2)+1
Line_Strt=-2  !in order to select the proper line for making area
```

```
*DO,i,1,NumbOfAgg-1
*SET,Agg_NOP_End1,NumbOfPix(i,2)
*SET,Agg_NOP_End2,NumbOfPix(i+1,2)
Agg_NOP_End=Agg_NOP_End2-Agg_NOP_End1



*DIM,Agg_Arr,ARRAY,Agg_NOP_End,2



!Keypoint
*DO,j,1,Agg_NOP_End
k=Agg_NOP_End1+j
Value1=Pix_arr(k,1)!!!
```

```
!THE OUTER AREA
K,Total_NumbOPix+1,0,0,0
K,Total_NumbOPix+2,0,5390
K,Total_NumbOPix+3,1622,539,0
K,Total_NumbOPix+4,1622,0,0
A,Total_NumbOPix+1,Total_NumbOPix+2,Total_NumbOPix+3,Total_NumbOPix
+4
ALLSEL,ALL

ASEL,S,AREA,,ALL
ASBA,41,ALL,  ,DELETE,KEEP



*DO,i,1,50
a_=mod(i,2)

*if,a_,EQ,1,THEN
ASBA,NumbOfAgg,i,,KEEP,KEEP
ADELE,NumbOfAgg,,1

*else
ASBA,NumbOfAgg+1,i,,KEEP,KEEP
ADELE,NumbOfAgg+1,,1

*endif
*enddo


ALLSEL,ALL



 FINISH          !Exits normally from a processor
!*****************************************************************
!             SOLUTION
!*****************************************************************
/SOLU



 FINISH          !Exits normally from a processor
!*****************************************************************
!             POSTPROCESSING
!*****************************************************************
/POST1


 FINISH
```

F. Synthetic Images Created by Particle Redistribution Method

In order to investigate the tensile variations of the HMA, particle redistribution method was created. This method was then applied separately for each of the finite element model. A sample was selected from each of the resilient modulus and creep experiments and 10 different synthetic images were produced by applying the particle redistribution method on these selected images. Below are the selected genuine and 10 different synthetic samples of these two sample types.

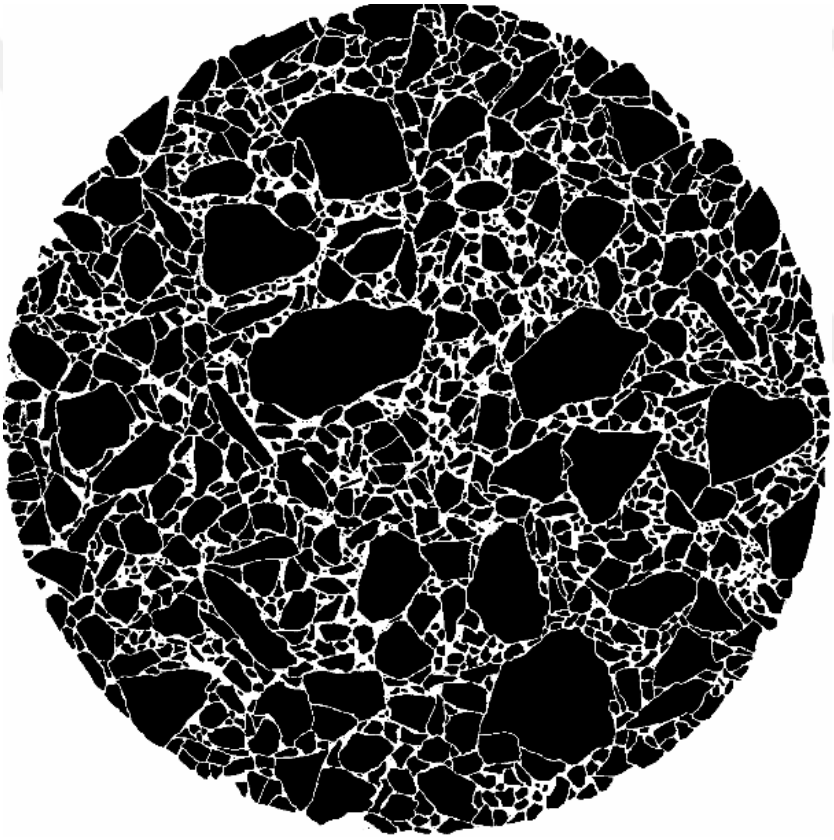

Figure F.1. Genuine image of sample ID LURM02-1

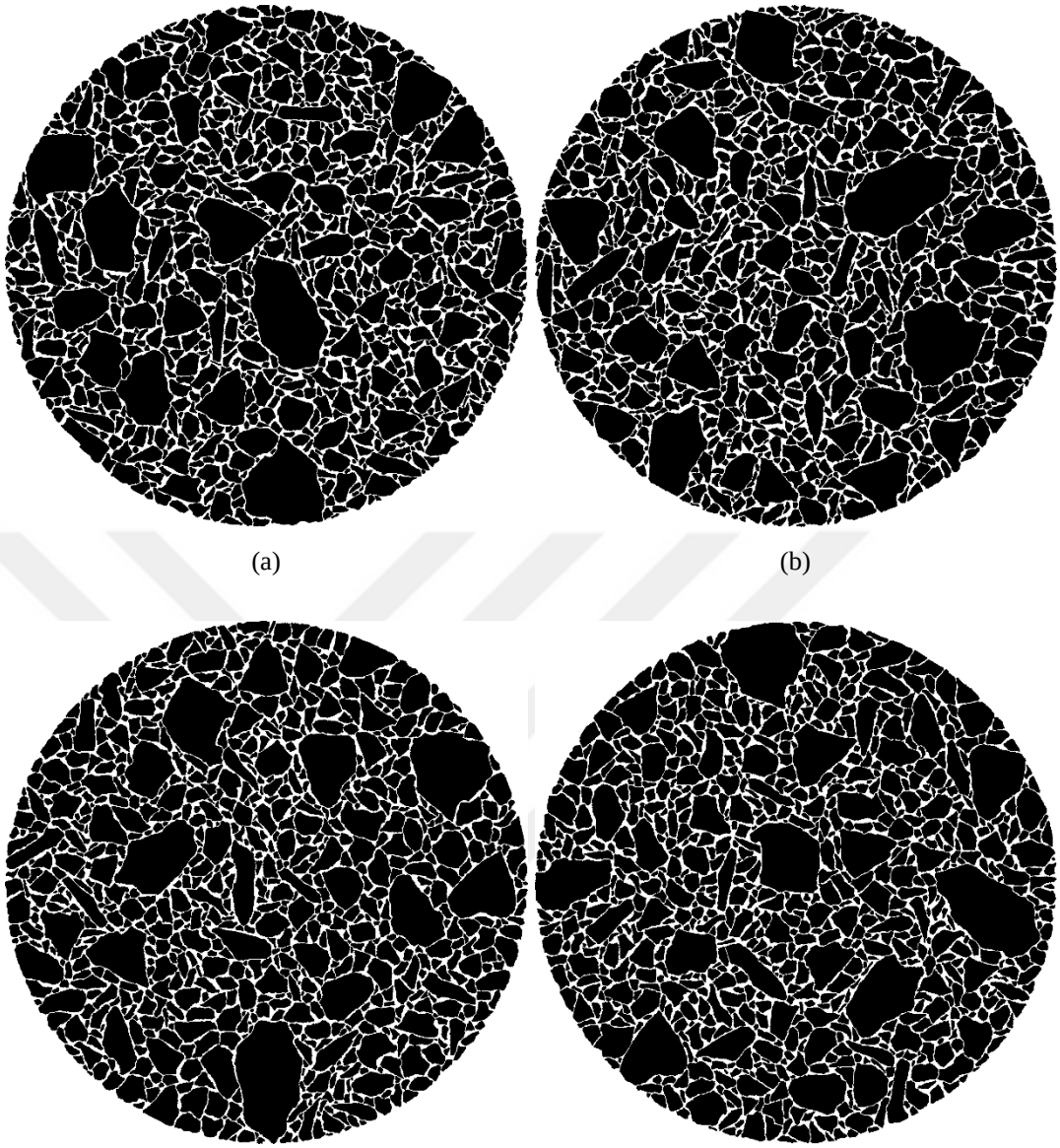

(a) (b)

(c) (d)

Figure F.2. Synthetic images of sample ID LURM02-1

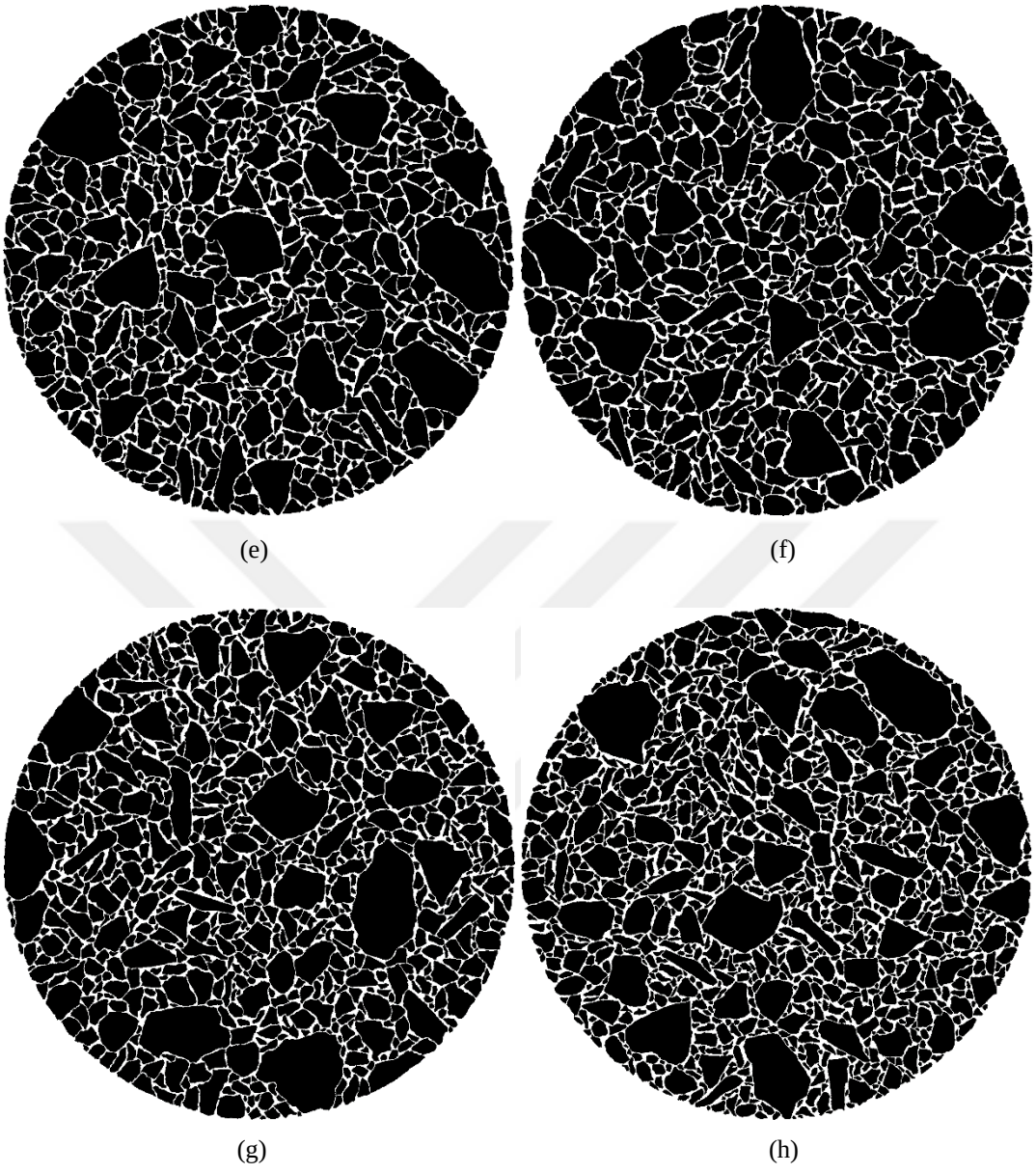

(e) (f)

(g) (h)

Figure F.2. (Continued)

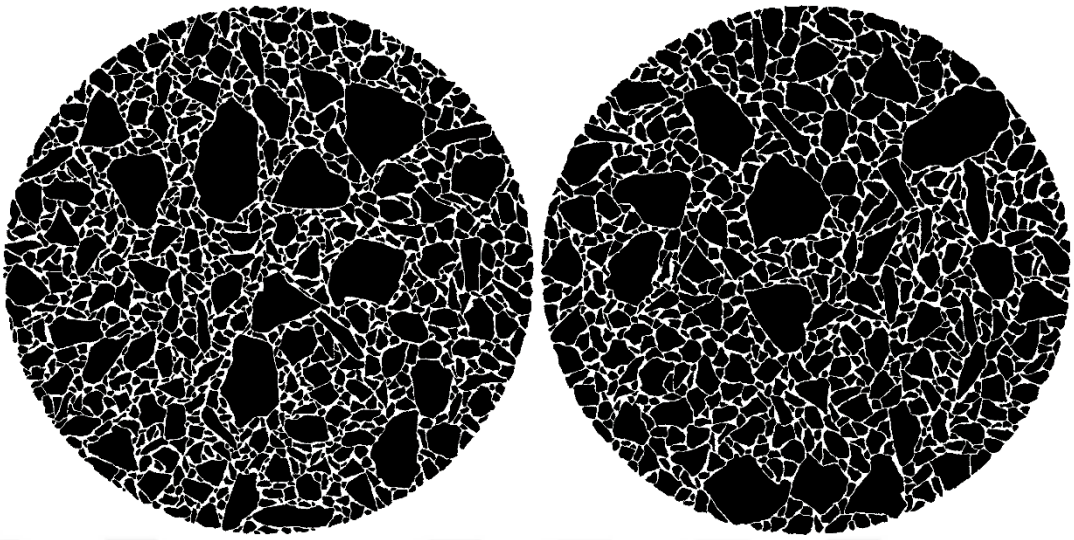

(i) (j)

Figure F.2. (Continued)

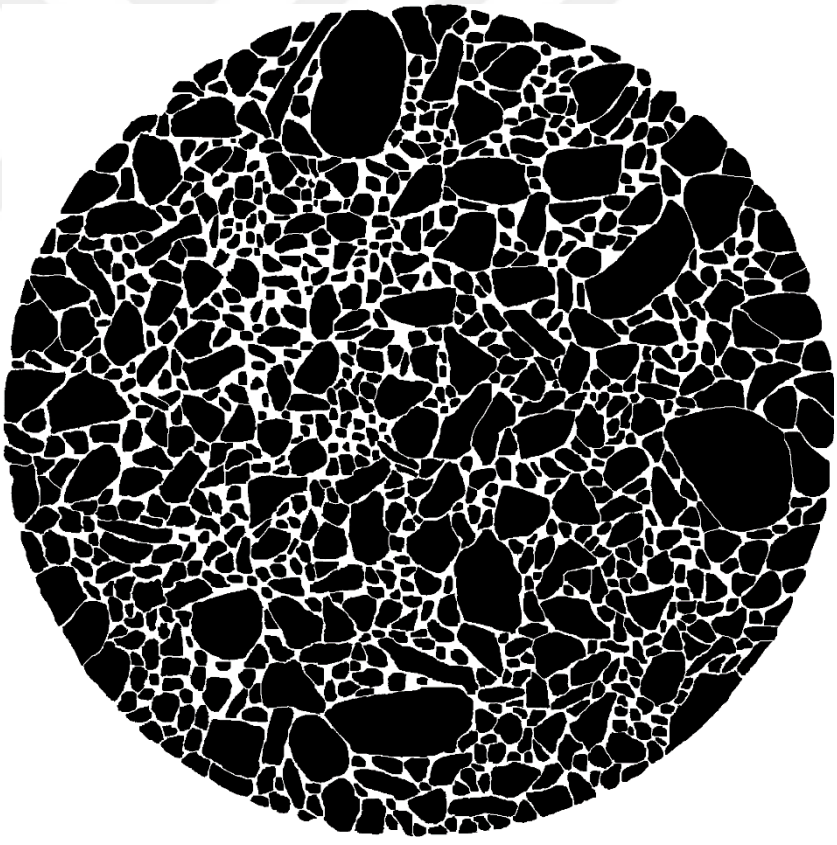

Figure F.3. Genuine image of the sample ID BMRM02-1

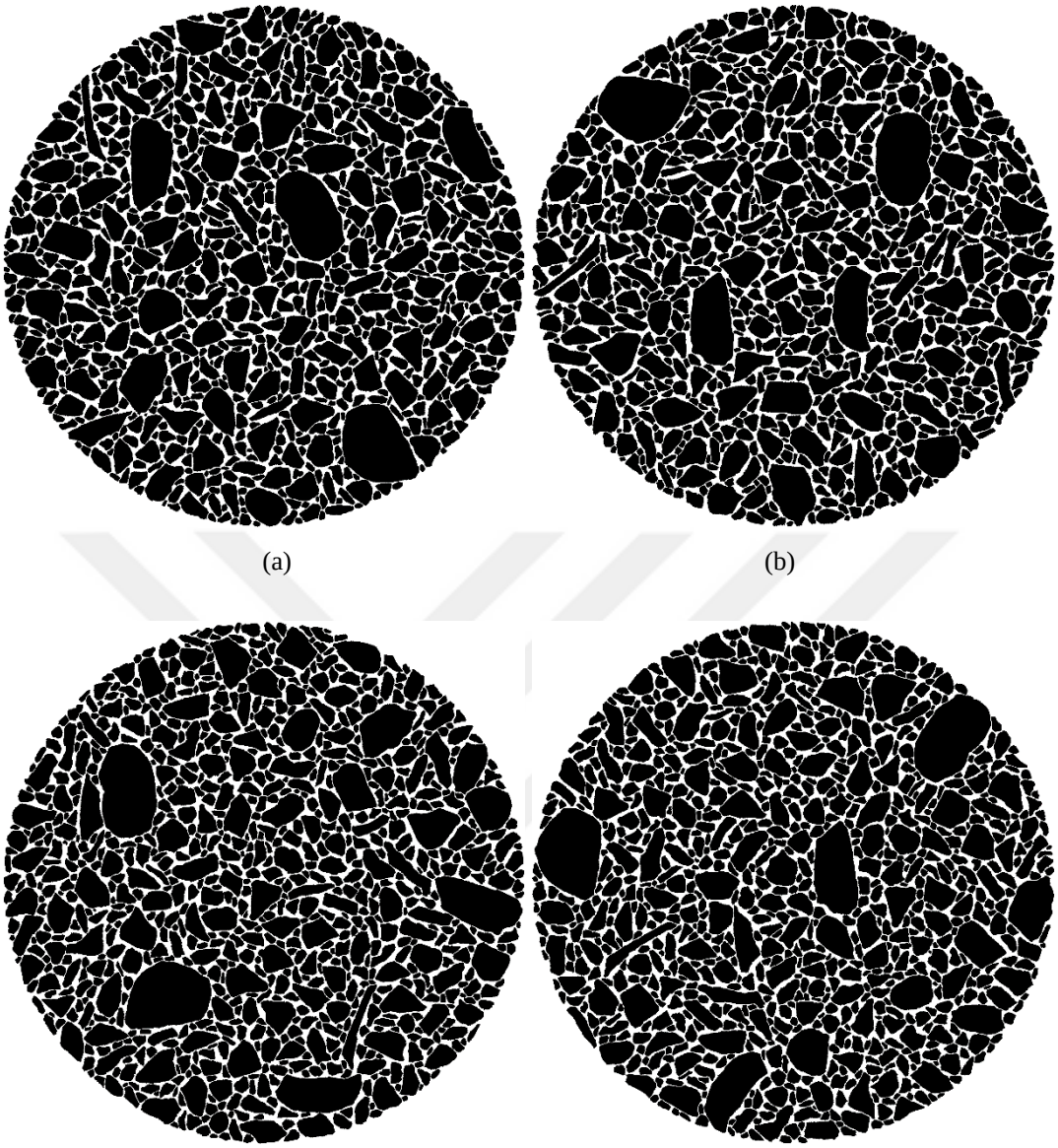

(a) (b)

(c) (d)

Figure F.4. Synthetic images of sample ID BMRM02-1

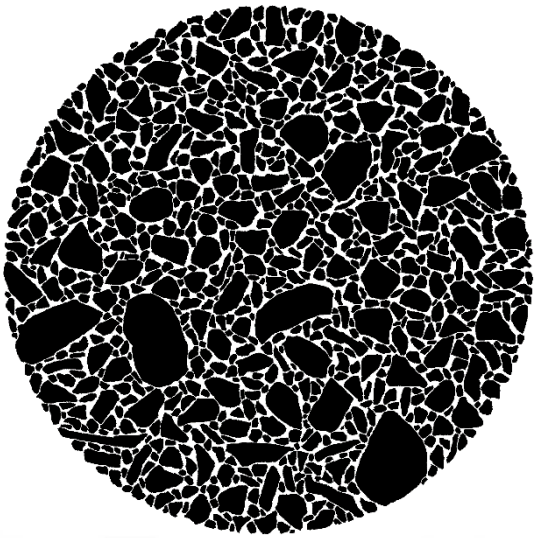

(e)

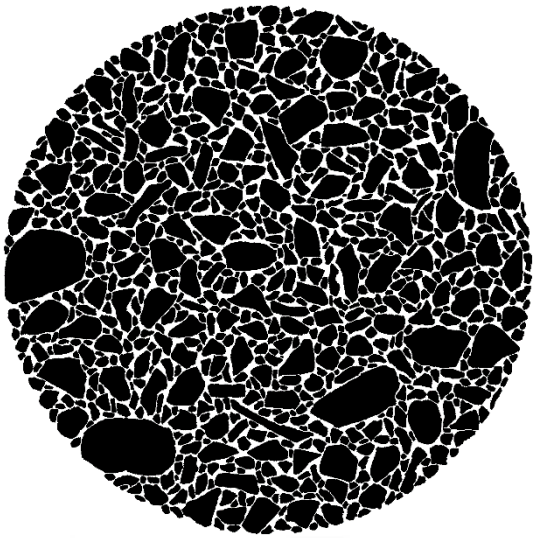

(f)

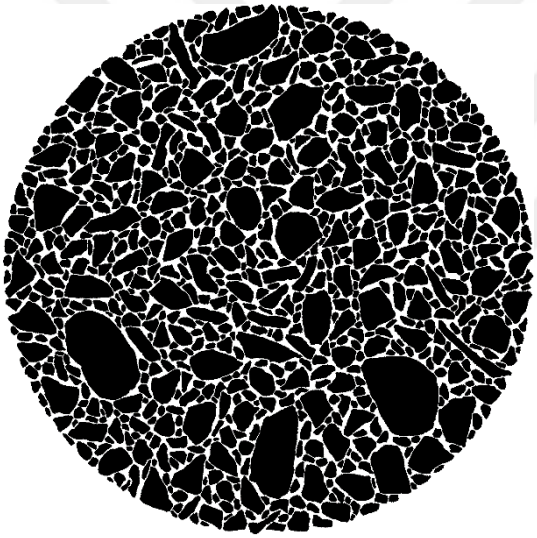

(g)

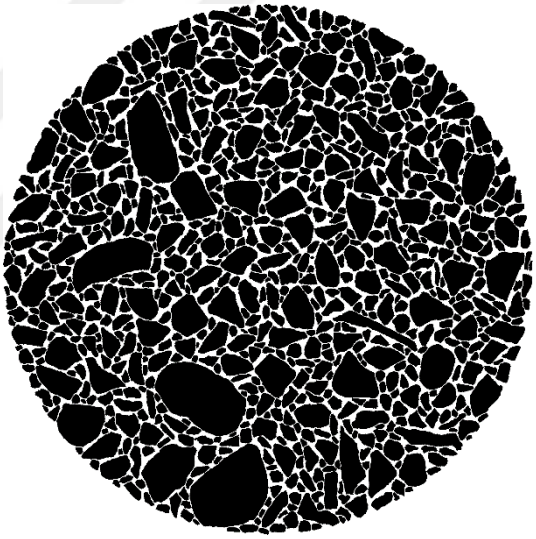

(h)

Figure F.4. (Continued)

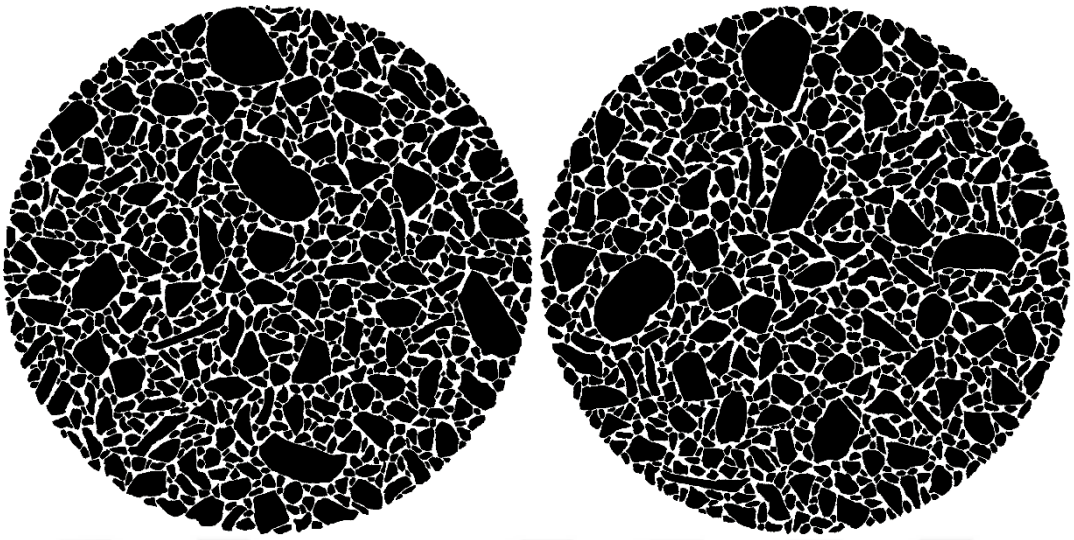

(i) (j)

Figure F.4. (Continued)

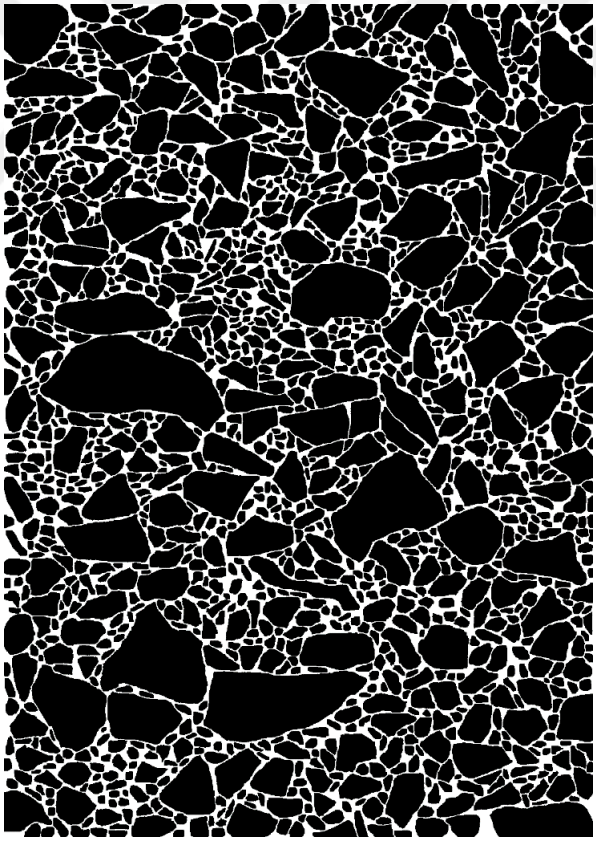

Figure F.5. Genuine image of sample ID LUCR06

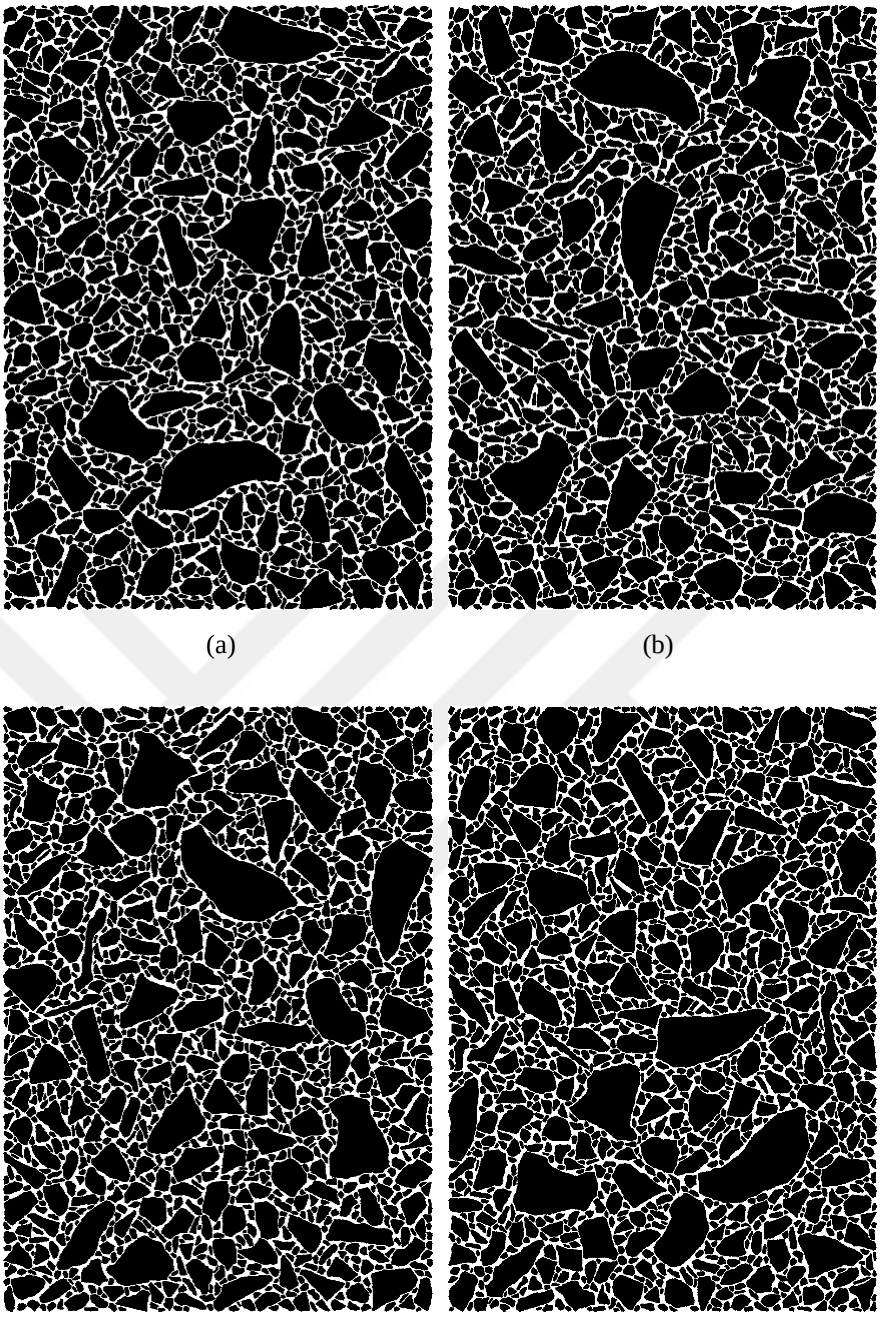

(a) (b)

(c) (d)

Figure F.6. Synthetic images of sample ID LUCR06

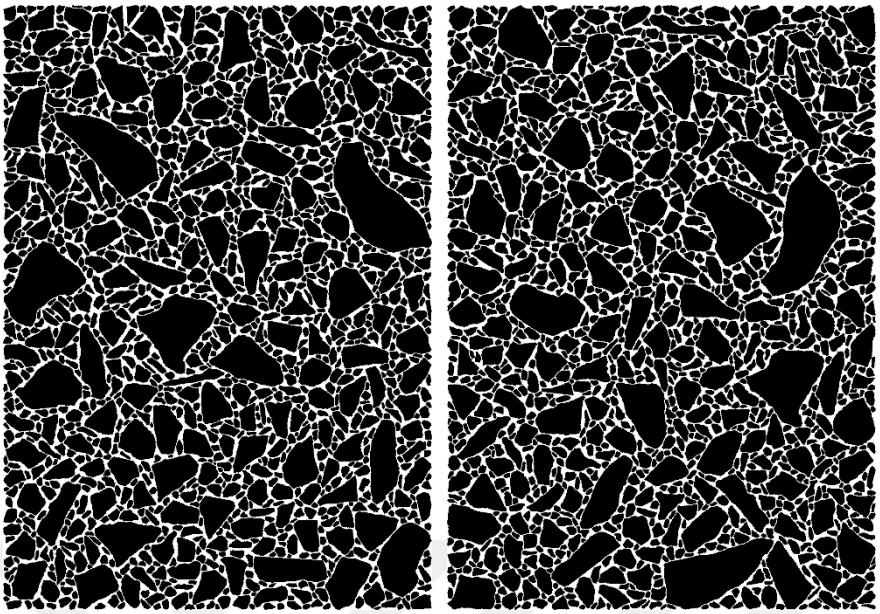

(e) (f)

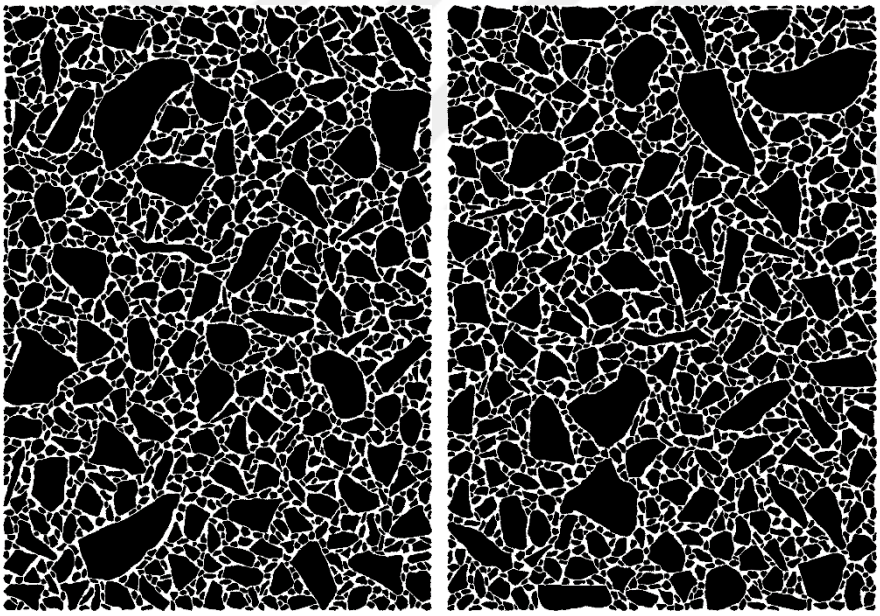

(g) (h)

Figure F.6. (Continued)

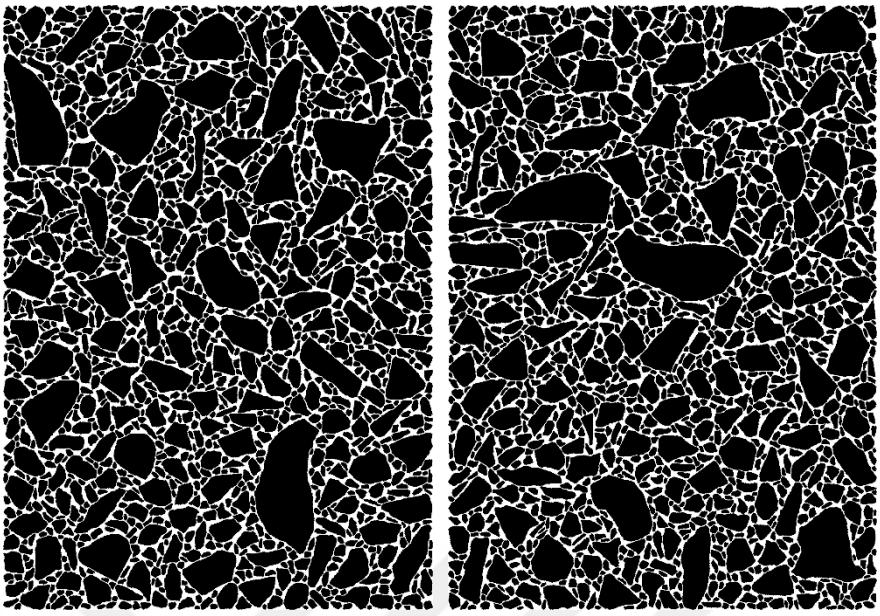

(i) (j)

Figure F.6. (Continued)

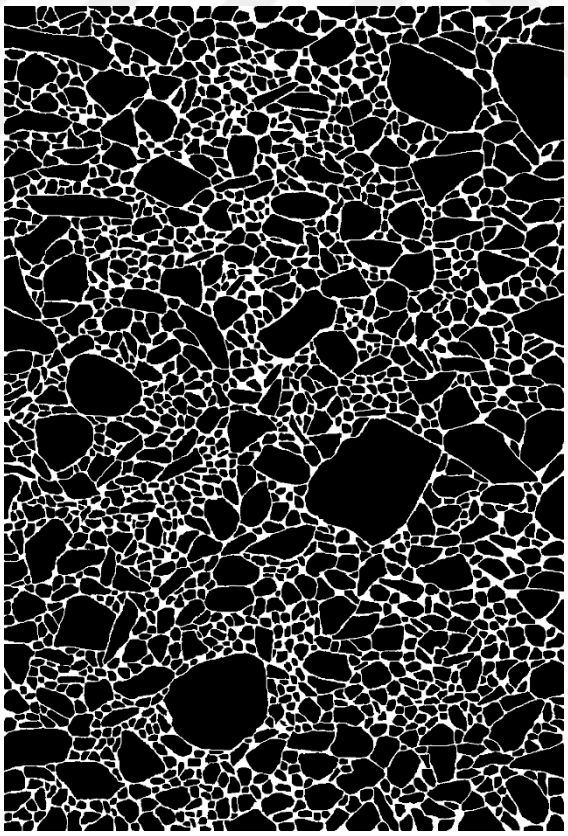

Figure F.7. Genuine image of sample ID BMCR03

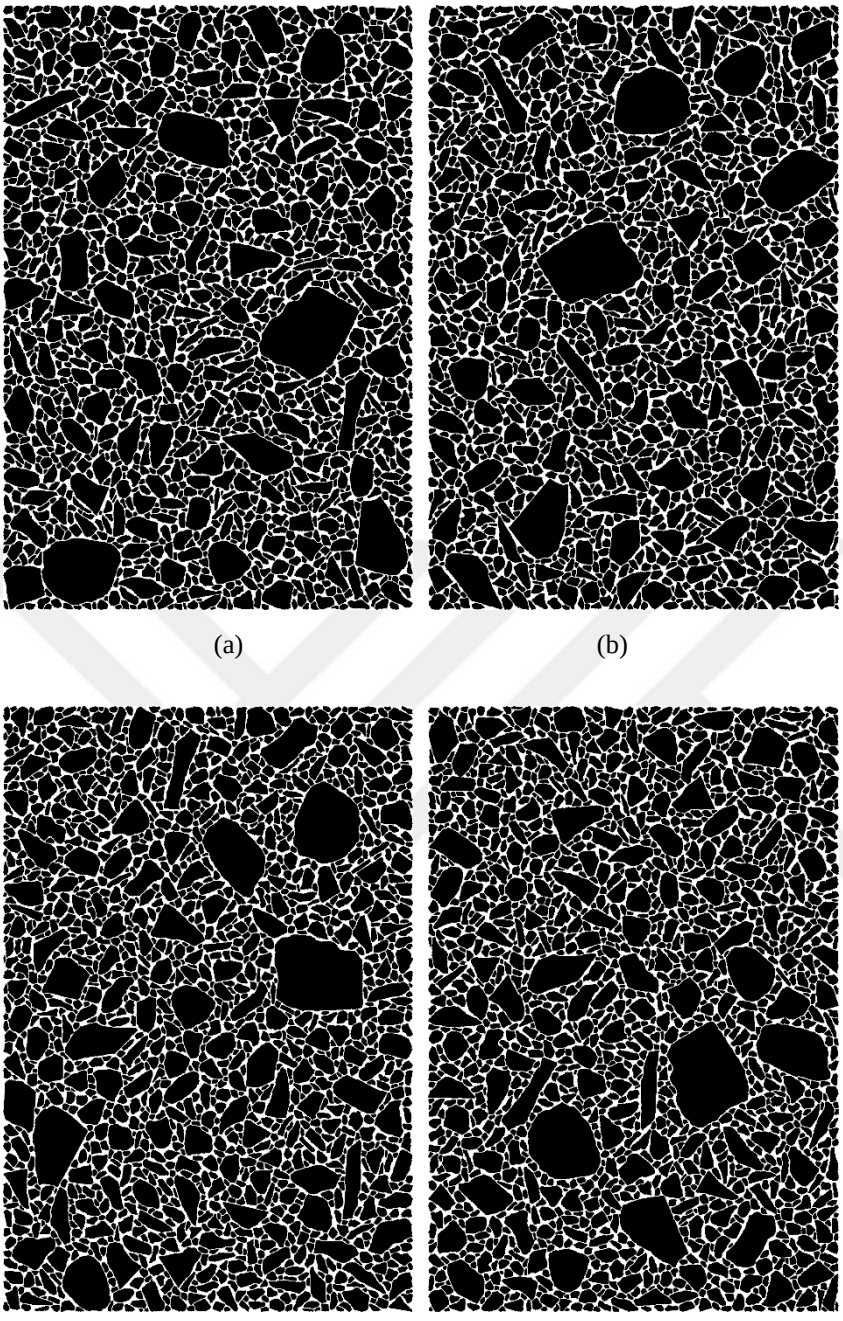

(a) (b)

(c) (d)

Figure F.8. Synthetic images of sample ID BMCR03

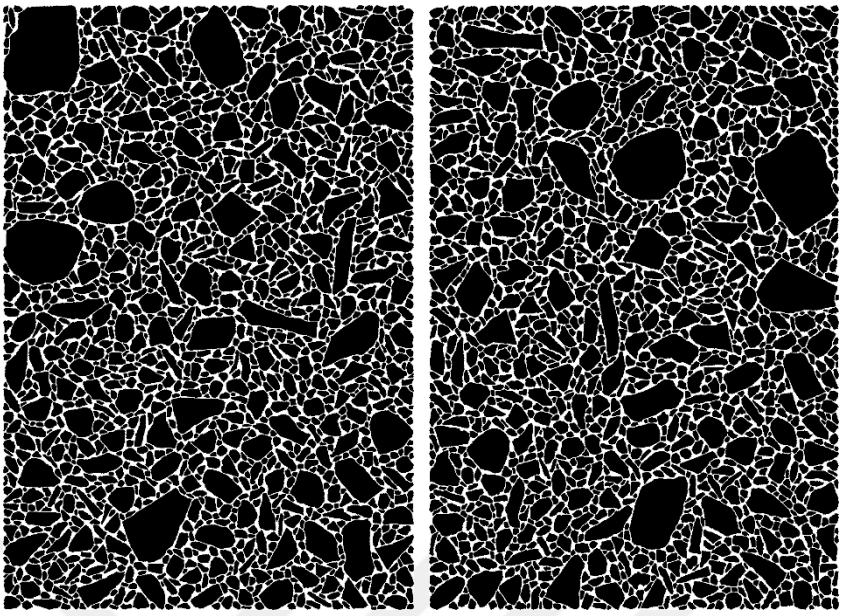

(e) (f)

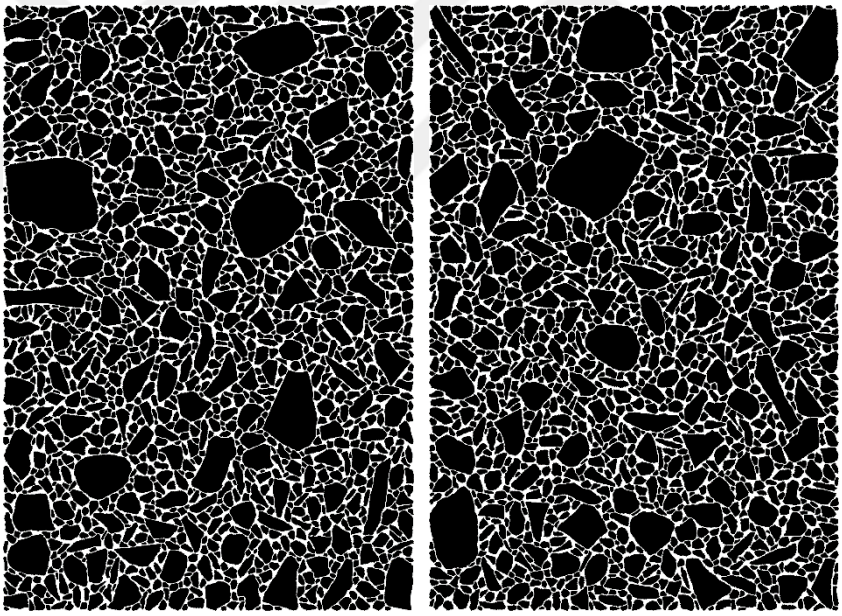

(g) (h)

Figure F.8. (Continued)

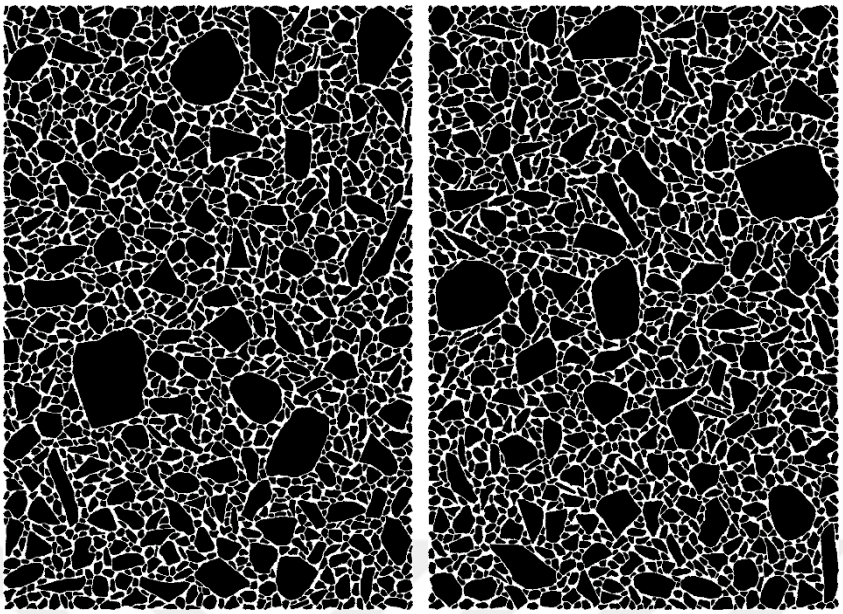

(i) (j)

Figure F.8. (Continued)

G. Finite Element Models of the Specimens

Image-based finite element model in this study is based on the captured, enhanced and vectorized 2D images of the laboratory compacted specimens. All the main image processing steps, i.e., capturing by the flatbed, image enhancement, and vectorization, along with their final FE model inside ABAQUS® are given for the entire samples used in this study, below.

In these images, the image processing section is divided into three main steps. First, RGB image right after scanned by a flatbed scanner is presented to demonstrate the effect of the scanner on capturing the structure of HMA samples. These images were scanned at 300 dpi resolution and consisted of approximately 2 to 3 million pixels, depending on the sample geometry. Next, their binary images are given before applying any further image enhancement technique. The effectiveness of high-resolution scanning on capturing the aggregate particle structure can be seen at this stage. After that, the images of the specimens after applying all the image enhancement procedures listed in Chapter 4 are given. It is worth mentioning that the images at this stage are ready to be vectorized. Finally, 2D FE models of the images inside ABAQUS® are given. The image vectorization method transformed the captured, enhanced, and processed images to a FE model through several steps applied using the software such as LabVIEW®, MATLAB®, ANSYS®, and ABAQUS®.

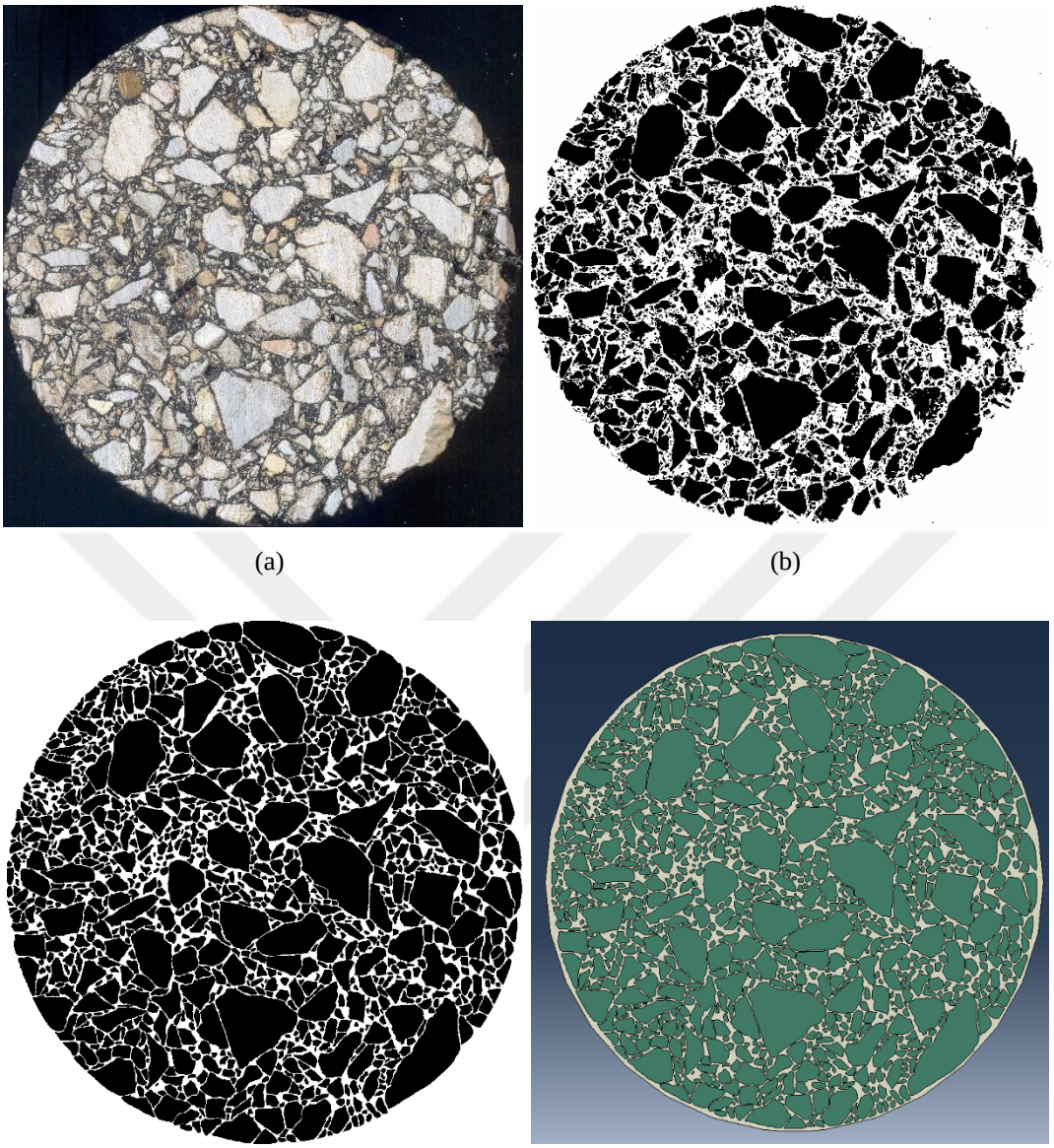

(a) (b)

(c) (d)

Figure G.1. Sample ID LURM01-1: a) Captured RGB image, b) Binary form, c) Processed image, d) 2D FE model in ABAQUS

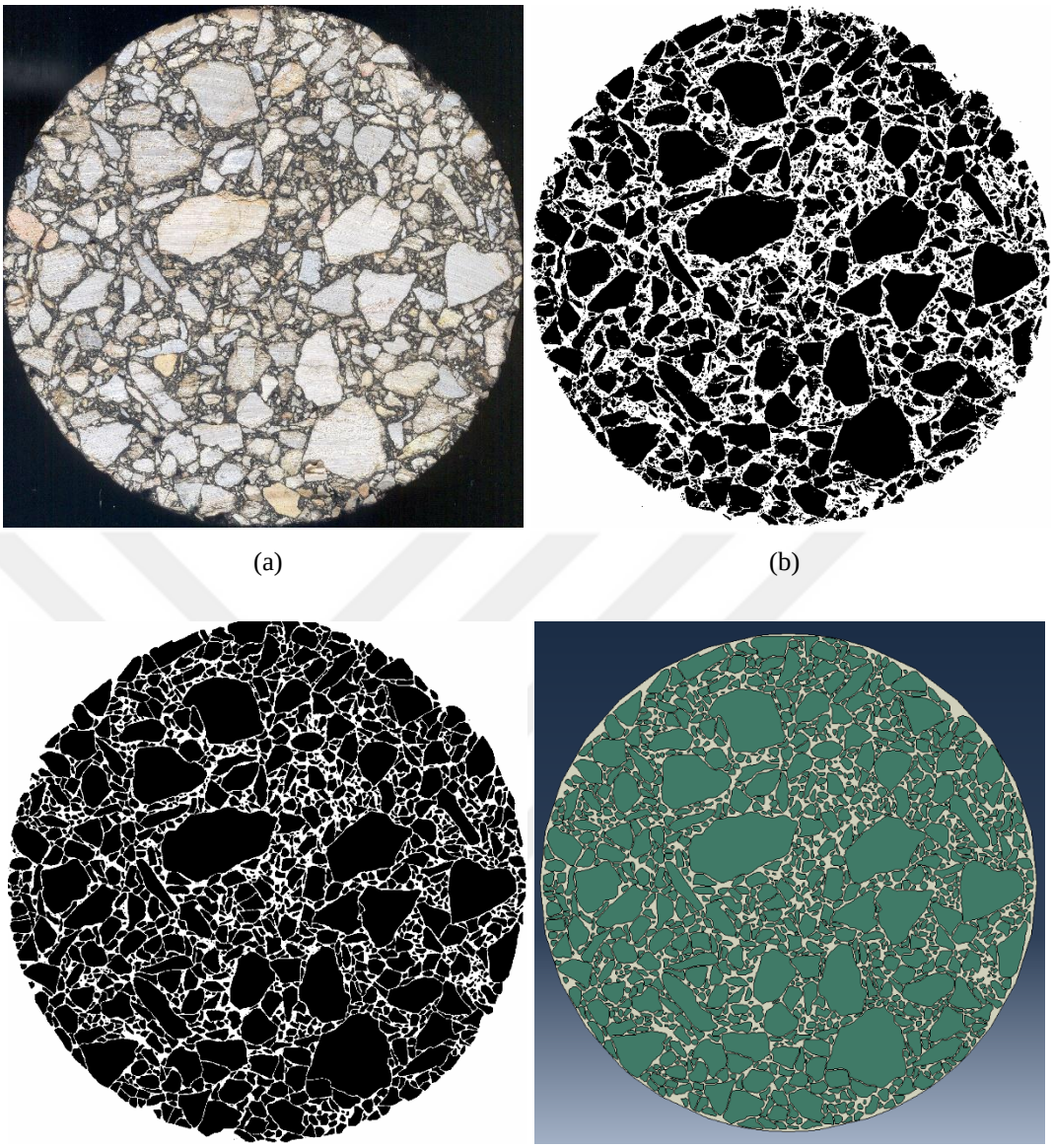

(a) (b)

(c) (d)

Figure G.2. Sample ID LURM02-1: a) Captured RGB image, b) Binary form, c) Processed image, d) 2D FE model in ABAQUS

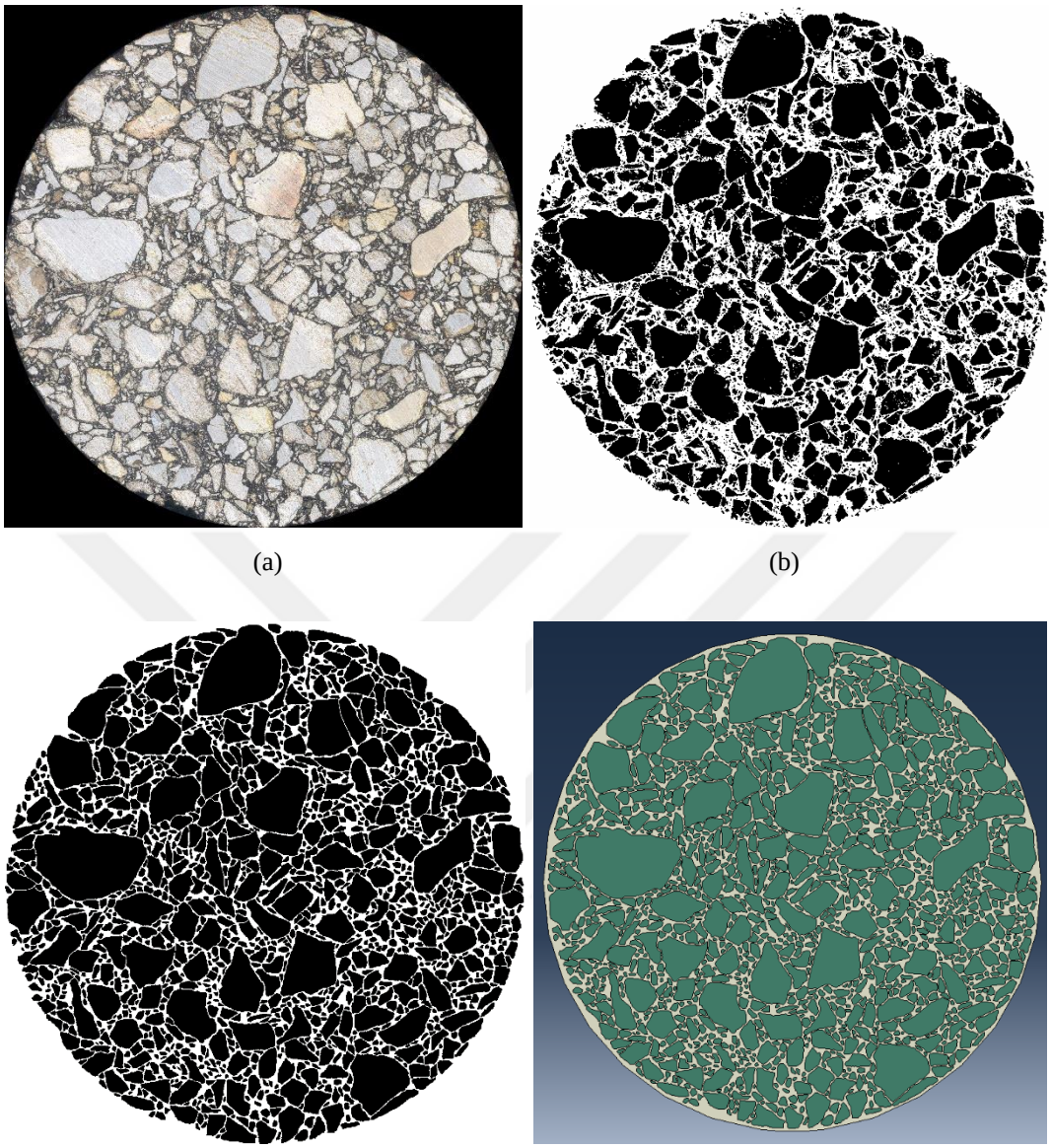

(a) (b)

(c) (d)

Figure G.3. Sample ID LURM03-1: a) Captured RGB image, b) Binary form, c) Processed image, d) 2D FE model in ABAQUS

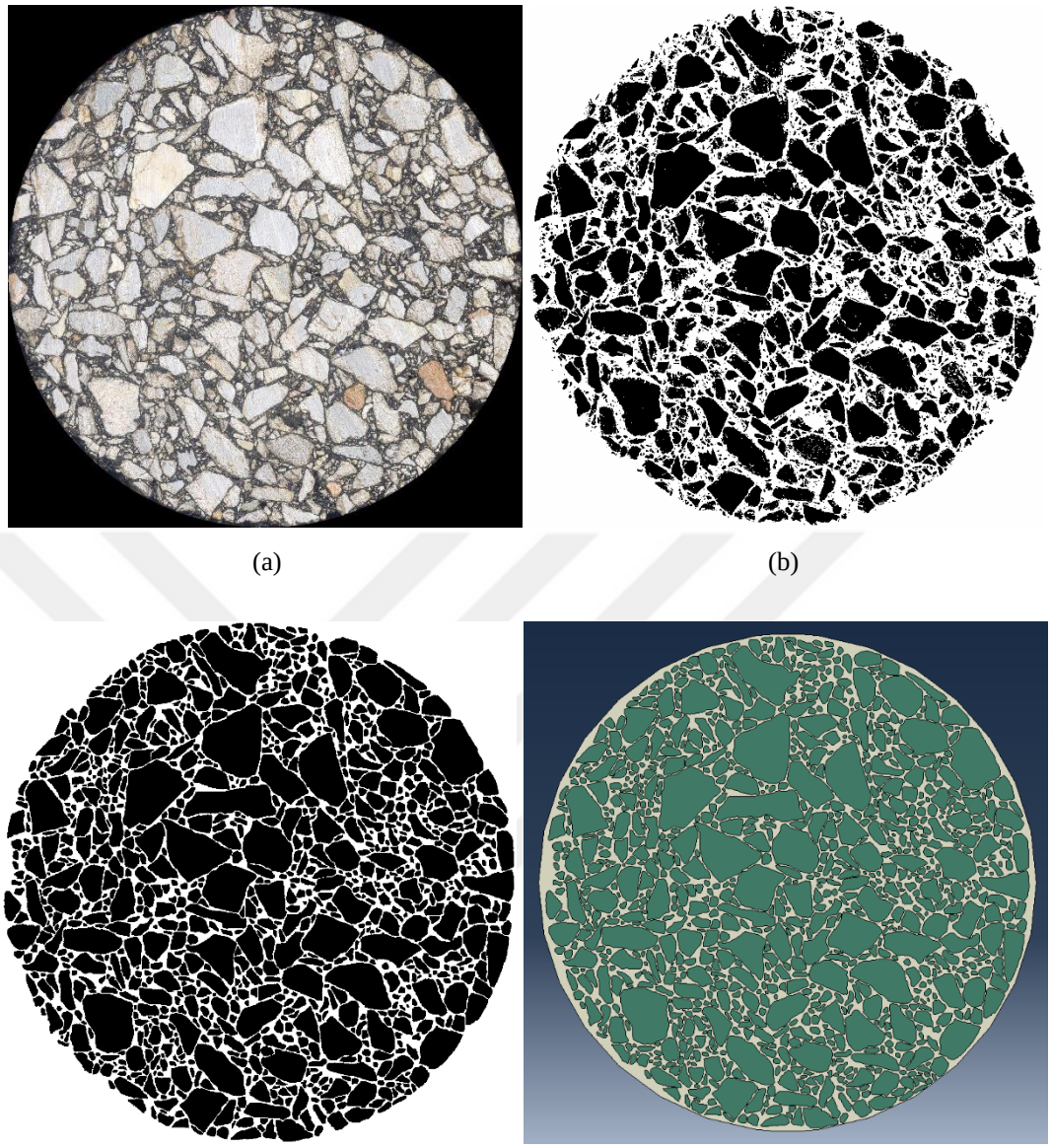

(a) (b)

(c) (d)

Figure G.4. Sample ID LURM06-1: a) Captured RGB image, b) Binary form, c) Processed image, d) 2D FE model in ABAQUS

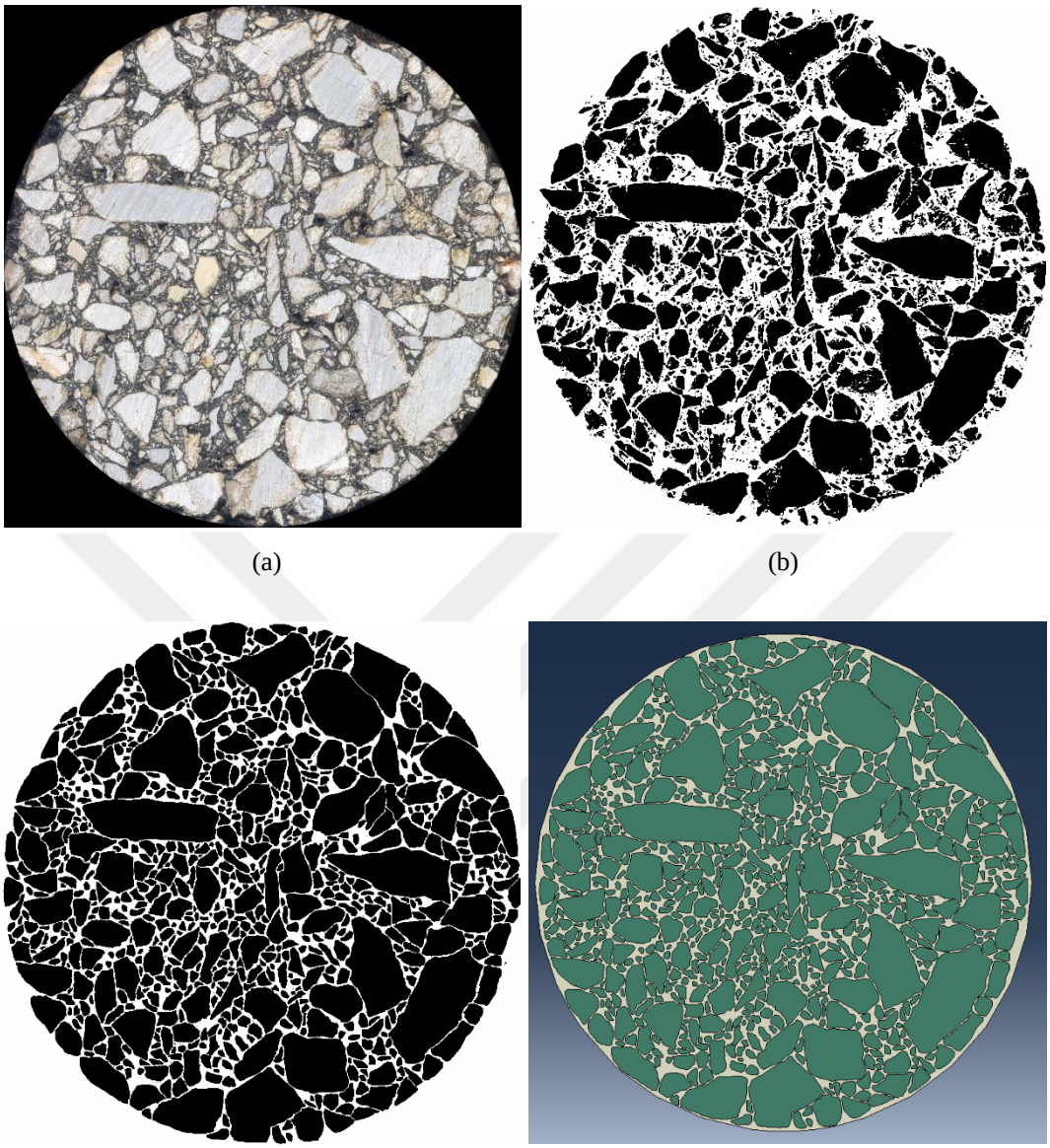

(a) (b)

(c) (d)

Figure G.5. Sample ID LURM07-1: a) Captured RGB image, b) Binary form, c) Processed image, d) 2D FE model in ABAQUS

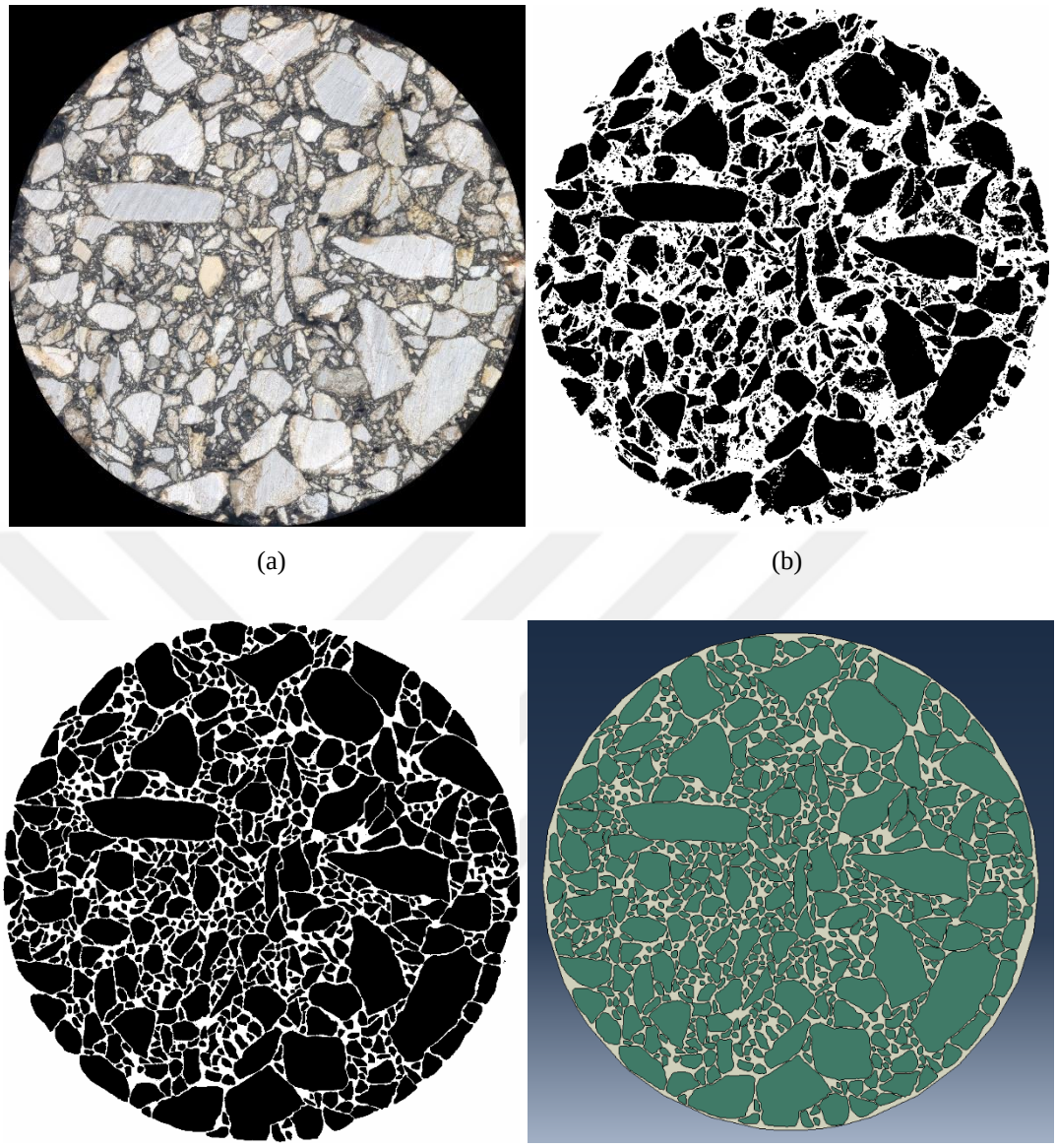

(a) (b)

(c) (d)

Figure G.6. Sample ID LURM08-1: a) Captured RGB image, b) Binary form, c) Processed image, d) 2D FE model in ABAQUS

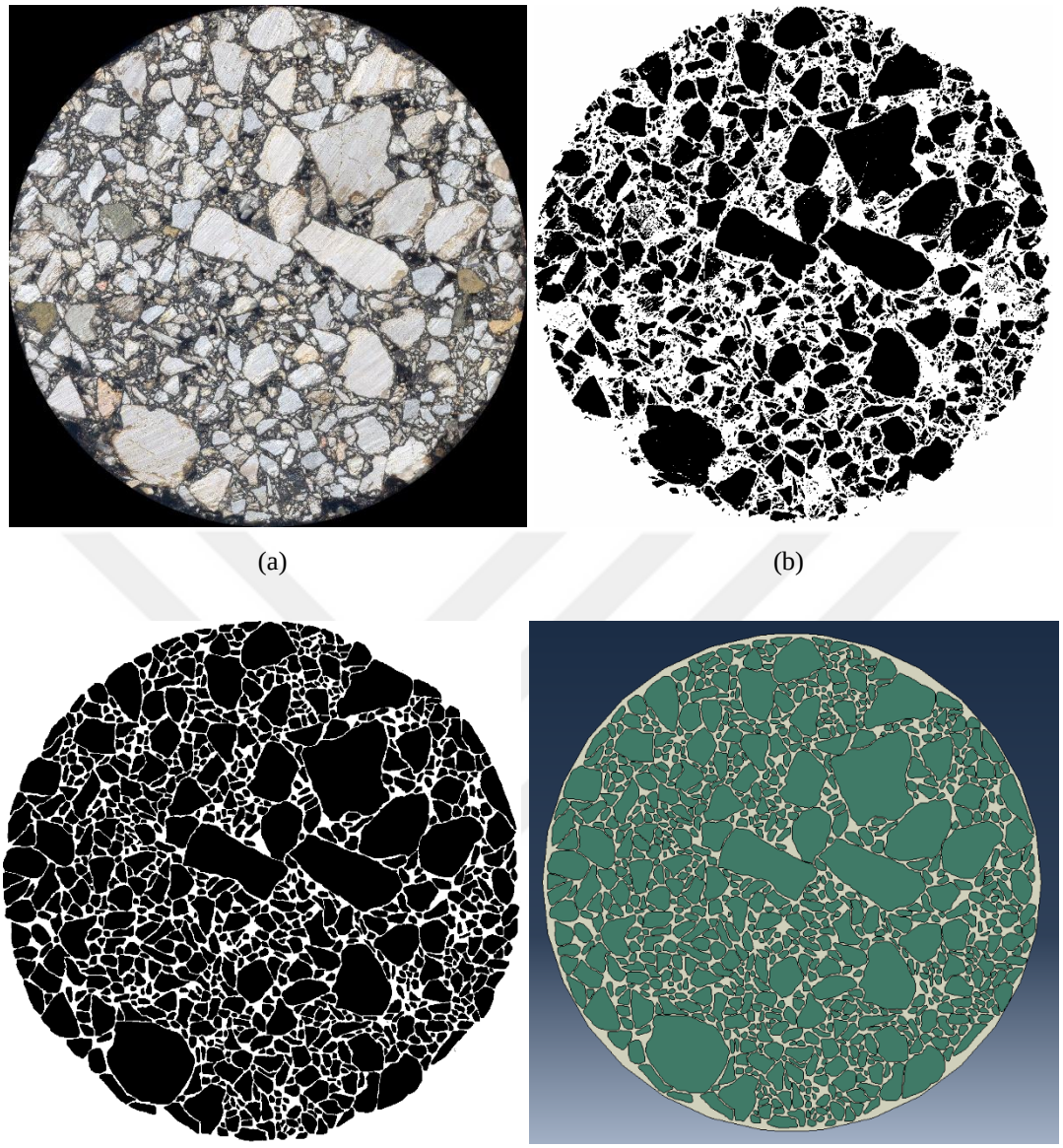

(a) (b)

(c) (d)

Figure G.7. Sample ID LURM09-1: a) Captured RGB image, b) Binary form, c) Processed image, d) 2D FE model in ABAQUS

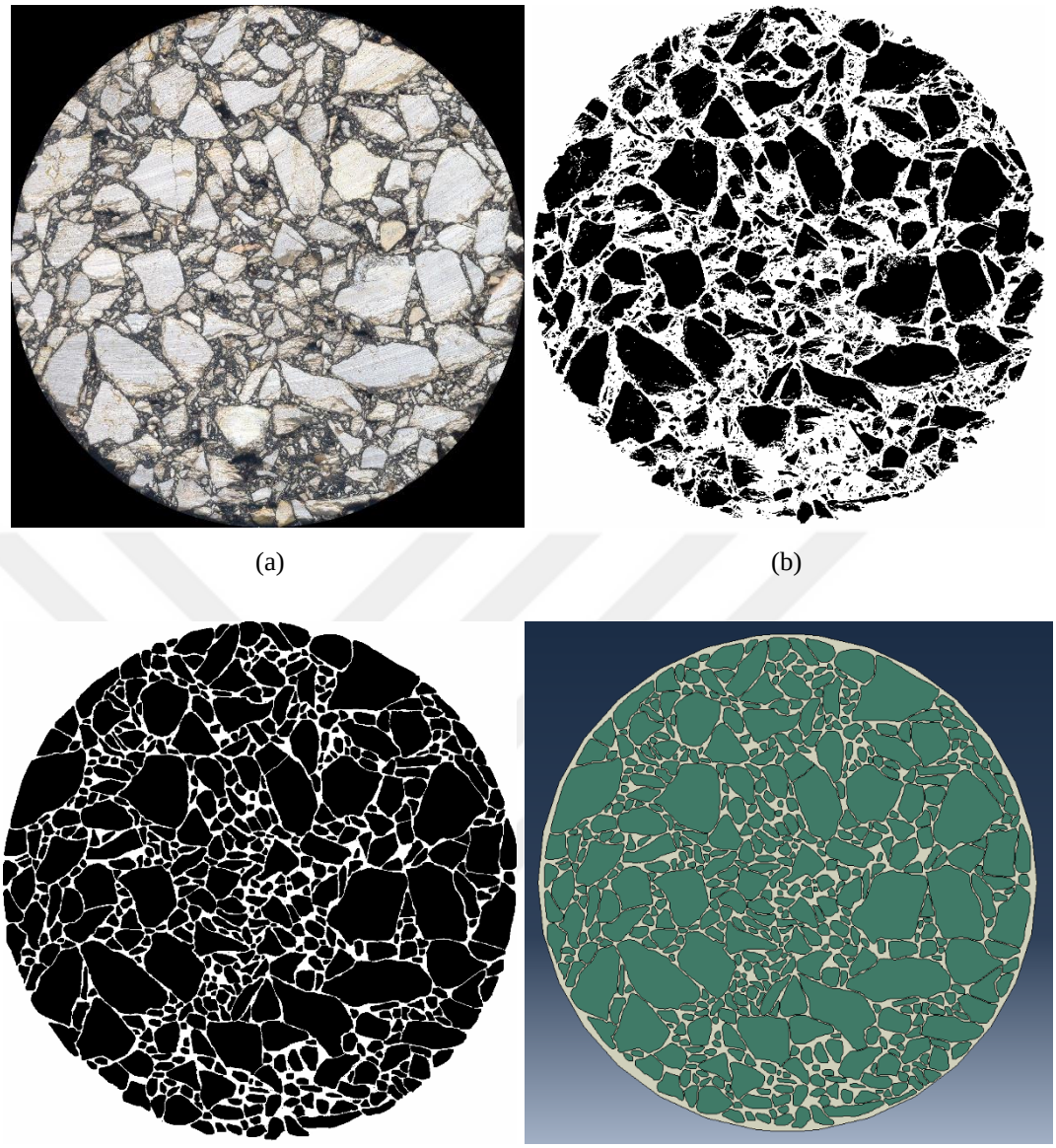

(a) (b)

(c) (d)

Figure G.8. Sample ID LURM10-1: a) Captured RGB image, b) Binary form, c) Processed image, d) 2D FE model in ABAQUS

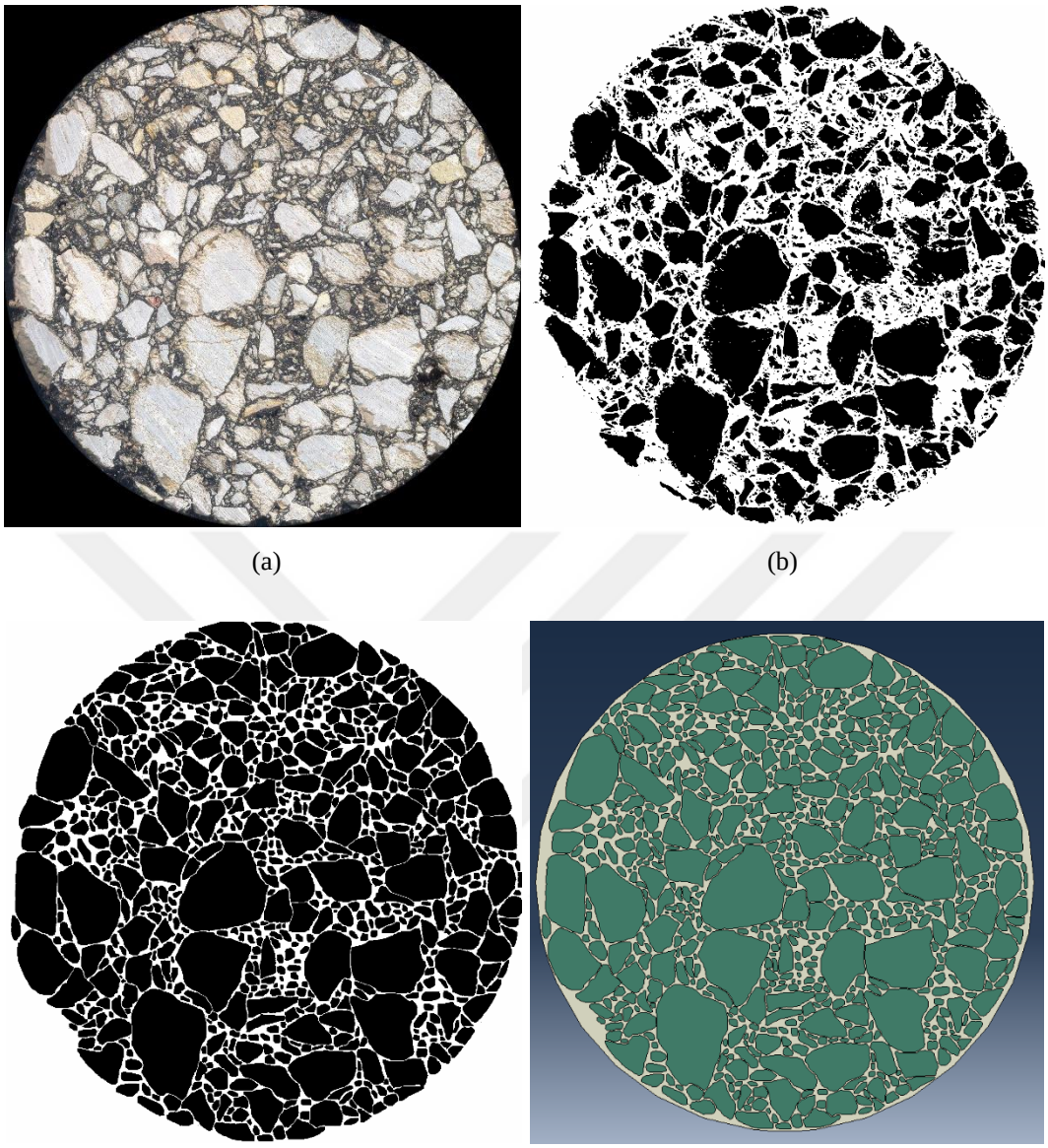

(a) (b)

(c) (d)

Figure G.9. Sample ID LURM11-1: a) Captured RGB image, b) Binary form, c) Processed image, d) 2D FE model in ABAQUS

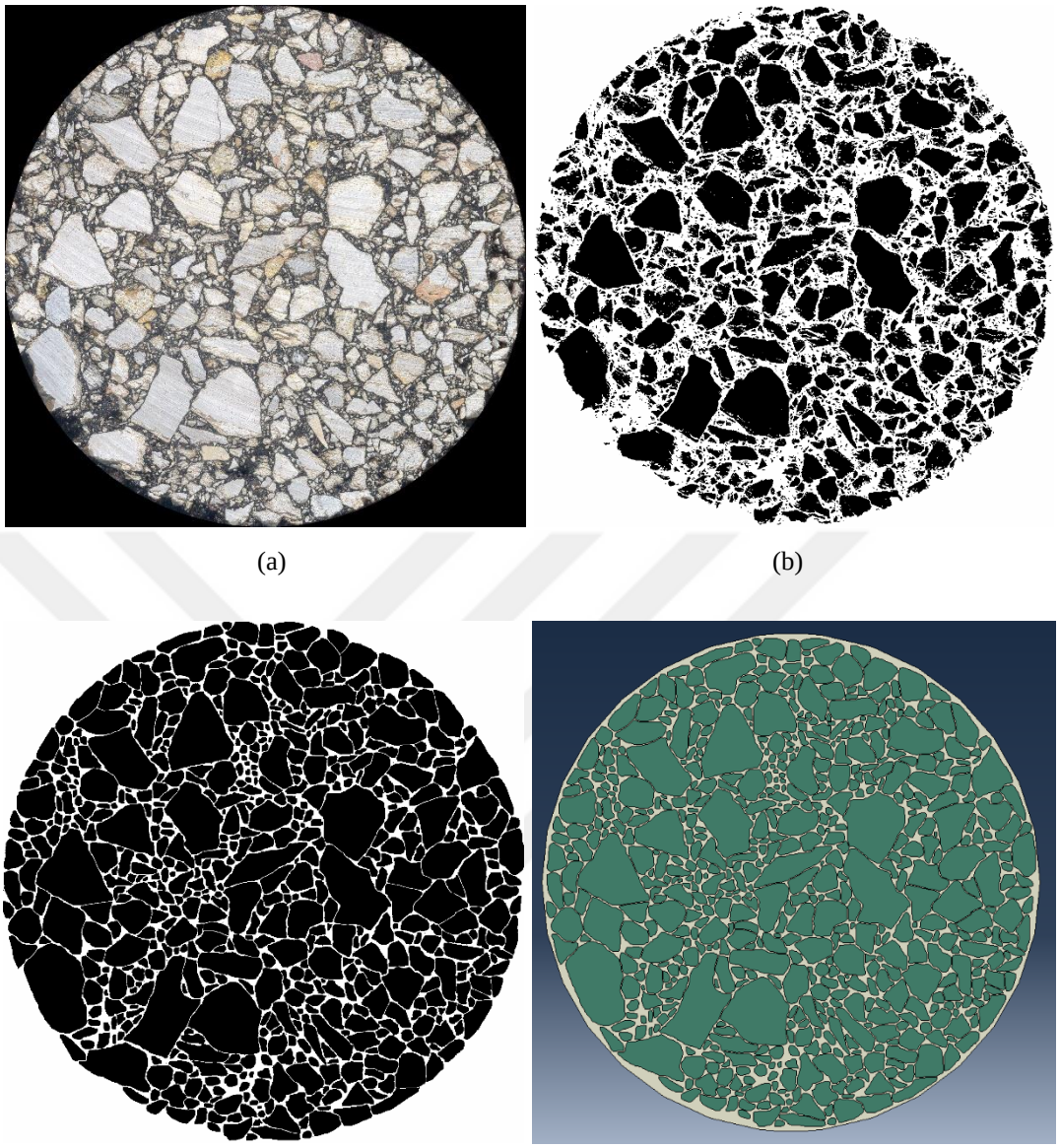

(a) (b)

(c) (d)

Figure G.10. Sample ID LURM12-1: a) Captured RGB image, b) Binary form, c) Processed image, d) 2D FE model in ABAQUS

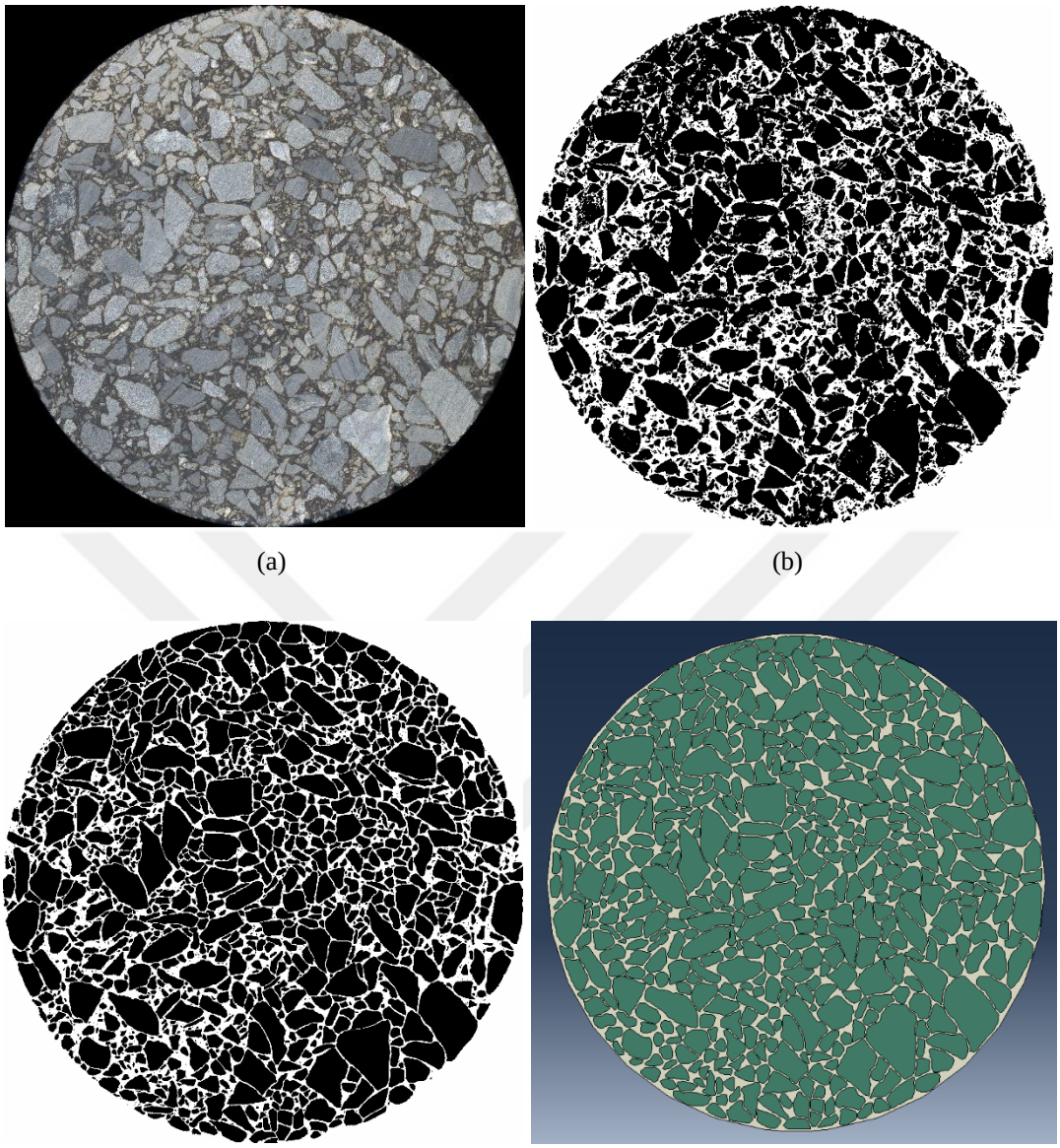

(a) (b)

(c) (d)

Figure G.11. Sample ID BMRM01-1: a) Captured RGB image, b) Binary form, c) Processed image, d) 2D FE model in ABAQUS

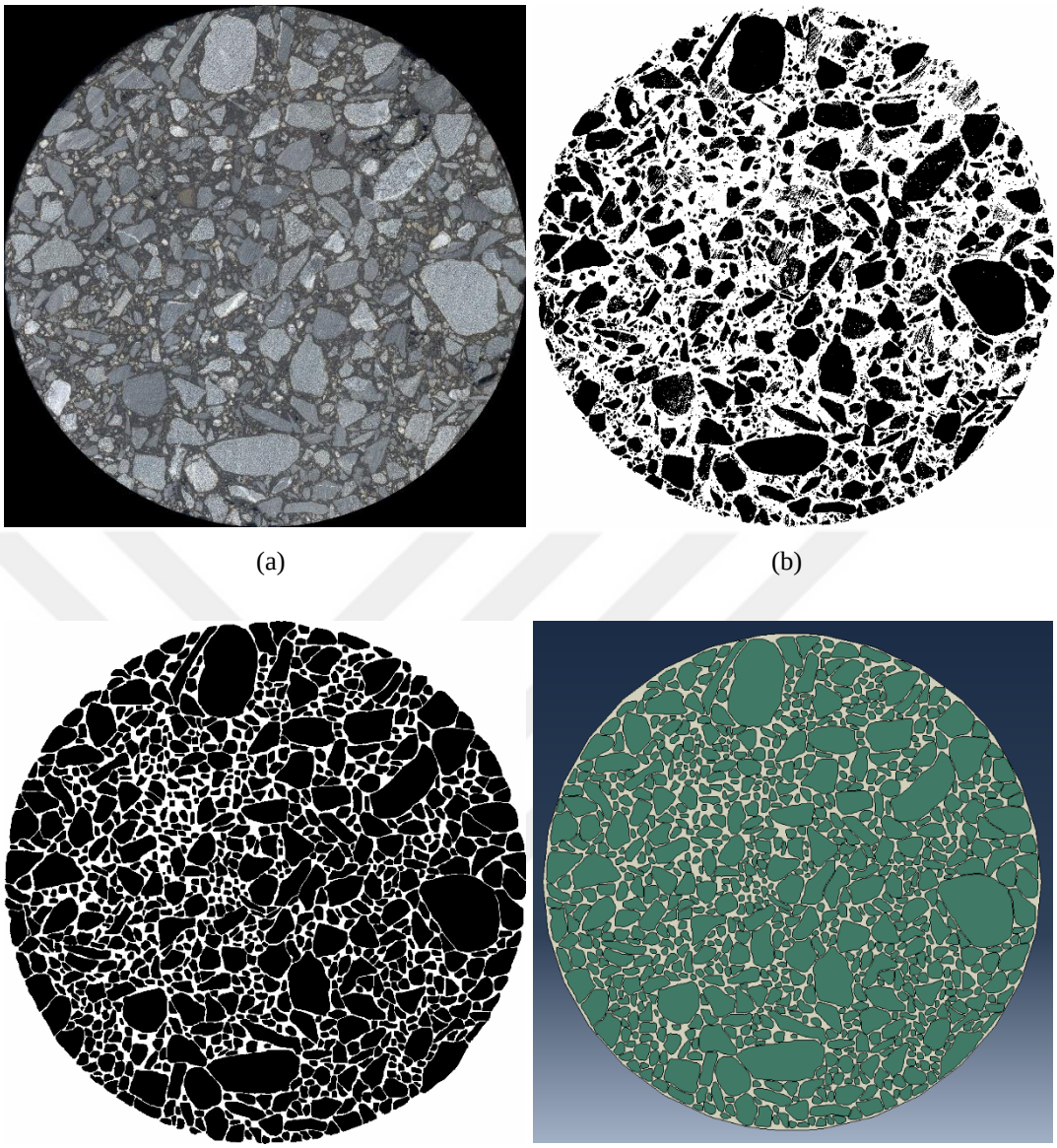

(a) (b)

(c) (d)

Figure G.12. Sample ID BMRM02-1: a) Captured RGB image, b) Binary form, c) Processed image, d) 2D FE model in ABAQUS

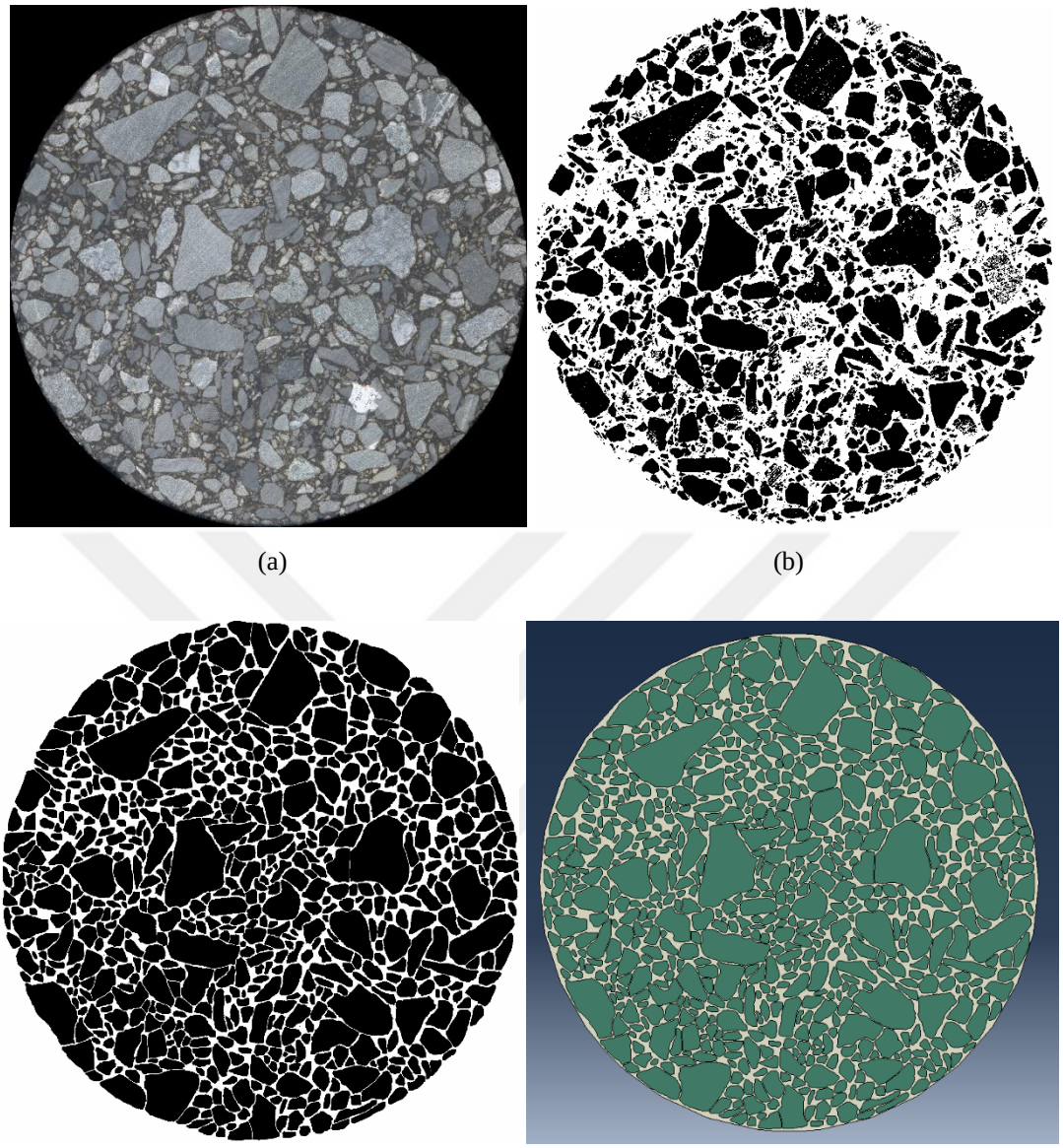

(a) (b)

(c) (d)

Figure G.13. Sample ID BMRM07-1: a) Captured RGB image, b) Binary form, c) Processed image, d) 2D FE model in ABAQUS

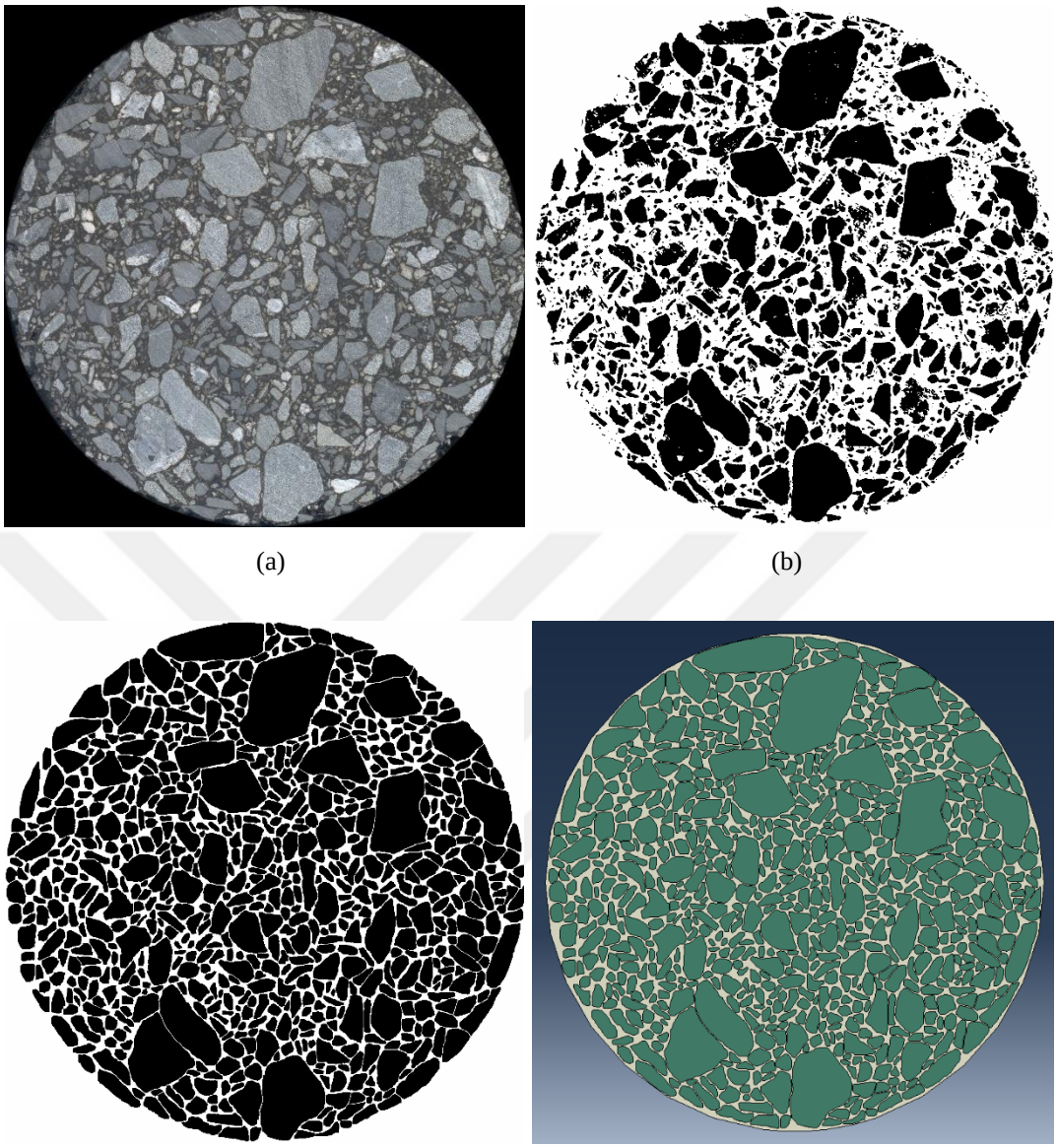

(a) (b)

(c) (d)

Figure G.14. Sample ID BMRM08-1: a) Captured RGB image, b) Binary form, c) Processed image, d) 2D FE model in ABAQUS

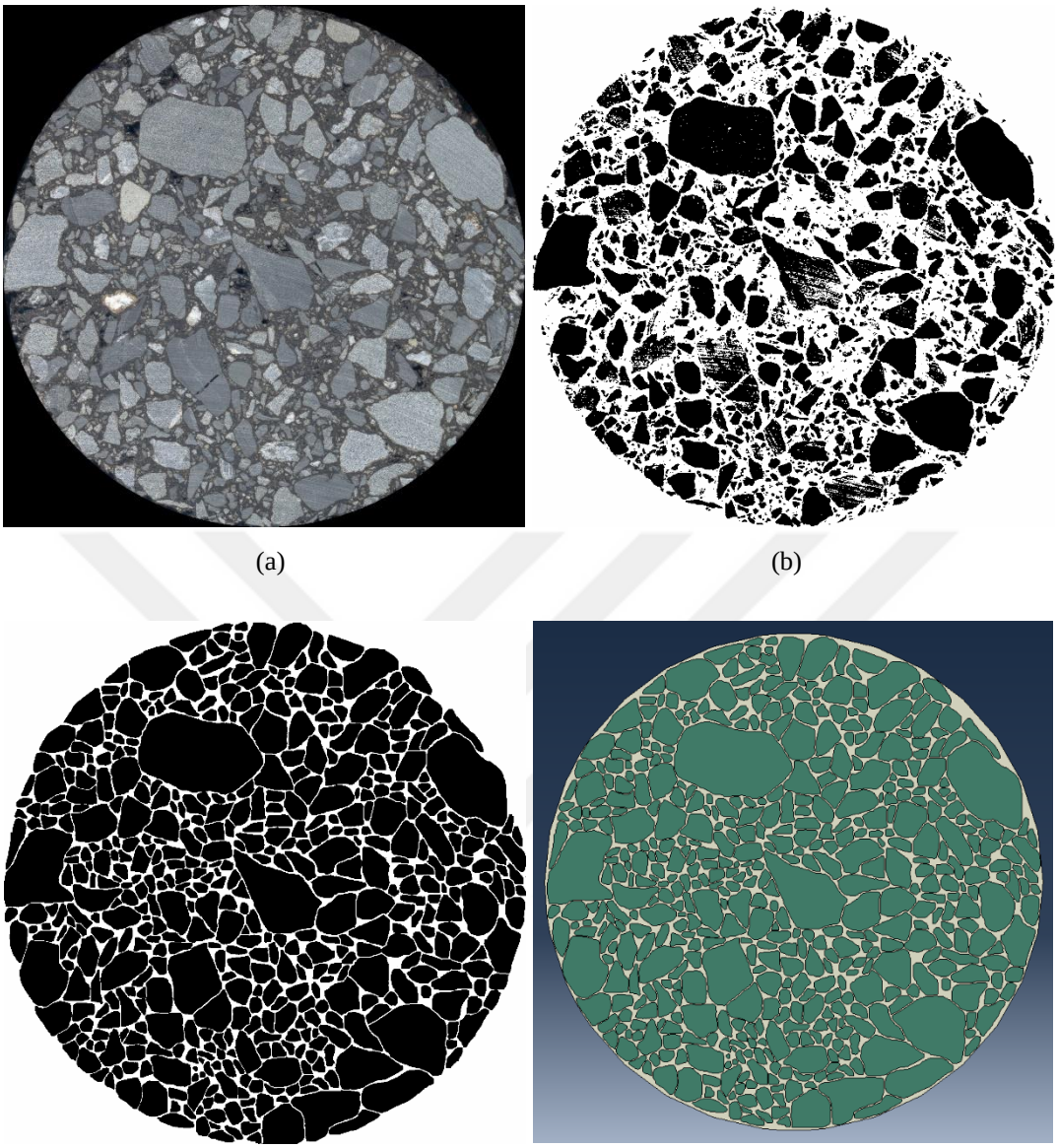

(a) (b)

(c) (d)

Figure G.15. Sample ID BMRM09-1: a) Captured RGB image, b) Binary form, c) Processed image, d) 2D FE model in ABAQUS

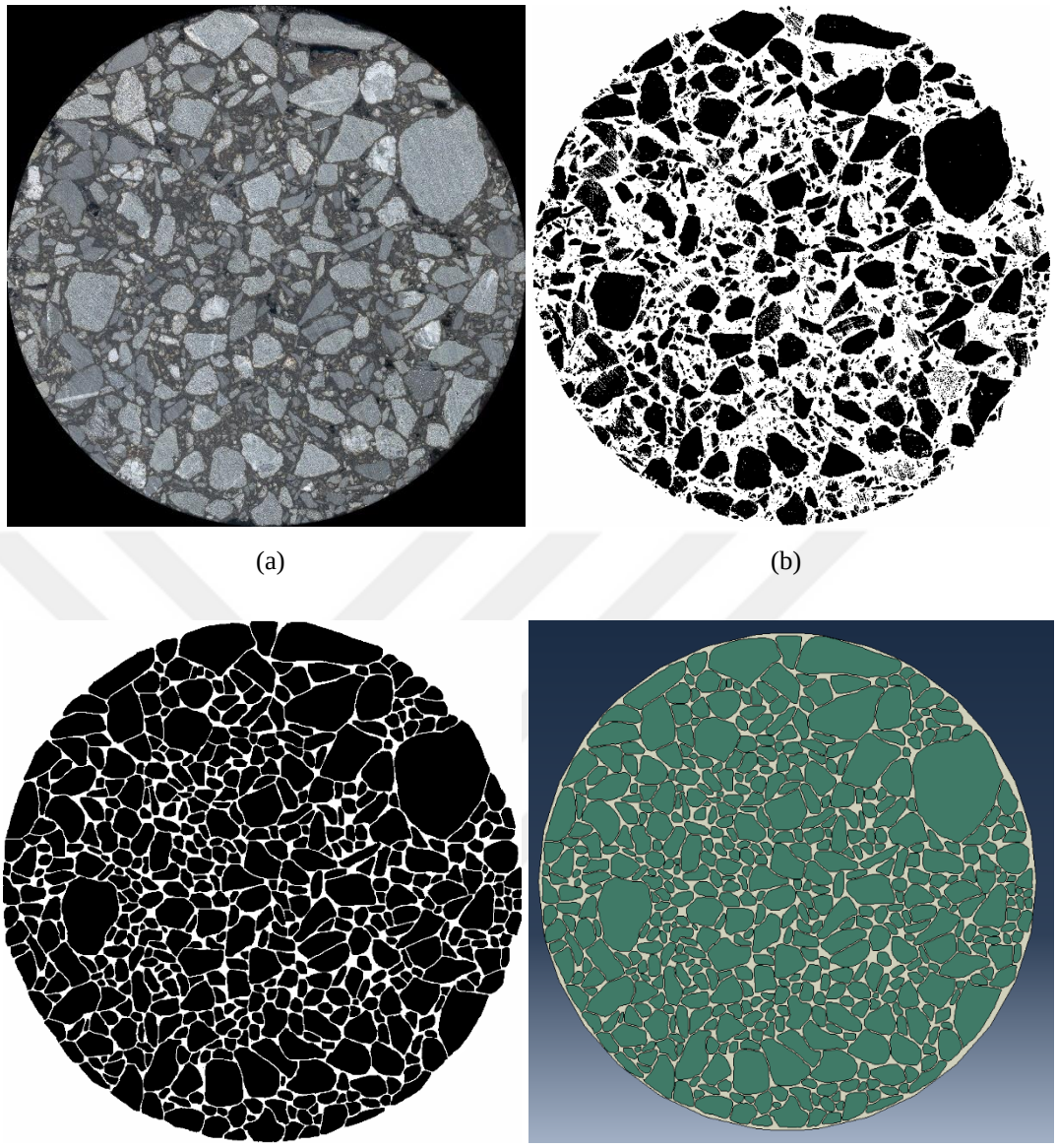

(a) (b)

(c) (d)

Figure G.16. Sample ID BMRM10-1: a) Captured RGB image, b) Binary form, c) Processed image, d) 2D FE model in ABAQUS

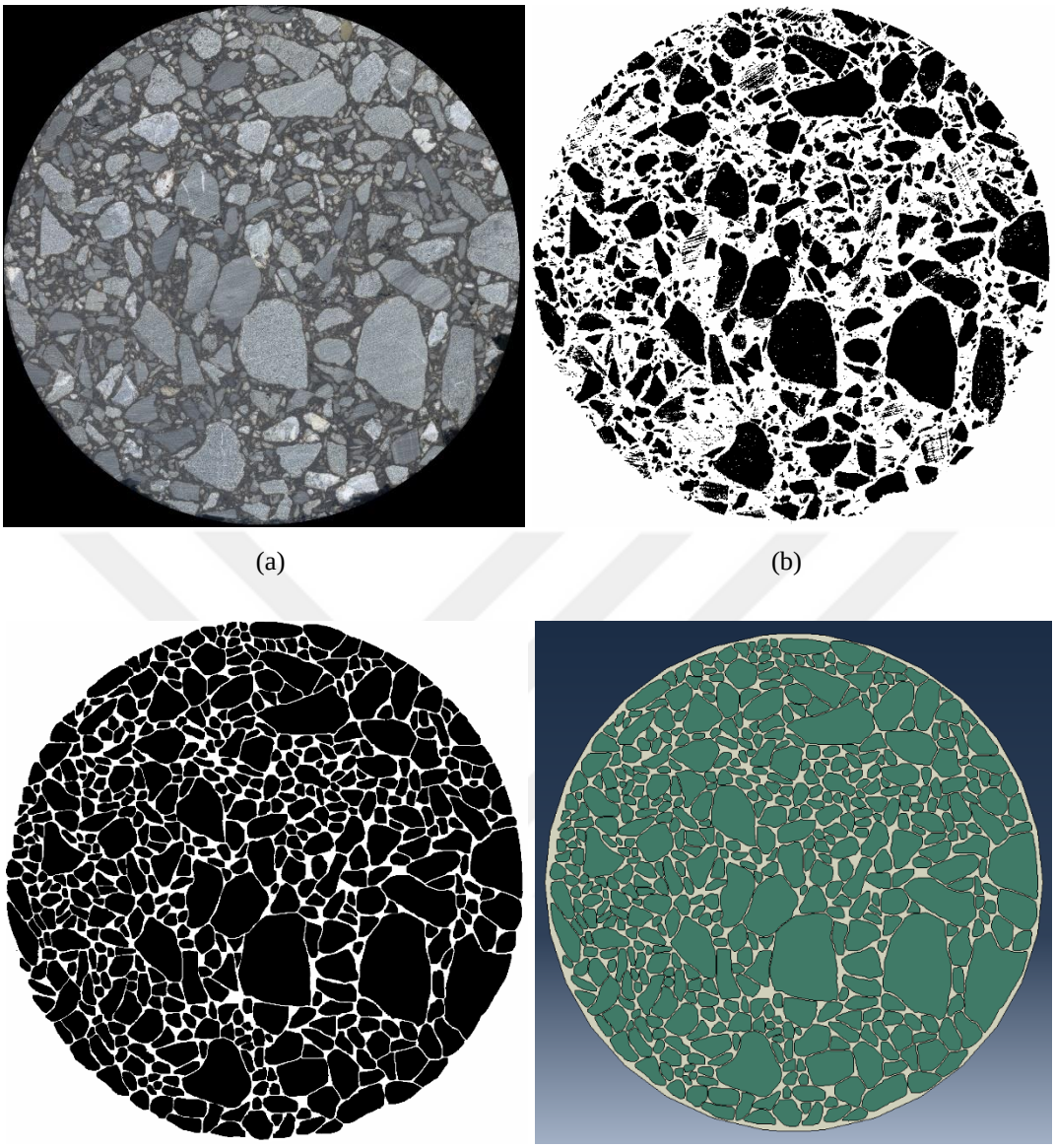

(a) (b)

(c) (d)

Figure G.17. Sample ID BMRM11-1: a) Captured RGB image, b) Binary form, c) Processed image, d) 2D FE model in ABAQUS

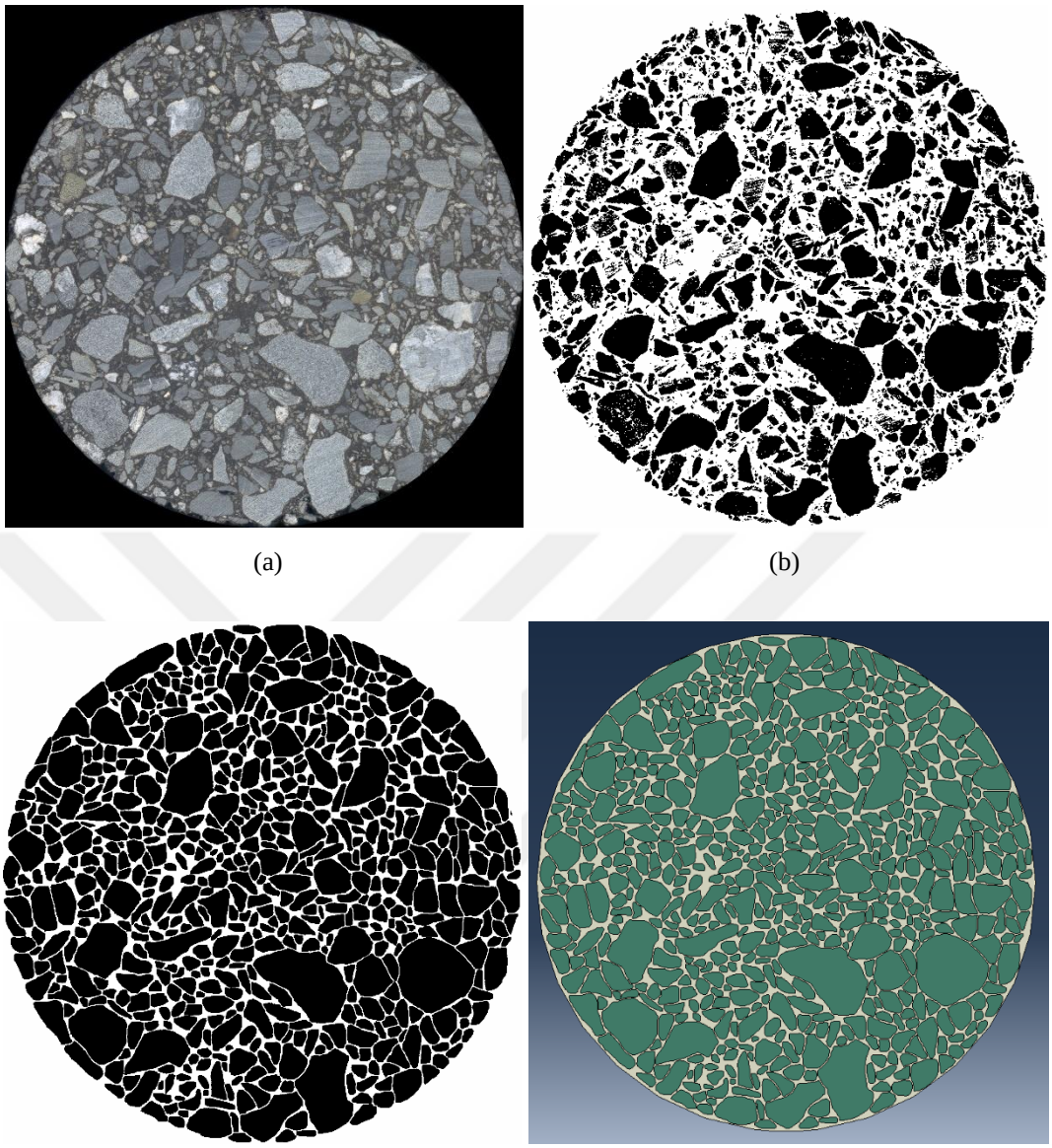

(a) (b)

(c) (d)

Figure G.18. Sample ID BMRM12-1: a) Captured RGB image, b) Binary form, c) Processed image, d) 2D FE model in ABAQUS

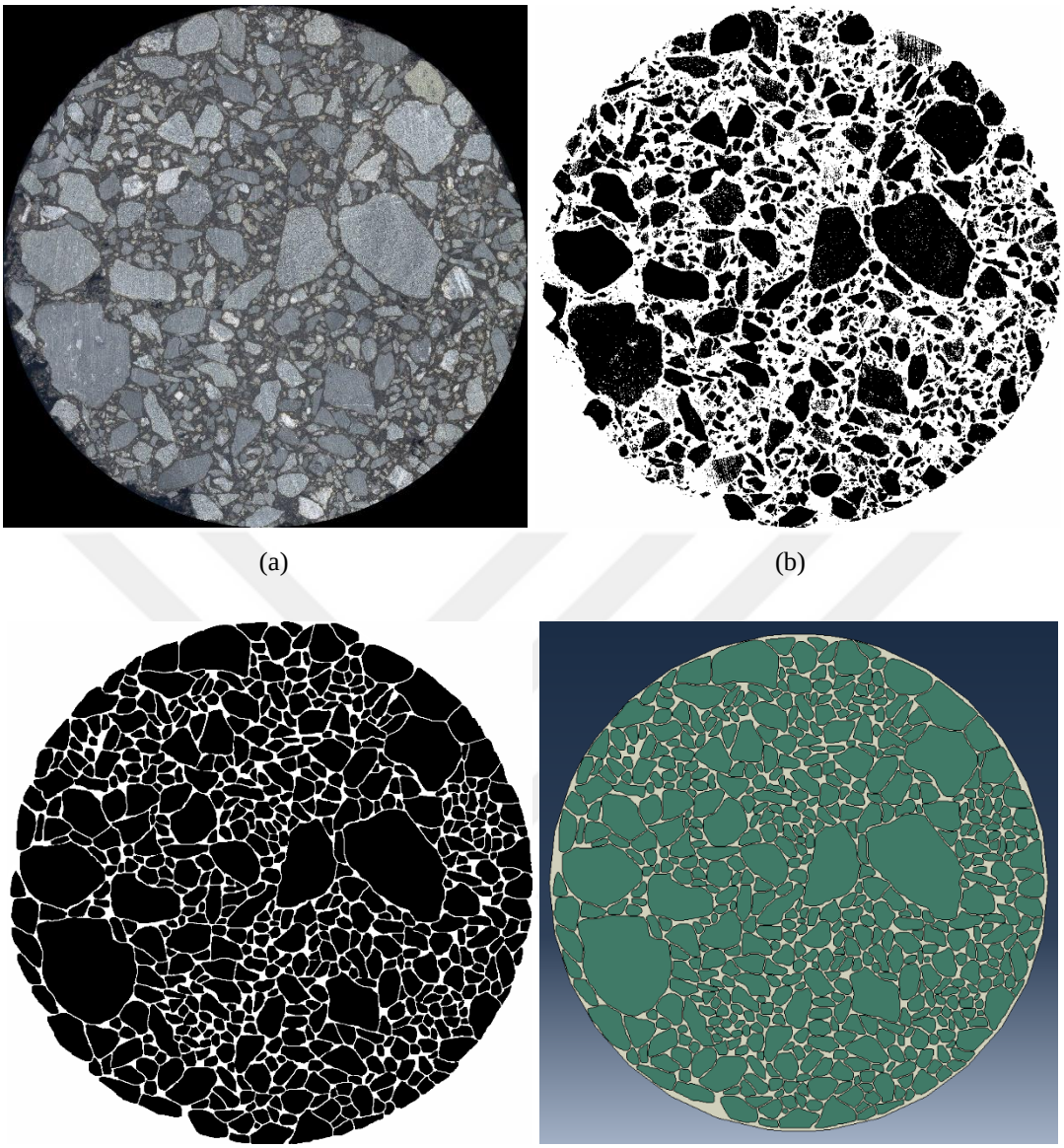

(a) (b)

(c) (d)

Figure G.19. Sample ID BMRM13-1: a) Captured RGB image, b) Binary form, c) Processed image, d) 2D FE model in ABAQUS

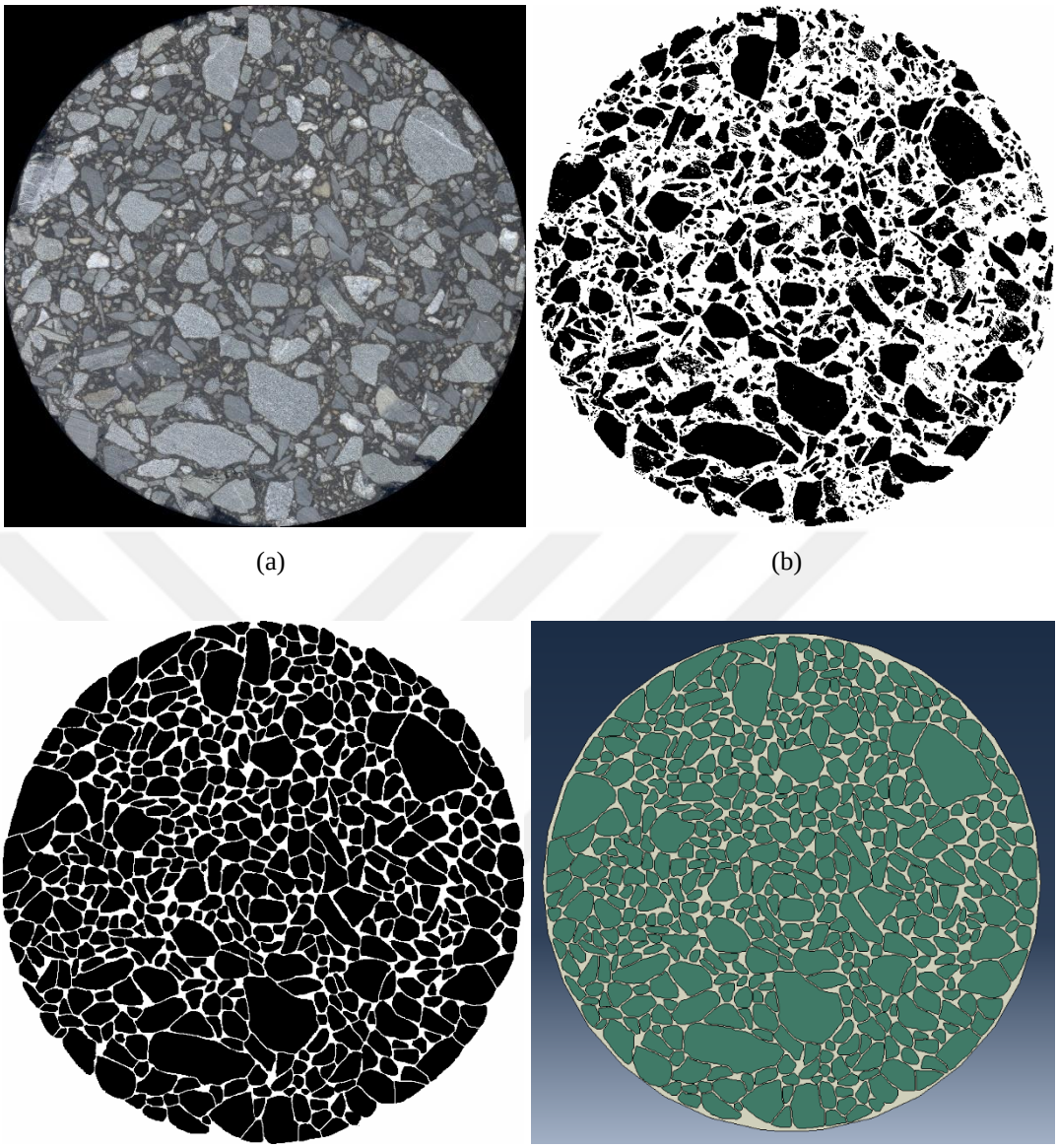

(a) (b)

(c) (d)

Figure G.20. Sample ID BMRM14-1: a) Captured RGB image, b) Binary form, c) Processed image, d) 2D FE model in ABAQUS

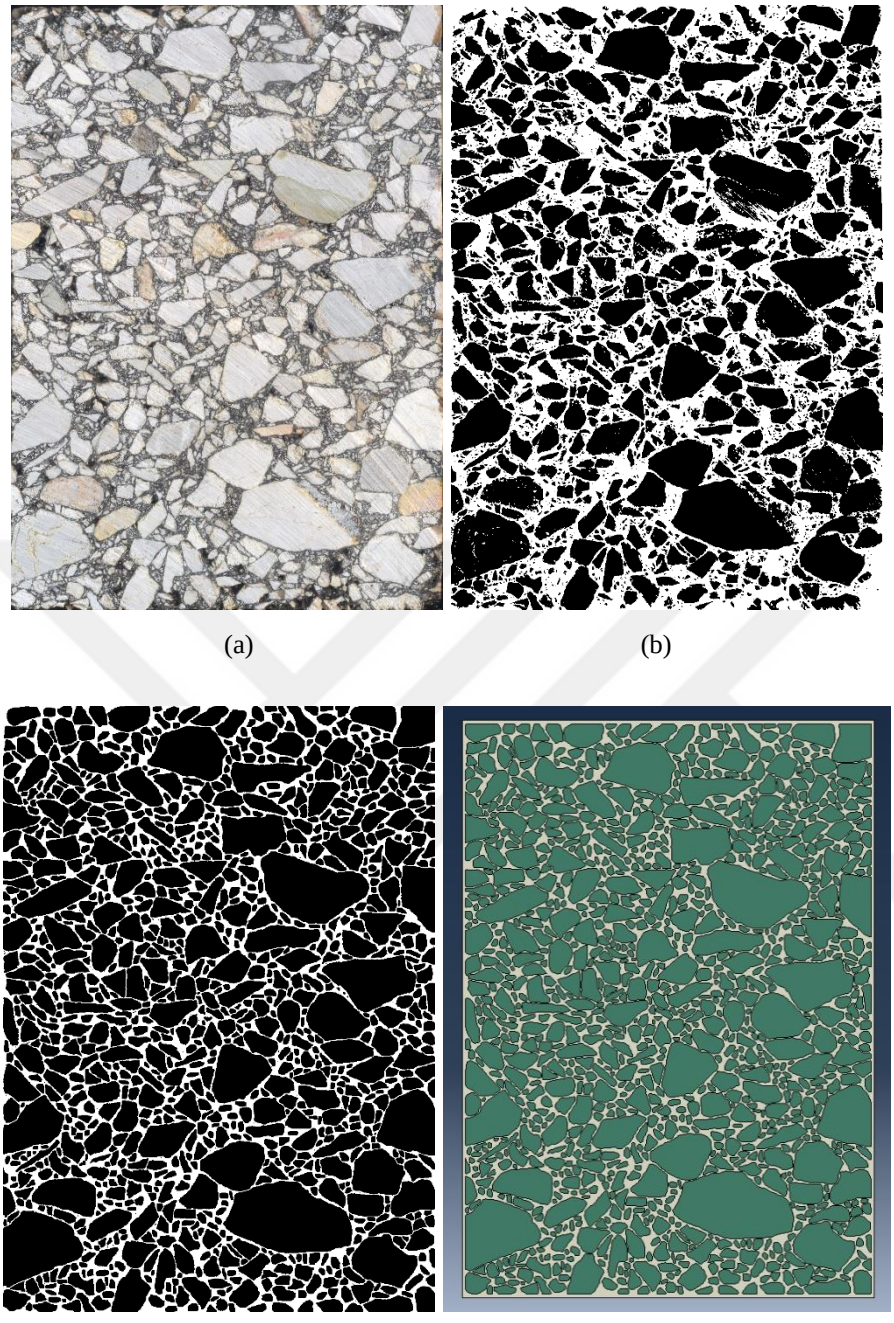

(a) (b)

(c) (d)

Figure G.21. Sample ID LUCR03: a) Captured RGB image, b) Binary form, c) Processed image, d) 2D FE model in ABAQUS

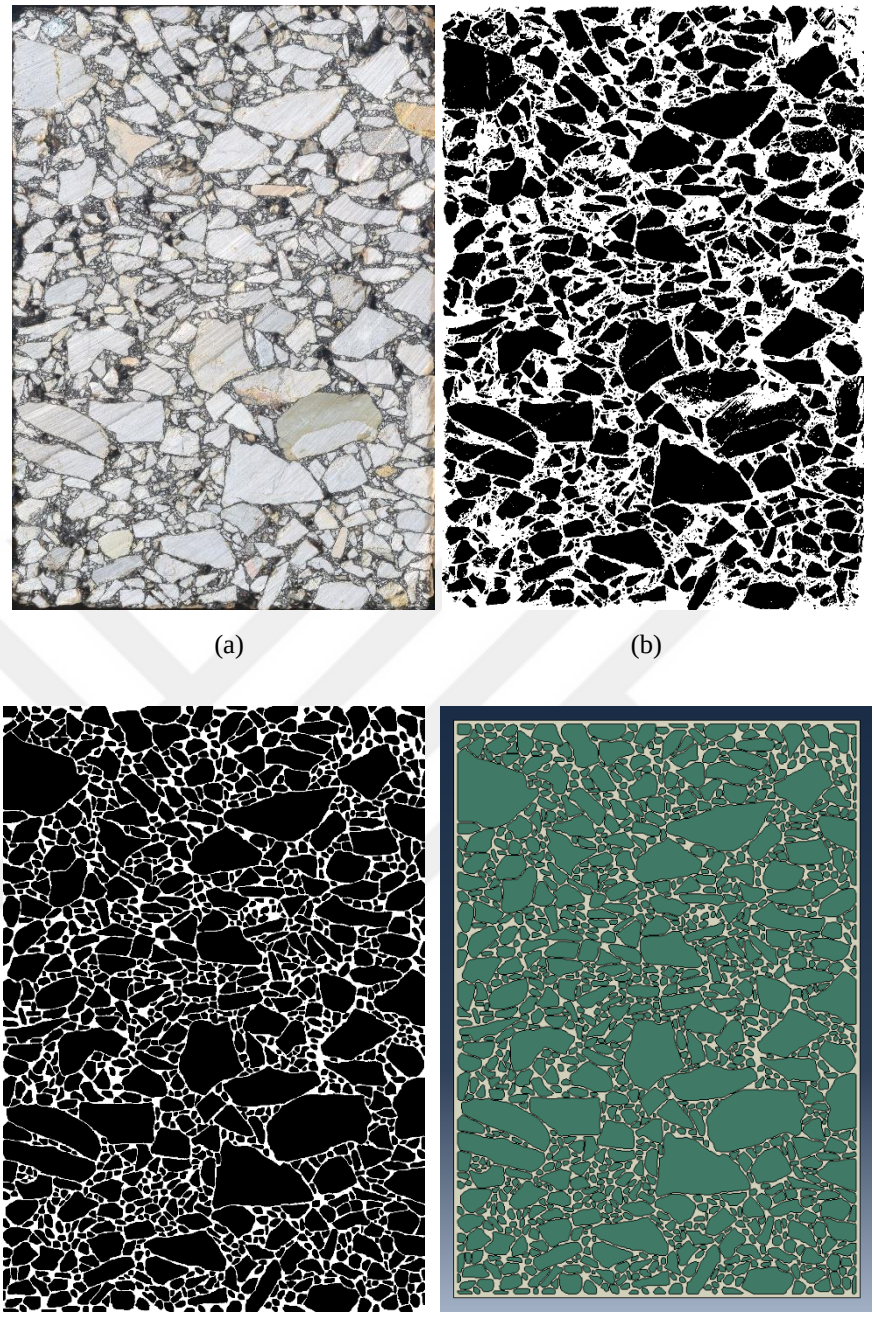

(a) (b)

(c) (d)

Figure G.22. Sample ID LUCR05: a) Captured RGB image, b) Binary form, c) Processed image, d) 2D FE model in ABAQUS

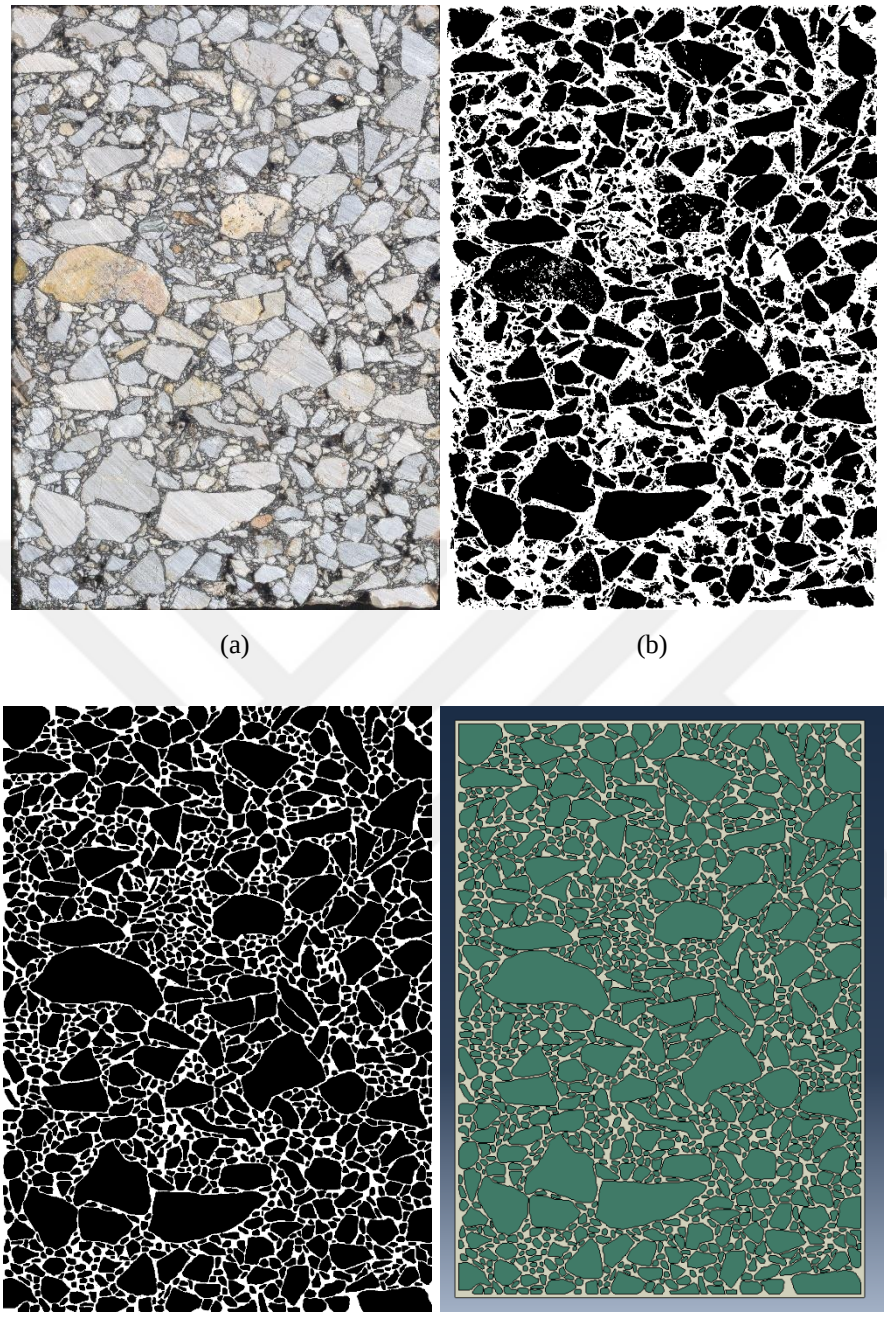

(a) (b)

(c) (d)

Figure G.23. Sample ID LUCR06: a) Captured RGB image, b) Binary form, c) Processed image, d) 2D FE model in ABAQUS

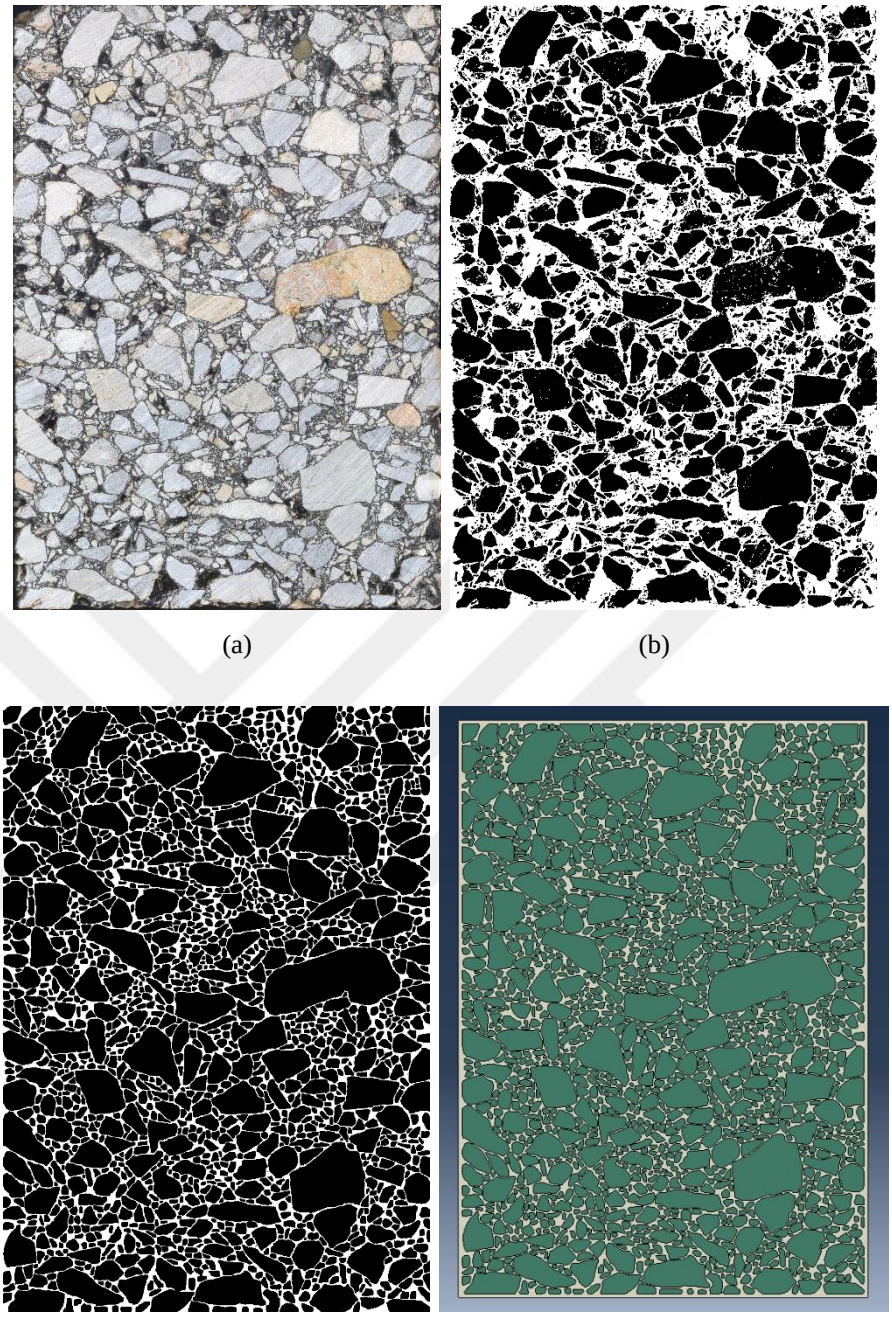

(a) (b)

(c) (d)

Figure G.24. Sample ID LUCR07: a) Captured RGB image, b) Binary form, c) Processed image, d) 2D FE model in ABAQUS

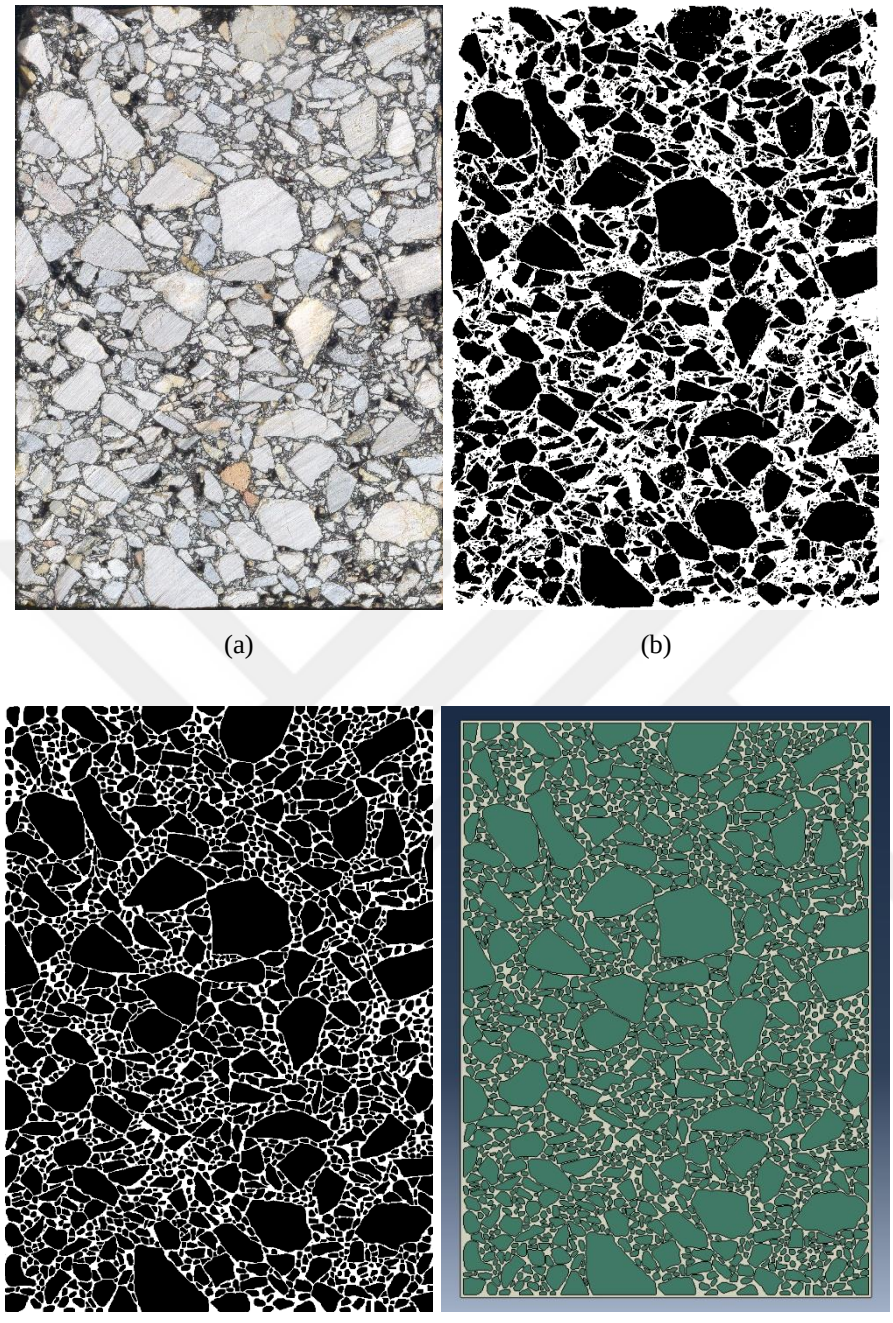

(a) (b)

(c) (d)

Figure G.25. Sample ID LUCR08: a) Captured RGB image, b) Binary form, c) Processed image, d) 2D FE model in ABAQUS

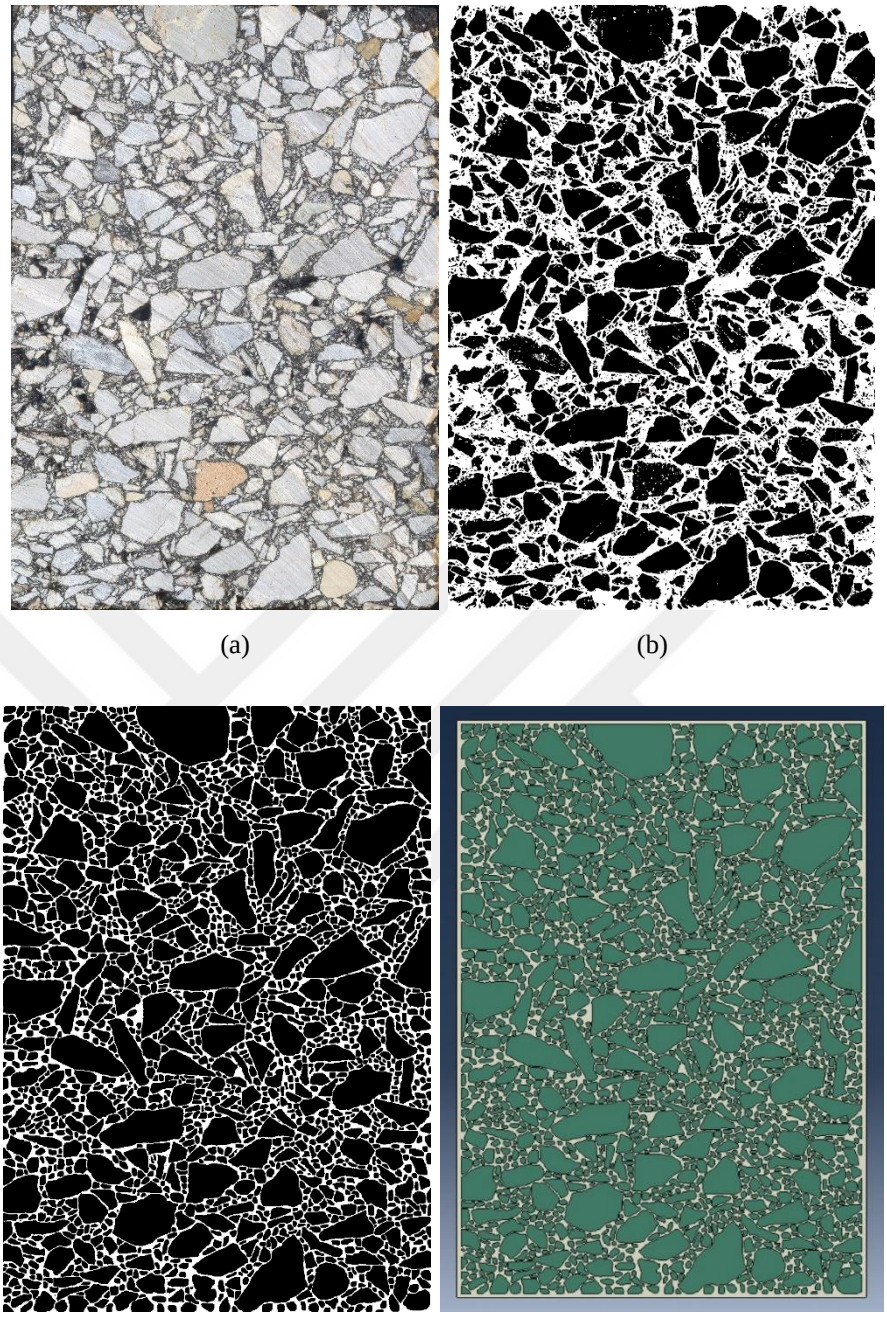

(a) (b)

(c) (d)

Figure G.26. Sample ID LUCR09: a) Captured RGB image, b) Binary form, c) Processed image, d) 2D FE model in ABAQUS

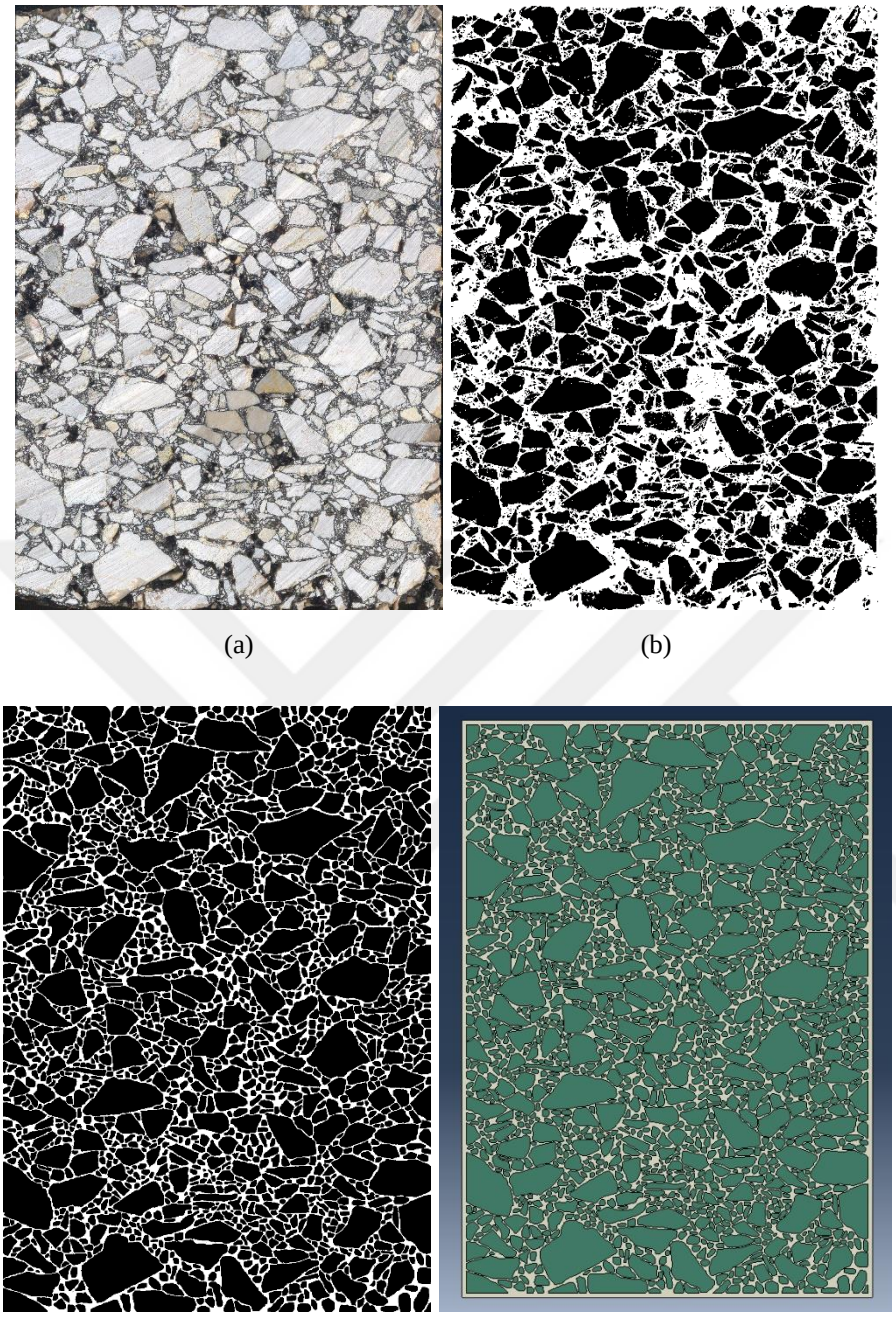

(a) (b)

(c) (d)

Figure G.27. Sample ID LUCR10: a) Captured RGB image, b) Binary form, c) Processed image, d) 2D FE model in ABAQUS

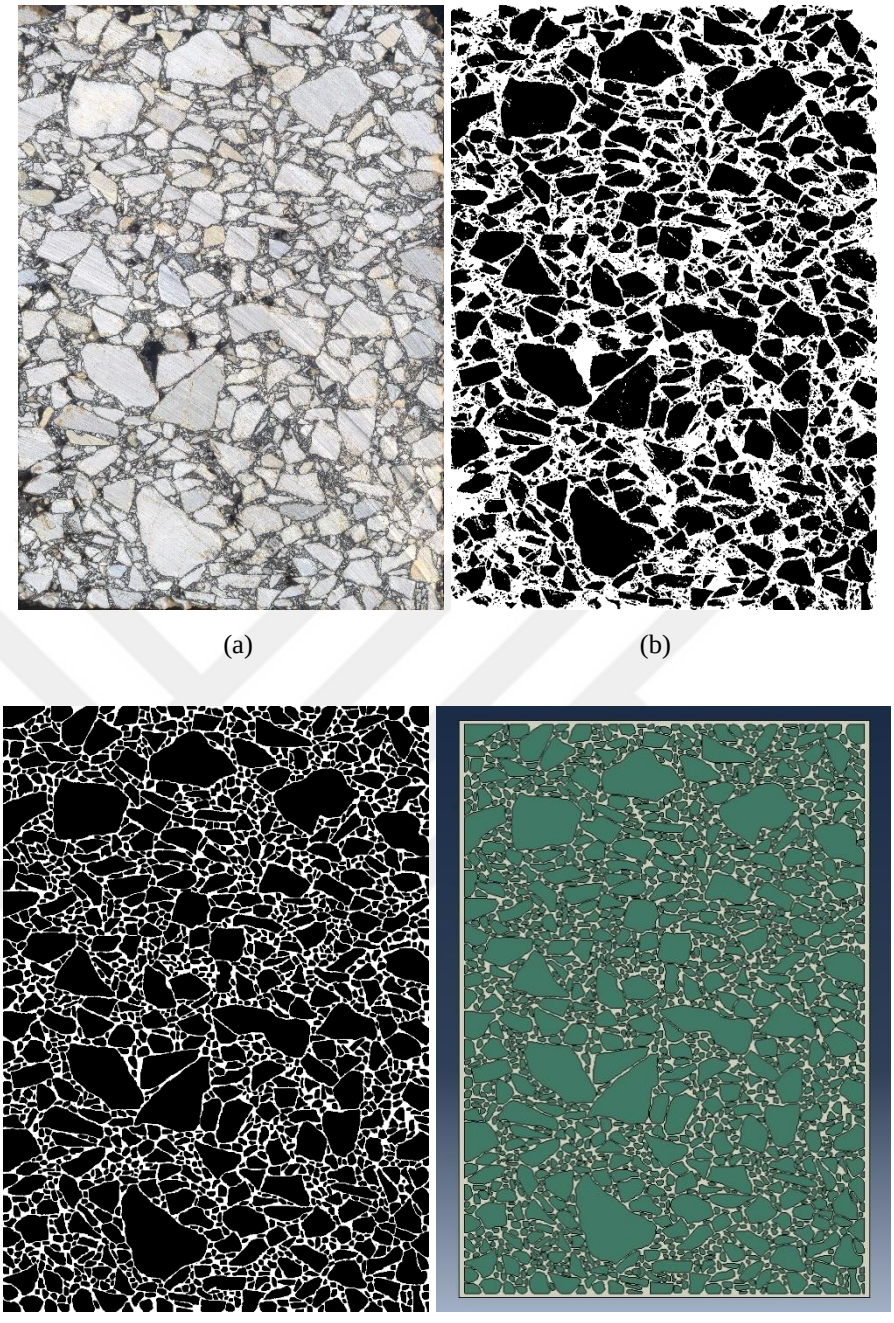

(a) (b)

(c) (d)

Figure G.28. Sample ID LUCR11: a) Captured RGB image, b) Binary form, c) Processed image, d) 2D FE model in ABAQUS

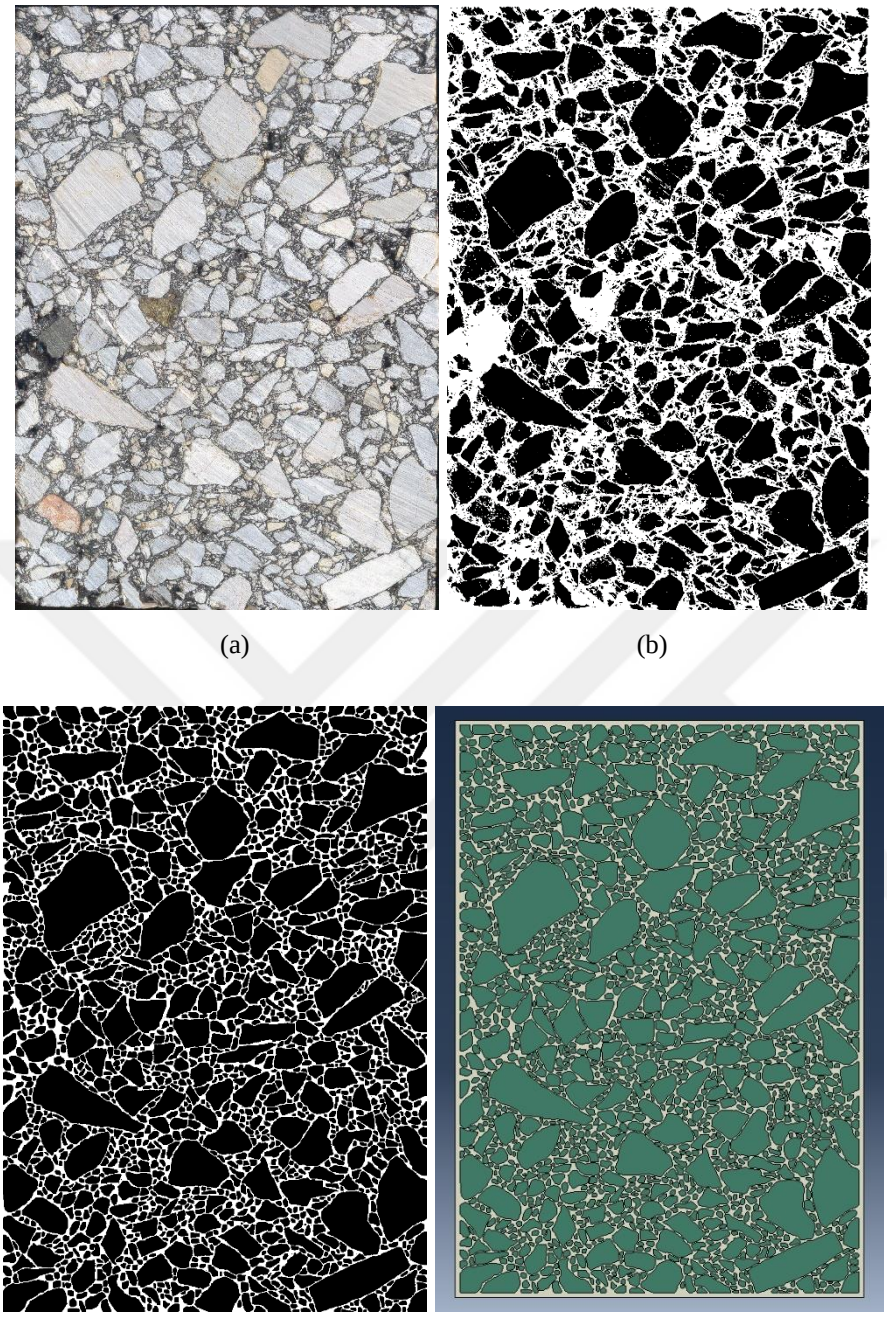

(a) (b)

(c) (d)

Figure G.29. Sample ID LUCR12: a) Captured RGB image, b) Binary form, c) Processed image, d) 2D FE model in ABAQUS

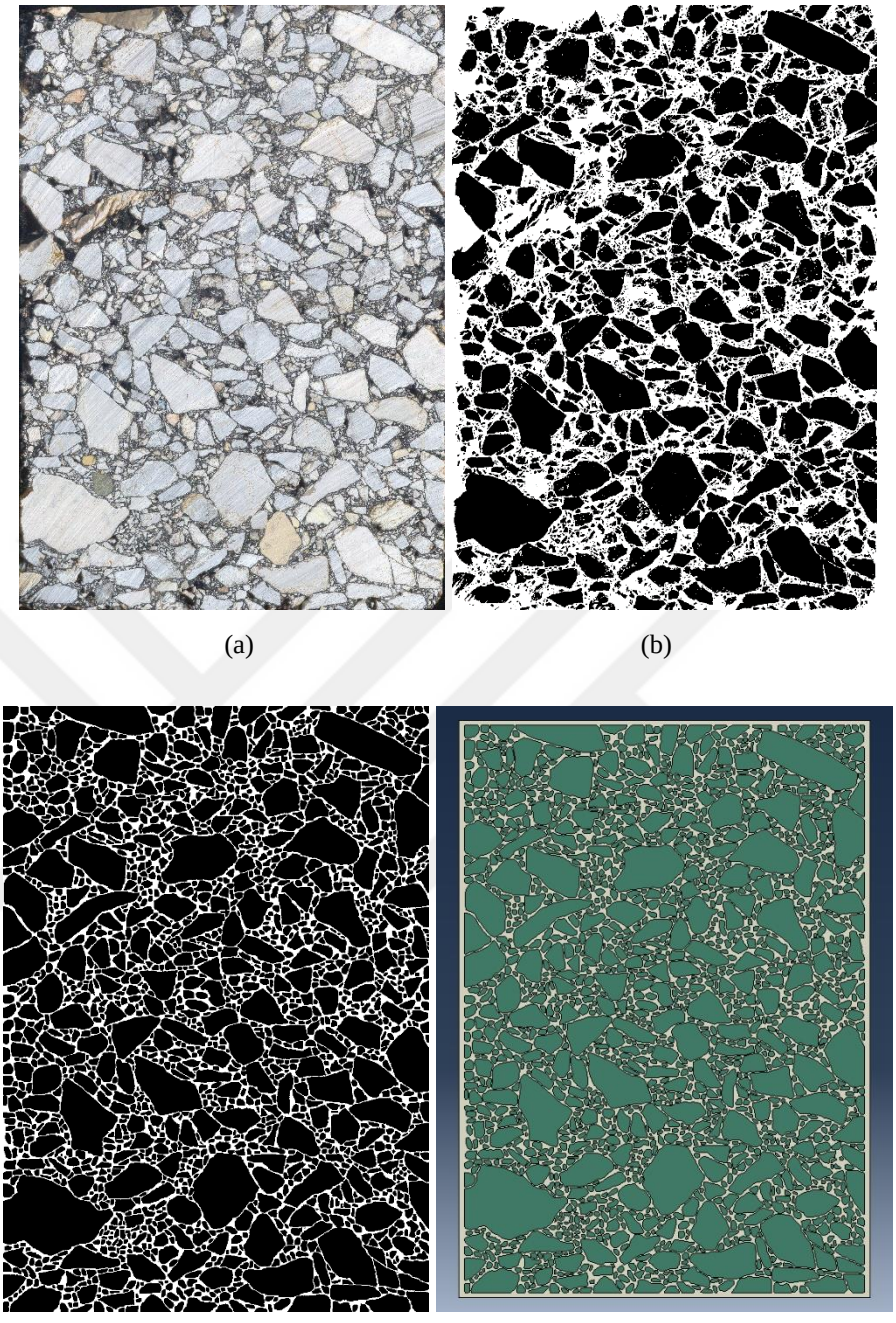

(a) (b)

(c) (d)

Figure G.30. Sample ID LUCR13: a) Captured RGB image, b) Binary form, c) Processed image, d) 2D FE model in ABAQUS

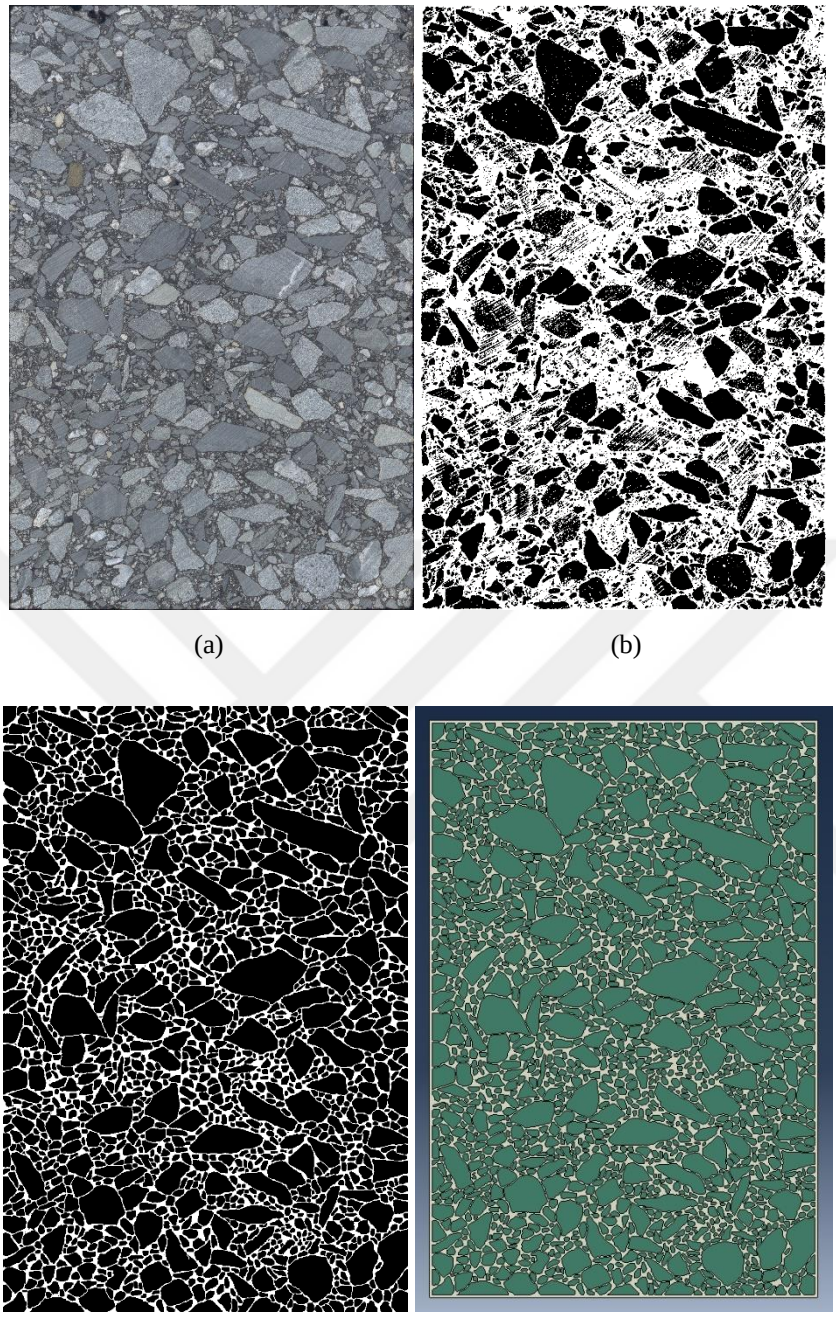

(a) (b)

(c) (d)

Figure G.31. Sample ID BMCR01: a) Captured RGB image, b) Binary form, c) Processed image, d) 2D FE model in ABAQUS

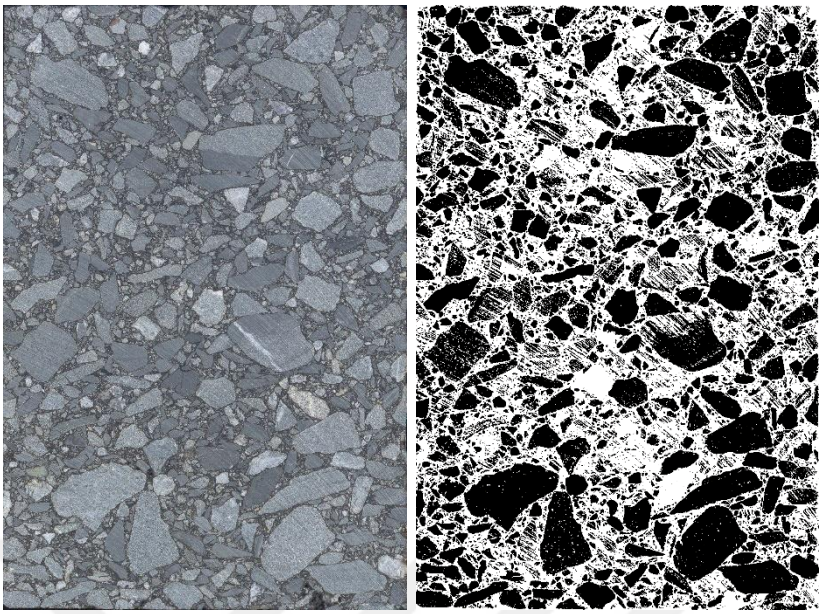

(a) (b)

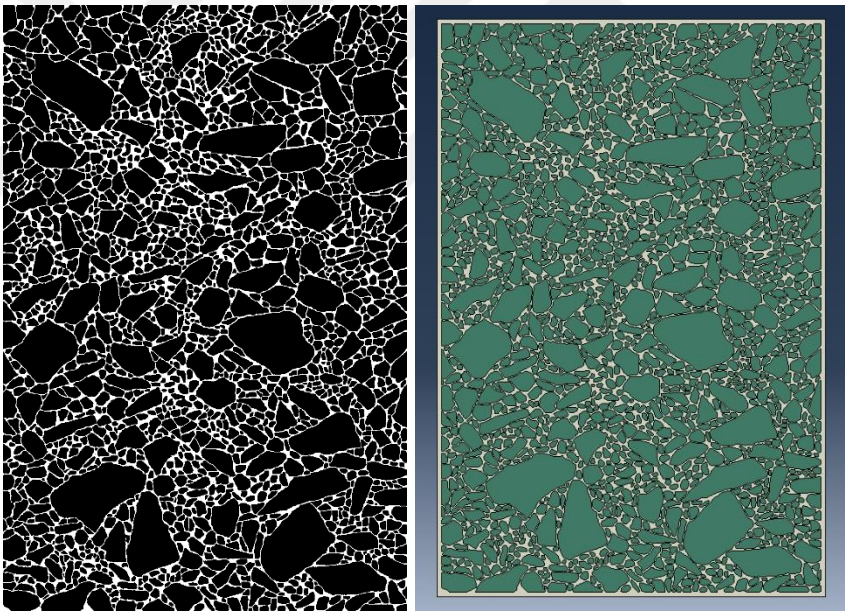

(c) (d)

Figure G.32. Sample ID BMCR02: a) Captured RGB image, b) Binary form, c) Processed image, d) 2D FE model in ABAQUS

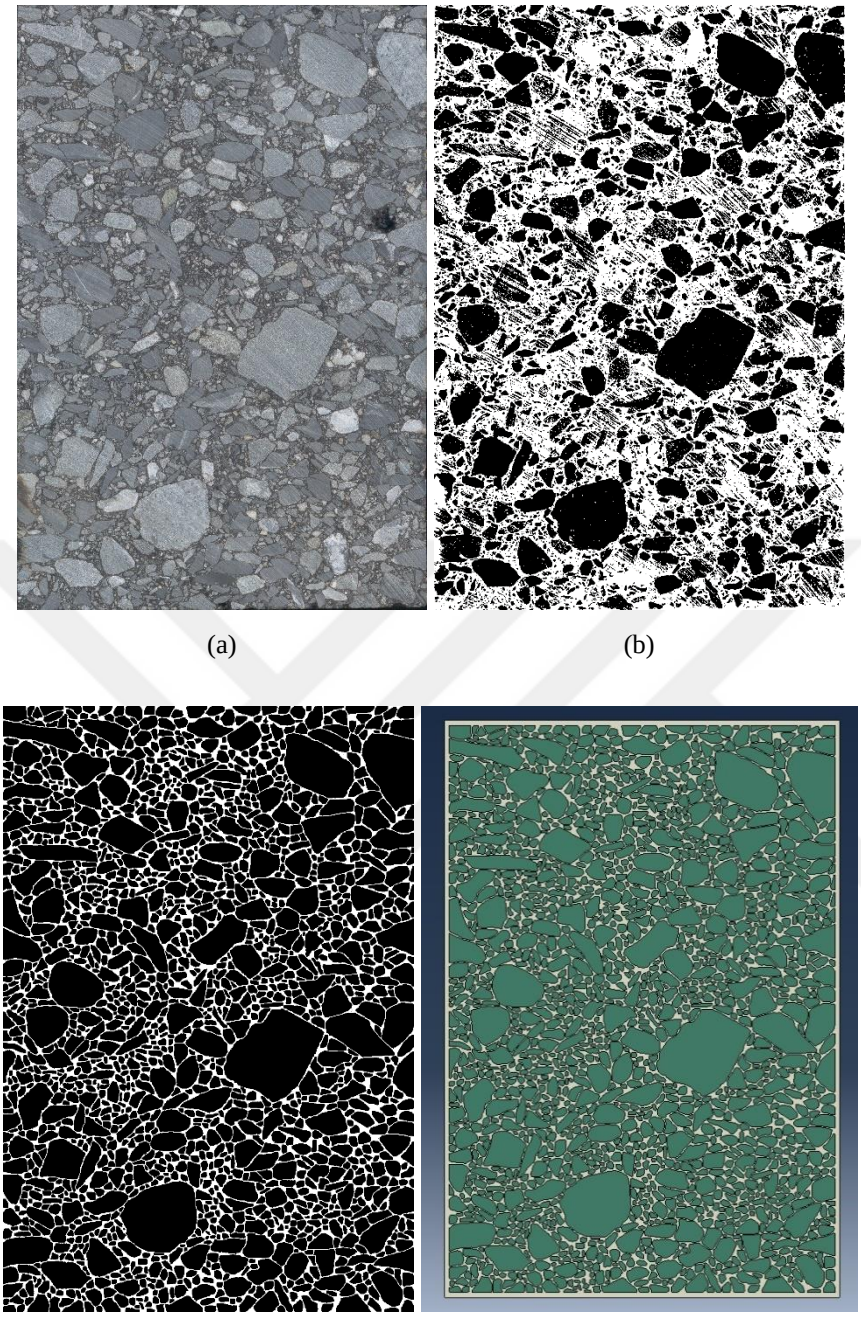

(a) (b)

(c) (d)

Figure G.33. Sample ID BMCR03: a) Captured RGB image, b) Binary form, c) Processed image, d) 2D FE model in ABAQUS

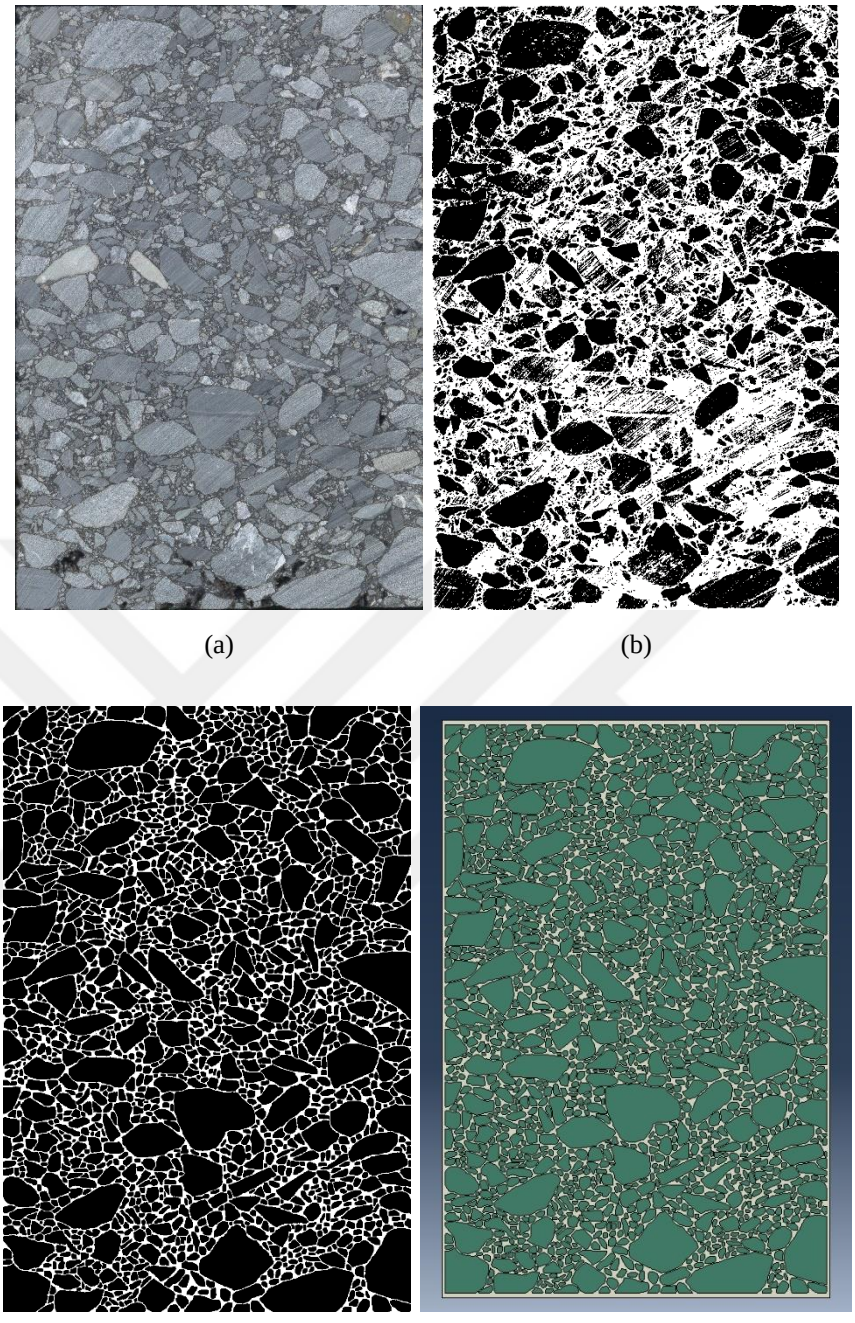

(a) (b)

(c) (d)

Figure G.34. Sample ID BMCR04: a) Captured RGB image, b) Binary form, c) Processed image, d) 2D FE model in ABAQUS

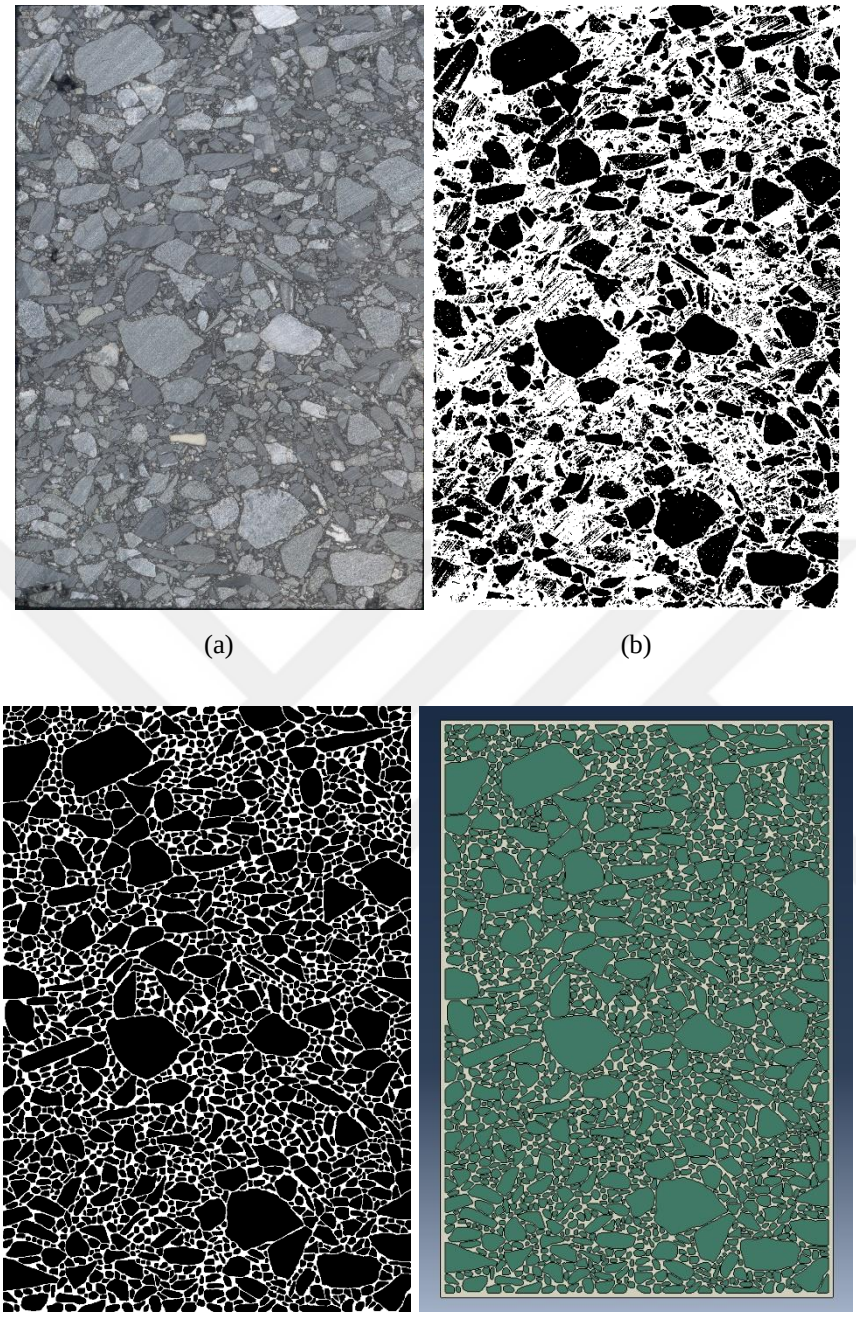

(a) (b)

(c) (d)

Figure G.35. Sample ID BMCR05: a) Captured RGB image, b) Binary form, c) Processed image, d) 2D FE model in ABAQUS

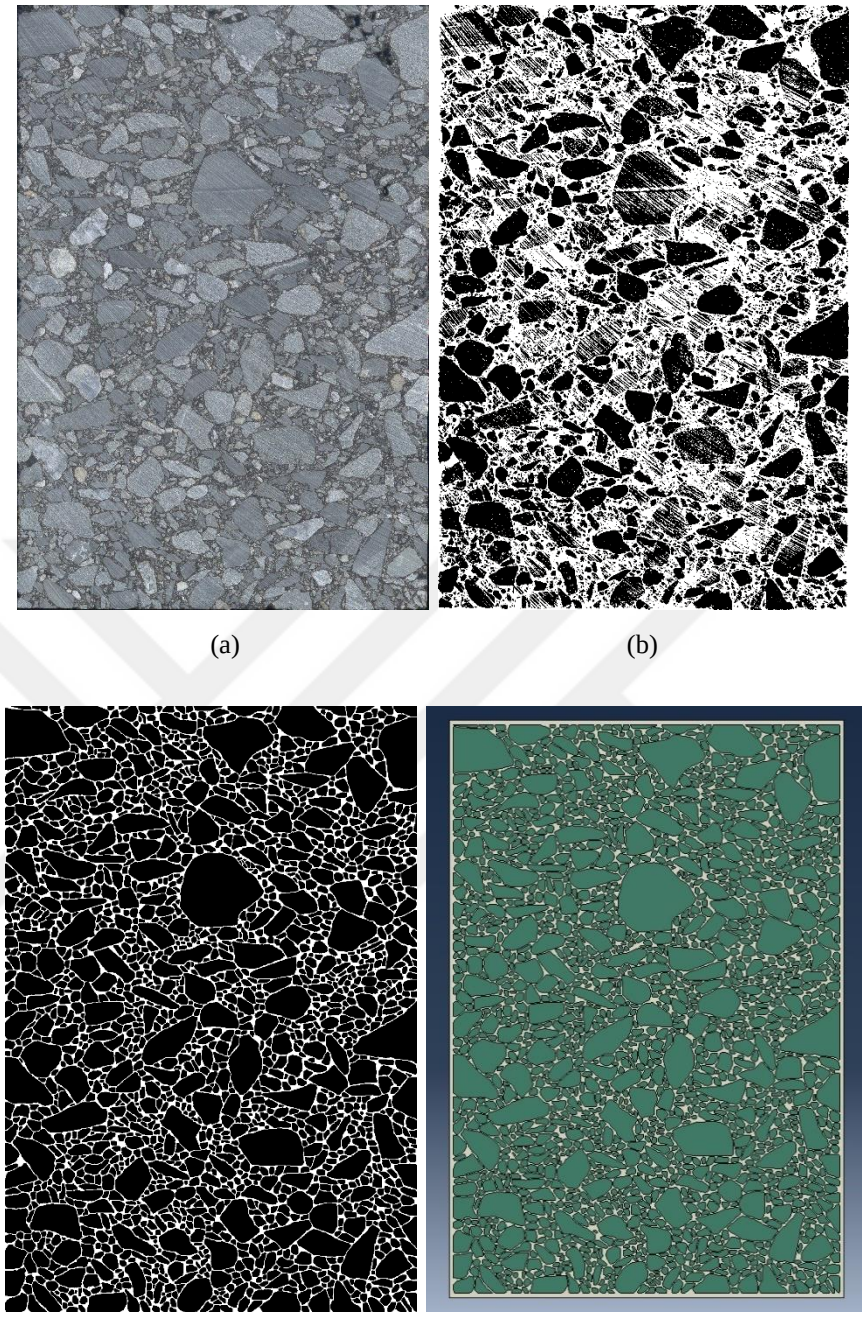

(a) (b)

(c) (d)

Figure G.36. Sample ID BMCR06: a) Captured RGB image, b) Binary form, c) Processed image, d) 2D FE model in ABAQUS

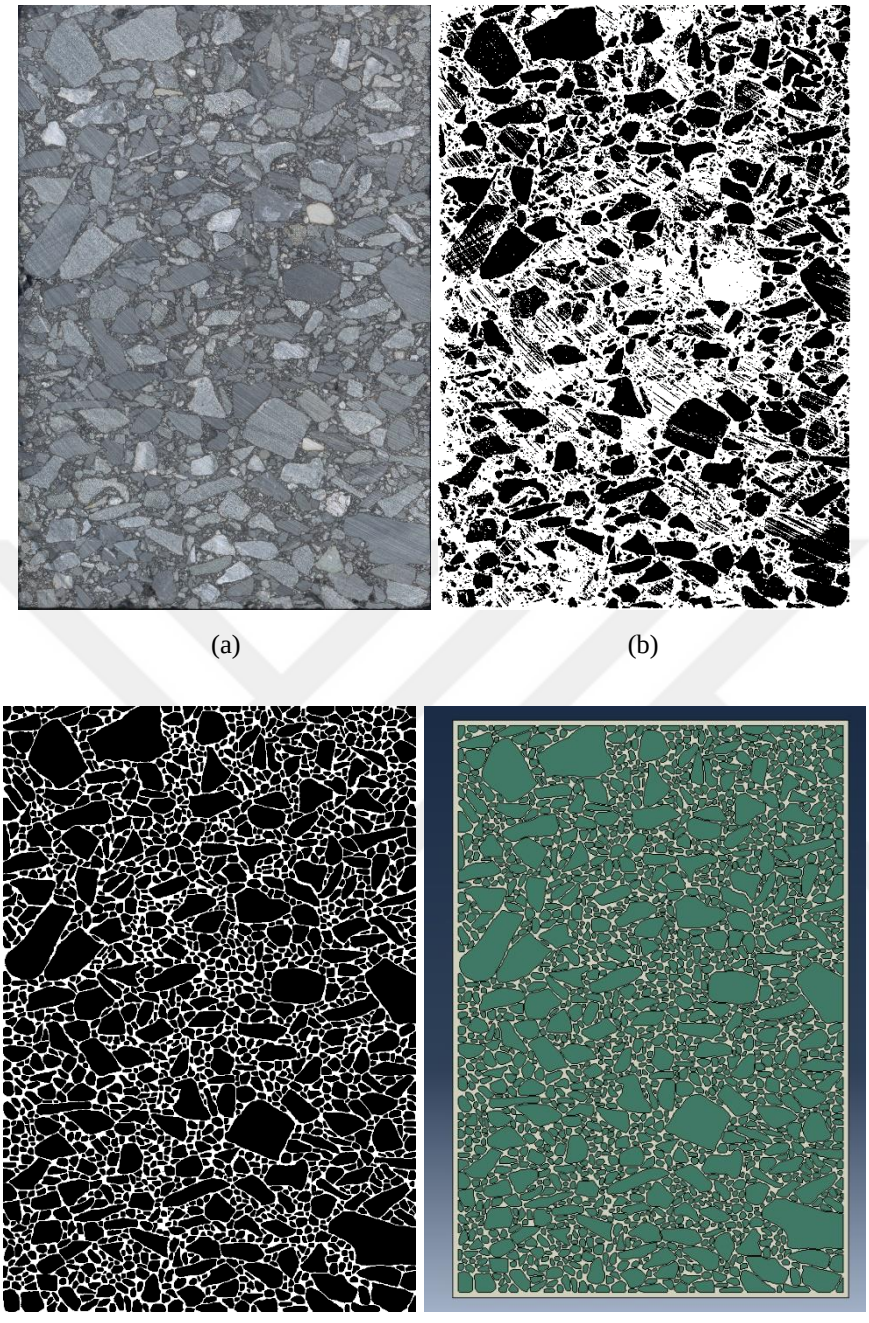

(a) (b)

(c) (d)

Figure G.37. Sample ID BMCR07: a) Captured RGB image, b) Binary form, c) Processed image, d) 2D FE model in ABAQUS

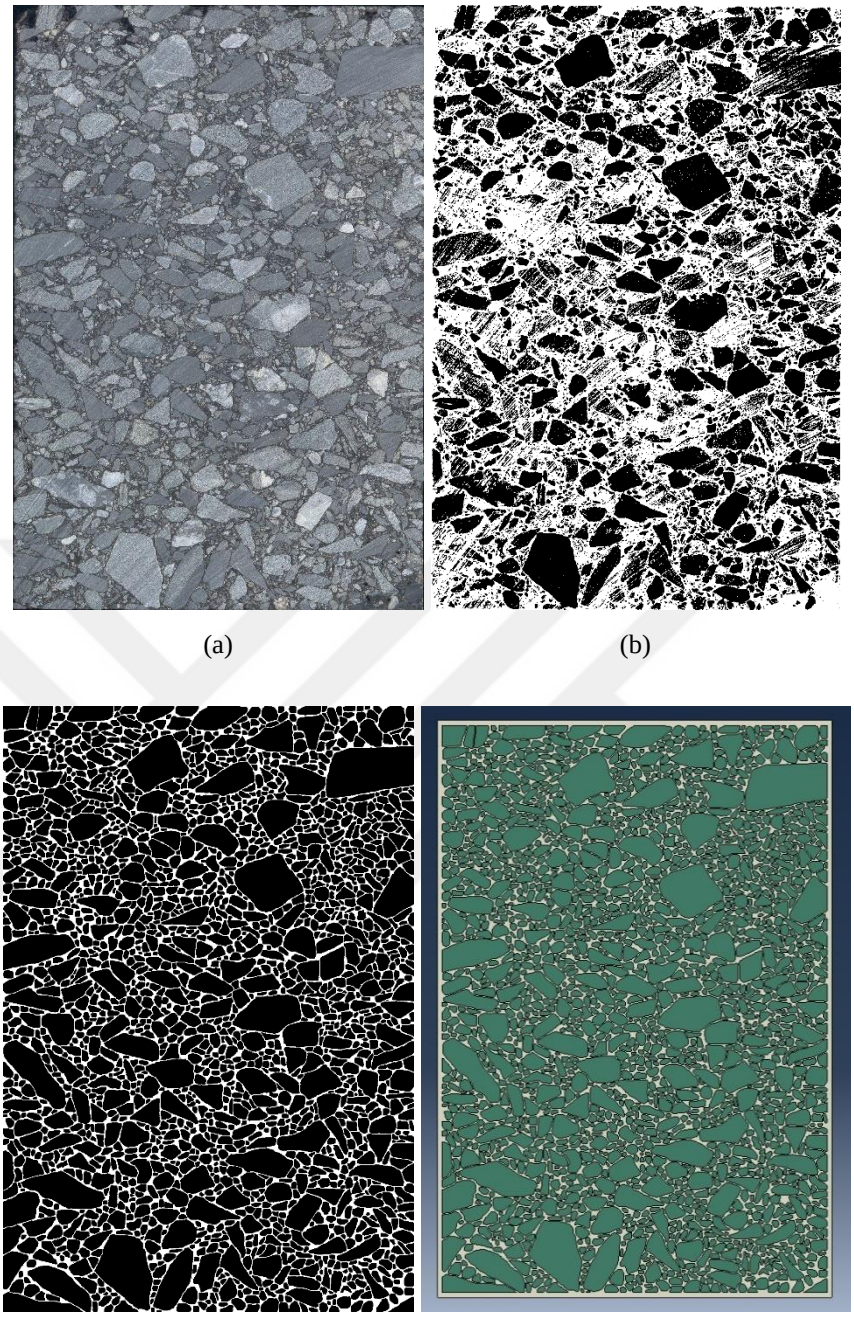

(a) (b)

(c) (d)

Figure G.38. Sample ID BMCR08: a) Captured RGB image, b) Binary form, c) Processed image, d) 2D FE model in ABAQUS

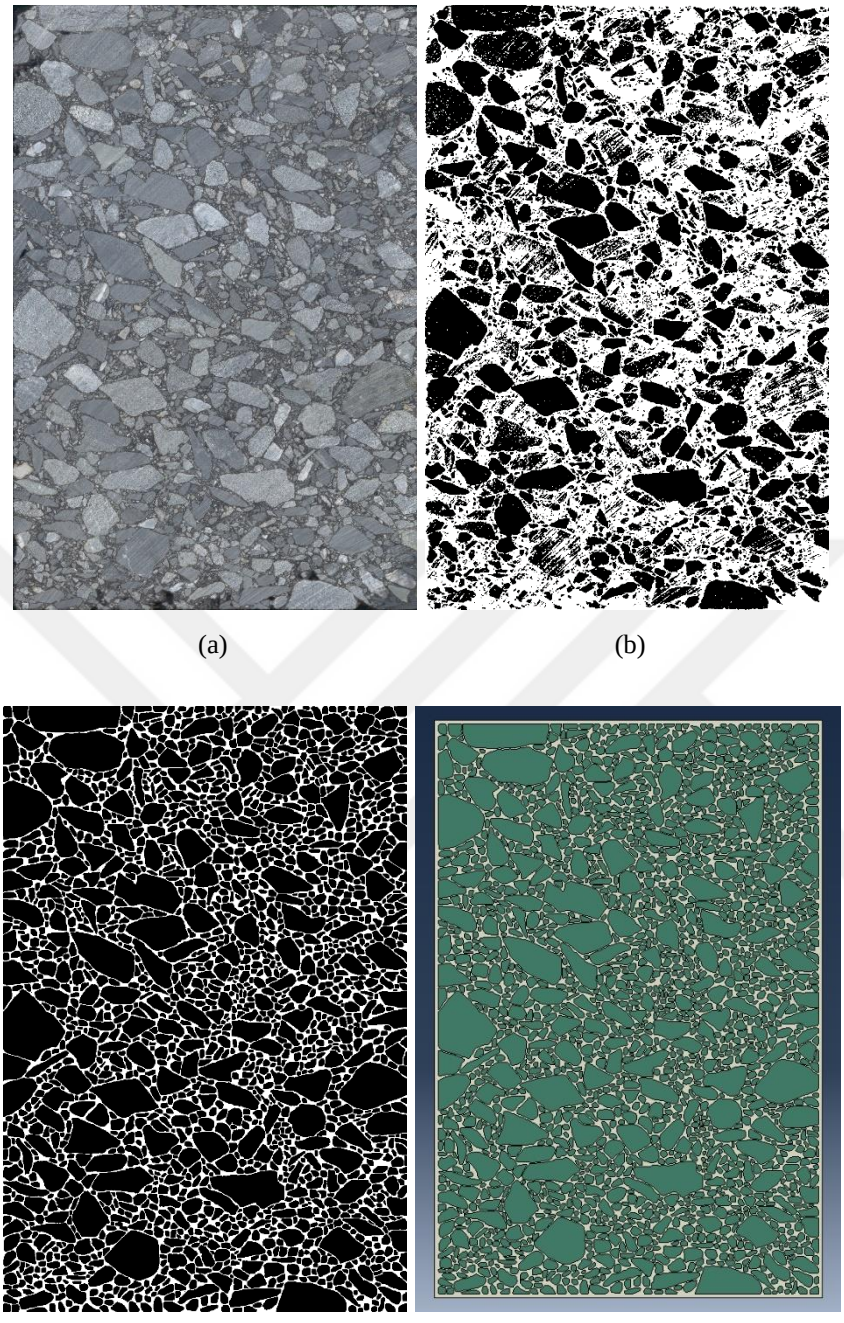

(a) (b)

(c) (d)

Figure G.39. Sample ID BMCR09: a) Captured RGB image, b) Binary form, c) Processed image, d) 2D FE model in ABAQUS

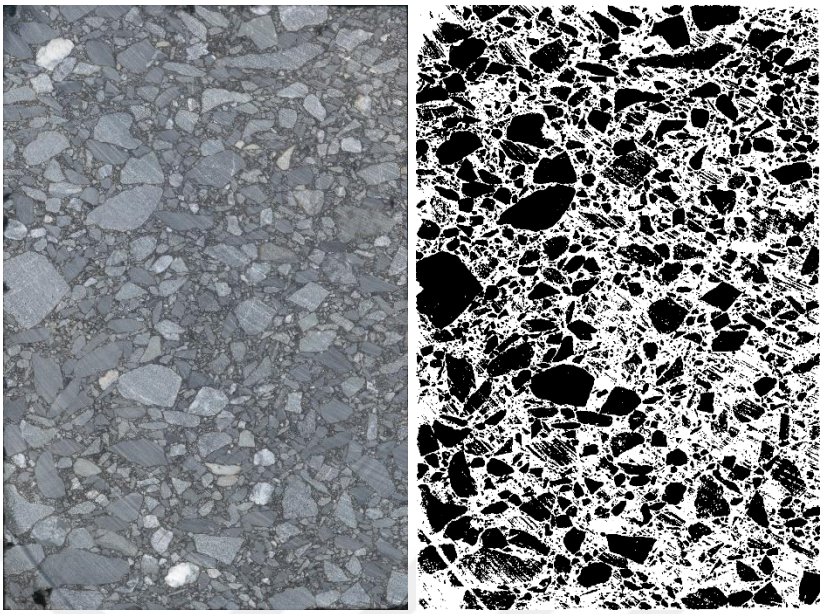

(a) (b)

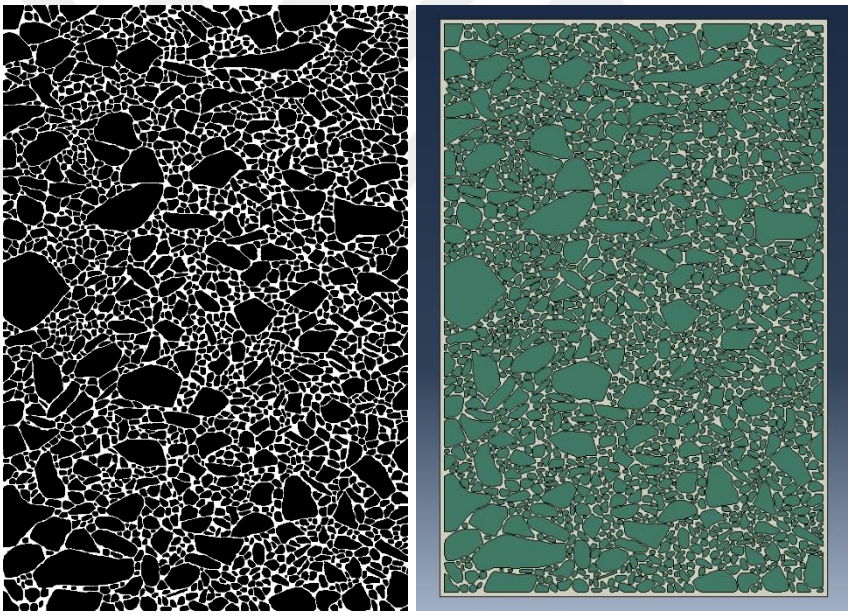

(c) (d)

Figure G.40. Sample ID BMCR10: a) Captured RGB image, b) Binary form, c) Processed image, d) 2D FE model in ABAQUS

H. FE Results of the Resilient Modulus Tests

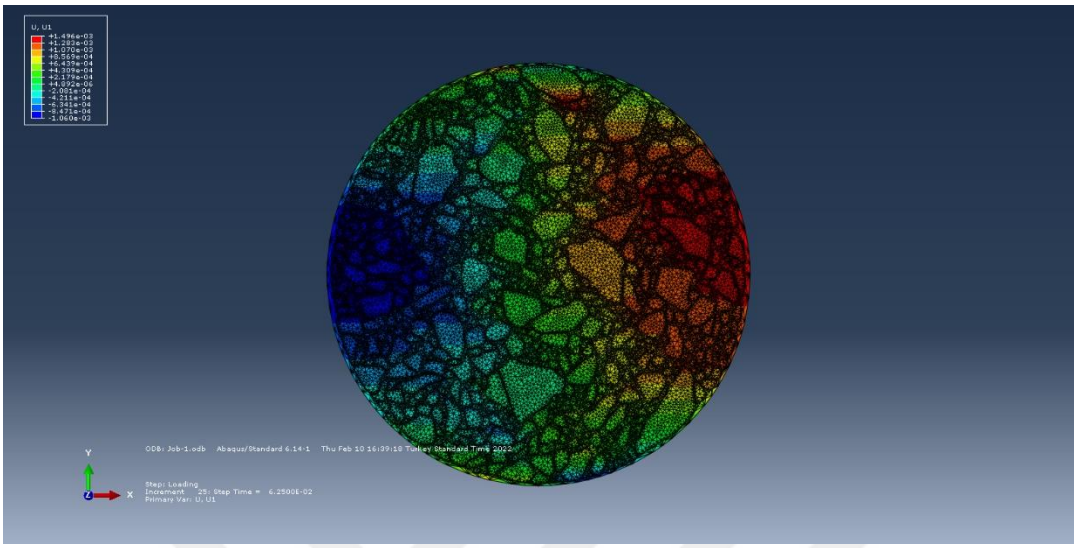

(a)

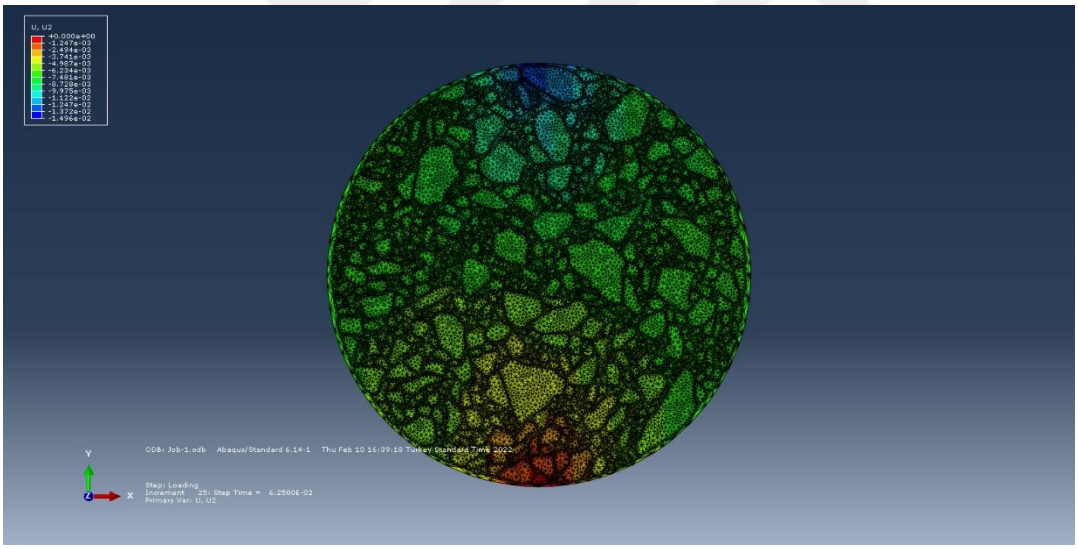

(b)

Figure H.1. Resilient modulus simulation results of the specimen ID LURM01-1: a) Maximum horizontal deformation, b) Maximum vertical deformation

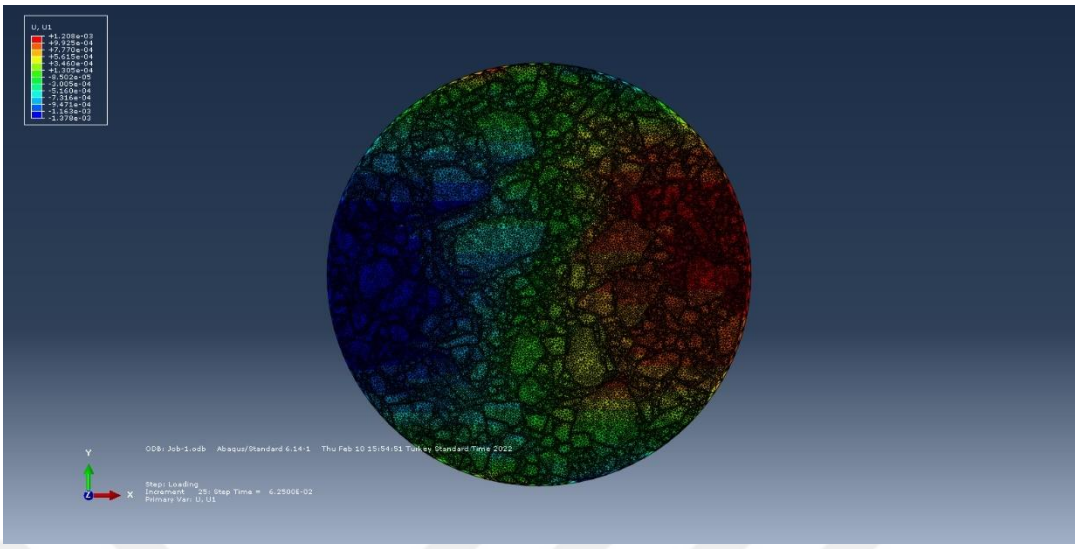

(a)

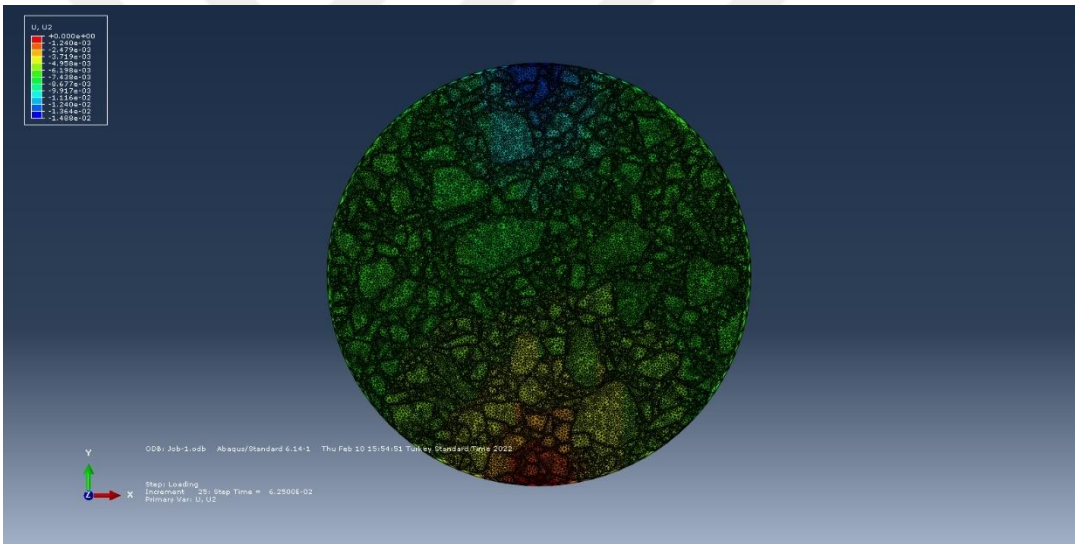

(b)

Figure H.2. Resilient modulus simulation results of the specimen ID LURM02-1: a) Maximum horizontal deformation, b) Maximum vertical deformation

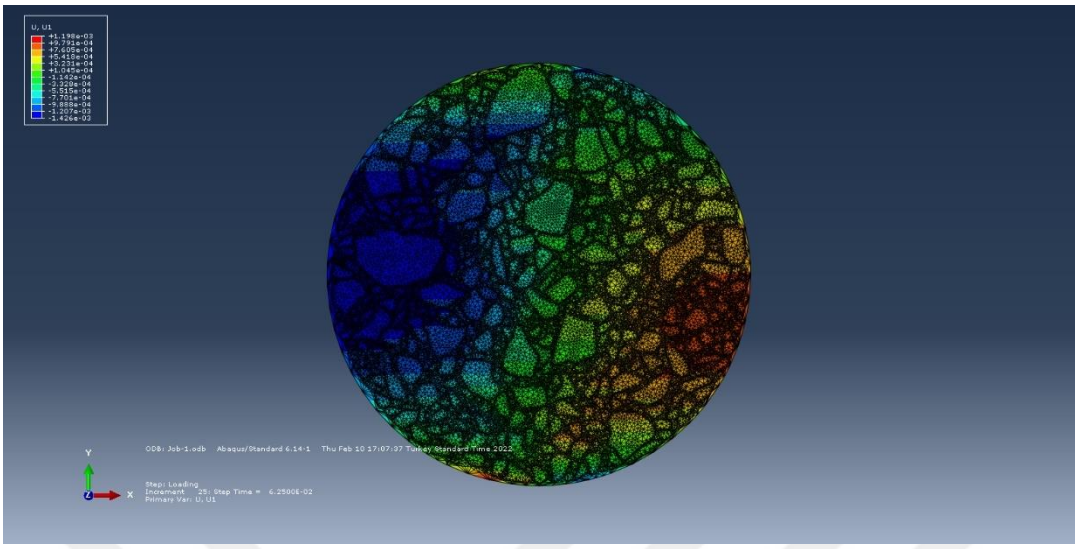

(a)

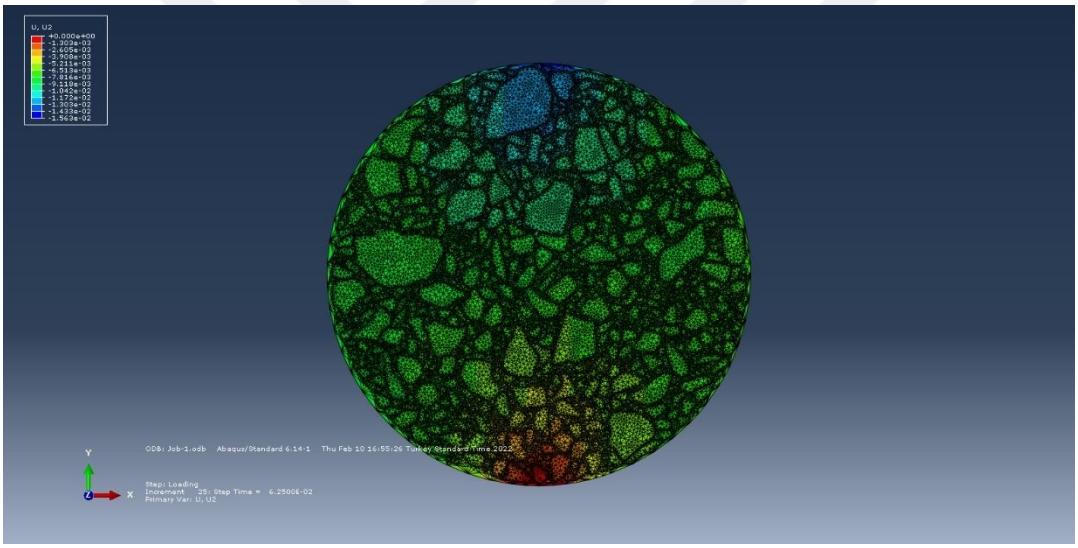

(b)

Figure H.3. Resilient modulus simulation results of the specimen ID LURM03-1: a) Maximum horizontal deformation, b) Maximum vertical deformation

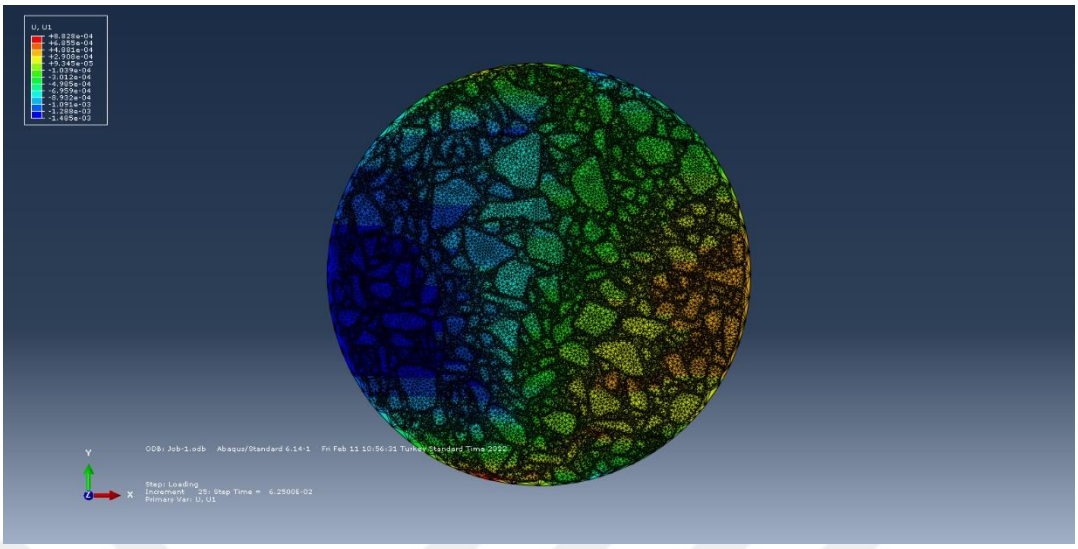

(a)

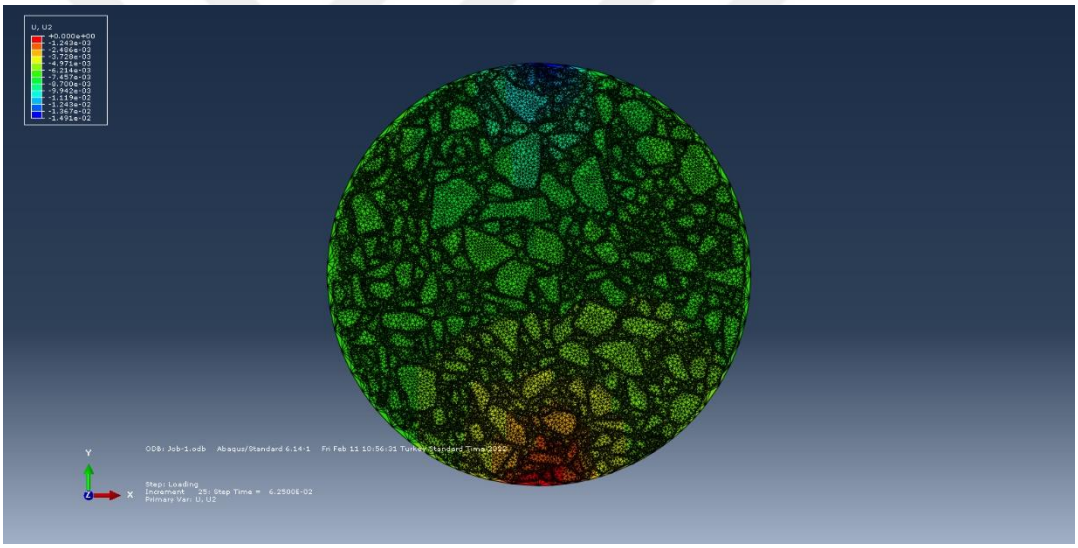

(b)

Figure H.4. Resilient modulus simulation results of the specimen ID LURM06-1: a) Maximum horizontal deformation, b) Maximum vertical deformation

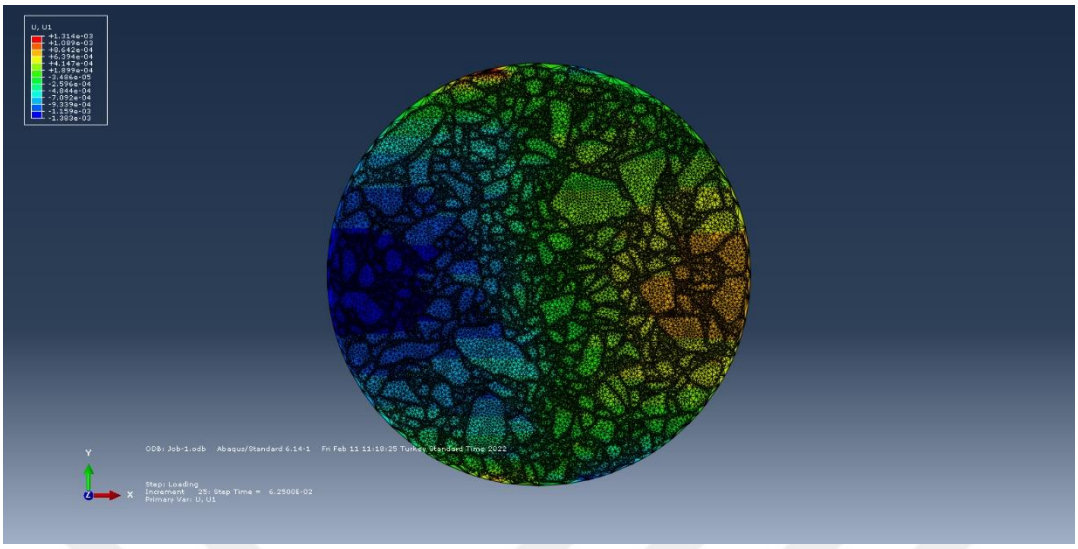

(a)

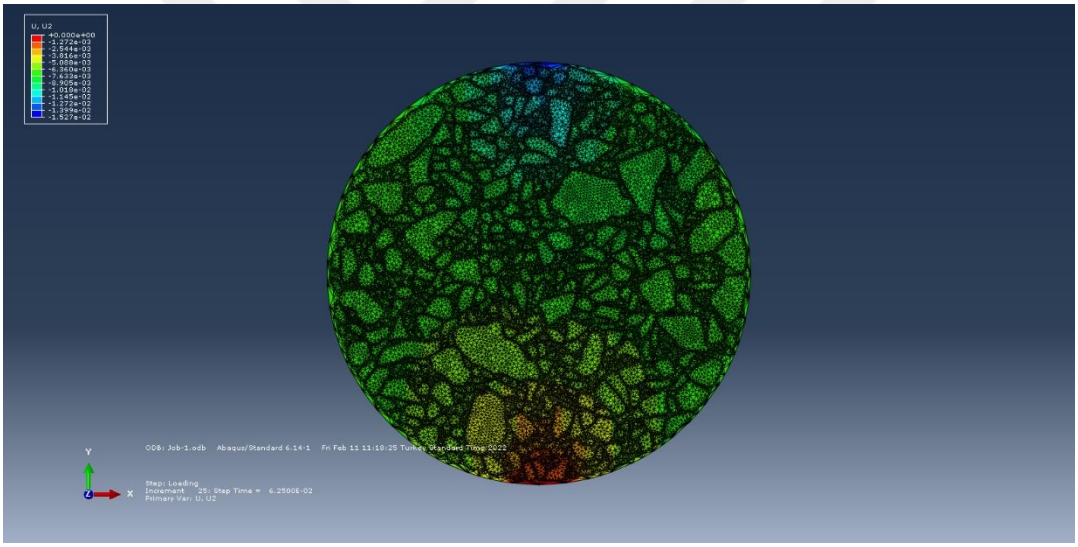

(b)

Figure H.5. Resilient modulus simulation results of the specimen ID LURM07-1: a) Maximum horizontal deformation, b) Maximum vertical deformation

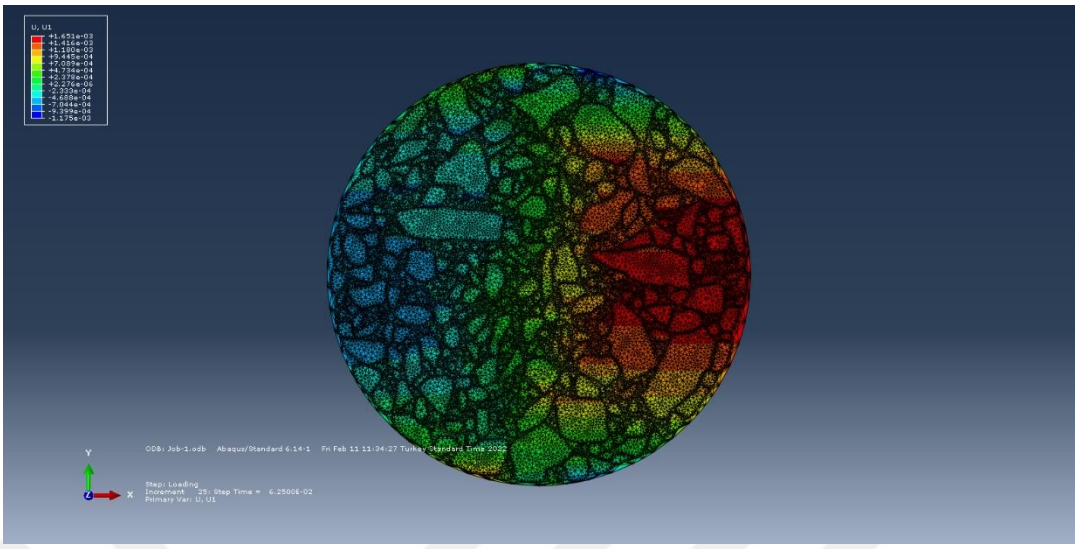

(a)

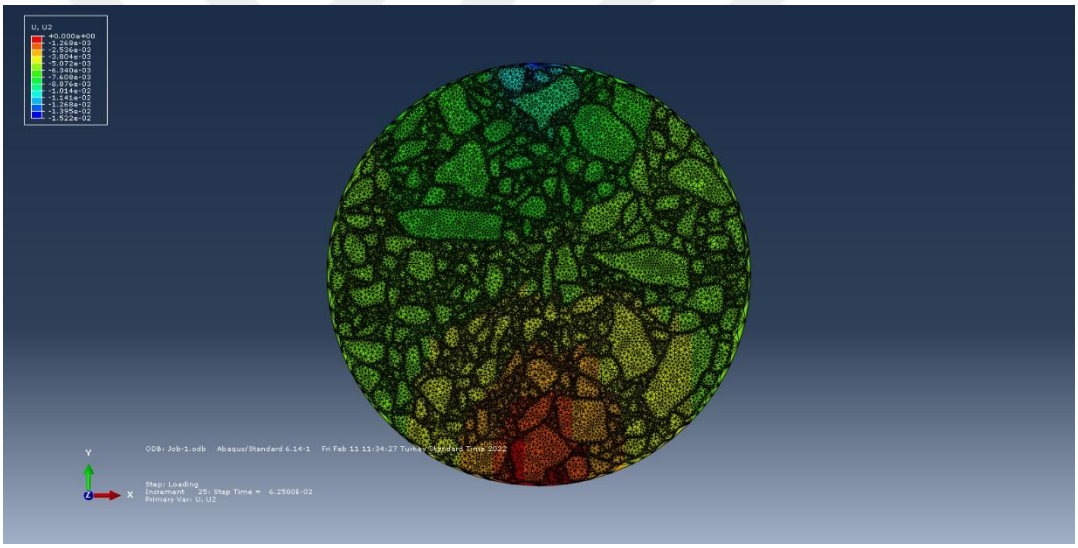

(b)

Figure H.6. Resilient modulus simulation results of the specimen ID LURM08-1: a) Maximum horizontal deformation, b) Maximum vertical deformation

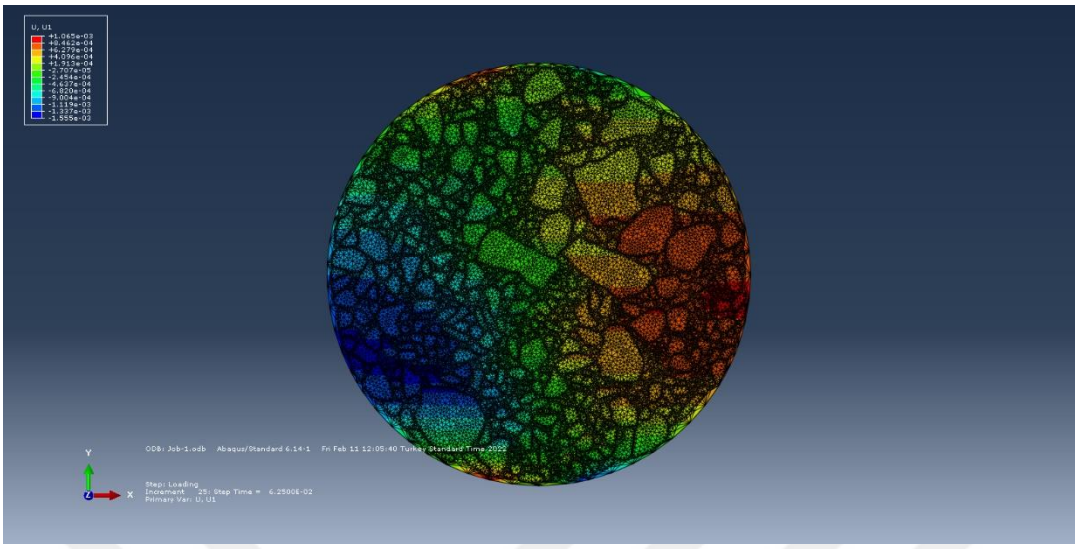

(a)

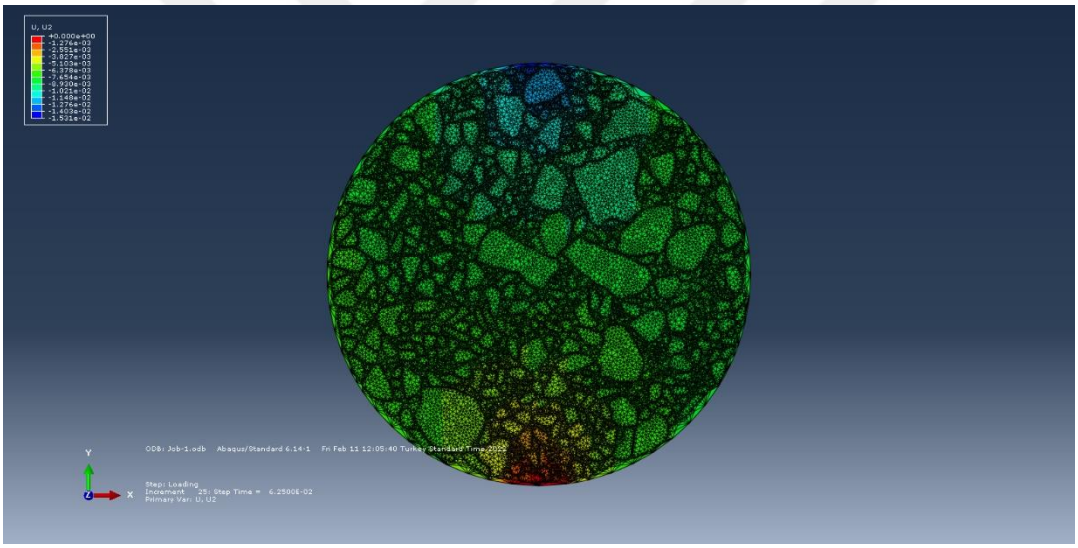

(b)

Figure H.7. Resilient modulus simulation results of the specimen ID LURM09-1: a) Maximum horizontal deformation, b) Maximum vertical deformation

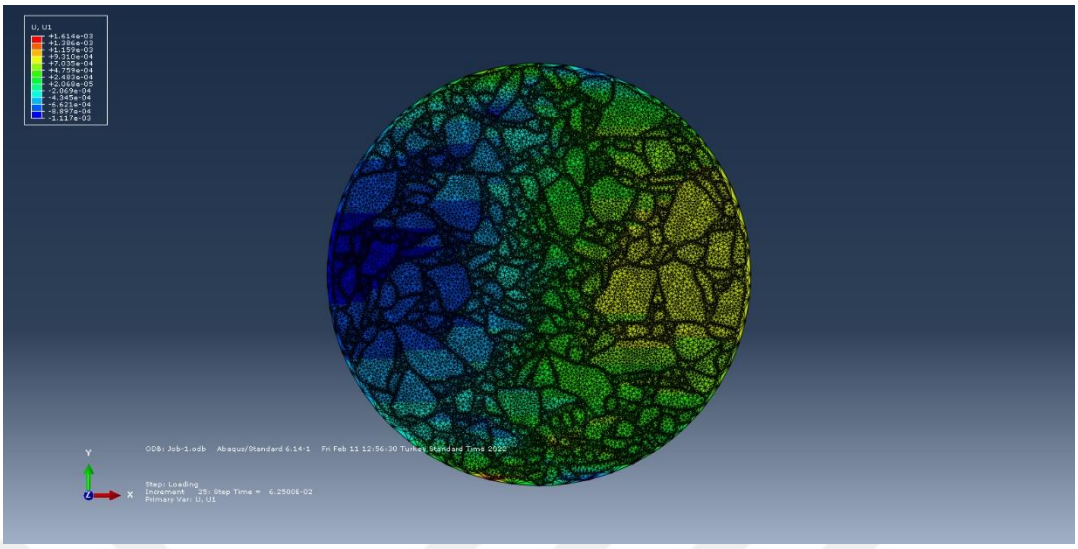

(a)

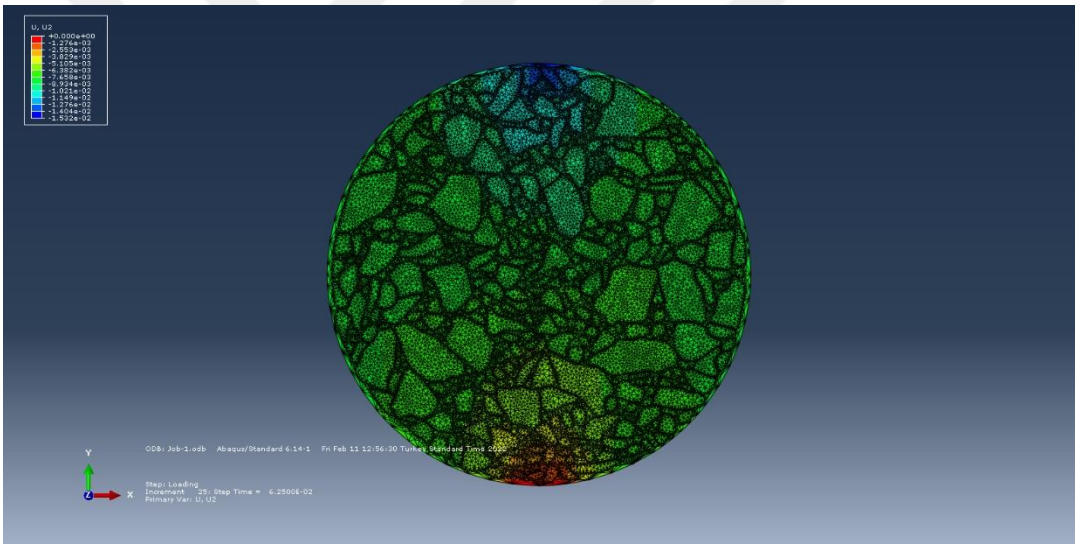

(b)

Figure H.8. Resilient modulus simulation results of the specimen ID LURM10-1: a) Maximum horizontal deformation, b) Maximum vertical deformation

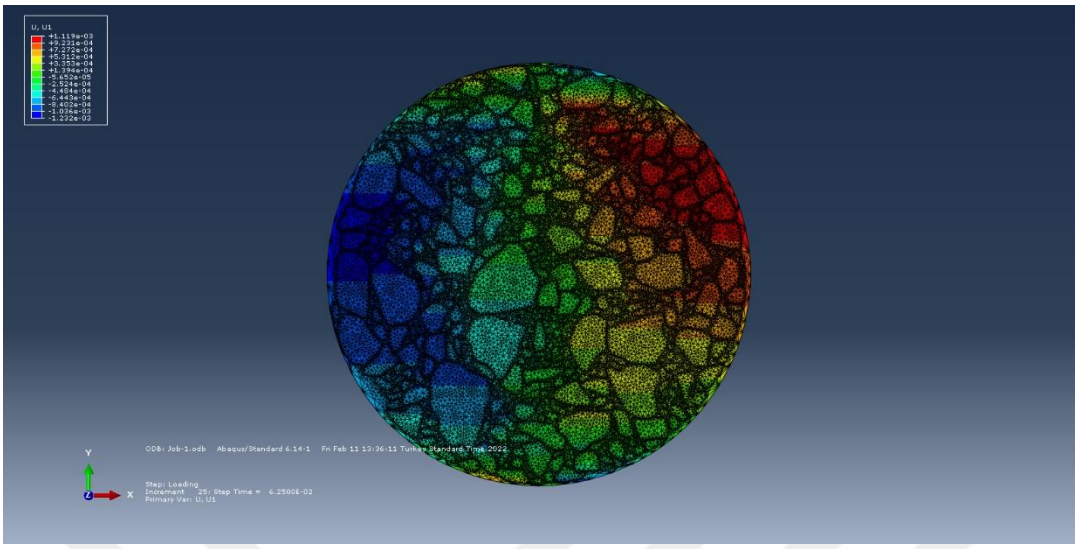

(a)

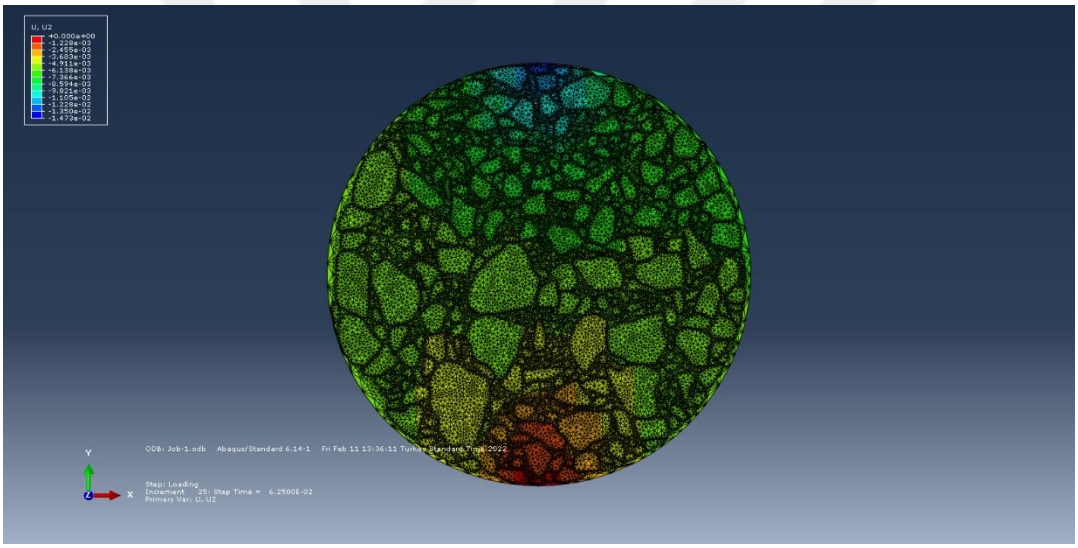

(b)

Figure H.9. Resilient modulus simulation results of the specimen ID LURM11-1: a) Maximum horizontal deformation, b) Maximum vertical deformation

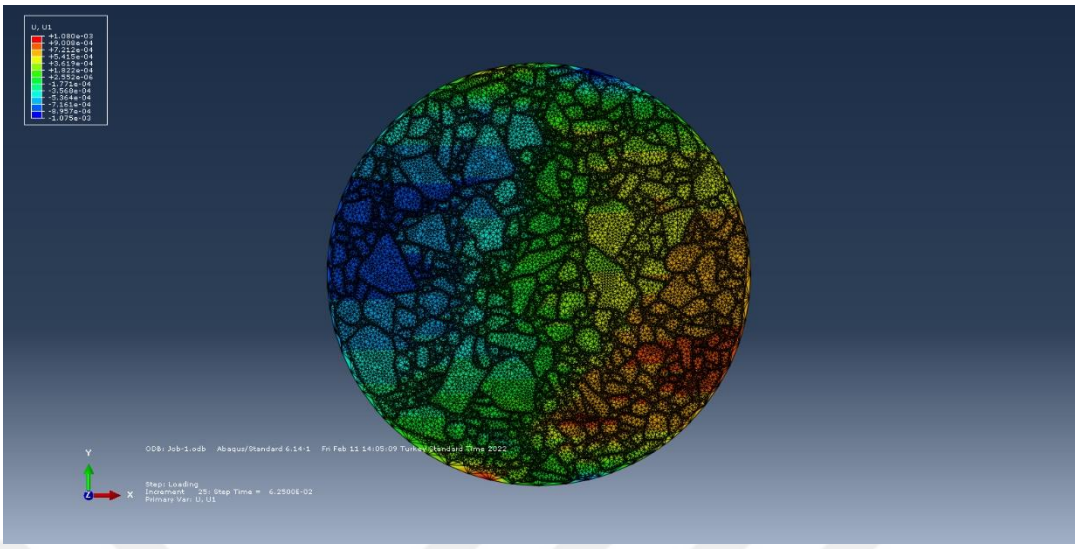

(a)

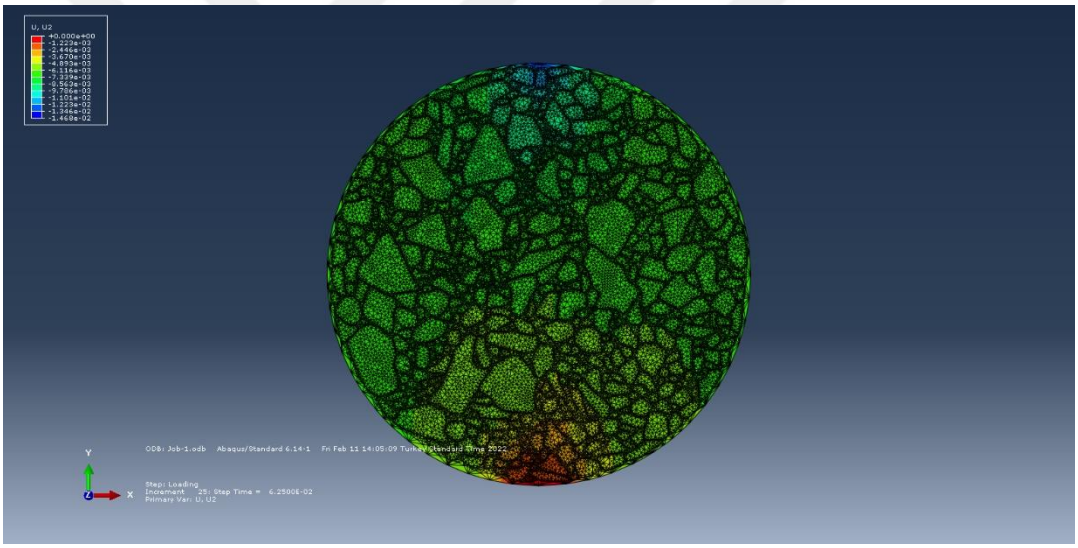

(b)

Figure H.10. Resilient modulus simulation results of the specimen ID LURM12-1: a) Maximum horizontal deformation, b) Maximum vertical deformation

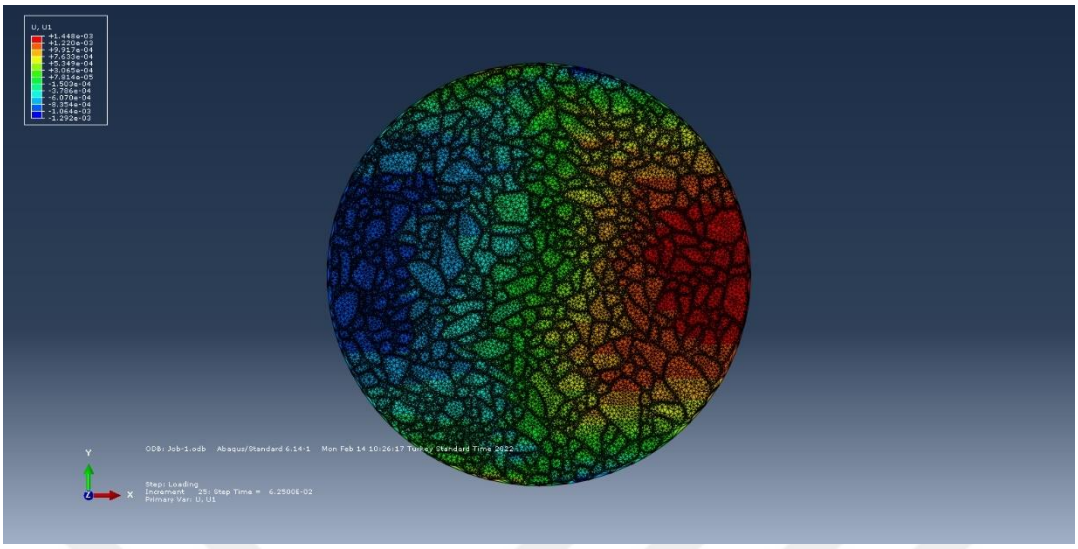

(a)

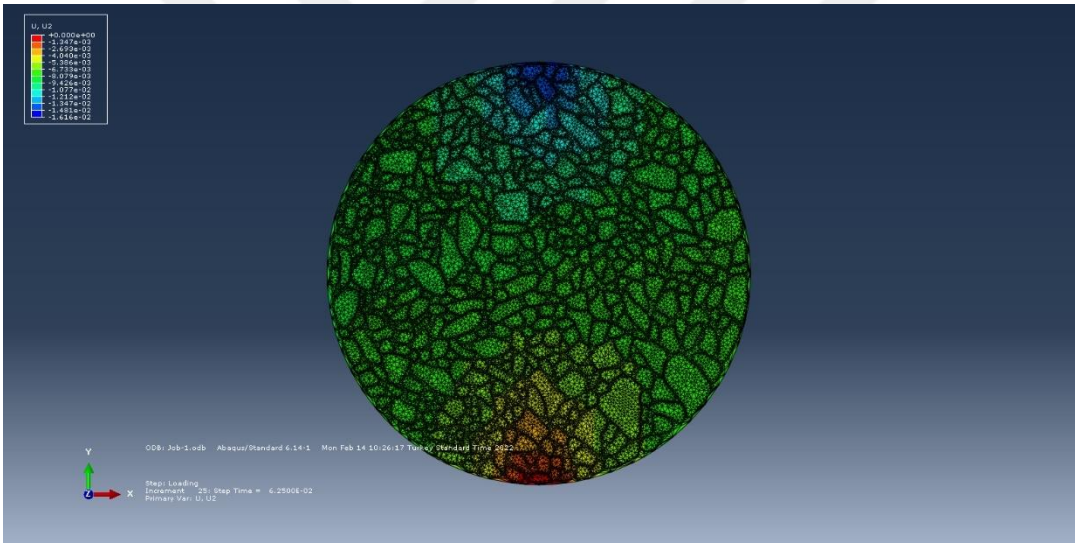

(b)

Figure H.11. Resilient modulus simulation results of the specimen ID BMRM01-1: a) Maximum horizontal deformation, b) Maximum vertical deformation

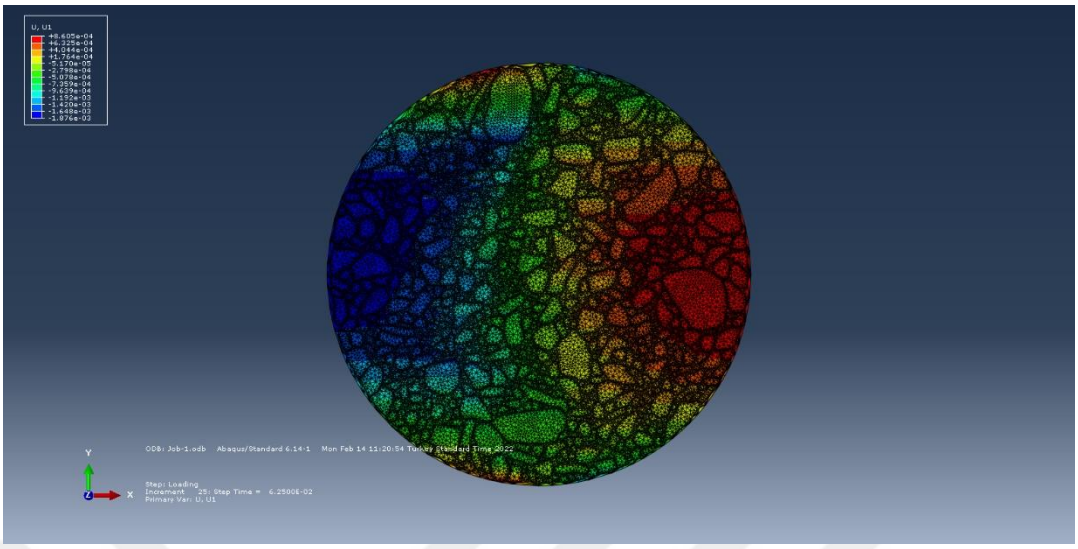

(a)

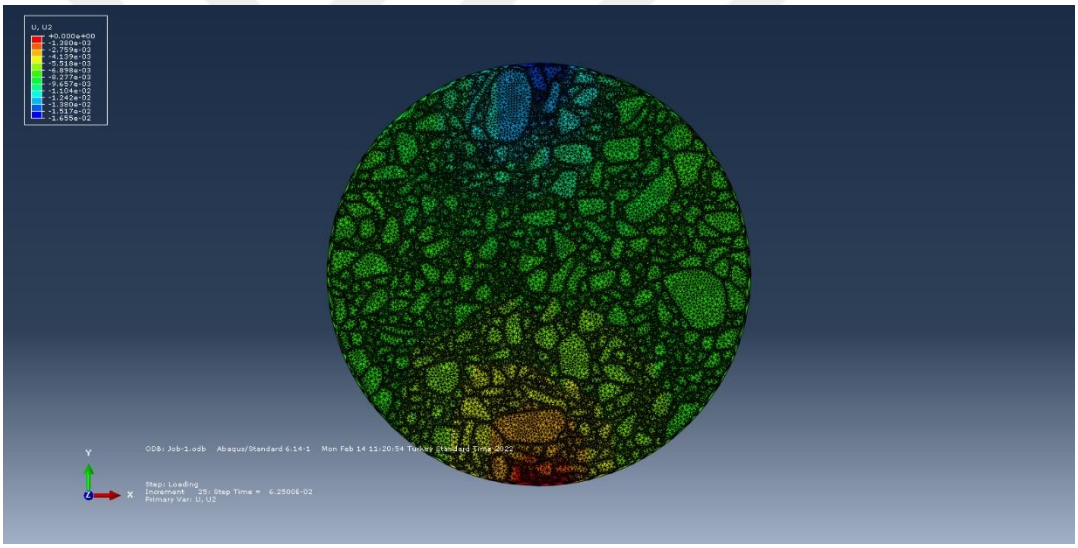

(b)

Figure H.12. Resilient modulus simulation results of the specimen ID BMRM02-1: a) Maximum horizontal deformation, b) Maximum vertical deformation

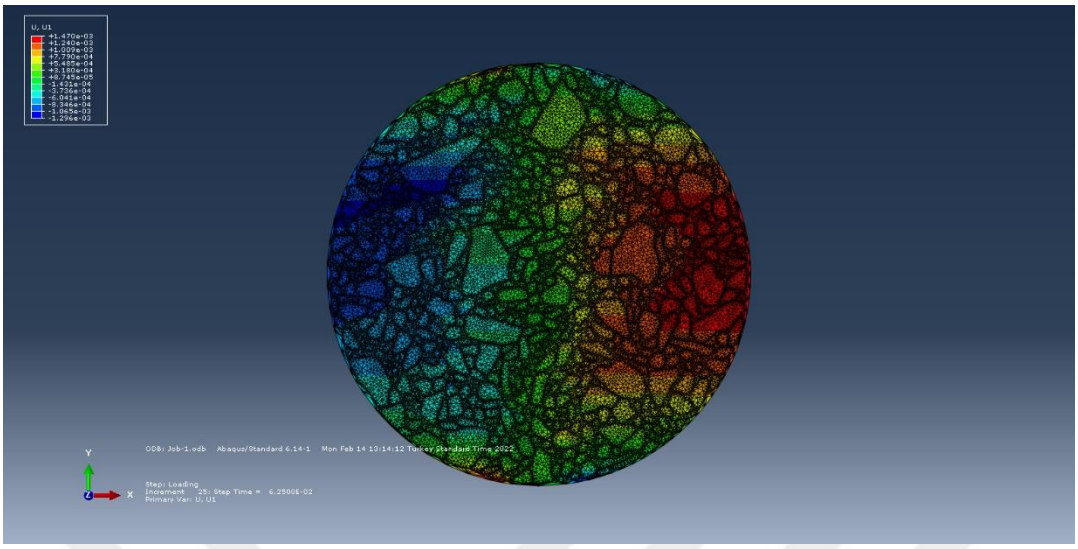

(a)

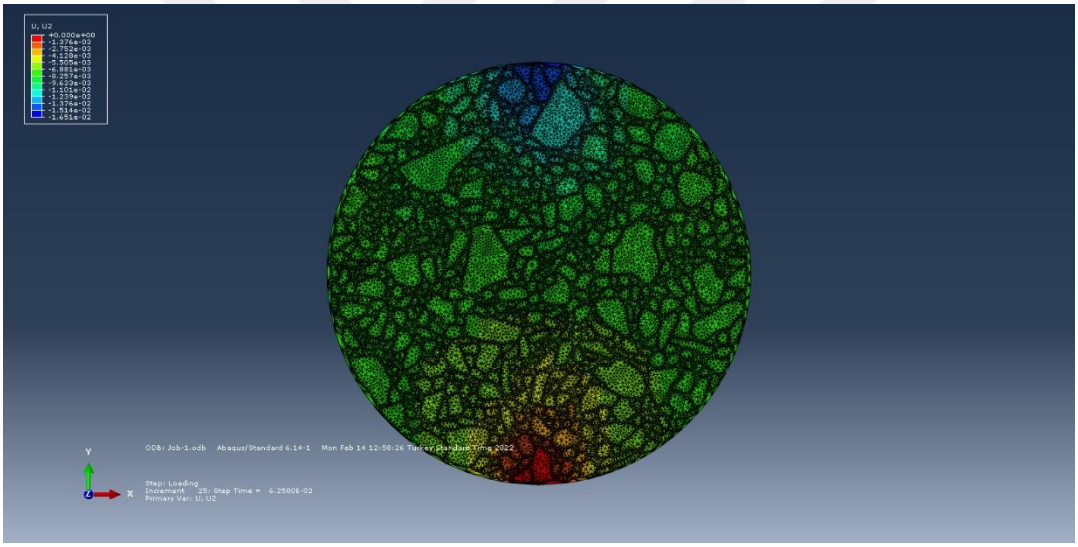

(b)

Figure H.13. Resilient modulus simulation results of the specimen ID BMRM07-1: a) Maximum horizontal deformation, b) Maximum vertical deformation

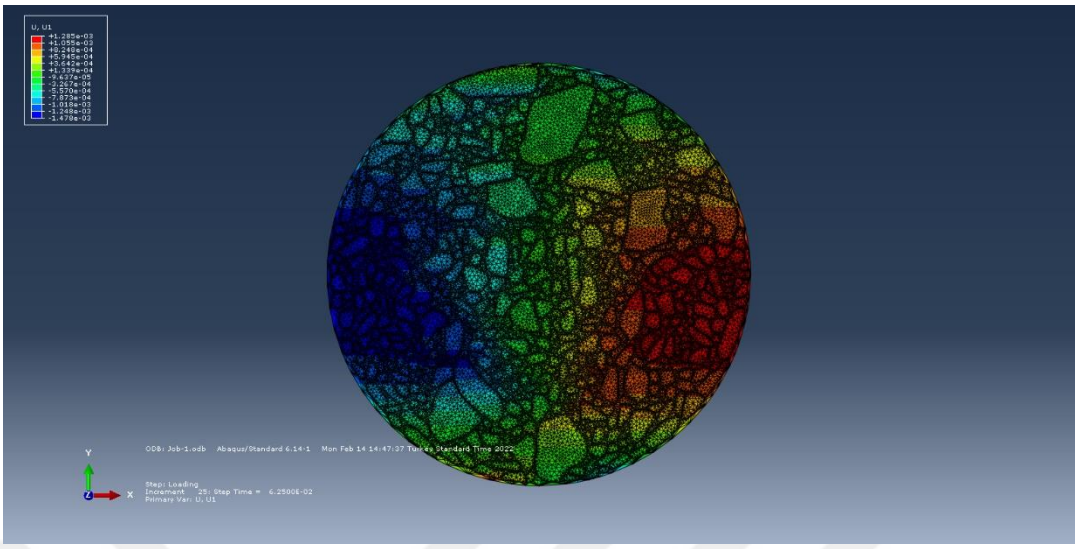

(a)

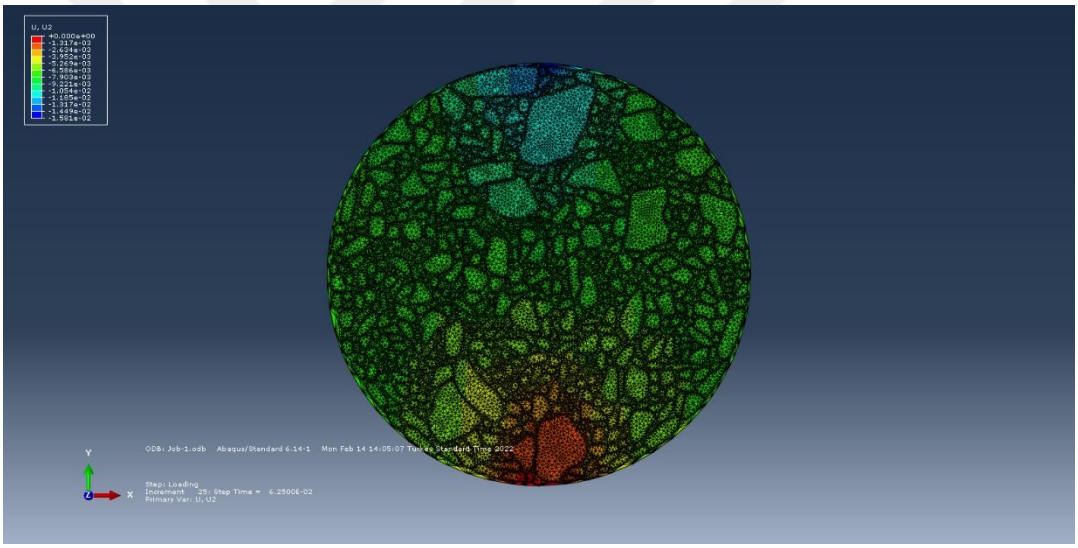

(b)

Figure H.14. Resilient modulus simulation results of the specimen ID BMRM08-1: a) Maximum horizontal deformation, b) Maximum vertical deformation

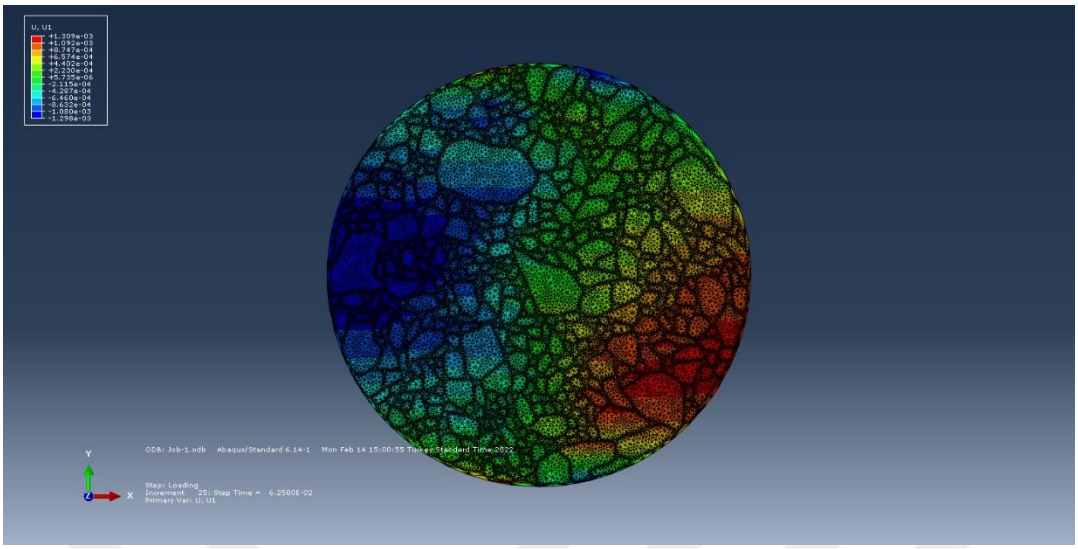

(a)

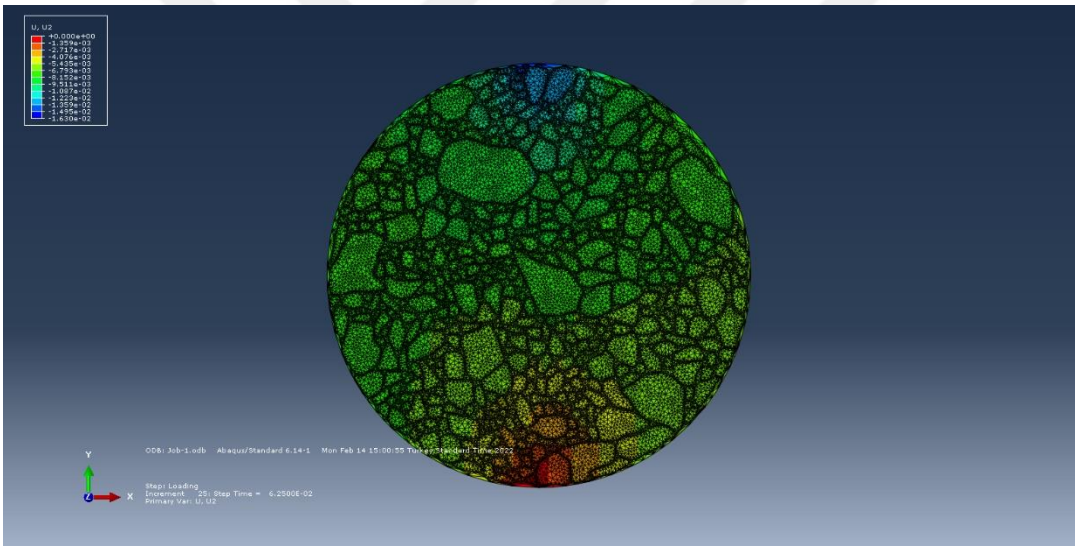

(b)

Figure H.15. Resilient modulus simulation results of the specimen ID BMRM09-1: a) Maximum horizontal deformation, b) Maximum vertical deformation

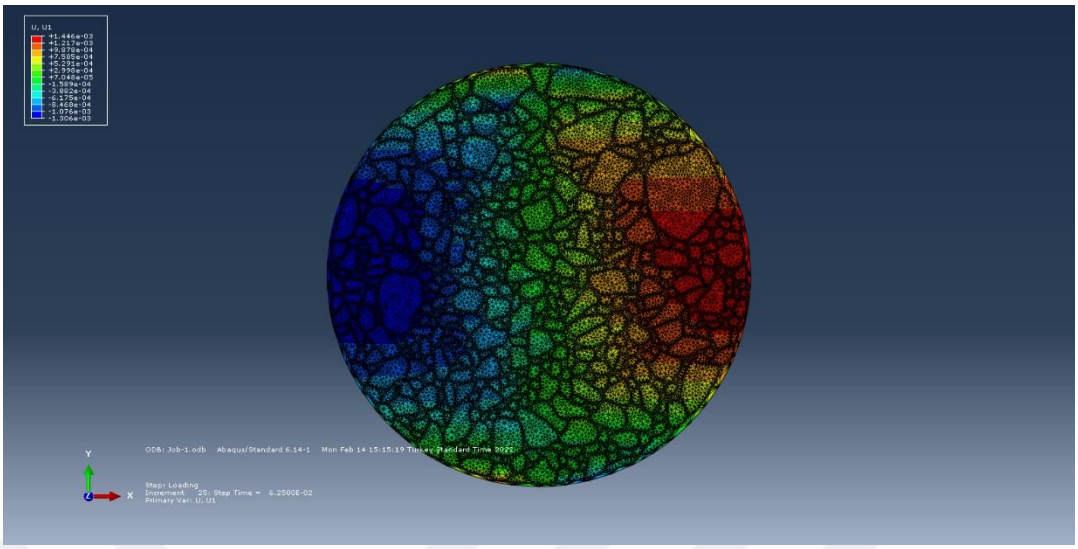

(a)

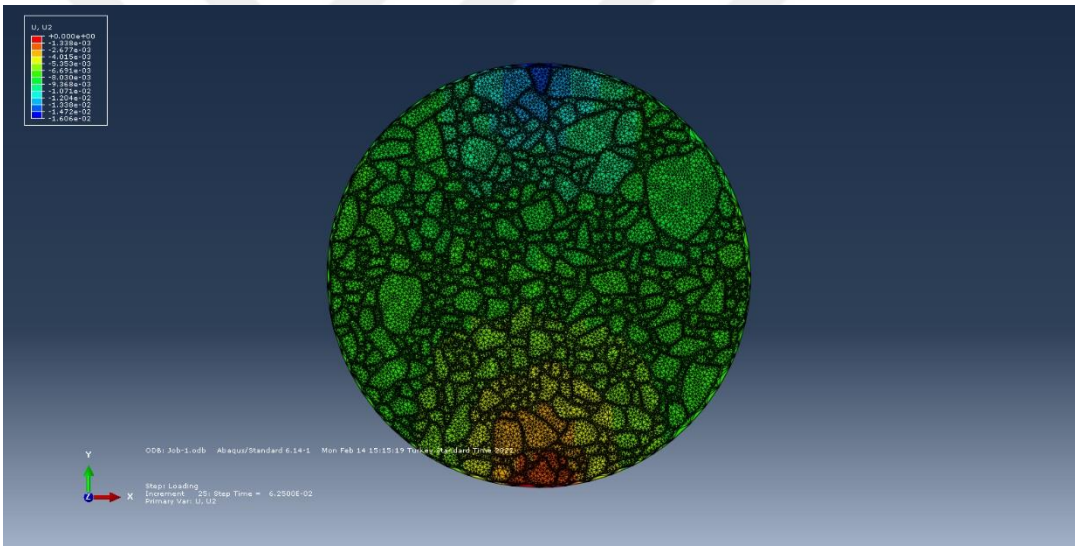

(b)

Figure H.16. Resilient modulus simulation results of the specimen ID BMRM10-1: a) Maximum horizontal deformation, b) Maximum vertical deformation

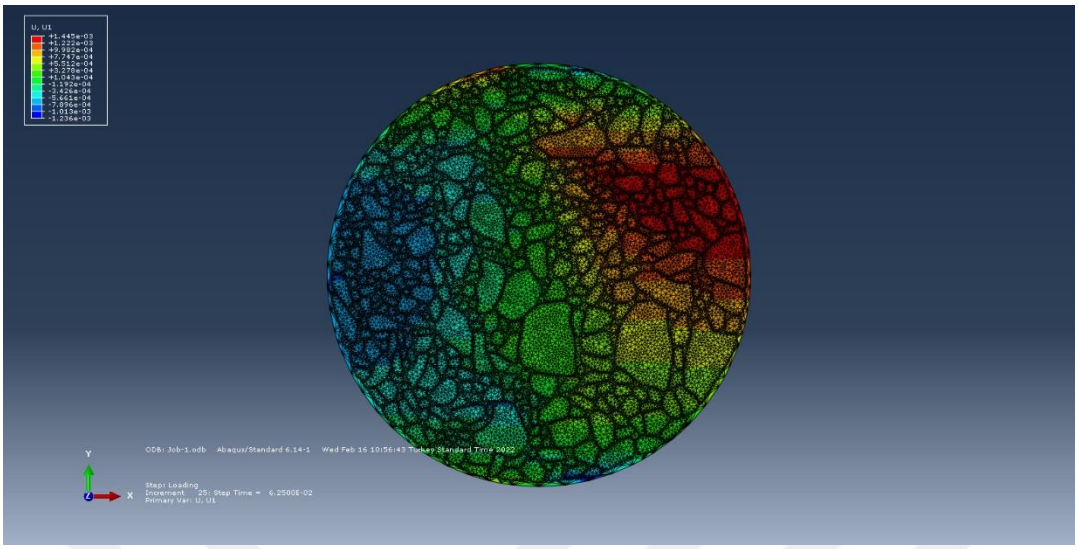

(a)

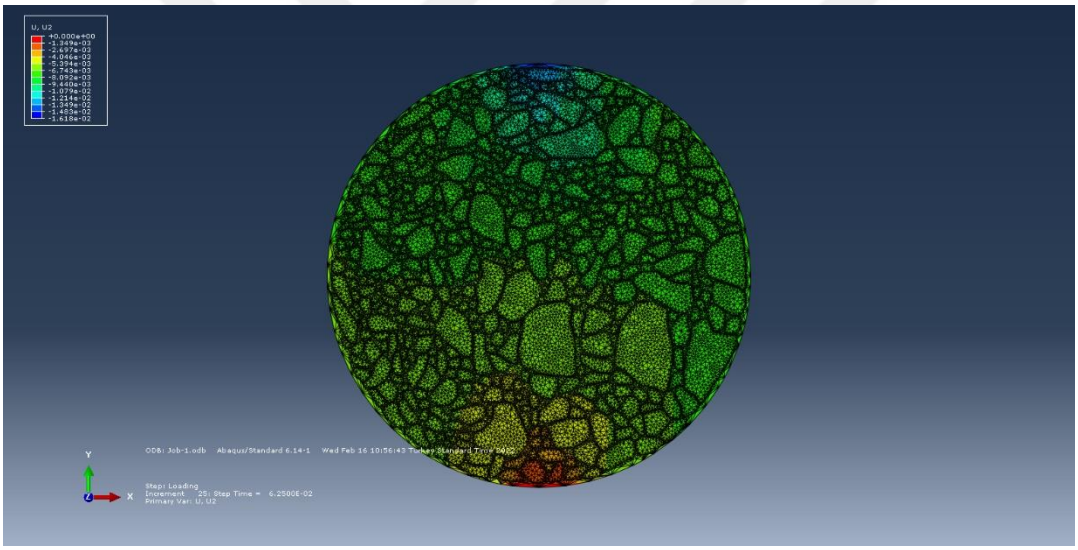

(b)

Figure H.17. Resilient modulus simulation results of the specimen ID BMRM11-1: a) Maximum horizontal deformation, b) Maximum vertical deformation

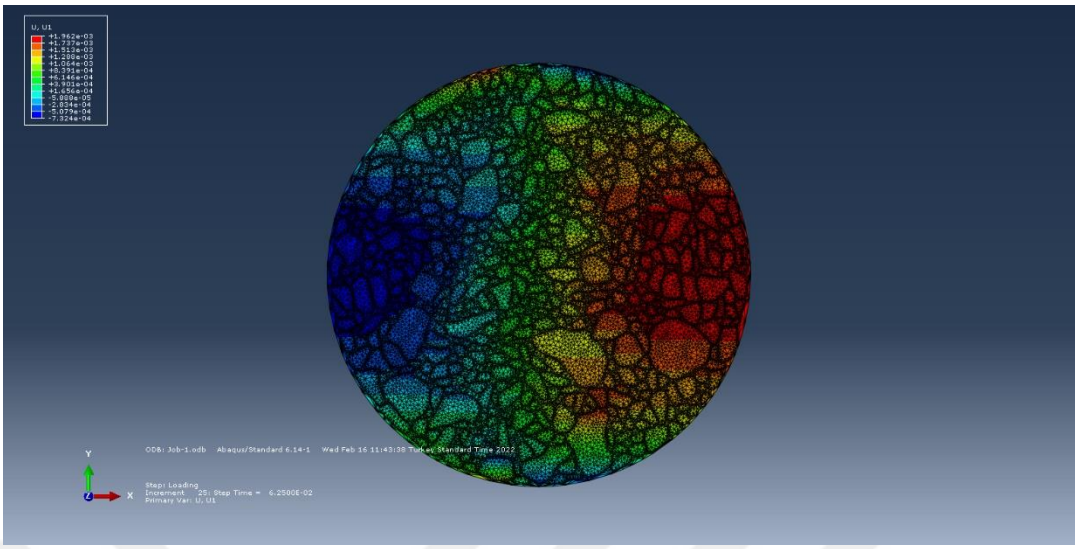

(a)

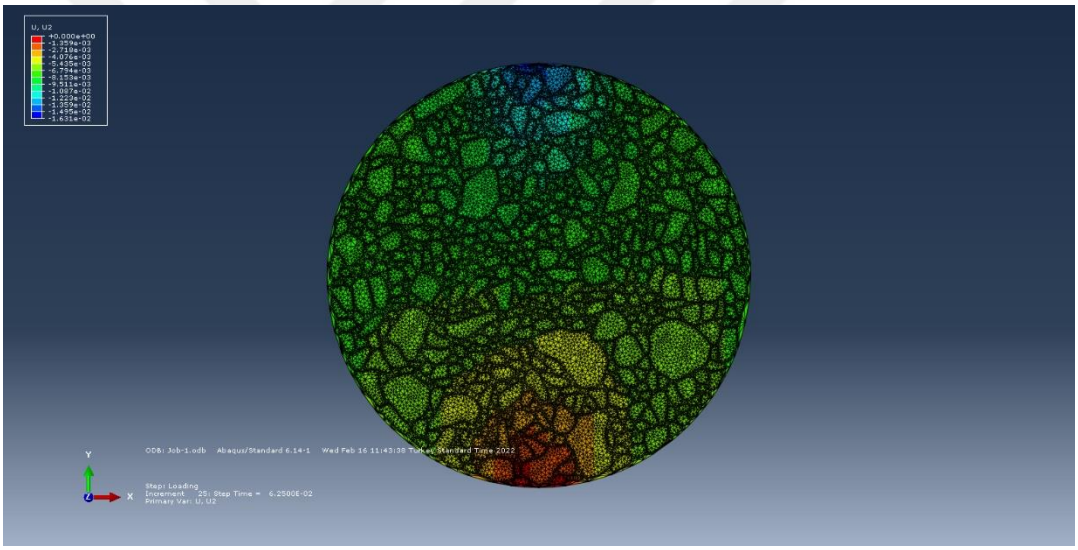

(b)

Figure H.18. Resilient modulus simulation results of the specimen ID BMRM12-1: a) Maximum horizontal deformation, b) Maximum vertical deformation

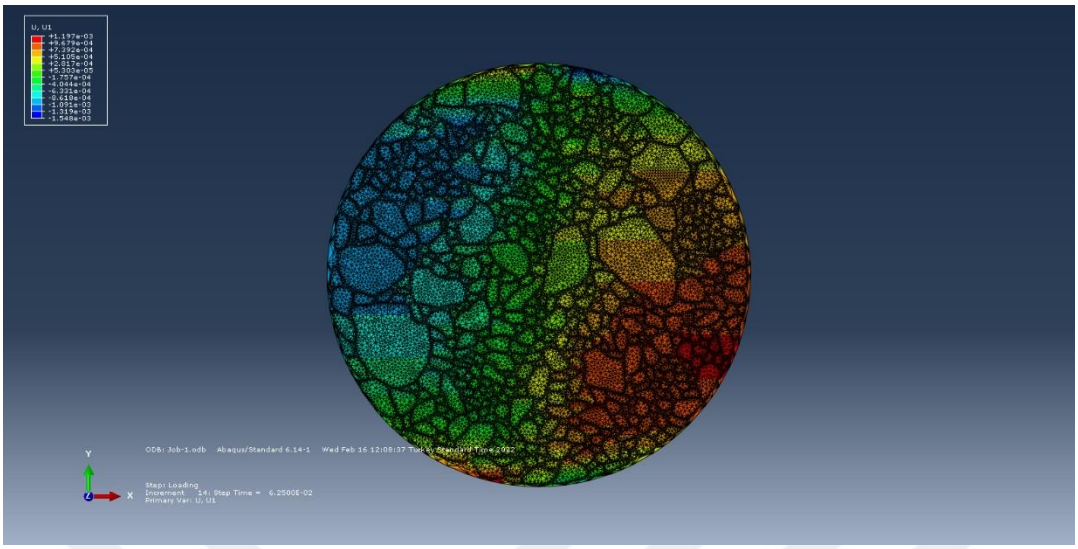

(a)

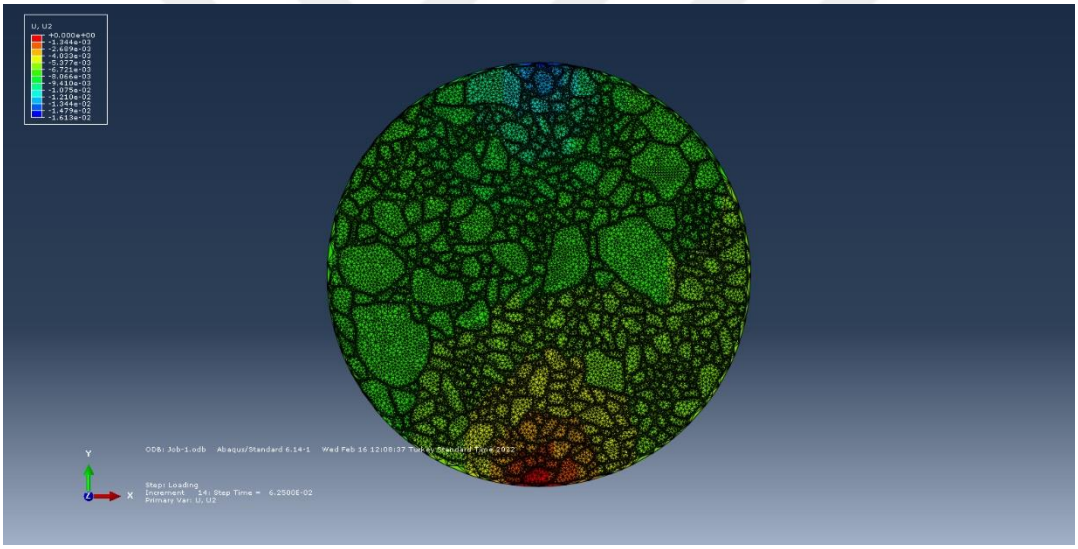

(b)

Figure H.19. Resilient modulus simulation results of the specimen ID BMRM13-1: a) Maximum horizontal deformation, b) Maximum vertical deformation

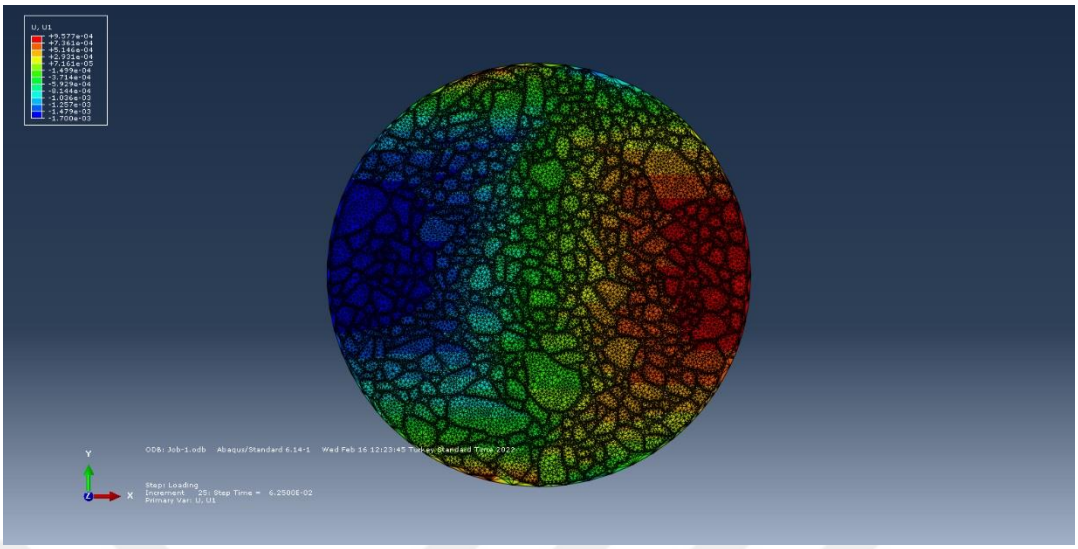

(a)

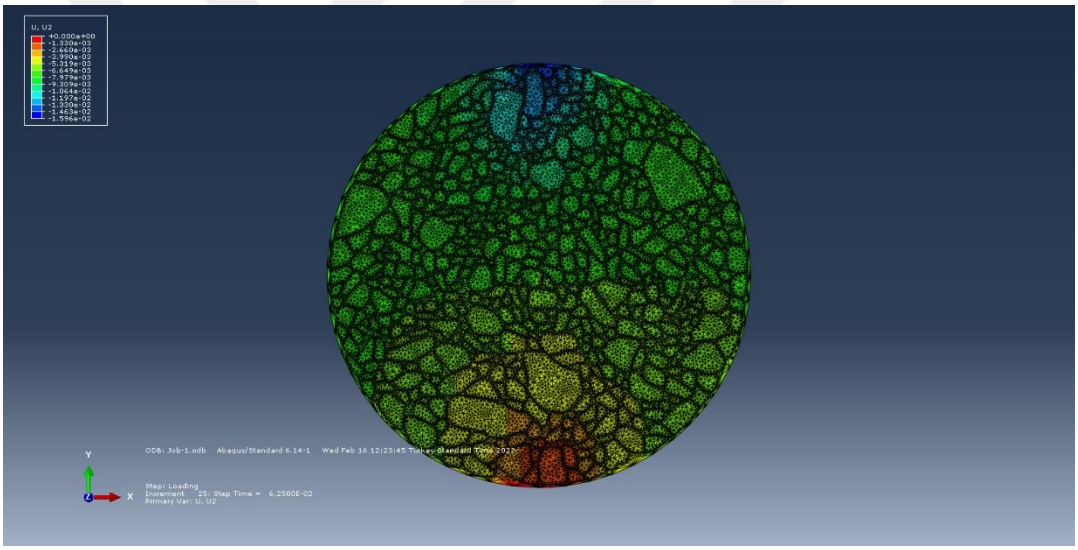

(b)

Figure H.20. Resilient modulus simulation results of the specimen ID BMRM14-1: a) Maximum horizontal deformation, b) Maximum vertical deformation

İ. FE Results of the Repeated Creep Tests

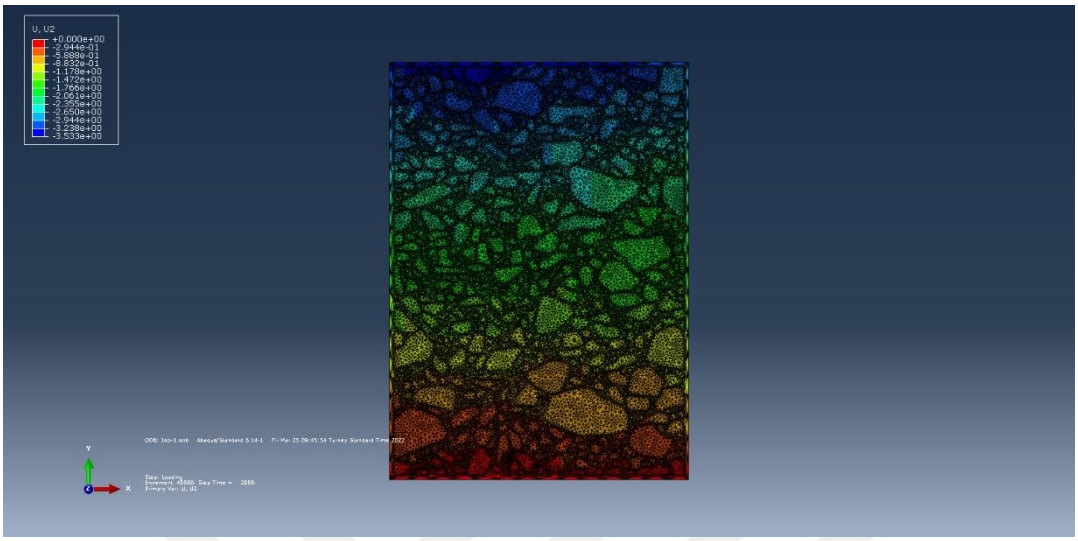

(a)

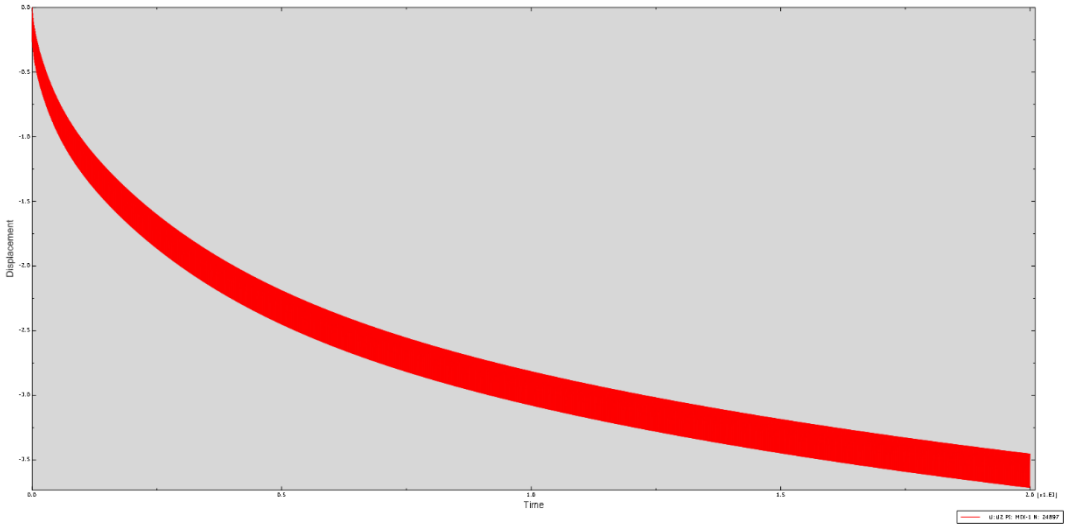

(b)

Figure İ.1. Repeated creep simulation results of the specimen ID LUCR03: a) Vertical deformations at the end of the test, b) Resulting vertical deformation graph

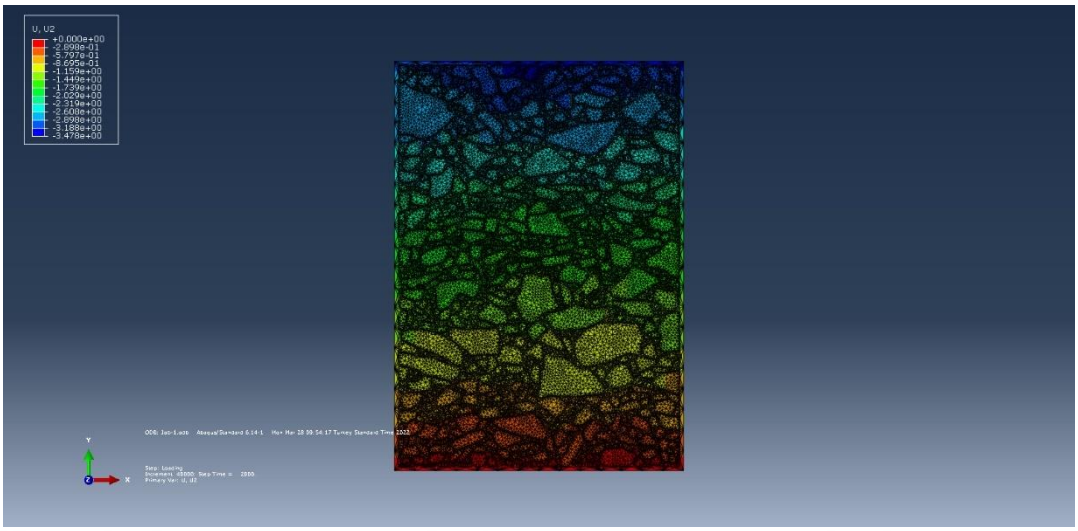

(a)

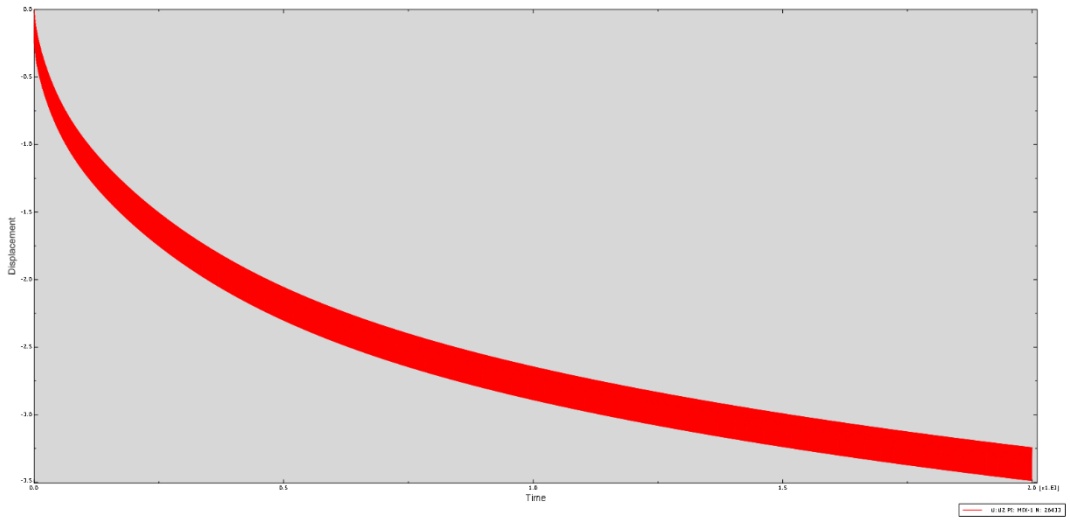

(b)

Figure İ.2. Repeated creep simulation results of the specimen ID LUCR05: a) Vertical deformations at the end of the test, b) Resulting vertical deformation graph

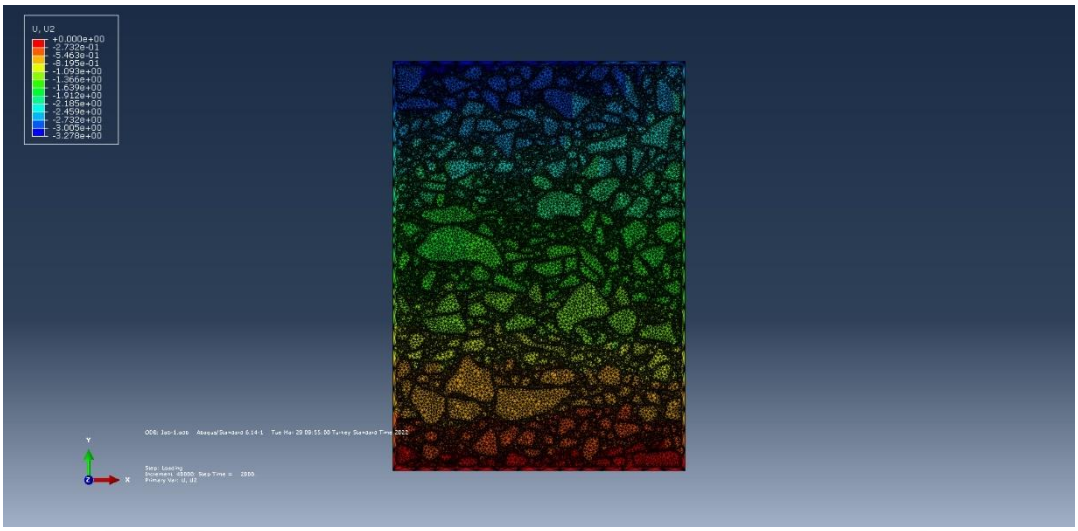

(a)

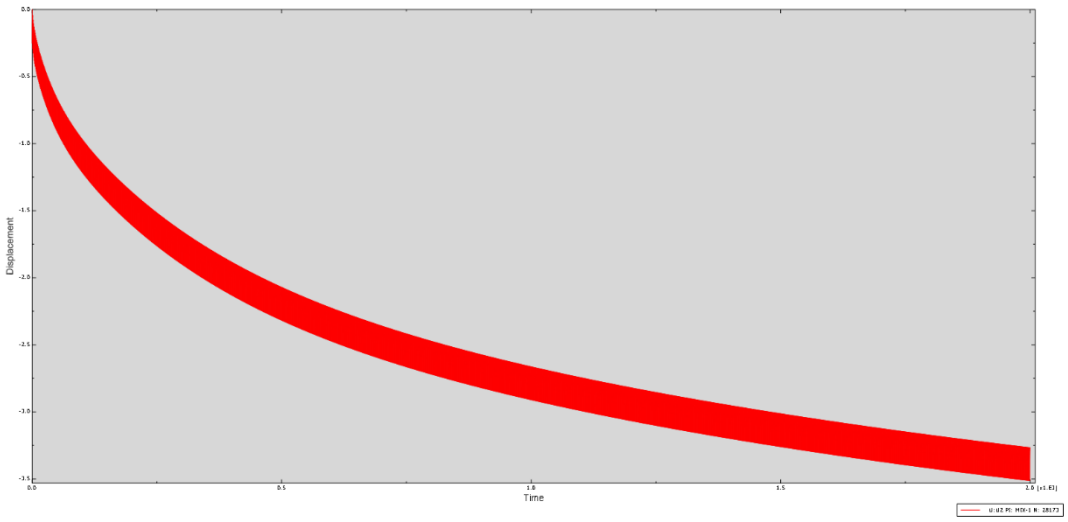

(b)

Figure İ.3. Repeated creep simulation results of the specimen ID LUCR06: a) Vertical deformations at the end of the test, b) Resulting vertical deformation graph

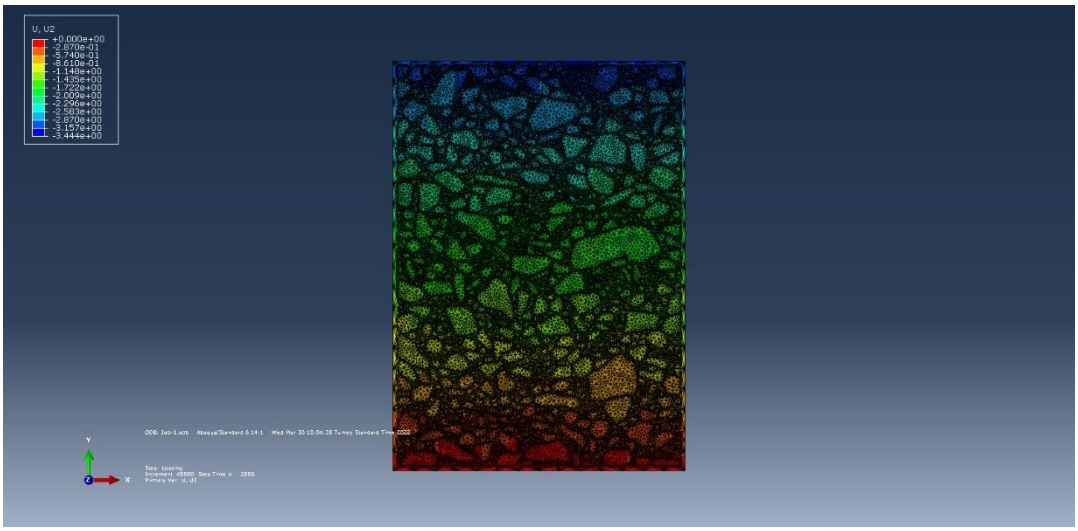

(a)

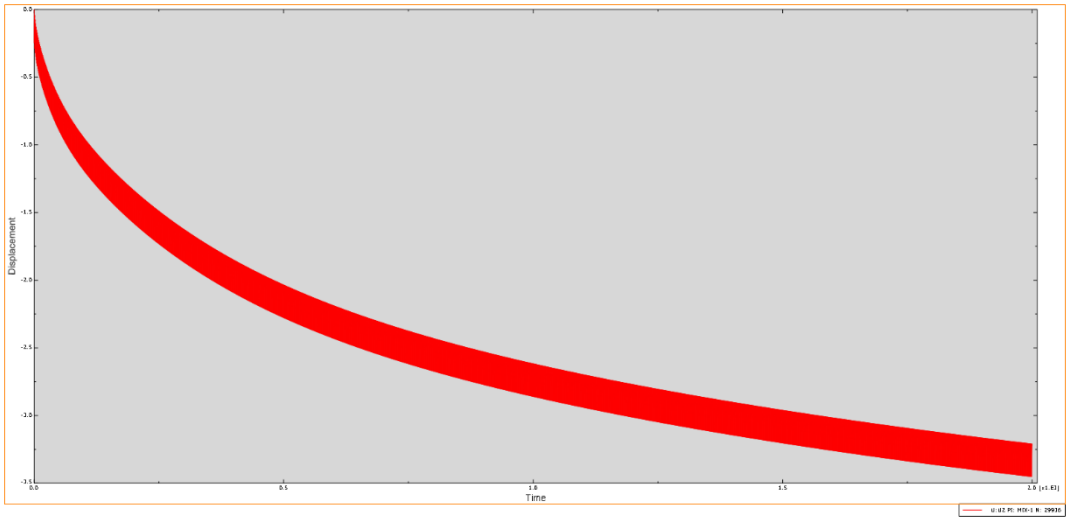

(b)

Figure İ.4. Repeated creep simulation results of the specimen ID LUCR07: a) Vertical deformations at the end of the test, b) Resulting vertical deformation graph

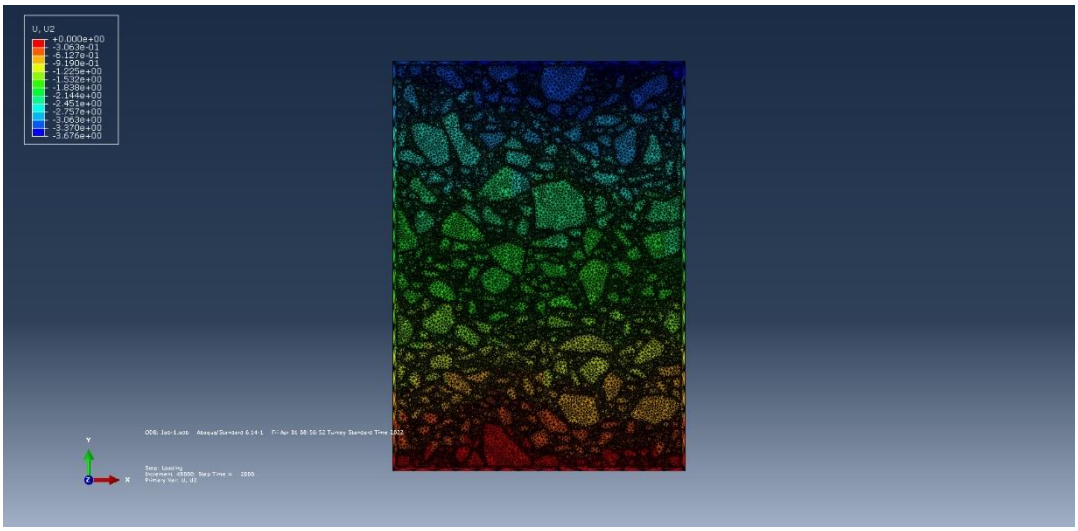

(a)

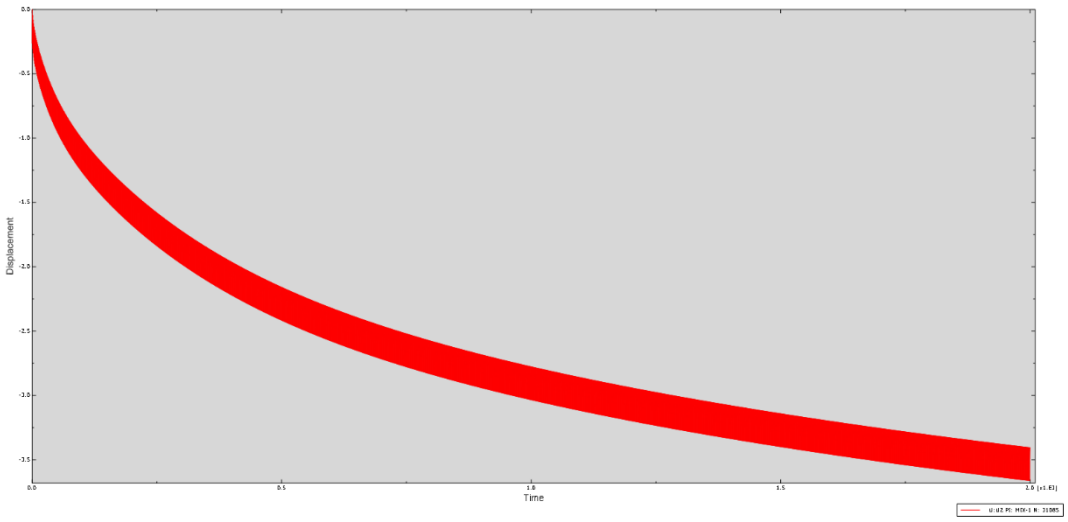

(b)

Figure İ.5. Repeated creep simulation results of the specimen ID LUCR08: a) Vertical deformations at the end of the test, b) Resulting vertical deformation graph

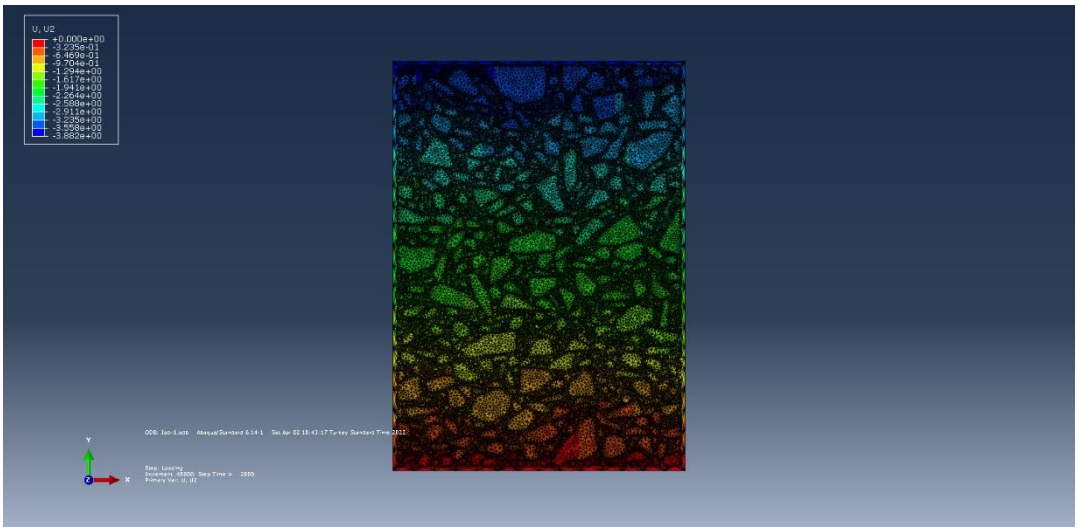

(a)

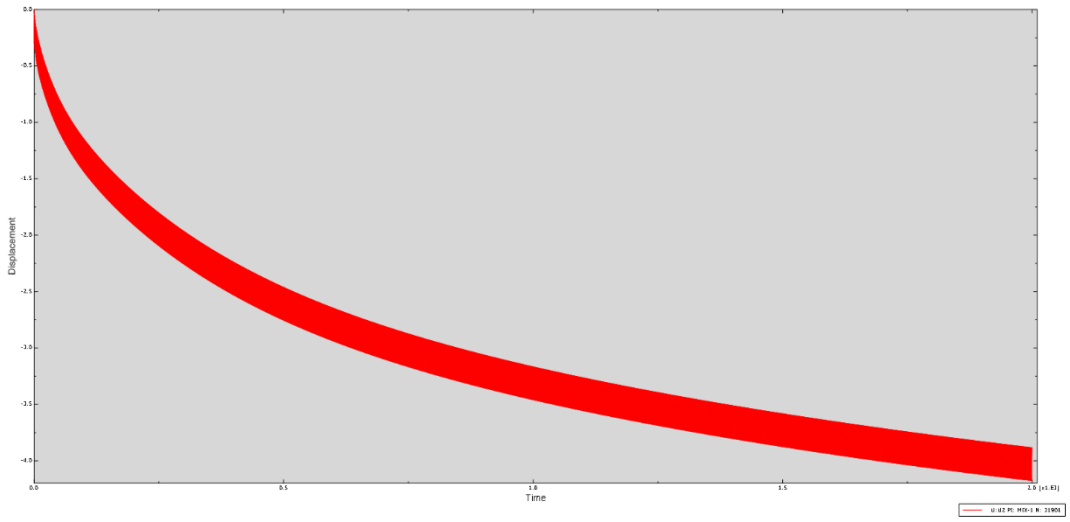

(b)

Figure İ.6. Repeated creep simulation results of the specimen ID LUCR09: a) Vertical deformations at the end of the test, b) Resulting vertical deformation graph

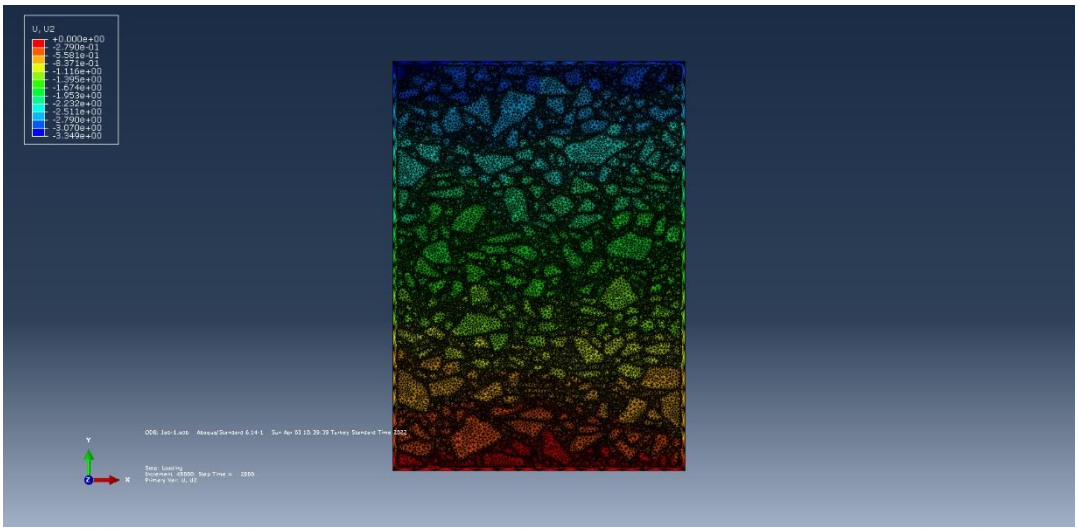

(a)

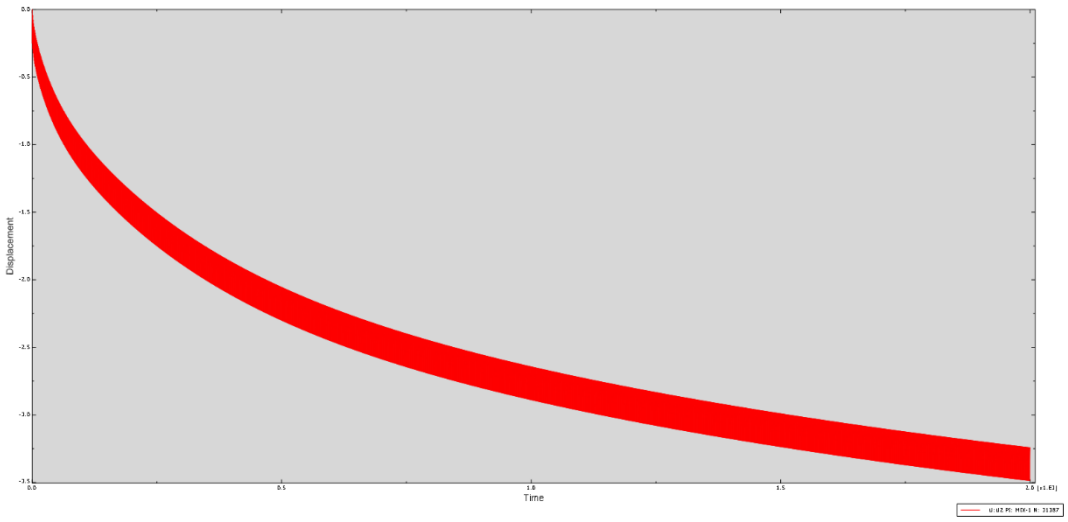

(b)

Figure İ.7. Repeated creep simulation results of the specimen ID LUCR10: a) Vertical deformations at the end of the test, b) Resulting vertical deformation graph

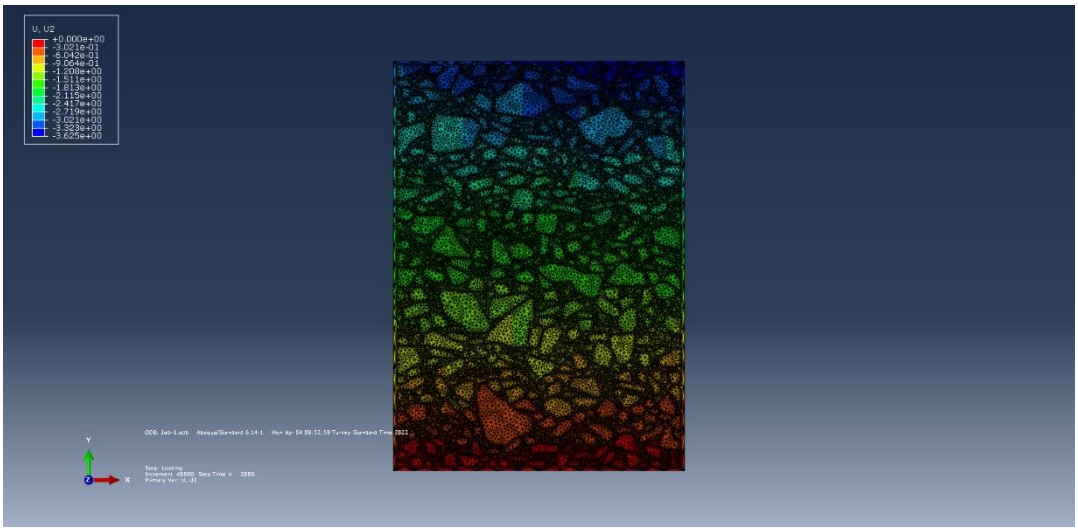

(a)

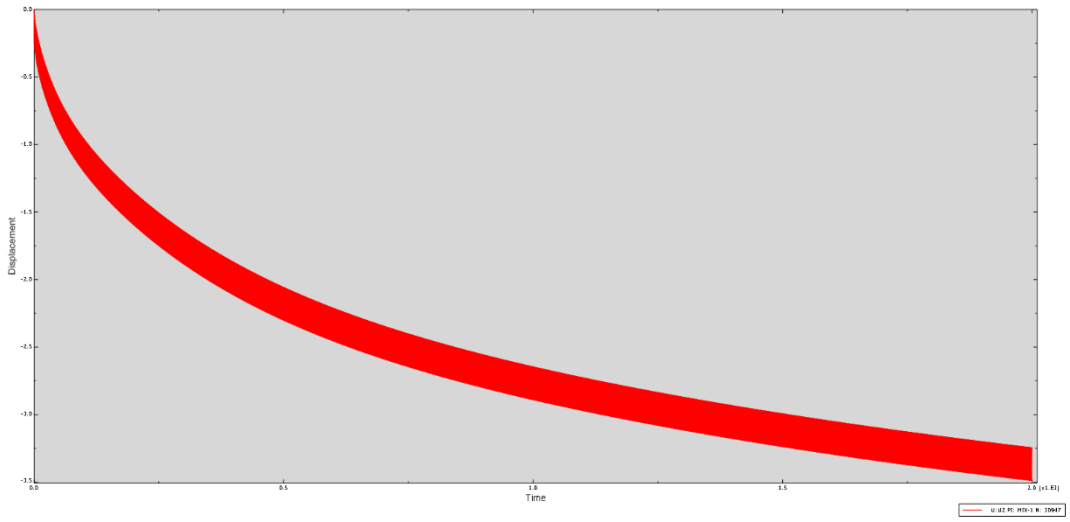

(b)

Figure İ.8. Repeated creep simulation results of the specimen ID LUCR11: a) Vertical deformations at the end of the test, b) Resulting vertical deformation graph

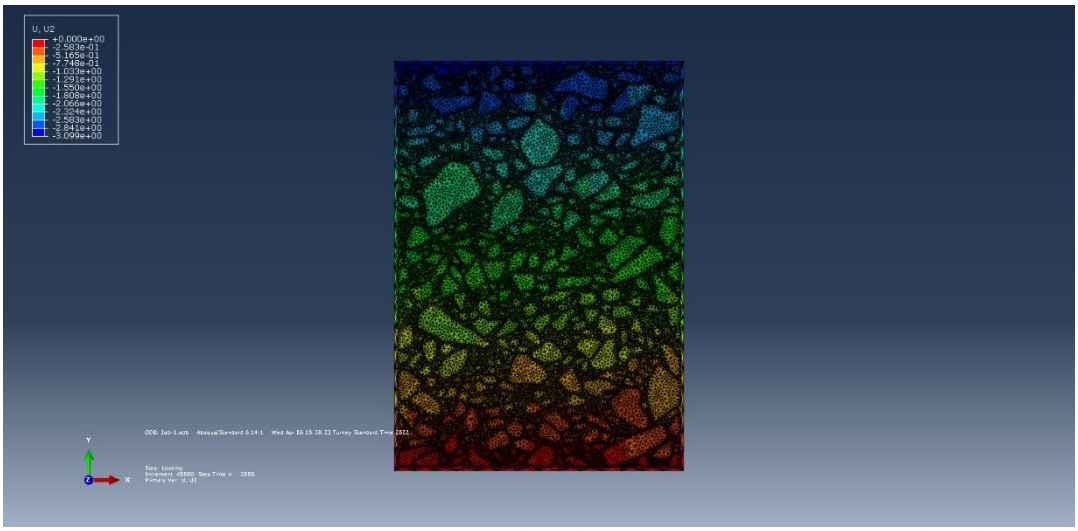

(a)

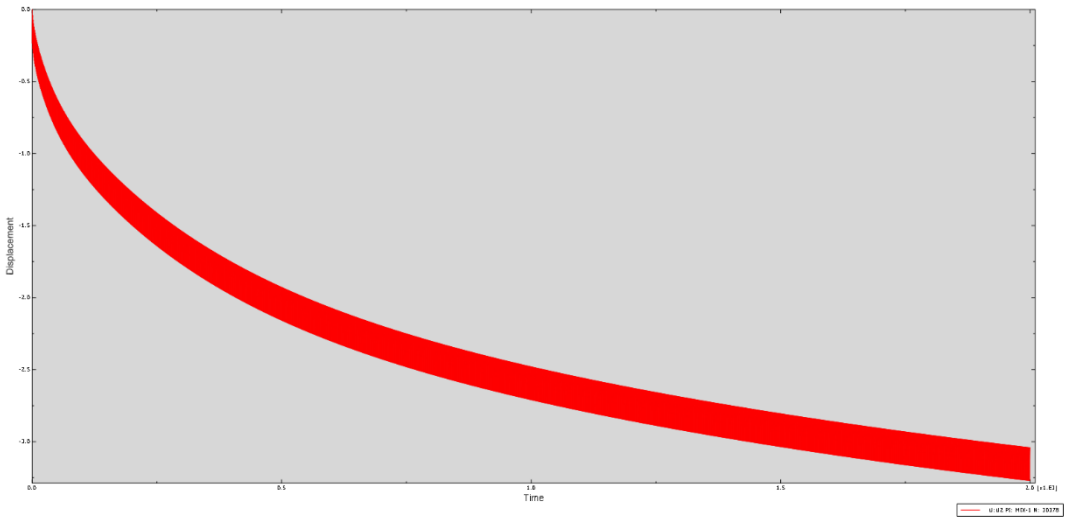

(b)

Figure İ.9. Repeated creep simulation results of the specimen ID LUCR12: a) Vertical deformations at the end of the test, b) Resulting vertical deformation graph

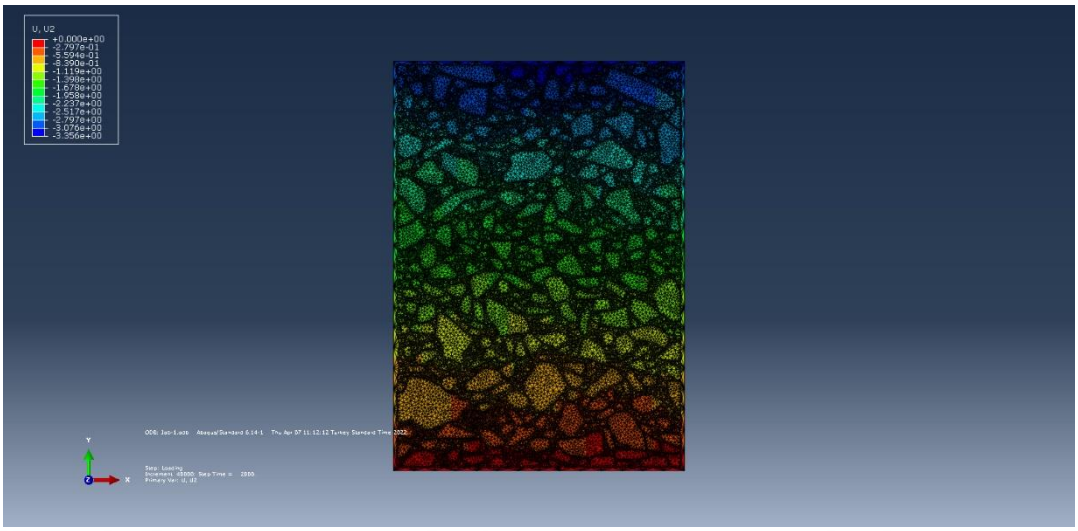

(a)

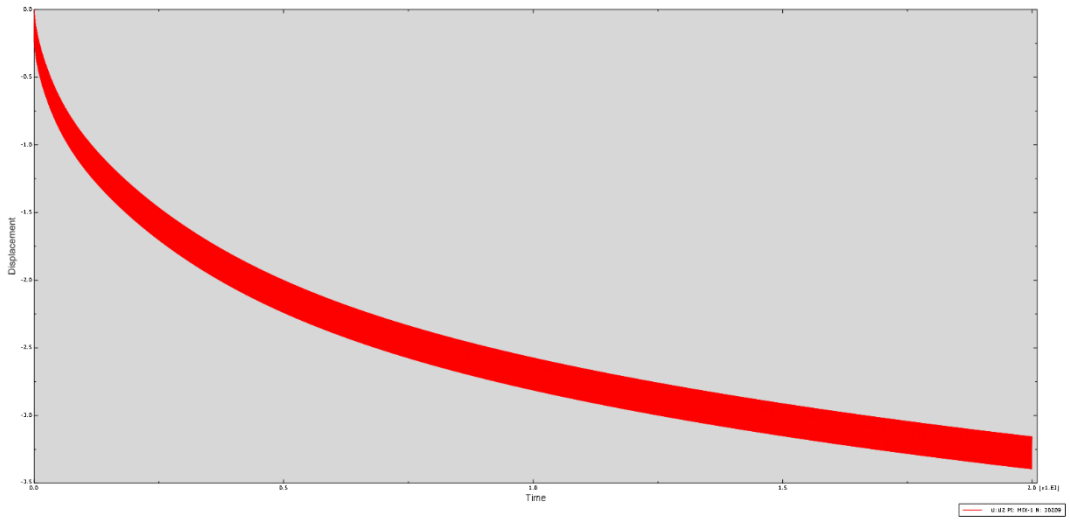

(b)

Figure İ.10. Repeated creep simulation results of the specimen ID LUCR13: a) Vertical deformations at the end of the test, b) Resulting vertical deformation graph

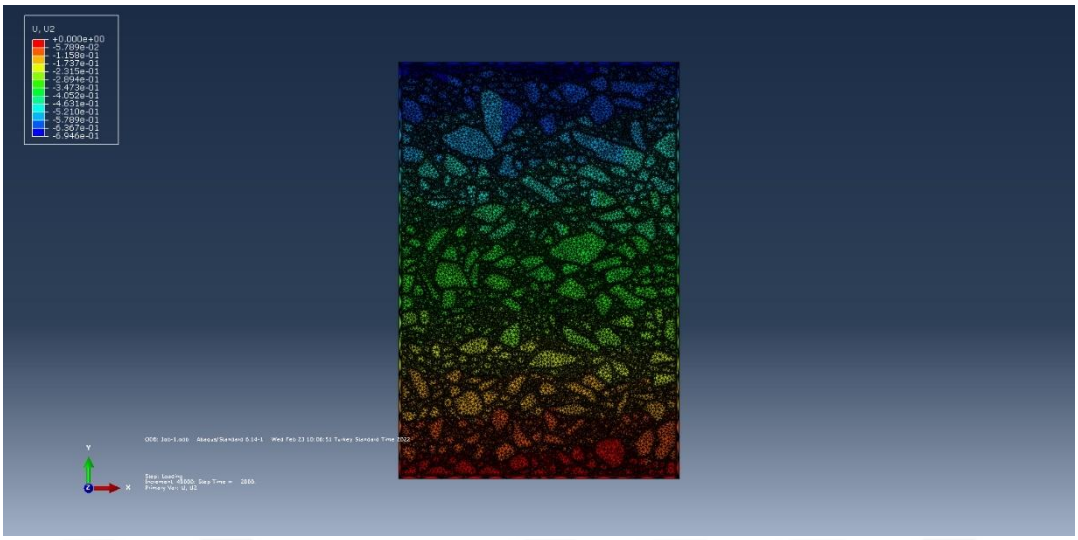

(a)

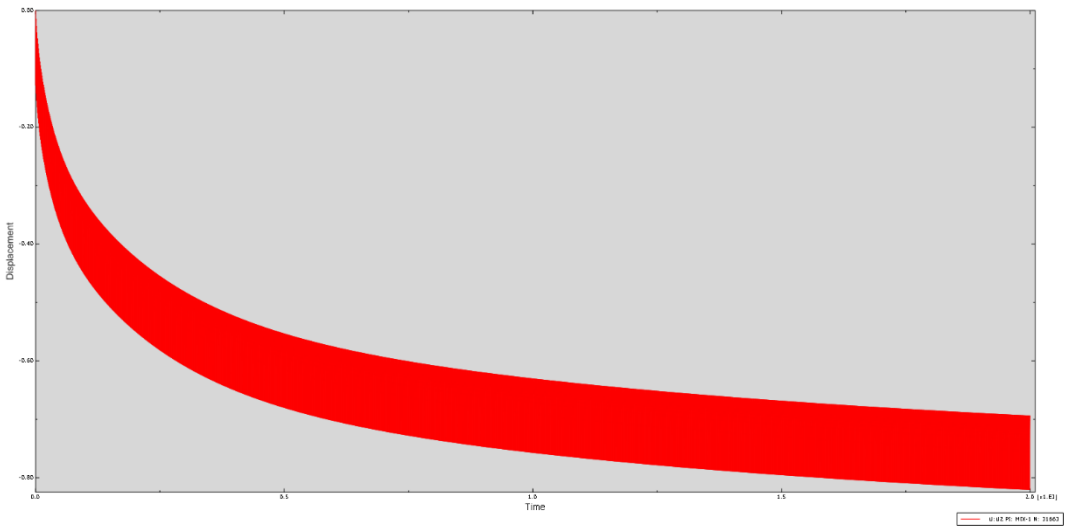

(b)

Figure İ.11. Repeated creep simulation results of the specimen ID BMCR01: a) Vertical deformations at the end of the test, b) Resulting vertical deformation graph

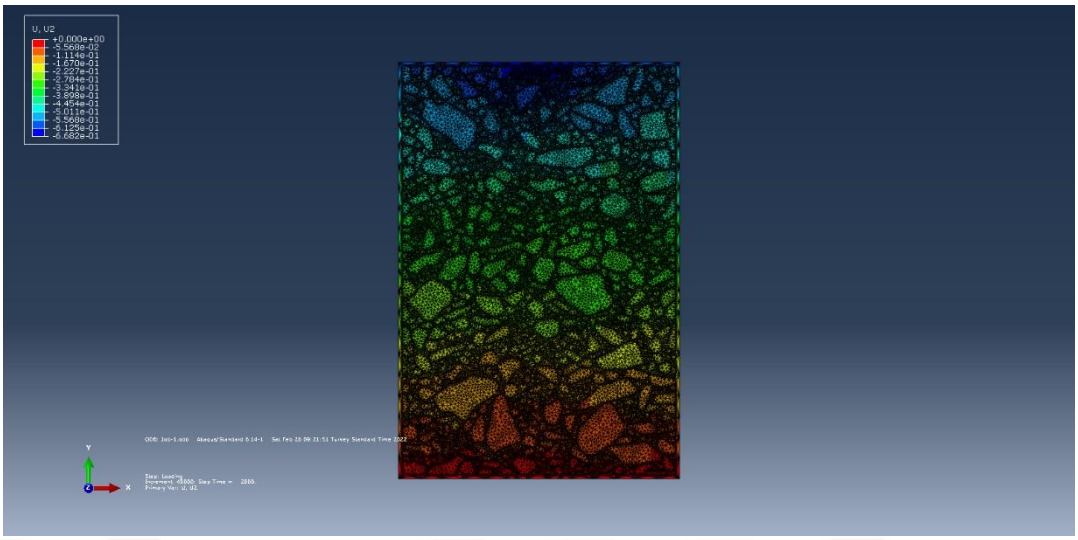

(a)

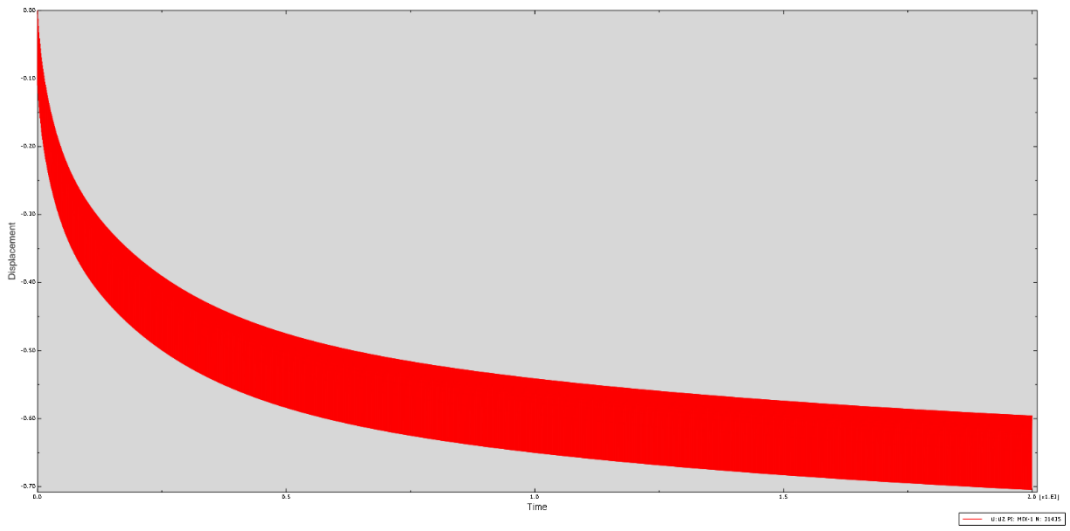

(b)

Figure İ.12. Repeated creep simulation results of the specimen ID BMCR02: a) Vertical deformations at the end of the test, b) Resulting vertical deformation graph

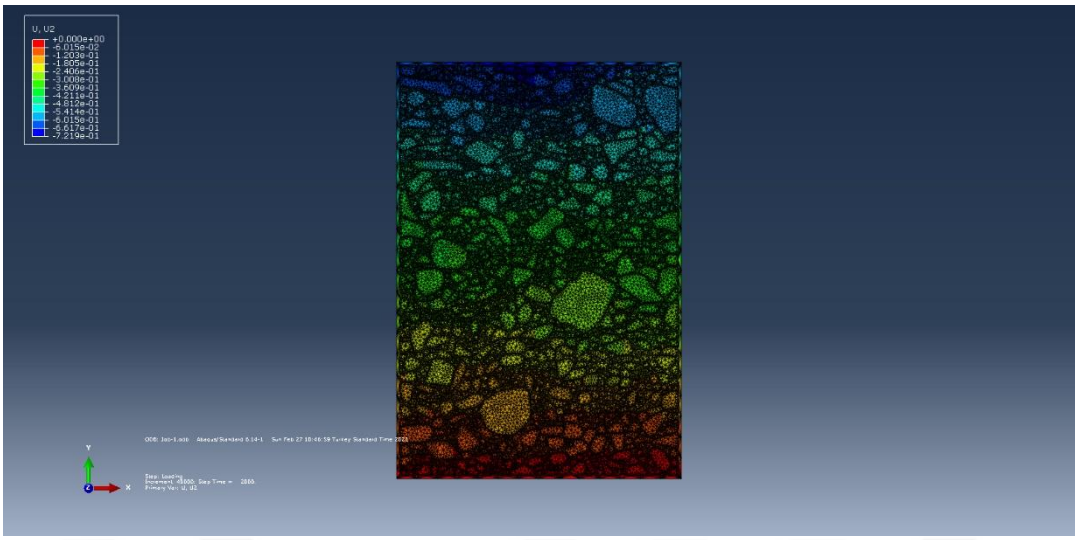

(a)

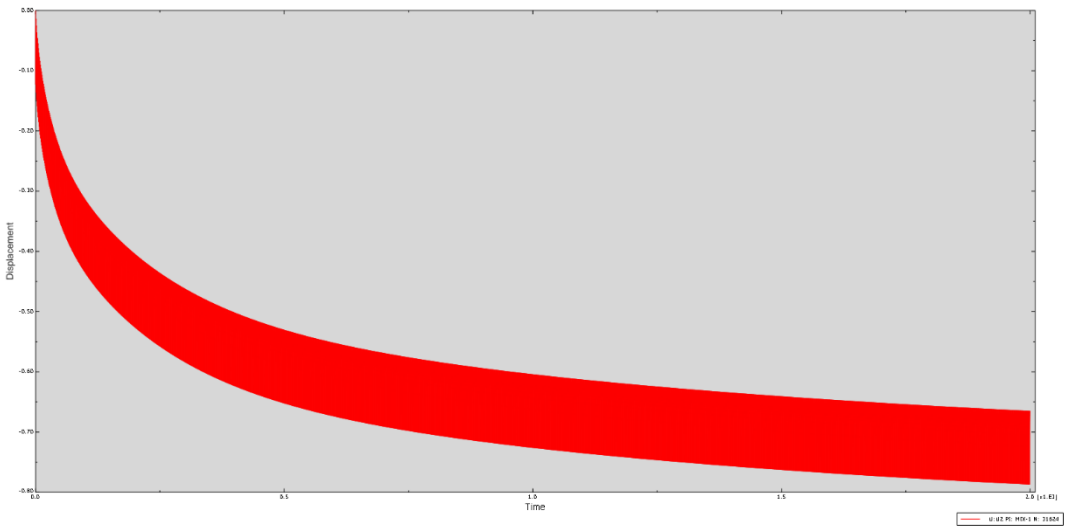

(b)

Figure İ.13. Repeated creep simulation results of the specimen ID BMCR03: a) Vertical deformations at the end of the test, b) Resulting vertical deformation graph

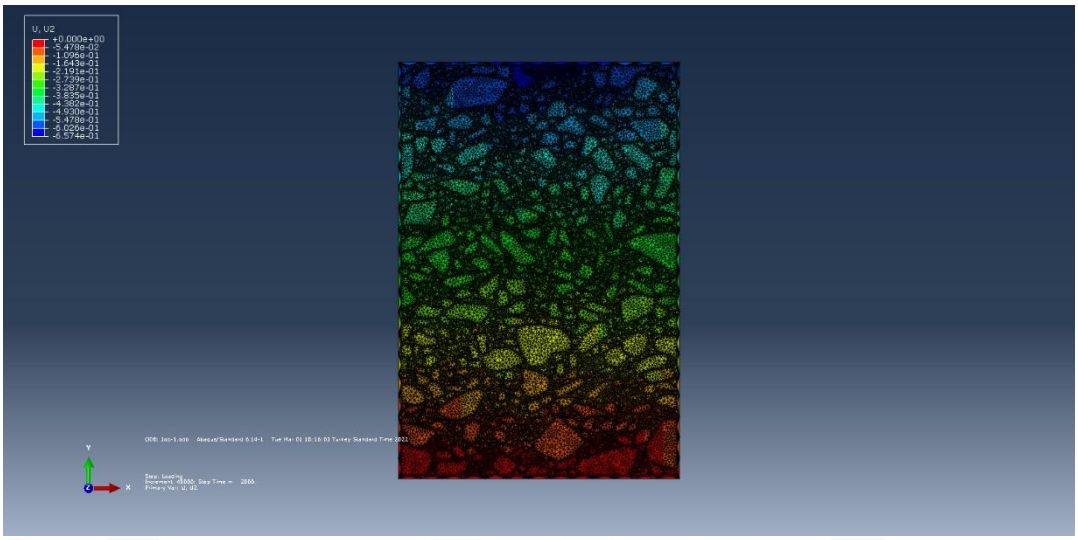

(a)

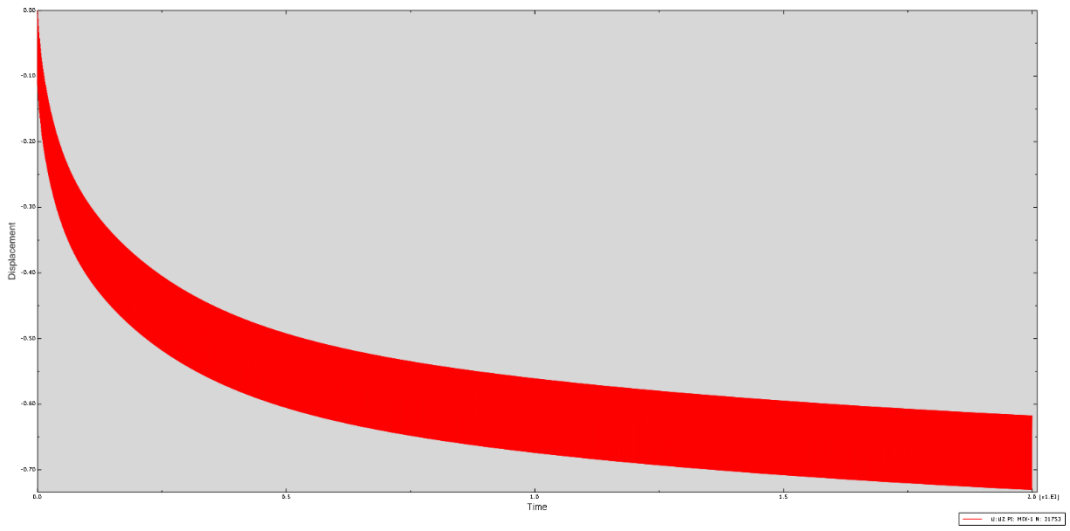

(b)

Figure İ.14. Repeated creep simulation results of the specimen ID BMCR04: a) Vertical deformations at the end of the test, b) Resulting vertical deformation graph

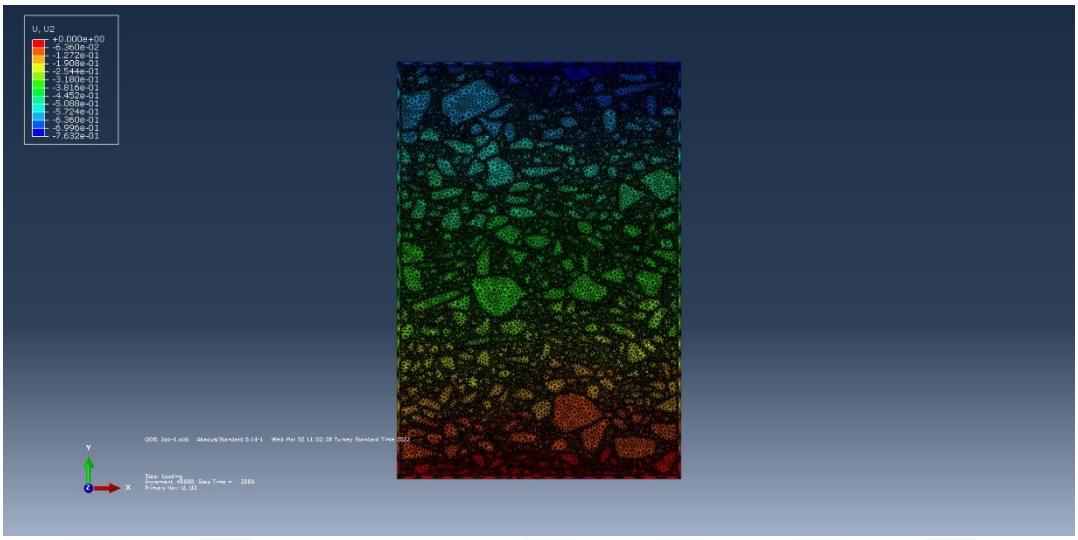

(a)

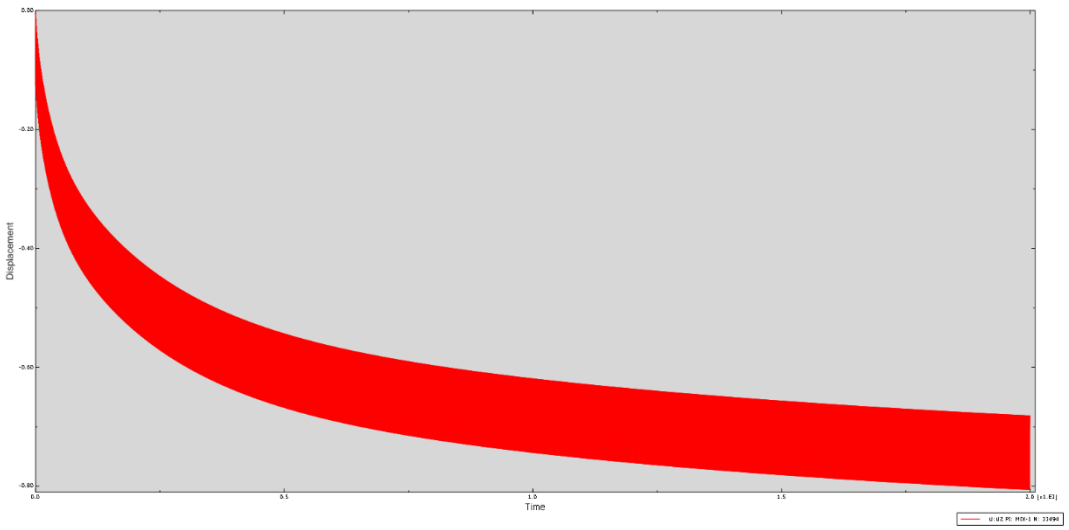

(b)

Figure İ.15. Repeated creep simulation results of the specimen ID BMCR05: a) Vertical deformations at the end of the test, b) Resulting vertical deformation graph

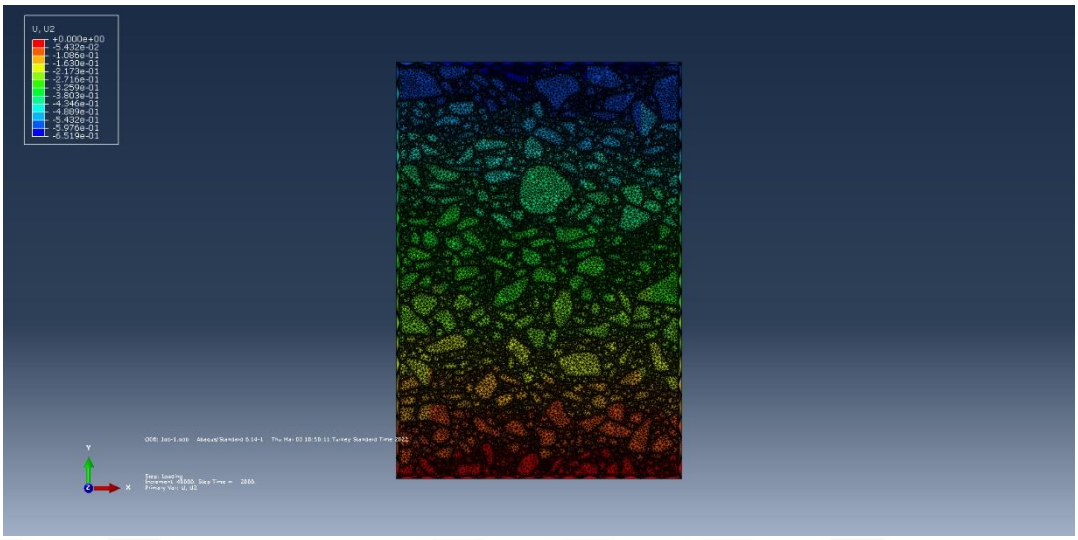

(a)

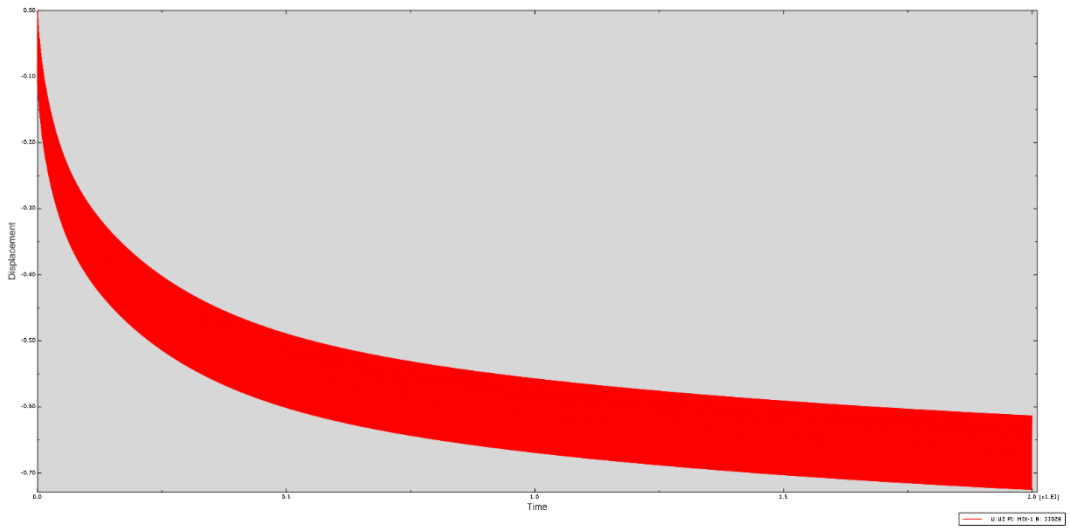

(b)

Figure İ.16. Repeated creep simulation results of the specimen ID BMCR06: a) Vertical deformations at the end of the test, b) Resulting vertical deformation graph

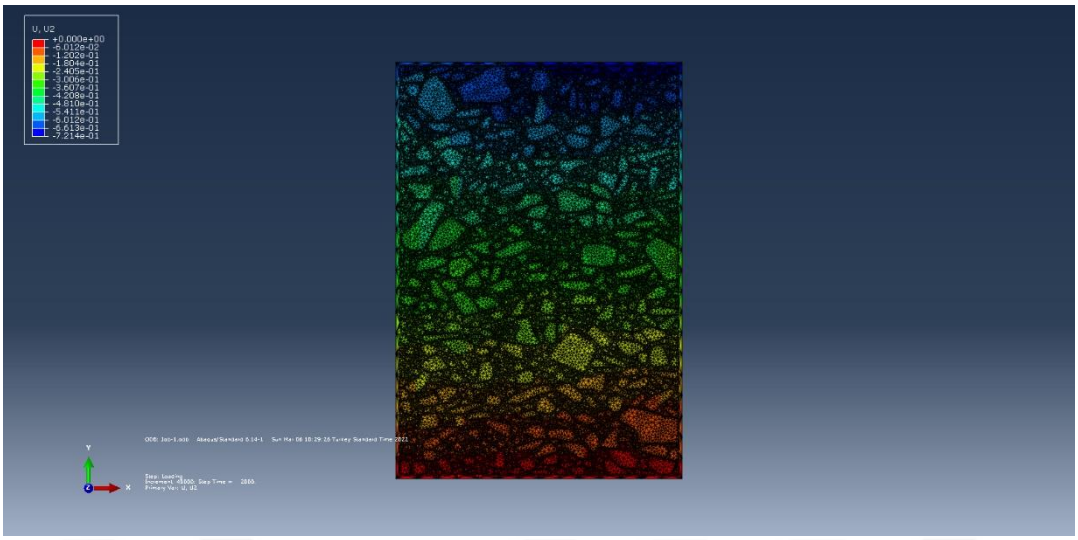

(a)

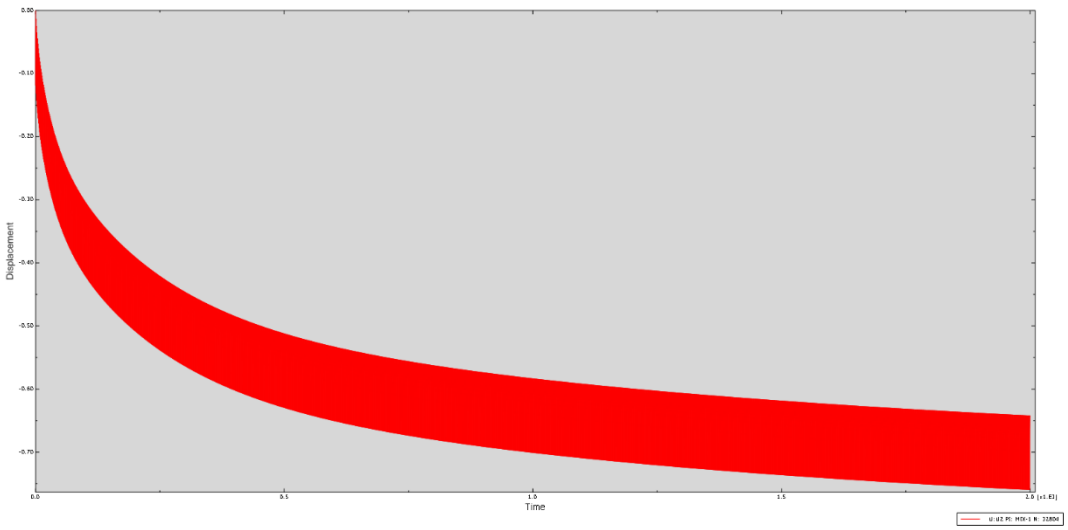

(b)

Figure İ.17. Repeated creep simulation results of the specimen ID BMCR07: a) Vertical deformations at the end of the test, b) Resulting vertical deformation graph

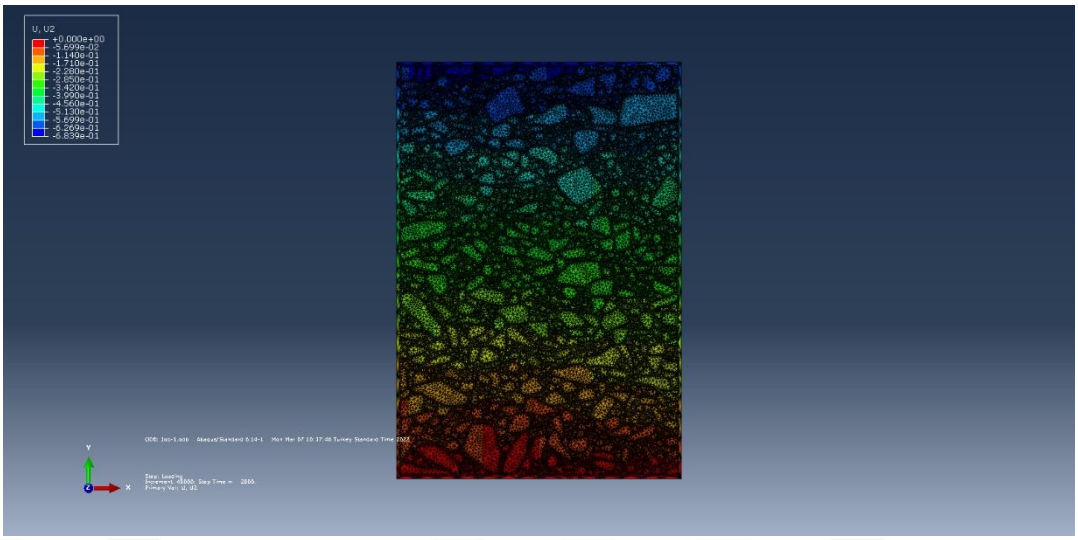

(a)

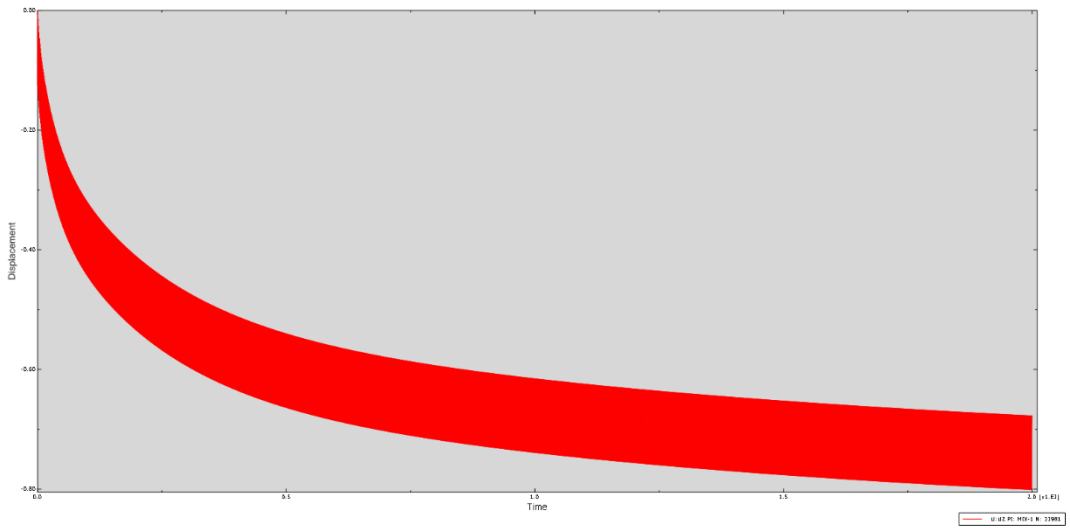

(b)

Figure İ.18. Repeated creep simulation results of the specimen ID BMCR08: a) Vertical deformations at the end of the test, b) Resulting vertical deformation graph

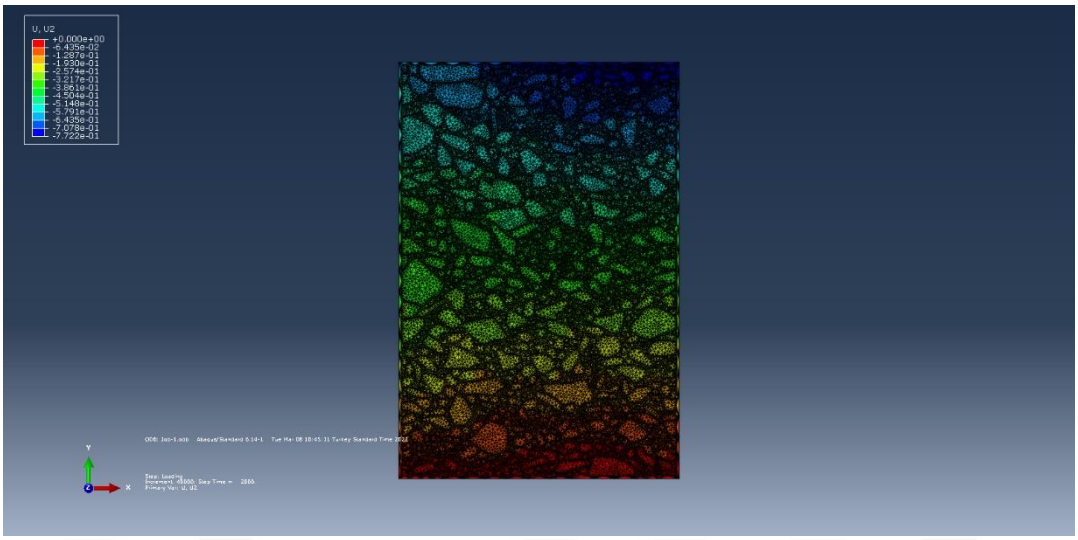

(a)

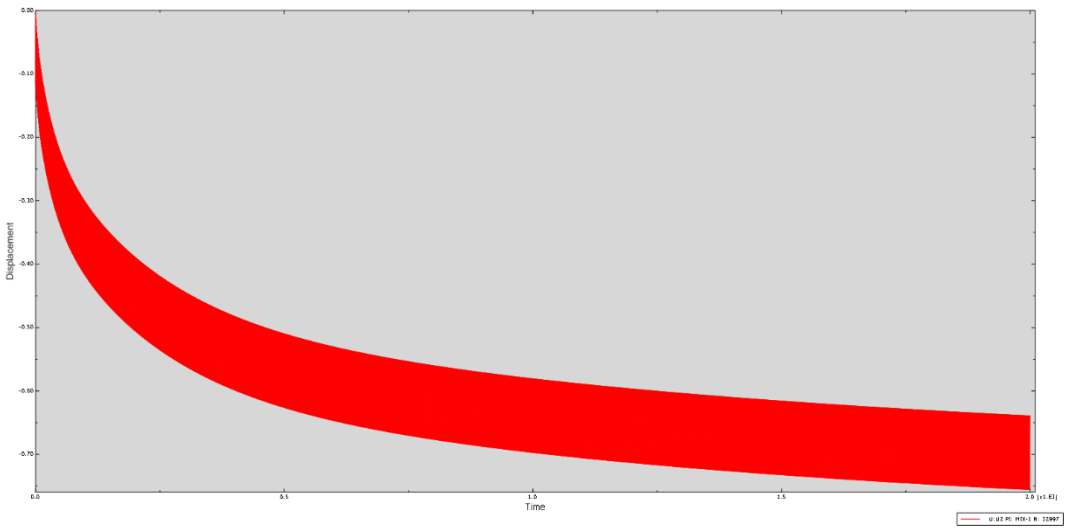

(b)

Figure İ.19. Repeated creep simulation results of the specimen ID BMCR09: a) Vertical deformations at the end of the test, b) Resulting vertical deformation graph

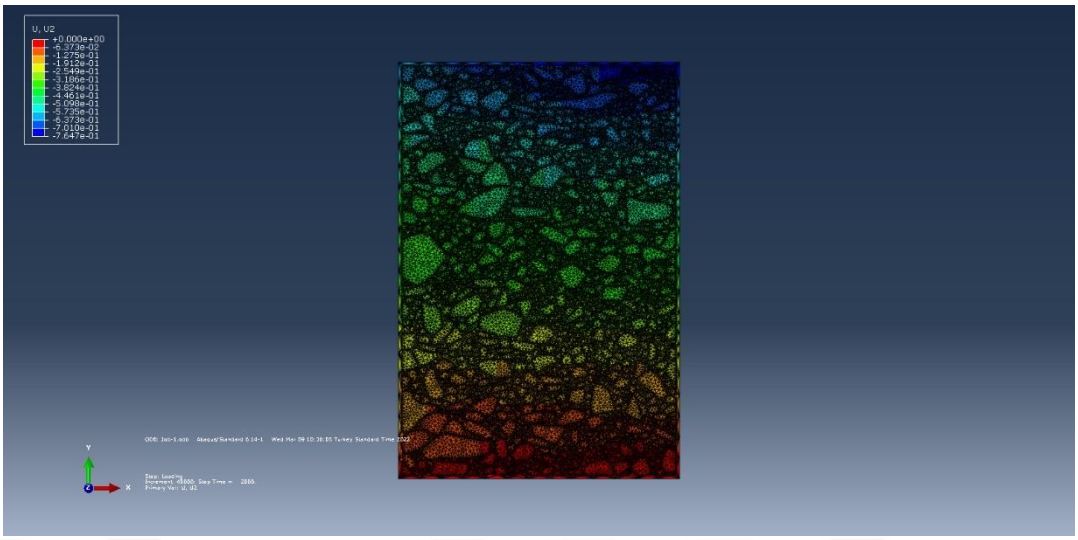

(a)

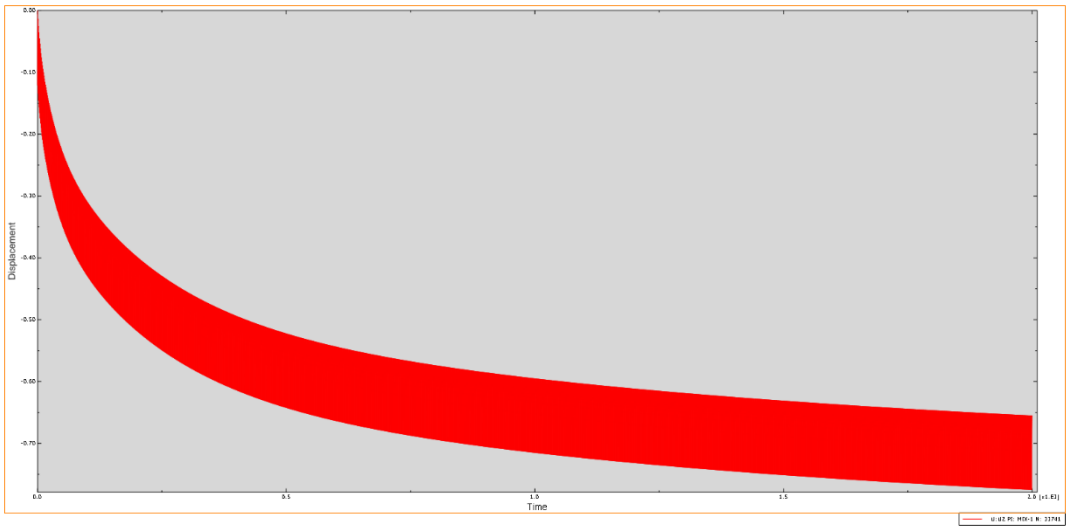

(b)

Figure İ.20. Repeated creep simulation results of the specimen ID BMCR10: a) Vertical deformations at the end of the test, b) Resulting vertical deformation graph

CURRICULUM VITAE

Surname, Name: Karakaya, Yalçın

EDUCATION

Degree	Institution	Year of Graduation
MS	METU Civil Engineering	2015
BS	KTU Civil Engineering	2011
High School	Milas High School, Mugla	2006

FOREIGN LANGUAGES

Advanced English

PUBLICATIONS

1. Arabzadeh, A., Karakaya, Y., & Güler, M. (2014). Thermal Fatigue Behavior of Asphalt Concrete Under Constant Amplitude Strain Loading, *Transportation Research Board*.

2. Karakaya, Y. & Güler, M. (2017). Asfalt Betonun Düşük Sıcaklık Performansının Doğrudan Çekme Deneyleri ile Belirlenmesi, *7. Ulusal Asfalt Sempozyumu ve Sergisi*, November 29-30, Ankara, Turkey.

3. Karakaya, Y. & Güler, M. (2018). Investigating Material Thoughness of Asphalt Concrete Under Direct Tension Loading, *13th International Congress on Advances in Civil Engineering*, October 12-14, Çeşme-İzmir, Turkey.

4. Karakaya, Y., Bingol, B. V., & Güler, M. (2019). Evaluation of Laboratory Performance of Zycotherm Additive for Extended Moisture Resistance of HMA Pavements, *International Civil Engineering & Architecture Conference (ICEARC 2019)*, April 17-20, Trabzon, Turkey.

5. Karakaya, Y., Yucel, A. O., & Güler, M. (2021), Evaluation of Performance Properties of Asphalt Mixtures Using Nano-Organosilane Additive, *7th Eurasphalt & Eurobitume Congress*, June 15-17.